Mathematical Modelling of an Aluminium Spray Process

Ian Alistair Frigaard, B.Sc., M.Sc.,

St. Hugh's College, Oxford.[1]

Hilary Term, 1993

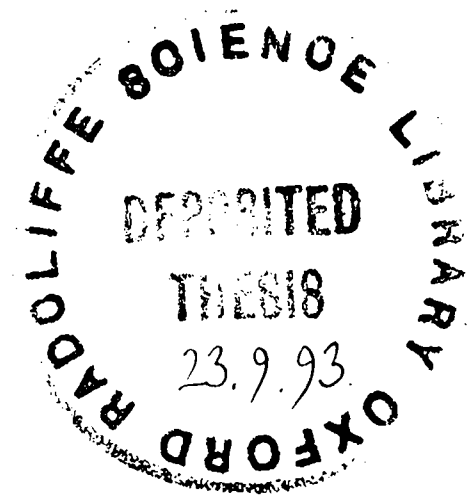

[1]This thesis is submitted in partial fulfilment of the requirements for the degree of Doctor of Philosophy. It was completed under the joint supervision of Dr P.W. Alexander, Alcan International Laboratories, Banbury, and of Dr O.L.R. Jacobs, Department of Engineering Science, University of Oxford.

Abstract

Spray-forming is a newly developed industrial metal forming process in which a cylindrical metal billet is produced by the incremental deposition and solidification of an atomised metal spray on a moving substrate. A mathematical model is developed to describe billet growth and heat flow within spray-formed aluminium alloy billets.

In the first part of the thesis, growth dynamics of the billet are considered. Conservation of mass at the billet surface yields a single first order quasi-linear partial differential equation for the movement of the billet surface; the nonlinearity arising from the possibility of surface shadowing.

The existence of two distinctly different timescales, amongst the process motions governing billet growth, prompts the use of an averaging method. The resulting averaged equations permit analysis and are shown to provide a valid asymptotic approximation to the billet surface motion on the timescale $1/\epsilon$, for a suitably defined class of billet surfaces. The parameter $\epsilon \ll 1$ is the ratio of the two process timescales.

Conditions under which the crown profile of the cylindrical billet becomes steady are analysed, through the averaged equations, and the stability of such profiles is examined. Computed examples of single and multiple steady state crown profiles are given. The averaged equations are also solved numerically to provide a model for transient billet growth on a "slow" timescale; results are presented.

The second part of the thesis considers heat flow within the growing billet. Phase change is incorporated using an enthalpy formulation of the energy equation. The resulting equation is a nonlinear heat equation that must be solved in an expanding domain, the boundary of which is determined by solution of the billet growth model equations.

Conduction on the billet length-scale takes place only on the slow timescale, with more rapid heat flow taking place only close to the billet surface. Accordingly, billet heat flow is analysed through the assumption that there is a thermal boundary layer close to the billet surface, which is driven by the "rapid" timescale spray deposition, with heat flow in the remainder of the billet driven by the time-averaged growth.

The boundary layer equation is a one dimensional nonlinear advection-diffusion equation, with a nonlinear boundary condition that incorporates the intermittent deposition from the spray in the form of an irregular pulse. This equation is solved numerically using an implicit finite difference method.

The slow-time heat flow is two dimensional, (assuming axisymmetric slow-time billet growth), and must also be solved numerically. For this an implicit predictor-corrector method is used. The predictor stage uses a "splitting" method, adapted from the fully implicit L.O.D. method to take account of the expanding domain. The method appears to be stable and consistent. Various numerical results are presented.

The model provides significant new understanding of the dynamics of billet growth and succeeds in providing a useful framework within which the transient heat flow that occurs during spray deposition, on a number of different timescales and length-scales, can be understood. Comparison of computed model predictions with real sprayed billets confirms the validity of the model.

The thesis is concluded with a summary of results and a look at possible future directions for research in this area.

Acknowledgements

I would like to thank the following for their assistance during the course of this research.

Dr Oliver Jacobs and Dr Peter Alexander for their guidance and support throughout, for keeping an open door, for helpful advice on presentation and for shared physical insight.

Alcan International Limited of Montreal, Canada, for paying my University and College fees, and for financial (and other) support towards the costs of preparing this thesis.

St. Hugh's College, Oxford, for financial support through the award of a graduate scholarship in 1991 and 1992.

My colleagues on the Teaching Company Scheme: Dr Brian Cantor, James Heath, Dr Duncan Hickman, Dr Ken Mingard and Dr James Myerscough. They have provided an interesting and enjoyable environment to work within, have given good criticism, much advice and practical help, (and have all shown great patience with my non-dimensional results).

Dr Steve Rogers, Dr Patrick Grant and Simon Langridge for data supplied, discussions and advice.

All in Cospray for their general friendliness and helpfulness, and for spraying aluminium billets which closely approximate the model.

Maureen Marshall in the Alcan library, for her efficiency in dealing with my (seemingly unending) lists of obscure reference requests.

Additionally, I would like to thank those whom I have shared my office in Oxford with, and my friends in Oxford and elsewhere, for their company, friendship, and the general preservation of my sanity. In particular, I would like to thank Sean for 426 lunchtime chess games, and for reading and commenting on large chunks of thesis, as well.

Finally, I thank my close family and my wife, Judy, for their love, encouragement, patience and understanding.

Contents

Chapter 1

Introduction

This thesis is concerned with the mathematical modelling of an industrial manufacturing process known as **spray-forming**. The process is relatively new (C. 1970's), and continues to develop with the technology employed. A variety of metals and composites are formed by this process, and a range of geometries are produced. The process is also referred to variously as **spray-casting**, **spray-deposition**, the **Osprey** process and **Liquid Dynamic Compaction**.

This chapter commences with a brief description of what spray-forming is, how it has developed and what the advantages are of this processing route over other more conventional processing routes. This is followed by a review of current mathematical understanding of the process as a whole, and of the various sub-processes involved. The chapter concludes by outlining the objectives of the research, the layout of the thesis, and the chief contributions that the thesis makes to knowledge in this field.

1.1 The spray-forming process

In the spray-forming process a stream of molten metal is gas atomised and the spray is directed towards a moving, shaped collector. Solidification takes place both in-flight and following deposition on the collector, where the spray droplets impact and coalesce into a near fully dense deposit. Deposit shape is mainly determined by the collector shape and by the relative motion of the atomiser and collector. Commonly produced shapes are metal strip, tubes and cylindrical billets or discs, see Fig. 1.1. This thesis only considers mathematical modelling of the spray-formation of cylindrical aluminium alloy billets.[1] Alloys of other metals that are produced by this method include copper, [143], nickel, [17, 31, 97, 98, 100], and magnesium, [71]. Special steels and metal matrix composites are also spray-formed, [6, 8, 131, 133, 145].

1.1.1 Process description

In producing aluminium alloys by this method inert atomising gases such as nitrogen or argon are used, due to the danger of exposing hot aluminium powder to oxygen. Thus, the basic apparatus depicted in Fig. 1.1 is enclosed within a sealed spraying chamber. A schematic of a billet spray-forming plant is shown in Fig.

[1] Both billets and discs are cylindrical. Billets are distinguished from discs by having larger length to diameter ratios.

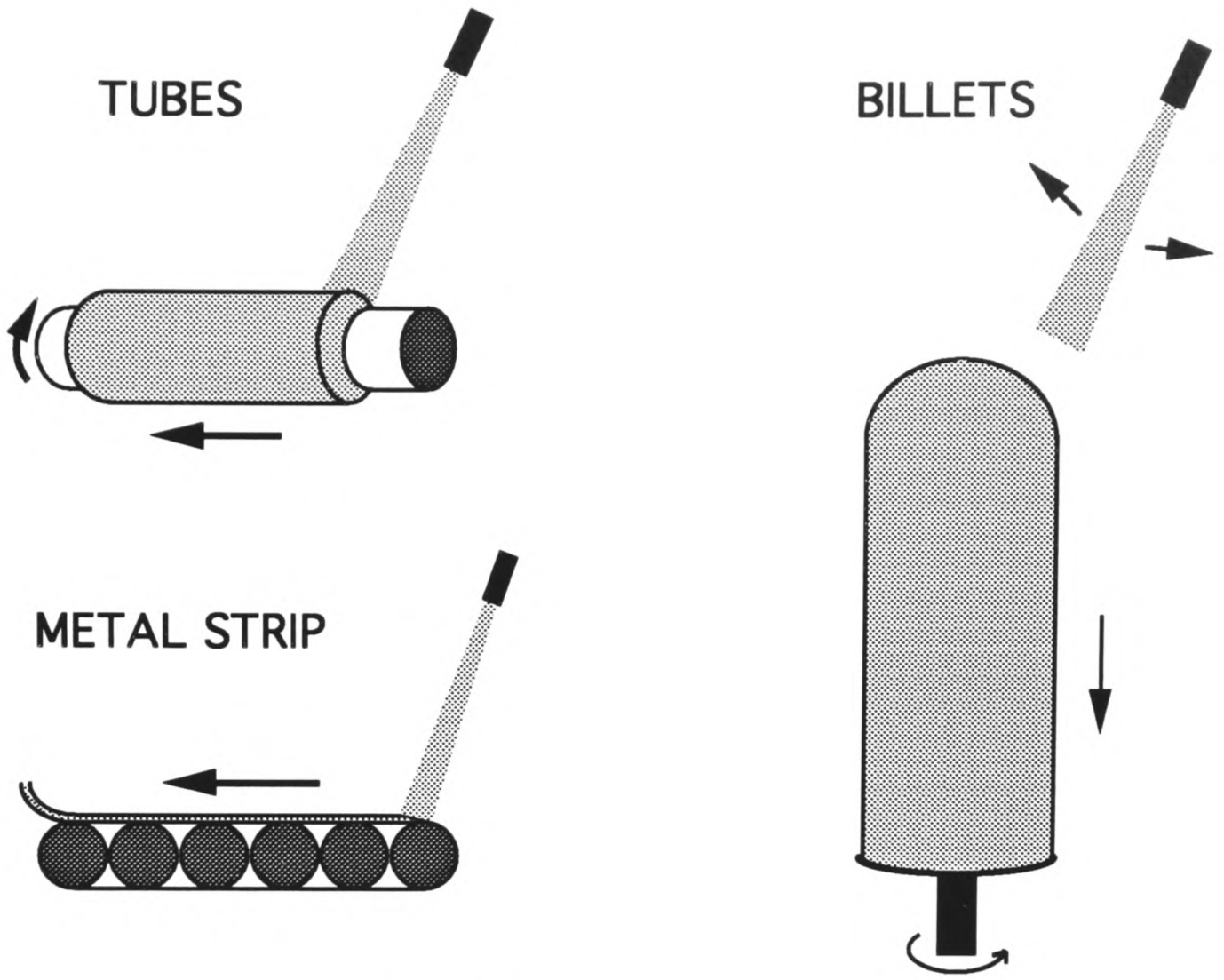

Figure 1.1: Different spray-formed geometries

1.2.

- Molten metal is heated in a pressurised crucible to a temperature which is between 10°C and 200°C above the alloy liquidus temperature. Metal flows from the crucible to the atomiser assembly, driven by gravity and gas overpressure.

- Atomisation is by means of a close coupled, twin fluid, spray ring atomiser. The liquid metal exits a central nozzle in a column and is immediately accelerated by a *primary* gas stream flowing nearly parallel to the metal. The metal stream is then atomised by *secondary* spray ring gas jets impacting the metal column at an angle. Both primary and secondary gas flows are subsonic.

- The atomised spray forms a tight diverging cone of spray droplets, with mass mean diameter typically lying in the range $50 - 150$ μm. The cone axis oscilates in a controlled manner, determined by a scanning movement of the spray ring gas jets. Scanning frequencies are in the range $10 - 25$ Hz. The spray cone axis points at an angle to the vertical, towards the circular collector top surface. Flight times taken for droplets to travel from the atomiser to the collector/deposit top surface are in the range 10^{-3} and 10^{-2} seconds.

- The collector rotates rapidly about a vertical axis and is withdrawn vertically downwards as the billet grows upwards. Rotation rates are in the range 100 to 1000rpm, and withdrawal speeds are $\sim 10^{-3}$m/s. The collector withdrawal ensures that an approximately constant *flight* distance, in the range $.3 - .7$m, is maintained between the atomiser and deposit top surface.

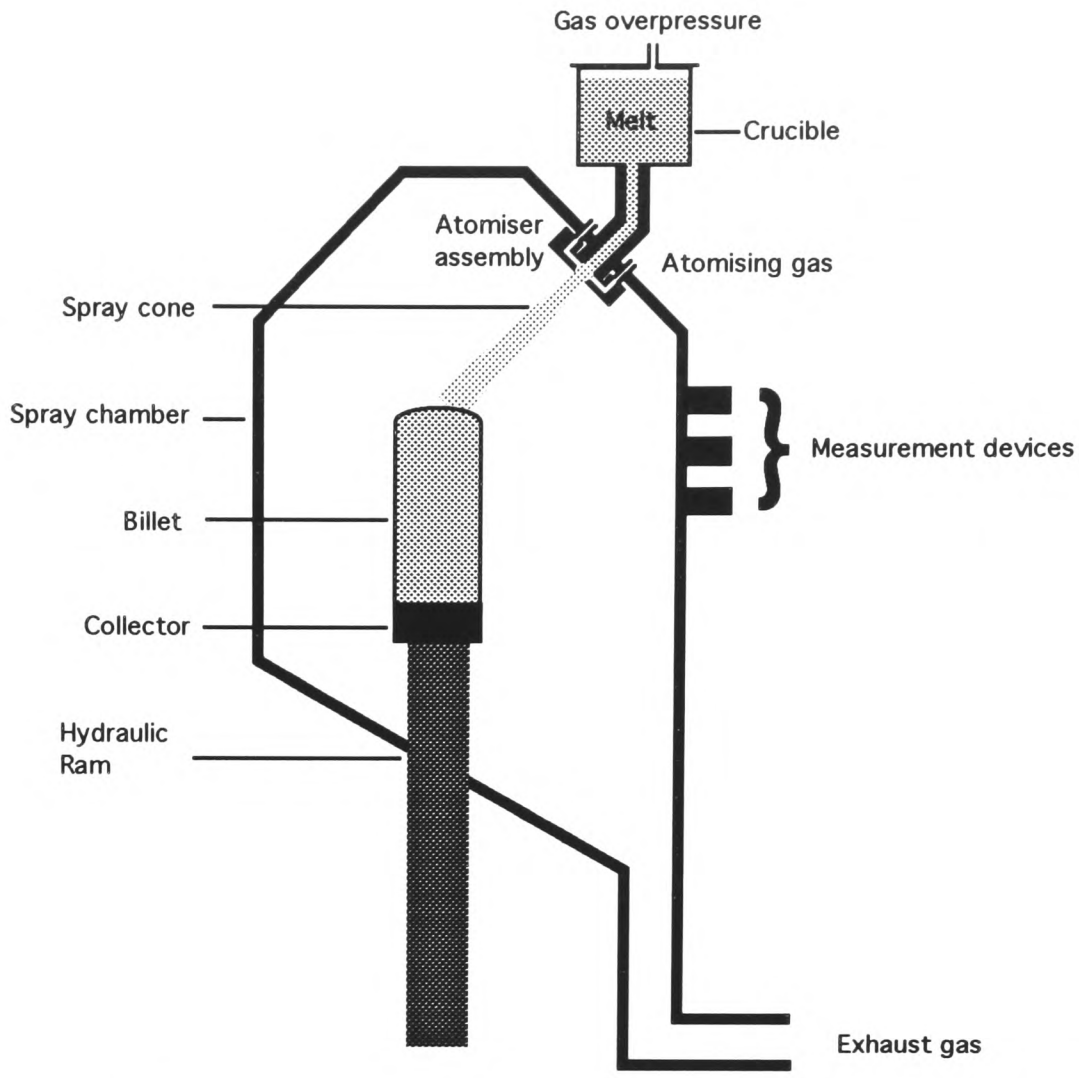

Figure 1.2: Apparatus for spray-forming billets

- Spray-formed aluminium-based billets of up to .3m diameter and over 1m length are produced, typically taking 20 – 30 minutes to spray.

Within the spraying chamber, spray droplets that are not deposited on the collector/billet tend to recirculate in the gas flow before exiting the spray chamber. Dense recirculating sprays can obscure the billet. This feature, coupled with the characteristically rapid movement of the collector/billet relative to the spray, makes measurement of the billet size, shape and surface temperature extremely difficult. The hostile environment within the chamber can also cause problems in attempting to measure characteristics of the metal spray.

The difficulty of measurement, (and consequently experimentation), combines with the process complexity, and a real need for effective regulation of microstructural variation in the end product, to generate a demand for physically based mathematical modelling of the process. Through such models it is hoped to gain insight into the causes of process variation, and hence to derive effective methods for control.

1.1.2 Historical perspective

According to Leatham *et al.* [80], the process of projecting hot, metallic particles onto a previously prepared base material to form a coating was invented by Dr M.U. Schoop in Switzerland in 1910 in the form of a variety of *metallising* guns. These devices were fairly impractical, (and dangerous), and were only ever seriously considered as a means of applying thin coatings.

Use of metal spraying for the production of nearly finished products of the type now produced via spray-

forming was first proposed by J.B. Brennan in the 1940's and 1950's, eventually resulting in the issue of a number of U.S. patents, e.g. [15, 16]. Brennan was concerned primarily with the production of spray-deposited metal strip. From [15], it is quite clear that Brennan saw the potential advantages of the production method in reducing porosity, oxidation, strip non-uniformity and post-processing costs. Since patent [16] was eventually granted to Brennan's executrix, it must be assumed that Brennan died before he was able to realise the commercial advantages of his ideas.

Laboratory scale production and the first strong suggestions that this might be a commercially viable process for manufacturing semi-finished products waited until the late 1960's, when much work was done by Professor A.R.E. Singer at the University of Wales, College of Swansea, [124, 125, 126, 127, 128]. It is not clear whether Singer was aware of Brennan's previous ideas. Singer proposed the production of both strip and tube geometries, and was able to report experimental work showing reductions in oxidation levels, segregation and potentially in post-processing costs, as well as improvements in various mechanical properties of the sprayed material.

In 1974 Osprey Metals Ltd. of Neath, South Wales, was formed as an offshoot of the group at Swansea, to develop and commercially exploit the process. Whist many of the early strip and tube prototype processes relied upon the collector to remove much of the latent heat of freezing, Osprey concentrated on developing means whereby the atomising gas extracted most of the latent heat, both in flight and after deposition. The main result of removing the dependence on the collector mass for cooling was to allow deposits of arbitrary thickness to be sprayed, [18, 19]. This has led naturally to billet production.

Many developments followed at Osprey, both in terms of the geometries that were able to be produced and in terms of the range of alloys that were able to be successfully sprayed. From 1980 until the present date Osprey have adopted a policy of licensing the existing process technology to interested companies and research organisations. This has resulted in a significant scale up in the amount of process research and development activity taking place, and in continuing diversification of the technology. Today about 30 large companies, Government and University departments worldwide are actively researching in this area, [80].

Comprehensive reviews of current process development and potential future directions for spray-forming are given in [73, 80, 130].

1.1.3 Comparative advantages

Today, high performance requirements of the leisure, aerospace, defence and automotive industries, (amongst others), generate an ongoing demand for improvements in the mechanical properties of metal alloys. The growing realisation that alloy microstructures can depend critically on the processing conditions, as well as on the alloying elements, has led to an increased interest in alternative metals manufacturing routes.

Spray-forming has evolved as one of these alternative routes, and has been able to produce improvements in mechanical properties for many of the materials sprayed, (i.e. over those mechanical properties exhibited by similar materials produced by more conventional methods), see e.g. [65, 72, 93, 145]. In order to understand the origin of these improvements it is helpful to view spray-forming in the context of other metal forming processes, and to consider some of the more generic processing problems that are experienced.

Many engineering alloys solidify over a range of temperatures and liquid concentrations. Consequently, the elements that make up a nominal alloy composition are able to segregate during solidification. Two types of segregation are commonly found.

1. **Macrosegregation** This occurs on length-scales of order $.01 - 1$ m and is related to global heat and fluid flow phenomena occurring during solidification.

2. **Microsegregation** This occurs on length-scales of order $1 - 1000$ μm, and is related to dendrite formation during solidification. The regions between dendrite arms are often found to be rich in those alloy elements which are retained in the solute. The dendrite arm spacing then corresponds to the length-scales over which gradients in alloy element concentration are found.

Conventional casting of alloys begins with a fully liquid alloy ingot and typically involves cooling rates in the range $0.1 - 1°C/s$. At these cooling rates there is plenty of time for fluid movement and solute redistribution to occur in a solidifying ingot. Thus, in castings both macrosegregation and microsegregation are commonplace.

Over a wide range of cooling rates dendrite arm spacing is found to vary inversely with the average cooling rate. At the low cooling rates that are found in conventional casting, large scale microsegregation can have detrimental effects on the mechanical properties of cast ingots. Other common casting problems include shrinkage defects, porosity formation and the development of coarse grain structures. Broadly speaking, these defects result from the relatively long time allowed for solidification and from the bulk of material present during solidification. The importance of these defects will depend on the material and intended application, but will often result in the need for some form of post-processing to achieve desired mechanical properties.

Both microsegregation and macrosegregation problems can be reduced by allowing less time for solidification. Macrosegregation in particular is eliminated by consolidating large numbers of metal particles, which are essentially microstructurally identical, into a bulk product. This approach is followed in powder metallurgy processes.

Powder metallurgy uses atomisation to produce metal spray droplets, typically with diameters much less than 1000μm. The scale of microsegregation is thus immediately limited by the droplet size. Further reduction in microsegregation arises from the high cooling rates experienced by the droplets, (typically in excess of 10^4 °C/s), due primarily to the increase in surface area to volume ratio.

After atomisation, liquid metal droplets are undercooled considerably below their liquidus temperature by strong convective cooling from the atomising gases. The likelihood of nucleation occurring and speed of subsequent solidification during recalescence increases with the degree of undercooling. At high cooling rates solidification does not take place in conditions of thermodynamic equilibrium at the solid/liquid interface. Such departures from equilibrium are believed to increase the stability of the solid/liquid interface. This reduces the wavelengths of perturbations to the interface that are required for dendrite formation, and hence the scale of microsegregation, [26].

Although powder metallurgy is able to produce low segregation, fine scale microstructures in the metal particulate, the following problems are characteristic of this processing route.

1. The need to use inert gases during atomisation, and consequent additional expense.

2. Particulate handling problems, (aluminium in particular);

   (a) formation of thin oxide films or precipitates,

   (b) explosive dangers.

3. Post-processing is required to achieve a useful product shape. This is

   (a) expensive, and

   (b) usually involves some degradation of the droplet microstructural properties.

The spray-forming process is clearly closely related to powder metallurgy, since both involve atomisation technology. However, since in spray-forming the spray droplets are collected whilst semi-solid, and further solidification takes place in the billet bulk, the process is also related to other casting processes. Potential advantages which spray-forming enjoys over other processes stem principally from this central position. These advantages include the following.

1. Fine scale, low segregation microstructure, (see [70] for a full and detailed review of microstructure development during spray-forming).

   - High cooling rates of droplets in the atomising gas allows nucleation of solidification in most droplets prior to deposition, see e.g. [43, 45, 47, 74, 87].
   - Impacting droplets "splat" and spread rapidly to their splatted size, causing intense shear between top and bottom of the spreading droplets. This shearing is thought to increase the number of potential nucleation sites, (e.g. by breaking off dendrite tips), [78, 79, 130].
   - Additional grain refinement, due to some primary nucleation in localised regions and to dendrite remelting, with the above, results in a fine equiaxed grain morphology,[2] [5, 47, 48, 62, 65, 72].

2. Potential reductions in porosity and contamination related defects.

   - Densities of up to 98-99% commonly reported, e.g. [62, 93].
   - Oxide formation and other contamination is reduced through inert gas atomisation and automatic consolidation, e.g. [93].
   - Oxides and contaminants are distributed uniformly during deposition/splatting, [70].

3. Economies in production.

   - In comparison with cast materials, there is less need for special treatments in order to attain desired mechanical properties.
   - In comparison with a powder metallurgy route, there is no need for consolidation and other post-processing to achieve a near net shape.
   - Possible attainment of improved mechanical properties that are not obtainable by other routes.

[2] Metallurgists' description of small round balls.

4. Production of novel materials possible.

   - Metal matrix composites.
   - Nickel and magnesium alloys, special steels.

Although the potential advantages of spray-formation are considerable, these are countered by the substantial problems of understanding the process, and controlling it to maximise the potential benefit in terms of the quality of material produced. It is towards these goals that this thesis and the majority of mathematically based research in this field is directed.

1.2 Process modelling; literature review

The physical processes underlying spray-forming span many different scientific disciplines, and this is reflected in the literature sources. A range of complex and interrelated fluid dynamic, dynamical, heat flow and solidification problems arise in the process. Although parallels can be drawn between parts of the spray-forming process and other physical processes, often the emphasis in spray-forming is subtly different.

For example, powder metallurgy and other rapid solidification processes form one main source of literature, (thanks to the atomisation involved in spray-forming). However, in powder metallurgy the objectives of atomisation are often to maximise the droplet cooling rates and atomiser efficiency,[3] whilst keeping the droplet size distribution within a certain range, see [42]. Thus, typical ultrasonic gas atomised powders have diameters less than 50 μm and cool at rates exceeding 10^4 °C/s, [4, 93]. This contrasts sharply with spray-forming, where objectives of efficiency are superceded by those of delivering the right amount of semi-solid material to the right point on the deposit surface, at the right temperature. Thus in spray-forming, atomisation is generally subsonic, droplet size ranges are broader, with slightly larger droplet diameters, and cooling rates are lower.

A second potential source of literature comes from mathematical modelling studies of other processes involving deposition. For example, the formation of ice on overhead electricity cables has been considered by Poots *et al.*, [10, 68, 108, 134]. Such work often gives insight into how various parts of the process can be modelled, (i.e. the mass conservation equations for surface motion due to deposition from the ice laden wind are essentially the same as those developed in chapter two). However, because the mathematical problems are motivated differently, results are rarely directly applicable.[4]

A third source of literature has emerged more recently with a number of mathematical modelling studies being carried out that are specific to the various spray-formed geometries. The process itself splits down into a series of complex sub-processes, (e.g. atomisation, deposit solidification), each of which must be understood through experimentation or modelling in order to understand and control the process. This natural break down has allowed researchers to focus on one or two particular sub-processes and subsequently

[3] Atomiser efficiency is defined as the ratio of the theoretical minimum power input required to turn bulk liquid into droplets, and the actual power input to the atomiser. Typically, this is about 2%, with most of the energy being transferred into droplet kinetic energy, (≈95%), or spent in viscous dissipation, (≈3%), [149].

[4] In fact many mathematical studies involving deposition are "coating" applications, thus considered one dimensional, e.g. paint spraying. The work by Poots *et al.* is very similar geometrically to the tube spray-forming process. In billet spray-forming there are possibilities for surface shadowing which do not arise in the tube geometry.

integrate their understanding of these sub-processes with models and/or experimental results describing the other sub-processes. In this way a number of "complete" process models have been derived, see e.g. [6, 7, 38, 49, 50, 54, 74, 77, 87, 88, 89, 90].

The main danger in deriving such "complete" process models arises when these models are used as process simulations, i.e. so as to be compared directly with experimental results. Since outputs from one stage of the process model become inputs to subsequent stages, there is the potential for a build up in predictive error as successive model stages are joined together. Because many of the physical processes involved in the process are extremely complex, (e.g. atomisation, deposition, solidification), significant errors are likely to accumulate and the direct predictive validity of the complete process model is likely to be severely diminished. This is especially true when either the component models are relatively simplistic, or rely on a large number of process parameters which are hard to measure.

Instead, the benefits of process modelling are likely to arise from the improved understanding of each sub-process and of the interactions between sub-processes. Following Mathur et al., [89], the process is split down into five sub-processes; atomisation, spray transport and solidification, spray impact and consolidation, deposit growth and deposit solidification. These sub-processes and most of the interacting process variables and parameters between sub-processes are depicted in Fig. 1.3. In the following subsections, relevant mathematical modelling of each sub-process in turn is reviewed. Where mathematical approaches have failed the current approach to quantitative understanding is outlined. Any mathematical literature relevant to the analytic and numerical techniques employed in this thesis is reviewed at the point of application. For reviews of the literature relevant to spray-forming, which focus more on metallurgical issues and experimental results the reader is referred to any of [6, 43, 87].

There is very little of the spray-forming literature that is specific to billet growth and solidification, (only [89]). However, much of the literature that focuses on other geometries is relevant to the atomisation, droplet flight and deposition stages of the process. Also, for the billet growth and solidification stages of the process, although dimensionally more complicated, it is still instructive to review approaches taken to, and results gained from, modelling the simpler geometries.

1.2.1 Atomisation

Atomisation is by means of a close coupled, twin fluid, spray ring atomiser. The liquid metal exits a central nozzle in a column and is accelerated by a primary gas stream, flowing nearly parallel to the metal. The liquid metal stream is then disintegrated into droplets by powerful secondary spray ring gas jets, angled in towards the metal stream.

When operating effectively, the primary gas is believed to create waves on the surface of the liquid metal column, through a mixture of pressure effects and viscous shearing stresses. These act to strip off liquid blobs, sheets and ligaments from the main column, and these are subsequently broken down into near spherical droplets by the secondary gas jets, according to the complex interaction of viscous, inertial and surface tension forces.

During twin fluid[5] atomisation, gas and liquid densities, liquid viscosity, liquid surface tension, gas-liquid

[5] i.e. gas and liquid metal.

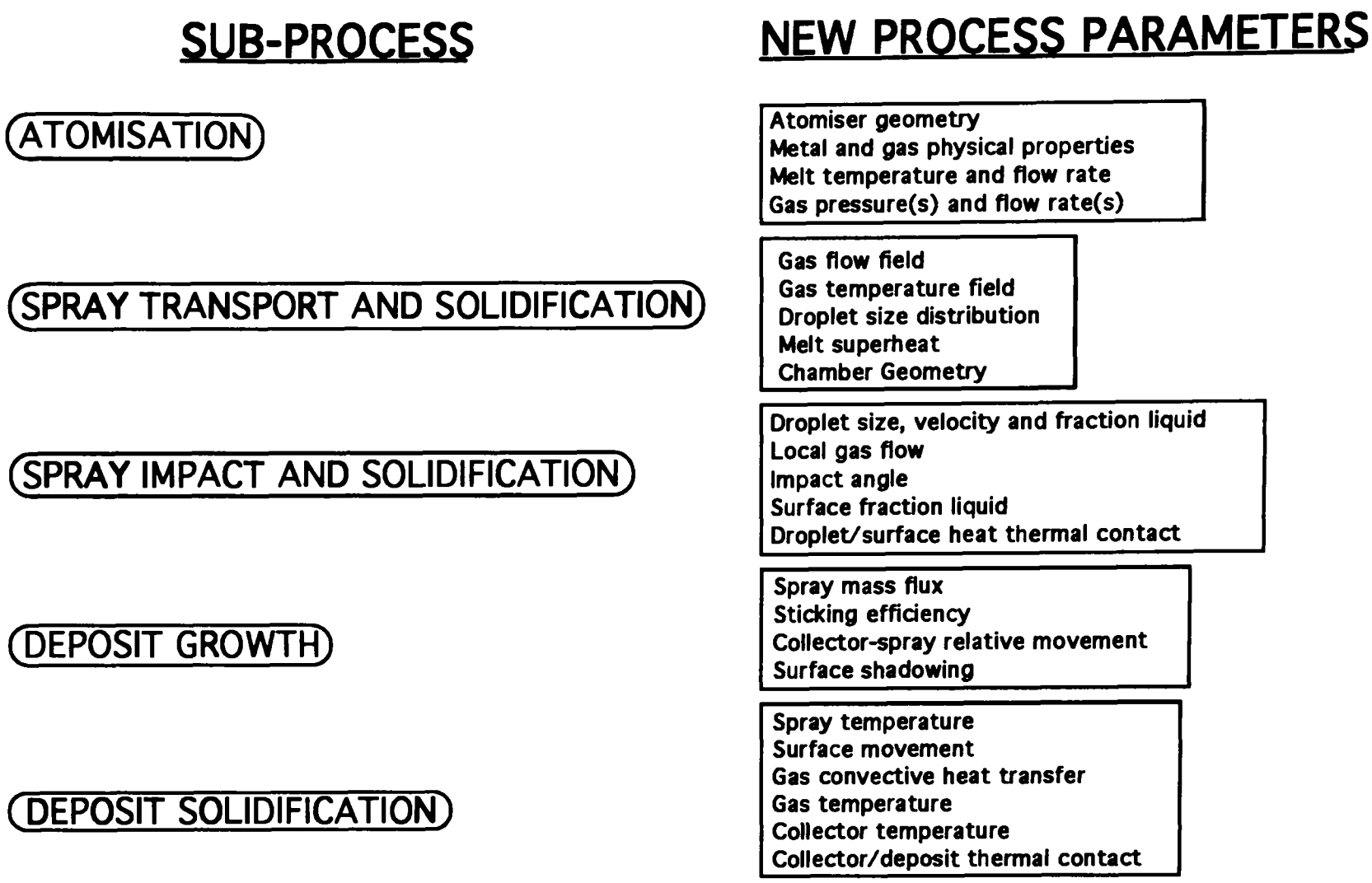

Figure 1.3: Sub-processes of spray-forming and interactions between them, after Mathur *et al.*.

relative velocity, gas and liquid flow rates, and atomiser geometry are all considered to be important in determining atomisation characteristics. Gas viscosity is rarely considered important since gas flow rates and atomiser geometries usually imply that the gas flow is turbulent, so that the shearing stresses at the gas liquid interface are dominated by pressure, (inertial), forces rather than by viscous forces, [149].

Relevant non-dimensional groups include the following.

1. The Reynolds number,

$$Re = \frac{\rho L U}{\mu}, \tag{1.1}$$

where ρ, L, U and μ denote respectively fluid density, length scale, velocity scale and fluid viscosity. A variety of Reynolds numbers can be defined according to the fluid and geometry in question, e.g. primary and secondary gas nozzles, liquid metal nozzle, liquid metal sheets, ligaments and droplets. The Reynolds number indicates the relative importance of viscous and inertial effects.

2. The Weber number,

$$We = \frac{\rho U^2 L}{\sigma}, \tag{1.2}$$

where σ is the liquid metal surface tension. The Weber number indicates the relative importance of inertial and surface tension forces, and again may be defined for the many different geometries present during atomisation. In (1.2), ρ refers to the gas density, U to the gas-liquid relative velocity and L refers to a liquid metal column, sheet, ligament or droplet length scale.

3. The Ohnesorge number,

$$Z = \frac{\mu}{(\rho L \sigma)^{1/2}}, \tag{1.3}$$

which compares the relative importance of viscous and surface tension forces.

Also considered relevant by some authors is the ratio of gas to liquid metal densities, although this can be expressed as a function of the above.

Exact physical properties of liquid aluminium alloys at high temperature are not easily measured. Viscosity and surface tension can vary strongly with both temperature and alloying elements. Approximate figures, (taken from [139], for an aluminium-copper alloy at 875 °C), are

$$\begin{aligned} \rho &= 2585 \text{ kg/m}^3, \\ \mu &= 0.00084 \text{ kg/m/s}, \\ \sigma &= 0.834 \text{ J/m}^2. \end{aligned}$$

With these figures as guidance, the liquid metal flow has an exit Reynolds number in the range $10^5 - 10^6$, and is likely to be turbulent. Exit Weber and Ohnesorge numbers are approximately 100 and 3×10^{-4} respectively. The most amplified instabilities, due to the action of the primary gas stream, (as predicted approximately by [85]), have wavelengths in the range $10^{-4} - 10^{-3}$m. At typical liquid metal flow rates such (linear) instabilities would be amplified by $O(e^{1.0})$ within $2 \times 10^{-5} - 2 \times 10^{-4}$ seconds; considerably less time than it takes to travel between the liquid metal exit nozzle and the approximate point of impact of the secondary gas jets with the metal stream. Thus, prior to impact by the secondary gas jets, there is plenty of time for initial disintegration of the liquid column into blobs, sheets and ligaments, and some further atomisation of these into smaller droplets.

Further breakup of blobs, sheets and ligaments by the mixed secondary and primary gases occurs. Effects leading to smaller sized droplets include

1. the breakup of smaller sized ligaments and sheets, or the spheroidisation of small blobs,

2. large Weber numbers, and

3. small Ohnesorge numbers.

For small enough droplet/blob Weber number, (i.e. when L becomes small or the gas stream accelerates the droplet/blob enough for U to become small), surface tension forces prevent further breakup and spheroidisation occurs. A critical Weber number, ($We \approx 13$), above which breakup occurs can be estimated for inviscid fluids, which approximate liquid metals during atomisation, (i.e. very small Z), [107, 140]. Lavernia, [70], reports an expression for the spheroidisation time, and computes a time $\sim 10^{-5}$ seconds for the formation of an 80 μm aluminium droplet.

Breakup of the liquid metal column into droplets in the vicinity of the atomiser thus takes $< 10^{-3}$ seconds. Since the liquid metal will initially be heated to well above its liquidus temperature, and since during atomisation the surface area to volume ratio of the liquid metal increases extremely rapidly, changes in temperature during atomisation are likely to be insignificant in comparison to overall changes occurring during flight towards the billet surface. Thus, immediately following atomisation droplet temperatures may

be approximated by the initial nozzle exit melt temperature. Gas and liquid metal nozzle exit velocities and temperatures may be measured and/or modelled. The ultimate goal for modelling the atomisation process then becomes the prediction of

1. the spray droplet size distribution, and

2. the gas velocity and temperature fields,

all within some vicinity of the atomiser. Although some further disintegration of spray droplets may occur downstream, due to collisions and to the survival of some large Weber number droplets, modern computational fluid dynamics techniques are able to model the evolution of the spray, as is further discussed in the next subsection.

The basic atomisation mechanisms outlined above have been understood qualitatively for some time, (see e.g. [22, 51]), and are described in various atomisation reviews, [76, 115]. There have been a large number of theoretical attempts to predict droplet sizes by considering the breakup of liquid columns, [23, 141, 144, 148], and of liquid sheets, [25, 28, 35, 52, 135].

These early theoretical attempts have not in general been successful in predicting droplet size distributions for the type of twin fluid atomisers commonly used in spray-forming. Reasons for this failure include the following.

1. The complex atomiser geometries involved do not reliably produce sheets and ligaments of easily identifiable dimensions. Predictive capabilities are much better, for example, for prefilming and fan spray atomisers, e.g. [28].

2. The reliance on linear perturbation theories to predict the wavelengths of the most unstable normal modes.

3. The unclear relationship between wavelengths of disturbances and final droplet diameters.

4. Over simplistic physical and geometrical assumptions, e.g. infinite columns and sheets, ideal fluids assumed, effects of the atomising gas ignored.

In short, the many theories made have involved assumptions that restrict the validity of their predictions to physical situations which lie outside the usual parameter regimes of interest in the atomisation of liquid metals. One exception, [14], which does include compressibility and viscosity effects, is still based on linear perturbation theory and simplistic geometric assumptions. This model has only been capable of order of magnitude predictions when applied to liquid metals, [14, 75, 76].

The fully mathematical, fluid dynamics based approach, at its very best, can provide predictions of spray droplet size only close to the point of atomisation, and usually only does so with limited accuracy. In a dense spray there will also be collisions and break up of droplets further downstream. It is only quite recently that such effects have begun to be accounted for, (e.g. [24, 102, 116]), and more promising semi-empirical predictive atomisation models have been produced, [114, 117]. The main motivation for these more successful models has come from the design of efficient diesel fuel injectors, where simpler round jet or prefilming atomiser designs predominate. Atomisers currently used in spray-forming incorporate many years

of progressive design from their initial ideas, (see for example the origins of current Osprey atomiser designs, [129]). Consequently, they are geometrically quite complex. Thus, it is likely that it will be many years before reliable theoretical predictions of droplet size distributions will be used in spray-forming applications.

As an alternative to direct physical modelling of the atomisation process in spray-forming, a number of empirical and semi-empirical methods have been used. In a semi-empirical method, mean droplet size and standard deviation are commonly assumed to be given by a correlation such as the Lubanska correlation, [83], (or by an atomiser specific modification of such a correlation, [112, 89]). Otherwise they are found directly from experiment. Mean and standard deviations are then fitted to assumed size distribution functions, (commonly log-normal). This same basic approach has been used in much recent work on spray-forming, [6, 7, 43, 45, 50, 74, 89].

Melt superheat, gas and metal flow rates, gas-metal impingement angle, atomiser geometry and atomising gas used are all known to affect atomisation of liquid metals, e.g. [13, 140]. Correlations such as the Lubanska correlation do include parameters describing gas and liquid mass flow rates, gas velocity at impact, surface tension, liquid density and the diameter of the liquid stream. However, each correlation is derived for only a finite number of different metals, atomiser geometries and other process parameters. Thus, although such correlations can give a useful guide to the possible effects of varying process parameters, they are not universally reliable, e.g. [139].

Unfortunately, it appears that reliable droplet size prediction in spray-forming is most likely to be based on atomiser specific measurements and/or subsequent correlations of droplet size distributions over a number of the alloys to be sprayed and over a range of typical operating parameters. Powder collection and sieving, laser and phase Doppler anemometry methods have all been used to this effect, e.g. [13, 87, 91].

1.2.2 Spray transport and solidification

Given the condition of the spray in the vicinity of the atomiser, (i.e. spray droplet distribution and temperature, gas velocity and temperature), the main goal of modelling the passage of the spray from the atomiser to the billet is to provide sensible predictions of the following.

1. The spray droplet trajectories and the spray mass flux at the billet surface.
2. The solidification characteristics of individual droplets.
3. The spray enthalpy at the billet surface.

Droplet trajectories and the spray mass flux

Atomisation gases exit the primary and secondary spray rings at velocities which are just subsonic. The gas flows occurring actually in the atomiser are thus compressible. Outside the vicinity of the atomiser, gas velocities decay significantly, but may still be in excess of 100m/s for significant parts of the flight, [13, 38, 43, 74, 87, 118]. Below such velocities the effects of compressibility become increasingly negligible, (see e.g. [11]), but to consider the chamber gas flows properly the assumption of incompressibility should not be made. The gas flow field is also turbulent. This is due to

- the rapid scanning motion of the atomiser secondary spray ring gas jets,
- the rapid rotational movement of the forming billet,
- the irregular geometries of both the atomiser and spray chamber,
- the high gas velocities, and
- the dispersal of droplets within the gas phase.

In order to compute the droplet trajectories it is necessary to derive some estimate of the gas flow field. This may be done either experimentally, using advanced measurement techniques, [13, 91], or it may be modelled. In view of the complexities of modelling turbulent, compressible, three dimensional two-phase flows, a considerable amount of semi-empirical approximation is used in current spray-forming models. Before reviewing these models, the approach used for the complex modelling of such flows is outlined.

Modelling of turbulent flows is carried out by considering the variables in the Navier-Stokes flow equations to consist of both a mean, (time-averaged), part and a fluctuating part, which is superimposed upon the mean part. Equations for the mean parts of quantities such as the velocity, pressure, temperature and density, are derived from the unsteady Navier-Stokes equations by averaging over time. The resulting equations are very similar to the Navier-Stokes equations in form, except that they contain additional transport terms due to the turbulent fluctuations.

The additional transport terms come from averaging quadratic products of the various fluctuating parts of the variables. These additional terms, called Reynold's stresses, (and turbulent heat flux, etc.), form additional unknowns. In the case of an incompressible flow, there are even more unknown quantities due to possible averaging of products of velocity component fluctuations with the density fluctuation. Since there are more unknowns than there are simultaneous partial differential equations to solve, some of the unknowns must be specified in order to solve for the mean flow variables. This is known as the turbulence closure problem.

Two basic methods of closing the set of turbulence equations are used. Firstly, values may be specified via algebraic expressions which are derived from experiments conducted on similar flows, or on flows where the same physical phenomena are dominant. Secondly, differential equations may be derived for the extra terms via algebraic manipulation and subsequent averaging of the Navier-Stokes equations. The equations derived in this way unfortunately also contain new unknown variables, comprised of averages of cubic combinations of the fluctuating variables, (i.e. third order moments). These new terms must then also be specified, algebraically or via the derivation of more differential equations. Hence, the turbulence closure problem recurs. At some stage one has to decide to close the system by specifying values for the remaining unknowns from empirically based estimates.

Ignoring for the moment the coupling of the droplet phase with the gas phase, problems in accurately computing the turbulent gas flow within the spray chamber include the following, [20].

1. The mean flow is three dimensional. Turbulent fluctuations are almost always three dimensional, but simplification can sometimes result if symmetries in the mean flow can be exploited.
2. The mean flow is probably unsteady, due to the billet/collector movement.

3. The underlying flow is compressible. Closure of the turbulence equations involves modelling additional terms, which involve averages of products that include the density fluctuation, as well as the usual terms.

4. The underlying flow involves recirculation, strong curvature and swirl. In such complex flows it is only very recently that new second moment closure models are being applied with success. Results and models are still anecdotal and being improved. Hence, they remain largely inaccessible to non-experts.

5. Even with improved higher order closures, there is no guarantee that in complex flows the accuracy of turbulence modelling will improve.[6]

Inclusion of the droplet phase in the computations may be done in one of two ways. Firstly, one may describe the droplet properties at all positions and times by means of a continuous, statistical distribution function. A conservation equation may then be derived to describe how this distribution changes spatially and temporally, and this equation can be solved along with the other turbulence equations. This approach is rarely used due to the additional computational expense.

A second approach more commonly used, is to consider the flight of a discrete number of droplets of representative sizes, thus approximating the continuous droplet model above. Eulerian gas phase equations are coupled with Lagrangian equations for the droplet motion. Additional source and sink terms are included in the conservation equations to account for the interactions between phases. Small "packets" of droplets of different sizes are introduced at intervals, near to the atomiser, and are tracked through the flow field. The number of droplets in each packet is adjusted so as to conserve the mass flow rate through the atomiser, and to conform to the initial droplet size distribution.

Aside from the additional complexity of working in both Eulerian and Lagrangian frameworks, problems with these models are

1. Without turbulence effects included in the gas flow equations the trajectories of all droplets of a given size released from the same position are identical. This enables an approximate computation of the spray mass flux, given an initial mass distribution near the atomiser. However, this then underestimates the turbulent dispersion of droplets in the gas stream.

2. With the turbulence effects included, computation of mass fluxes requires that large numbers of droplet trajectories be computed, which is expensive computationally.

3. Thus, additional models should be included to account for effects such as droplet dispersion, droplet breakup and droplet collisions.

4. Solution procedures usually involve iterative inclusion of the interphase source/sink terms, i.e. solve for gas phase alone, use gas phase solution to solve for the droplet phase, include the droplet source/sink terms in the gas phase equations and solve again, etc. When gas and metal mass flow rates are of the same order of magnitude, (as they are in many spray-forming situations), the interphase coupling is

[6]The whole point about turbulence is that the fluctuations are not perturbations to the mean flow, but are characteristic of the flow itself. Thus, there is no guarantee that higher order moments of these quantities are small, and that higher order closures will be more accurate.

quite strong and the amount of iteration required will thus contribute significantly to the computational expense.

5. Numerical effects arising from solution of the gas phase equations can have a large effect on individual droplet behaviour.

6. Discrepancies in the gas phase flow equations, resulting from the use of different turbulence models, can have a relatively large effect on individual droplet behaviour.

7. Complex boundary conditions, which are often not well understood physically, must be approximated relatively simplistically for the droplet phase, e.g. deposition/impacts.

In spite of the above problems, the ability to solve complex, turbulent, two-phase flows in irregular geometries with even approximate models is an extremely impressive achievement.

Current commercial software packages, motivated chiefly by combustion applications, are able to make such computations accessible to non-experts, [34, 106], (or at least, those with large enough computers and some understanding of the physics). Unfortunately, the commercial software tends to lag behind leading edge academic research in turbulence modelling. When cautiously used, and when the results are assessed in light of the model(s) limitations, these techniques represent a valuable alternative to direct experimentation.

Rogers and Katgerman, [118], and Grant *et al.*, [43, 46], have both used this type of modelling technique to compute gas flow fields and droplet trajectories within an axisymmetric spraying chamber, with fixed axial atomising gas jets impinging on a fixed circular collector. Aside from the geometrical simplifications, parameters used in both of these models are representative of current aluminium billet spray-forming processes. The computations in both cases used the $k - \epsilon$ model of turbulence, and were carried out using PHOENICS software, [106].

In [118] it is demonstrated that recirculatory gas flows exist in the chamber, and example trajectories are shown for different droplet sizes. Small, $2 - 10$ μm, droplets accelerate rapidly in the gas stream and are carried round the collector in the gas stream, whilst larger, $50 - 100$ μm, droplets accelerate more slowly, remain more central in the gas stream and impact the collector. Very similar results are presented in [43, 46].

Although in both of the above cases droplet velocities and trajectories are computed for a range of droplet sizes, in neither case is a mass flux computed from these results. This is probably due to the excessive amount of computation required. Other approaches have been as follows.

- Lavernia *et al.*, [50, 74], assume a one dimensional gas flow field with velocity that decays quadratically with distance from the atomiser nozzle. Only thin one dimensional deposits are considered. A mass flux at the deposit surface is not computed, but droplet velocities are computed in order that droplet solidification may be studied in parallel.

- Gillen *et al.*, [9, 38], also assume a one dimensional decaying gas velocity, (unspecified source), and compute droplet velocities.

- Mathur *et al.*, [6, 87, 89, 90], use empirically based predictions of the decaying axial gas velocity in an axisymmetric jet. Spray chamber geometry is axisymmetric with a centrally positioned atomiser.

The approach is essentially one dimensional, as above. In [90] experimental results are presented, demonstrating the radial variation across the spray jet of the mass median droplet size, but these results are not used further in droplet velocity computations. Droplet velocity profiles are computed for a range of droplet sizes. The mass flux is not computed.

- Grant, [43], uses a one dimensional exponentially decaying axial gas velocity to compute droplet velocities.

Droplet velocity, $\boldsymbol{v}_d$, is governed by

$$\rho_d V_d \frac{\mathrm{d}\boldsymbol{v}_d}{\mathrm{d}t} = V_d(\rho_d - \rho_g)g + \frac{A_d}{8} C_{drag} \rho_g (\boldsymbol{v}_g - \boldsymbol{v}_d)|\boldsymbol{v}_g - \boldsymbol{v}_d|, \tag{1.4}$$

in [50, 74], where ρ_d, V_d, A_d, ρ_g, C_{drag} and $\boldsymbol{v}_g$ are respectively the droplet density, volume, surface area, the gas density, the drag coefficient and the gas velocity. In [6, 9, 38, 87, 89, 90] equation (1.4) is replaced by

$$\rho_d V_d \frac{\mathrm{d}\boldsymbol{v}_d}{\mathrm{d}t} = V_d \rho_d g + \frac{A_d}{8} C_{drag} \rho_g (\boldsymbol{v}_g - \boldsymbol{v}_d)|\boldsymbol{v}_g - \boldsymbol{v}_d|, \tag{1.5}$$

and Grant, [43], neglects gravitational effects altogether. Gravitational effects on a droplet will usually be negligible in comparison to the influence of gas friction, thus the discrepancy in model equations is not serious. The drag coefficient is given in all cases by

$$C_{drag} = 0.28 + \frac{6}{Re^{1/2}} + \frac{21}{Re}, \tag{1.6}$$

where Re is a Reynolds number based upon the relative gas-droplet velocity and the droplet diameter.

The one dimensional results described above are all fairly similar. Droplets are accelerated to a maximum velocity by the gas stream and then, as the gas velocity decays below their maximum velocity, they are decelerated. Maximum velocities are higher and reached sooner in the case of smaller droplets. Droplet velocities are of order 100m/s in most computations. The main failings of these models are that the rapid deceleration of the gas stream impinging on the deposit surface is not accounted for, that the velocity field is not influenced by the droplet size distribution and/or metal mass flow rate, and that the axial velocity of a decaying gas jet is not representative of the velocity field experienced by the majority of droplets in passage.

In none of the spray-forming literature are spray droplet velocity computations used to give an estimate of the mass flux at the deposit surface. The reason for this is probably because most of the literature refers to fixed atomiser configurations and deposit shapes are assumed to be one dimensional. In such cases the deposit growth may be measured fairly accurately and the droplet velocity computations are carried out in order to determine droplet solidification behaviour. The assumptions of one dimensional geometries are usually justified in the above by the relatively thin deposits grown, and not by lack of variation in the mass flux produced by the atomised spray. For example, in [87] the measured deposition rate is shown to have considerable radial variation across the width of the spray cone.

In billet production deposits are thick and the mass flux will vary considerably over the deposit surface. It is desirable to be able to predict this variation. It is felt that in view of the relative simplicity of the equations describing droplet motion, sensible estimates of the spray mass flux field could be gained by integration of, for example (1.4), over representative droplet distributions released from a range of atomiser inlet start positions. This could be coupled with approximate measurements of the velocity field. If the gas

flow measurements are made when droplet laden then this gives at least some approximation of the effects of interphase interactions.

Inflight droplet solidification

Five different regimes may be identified in the thermal histories of droplets in flight, [43, 46].

1. Cooling in the liquid state to below the liquidus temperature of the alloy.
2. Nucleation at a given undercooling, and subsequent recalescence to near the liquidus temperature.
3. Segregated solidification.
4. Solidification at the eutectic temperature, until fully solid.
5. Cooling whilst solid.

Heat removal from the droplet surface into the droplet boundary layer gas flow is governed by the Biot number, B, given by

$$B = \frac{h_d d_d}{K_d}, \tag{1.7}$$

where h_d, d_d and K_d are the droplet heat transfer coefficient, diameter and thermal conductivity.

In the most complex models, B will vary with different points on the droplet surface, and there will exist temperature gradients within the droplet volume. More commonly however, B is considered to be an average Biot number. For typical droplet sizes and gas velocities encountered during spray-forming Biot numbers are small, $B < 0.1$. For Biot numbers in this range, temperature gradients within the droplet can usually be ignored, i.e. Newtonian cooling. This treatment is not exact. Levi and Mehrabian have shown that at large undercoolings, significant thermal gradients may exist for Biot numbers as low as $B \approx 10^{-4}$, [82]. For the majority of spray-forming models the Newtonian model is adopted.

During the first cooling regime, heat is removed by convection from the droplet surface, according to

$$\rho_d d_d c_d \frac{\mathrm{d}T_d}{\mathrm{d}t} = -6h_d(T_d - T_g), \tag{1.8}$$

where ρ_d, c_d, T_d and T_g denote respectively the droplet density, specific heat capacity, temperature and the gas temperature. The heat transfer coefficient is assumed to be given by the Ranz-Marshall correlation,

$$B = 2 + 0.6Re^{1/2}Pr^{1/3}, \tag{1.9}$$

where

$$Pr = \frac{c_g \mu_g}{K_g},$$

is the Prandtl number, c_g is the gas specific heat capacity, μ_g is the gas viscosity and K_g is the gas thermal conductivity. The Reynolds number is based on the gas properties, the droplet diameter and the relative gas-droplet velocity. Gas and droplet velocities are computed and/or specified by the methods outlined in the previous section. Gas temperatures are treated as either constant or are estimated from empirical/computational results. Slight model variations are

- Inclusion of radiative effects, (usually negligible), [87], and

- slight modifications of the Ranz-Marshall correlation to account for the sharp temperature gradients in the gas close to the droplet, [89].

According to Lavernia, [70], nucleation occurs heterogeneously in all but the smallest of droplets, due to one of the following processes.

1. Bulk heterogeneous nucleation within the droplet, i.e. alloy composition is not fully homogeneous.
2. Surface heterogeneous nucleation, i.e. due to the lower droplet surface temperatures than within the droplet bulk.
3. Surface oxidation processes
4. Interparticle collisions

The physics underlying the nucleation process is complex and not reviewed here. The essential features are that the probability of nucleation occurring by one of the above processes, (or homogeneously), increases with both the size of undercooling achieved and the volume of liquid material present. Most models assume that nucleation takes place at a fixed undercooling temperature, which depends inversely on the droplet size, [45, 46, 50, 74], or is determined by some other means, [87].

Recalescence is the rapid rise in droplet temperature immediately following nucleation. It results from both the rapid release of latent heat and the inability of the surrounding gas to convect this heat away quickly enough. During recalescence the solidification rate is assumed proportional to the undercooling, and convective cooling effects are considered negligible, [45, 46, 50, 74], (or a more complex model is utilised, [87]). The exact details of the model used during this part of the droplet thermal history are probably not significant. Recalescence usually takes only microseconds to complete and it is only when particularly large undercooling occurs, prior to nucleation, that large proportions of the droplet can solidify during recalescence. Unless this happens the influence of microstructural formation that occurs during recalescence is likely to be small. Recalescence is considered complete when the rate of latent heat release is equal to the rate of convective heat loss.

Segregated solidification is governed by

$$\rho_d d_d [c_d \frac{\mathrm{d}T_d}{\mathrm{d}t} - L \frac{\mathrm{d}f_s}{\mathrm{d}t}] = -6h_d(T_d - T_g), \tag{1.10}$$

where f_s is the droplet solid fraction. The Scheil equation is used to express f_s as a function of temperature, see e.g. [43, 45, 46, 87, 89, 90].

If there is a eutectic temperature, then the temperature remains constant at that temperature whilst the remainder of the heat is extracted, [43, 45]. Subsequent cooling of fully solid droplets is governed again by (1.8).

Microstructural evolution in each of the above stages has not been reviewed. The interested reader may refer to [43, 74, 70, 87, 89, 90]. The following general conclusions may be drawn collectively from the results of models of this part of the spray-forming process.

- Droplet solidification depends strongly on droplet size. At typical atomiser-collector flight distances smaller droplets generally contain larger fractions of solid. At particularly short flight distances, (e.g. 100mm), this may not be true since smaller droplets may still not have achieved the undercooling necessary for nucleation.
- Provided flight distances are not too short, the effect of including the nucleation, undercooling and recalescence phases is minimal.
- Flight distance has a large effect on the thermal history of individual droplets.
- At typical flight distances and with typical droplet size distributions it is possible for fully solid, mushy and fully liquid droplets to be deposited.
- Changes in the models affecting droplet dynamic behaviour can have large effects on the droplet temperature at a given flight distance, even when the effect on overall cooling rate is much less pronounced, [43].
- Changing the model assumptions regarding definition of the heat transfer coefficient can have a large effect on droplet temperature profiles, [43].
- In comparison to the above two effects, changes in the detailed modelling of the solidification process have little effect, [43].
- Droplet thermal behaviour is influenced by the amount of melt superheat; this effect being larger for larger droplets.
- Changes in atomising gas used and in atomising gas pressure can have a large effect on the thermal behaviour of individual droplets, [74, 87].
- The one dimensional gas velocities assumed in these models are capable of producing physically sensible results, consistent both with experiment and with more complex computational results.

Spray enthalpy at the billet surface

Most models of deposit solidification are continuum models, implicitly involving the assumption that temperature differences on the scale of flattened droplets and/or grains are insignificant within the deposit. In these models, it is necessary to specify the heat flux across the deposit top surface. For computational efficiency and for consistency with the continuum approach, the heat influx normal to the deposit surface due to deposition from the spray is given by the product of the surface normal velocity and the mass averaged enthalpy of the spray. This last quantity is obtained by averaging the enthalpy of individual droplets over a representative droplet size distribution. Individual droplet temperatures are computed using the methods described above. Several authors have computed spray enthalpies in such a way.

Annavarapu, Mathur *et al.*, [6, 7, 87, 89, 90], have computed the spray enthalpy for a variety of different alloys and over a range of different flight distances. At a flight distance of 400mm spray enthalpy variations correspond to variations in spray fraction liquid of between 10% and 45%, for different steels, copper and

nickel alloys. Not surprisingly, the droplet size distribution is reported to have a critical effect on the computed spray enthalpy at a given flight distance. Over the radius of the spray cone, ($\approx$ 50mm), computed variations in spray enthalpy are reported as being insignificant, [7, 90]. In [89] it is shown that for a copper-titanium alloy, changes in the gas to metal mass flow rate ratio through the atomiser can have a marked effect on the computed spray enthalpy; e.g. approximately a 14 % reduction in spray fraction liquid over a range of flight distances results from doubling this ratio.

Grant, [43], computes the spray enthalpy for aluminium-copper alloys, with similar material properties to the alloys considered later in this thesis. At a flight distance of 350mm the computed spray enthalpy corresponds to $\approx$ 65 % spray fraction liquid. In [45] Grant presents results demonstrating the sensitivity of the spray fraction liquid to variations in the assumed model gas velocity, melt flow rate and melt superheat, all at a range of flight distances. The spray fraction liquid is observed to vary approximately linearly with gas velocity and melt superheat, and inversely with melt flow rate.

Grant points out that the effects on the computed spray enthalpy of varying process parameters are extremely difficult to predict and/or to summarise, due to the variability of both materials and atomisers. For example, increasing the melt superheat increases the amount of heat that must be extracted from the droplets, but may also decrease the mean droplet size through a decrease in liquid metal viscosity.

Perhaps the only conclusions to be drawn are that, in general,

- the spray fraction liquid decreases with flight distance,
- at typical flight distances, (i.e. usually in the range $300 - 700$ mm), sprays of most metals are not fully solid,[7]
- an order of magnitude guide for the decrease in fraction liquid with distance, over typical flight distances, is $0.5 - 1$ % fraction liquid per 1cm,
- the computed spray fraction liquid will vary with different atomisation conditions and alloys.

This remains an area of active research.

1.2.3 Spray impact and consolidation

This part of the spray-forming process is probably the part for which there is least quantitative understanding, but which is also the most critical. Models describing the process prior to deposition and consolidation are generally discrete, (i.e. droplet based), whilst those that describe deposit growth and solidification assume a continuum. Boundary conditions for the deposit growth and solidification models include continuous functions that represent the surface velocity and the spray enthalpy, (e.g. [43, 49, 50, 87, 90]), both of which are defined, (implicitly), by spatio-temporal averaging of the spray properties. The basic unit of the deposition/consolidation process is the "splatting", (i.e. impact and spreading), of a single droplet on the deposit surface and the subsequent heat flow between it and the deposit. Fundamental questions relating to this part of the process include the following.

[7] In practice, collector positioning has been determined at some stage during process development by trial and error so that this is true!

1. In what way, (qualitatively), can the conditions present during deposition effect the subsequent deposit microstructure.

2. In what sense are the continuum models, which use averaged boundary conditions at the deposit surface, the limiting case of the real discrete stochastic process.

3. How different are predictions gained from discrete and continuous models.

4. What process factors influence

   (a) whether or not a droplet is deposited on the surface,

   (b) the deformation of an individual droplet that impacts the surface,

   (c) the heat flow between a newly deposited droplet and the rest of the deposit.

Qualitative understanding of the relationship between local deposition conditions and subsequent microstructure is fairly good. Commonly, four different combinations of droplet and deposit thermal conditions are distinguished, each of which is related to a characteristic microstructure, e.g. [87].

- Both droplet and deposit surface are solid. In this case, due to the rapid collector movement and strong turbulent gas flows, it is unlikely that any deposit will form.

- The deposit surface is fully solid when impacted by each droplet, (on average), and droplets contain some fraction liquid. In this case droplets with significant liquid fractions are believed to splat and adhere to the deposit surface. Successive droplets do weld together, but because of the long interval between droplet impacts there is no surplus liquid on the deposit surface when each new droplet arrives. This condition is associated with observed microstructures in which the grains are columnular and there is significant porosity at the intergrain boundaries.

- The deposit surface is only partially solid, and is impacted by droplets which are also semisolid. This case, where the surface fraction liquid is not so great as to allow lateral flow of liquid, has been termed incremental solidification by Singer *et al.*, [30, 132]. Singer *et al.* assume that there is a thin surface film of liquid whose lateral flow is restricted by surface tension and friction between solid particles. Segregation is minimal because of the restricted surface liquid flow, and because the excess liquid is able to fill interstitial pores, porosity in the formed microstructure is also minimal. This is considered to be the optimal spraying condition and is associated with fine equiaxed grain structures that are commonly observed in spray-formed materials. In [132] this deposition regime is distinguished from that above by the mean time required for a spray droplet to solidify, first exceeding the mean time between successive droplet impacts at a point on the surface. An expression is derived for this critical time interval between droplets, and is related to process parameters.

- Both deposit surface and droplet have liquid fractions that are "too high". In this case the viscosity of the semi-solid surface layer becomes low enough to allow fluid movement. Macrosegregation then becomes possible, but more serious usually will be the possibility of porosity due to gas entrapment during disturbances of this surface layer, (i.e. instabilities such as waves, splashes, re-atomisation).

Specification of a critical surface fraction liquid at which this deposition regime becomes operative is hard. Although here is a considerable literature on turbulence induced surface instabilities on thin liquid films, (e.g. [27, 53]), theoretical critical stability results are usually presented in terms of the gas velocity scale and the liquid film Reynolds number. Whilst the former is relatively easy to estimate, the latter relies on being able to specify a viscosity for the mushy surface layer. This is a notoriously difficult problem; semi-solid alloy slurries exhibit complex thixotropic, temperature dependant behaviour which is not well understood or predicted, [33].

Aside from the inclusion of porosity resulting from fluid instabilities, other mechanisms by which porosity may enter the deposit have been considered by Lavernia, [70]. These are:

1. Gas entrapped in spray droplets. This is possible in any of the above deposition regimes and can be modelled to give reasonable agreement with experiments. The amount of trapped gas decreases with droplet size and the total porosity is not usually significant, [111].

2. Porosity due to solid shrinkage. This is likely only when there is significant surface liquid fraction, i.e. in the last of the four regimes described above. Shrinkage porosity will usually be identifiable by its morphology, but since it occurs with other high liquid fraction related porosity it is hard to quantify alone.

3. Interstitial porosity. This is probably due to micron sized cavities trapped during impact, and may potentially happen in any of the last three deposition regimes. See [101] for possible cavitation mechanisms during contact between liquid surfaces.

The sense in which the continuum boundary conditions are the limiting case of the discrete stochastic deposition process appears to have recieived no formal mathematical treatment.

Annavarapu, [6, 7], has computed the temperature within a one dimensional growing deposit using both a continuum approach in which growth and heat flow are represented as continuous functions of time, and a discrete event approach. In the latter model, splats of an appropriate thickness are added to the deposit at regular intervals. The splats have temperature dictated by the mass averaged spray enthalpy. The interval between splats is determined from an estimate of the spray density, (slightly modified from the analysis of [132]). The discrete model also includes a parameter which may be adjusted to simulate the efficiency of the thermal contact between successive splats. Results predicted from both models are shown to converge approximately 0.3 seconds after commencement of deposition. The strip thicknesses and times considered in [6, 7] are both very small, (i.e. $\approx 2-3$ mm, and $\approx$ .5s). These appear to be the only published numerical results which compare discrete and continuous effects during deposition.

Whether or not a droplet is deposited on the surface depends on two separate sequential processes. Firstly, whether or not the droplet actually hits the surface, and secondly, whether a droplet that hits the surface will stick there. This distinction is important if both the heat and mass transfer processes occurring during deposition are to be studied on the droplet scale. For example, although there is only a positive mass flux into the deposit when an impacting droplet adheres to the deposit, a significant positive heat flux can

occur during the elastic collision between a small spray droplet and the deposit surface, even when there is no adhesion, (see e.g. [136]).

Large diameter droplets are effected less by the turbulent gas velocity fluctuations than are small diameter droplets. Impact and deposition of the larger diameter spray droplets is thus determined chiefly by the mean gas flow velocity field. The mean velocity of the atomising gas jets will decelerate rapidly as they impinge upon the deposit surface, and as the gas flows around the sides of the deposit and collector. Larger droplets will not be decelerated as rapidly as smaller droplets in the impingement region, and thus are likely to impact the billet surface. Grant, Rogers *et al.*, [46, 118], have shown that for droplet diameters $\approx 10\mu$m and less, the majority of droplets have insufficient momentum to impact the collector directly and are carried away in the gas stream.

The dominant mechanism of deposition for the smaller[8] diameter droplets is thought to be turbulent diffusion, taking over gradually from purely inertial deposition as the droplet size decreases. Turbulence dominated deposition has received much attention in recent years, due to the importance of spray cooling systems and other two-phase flows in nuclear reactors. Relevant parameters include the viscous sublayer thickness, the gas kinematic viscosity, the realtive gas-droplet velocity and a "stopping distance" length-scale, based on the distance a droplet with prescribed initial velocity would travel through a stagnant fluid. The reader is referred to [37] for more information. Although quantitative models of turbulent deposition processes have been derived, they have not been applied to metal spray-forming processes. Without understanding, and being able to accurately model or measure the near-deposit gas flow, it is doubtful whether any predictive model based on the fundamentals of droplet deposition will be applied.

Adhesion of droplets to the surface after impact is also an area where there has been some fundamental study, e.g. [39]. The effectiveness of adhesion to the surface is determined by the area of contact between the impacting droplet and surface, and the drag on the droplet due to the gas stream during the impact process. Contact area is determined by droplet impact velocity and subsequent deformation. Hence, factors such as the impact angle can have a significant effect on the effectiveness of both deposition and adhesion. In the case where the droplet effective viscosity varies strongly with its fraction liquid, the situation is clearly much harder to analyse.

In response to the complexity of the deposition process, spray-forming models have tended to either "sidestep" the question of the deposition efficiency by using empirical measurements of deposit growth, or more recently have proposed lumped parameter models of "sticking efficiency", [89].

Mathur *et al.*, [89], assume that the sticking efficiency of the spray and surface at any particular point is composed of two components. One of these is a geometric component, which is discussed later. This component multiplies a thermal sticking efficiency coefficient, SE_T, defined by

$$SE_T = (\eta_s(1-f_l)+\eta_l f_l)\epsilon, \tag{1.11}$$

$$\eta_s = 1. - 0.75(1-F_l), \tag{1.12}$$

$$\eta_l = 0.98. \tag{1.13}$$

[8]Here, submicron sized droplets are excluded since Brownian motion is believed to dominate in this size range.

The functions f_l and F_l denote the fraction liquids of the spray and deposit surface respectively, $\epsilon \in [0, 1]$ is a viscosity dependant parameter. The model predicts that 25% of a fully solid spray impacting a fully solid surface would remain deposited, increasing to 100% for a fully liquid surface, (ignoring ϵ). In contrast, 98% of a fully liquid spray remains deposited. At 60% surface liquid fraction, ϵ is assumed to drop drastically, to describe the ejection of liquid metal from the deposit surface.

Although phenomenological in its derivation, and although this model ignores entirely droplet size effects, the thermal component of the "sticking efficiency" model in [89] represents the only attempt to account quantitatively for process variation of this kind, and as such is extremely valuable. In [89] it is demonstrated how variations in spray liquid fraction may result in significant variations in both material yield and billet shape.

The deformation of an individual isothermal droplet that impacts the surface has recently been considered by Trapaga and Szekely, [138], focussing specifically on droplet size and velocity ranges occurring in spray-forming operations. Liquid droplet impacts on both solid and liquid surfaces are modelled. Droplets are shown to impact and spread to their final diameters in microseconds. The computational results in [138] are compared with earlier asymptotic results, [84], and reported to give good agreement. The ratio of splat diameter to droplet diameter, ζ_m, and the spreading time, τ_s, are given for typical spray-forming parameters as

$$\zeta_m \approx Re^{1/5}, \tag{1.14}$$

$$\tau_s \approx \frac{2d}{3V_i} Re^{1/5}, \tag{1.15}$$

where d and V_i are the droplet diameter and impact velocity.

Typical semi-solid droplet Reynolds numbers prior to impact are in the range $10-10^4$, (heavily dependant on viscosity, i.e. fraction liquid), giving ζ_m in the range $1.5 - 6.3$. Assuming the smaller values of ζ_m to correspond to the smaller diameter, more viscous droplets, splat thickness is likely to be of order $5 - 10$ μm. Thermal conduction within the droplet will have an approximate timescale

$$\frac{\rho c d^2}{K},$$

(assuming perfect thermal contact), or slower. For a typical 100 μm aluminium alloy droplet this timescale is $\approx 10^{-4}$ seconds, much slower than the splatting times predicted above. Thus, in considering the thermal equilibriation of the droplet, the splatting and heat flow problems have been considered separately, as seems reasonable. In view also of the typical splat diameter–thickness aspect ratios, of order 10, thermal equilibriation in splat cooling is usually considered one dimensional.

There have been a number of studies of heat flow during splat cooling. Early experimental and mathematical work, [60, 59, 109, 119], suggested that the type of cooling occurring could be characterised by a Biot number, based on the heat transfer coefficient between splat and deposit, the splat thickness and the thermal conductivity of the splat. For Biot numbers less than about 0.015, thermal gradients across the splat were considered negligible, and Newtonian cooling assumed. Biot numbers above 30 were approximated by assumed perfect thermal contact. For both these cases, analytical approximations of the cooling rates have been derived.

More recently Wang and Matthys, [142], have considered the problem again in far greater detail, numerically solving a Stefan problem through the splat thickness for a range of different materials and Biot numbers. They show that the Newtonian approximation can give good agreement with the computed results for Biot numbers as high as 0.5, and that for higher Biot numbers these results provide a lower bound for splat cooling rates with more perfect thermal contact.

Consider then, a semi-solid splat with initial fraction liquid, f_l, and remaining latent heat of freezing, $f_l L$, that is assumed to be released linearly over the remaining freezing range. Define an initial temperature, T_i, a deposit temperature T_d, a solidus temperature T_s, and the remaining temperature freezing range

$$\Delta T = T_i - T_s.$$

With these assumptions, Newtonian cooling of the splat is governed by

$$\begin{aligned} \frac{\mathrm{d}T}{\mathrm{d}t} &= \frac{h}{\rho Z(c + \frac{f_l L}{\Delta T})}[T_d - T], \\ &= \beta[T_d - T], \end{aligned} \tag{1.16}$$

for $T > T_s$. In the above, Z denotes the splat thickness and h the heat transfer coefficient. Defining an "equilibriation" time, $\tau_{0.9}$, as the time taken for the splat–deposit temperature difference to reach one tenth of its initial size, and assuming that $T_d \geq T_s$, an approximate equilibriation time is given by

$$\tau_{0.9} \approx \frac{2.3\rho Z(c + \frac{f_l L}{\Delta T})}{h}. \tag{1.17}$$

Typically, $h > 10^5 \mathrm{W/m^2/^\circ C}$ in splat cooling, [142], (often $h \gg 10^5 \mathrm{W/m^2/^\circ C}$). Thus, an approximate upper bound for the equilibriation time between droplets and the deposit is 3×10^{-3} seconds. For larger, more liquid, droplets where thermal contact is better, equilibriation times might be expected in the range $10^{-5} - 10^{-4}$ seconds.

1.2.4 Deposit growth

Mathematical modelling of deposit growth has been motivated in main by the need to know both the deposit size and surface velocity in order to solve the solidification problem within the growing deposit. Gutierrez *et al.*, [49, 50], and later Grant, [43], consider one dimensional deposit growth. In both cases growth rate is assumed constant in time, and is determined experimentally as the average growth rate from the end deposit thickness and spraying time.

Obvious limitations of the one dimensional assumption, many of which are discussed in these references, include the following.

1. Spatial variations in mass flux will exist across the diameter of the spray cone. Thus, the one dimensional growth assumption requires that some symmetry of the deposit is exploited, if the models are to be in some way representative of the whole deposit.

   (a) In the case of thin tube or strip geometries this might be a realistic assumption. However, the deposit-spray relative motion in these geometries means that any position on the deposit will pass through the spray and thus not have a growth rate constant in time.

(b) In the case of a cylindrical disc/billet geometry, the only point of symmetry is along the axis of rotation. When the atomiser is positioned directly above the collector surface, velocities here will typically be larger here than elsewhere. Thus, caution should be exercised in generalising such results. Where disc shapes are more uniform radially this is likely to be achieved with a non constant growth rate.

2. Temporal variations in mass flux are likely to exist due to the difficulties of effectively controlling the atomiser throughput and, in the case of very short spraying runs, atomiser start-up and shut-down effects.

A slightly less empirical model has been developed by Mathur, [87], and has been used extensively in many future publications, [6, 7, 77, 88, 89, 90]. This model has been used to predict both strip and disc/billet geometries. A fundamental failing of this model for any but truly one dimensional geometries is exposed in the critique below.

Mathur defines a deposition rate function, $\dot{D}(r)$, dependant on the radial distance, r, from the axis of the, (axisymmetric), spray cone. The function $\dot{D}$ is defined as, "the thickness of a deposit that would build up per unit time on a flat stationary substrate positioned normal to the spray axis.", ([87], p. 29). Thus, for alloy density ρ, the mass flux due to the spray is assumed to be parallel to the direction of the spray axis, and is given by $\rho\dot{D}(r)$. Estimated values of $\dot{D}(r)$ are gained from videoing the build up of the deposit formed when spraying onto a flat plate fixed perpendicular to the spray cone. The function $\dot{D}(r)$ is found to be approximately Gaussian, [6, 87].

Defining position on the collector by coordinates (x, y), Mathur denotes the deposit thickness $L(x, y, t)$ and equates

$$\frac{\partial L}{\partial t}(x, y, t) = \dot{D}(r[x, y]). \tag{1.18}$$

This equation is wrong, and can have serious implications. Neglecting the efficiency of the deposition step, a corrected version of (1.18), (see chapter two for derivation), is given by

$$\frac{\partial L}{\partial t}(x, y, t) = \dot{D}(r[x, y])\boldsymbol{k}'.\boldsymbol{\nabla}[z - L(x, y, t)], \tag{1.19}$$

where $\boldsymbol{k}'$ denotes the unit vector in the direction of the spray cone axis and z denotes the coordinate perpendicular to the collector, (i.e. $z = L(x, y, t)$ is the deposit surface).

The model given by (1.18) is correct only when the surface is planar and perpendicular to the spray cone axis. Such a situation may correspond approximately, for example, to a strip forming process. However, when either the collector is not initially perpendicular to the spray axis, or when the surface becomes non-planar, the formulation (1.18) will not conserve the mass of the spray. Deposit growth results have been presented explicitly in [6, 7, 87], using this model. In [87], results for disc/billet geometries are computed, for which (1.18) will certainly not be accurate. Even for the strip spraying results computed in [6, 7], significant longitudinal and transverse variations in strip thickness can result,[9] effecting the accuracy of (1.18).

In the later work by Mathur *et al.*, [89], the situation is confused further by the inclusion of a spray-surface "sticking efficiency" term. The thermal component of this term has been considered in the previous

[9]This depends on the relative speeds of the strip thickness growth and the strip velocity under the spray.

section. The "geometric component" of the sticking efficiency component used to compute results in [89] is not actually given, but it is assumed to depend upon the angle, θ, between the surface normal and the spray axis. Suggested forms for this coefficient are $\cos\theta$ or $\cos^2\theta$. With the former of these two options, (1.18) becomes

$$\frac{\partial L}{\partial t}(x,y,t) = \dot{D}(r[x,y])\boldsymbol{k}'.\boldsymbol{\nabla}[z - L(x,y,t)]\|\boldsymbol{\nabla}[z - L(x,y,t)]\|^{-1}, \tag{1.20}$$

which is closer to (1.19), but still inaccurate when $\|\boldsymbol{\nabla}[z - L(x,y,t)]\| > 1$, (as in [89]).

There are likely to be geometric effects on the efficiency of deposition, due purely to the variations in local gas velocity and droplet impact angle making it "mechanically" harder for droplets to hit the surface. There are also effects that are due purely to incorrectly specifying the velocity of a point on a curved surface that is moving due to a specified mass flux through it, i.e. equation (1.18) versus equation (1.19). It is felt that investigation of the former of these effects, for example by comparison of model based predictions and experiment, (e.g. [89]), will remain obscured unless a model such as (1.19) is adopted *a priori*.

Other than the results mentioned above in [87, 89], there have been no other published results relating to the growth of disc/billet shaped deposits. Those results that have been presented in [87, 89] relate to th growth of fairly small "discs", rather than larger billets, and are chiefly motivated by wanting to model the heat flow within the discs.

When the length to diameter ratio becomes larger and full size production billets are grown the dynamics of billet growth become of interest in their own right. Not only is there more scope for larger changes in billet shape to manifest, due to the length of time involved, but billet solidification becomes progressively less influenced by the collector cooling and more influenced by geometric effects as it grow larger. Thus, there are many additional considerations, which have not to date appeared in the literature.

Billet growth dynamics is considered in detail later in this thesis, and also in a parallel study, [99], focussed primarily on development of a billet shape control algorithm. Other problems peculiar to production scale billet growth dynamics include

- properly multi-dimensional growth must be considered,
- possible shadowing of the spray mass flux by the billet surface can occur,
- minimisation of subsequent machining wastage becomes an added objective, e.g. [99].

1.2.5 Deposit solidification

For pure metals, solidification occurs by the release of all the latent heat of freezing at one particular melting temperature. The mathematical formulation of such a problem is a Stefan problem, which has received much attention in the mathematical literature; see e.g. [56]. Spray-formed metals are usually alloys of two or more elements. These alloys typically release their latent heat over a range of temperatures, (the freezing range). For this reason the Stefan formulation is inappropriate, although it may give useful approximate results.

A generic alloy solidification problem for a binary alloy consists of solid, liquid and mushy regions. In the later region, both solid and liquid phases will coexist. In the spray-forming process the spray is only partially liquid on deposition, and subsequent solidification of the remaining liquid fraction is generally rapid.

Thus, only solid and mushy regions are present. In the case of strip and tube geometries the solidification is dominated by the chill effect of the collector. In the case of the billet geometry this is not so, but the rapid rotational movement of the billet implies that the mushy region necessarily be confined to a small part of the billet, to avoid disintegration. Thus, in billet production the mass and heat fluxes from the spray must be carefully controlled so that a combination of chilling from the formed billet and convective cooling from the atomising gas is sufficient to solidify each deposited layer of spray before the next layer is deposited.

In such situations solidification is conduction-controlled and an appropriate governing equation in both solid and mushy regions is

$$\frac{\partial H}{\partial t} = \nabla.[K\nabla T]. \tag{1.21}$$

Here H, K and T are "mixture-based" enthalpy, thermal conductivity and temperature respectively.[10] The mixture-based formulation relies upon the prescription of densities, specific heat capacities and thermal conductivities for both solid and liquid phases. It is also reliant upon the prescription of the liquid fraction as a function of the other solidification variables. Liquid fractions may vary with cooling rates and with the local concentration of alloying elements, as well as with the temperature. However, the approximation of a purely temperature dependant liquid fraction is commonly made, and is particulary relevant in spray-forming studies where product homogeneity is high. Rate dependency is usually neglected and a fraction liquid curve, $f_l(T)$, is prescribed either directly from experiment or via the Scheil equation.

Equation (1.21) may be re-written in many different ways, but the basic formulation described above is consistent across all published spray-forming deposit solidification studies. This equation is a nonlinear heat equation. Most solidification studies are one dimensional, corresponding to the deposit growth models utilised.

It should be noted that the assumption of a one dimensional heat flow does not follow automatically from the one dimensional geometry. In the case of a strip or tube geometry, different points on the deposit are growing at different times. Thus, the relative velocity of the spray across the deposit surface must be fast enough to dominate conduction in the same direction.

Boundary conditions at the billet surface involve the sum of a heat influx from the spray, which is represented by the surface velocity multiplied by the enthalpy difference between the spray and top surface, and a standard Newtonian cooling effect. In some cases radiative cooling is also included, but radiative effects are typically much smaller than convective effects, and may be included within the Newtonian cooling term.

The heat transfer coefficient between the top surface and the gas is only approximately known. Although empirical correlations do exist for the heat transfer between impinging jets and flat plates the spray-forming situation is complicated by the following, (see e.g. [86]).

1. Formulas rely on an effective nozzle length-scale which is more difficult to interpret in a multi-nozzle arrangement.

2. Formulas are usually valid only within a relatively close distance from the jet nozzle, (i.e. close relative to the above nozzle length-scale). The flight distance in many spray-forming applications is relatively long.

[10] i.e. weighted with the volume fraction liquid

3. Presence of the droplet phase will effect the heat transfer.

4. Heat transfer is effected by surface roughness.

5. Heat transfer is effected by jet-surface impingement angle and surface concavity.

This difficulty is compounded by the differences in gas flow rates used in different spray-forming rigs for different geometries. Assumed values vary from $21 W/m^2/°C$, [49, 50], to $500 W/m^2/°C$, [7].

For the assumed model gas-deposit heat transfer coefficients, one dimensional results computed by different authors are qualitatively similar, see [6, 7, 43, 49, 50, 87, 88, 90]. For constant deposition rates, top surface temperatures rise to a maximum which is less than the spray temperature. For a sufficiently long spraying time, a steady maximum temperature will be attained at the surface, [43]. Grant and Cantor, [45], argue that in this situation conduction into the deposit can be ignored, and produce an equation for the steady top surface temperature.

Newtonian cooling at the collector-deposit interface is assumed universally in published work. Heat transfer coefficients here are of order $1000 - 3000\ W/m^2/°C$. When deposition stops, cooling is mainly dominated by the collector. This is due mainly to the thinness of deposits modelled, (i.e. usually much less than 10cm thick). Changes in both the deposition rate and the spray enthalpy are both shown to have significant effects on the computed solidification times, e.g. [49, 50]. These parameters both effect the total heat in the spray which must be extracted by the collector and atomising gas cooling effects.

Numerical algorithms used to solve the one dimensional equations are usually based on standard explicit finite difference methods, (except [43], which uses an implicit method). A variety of methods are used to cope with the moving boundary. These are discussed further in chapter seven.

Two dimensional results have been computed by Mathur *et al.* inside small discs, [89]. However, the model used to predict the disc geometry is that described in the previous section. This model does not conserve mass at the deposit surface, and therefore does not conserve heat either. From [89] and the literature cited therein, it is not possible to ascertain whether the heat flow computations are properly two dimensional or are one dimensional, nor is it possible to ascertain any details of the numerical algorithm used. Further comments are made in chapter seven.

1.3 Project overview

Research in this thesis was carried out by the author during 1990-1993 as part of a collaborative "Teaching Company Scheme" project[11] run jointly between the Oxford Centre for Advanced Materials and Composites, in the Departments of Engineering Science and Materials at Oxford University, and the Cospray division of Alcan International Limited, at Banbury. Cospray produce spray-formed aluminium alloy billets for commercial purposes. Cospray's original (research and development) plant was supplied by Osprey Metals in 1986, and a larger, modified production unit was commissioned in May 1988.

The main project aims were to apply advanced control engineering and metallurgical expertise to improve recovery rates. The mathematical modelling part of the project, which is described in this thesis, was thus

[11] Teaching company scheme grant number GR/F/12006

motivated by the needs of both disciplines for greater understanding of the process.

- Improved recovery rates can result from a reduction in the amount of material that is wasted, on each billet produced, that is of sufficient quality to sell.
- Improved recovery rates can also result from increasing the percentage of billets produced that are of sufficient quality to sell.

Each of these objective ways of improving recovery can generate different demands for mathematical analyses. Meeting the first objective is better suited to control engineering methods, whilst meeting the second objective requires an understanding of the process metallurgical issues.

The research in this thesis is concerned primarily with billet growth and billet solidification. This choice is partly motivated by the lack of research in these areas within the literature, partly by the project aims outlined above, and partly by personal taste. The project aims influence not only the choice of the area in which this research is carried out, but also the approach which has been taken and the results derived from the analysis.

1.3.1 Thesis outline

The thesis presents its analysis in six main chapters; chapters two to four are concerned with billet growth and chapters five to seven are concerned with billet solidification. Each of these chapters ends with a brief summary, outlining the main points of the chapter. In chapter eight the whole thesis is summarised; the main results of the research are presented and suggestions for further work are made.

- Chapter two derives model equations governing three dimensional billet growth. An averaging method is applied to the model equations. Under appropriate assumptions, the validity of the method is demonstrated for a class of billet surfaces. The solution of the resulting averaged equations forms an asymptotic approximation to the solution of the full equations, valid uniformly over the length of the modelled production run.

  The averaged equations are two dimensional. Conditions are derived under which there exists a unique steady state billet crown shape for a given ratio of withdrawal rate to mass flow rate. The stability of steady states is investigated, and a stability theorem proven. The chapter concludes with a discussion of the likely alternative dynamics that are possible when these conditions are not met.

- Chapter three presents a numerical method for computing steady state billet crown shapes. The computed results confirm the analytic results of chapter two. For a fixed angle spray, (i.e. no scanning motion), variations in steady state dynamics with spraying angle and with spray cone radius are investigated numerically. For a sinusoidal scanning motion, and for a more realistic scanning motion, the effect of increasing the scanning range of the atomiser is studied. The possible multiple existence of steady state crown shapes, at the same ratio of withdrawal rate to mass flow rate, is demonstrated computationally. An optimisation method is developed that allows the design of scanning angle motions for which there can be only one steady state crown shape for any one ratio of withdrawal rate to mass flow rate.

- Chapter four presents a method for computing transient motions of the billet surface. The computational solution method is applied to the problem of determining a suitable initial strategy for controlling billet growth. Results are also presented of simulating a production run using the model, and are compared with measurements taken during the run. This provides some validation for the model. A study is made of the generic transient surface motion between steady state crown shapes. Results are also presented of a numerical simulation of hysteresis between two coexisting steady states.

- Chapter five derives field equations and boundary conditions for the heat flow occurring within the growing billet. Relevant non-dimensional groups are discussed. A boundary layer approximation is derived for rapidly varying heat flow, close to the billet surface. Averaged equations are also derived, modelling the more macroscopic heat fluxes within the bulk of the billet

- Chapter six describes the computational algorithm used for solution of the boundary layer approximation. Results are presented demonstrating the effects of varying both billet shape and the rotation/scanner frequency on the transient boundary layer heat flow.

- Chapter seven presents an efficient and robust computational algorithm for solution of the averaged heat flow equations. The flexibility of the algorithm for computing heat flow within irregularly shaped billets, and with sharp variations in process parameters, is demonstrated. The initial strategy for billet growth, (investigated in chapter four), is re-examined in the context of the heat flow occurring. Computations are also carried out over a longer time period. These computations strongly suggest that a thermal, billet crown steady state is approached following the convergence of the crown geometry to a steady state shape, and when the billet crown has grown sufficiently far from the influence of the collector.

1.3.2 Main contributions of the thesis

- The derivation of mathematical equations describing a novel industrial process.

- Incorporation of surface shadowing effects in the derivation of mass conservation equations, describing the movement of the billet surface.

- The application of an averaging method to the billet growth equations, and consequent derivation, for a class of billet surfaces, of an asymptotically valid two dimensional approximation to the three dimensional billet growth.

- The analysis of the averaged equations, to demonstrate necessary conditions for the existence of a unique steady state billet crown shape. An exploration of the stability of the unique steady state. Presentation of computational results confirming the analytical results, and indicating the effects on both steady state geometry and stability of varying different model process parameters. In particular, identification of the ratio of withdrawal rate to mass flow rate as a critical parameter in determining growth dynamics of the averaged equations.

- Computation of transient solutions of the averaged equations of motion for the billet surface. Results showing generic billet surface motion in response to a change in the ratio of withdrawal rate to mass flow rate.

- Identification of the possibility, under certain conditions, of the coexistence of stable steady state crown shapes. When multiple steady states coexist, identification of the possibility of hysteresis in the transient billet motions. Computational results both confirming the coexistence of steady states, and showing an idealised case of hysteresis between steady states. Derivation of an optimisation method for scanner angle design, so as to ensure the uniqueness of steady state billet crown shapes that exist at any given ratio of withdrawal rate to mass flow rate.

- Derivation of a boundary layer approximation to describe rapid transient surface movement occurring during deposition at a point on the surface, and the related heat flow occurring just beneath the billet surface. For typical process parameters it is shown that cooling rates of up to $\sim 10^3$ °C/s may be found in the boundary layer.

- Results showing the possible critical effect of changes in surface shape and in rotation/scanner frequencies on the rapid solidification occurring in the boundary layer. Typical radial variations in solidification behaviour are discussed, as is the interaction between scanner and rotational movements.

- Derivation of averaged equations describing the solidification of the billet bulk and development of an efficient and robust computational algorithm for the solution of these equations.

- Investigation of the effects of choosing different idealised control strategies for the initial part of a production run, considering both thermal and geometric variations.

- Identification of the likelihood of thermal steady states existing during (geometric) steady state billet production.

The thesis is biased towards the derivation of models for billet growth and solidification within a unified framework that emphasises and exploits the different length and time scales present in the process, and also towards the analysis and computational solution of these models. It is not the aim of the thesis to present parametric studies of process variations. Instead the thesis aims to provide the tools with which such studies might economically be carried out, and to provide non-exhaustive examples demonstrating the applicability of the models to a variety of investigative tasks. Computational efficiency of the numerical methods employed is reflected by the fact that even the most computationally intensive model, (that describing solidification of the growing billet), is able to run in "real-time" on a 35MIP, dual processor, DEC VAX 6000/620 computer. This lies within the processing power range of currently available, (and affordable), workstations. It is hoped that these features will make the models and analysis of value to both process metallurgists and control engineers.

Chapter 2

Mathematical Modelling of Billet Growth

The layout of this chapter is as follows. Section one introduces the different frames of reference that are used throughout the thesis. Approximate equations are derived describing conservation of mass, both within the spray and at the billet surface. Section two introduces the averaging method, and applies it to the mass conservation equations. Section three analyses the averaged equations, deriving various results concerning steady state billet crown shapes and associated dynamics. A summary is presented in section four.

In the thesis dimensional quantities $\bullet$ are differentiated from their non-dimensional counterparts by a hat, i.e. $\hat{\bullet}$. Vector quantities are denoted in bold print, i.e. $\boldsymbol{x}$. Other notation is introduced en-route.

2.1 Formulation

Molten metal spray travels rapidly from an atomiser towards a flat-topped cylindrical collector of radius $\hat{r}_c$. At time $\hat{t} \geq 0$ the collector rotates about a vertical axis with angular velocity $\hat{\omega}(\hat{t})$ and is withdrawn vertically downwards with speed $\hat{U}(\hat{t})$. The initial vertical displacement of the collector top below the atomiser nozzle is denoted $\hat{z}_n$ and the radial distance of the atomiser nozzle from the collector axis of rotation is denoted $\hat{r}_n$.

Infra-red photography reveals that the molten spray remains largely confined within a narrow and slightly diverging cone. Spraying directly onto a flat aluminium plate positioned perpendicular to the spray cone reveals that mass is distributed approximately axisymmetrically about the cone axis and decreases monotonically from centre to edge. The spray cone axis is angled radially inwards towards the collector axis of rotation, at an angle $a(\hat{t})$ with the vertical, and is scanned to generate a required distribution of the spray. The unit vector oscillating in the direction of the spray cone axis is denoted by $\boldsymbol{k}'(\hat{t})$. This geometry is illustrated in Fig. 2.1.

It can be assumed that $\hat{U}(\hat{t}) \geq 0$, that $a(\hat{t})$ is bounded and periodic, (say $a(\hat{t}) \in [a_1, a_2] \subset [0, \pi/2]$), and that both functions are C^∞. The angular velocity $\hat{\omega}(\hat{t})$ will normally be kept constant throughout the process.

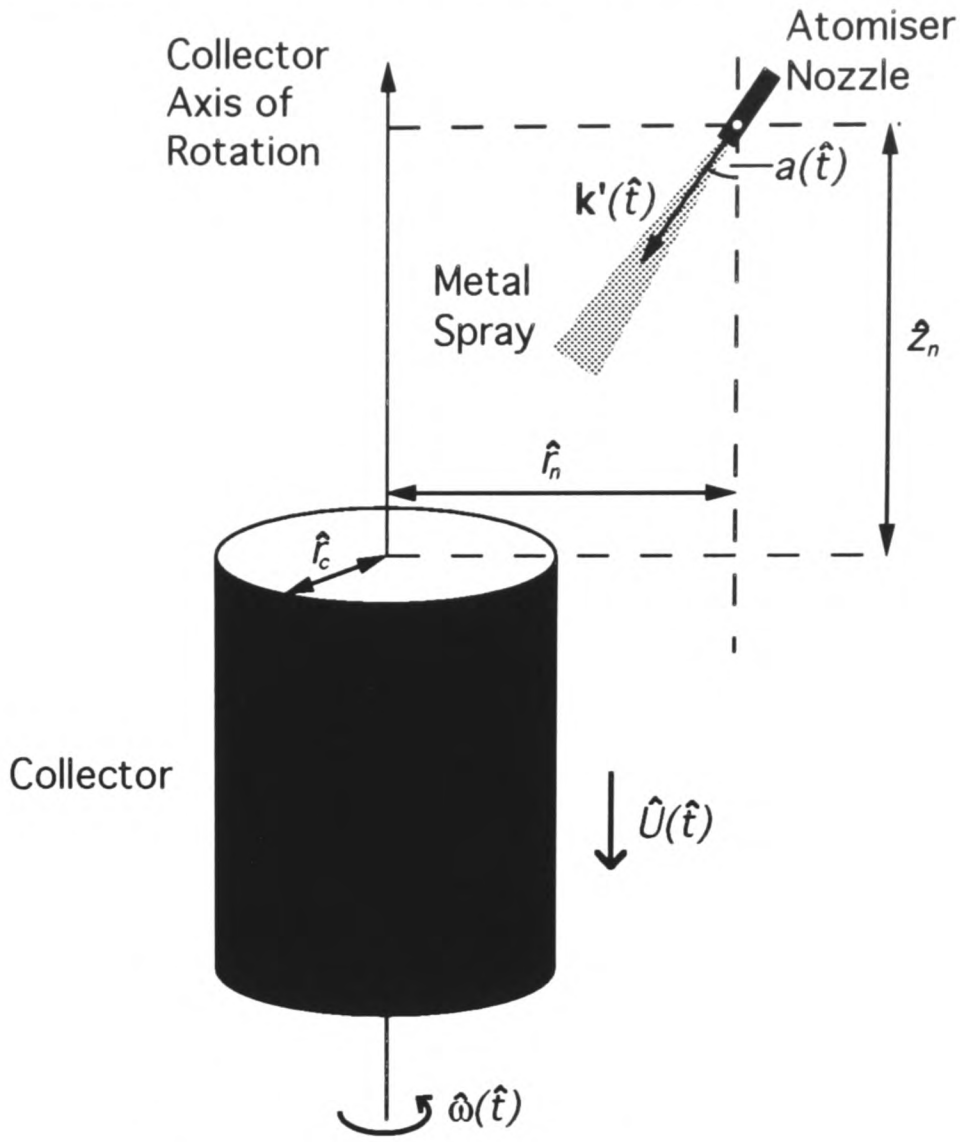

Figure 2.1: Process motions and geometry.

In addition to the fixed **global** frame of reference three more frames of reference are needed in order to clearly describe the process, (see Fig. 2.2).

- Firstly, a **spray** frame of reference is defined, with origin fixed at the atomiser nozzle and which oscillates with the spray cone axis. Within this frame of reference a cylindrical polar coordinate system will be used; $\boldsymbol{x}' = (\hat{r}', \theta', \hat{z}')$, with $\hat{z}' > 0$ measuring distance in the direction of the vector $\boldsymbol{k}'(\hat{t})$.

  A nominal **spray cone radius**, $\hat{r}_s$, is defined to be the radial distance from the spray cone axis within which 95% of the mass is contained. Clearly, in reality $\hat{r}_s$ varies with distance from the atomiser, since the cone diverges. However, the spray cone is not strictly conical, (more "plume" shaped), and its apex is hard to define precisely due to the spray ring atomiser geometry. Additionally, divergence of the spray cone radius at a typical flight distance between the atomiser and billet surface is only slight, e.g.

$$\frac{\mathrm{d}\hat{r}_s}{\mathrm{d}z'} \approx \frac{1}{17}.$$

  Thus, for the model the spray cone radius is defined as above, but at a fixed distance, $\hat{z}' = D_F$, from the atomiser, i.e. in the model $\hat{r}_s$ is assumed not to vary with z'. Here D_F denotes a typical flight distance for the spray, between atomiser and billet surface.

  The line that passes through the point that is displaced a distance $\hat{r}_s/\sin a_1$ below the atomiser nozzle, and which runs parallel to the spray cone axis when $a(\hat{t}) = a_1$, is called the **lower spray boundary**. Similarly, the line that passes through the point that is displaced a distance $\hat{r}_s/\sin a_2$ above the atomiser nozzle, and which runs parallel to the spray cone axis when $a(\hat{t}) = a_2$, is called the **upper**

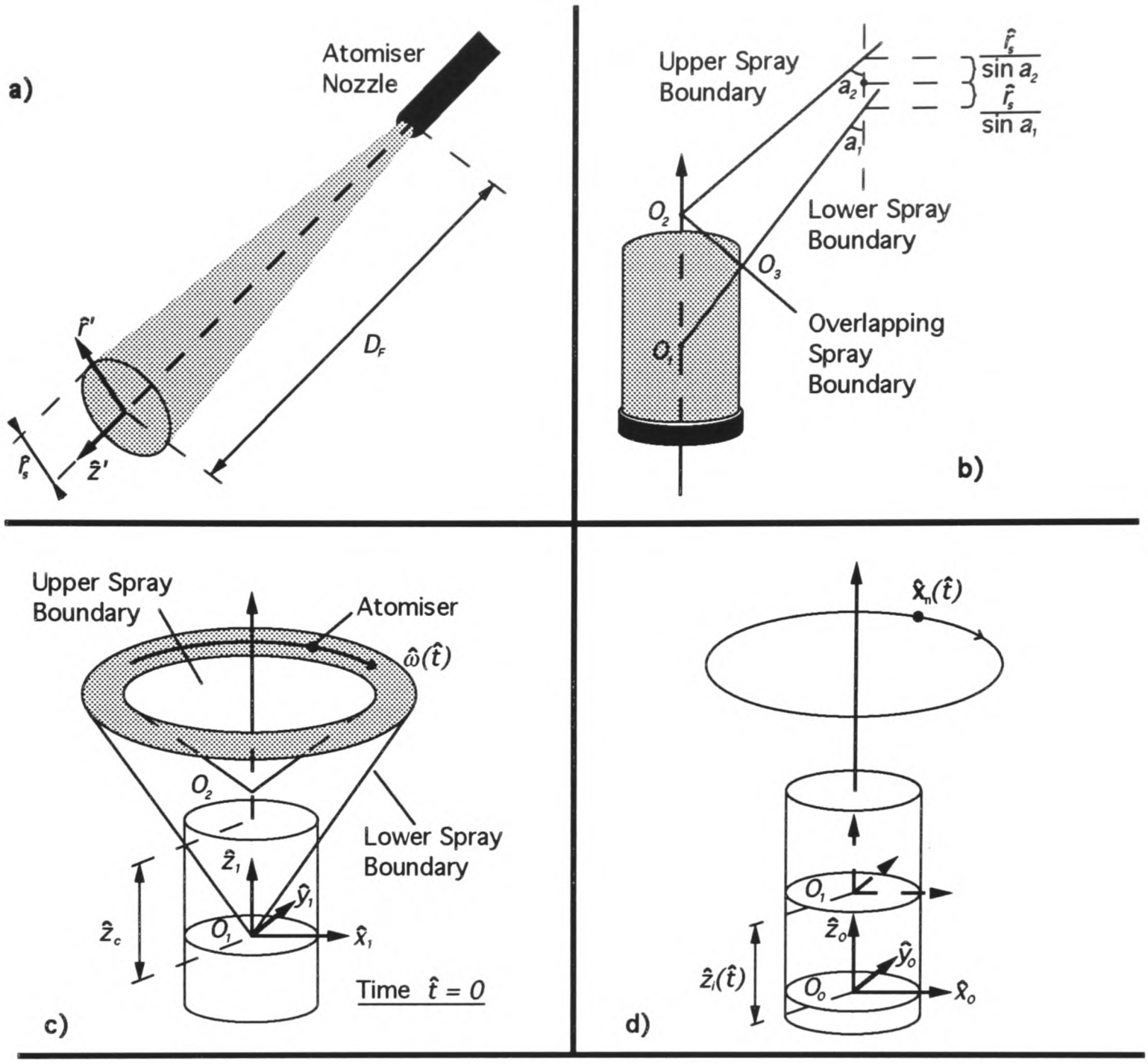

Figure 2.2: Frames of reference: a) position, $\boldsymbol{x}'$, in the cylindrical spray coordinate system, b) spray boundaries, c) position, $\boldsymbol{x}_1$, in the crown frame of reference, d) position, $\boldsymbol{x}_0$, in the billet frame of reference.

spray boundary. The two points on the collector axis of rotation where the lower and upper spray boundaries cross are denoted by O_1 and O_2 respectively. Extending the upper spray boundary beyond O_2, and reflecting through π radians about the axis of rotation produces the **overlapping spray boundary**. The overlapping spray boundary intersects the lower spray boundary at the point O_3.

- A second, **crown** frame of reference is defined with origin at O_1, and which rotates about the collector axis of rotation with angular velocity $\hat{\omega}(\hat{t})$. Since very little metal spray will pass below O_1 on the axis of rotation, the top surface of the collector will initially be positioned above O_1 and this displacement is denoted by $\hat{z}_c$ (> 0). In the crown frame of reference the loci of the lower, upper (and overlapping) spray boundaries are cones; bounding the regions within which deposition takes place.

- Thirdly, a **billet** frame of reference is defined, with origin O_0 that is displaced a distance $\hat{z}_i(\hat{t})$ below O_1 on the axis of rotation, where

$$\hat{z}_i(\hat{t}) \equiv \int_0^{\hat{t}} \hat{U}(s)ds. \tag{2.1}$$

The billet frame of reference also rotates with the collector angular velocity $\hat{\omega}(\hat{t})$, and since $\hat{z}_i(0) = 0$

it can be seen that the crown and billet frames of reference coincide at $\hat{t} = 0$.

The three frames of reference and other geometry are illustrated in Fig. 2.2. The convention is adopted, of denoting coordinates in the billet and in the crown frames of reference by the subscripts 0 and 1 respectively, whenever confusion might arise. Transformations between coordinate systems are listed in Appendix A.

In terms of a cartesian coordinate system fixed within the billet frame of reference the atomiser nozzle has position $\hat{\boldsymbol{x}}_{n,0}(\hat{t})$ given by

$$\hat{\boldsymbol{x}}_{n,0}(\hat{t}) \equiv (\hat{r}_n \cos\phi_n(\hat{t}), -\hat{r}_n \sin\phi_n(\hat{t}), \hat{z}_n + \hat{z}_c + \hat{z}_i(\hat{t})), \tag{2.2}$$

where

$$\phi_n(\hat{t}) = \int_0^{\hat{t}} \hat{\omega}(s)ds, \tag{2.3}$$

whilst in the crown frame of reference the atomiser nozzle has position $\hat{\boldsymbol{x}}_{n,1}(\hat{t})$ given by

$$\hat{\boldsymbol{x}}_{n,1}(\hat{t}) \equiv (\hat{r}_n \cos\phi_n(\hat{t}), -\hat{r}_n \sin\phi_n(\hat{t}), \hat{z}_n + \hat{z}_c). \tag{2.4}$$

2.1.1 Mass Flux Characterisation

A vector field $\hat{\boldsymbol{G}}$ is defined representing the mass flux due to the metal phase in the spray, relative to the global frame of reference, (i.e. $\hat{\boldsymbol{G}}(\hat{\boldsymbol{x}}, \hat{t})$ is the mass flux at $(\hat{\boldsymbol{x}}, \hat{t})$ assuming that no spray directed towards $\hat{\boldsymbol{x}}$ has been obstructed en-route). It is assumed that the spray may be approximated as a continuum. More specifically, it is assumed that differentiable functions, $\hat{\rho}_s(\boldsymbol{x}, t)$ and $\hat{\boldsymbol{V}}(\boldsymbol{x}, t)$, can be defined such that

$$\hat{\rho}_s(\boldsymbol{x}, t) \approx \frac{1}{\|S_{\boldsymbol{x}}\|T} \int_{t-T/2}^{t+T/2} \sum_{j=1}^{N(\tau, S_{\boldsymbol{x}})} \hat{m}_j(\tau, S_{\boldsymbol{x}})\, \mathrm{d}\tau, \tag{2.5}$$

$$\hat{\boldsymbol{V}}(\boldsymbol{x}, t) \approx \frac{\int_{t-T/2}^{t+T/2} \sum_{j=1}^{N(\tau, S_{\boldsymbol{x}})} \hat{m}_j(\tau, S_{\boldsymbol{x}}) \hat{\boldsymbol{v}}_j(\tau, S_{\boldsymbol{x}})\, \mathrm{d}\tau}{\int_{t-T/2}^{t+T/2} \sum_{j=1}^{N(\tau, S_{\boldsymbol{x}})} \hat{m}_j(\tau, S_{\boldsymbol{x}})\, \mathrm{d}\tau}, \tag{2.6}$$

uniformly within the spray chamber. In equations (2.5) and (2.6), $S_{\boldsymbol{x}}$ is a small sphere surrounding $\boldsymbol{x}$, $N(\tau, S_{\boldsymbol{x}})$ is the number of droplets having some part of their volume within $S_{\boldsymbol{x}}$ at time $t = \tau$, $\hat{m}_j(\tau, S_{\boldsymbol{x}})$ and $\hat{\boldsymbol{v}}_j(\tau, S_{\boldsymbol{x}})$ are respectively the mass of the jth droplet within $S_{\boldsymbol{x}}$ and the velocity of the jth droplet. It is assumed that T and the length-scale characterising $S_{\boldsymbol{x}}$ are an order of magnitude smaller than other time and length-scales appearing subsequently.

The functions $\hat{\rho}_s(\boldsymbol{x}, t)$ and $\hat{\boldsymbol{V}}(\boldsymbol{x}, t)$ are called the **spray density** and the **spray velocity** respectively. The spray mass flux field, $\hat{\boldsymbol{G}}(\hat{\boldsymbol{x}}, \hat{t})$, may be written as

$$\hat{\boldsymbol{G}}(\hat{\boldsymbol{x}}, \hat{t}) = \hat{\rho}_s(\hat{\boldsymbol{x}}, \hat{t})\hat{\boldsymbol{V}}(\hat{\boldsymbol{x}}, \hat{t}). \tag{2.7}$$

Conservation of mass within the spray is described by

$$\frac{\partial \hat{\rho}_s}{\partial \hat{t}} = -\hat{\boldsymbol{\nabla}}.\hat{\boldsymbol{G}}. \tag{2.8}$$

Approximation of the functions $\hat{\rho}_s(\boldsymbol{x}, t)$ and $\hat{\boldsymbol{V}}(\boldsymbol{x}, t)$ through equations (2.5) and (2.6) requires the computation of individual droplet trajectories by the methods discussed in chapter one. Apart from being very

expensive computationally, such methods will not succeed in relating the characteristics of the mass flux field to the process variables in any easily defined way. Instead, the following form is assumed for $\hat{\boldsymbol{G}}(\hat{\boldsymbol{x}}, \hat{t})$.

$$\hat{\boldsymbol{G}}(\hat{\boldsymbol{x}}, \hat{t}) = \hat{\dot{M}}(\hat{t})\hat{g}(\hat{r}'[\hat{\boldsymbol{x}}, \hat{t}])\boldsymbol{k}'(\hat{t}) + O(\hat{\boldsymbol{\xi}}_1). \tag{2.9}$$

In equation (2.9) $\hat{\dot{M}}(\hat{t})$ is the total metal mass flow rate into the atomiser. The function $\hat{g}(\hat{r}')$ is a distribution function; $\hat{g}(\hat{r}')$ will be a monotonically decreasing function of $\hat{r}' > 0$ which may be assumed to be C^∞ and will satisfy

$$\hat{g}(\hat{r}') = 0, \qquad \hat{r}' \geq \hat{r}_s, \tag{2.10}$$

for spray cone radius, $\hat{r}_s$, as defined earlier.

Later, in deriving the model equations, the approximation

$$\hat{\boldsymbol{G}}(\hat{\boldsymbol{x}}, \hat{t}) \approx \hat{\dot{M}}(\hat{t})\hat{g}(\hat{r}'[\hat{\boldsymbol{x}}, \hat{t}])\boldsymbol{k}'(\hat{t}), \tag{2.11}$$

will be made. This approximation assumes that the mass flux may be characterised by a spray that is distributed axisymmetrically about the spray cone axis and travels parallel to the spray cone axis. The mass flux is assumed to be non-zero only within a fixed radial distance, $\hat{r}_s$, of the spray cone axis at any time, see Fig. 2.3. The mass flux approximation (2.11) is similar to that made in [87]. The narrowly diverging spray cone of turbulent gas and molten metal droplets has been replaced with a specified smooth cylindrical mass flux field. The axis of the cylinder oscillates as did the spray cone, and the radius of the cylinder is representative of that of the spray cone at a typical flight distance between atomiser and billet surface. All approximation error is contained in the $O(\hat{\boldsymbol{\zeta}}_1)$ term in (2.9), which is assumed uniformly bounded in time and on any closed domain. Contributions to this error term include the following.

1. Stochastic errors associated with the continuum approximation of the discrete spray mass flux field through (2.5) and (2.6).

2. Small errors resulting from asymmetry of the mass flux field within the spray cone, and from there being in reality a small non-zero mass flux outside the spray cone radius, (which has been rather arbitrarily defined).

3. Errors associated with the fact that the spray cone radius will depend upon $\hat{z}'$, due to the spray diverging slightly.

4. Errors resulting from variation in the distribution $\hat{g}$ due to changes in $\hat{\dot{M}}(\hat{t})$, which has been disallowed in (2.9).

These errors are hard to quantify, but will be assumed to be small. Spraying on to a flat plate held perpendicular to the spray cone axis, (as in [87]), has shown the mass flux to be approximately axisymmetrically distributed. When the variation in flight distances experienced at different points on the billet surface is small, errors in 3 above will also be small, due to the only slight divergence of the spray cone. Although variation in $\hat{g}$ is likely with the atomising conditions, it will be assumed that this dependency is weak. Typically the mass flow rate, $\hat{\dot{M}}(\hat{t})$, is kept fairly static throughout the process.

Aside from computational ease, the benefits of this characterisation of the mass flux arise from including directly, (although in a simplistic way), the effects of

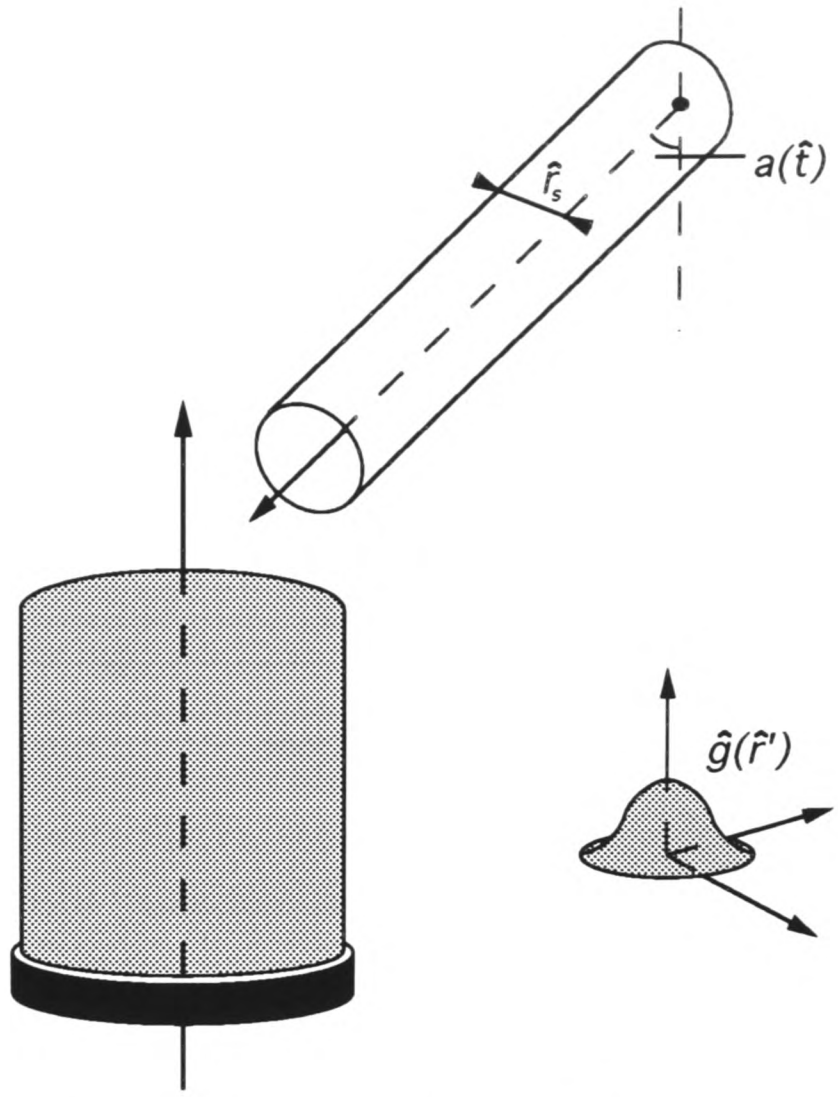

Figure 2.3: Spray characterisation

- the mass distribution within the spray cone,
- the scanning motion of the spray cone, and
- variations in the mass flow rate through the atomiser.

This latter inclusion puts a constraint on the function $\hat{g}$. Conservation of mass flowing through the atomiser is represented by

$$2\pi \int_0^{\hat{r}_s} \hat{r}' \hat{g}(\hat{r}') d\hat{r}' = 1. \tag{2.12}$$

2.1.2 Surface Motion

Denote by $\hat{\Omega}(\hat{t})$ the volume occupied by the billet at time $\hat{t}$, and by $\partial\hat{\Omega}(\hat{t})$ the billet surface. At time $\hat{t}$ the position of the billet surface is given by

$$\partial\hat{\Omega}(\hat{t}) = \{\hat{\boldsymbol{x}}_0 \in \mathcal{R}^3 : \hat{F}(\hat{\boldsymbol{x}}_0, \hat{t}) = 0\}, \tag{2.13}$$

where $\hat{\boldsymbol{x}}_0$ denotes position in the billet frame of reference. The function $\hat{F}$ is chosen so that $\hat{\nabla}\hat{F}$ is pointing in the direction of the outward normal to $\partial\hat{\Omega}(\hat{t})$.

Initial conditions for $\hat{F}$, in the billet frame of reference, are given in cylindrical polar coordinates by the initial position and size of the collector. These are

$$\hat{F}(\hat{\boldsymbol{x}}_0, 0) = \left\{ \begin{array}{ll} \hat{z}_0 - \hat{z}_c, & 0 \le \hat{r}_0 \le \hat{r}_c \\ \hat{r}_0 - \hat{r}_c, & 0 \le \hat{z}_0 \le \hat{z}_c \end{array} \right\}. \tag{2.14}$$

At time $\hat{t}$ a point $P \in \partial\hat{\Omega}(\hat{t})$ is moving relative to the collector and in the outward normal direction with speed $\hat{v}_P$ given by

$$\hat{v}_P = -\frac{\partial \hat{F}}{\partial \hat{t}} |\hat{\nabla}\hat{F}|^{-1}. \tag{2.15}$$

Hence, the rate at which material of constant density ρ flows inwards across a small surface element $\partial\hat{A} \subset \partial\hat{\Omega}(\hat{t})$ and is added to the billet is

$$-\int_{\partial\hat{A}} \rho \frac{\partial \hat{F}}{\partial \hat{t}} |\hat{\nabla}\hat{F}|^{-1} \mathrm{d}s. \tag{2.16}$$

Movement of the billet surface described in (2.16) is due solely to deposition from the spray. The rate at which mass flows inwards across $\partial\hat{A}$ is

$$-\int_{\partial\hat{A}} \hat{\boldsymbol{G}}_0 . \boldsymbol{n} \mathrm{d}s, \tag{2.17}$$

where $\hat{\boldsymbol{G}}_0$ is the spray mass flux field, *relative to the billet frame of reference*, and $\boldsymbol{n}$ defined by

$$\boldsymbol{n} = \hat{\boldsymbol{\nabla}}\hat{F} |\hat{\boldsymbol{\nabla}}\hat{F}|^{-1}, \tag{2.18}$$

is the outward unit normal vector to $\partial\hat{\Omega}(\hat{t})$. All quantities have been evaluated on the billet surface.

The spray mass flux field in the billet frame of reference, $\hat{\boldsymbol{G}}_0$, is related to the spray mass flux field in the global frame of reference, $\hat{\boldsymbol{G}}$, by

$$\begin{aligned} \hat{\boldsymbol{G}}_0(\hat{\boldsymbol{x}}_0, \hat{t}) &= \hat{\boldsymbol{G}}(\hat{\boldsymbol{x}}[\hat{\boldsymbol{x}}_0, \hat{t}], \hat{t}) + \hat{\rho}_s(\hat{\boldsymbol{x}}[\hat{\boldsymbol{x}}_0, \hat{t}], \hat{t}) \hat{\boldsymbol{V}}_0(\hat{t}), \\ &= \hat{\rho}_s(\hat{\boldsymbol{x}}[\hat{\boldsymbol{x}}_0, \hat{t}], \hat{t}) [\hat{\boldsymbol{V}}(\hat{\boldsymbol{x}}_0, \hat{t}) + \hat{\boldsymbol{V}}_0(\hat{t})], \end{aligned} \tag{2.19}$$

where

$$\begin{aligned} \hat{\boldsymbol{V}}_0(\hat{t}) &\equiv (\hat{V}_{\hat{x}_0}, \hat{V}_{\hat{y}_0}, \hat{V}_{\hat{z}_0}), \\ &= (-\hat{\omega}(\hat{t})\hat{r}_n \sin\phi_n(\hat{t}), -\hat{\omega}(\hat{t})\hat{r}_n \cos\phi_n(\hat{t}), \hat{U}(\hat{t})). \end{aligned} \tag{2.20}$$

Assuming that all spray passing through $\partial\hat{A}$ "sticks where it hits", and neglecting the slight shrinkage that will occur during solidification, mass conservation implies the equality of (2.16) and (2.17). This will describe surface movement during 100% efficient deposition and in the absence of shadowing effects.

Sticking efficiency and shadowing

In reality 100% efficiency is never achieved. Apart from the possibility of mass redistribution on the billet surface due to fluid flow, it is also likely that firstly, some spray will not reach the billet surface due to the turbulent nature of the chamber gas flow, and secondly, that some spray reaching the billet surface will not stick. Local "sticking efficiencies" will depend upon the local gas flow, the spray droplet size distribution, the surface geometry, and the temperature of both billet and spray (see the discussion in chapter one).

These effects are not well understood, due mainly to the interaction of many different complex physical processes, and no attempt will be made to model them here. Mean sticking efficiencies, averaged over the length of the process, can vary between 60% and 90%, [104], and it will be assumed that local spatial and temporal variations about this mean are small.

Shadowing introduces nonlinearity into the problem. The mass flux reaching a point P on the billet surface depends not only on the position of P relative to O_0, but can also depend critically on the intervening surface profile, as is illustrated in Fig. 2.4.

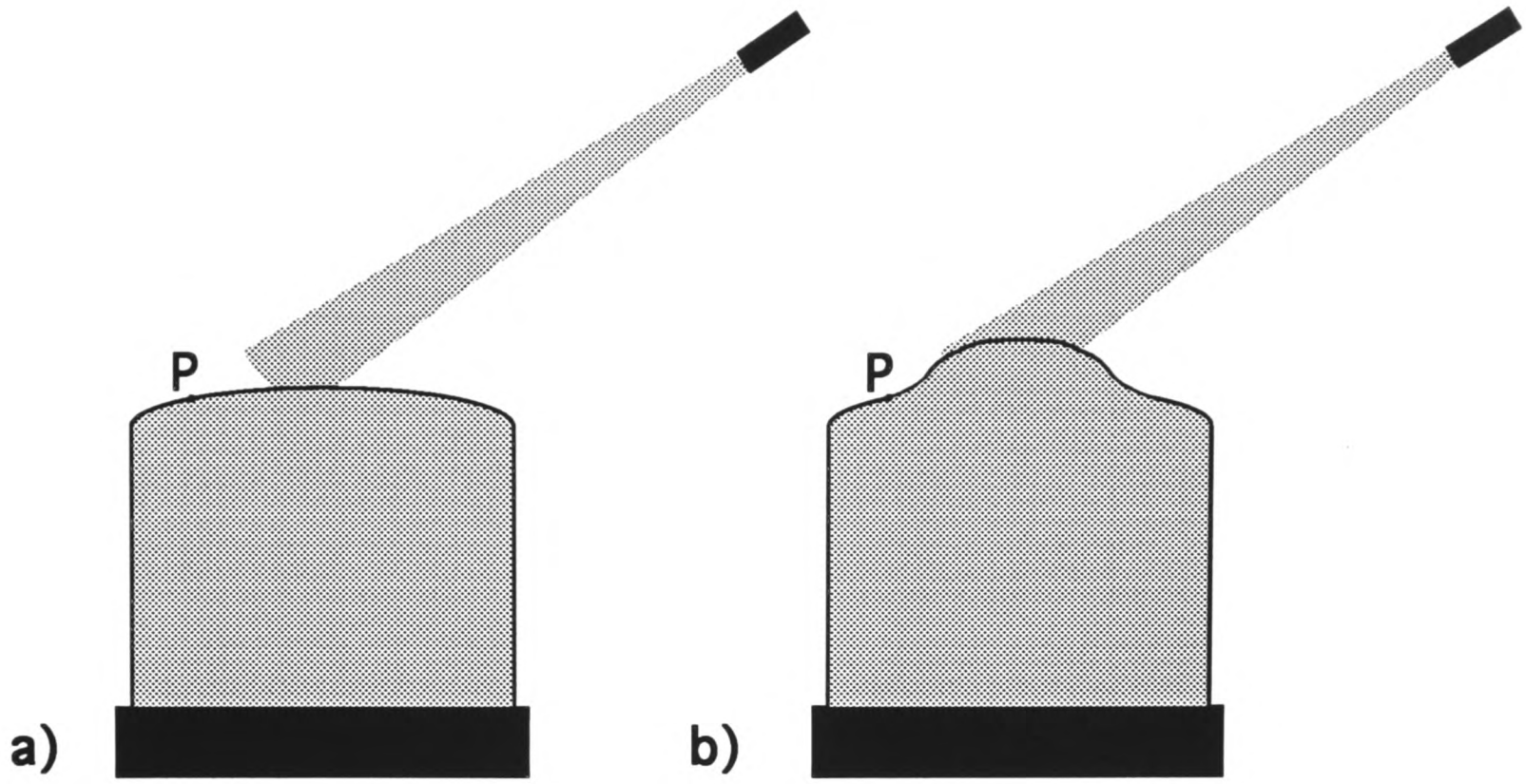

Figure 2.4: Nonlinearity due to surface shadowing

Two main ways in which shadowing occurs can be identified.

- Firstly, billet rotation means that there may be regions on the billet surface, (e.g. opposite the atomiser nozzle), within which

$$\hat{G}_0.\boldsymbol{n} > 0, \tag{2.21}$$

but which only border other surface regions for which $\hat{G}_0.\boldsymbol{n} \leq 0$ and within which there is no shadowing. This type of shadowing is called type A shadowing. Regions where it occurs may be identified through (2.21). It will occur mainly on the billet sides, (see Fig. 2.5a), but can also occur on the billet crown.

- A second, more complicated type of shadowing is depicted in Fig. 2.5b. This type of shadowing is called type B shadowing. Here, previous growth at points such as P_1 has shadowed the mass flux from points such as P_2 and P_3. In this case (2.21) is satisfied by some points in the shadowed region, (e.g. P_2), but not by all points, (e.g. P_3). Thus, regions within which (2.21) holds are now surrounded by other surface regions within which $\hat{G}_0.\boldsymbol{n} \leq 0$, as before, but within which shadowing may now occur.

To account for both shadowing and sticking efficiency phenomena a function $\hat{\Gamma}$ is introduced, which takes values in $[0, 1]$ according to the amount of spray arriving at each point and the proportion of it which sticks. A complete description of surface movement is then provided by

$$\int_{\partial \hat{A}} \rho \frac{\partial \hat{F}}{\partial \hat{t}} |\hat{\boldsymbol{\nabla}} \hat{F}|^{-1} \mathrm{d}s = \int_{\partial \hat{A}} |\hat{\boldsymbol{\nabla}} \hat{F}|^{-1} \hat{\Gamma} \hat{G}_0.\hat{\boldsymbol{\nabla}} \hat{F} \mathrm{d}s. \tag{2.22}$$

The mass flux $\hat{G}_0$ will be nonzero only within a tight cone of metal spray at any one time, and has been assumed to be smooth. Where shadowing occurs on the billet surface $\hat{\Gamma}$ must change to zero from an otherwise positive value. If the shadowing is of type A, then $\hat{G}_0.\boldsymbol{n}$ will also approach zero at the boundary

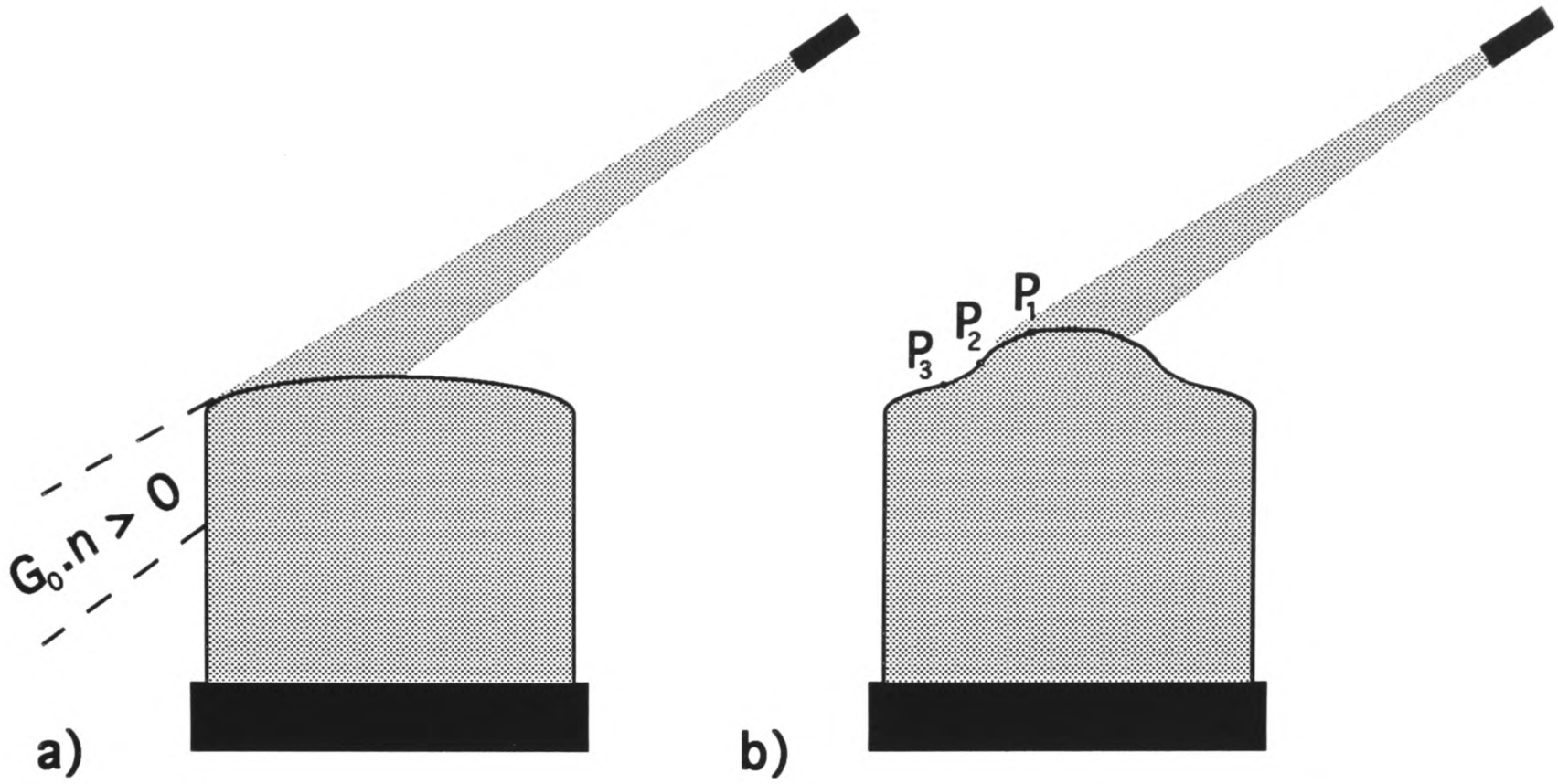

Figure 2.5: Type A and type B shadowing

of a shadowed region, but smoothly. Hence, when the jump in $\hat{\Gamma}$ takes place on the boundary of a type A shadowed region, smoothness of the integrand on the right-hand side of (2.22) is preserved and

$$\rho \frac{\partial \hat{F}}{\partial \hat{t}} = \hat{\Gamma} \hat{\boldsymbol{G}}_0 . \hat{\boldsymbol{\nabla}} \hat{F} \qquad \hat{\boldsymbol{x}} \in \partial \hat{A}. \tag{2.23}$$

Assuming that outside of shadowed regions $\hat{\Gamma}$ varies smoothly with the local physical conditions discussed earlier then $\hat{F}$ will remain as smooth as its initial conditions, (at least locally), as has been implicit in the formulation.

In contrast, type B shadowing does not require that $\hat{\boldsymbol{G}}_0 . \boldsymbol{n}$ tend to zero at the boundaries of shadowed regions. A jump in $\hat{\Gamma}$ leads to a discontinuous surface deposition rate and a non-smooth surface profile, $\hat{F}$. Only the weak formulation, (2.22), will be valid in this case. The "shock" phenomena resulting from type B shadowing have many physical parallels and are of some mathematical interest. Fortunately, they are rarely observed in practice, and it will be assumed for the remainder of this thesis that only type A shadowing occurs.

Under this assumption, surface movement is determined by

$$\rho \frac{\partial \hat{F}}{\partial \hat{t}} = \hat{\Gamma} \hat{\boldsymbol{G}}_0 . \hat{\boldsymbol{\nabla}} \hat{F}, \qquad \hat{\boldsymbol{x}}_0 \in \partial \hat{\Omega}(\hat{t}). \tag{2.24}$$

2.1.3 Coordinate transformation and non-dimensionalisation

In producing long cylindrical billets the billet sides are withdrawn out of the spray region as the billet grows. Deposition occurs mostly at the top of the billet, and this becomes the main region of interest. Thus, whilst it has been convenient to characterise the mass flux field in the spray frame of reference, and to formulate

the equation of motion for the billet surface within the billet frame of reference, to analyse the dynamics of billet growth it is more sensible to look at surface movement relative to the crown frame of reference.

Equations (2.8) and (2.24), representing conservation of mass in the spray and at the billet surface respectively, transform to

$$\frac{\partial \hat{\rho}_s}{\partial \hat{t}} + \hat{\omega}(\hat{t})\hat{y}_1 \frac{\partial \hat{\rho}_s}{\partial \hat{x}_1} - \hat{\omega}(\hat{t})\hat{x}_1 \frac{\partial \hat{\rho}_s}{\partial \hat{y}_1} = -\hat{\boldsymbol{\nabla}}.\hat{\boldsymbol{G}}, \qquad \hat{\boldsymbol{x}}_1 \in \mathcal{R}^3 | \hat{\Omega}(\hat{t}), \tag{2.25}$$

$$\rho \left[\frac{\partial \hat{F}}{\partial \hat{t}} - \hat{U}(\hat{t}) \frac{\partial \hat{F}}{\partial \hat{z}_1} \right] = \hat{\Gamma} \hat{\boldsymbol{G}}_0 . \hat{\boldsymbol{\nabla}} \hat{F}, \qquad \hat{\boldsymbol{x}}_1 \in \partial \hat{\Omega}(\hat{t}). \tag{2.26}$$

Non-dimensional forms of (2.26) and (2.25) may be derived by introducing the following scaling

$$\begin{aligned}
\boldsymbol{x} &= \frac{\hat{\boldsymbol{x}}}{R}, & \dot{m}(t) &= \frac{\hat{\dot{M}}(\hat{t})}{\hat{\dot{M}}_0}, \\
t &= \frac{\hat{\omega}_0 \hat{t}}{2\pi}, & u(t) &= \frac{\hat{U}(\hat{t})}{\hat{U}_0}, \\
F(\boldsymbol{x}_1, t) &= \frac{\hat{F}(\hat{\boldsymbol{x}}_1, \hat{t})}{R}, & \omega(t) &= \frac{\hat{\omega}(\hat{t})}{\hat{\omega}_0}, \\
\boldsymbol{v}(\boldsymbol{x}, t) &= \frac{\hat{\boldsymbol{V}}(\hat{\boldsymbol{x}}, \hat{t})}{\overline{V}}, & \boldsymbol{G}(\boldsymbol{x}, t) &= \pi R^2 \frac{\hat{\boldsymbol{G}}(\hat{\boldsymbol{x}}, \hat{t})}{\hat{\dot{M}}_0}, \\
\rho_s &= \frac{\hat{\rho}_s}{\hat{\rho}_{s,0}}, & g(r') &= \pi R^2 \hat{g}(\hat{r}'), \\
\Gamma &= \frac{\hat{\Gamma}}{\overline{Y}}.
\end{aligned} \tag{2.27}$$

In (2.27), R is a length-scale, chosen to reflect the desired radius of the billet. Constants $\hat{\dot{M}}_0$ and $\overline{Y}$ respectively represent a typical mass flow rate and a typical average yield, ($\overline{Y} < 1$), for the process. Scalings $\hat{\omega}_0$ and $\overline{V}$ are a typical rotation rate and metal spray velocity for the process. The withdrawal velocity scale, $\hat{U}_0$, is defined by

$$\frac{\overline{Y} \hat{\dot{M}}_0}{\pi \rho \hat{U}_0 R^2} = 1, \tag{2.28}$$

which corresponds to the withdrawal velocity required to produce a perfectly cylindrical billet of radius R from a constant mass flow rate $\hat{\dot{M}}_0$. The control volume analysis leading to the mass balance (2.28) is due to Alexander, [3], see Fig. 2.6.

The mass flux field has been scaled with $\hat{\dot{M}}_0/\pi R^2$. This corresponds to scaling with a mass flux that is averaged over the top of a cylinder of radius R. Since the spray is in fact confined to a cone of radius $\hat{r}_s$, the magnitude of the non-dimensional mass flux field will be of order $(R/\hat{r}_s)^2$ within the spray cone, and zero outside. An alternative scaling for $\hat{\boldsymbol{G}}$ is given by

$$\frac{\hat{\dot{M}}_0}{\pi R^2} = \hat{\rho}_{s,0} \overline{V}, \tag{2.29}$$

thus defining the spray density scaling $\hat{\rho}_{s,0}$. Note that since the mass flux field scaling on the left-hand side of (2.29) corresponds in a sense to the "average" mass flux through the billet top surface, the scaling for the spray density should also correspond to an averaged spray density. Hence, fluctuations of order $(R/\hat{r}_s)^2$ should also be expected in the non-dimensional spray density on passing through the spray cone.

There are three timescales associated with the process.

1. Withdrawal: $R/\hat{U}_0$.

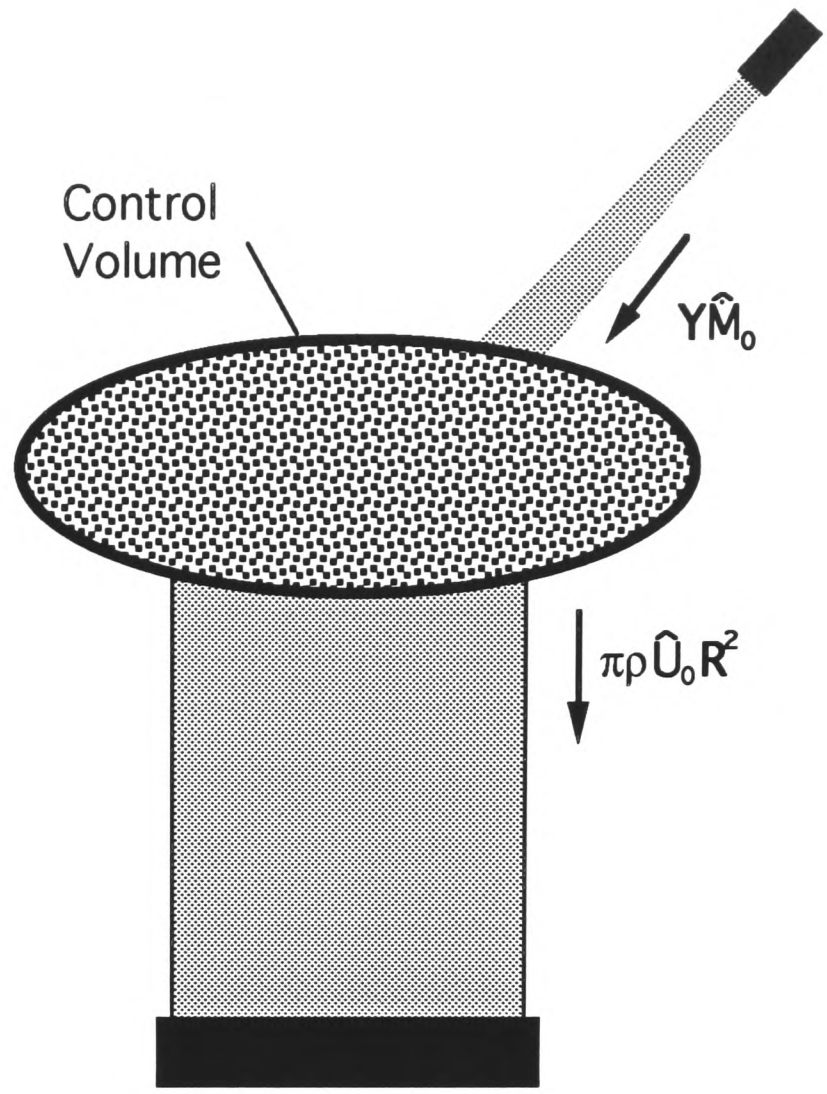

Figure 2.6: Mass balance by control volume analysis

2. Rotation: $2\pi/\hat{\omega}_0$.

3. Scanning: $\hat{t}_s$ = period of $a(\hat{t})$.

Typically,

$$\frac{R}{\hat{U}_0} \gg \frac{2\pi}{\hat{\omega}_0} \sim \hat{t}_s, \tag{2.30}$$

which reflects the purpose of the rotational and scanning movements in distributing mass evenly over the billet top surface. Hence, scaling with $\frac{2\pi}{\hat{\omega}_0}$ corresponds to taking a timescale on which all transient surface movement should be observable.

Defining two dimensionless groups, ξ_2 and ϵ, by

$$\xi_2 \equiv \frac{\hat{U}_0}{\overline{\hat{V}}}, \tag{2.31}$$

$$\epsilon \equiv \frac{2\pi}{\hat{\omega}_0}\frac{\hat{U}_0}{R}, \tag{2.32}$$

equations (2.25) and (2.26) become

$$\frac{\xi_2}{\epsilon}\left(\frac{\partial}{\partial t} + 2\pi\omega(t)[y_1\frac{\partial}{\partial x_1} - x_1\frac{\partial}{\partial y_1}]\right)\rho_s(\boldsymbol{x}[\boldsymbol{x}_1,t],t) = -\boldsymbol{\nabla}.\boldsymbol{G}(\boldsymbol{x}[\boldsymbol{x}_1,t],t), \tag{2.33}$$

and

$$\begin{aligned}\frac{\partial F}{\partial t}(\boldsymbol{x}_1,t) &= \epsilon\Gamma[-\frac{2\pi\omega(t)r_n\xi_2}{\epsilon}(\sin\phi_n(t),\cos\phi_n(t),-\frac{\epsilon u(t)}{2\pi\omega(t)r_n})\rho_s(\boldsymbol{x}[\boldsymbol{x}_1,t],t) \\ &\quad +\boldsymbol{G}(\boldsymbol{x}[\boldsymbol{x}_1,t],t)].\boldsymbol{\nabla}F(\boldsymbol{x}_1,t) + \epsilon u(t)\frac{\partial F}{\partial z_1}(\boldsymbol{x}_1,t).\end{aligned} \tag{2.34}$$

Here ξ_2 represents the ratio between the withdrawal velocity scale and the spray droplet velocity scale whilst ϵ represents the ratio of rotation to withdrawal timescales. Typically, process parameters give

$$\xi_2 \ll \epsilon \ll 1. \tag{2.35}$$

Non-dimensionalisation of the mass flux characterisation (2.9) produces

$$\boldsymbol{G}(\boldsymbol{x}[\boldsymbol{x}_1, t], t) = \dot{m}(t) g(r'[\boldsymbol{x}_1, t], t) \boldsymbol{k}'(t) + O(\boldsymbol{\xi}_1), \tag{2.36}$$

where the $O(\boldsymbol{\xi}_1)$ term results from scaling the $O(\hat{\boldsymbol{\xi}}_1)$ term in (2.9) with $\hat{\dot{M}}_0/\pi R^2$. In terms of the spray coordinate system, (scaled with R also), and the non-dimensional spray cone radius, $r_s = \hat{r}_s/R$, the function $g(r')$ now satisfies

$$\int_0^{r_s} r' g(r') dr' = \frac{1}{2}, \tag{2.37}$$

representing conservation of mass through the atomiser, with

$$g(r') \begin{cases} > 0, & r' < r_s, \\ = 0, & r' \geq r_s, \end{cases} \tag{2.38}$$

and $g(r')$ will typically decrease monotonically in $[0, r_s)$. Non-dimensional spray cone radii typically satisfy

$$0 \ll r_s < 1, \tag{2.39}$$

so that $g(r') = O(1)$ within the spray cone.

2.1.4 Approximate model equations

The preponderance of small parameters in equations (2.33), (2.34) and (2.36) suggests that numerical solution would not be feasible in the present form. Before further progress can be made analytically, some form of approximation of both the function Γ and of the equations (2.33), (2.34) and (2.36) is needed.

The sticking efficiency, Γ

The function Γ, which defines the fraction of the spray mass flux that sticks at any particular point on the billet surface, will depend upon the spray mass fiux field, the billet surface profile and a host of other local physical parameters. Using $\boldsymbol{P}$ to denote parameters other than the spray mass flux field and the billet surface profile,[1] Γ may be written as

$$\Gamma = \Gamma(\boldsymbol{G}, F, \boldsymbol{P}),$$

for arbitrary mass flux field $\boldsymbol{G}$ and billet surface F.

A function $\gamma(\dot{m}g\boldsymbol{k}', F)$ is defined, which takes the values 0 and 1, and depends only on the approximate mass flux field, $\dot{m}g\boldsymbol{k}'$, and on F. The function $\gamma(\dot{m}g\boldsymbol{k}', F)$ takes the value 0 whenever

$$\dot{m}g\boldsymbol{k}'.n > 0,$$

or when the mass flux field $\dot{m}g\boldsymbol{k}'$ is obstructed by the billet surface; otherwise

$$\gamma(\dot{m}g\boldsymbol{k}', F) = 1.$$

[1] e.g. spray and surface temperatures, local spray droplet distribution, local gas flow field.

Clearly, $\Gamma(\boldsymbol{G}, F, \boldsymbol{P})$ may be written as

$$\Gamma(\boldsymbol{G}, F, \boldsymbol{P}) = \gamma(\dot{m}g\boldsymbol{k}', F) + [\Gamma(\dot{m}g\boldsymbol{k}', F, \boldsymbol{P}) - \gamma(\dot{m}g\boldsymbol{k}', F)] + [\Gamma(\boldsymbol{G}, F, \boldsymbol{P}) - \Gamma(\dot{m}g\boldsymbol{k}', F, \boldsymbol{P})], \tag{2.40}$$

The first square bracket on the right-hand side of (2.40) represents the difference in surface sticking efficiencies on F, due to the mass flux field $\dot{m}g\boldsymbol{k}'$, between the average efficiency, γ, and the efficiency, Γ, that is affected by the local parameters $\boldsymbol{P}$. The second square bracket on the right-hand side of (2.40) represents the difference in surface sticking efficiencies on F, when influenced by the local parameters, $\boldsymbol{P}$, due to the different mass flux fields $\dot{m}g\boldsymbol{k}'$ and $\boldsymbol{G}$.

Instead of (2.40) write

$$\Gamma(\boldsymbol{G}, F, \boldsymbol{P}) = \gamma(\dot{m}g\boldsymbol{k}', F) + \xi_3 + \xi_4, \tag{2.41}$$

where the ξ_3 and ξ_4 terms correspond directly to the first and second sets of square brackets on the right hand side of (2.40).

Assuming that local fluctuations from the average sticking efficiency throughout the run are small in comparison to the average efficiency, $\overline{Y}$, the ξ_3 term will be small. The same assumption may not be made about the ξ_4 term. Although $\dot{m}g\boldsymbol{k}'$ is assumed to approximate the mass flux field $\boldsymbol{G}$, there may be times when shadowing effects for the two mass flux fields $\dot{m}g\boldsymbol{k}'$ and $\boldsymbol{G}$ are different, and this will result in an $O(1)$ contribution to the term ξ_4. However, since type B shadowing is not considered, these $O(1)$ differences between the sticking efficiencies for the two different mass flux fields are most likely to occur either near the edge of the spray cone, or where $\boldsymbol{G}.\boldsymbol{n}$, (or $\dot{m}g\boldsymbol{k}'.\boldsymbol{n}$), is small. In either of these cases, Γ will be multiplying terms of order $O(\epsilon\boldsymbol{\xi}_1 + \xi_2)$.

The model equations

Approximate model equations are derived from equation (2.33), by neglecting terms of orders $\boldsymbol{\xi}_1$ and ξ_2/ϵ, and from equation (2.34) by neglecting terms of orders $\epsilon\boldsymbol{\xi}_1$, ξ_2 and $\epsilon\xi_3$. These simplified equations describe mass conservation in the spray and three dimensional growth of the billet surface. They are given by

$$\begin{aligned} 0 &= \boldsymbol{\nabla}.[\dot{m}(t)g(r'[\boldsymbol{x}_1, t])\boldsymbol{k}'(t)], \\ &\quad \boldsymbol{x}_1 \in \mathcal{R}^3 | \Omega(t) \end{aligned} \tag{2.42}$$

$$\begin{aligned} \frac{1}{\epsilon}\frac{\partial F}{\partial t}(\boldsymbol{x}_1, t) - u(t)\frac{\partial F}{\partial z_1}(\boldsymbol{x}_1, t) &= \gamma(\dot{m}g\boldsymbol{k}', F)\dot{m}(t)g(r'[\boldsymbol{x}_1, t])\boldsymbol{k}'(t).\boldsymbol{\nabla}F(\boldsymbol{x}_1, t) \\ &\quad \boldsymbol{x}_1 \in \partial\Omega(t). \end{aligned} \tag{2.43}$$

Initial conditions for F in the crown frame of reference are

$$F(\boldsymbol{x}_1, 0) = \left\{ \begin{array}{ll} z_1 - z_c, & 0 \leq r_1 \leq r_c \\ r_1 - r_c, & 0 \leq z_1 \leq z_c \end{array} \right\}. \tag{2.44}$$

The somewhat simplistic approximations of the spray mass flux and the deposition stage of the process has yielded a set of equations that are simple enough to permit some analysis in the following sections, but which also preserve the essential process control variables and controlled process motions, as well as the timescales on which they occur. The validity of the model will always depend upon the size of the $O(\xi)$ terms

neglected. When valid, the model equations should allow the investigation of those billet growth phenomena for which process control will be feasible.

2.2 Averaging Methods

The non-dimensional equation (2.43) has been derived by scaling time with the rotation period and indicates that changes in billet shape are small, of order ϵ, on the rotation/scanner timescale. However, $O(1)$ changes in the spray distribution $g(r')$ are occurring on the rotation timescale. These are caused by billet rotation and atomiser scanning motion, both of which effectively move the billet surface through the spray cone. The desired effect of this rapid movement of the spray cone over the billet surface is to even out the deposition at different points on the surface.

For a numerical solution of (2.43) the $O(1)$ changes in $g(r')$ dictate that a small timestep be used, while the $O(\epsilon)$ growth terms indicate that integration must take place over an $O(\epsilon^{-1})$ time period. Hence, although possible, a straightforward numerical solution of (2.43) is unlikely to be productive. Instead, an attempt is made to exploit the smallness of ϵ and the existence of two distinct process timescales in deriving an asymptotic approximation to the solution of (2.43).

A regular perturbation approximation to (2.43) leads to the trivial approximation of F by its initial conditions,

$$F(\boldsymbol{x}_1, t) \approx F_0(\boldsymbol{x}_1, t) = F(\boldsymbol{x}_1, 0).$$

This gives an $O(\epsilon)$ approximation to F, provided that $t \ll \epsilon^{-1}$. When $t \sim \epsilon^{-1}$, billet growth of $O(1)$ may have occurred and it is unlikely that the above approximation will be valid; hence this simplistic method fails.

Non-uniform validity of an approximation with time, as above, is commonly found when applying a *regular* perturbation method to a *singular* perturbation problem such as (2.43). In order to extend the interval of validity more advanced approximation methods are needed. In this section an averaging method is applied to (2.43). It is shown that for appropriate scanning and rotation periods, and for suitable billet crown shapes, the averaged equations give an $O(\epsilon)$ approximation to the billet surface motion that is valid uniformly over the timescale ϵ^{-1}.

In a typical situation for which averaging may be deemed suitable one is faced with a dynamical system that exhibits some kind of slow characteristic global behaviour about which small rapid perturbations may also be observed. In applying an averaging method one averages the dynamical system, (i.e. the equations), and not the observed behaviour (the solution). The fundamental question to be asked then is how closely the solution of the averaged system approximates the slow ("averaged") behaviour of the original system.

For finite-dimensional initial value problems such questions have been considered for some time and the theory is fairly complete, see e.g. [64, 122]. In contrast, the theory of averaging for partial differential equations is much less complete. Asymptotic methods, when applied to dynamical systems, are usually directed towards exploiting some physical feature of the problem. Perhaps it has traditionally been the case that less of the initial-boundary value problems that have been tackled have been physically suited to an averaging approach, rather than to a different asymptotic technique.

Where initial-boundary value problems have been tackled the approach has often been to convert the partial differential equation into an infinite system of ordinary differential equations via an eigenfunction expansion, truncate the expansion, and then apply the established averaging theory to the reduced system, e.g. [63, 66, 69]. Such methods are not suitable here. Instead, the averaging method is applied directly to the ordinary differential equations that govern the characteristic projections of (2.43).

2.2.1 Definitions and Theory

Let $\epsilon \in (0, \epsilon_0]$ for ϵ_0 some small positive constant.

Definition 2.2.1 *The continuous function $\boldsymbol{f}(t)$ is* **almost periodic** *if from every sequence $\{c'_n\}$ one can extract a subsequence $\{c_n\}$ such that $\lim_{n\to\infty} \boldsymbol{f}(t + c_n)$ exists uniformly on the real line.*

Definition 2.2.2 *Consider the vectorfield $\boldsymbol{f}(\boldsymbol{x}, t)$ with $\boldsymbol{f} : \mathcal{R}^n \times \mathcal{R} \to \mathcal{R}^n$, Lipschitz continuous in $\boldsymbol{x}$ on $\mathcal{D} \subset \mathcal{R}^n$, $t \geq 0$; $\boldsymbol{f}$ continuous in $\boldsymbol{x}$ and t on $\mathcal{D} \times \mathcal{R}^+$. If the average*

$$\boldsymbol{f}^0(\boldsymbol{x}) = \lim_{T\to\infty} \frac{1}{T} \int_0^T \boldsymbol{f}(\boldsymbol{x}, t)dt$$

exists, $\boldsymbol{f}$ is called a **KBM-vectorfield**.

Theorem 2.2.3 (General Averaging) *Consider the initial value problems*

$$\frac{\mathrm{d}}{\mathrm{d}t}\boldsymbol{x} = \epsilon \boldsymbol{f}(\boldsymbol{x}, t), \qquad \boldsymbol{x}(0) = \boldsymbol{x}_0,$$

with $\boldsymbol{f} : \mathcal{R}^n \times \mathcal{R} \to \mathcal{R}^n$, and

$$\frac{\mathrm{d}}{\mathrm{d}t}\boldsymbol{y} = \epsilon \boldsymbol{f}^0(\boldsymbol{y}), \qquad \boldsymbol{y}(0) = \boldsymbol{x}_0,$$

where $\boldsymbol{x}$, $\boldsymbol{y}$, $\boldsymbol{x}_0 \in \mathcal{D} \subset \mathcal{R}^n$, $t \in [0, \infty)$, $\epsilon \in (0, \epsilon_0]$. Suppose that

a) $\boldsymbol{f}$ is a KBM-vectorfield with average $\boldsymbol{f}^0$, and

b) $\boldsymbol{y}(t)$ belongs to an interior subset of $\mathcal{D}$ on the timescale ϵ^{-1}.

Then

$$\boldsymbol{x}(t) - \boldsymbol{y}(t) = O(\delta^{1/2}(\epsilon)) \quad \text{as } \epsilon \to 0 \text{ on the timescale } \epsilon^{-1},$$

where

$$\boldsymbol{f}^0(\boldsymbol{x}) = \lim_{T\to\infty} \frac{1}{T} \int_0^T \boldsymbol{f}(\boldsymbol{x}, t)dt,$$

and

$$\delta(\epsilon) = \sup_{\boldsymbol{x}\in\mathcal{D}} \sup_{t\in[0, \frac{L}{\epsilon})} \epsilon \left\| \int_0^t \boldsymbol{f}(\boldsymbol{x}, \tau) - \boldsymbol{f}^0(\boldsymbol{x})d\tau \right\|.$$

Proof See [122], page 41.

Theorem 2.2.4 (Improved Averaging) *Consider the initial value problems*

$$\frac{\mathrm{d}}{\mathrm{d}t}\boldsymbol{x} = \epsilon \boldsymbol{f}(\boldsymbol{x}, t), \qquad \boldsymbol{x}(0) = \boldsymbol{x}_0,$$

and

$$\frac{\mathrm{d}}{\mathrm{d}t}\boldsymbol{u} = \epsilon \boldsymbol{f}^0(\boldsymbol{u}) + \epsilon\delta_1(\epsilon)\boldsymbol{f}^{1_0}(\boldsymbol{u}), \qquad \boldsymbol{u}(0) = \boldsymbol{x}_0,$$

with $\boldsymbol{f} : \mathcal{R}^n \times \mathcal{R} \to \mathcal{R}^n$; $\boldsymbol{x}$, $\boldsymbol{y}$, $\boldsymbol{x}_0 \in \mathcal{D} \subset \mathcal{R}^n$, $t \in [0, \infty)$, $\epsilon \in (0, \epsilon_0]$, *and*

$$\boldsymbol{f}^1(\boldsymbol{x}, t) = [\mathbf{D}\boldsymbol{f}(\boldsymbol{x}, t)]\boldsymbol{u}^1(\boldsymbol{x}, t) - [\mathbf{D}\boldsymbol{u}^1(\boldsymbol{x}, t)]\boldsymbol{f}^0(\boldsymbol{x}),$$

where

$$\delta_1(\epsilon)\boldsymbol{u}^1(\boldsymbol{x}, t) = \epsilon \int_0^t [\boldsymbol{f}(\boldsymbol{x}, \tau) - \boldsymbol{f}^0(\boldsymbol{x})]d\tau$$

and

$$\delta_1(\epsilon) = \sup_{\boldsymbol{x}\in\mathcal{D}} \sup_{t\in[0,\frac{L}{\epsilon})} \epsilon \left\| \int_0^t [\boldsymbol{f}(\boldsymbol{x}, \tau) - \boldsymbol{f}^0(\boldsymbol{x})]d\tau \right\|.$$

Suppose that

a) $\boldsymbol{f}$ *and* $\boldsymbol{f}^1$ *are KBM-vectorfields with averages* $\boldsymbol{f}^0$ *and* $\boldsymbol{f}^{1_0}$, *and*

b) $\boldsymbol{u}(t)$ *belongs to an interior subset of* $\mathcal{D}$ *on the timescale* ϵ^{-1}.

Then, on the timescale ϵ^{-1},

$$\boldsymbol{x}(t) = \boldsymbol{u}(t) + \delta_1(\epsilon)\boldsymbol{u}^1(\boldsymbol{u}(t), t) + O(\delta_1(\epsilon)[\delta_2^{1/2}(\epsilon) + \delta_1(\epsilon)]),$$

where

$$\boldsymbol{f}^0(\boldsymbol{x}) = \lim_{T\to\infty} \frac{1}{T} \int_0^T \boldsymbol{f}(\boldsymbol{x}, t)dt,$$

and

$$\delta_2(\epsilon) = \sup_{\boldsymbol{x}\in\mathcal{D}} \sup_{t\in[0,\frac{L}{\epsilon})} \epsilon \left\| \int_0^t [\boldsymbol{f}^1(\boldsymbol{x}, \tau) - \boldsymbol{f}^{1_0}(\boldsymbol{x})]d\tau \right\|.$$

Proof See [122], page 46.

Theorem 2.2.5 *Consider the initial value problems*

$$\frac{\mathrm{d}}{\mathrm{d}t}\boldsymbol{x} = \epsilon \boldsymbol{f}(\boldsymbol{x}, t), \qquad \boldsymbol{x}(0) = \boldsymbol{x}_0,$$

and

$$\frac{\mathrm{d}}{\mathrm{d}t}\boldsymbol{y} = \epsilon \boldsymbol{f}^0(\boldsymbol{y}), \qquad \boldsymbol{y}(0) = \boldsymbol{x}_0.$$

Then, with the assumptions of Theorem 2.2.4,

$$\boldsymbol{x}(t) = \boldsymbol{y}(t) + O(\delta_1(\epsilon)) \quad \textit{as } \epsilon \to 0 \textit{ on the timescale } \epsilon^{-1},$$

where

$$\delta_1(\epsilon) = \sup_{\boldsymbol{x}\in\mathcal{D}} \sup_{t\in[0,\frac{L}{\epsilon})} \epsilon \left\| \int_0^t \boldsymbol{f}(\boldsymbol{x}, \tau) - \boldsymbol{f}^0(\boldsymbol{x})d\tau \right\|.$$

Proof See [122], page 47.

Remarks Only the basic theorems needed have been given above. A more complete discussion of the averaging method and its applications can be found in the very readable book by Sanders and Verhulst, [122]. The above three theorems are very interesting. Theorem 2.2.3 is most general, but gives only a relatively low order of approximation. The approximation is improved by theorem 2.2.4, where additional

conditions must be satisfied. The estimate $\mathbf{u}$ of theorem 2.2.4 is an order $\delta_1(\epsilon)$ approximation, and leads naturally to an even higher order approximation, by computing $\mathbf{u}^1$. However, in comparison to the estimate $\mathbf{y}$ of theorem 2.2.3, $\mathbf{u}$ is extremely cumbersome to compute. Since an averaging method is generally used to simplify a problem, perhaps to allow some analytic insight to be gained, it is doubtful whether computation of the estimate $\mathbf{u}$ will ever be of real practical use. However, the value of theorem 2.2.4 is in establishing theorem 2.2.5. Theorem 2.2.5 relies upon the conditions of theorem 2.2.4, but demonstrates that the more simple estimate, $\mathbf{y}$, of theorem 2.2.3 then gives as good an order of approximation as does $\mathbf{u}$. Since the estimate $\mathbf{y}$ is both more accessible than $\mathbf{u}$, and is intuitively "the averaged solution", this result is quite valuable. In application, one thus attempts to show that the conditions of theorem 2.2.4 are applicable, then works with the estimate of theorems 2.2.3 and 2.2.5.

2.2.2 Application

Equation (2.43) is a first order quasi-linear partial differential equation that describes the evolution of the billet surface from its initial conditions, (2.44), for a specified mass flux. It is quasi-linear due to the dependence of the sticking efficiency γ on the billet surface F. Only the subset $\mathcal{S}$, of all possible billet surfaces for which type B shadowing does not occur, is considered. For these surfaces the deposition terms on the right-hand side of (2.43) are smooth.

The motion of the billet surface may either be followed by integrating (2.43) forward in time directly, or by integrating forward the equations for each of the characteristic projections of (2.43) that pass through points on the initial surface, and then considering the union of all points on these characteristic projections at time t. A point on a characteristic projection of (2.43) at time t_0 lies at a point P on the billet surface at time t_0 and moves with the velocity of the billet surface at P, relative to O_1, thus remaining on the billet surface for times $t \geq t_0$, see Fig. 2.7. A characteristic projection $\boldsymbol{x}_1(t)$ of (2.43) satisfies the equations[2]

$$\frac{\mathrm{d}x_1}{\mathrm{d}t} = -\epsilon\gamma(\dot{m}g\boldsymbol{k}', F)\dot{m}(t)g(r'[\boldsymbol{x}_1, t])\boldsymbol{k}'_{x_1}(t), \tag{2.45}$$

$$\frac{\mathrm{d}y_1}{\mathrm{d}t} = -\epsilon\gamma(\dot{m}g\boldsymbol{k}', F)\dot{m}(t)g(r'[\boldsymbol{x}_1, t])\boldsymbol{k}'_{y_1}(t), \tag{2.46}$$

$$\frac{\mathrm{d}z_1}{\mathrm{d}t} = -\epsilon\gamma(\dot{m}g\boldsymbol{k}', F)\dot{m}(t)g(r'[\boldsymbol{x}_1, t])\boldsymbol{k}'_{z_1}(t) - \epsilon u(t), \tag{2.47}$$

where $\boldsymbol{k}'_{x_1}$, $\boldsymbol{k}'_{y_1}$ and $\boldsymbol{k}'_{z_1}$ are the three cartesian components of $\boldsymbol{k}'$ in the crown frame of reference, and where $\boldsymbol{x}_1$ satisfies the initial conditions given by (2.44), i.e.

$$F(\boldsymbol{x}_1(0), 0) = 0. \tag{2.48}$$

[2]Strictly speaking, a time-like variable τ should replace t in (2.45), (2.46) & (2.47), and these equations should be supplemented with

$$\frac{\mathrm{d}t}{\mathrm{d}\tau} = 1.$$

If the equations for a *characteristic*, rather than a characteristic *projection*, are required then

$$\frac{\mathrm{d}F}{\mathrm{d}\tau} = 0,$$

must also be included. Both of these equations are unnecessary complications.

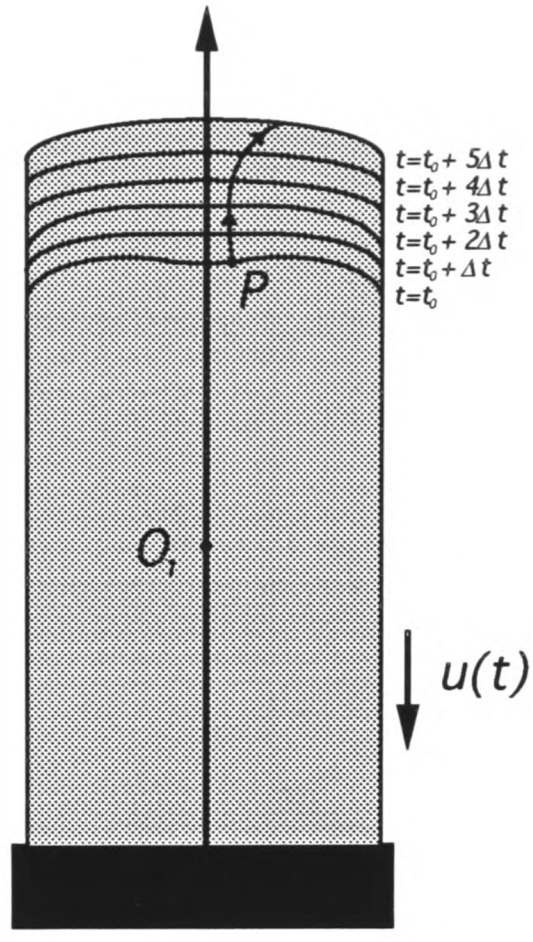

Figure 2.7: A characteristic projection

In the spray-forming process, withdrawal rate, $u(t)$, is varied smoothly in response to observed changes in billet shape. These changes occur on the timescale ϵ^{-1}. The mass flow rate, $\dot{m}(t)$, is not generally varied a great deal. This is because variations in mass flow rate vary not just the spray mass flux but also the spray heat flux, (and consequently billet solidification), in a very direct way. Thus, $\dot{m}(t)$ can also be assumed to vary only[3] on the timescale ϵ^{-1}. Other variations with time in (2.45), (2.46) and (2.47) occur on the rotation/scanner timescale. Accordingly, a **slow-time** variable η is defined by

$$\eta(t) = \epsilon t, \tag{2.49}$$

and equations (2.45), (2.46), (2.47) and (2.48) are supplemented with

$$\frac{\mathrm{d}\eta}{\mathrm{d}t} = \epsilon, \qquad \eta(0) = 0. \tag{2.50}$$

The initial surface, (and thus the characteristic projections), can be parameterised through a vector $\boldsymbol{\nu} = (\nu_1, \nu_2)$; which may be chosen so that $\nu_i \in [-1, 1]$, $i = 1, 2$, as is illustrated schematically in Fig. 2.8. Then, for convenience defining

$$\boldsymbol{c}_\nu(t) \equiv (x_1(t), y_1(t), z_1(t), \eta(t)), \tag{2.51}$$

and

$$\boldsymbol{f}_F(F, \boldsymbol{c}_\nu, t) \equiv \begin{pmatrix} -\gamma(\dot{m}g\boldsymbol{k}', F)\dot{m}(\eta)g(r'[\boldsymbol{x}_1, t])\boldsymbol{k}'_{x_1}(t) \\ -\gamma(\dot{m}g\boldsymbol{k}', F)\dot{m}(\eta)g(r'[\boldsymbol{x}_1, t])\boldsymbol{k}'_{y_1}(t) \\ -\gamma(\dot{m}g\boldsymbol{k}', F)\dot{m}(\eta)g(r'[\boldsymbol{x}_1, t])\boldsymbol{k}'_{z_1}(t) - u(\eta) \\ 1 \end{pmatrix}, \tag{2.52}$$

[3]Sharper changes in $\dot{m}(t)$ might result, for example, from a blockage of the atomiser nozzle. Such events are likely to result either in the end of the production run or, if a temporary/partial blockage, in an end product that is scrapped.

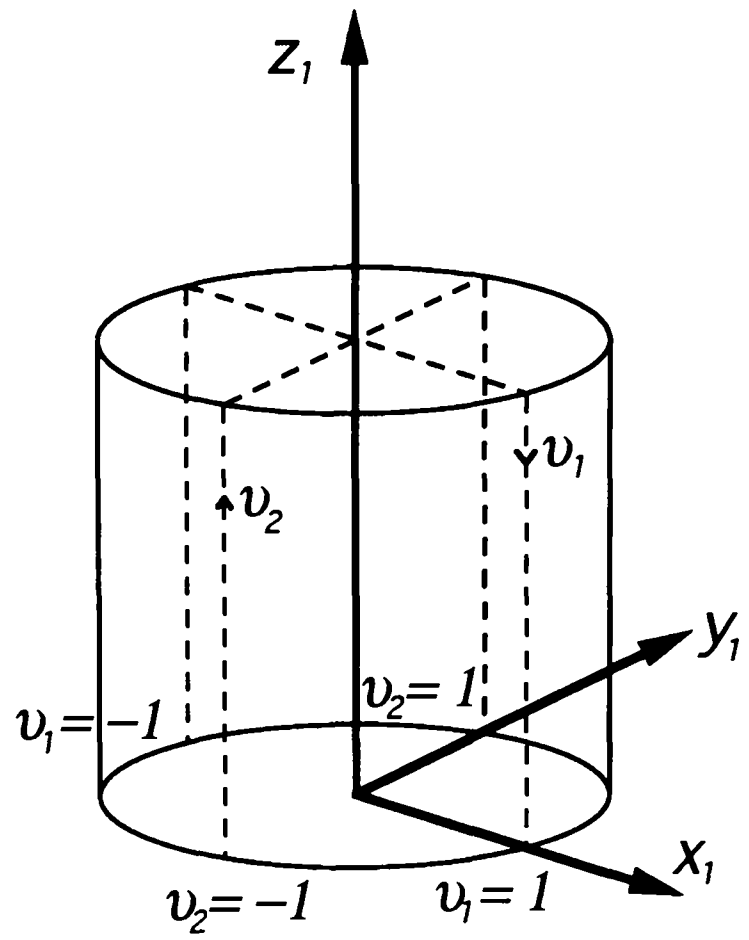

Figure 2.8: Initial surface parameterisation

equations for the characteristic projections may be rewritten as

$$\frac{\mathrm{d}}{\mathrm{d}t}\boldsymbol{c}_{\boldsymbol{\nu}} = \epsilon \boldsymbol{f}_F(F, \boldsymbol{c}_{\boldsymbol{\nu}}, t), \tag{2.53}$$

$$\boldsymbol{c}_{\boldsymbol{\nu}}(0) = (x_{1,\boldsymbol{\nu}}(0), y_{1,\boldsymbol{\nu}}(0), z_{1,\boldsymbol{\nu}}(0), 0). \tag{2.54}$$

The equations (2.53) and (2.54) differ from a standard, initial value averaging problem only in that the function $\boldsymbol{f}_F$ depends upon F, which is found by solving (2.53) for $\boldsymbol{\nu} \in [-1,1] \times [-1,1]$. Unfortunately, this nonlinearity in the partial differential equation, (2.43), causes great problems when considering the validity of the averaging method in full generality for the equivalent system (2.53). Whilst the right-hand side of (2.43) was smooth for $\boldsymbol{x}_1 \in \partial\Omega(t)$, the same is not true of the right-hand side of (2.53) which may have finite discontinuities, due to the jump in γ at the boundaries of shadowed regions. Additionally, the function γ has only been defined for $\boldsymbol{x}_1 \in \partial\Omega(t)$, whereas the averaging theorems require $\boldsymbol{f}_F$ to be defined in some wider domain $\mathcal{D}$. In order to apply the averaging method to these equations it is necessary to consider those billet surfaces for which $\boldsymbol{f}_F$ can be extended smoothly to some such domain.

"Linearising" the problem

One way of doing this is to consider a subclass of billet crown shapes for which it will be possible to redefine γ so that γ does not depend upon F, but still retains the same values as before, (i.e. effectively making (2.43) linear). If this redefined γ is sufficiently smooth, then the averaging method can be successfully applied to this subclass of billet crown shapes.

Since $\dot{m}$, g and $\boldsymbol{k}'$ vary smoothly, it is necessary to restrict the subclass of surfaces considered to those for which γ changes from 1 to 0 only when $g = 0$. Such a profile is depicted in Fig. 2.9a. Since γ changes

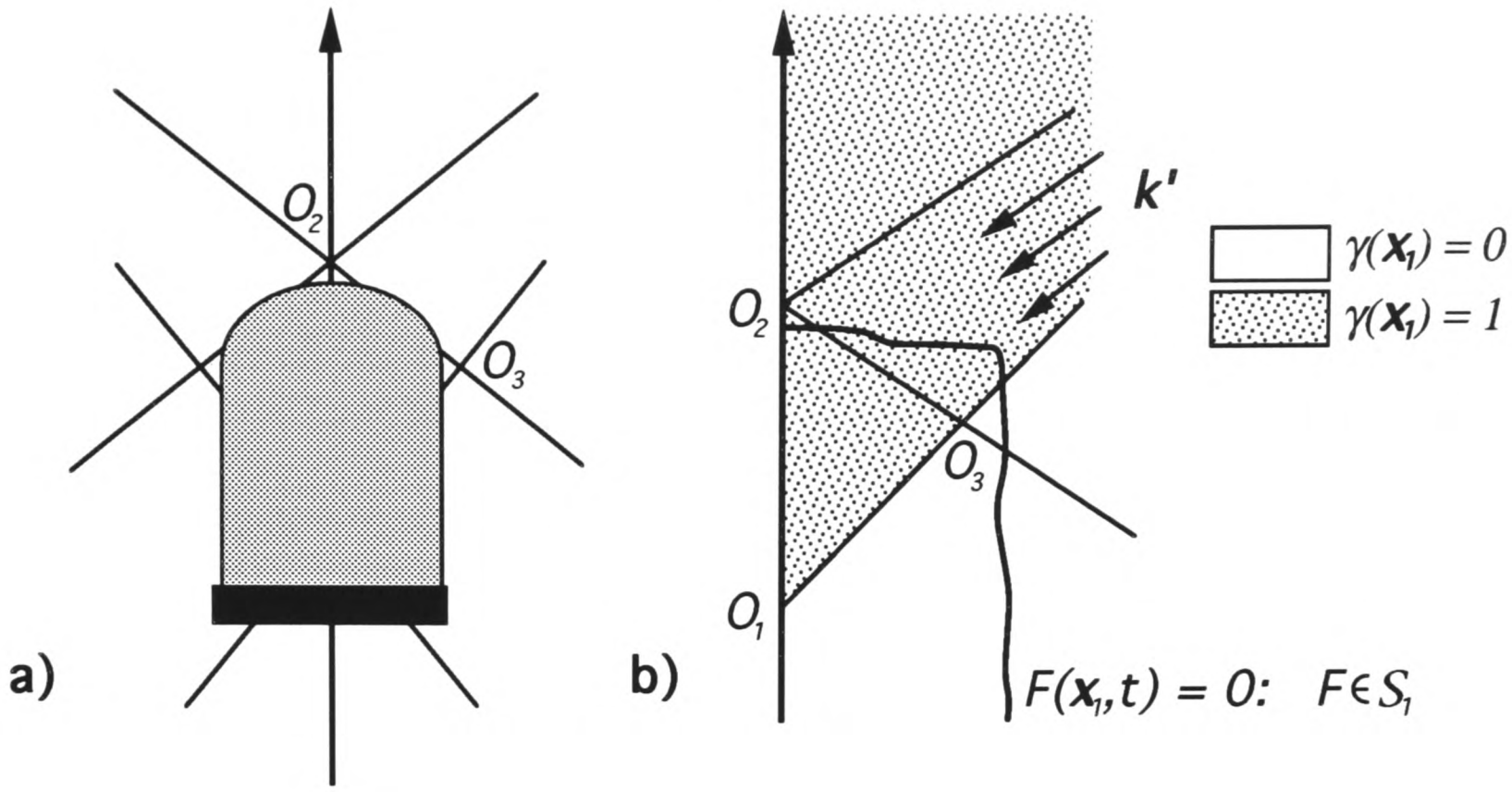

Figure 2.9: a) Radial surface cross-section for which $\boldsymbol{f}_F$ is smooth, b) definition of $\gamma(\mathbf{x}_1)$, and a surface in $\mathcal{S}_1$.

value only when $\boldsymbol{k}'.\boldsymbol{n} \to 0$, this condition can be given more formally by

$$\dot{m}g\boldsymbol{k}'.\boldsymbol{n} < 0 \Longrightarrow -\boldsymbol{k}'.\boldsymbol{n} = O_S(1), \tag{2.55}$$

which bounds $\boldsymbol{k}'.\boldsymbol{n}$ away from 0 whenever deposition is occurring. Now, define a subclass of billet crown surfaces, $\mathcal{S}_1$, by

$$F \in \mathcal{S}_1 \Longleftrightarrow$$

1. $F \in \mathcal{S}$, (i.e. type B shadowing does not occur on F).
2. Equation (2.55) holds at all points on F.
3. Any radial cross-section of F intercepts the overlapping spray boundary at most once between O_2 and O_3.

For $F \in \mathcal{S}_1$ redefine γ as taking the value 1 at all points above the lower spray boundary, and 0 otherwise. In terms of a cylindrical polar crown coordinate system,

$$\gamma(\boldsymbol{x}_1) = \begin{cases} 1, & z_1 \geq \frac{r_1}{\tan a_1}, \\ 0, & z_1 < \frac{r_1}{\tan a_1}. \end{cases} \tag{2.56}$$

A radial cross-section of a surface in $\mathcal{S}_1$, and the definition of γ, are depicted in Fig. 2.9b. It can be seen that for such a surface the definition of $\gamma(\boldsymbol{x}_1)$ given by (2.56) above, will correspond to that given earlier for $\gamma(\dot{m}g\boldsymbol{k}', F)$; and also that provided the surface remains in $\mathcal{S}_1$ the function $\boldsymbol{f}_F$ will not depend upon F and will be as smooth as $\dot{m}g\boldsymbol{k}'$.

Condition 3 above allows the redefinition of γ in such a simple way. However, this condition is non-essential, and for surfaces which cross the lower spray boundary more than once between O_2 and O_3, (e.g. Fig. 2.9a), one will often still be able to define γ as a function of $(\boldsymbol{x}_1, t)$, and apply the averaging theorems, provided that conditions 1 and 2 still hold.

Applying the general averaging theorem

Suppose that the rotation rate, $\omega(t)$, remains constant throughout the process.[4] For constant $\omega(t)$ both $g(r')$ and $\boldsymbol{k}'$ are smooth functions of additive and multiplicative combinations of periodic functions of t, each having periods 1 and t_s. Consequently, (see [32] page 5), the mass flux field $\dot{m}g\boldsymbol{k}'$ is an almost periodic function, (see definition 2.2.1). These functions are in a sense a generalisation of periodic functions, and share certain properties. In particular, all smooth almost periodic vector-fields are KBM-vector-fields, (see [122] page 55). This means that the average of the mass flux vectorfield,

$$\lim_{T\to\infty} \frac{1}{T} \int_0^T \dot{m}(\eta) g(r'[\boldsymbol{x}_1, t]) \boldsymbol{k}'(t) dt, \tag{2.57}$$

exists.

For $F \in \mathcal{S}_1$, replacing $\gamma(\dot{m}g\boldsymbol{k}', F)$ by $\gamma(\boldsymbol{x}_1)$, the "linearised" equations for the characteristic projections become

$$\frac{\mathrm{d}}{\mathrm{d}t}\boldsymbol{c}_\nu = \epsilon \boldsymbol{f}(\boldsymbol{c}_\nu, t), \tag{2.58}$$

where

$$\boldsymbol{f}(\boldsymbol{c}_\nu, t) \equiv \begin{pmatrix} -\gamma(\boldsymbol{x}_1)\dot{m}(\eta)g(r'[\boldsymbol{x}_1,t])\boldsymbol{k}'_{x_1}(t) \\ -\gamma(\boldsymbol{x}_1)\dot{m}(\eta)g(r'[\boldsymbol{x}_1,t])\boldsymbol{k}'_{y_1}(t) \\ -\gamma(\boldsymbol{x}_1)\dot{m}(\eta)g(r'[\boldsymbol{x}_1,t])\boldsymbol{k}'_{z_1}(t) - u(\eta) \\ 1 \end{pmatrix}. \tag{2.59}$$

The equations (2.58) correspond to a linear version of the quasi-linear partial differential equation (2.43).

For as long as F remains in $\mathcal{S}_1$, (2.58) satisfies the conditions of the general averaging theorem 2.2.3. Denoting by $t = A/\epsilon$ the end time of the process, it follows that if $F \in \mathcal{S}_1$ on $[0, A/\epsilon)$ the solution $\boldsymbol{y}$ of the system

$$\frac{\mathrm{d}}{\mathrm{d}t}\boldsymbol{y} = \epsilon \boldsymbol{f}^0(\boldsymbol{y}), \tag{2.60}$$

$$\boldsymbol{y}(0) = \boldsymbol{c}_\nu(0), \tag{2.61}$$

where

$$\boldsymbol{f}^0(\boldsymbol{y}) = \lim_{T\to\infty} \frac{1}{T} \int_0^T \boldsymbol{f}(\boldsymbol{y}, t) dt, \tag{2.62}$$

is an $O(\delta^{1/2}(\epsilon))$ asymptotic approximation to $\boldsymbol{c}_\nu(t)$ on the interval $[0, A/\epsilon)$. The order function $\delta(\epsilon)$ is given by

$$\delta(\epsilon) = \sup_{\boldsymbol{y}\in\mathcal{D}} \sup_{t\in[0,\frac{A}{\epsilon})} \epsilon \left\| \int_0^t \boldsymbol{f}(\boldsymbol{y}, \tau) - \boldsymbol{f}^0(\boldsymbol{y}) d\tau \right\|, \tag{2.63}$$

and it is assumed, from observation, that the integral

$$I(\boldsymbol{y}, t) = \int_0^t \boldsymbol{f}(\boldsymbol{y}, \tau) - \boldsymbol{f}^0(\boldsymbol{y}) d\tau \tag{2.64}$$

[4] Slow variation of ω with η could also be allowed.

is uniformly bounded for $\boldsymbol{y} \in \mathcal{D}$ and $t \in [0, \frac{A}{\epsilon})$, i.e. there is no evident build up of mass flux during averaging at any point in $\mathcal{D}$. With this assumption,

$$\delta(\epsilon) = \epsilon.$$

Since the result will hold uniformly for $\|\boldsymbol{\nu}\| \leq 1$, the solution of the averaged equations for the billet surface will remain close, $O(\epsilon^{1/2})$, to F for $t \in [0, A/\epsilon)$, i.e. throughout the length of the process.

Improved approximation

The assumption of the boundedness of the integral in (2.64) might be validated with some *a priori* knowledge of the generalized Fourier expansion of $\boldsymbol{f}$, see [32]. This is not pursued. When the integral $I(\boldsymbol{y}, t)$ in (2.64) is uniformly bounded, then it may also be shown to be an almost periodic function. Provided $\boldsymbol{f}$ is smooth in $\mathcal{D}$, then both matrices of partial derivatives

$$[\mathbf{D}\boldsymbol{f}] \text{ and } [\mathbf{D}I(\boldsymbol{y}, t)]$$

will also be almost periodic. Since $\boldsymbol{f}$ and $\boldsymbol{f}^1$ in theorem 2.2.4 are consequently both KBM-vectorfields, theorems 2.2.4 and 2.2.5 can then both be applied to improve the order of approximation to $O(\epsilon)$, valid on the timescale ϵ^{-1}.

Limitations

Sufficient conditions for the solutions of the averaged equations, (2.60), to give an $O(\epsilon)$ asymptotic approximation to the billet surface movement over the duration of the run are

1. Constant $\omega(t)$.
2. $I(\boldsymbol{y}, t) = O(1)$ uniformly for $t \in (0, A/\epsilon]$ and for $\boldsymbol{y} \in \mathcal{D}$.
3. $F \in \mathcal{S}_1$ for $t \in (0, A/\epsilon]$.

The first of these conditions is nearly always met in real production runs. The second of these conditions is needed only to ensure the approximation is $O(\epsilon)$, rather than $O(\delta^{1/2}(\epsilon))$. This condition must be assumed, but does not appear unreasonable. It is the third condition that is most likely to fail.

Possible reasons for F not to remain in $\mathcal{S}_1$ for $t \in (0, A/\epsilon]$ include the following

1. The averaged function $\boldsymbol{f}^0$ is not symmetric about the billet axis of rotation. The solution to the averaged equations will thus be asymmetric. Asymmetries result from synchronisation of the scanner and rotation period, (e.g. when t_s is a rational number), and will evolve over the timescale ϵ^{-1}. Geometrically, such $O(1)$ asymmetric growth will be seen as a "fold" on the billet crown surface, see Fig. 2.10a, and is likely to result eventually in type B shadowing occurring, (i.e. $F \notin \mathcal{S} \supset \mathcal{S}_1$). In reality, scanner-rotation synchronisation and $O(1)$ asymmetric growth is observed only extremely rarely, (even though t_s may be a rational number). This is probably due to the stochastic nature of the spray and to a certain amount of machine wear.
2. Billet growth results in a situation where $-\boldsymbol{k}'.\boldsymbol{n} \ll 1$ while $\dot{m}g\boldsymbol{k}'.\boldsymbol{n} < 0$. This may result, for example, at the start of a production run when rapid upwards growth of the part of the billet surface closest to

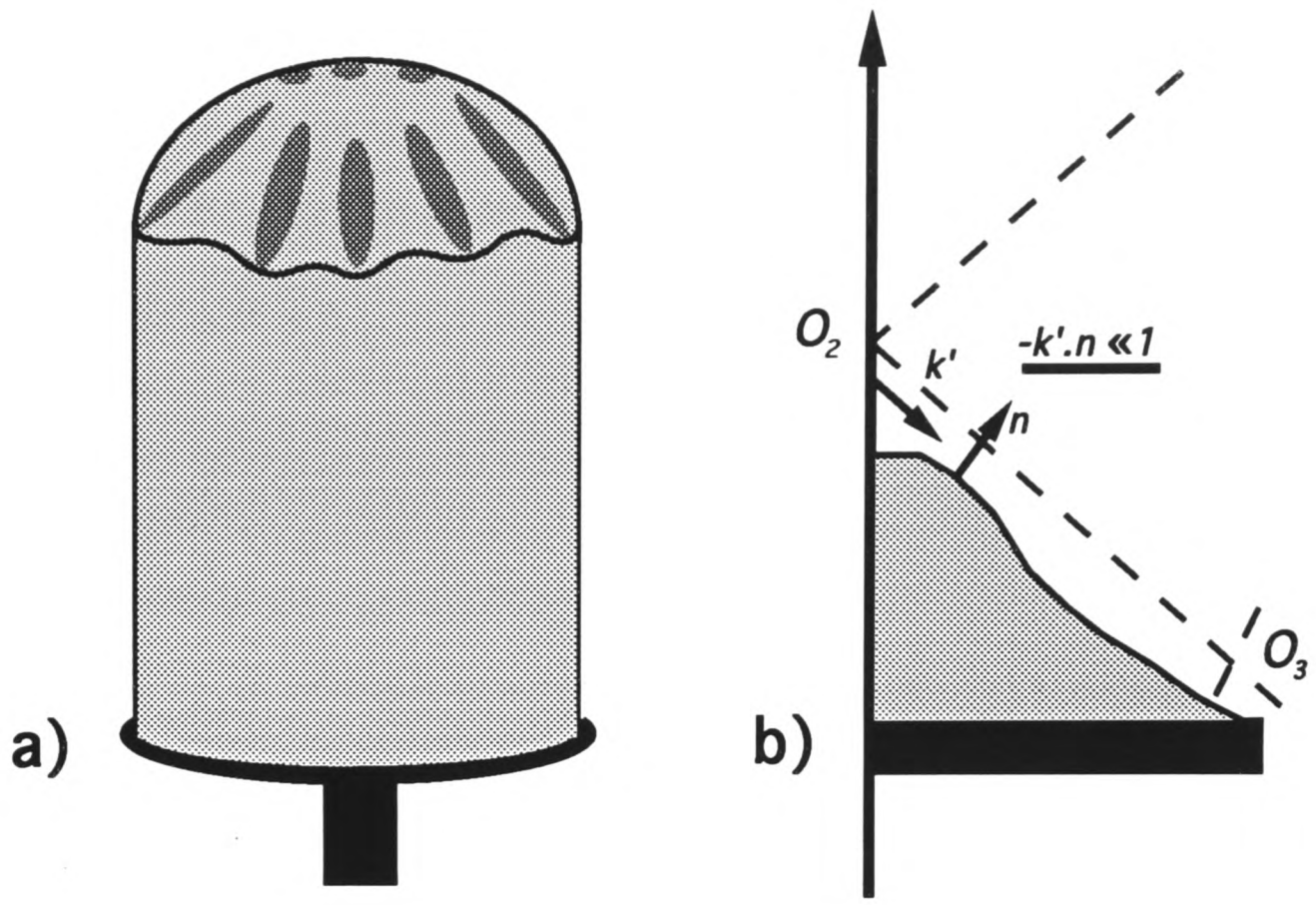

Figure 2.10: Failures of the averaging method; a) surface "folds", b) $O(\epsilon)$ growth causing shadowing when $-\boldsymbol{k}'.\boldsymbol{n} \ll 1$.

the billet axis of rotation is often observed. This situation is shown schematically, in a radial cross-section, in Fig. 2.10b. Although the function $\boldsymbol{f}$ remains smooth for a surface such as that depicted in Fig. 2.10b, and although the average $\boldsymbol{f}^0$ is well defined, the averaged equations may fail to give a valid approximation.

Physically, the problem may be explained as follows. The averaged system, relying on $\boldsymbol{f}^0$, assumes that the deposition at a point such as P in Fig. 2.10b occurs at a constant rate during the rotation of the billet. However, in reality the deposition occurring at P varies throughout the rotation of the billet. When P faces the atomiser directly, then $-\boldsymbol{k}'.\boldsymbol{n} = O_S(1)$, and growth at P will be $O(\epsilon)$. Later, as the billet rotates, the atomiser nozzle is on the opposite side of the billet to P. Supposing $-\boldsymbol{k}'.\boldsymbol{n} \ll 1$ while $\dot{m}g\boldsymbol{k}'.\boldsymbol{n} < 0$ at P, on the previous rotation of the billet, as is depicted in Fig. 2.10b; then the $O(\epsilon)$ growth that has occurred at P when facing the atomiser, may shadow the spray deposited from the other side of the billet when P is opposite the atomiser. In this situation the averaged equations clearly do not represent physical reality.

3. The billet crown may grow in such a way that radial cross-sections of the billet crown fail to intercept the overlapping spray boundary only once between O_2 and O_3. This might result, for example, from either the billet radius growing inwards, inside O_3, or from rapid withdrawal of the billet below the overlapping spray boundary. Provided that both (2.55) remains valid and that type B shadowing does not occur, this should present no real problem for the validity of the averaging method, although the validity of the definition of $\gamma(\boldsymbol{x}_1)$ should be examined.

2.3 Analysis of the averaged equations

Application of the averaging method leads to an asymptotic approximation of the billet surface motion responding only on the slow timescale η,

$$F \equiv F(\boldsymbol{x}_1, \eta, t) \sim F_0(\boldsymbol{x}_1, \eta) + o(\epsilon).$$

Axisymmetric averaged billet growth is of greatest practical interest, not only because real billets are nearly always observed to be axisymmetric, but also because the assumption of symmetry means that the averaged equations are two dimensional. The following economies are gained by averaging, and when the averaged equations are axisymmetric.

- The three dimensional averaged equations are much quicker to solve computationally than the three dimensional non-averaged equations, since they need only be integrated with respect to the slow-time variable $\eta \in (0, A]$.
- The two dimensional averaged equations are much quicker to solve computationally than the three dimensional averaged equations.
- An **axisymmetric averaged mass flux field** can be quickly computed for the axisymmetric equations by averaging the mass flux field over one scanner period and over one rotation of the billet.
- The two dimensional averaged equations are simple enough to allow some analytic techniques to be applied.

Slow-time axisymmetric billet growth is governed by the partial differential equation

$$\frac{\partial F_0}{\partial \eta}(\boldsymbol{x}_1, \eta) = [u(\eta)\boldsymbol{k}_1 + \dot{m}(\eta)\bar{\boldsymbol{g}}(\boldsymbol{x}_1, \eta)].\nabla F_0(\boldsymbol{x}_1, \eta), \tag{2.65}$$

where $\boldsymbol{k}_1$ is the unit vector in the direction of the billet axis of rotation and $\bar{\boldsymbol{g}}(\boldsymbol{x}_1, \eta)$ is the axisymmetric averaged mass flux distribution vector field. The function $\bar{\boldsymbol{g}}(\boldsymbol{x}_1, \eta)$ has not been allowed to depend upon F_0 in equation (2.65). Correspondingly, in the following subsections attention will be restricted to surfaces in $\mathcal{S}_1$.

To define $\bar{\boldsymbol{g}}(\boldsymbol{x}_1, \eta)$ more formally, first write $\tau_1 = t/t_s$ and $\tau_2 = t - 1/4$. Then, in the cartesian crown coordinate system,

$$\begin{aligned} \boldsymbol{k}'(t) &\equiv (-\cos 2\pi t \sin a(t), \sin 2\pi t \sin a(t), -\cos a(t)) \\ &= (-\cos 2\pi(\tau_2 + 1/4) \sin a(\tau_1 t_s), \sin 2\pi(\tau_2 + 1/4) \sin a(\tau_1 t_s), -\cos a(\tau_1 t_s)) \end{aligned} \tag{2.66}$$

and

$$r'(\boldsymbol{x}_1, t) \equiv [x'(\boldsymbol{x}_1, t)^2 + y'(\boldsymbol{x}_1, t)^2]^{1/2}$$

where

$$\begin{aligned} x' &= (-x_1 \cos 2\pi t + y_1 \sin 2\pi t + r_n) \cos a(t) + (z_1 - z_n - z_c) \sin a(t), \\ &= (-x_1 \cos 2\pi(\tau_2 + 1/4) + y_1 \sin 2\pi(\tau_2 + 1/4) + r_n) \cos a(\tau_1 t_s) \end{aligned}$$

$$+(z_1 - z_n - z_c)\sin a(\tau_1 t_s), \tag{2.67}$$

$$\begin{aligned} y' &= x_1 \sin 2\pi t + y_1 \cos 2\pi t, \\ &= x_1 \sin 2\pi(\tau_2 + 1/4) + y_1 \cos 2\pi(\tau_2 + 1/4). \end{aligned} \tag{2.68}$$

Writing the functions $g(r'[\boldsymbol{x}_1, t])$ and $\boldsymbol{k}'(t)$ as $g(r'[\boldsymbol{x}_1, \tau_1, \tau_2])$ and $\boldsymbol{k}'(\tau_1, \tau_2)$, the axisymmetric average mass flux distribution vector field $\bar{\boldsymbol{g}}$ is given by

$$\bar{\boldsymbol{g}}(\boldsymbol{x}_1, \eta) = \int_0^1 \int_0^1 \gamma(\boldsymbol{x}_1, \eta) g(r'[\boldsymbol{x}_1, \tau_1, \tau_2]) \boldsymbol{k}'(\tau_1, \tau_2) \mathrm{d}\tau_1 \mathrm{d}\tau_2. \tag{2.69}$$

This corresponds to averaging the mass flux distribution independently over one rotation period and over one scanner period, thus producing an axisymmetric distribution. The form $\gamma = \gamma(\boldsymbol{x}_1, \eta)$ has been used in (2.69), and is clearly suitable for surfaces in $\mathcal{S}_1$. However, one also wishes to define $\bar{\boldsymbol{g}}$ for other surfaces which may not be in $\mathcal{S}_1$, but for which the averaging method is still valid. For this purpose (2.69) is less restrictive. Averaging of the mass conservation equation (2.42), also over one rotation and one scanner period, gives

$$\boldsymbol{\nabla}.\bar{\boldsymbol{g}} = 0, \tag{2.70}$$

for $F_0 \in \mathcal{S}_1$. For the remainder of this section only surfaces $F_0 \in \mathcal{S}_1$ are considered. For these surfaces, conditions are demonstrated for the existence, uniqueness and stability of a steady state axisymmetric averaged billet crown shape.

2.3.1 Steady state crown shapes; local analysis

A primary objective of the process is to be able to reliably produce cylindrical billets of a desired radius and length. Process control is thus made far easier if the underlying dynamical system allows the steady and stable growth of billets of fixed radius and crown profile. Therefore, it is important to investigate the possibility of steady state solutions to (2.65) existing, and to examine their uniqueness and stability properties.

In terms of a spherical polar crown coordinate system with coordinates (σ, θ, ϕ) as in Fig. 2.11, the axisymmetric average mass flux distribution vector field $\bar{\boldsymbol{g}}$ has components

$$\bar{\boldsymbol{g}}(\sigma, \theta) = (\bar{g}_\sigma(\sigma, \theta), \bar{g}_\theta(\sigma, \theta), 0).$$

Since $F_0 \in \mathcal{S}_1$ is initially axisymmetric, analysis can be confined to the (σ, θ)-plane. Equation (2.65) becomes

$$\frac{\partial F_0}{\partial \eta} = [\dot{m}(\eta)\bar{g}_\sigma(\sigma, \theta) + u(\eta)\cos\theta]\frac{\partial F_0}{\partial \sigma} + \frac{\dot{m}(\eta)\bar{g}_\theta(\sigma, \theta) - u(\eta)\sin\theta}{\sigma}\frac{\partial F_0}{\partial \theta}. \tag{2.71}$$

Writing

$$F_0(\sigma, \theta, \eta) \equiv \sigma - f(\theta, \eta),$$

it is seen that a steady state solution of (2.71), $f = f(\theta)$, satisfies the ordinary differential equation

$$\frac{\mathrm{d}f}{\mathrm{d}\theta}(\theta) = \mathcal{H}(f(\theta), \theta, \mu) \equiv f(\theta)\frac{\bar{g}_\sigma(f(\theta), \theta) + \mu\cos\theta}{\bar{g}_\theta(f(\theta), \theta) - \mu\sin\theta}, \tag{2.72}$$

where

$$\mu \equiv \frac{u(\eta)}{\dot{m}(\eta)} = \text{ constant}, \tag{2.73}$$

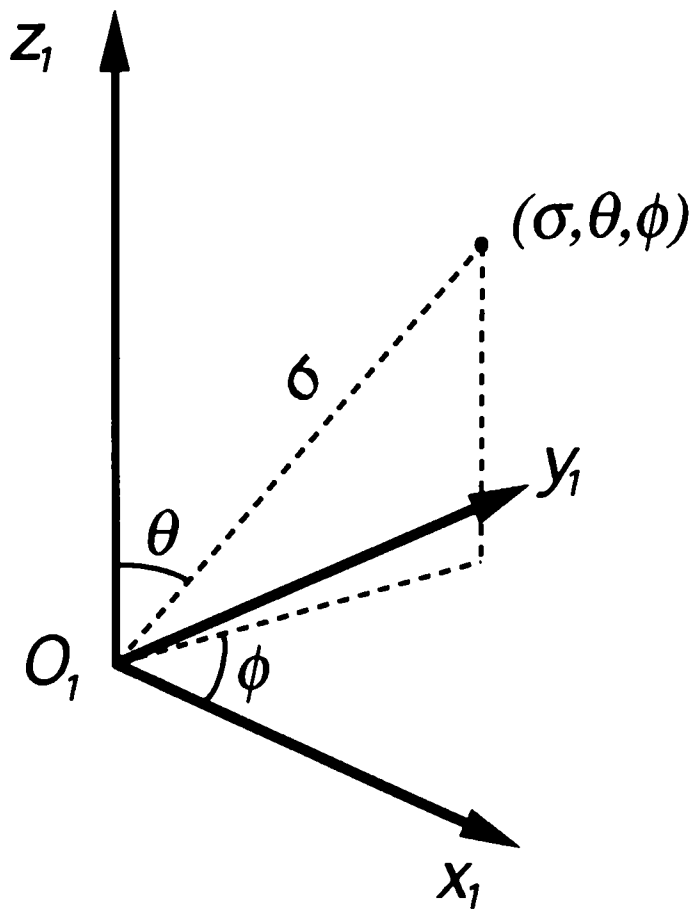

Figure 2.11: Spherical crown coordinate system

since f is independent of η.

To ensure existence of a steady state the Picard-Lindelöf theorem can be applied at an initial point $(f(\theta),\theta) = (\sigma_0,\theta_0)$ to prove local existence, and an attempt can then be made to extend the local solution smoothly to the interval[5] $\theta \in [0, a_1]$, (see e.g. [113]). For a straightforward application of this theorem it is required that

$$\bar{g}_\sigma, \bar{g}_\theta \in C^1(\mathcal{D}), \tag{2.74}$$

where $\mathcal{D}$ is some domain in the (σ,θ)-plane that encloses the steady state. Also, within $\mathcal{D}$ it is required that

$$\bar{g}_\theta(\sigma,\theta) - \mu\sin\theta \neq 0. \tag{2.75}$$

These conditions ensure that $\mathcal{H}$ is sufficiently smooth for the local result to be extended globally within $\mathcal{D}$. Condition (2.74) is satisfied immediately for surfaces in $\mathcal{S}_1$. Condition (2.75), unfortunately, needs further consideration.

By a symmetry argument, it is clear that

$$\bar{g}_\theta \to 0, \quad \text{as} \quad \theta \to 0, \tag{2.76}$$

$$\frac{\partial \bar{g}_\sigma}{\partial\theta} \to 0, \quad \text{as} \quad \theta \to 0. \tag{2.77}$$

Thus, (2.72) implies that $\frac{\mathrm{d}f}{\mathrm{d}\theta} \to \pm\infty$ as $\theta \to 0$, unless also

$$\mu\cos\theta + \bar{g}_\sigma(f(\theta),\theta) \to 0, \text{ as } \theta \to 0. \tag{2.78}$$

[5]For $\theta \geq a_1$ the steady state crown profile will have exited the lower spray boundary and will be given by

$$\sigma\sin\theta = \text{ constant.}$$

Solutions of (2.78) represent points at which solutions of (2.72) could be extended smoothly onto the billet axis of rotation. Note that, on the billet axis of rotation $u(\eta)$ is the rate at which mass is being withdrawn downwards away from the spray, and $-\dot{m}(\eta)\bar{g}_\sigma(\sigma,0)$ is the rate at which mass from the spray passes through the billet surface due to deposition. Hence, (2.78) says that for a steady state to exist these two quantities must balance. Since, (after algebra),

$$\bar{g}_\sigma(\sigma,0) = -\int_0^1 \gamma(\sigma,0)g(r'[\sigma,\tau_1])\cos a(\tau_1 t_s)\mathrm{d}\tau_1, \tag{2.79}$$

and $g(r') \to 0$ as $r' \to r_s$, it follows that (2.78) can only be satisfied on the open line segment $\overline{O_1O_2}$, for $\mu > 0$. This open line segment represents the limits, on the billet axis of rotation, of where there is a positive mass flux from the spray into the billet.

Although necessary, (2.78) is insufficient to guarantee the boundedness of $\frac{\mathrm{d}f}{\mathrm{d}\theta}$ as $\theta \to 0$. Applying L'Hopital's rules and using (2.70)

$$\begin{aligned}\lim_{\theta\to 0}\left[\frac{\mathrm{d}f}{\mathrm{d}\theta}\right] &= \lim_{\theta\to 0}\left[f\,\frac{\dfrac{\partial\bar{g}_\sigma}{\partial\theta}+\dfrac{\partial\bar{g}_\sigma}{\partial\sigma}\dfrac{\mathrm{d}f}{\mathrm{d}\theta}-\mu\sin\theta}{\dfrac{\partial\bar{g}_\theta}{\partial\theta}+\dfrac{\partial\bar{g}_\theta}{\partial\sigma}\dfrac{\mathrm{d}f}{\mathrm{d}\theta}-\mu\cos\theta}\right],\\ &= \lim_{\theta\to 0}\left[-f\,\frac{\dfrac{\partial\bar{g}_\sigma}{\partial\sigma}\dfrac{\mathrm{d}f}{\mathrm{d}\theta}}{f\dfrac{\partial\bar{g}_\sigma}{\partial\sigma}+\mu}\right],\end{aligned} \tag{2.80}$$

Hence, provided that

$$\frac{\partial\bar{g}_\sigma}{\partial\sigma}(f(0),0) \neq -\frac{\mu}{f(0)},\ \text{or}\ -\frac{\mu}{2f(0)}, \tag{2.81}$$

it follows that

$$\frac{\mathrm{d}f}{\mathrm{d}\theta}(0) = 0, \tag{2.82}$$

and any steady states that do exist will be flat-topped on the billet axis of rotation.

Three conclusions can be drawn from this local analysis.

1. Existence of a solution to (2.78), for given μ, is a necessary condition for the existence of a steady state. Solutions, σ, of (2.78) represent the heights, above O_1, of possible points of intersection of steady state crown shapes with the billet axis of rotation.

2. In general a steady state billet crown must lie below O_2. Thus, some of the spray will pass over the billet centre on each scan of the atomiser.

3. Since $-\bar{g}_\sigma > 0$ below O_2 and $-\bar{g}_\sigma \to 0$ at O_2, the solution of (2.78) nearest to the upper spray boundary will satisfy (2.81). Thus, if it exists, the uppermost steady state will be flat-topped at the billet axis of rotation.

2.3.2 Analysis in the phase plane

To progress further in understanding the likelihood of being able to extend globally the local analysis above, and to understand the transient motions of the billet surface, requires reconsideration of (2.71). Projections

of the characteristic curves of (2.71) onto the (σ,θ)-plane are those curves $(\sigma(\eta),\theta(\eta))$ governed by

$$\frac{\mathrm{d}\sigma}{\mathrm{d}\eta} = -u(\eta)\cos\theta - \dot{m}(\eta)\bar{g}_\sigma(\sigma,\theta), \tag{2.83}$$

$$\frac{\mathrm{d}\theta}{\mathrm{d}\eta} = \frac{u(\eta)\sin\theta - \dot{m}(\eta)\bar{g}_\theta(\sigma,\theta)}{\sigma}. \tag{2.84}$$

Superimposing a billet crown profile $F_0 \equiv \sigma - f(\theta,\eta) = 0$ onto the (σ,θ)-plane, the motion of the point $(\sigma,\theta) = (f,\theta)$ within the (σ,θ)-plane is given instantaneously by the vector

$$(-u(\eta)\cos\theta - \dot{m}(\eta)\bar{g}_\sigma(f,\theta), \frac{u(\eta)\sin\theta - \dot{m}(\eta)\bar{g}_\theta(f,\theta)}{f}), \tag{2.85}$$

which also describes the instantaneous motion of the point (f,θ) on the billet surface, within the (σ,θ)-plane. Hence, instead of analysing (2.71) directly, (2.83) and (2.84) can be analysed, to determine the possible motions of the billet surface.

The system (2.83) and (2.84) is two dimensional and is not autonomous. Dependence on η enters (2.83) and (2.84) only through $u(\eta)$ and $\dot{m}(\eta)$, which represent the control parameters of the process. These are varied smoothly throughout the process. Thus, the behaviour of solutions to (2.83) and (2.84) can be analysed in their phase space, as if the phase space for (2.83) and (2.84) were composed from a continuous smooth distortion of possible phase planes for the fully autonomous system

$$\frac{\mathrm{d}\sigma}{\mathrm{d}\eta} = -u\cos\theta - \dot{m}\bar{g}_\sigma(\sigma,\theta), \tag{2.86}$$

$$\frac{\mathrm{d}\theta}{\mathrm{d}\eta} = \frac{u\sin\theta - \dot{m}\bar{g}_\theta(\sigma,\theta)}{\sigma}. \tag{2.87}$$

where u and $\dot{m}$ are treated as constant parameters, (≥ 0). A number of general observations can be made about the phase plane for (2.86) and (2.87).

- With the assumption of symmetry about the axis $\theta = 0$, the spray can be considered to be confined to a bounded region of the phase plane $(\sigma,\theta) \in [0,\infty) \times [0,\pi/2]$. In the spherical coordinate system the lower, upper and overlapping spray boundaries are respectively the lines

$$\begin{aligned} \theta &= a_1, \\ \sigma\cos\theta &= z_u + \sigma\sin\theta\cot a_2, \\ \sigma\cos\theta &= z_u - \sigma\sin\theta\cot a_2, \end{aligned}$$

  where z_u is the displacement of O_1 below O_2 on the billet axis of rotation.

- Phase paths of (2.86) and (2.87) are those lines $\sigma(\theta)$ with gradient

$$\frac{\mathrm{d}\sigma}{\mathrm{d}\theta} = \mathcal{H}(\sigma,\theta,\mu), \tag{2.88}$$

  where $\mathcal{H}$ is as defined in (2.72). It follows that steady state crown profiles are represented by phase paths that run from $\theta = 0$ to $\theta = \pi/2$.

- Where $\bar{g}_\theta$ and $\bar{g}_\sigma$ are zero there is no deposition, only withdrawal. Phase paths are given by the lines

$$r_1 \equiv \sigma\sin\theta = \text{ constant}. \tag{2.89}$$

- Equilibrium points, (EP's), of (2.86) and (2.87) are located at the intersections of those lines, (nullclines), on which

$$0 = \mu\cos\theta - \bar{g}_\sigma(\sigma,\theta), \tag{2.90}$$

$$0 = \frac{\mu\sin\theta - \bar{g}_\theta(\sigma,\theta)}{\sigma}, \tag{2.91}$$

  Hence, EP's can exist only on the billet axis, $\theta = 0$, or where $\bar{g}_\sigma$ and $\bar{g}_\theta$ are non-zero, since otherwise (2.90) and (2.91) cannot be satisfied simultaneously there. Positions of the σ and θ-nullclines, (which are given by (2.90) and (2.91) respectively), will vary with μ, making characterisation hard. However, the lines $\theta = \pi/2$ and $\theta = 0$ are respectively, σ and θ-nullclines always.

  Both $\bar{g}_\sigma$ and $\bar{g}_\theta$ are zero at $\sigma = 0$, and for $\theta > a_1$. For $\theta \in (0, a_1)$, for sufficiently large σ and for $u > 0$, $\frac{\mathrm{d}\sigma}{\mathrm{d}\eta} < 0$. On the open line segment $\overline{O_1O_3}$, along $\theta = a_1$, there is a jump discontinuity in both $\bar{g}_\sigma$ and $\bar{g}_\theta$, due to the jump discontinuity in the definition of $\gamma(\boldsymbol{x}_1)$ for surfaces in $\mathcal{S}_1$. Nullclines will not generally terminate at regular points in the interior of the phase plane. Hence, additional σ and θ-nullclines will either be isolated closed curves or will enter and leave the phase plane through the open line segments $\overline{O_1O_2}$ and $\overline{O_1O_3}$.

- Within the region $\theta \in (0, a_1)$, $\sigma > 0$, the right-hand sides of both (2.86) and (2.87) are smooth. Application of Bendixson's negative criterion to (2.86) and (2.87) within this region, (see e.g. [61], page 84), and by using (2.70), implies that there are no closed phase paths for $u > 0$. The Poincaré-Bendixson (PB) theorem then implies that all phase paths of (2.86) and (2.87) must either be/approach equilibrium points within this region, leave the region through the lower spray boundary, or become unbounded as $\eta \to \infty$.

- From (2.90) and (2.91) it is seen that the physical interpretation of an EP is a point at which mass transfer across the billet surface due to deposition and withdrawal is balanced exactly, in both radial and polar directions. Thus, a billet surface moving in the phase plane will not be able to "pass through" such a point. Since withdrawal is parallel to the billet axis, it follows that at an EP, (σ^*, θ^*), the averaged mass flux field must also be parallel to the billet axis, i.e.

$$\bar{g}_\sigma(\sigma^*,\theta^*)\sin\theta^* + \bar{g}_\theta(\sigma^*,\theta^*)\cos\theta^* = 0. \tag{2.92}$$

$$-\bar{g}_\sigma(\sigma^*,\theta^*)\cos\theta^* + \bar{g}_\theta(\sigma^*,\theta^*)\sin\theta^* = \mu, \tag{2.93}$$

  Because metal is sprayed in towards the billet axis, this can only happen at points where sufficient spray arrives from all directions to "cancel out" the mass flux component perpendicular to the billet axis, i.e. within the area bounded by the lower and overlapping spray boundaries and by the billet axis of rotation. This area is shaded in Fig. 2.12.

- A local, linear stability analysis reveals that all EP's are unstable for $u > 0$. They will correspond to either saddle points, unstable nodes or unstable spirals, according to the sign of

$$\mathcal{Q} \equiv [\frac{\partial\bar{g}_\sigma}{\partial\sigma}(\bar{g}_\sigma + \frac{\partial\bar{g}_\theta}{\partial\theta}) + \frac{\partial\bar{g}_\theta}{\partial\sigma}(\bar{g}_\theta - \frac{\partial\bar{g}_\sigma}{\partial\theta})],$$

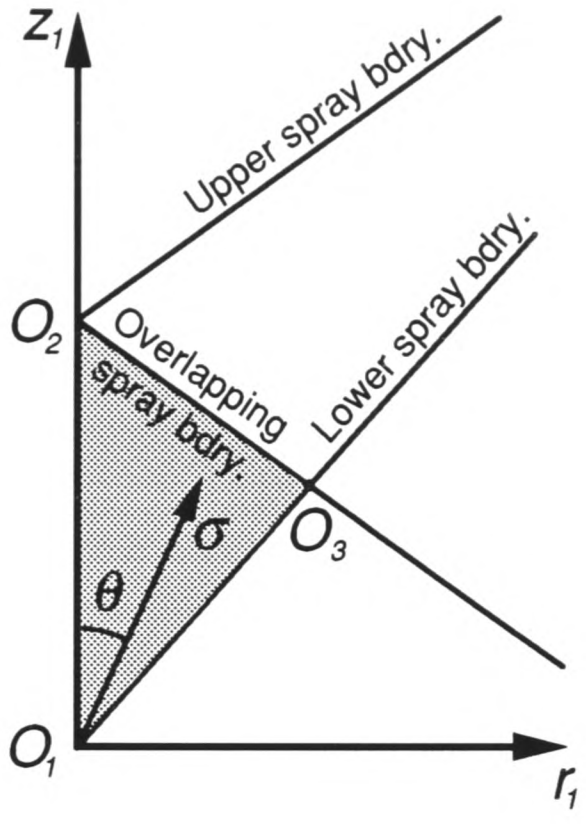

Figure 2.12: Shaded region within which equilibrium points may exist

(all functions evaluated at the EP). EP's are classified as follows

$$\begin{aligned} -\infty \;&<\mathcal{Q}<\; 0 && \Rightarrow \text{ saddle,} \\ 0 \;&<\mathcal{Q}<\; \frac{(\mu\cos\theta^*)^2}{4\sigma^*} && \Rightarrow \text{ unstable node,} \\ \frac{(\mu\cos\theta^*)^2}{4\sigma^*} \;&<\mathcal{Q}<\; \infty && \Rightarrow \text{ unstable spiral.} \end{aligned} \tag{2.94}$$

- From (2.76) and (2.78), it is seen that the points at which steady state crown shapes cross the billet axis are EP's for the system (2.86) and (2.87). Considerable simplification results from calculating $\mathcal{Q}$ on the billet axis. EP's $(\sigma^*, 0)$ are classified by

$$\begin{aligned} -\infty \;&<\frac{\partial\bar{g}_\sigma}{\partial\sigma}(\sigma^*,0)<\; -\tfrac{\mu}{\sigma^*} && \Rightarrow \text{ saddle,} \\ -\tfrac{\mu}{\sigma^*} \;&<\frac{\partial\bar{g}_\sigma}{\partial\sigma}(\sigma^*,0)<\; 0 && \Rightarrow \text{ node,} \\ 0 \;&<\frac{\partial\bar{g}_\sigma}{\partial\sigma}(\sigma^*,0)<\; \infty && \Rightarrow \text{ saddle.} \end{aligned} \tag{2.95}$$

  The stable and unstable separatrices of the saddle are reversed for $\frac{\partial\bar{g}_\sigma}{\partial\sigma}(\sigma^*,0) > 0$ and $\frac{\partial\bar{g}_\sigma}{\partial\sigma}(\sigma^*,0) < -\frac{\mu}{\sigma^*}$. The node is inflected at $\frac{\partial\bar{g}_\sigma}{\partial\sigma}(\sigma^*,0) = -\frac{\mu}{2\sigma^*}$.

2.3.3 Steady state crown shapes; global analysis

Clearly, all possible phase planes cannot be accounted for, since each choice of $g(r')$, $a(t)$ or μ produces a new phase portrait. However, (2.95) implies that many of the qualitative features of the phase plane close to the billet axis will depend on the function $\bar{g}_\sigma(\sigma, 0)$, and at least those phase planes corresponding to "typical" $\bar{g}_\sigma(\sigma, 0)$ can be considered.

From (2.79) it is seen that $\bar{g}_\sigma(\sigma, 0)$ is the convolution of $g(r')$ and $\cos a(t)$. Since the spray distribution, $g(r')$, is known to be unimodal across the diameter of the spray cone, the shape of $\bar{g}_\sigma(\sigma, 0)$ will depend

largely on $a(t)$. Due to the scanning motion, the region between upper and lower spray boundaries diverges with distance from the atomiser nozzle. The more the region has diverged, the greater effect the convolution (2.79) can have in disturbing the unimodality of $g(r')$. If either $|a_1 - a_2|$ or the distance $[r_n^2 + (z_n + z_c)^2]^{1/2}$ is small enough, then it is likely that $-\bar{g}_\sigma(\sigma, 0)$ will be unimodal also. It is this case that is investigated.

Existence of a steady state for unimodal $-\bar{g}_\sigma(\sigma, 0)$

Suppose that $-\bar{g}_\sigma(\sigma, 0)$ is unimodal with maximum value K at $\sigma_K \in (0, z_u)$. Then for any $\mu \in (0, K)$ there are exactly two solutions of (2.78), say $f = \sigma_1, \sigma_2 : \sigma_1 > \sigma_2$. Hence there is the possibility of at most two steady state crown shapes existing, if any.

The EP nearest O_2, $(\sigma_1, 0)$, is a saddle with stable separatrices lying along the axis $\theta = 0$. The unstable separatrix extends out into the phase plane $\theta > 0$ and can represent a steady state crown profile only if it crosses the line $\theta = a_1$. The PB theorem implies that it will do so unless it approaches another EP.

If the unstable separatrix approaches $(\sigma_2, 0)$ then this EP must be a saddle also, (since all EP's are unstable), and the unstable separatrix of $(\sigma_1, 0)$ will become the stable separatrix of $(\sigma_2, 0)$. The unstable separatrix of $(\sigma_2, 0)$ lies along the billet axis and joins the stable separatrix of $(\sigma_1, 0)$. Hence, this hypothesis implies a hetroclinic orbit between the two saddles, see Fig. 2.13.

Within this orbit there must be an EP of index 1, (i.e. an unstable node or spiral), and hence a limit cycle. This leads to a contradiction, via Bendixson's negative criterion. Thus, unless the unstable separatrix from $(\sigma_1, 0)$ approaches another EP in the region $\theta \in (0, a_1),\ \sigma > 0$, it will cross $\theta = a_1$.

Recall that at an EP the mass flux field must be parallel to the billet axis and must balance the withdrawal rate exactly. Consider now the computation of the averaged mass flux field. Fixing $\phi = 0$, evaluate $\bar{\boldsymbol{g}}$ through (2.69), by integrating with respect to τ_2 over the two intervals $[0, 1/2]$ and $[1/2, 1]$ separately. The first of these gives the mass flux travelling direct to $(\sigma, \theta, 0)$, when the point $(\sigma, \theta, 0)$ is facing the atomiser; the second gives the mass flux at $(\sigma, \theta, 0)$ that travels from the far side of the billet to get there. The two mass flux fields, say $\bar{\boldsymbol{g}}_1$ and $\bar{\boldsymbol{g}}_2$, combine to give $\bar{\boldsymbol{g}}$, see Fig. 2.14a.

Unimodality of $-\bar{g}_\sigma(\sigma, 0)$ implies that the averaged mass fluxes $\|\bar{\boldsymbol{g}}_1\|$ and $\|\bar{\boldsymbol{g}}_2\|$ across any line, $r_1 \equiv \sigma \sin\theta = \lambda$, parallel to the billet axis of rotation, will also be unimodal. For $\lambda \geq 0$, denote the vertical height in the crown frame of reference at which $\|\bar{\boldsymbol{g}}_1\|$, attains its maximum by $z_{m,1}(\lambda)$, similarly defining $z_{m,2}(\lambda)$ with $\|\bar{\boldsymbol{g}}_2\|$, Fig. 2.14b. Note that $z_{m,1}(\lambda)$ increases with λ whilst $z_{m,2}(\lambda)$ decreases.

For (2.92) to be satisfied, the components of the two mass fluxes perpendicular to the billet axis must be of equal size and of opposite sign. This happens at all points on the billet axis. Starting at any point $(\sigma, 0) : \sigma \in (0, z_u)$, attempt to construct a line $\mathcal{L}(\lambda)$ along which (2.92) is satisfied. For $\sigma > \sigma_K$, moving perpendicular to the billet axis, one moves initially away from $z_{m,2}(\lambda)$ and towards $z_{m,1}(\lambda)$. For $\sigma < \sigma_K$, this is reversed. It is soon apparent that $\mathcal{L}(\lambda)$ must run from $(\sigma_K, 0)$ out towards the point of intersection of the overlapping and lower spray edges, O_3.

In traversing along $\mathcal{L}(\lambda)$ the mass flux

$$\|\bar{\boldsymbol{g}}\| = |-\bar{g}_\sigma \cos\theta + \bar{g}_\theta \sin\theta|$$

will decrease to zero with λ. Thus, there can be at most one point on this line where (2.93) can be satisfied, and can be at most one further EP in the region $\theta \in (0, a_1),\ \sigma > 0$.

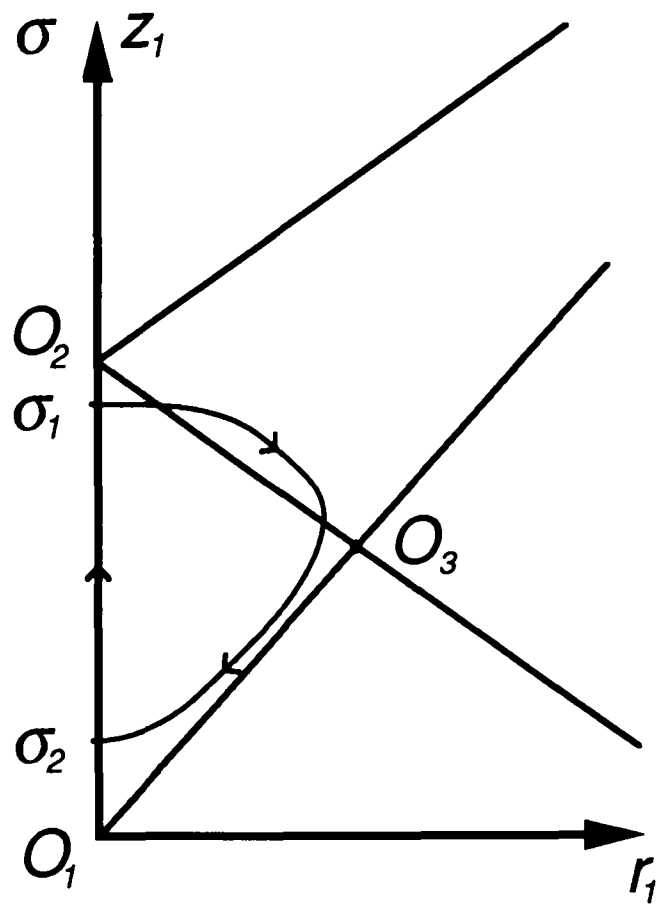

Figure 2.13: Hetroclinic orbit in the phase plane

By defining $\gamma(\boldsymbol{x}_1) = 1$ everywhere, and integrating a new axisymmetric averaged mass flux field, as before, a new phase plane can be defined, which is exactly the same as that for equations (2.86) and (2.87) in the region $\theta \in [0, a_1]$, but which extends smoothly below the lower spray boundary in a natural way.[6] For this new phase plane there can also only exist EP's in the shaded region of Fig. 2.12, by the same arguments as before. This new phase plane is now considered briefly, in order to classify the extra EP.

On the line segment $\overline{O_1O_2}$, σ-nullclines enter and leave the phase plane $\theta > 0$ only at EP's and θ-nullclines enter and leave the phase plane at points $(\sigma, 0)$ satisfying

$$\frac{\mu}{\sigma} + \frac{\partial \bar{g}_\sigma}{\partial \sigma}(\sigma, 0) = 0. \tag{2.96}$$

The σ-nullcline must run in a loop between $(\sigma_1, 0)$ and $(\sigma_2, 0)$. The existence of an additional EP in the phase plane implies its intersection with a θ-nullcline. Intersections of closed nullclines with each other or of a closed θ-nullcline with the looped σ-nullcline will produce $2k$ extra EP's. Similarly, if a θ-nullcline loops between two solutions of (2.96) and intercepts the looped σ-nullcline there will be $2k$ extra EP's, unless the two solutions of (2.96) straddle $(\sigma_2, 0)$ on the billet axis, (when there are $2k + 1$ intersections with the σ-nullcline).

Since there is at most one extra EP, the last case is the only one of interest. When solutions of (2.96) straddle $(\sigma_2, 0)$, this lower EP will be a saddle point, see (2.95). The new EP at the intersection of the two loops has index 1, and so is an unstable node or spiral. In either case the unstable separatrix from $(\sigma_1, 0)$ cannot approach it. It follows that the unstable separatrix from $(\sigma_1, 0)$ must cross the line $\theta = a_1$.

The above argument proves that for unimodal $-\bar{g}_\sigma(\sigma, 0)$ there will exist a phase path of the system (2.86) and (2.87) that corresponds directly to a steady state solution of the equation (2.71). Equation (2.71) describes transient, axisymmetric, slow-time growth of billet crown shapes $F_0 \in \mathcal{S}_1$. What the above

[6] This new phase plane is that which results from assuming that there is absolutely no shadowing.

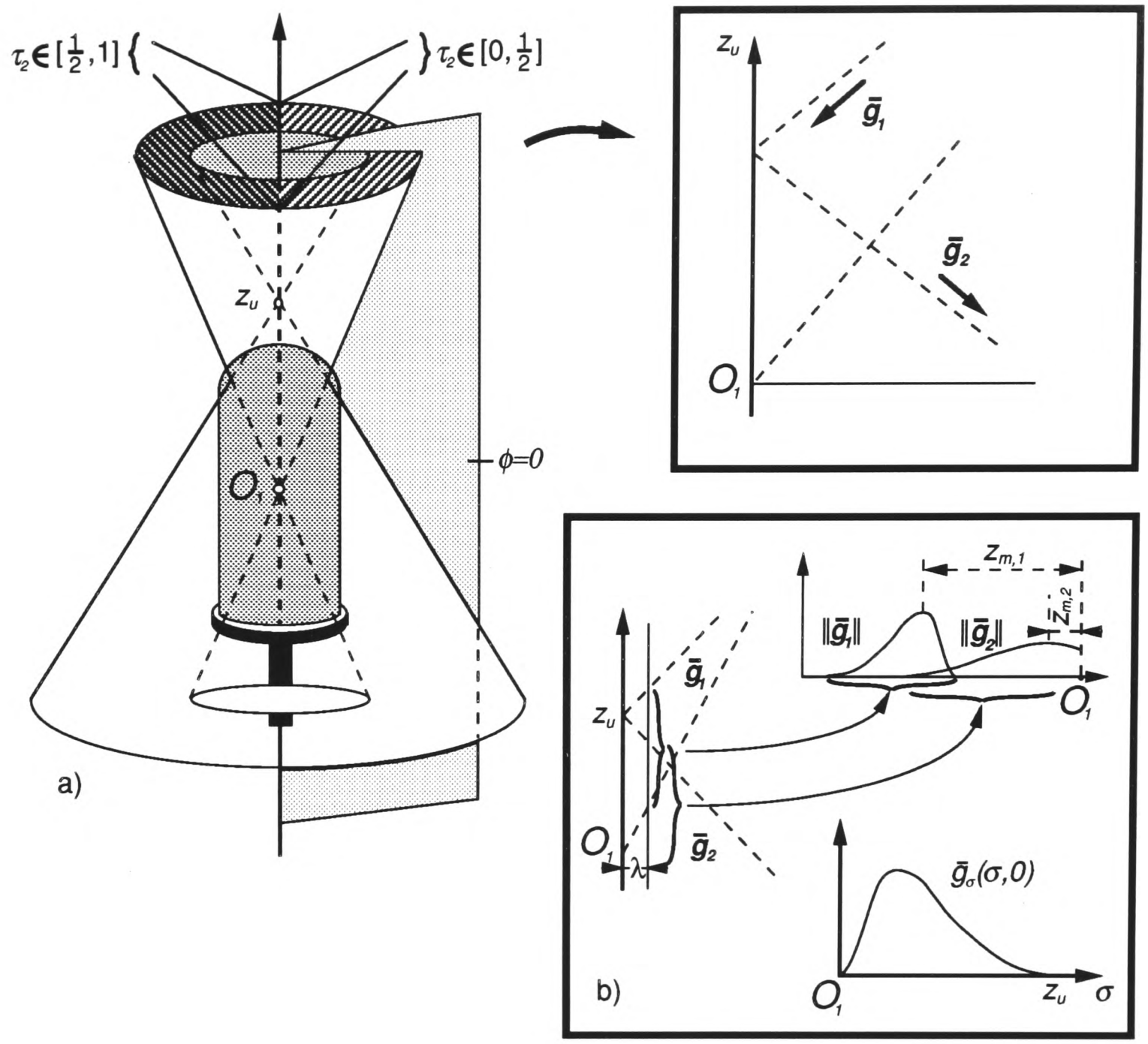

Figure 2.14: Averaging the mass flux distribution field, defining $z_{m,1}$, $z_{m,2}$.

argument does not prove is that the steady state solution computed corresponds to a surface that is in $\mathcal{S}_1$. This must be verified after computation of the steady state. The following algorithm can be used to demonstrate the global existence of a steady state billet crown profile.

1. Compute $\overline{g}$ using the sticking efficiency $\gamma(\boldsymbol{x}_1)$ defined by (2.56).

2. If $-\overline{g}_\sigma(\sigma, 0)$ is unimodal and $\mu \in (0, K)$, then there exists a phase path, entering the phase plane from $(\sigma_1, 0)$ and exiting through $\theta = \pi/2$.

3. Compute the phase path, call it F_0.

4. If $F_0 \in \mathcal{S}_1$ then F_0 corresponds to $F_0 = \sigma - f(\theta)$ given by (2.72), and is a steady state crown profile, (as well as a steady state solution of (2.71)).

Uniqueness

It is clearly of interest, from an operational point of view, to determine whether there can be a second steady state emanating from the point $(\sigma_2, 0)$ on the billet axis of rotation. The EP, $(\sigma_2, 0)$, will be either a node or a saddle. If it is a node then the phase path that satisfies

$$\frac{d\sigma}{d\theta} \to 0, \text{ as } (\sigma, \theta) \to (\sigma_2, 0),$$

can be followed from the phase plane, and this will give a second steady state profile. However, since all other phase paths from $(\sigma_2, 0)$ will also cross $\theta = a_1$, this path is non-unique.

If $(\sigma_2, 0)$ is a saddle then, as discussed previously, there exists a single additional EP, not on the billet axis, which will be either a node or a spiral. The unstable separatrix of $(\sigma_2, 0)$ will lie along the billet axis, whilst the stable separatrix extends into the phase plane and approaches the extra node/spiral as $\eta \to -\infty$. Whether a node or a spiral there are infinitely many phase paths between the extra EP and $\theta = a_1$.

Clearly, this non-uniqueness of paths from $(\sigma_2, 0)$ to $\theta = a_1$ implies that any steady state profile from $(\sigma_2, 0)$ will be unstable. Thus, a steady state crown profile that starts at $(\sigma_1, 0)$, (for any fixed value of μ), will be unique in the sense that it will be the only steady state crown profile that is uniquely defined and can be stable. For unimodal $-\bar{g}_\sigma(\sigma, 0)$, there are thus only two qualitatively different phase planes possible. These are sketched schematically in Fig. 2.15.

Stability

From Fig. 2.15 the stability of the single steady state is self evident. Phase paths close to the σ-axis, (above $(\sigma_2, 0)$), follow the σ-axis until close to $(\sigma_1, 0)$ where they turn and follow the unstable separatrix/steady state out through $\theta = \pi/2$. If a transient crown profile is superimposed on the phase plane, it can be seen that a small interval of the surface that is initially close to the billet axis will eventually expand to represent a large proportion of the billet crown. Since the phase paths close to the billet axis remain close to the steady state, the transient profile will eventually become closer to the steady state profile. Thus, the steady state is stable in the sense that

$$\lim_{\eta \to \infty} \sup_{\theta \in [0, \pi/2]} |\tilde{f}(\theta, \eta)| = 0, \tag{2.97}$$

where $\sigma = f(\theta)$ is the steady state profile and $\sigma = f(\theta) + \tilde{f}(\theta, \eta)$ is the transient profile.

This type of stability effectively "waits" for the part of the crown profile nearest the billet axis to grow outwards. However, since $\eta \in [0, A]$ during a production run, and $A = O_S(1)$, there may not be enough time during a production run to "wait" for this type of stability to develop, especially since some points on the transient billet profile may still actually be moving away from the steady state. More useful is to know when the transient billet crown is approaching the steady state crown at all points where deposition is taking place and at all times during the production run, i.e. when

$$\frac{\mathrm{d}}{\mathrm{d}\eta}|\tilde{f}(\theta, \eta)| < 0, \ \forall\, \theta \in [0, a_1], \ \eta \in [0, A].$$

To this end, the following theorem may be proven.

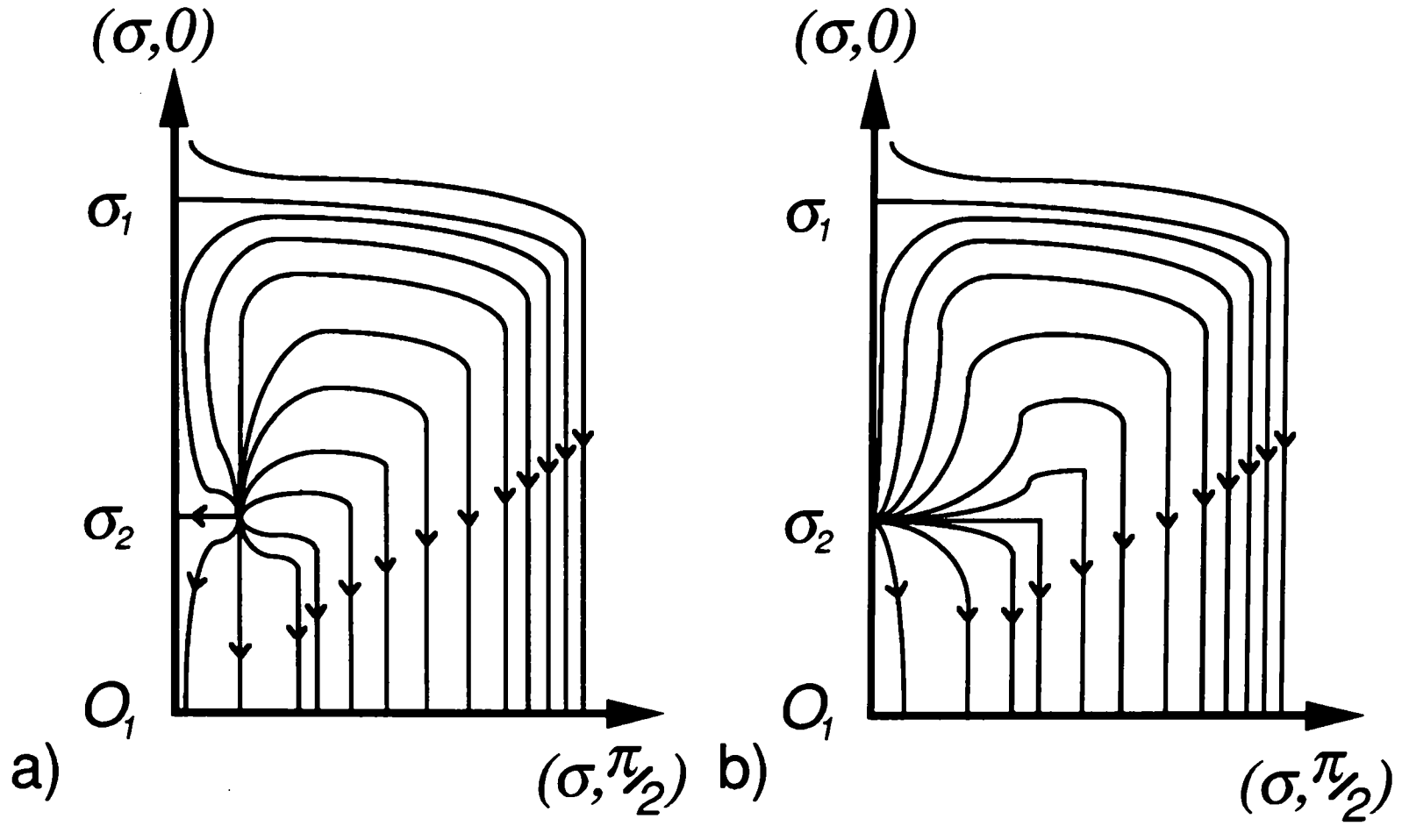

Figure 2.15: Schematic of the two possible phase planes for unimodal $-\bar{g}_\sigma(\sigma,0)$, and surfaces in $\mathcal{S}_1$.

Theorem 2.3.1 *Let $-\bar{g}_\sigma(\sigma,0)$ be unimodal with maximum value K, and let $\mu < K$ be fixed so that there exists a single steady state solution of (2.71). Also, let b and $\kappa > 0$ be such that for $\theta \in (0,b] \subseteq (0,a_1]$,*

$$|\tilde{f}| < \kappa \Longrightarrow$$

a) $\mu \sin\theta - \bar{g}_\theta(f+\tilde{f},\theta) > 0$, and

b) $\frac{\partial \mathcal{H}}{\partial \sigma}(f+\tilde{f},\theta,\mu) < 0$.

Then, there exists $\kappa_1 > 0$ such that $|\tilde{f}(\theta,\eta_0)| < \kappa_1 \quad \forall \theta \in [0,b] \Rightarrow$

$$\frac{\partial}{\partial \eta}|\tilde{f}| < 0, \ \forall \theta \in [0,b], \ \eta > \eta_0.$$

Proof Define $\mathcal{A}(\sigma,\theta,\mu)$ by

$$\mathcal{A}(\sigma,\theta,\mu) = \frac{\mu \sin\theta - \bar{g}_\theta(\sigma,\theta)}{\sigma}, \tag{2.98}$$

so that the steady state crown profile, $\sigma = f(\theta)$, and transient crown profile, $\sigma = f(\theta) + \tilde{f}(\theta,\eta)$, respectively satisfy

$$\dot{m}(\eta)\mathcal{A}(f,\theta,\mu)\frac{\mathrm{d}f}{\mathrm{d}\theta} = \dot{m}(\eta)\mathcal{A}(f,\theta,\mu)\mathcal{H}(f,\theta,\mu), \tag{2.99}$$

$$\frac{\partial \tilde{f}}{\partial \eta} + \dot{m}(\eta)\mathcal{A}(f+\tilde{f},\theta,\mu)\left(\frac{\mathrm{d}f}{\mathrm{d}\theta} + \frac{\partial \tilde{f}}{\partial \theta}\right) = \dot{m}(\eta)\mathcal{A}(f+\tilde{f},\theta,\mu)\mathcal{H}(f+\tilde{f},\theta,\mu). \tag{2.100}$$

Recall that $\mathcal{H}(\sigma,\theta,\mu)$ is defined by equation (2.72). Using a Taylor expansion, (mean value theorem),

$$\mathcal{A}(f+\tilde{f},\theta,\mu) = \mathcal{A}(f,\theta,\mu) + \tilde{f}\frac{\partial \mathcal{A}}{\partial \sigma}(f+\tilde{f}_1,\theta,\mu), \tag{2.101}$$

$$\mathcal{H}(f+\tilde{f},\theta,\mu) = \mathcal{H}(f,\theta,\mu) + \tilde{f}\frac{\partial \mathcal{H}}{\partial \sigma}(f+\tilde{f}_2,\theta,\mu), \tag{2.102}$$

where

$$0 < |\tilde{f}_1| < |\tilde{f}|,$$

$$0 < |\tilde{f}_2| < |\tilde{f}|.$$

Rewrite equations (2.99) and (2.100) as

$$\begin{aligned} 0 &= -\dot{m}(\eta)\left[\mathcal{A}(f+\tilde{f},\theta,\mu) - \tilde{f}\frac{\partial \mathcal{A}}{\partial \sigma}(f+\tilde{f}_1,\theta,\mu)\right]\frac{\mathrm{d}f}{\mathrm{d}\theta} \\ &+ \dot{m}(\eta)\mathcal{A}(f,\theta,\mu)\left[\mathcal{H}(f+\tilde{f},\theta,\mu) - \tilde{f}\frac{\partial \mathcal{H}}{\partial \sigma}(f+\tilde{f}_2,\theta,\mu)\right], \qquad (2.103) \\ \frac{\partial \tilde{f}}{\partial \eta} &= -\dot{m}(\eta)\mathcal{A}(f+\tilde{f},\theta,\mu)\left(\frac{\mathrm{d}f}{\mathrm{d}\theta} + \frac{\partial \tilde{f}}{\partial \theta}\right) \\ &+ \dot{m}(\eta)\left[\mathcal{A}(f,\theta,\mu) + \tilde{f}\frac{\partial \mathcal{A}}{\partial \sigma}(f+\tilde{f}_1,\theta,\mu)\right]\mathcal{H}(f+\tilde{f},\theta,\mu). \qquad (2.104) \end{aligned}$$

Subtracting (2.103) from (2.104) produces

$$\begin{aligned} \frac{\partial \tilde{f}}{\partial \eta} &= -\dot{m}(\eta)\mathcal{A}(f+\tilde{f},\theta,\mu)\frac{\partial \tilde{f}}{\partial \theta} + \tilde{f}\dot{m}(\eta)\left[\mathcal{A}(f,\theta,\mu)\frac{\partial \mathcal{H}}{\partial \sigma}(f+\tilde{f}_2,\theta,\mu)\right. \\ &+ \left.(\mathcal{H}(f+\tilde{f},\theta,\mu) - \frac{\mathrm{d}f}{\mathrm{d}\theta})\frac{\partial \mathcal{A}}{\partial \sigma}(f+\tilde{f}_1,\theta,\mu)\right], \qquad (2.105) \end{aligned}$$

which, on using (2.99) to substitute for $\frac{\mathrm{d}f}{\mathrm{d}\theta}$, and using (2.101) and (2.102) once more, becomes

$$\frac{\partial \tilde{f}}{\partial \eta} + \dot{m}(\eta)\mathcal{A}(f+\tilde{f},\theta,\mu)\frac{\partial \tilde{f}}{\partial \theta} = \tilde{f}\dot{m}(\eta)\mathcal{A}(f+\tilde{f},\theta,\mu)\frac{\partial \mathcal{H}}{\partial \sigma}(f+\tilde{f}_2,\theta,\mu). \qquad (2.106)$$

Multiplying through by $2\tilde{f}$ produces

$$\frac{\partial}{\partial \eta}|\tilde{f}|^2 + \dot{m}(\eta)\mathcal{A}(f+\tilde{f},\theta,\mu)\frac{\partial}{\partial \theta}|\tilde{f}|^2 = 2|\tilde{f}|^2\dot{m}(\eta)\mathcal{A}(f+\tilde{f},\theta,\mu)\frac{\partial \mathcal{H}}{\partial \sigma}(f+\tilde{f}_2,\theta,\mu). \qquad (2.107)$$

This equation governs the behaviour of the positive quantity $|\tilde{f}|^2$. Along the characteristics of (2.107), $|\tilde{f}|^2$ and θ vary with η according to

$$\begin{aligned} \frac{\mathrm{d}}{\mathrm{d}\eta}|\tilde{f}|^2(\eta) &= 2|\tilde{f}|^2\dot{m}(\eta)\mathcal{A}(f+\tilde{f},\theta,\mu)\frac{\partial \mathcal{H}}{\partial \sigma}(f+\tilde{f}_2,\theta,\mu), \qquad (2.108) \\ \frac{\mathrm{d}}{\mathrm{d}\eta}\theta(\eta) &= \dot{m}(\eta)\mathcal{A}(f+\tilde{f},\theta,\mu). \qquad (2.109) \end{aligned}$$

For $|\tilde{f}(\theta,\eta_0)| < \kappa$ and $\theta \in (0,b]$, plot $|\tilde{f}|^2$ against θ along any of the characteristic curves.

- The right-hand side of (2.109) is positive, (according to condition a) of the theorem), so θ increases with η, at least when $\theta < b$.
- The right-hand side of (2.108) is negative, (according to conditions a) and b) of the theorem), so $|\tilde{f}|^2$ decreases with η.

Thus, for $|\tilde{f}| < \kappa$ and $\theta \in (0,b]$, $|\tilde{f}|$ will be decreasing for $\eta > \eta_0$. The same is true for any $\kappa_1 \leq \kappa$. This completes the proof, since it is qualitatively clear from the phase plane that when $\mu < K$, the two EP's on the billet axis of rotation are separated by a finite distance, say κ_2. Then, defining $\kappa_1 = \min[\kappa, \kappa_2]$ the stability of $|\tilde{f}|$ can be extended onto the axis $\theta = 0$. □

Remarks

1. This theorem provides sufficient, but not necessary, conditions for an interval of the steady state solution to be stable to finite perturbations. In the next chapter, steady state solutions are computed for a range of different process parameters and their stability is examined by considering those parts of the phase plane for which both these conditions hold. Where conditions a) and b) do not hold, it is readily seen from (2.108) and (2.109) in the proof of the theorem that the alternative conditions

(a) $\mu \sin\theta - \bar{g}_\theta(f + \tilde{f}, \theta) < 0$, and

(b) $\frac{\partial \mathcal{H}}{\partial \sigma}(f + \tilde{f}, \theta, \mu) > 0$,

also result in stable intervals of billet surface. Thus, regions where either or both of conditions a) and b) fail must be examined closely.

2. In practice, $\dot{m}(\eta)$ and $u(\eta)$ will vary during the run. Since, for different values of μ, $(= \mu(\eta))$, the same steady state profile will not exist, it is also necessary to consider stability to finite perturbations of μ. This can be done using the above methods.

3. The above theorem considers only the interval of the steady state solution with $\theta \in [0, b] \subseteq [0, a_1]$. The region below the lower spray boundary is of little interest, since if $F \in \mathcal{S}_1$, no deposition can occur here.

4. The theorem gives conditions for the nonlinear stability of the steady state solution of (2.71). When this steady state solution corresponds to a surface in $\mathcal{S}_1$, and when finite perturbations of the steady state satisfy the conditions of the theorem and also lie in $\mathcal{S}_1$, then these surfaces will approach the steady state billet surface for all $\theta \in [0, b]$.

Simplified analysis

Whilst determination of the exact steady state profile requires computation of the averaged mass flux distribution field, for the subclass of billet surfaces considered, the endpoints of the profile can be identified more simply.

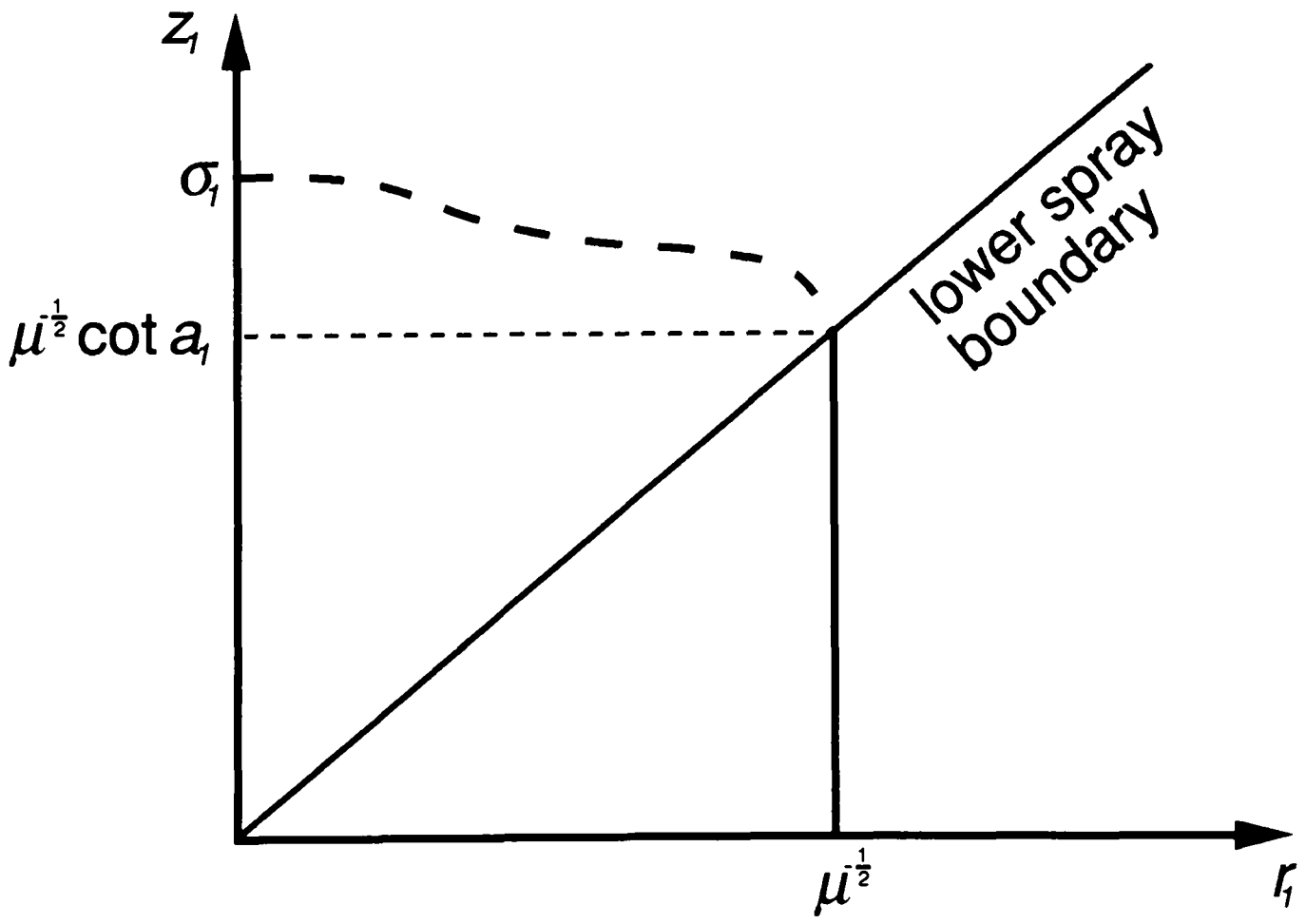

Figure 2.16: Determination of the endpoints of a steady state crown profile in $\mathcal{S}_1$.

The crown profile intercepts the axis of rotation horizontally at a height

$$z_1 = \sigma_1$$

above O_1, where σ_1 is the uppermost solution of (2.78). The crown profile then collects all the spray before exiting the deposition region vertically through the lower spray boundary. The billet radius, r_1, is thus given by the simple mass balance (2.28), which non-dimensionally becomes

$$\mu = \frac{1}{r_1^2},$$

so that the height at which the crown profile exits the deposition region is given by

$$z_1 = \mu^{-1/2} \cot a_1,$$

see Fig. 2.16.

2.3.4 Alternative dynamics

The preceding sections have described situations where scanning of the atomiser has little effect, except in "spreading out" the unimodal flux distribution, $g(r')$. The dynamics in this case are straightforward. Initial positioning of the collector plate above $(\sigma_2, 0)$, (and above the internal EP when it exists), and maintaining μ constant will result in a crown profile that eventually approaches the steady state profile. If the collector profile is initially close enough to the steady state profile then the steady state may be approached at all points $(\sigma, \theta) : \ \theta \in [0, b]$, according to the validity of theorem 2.3.1. Continuous variation of μ will result in continuous variation of the phase plane, but the underlying topology will remain the same.

As either $|a_1 - a_2|$ or the distance $[r_n^2 + (z_n + z_c)^2]^{1/2}$ becomes larger, unimodal $-\overline{g}_\sigma(\sigma, 0)$ becomes less likely. Mechanical constraints on turnaround times for the scanning atomiser nozzle can often give rise to bimodal $-\overline{g}_\sigma(\sigma, 0)$, for which the dynamics are more interesting. A bimodal $-\overline{g}_\sigma(\sigma, 0)$ introduces the possibility of there being more than one stable steady state crown profile for a given withdrawal to mass flow rate ratio, μ.

For a typical bimodal $-\overline{g}_\sigma(\sigma, 0)$, small and large enough μ give rise to two solutions of (2.78), whereas moderate μ allows four solutions to exist, see Fig. 2.17. The former case is similar to that discussed above. However, the added complexity of the bimodal mass distribution makes physical insight difficult. In particular, there is no guarantee that there will be no more than one EP in the interior of the phase plane. This allows the possible existence of a saddle point in the interior of the phase plane, and hence the possibility that the unstable separatrix from $(\sigma_1, 0)$ does not cross $\theta = a_1$. Since each saddle in the interior of the phase plane has two unstable separatrices it follows from a simple parity argument that successive separatrices can be pieced together, moving from saddle to saddle, and eventually the line $\theta = a_1$ will be crossed.

Such a path corresponds to a steady state solution of (2.71), and hence possibly to a steady state crown shape. However, such phase planes are structurally unstable, (see e.g. [81]); a small perturbation in μ can potentially result in a large change in steady state profile, as shown schematically in Fig. 2.18. Note that the effect of this type of instability, (saddlenode bifurcation), is not felt close to the billet axis, where the

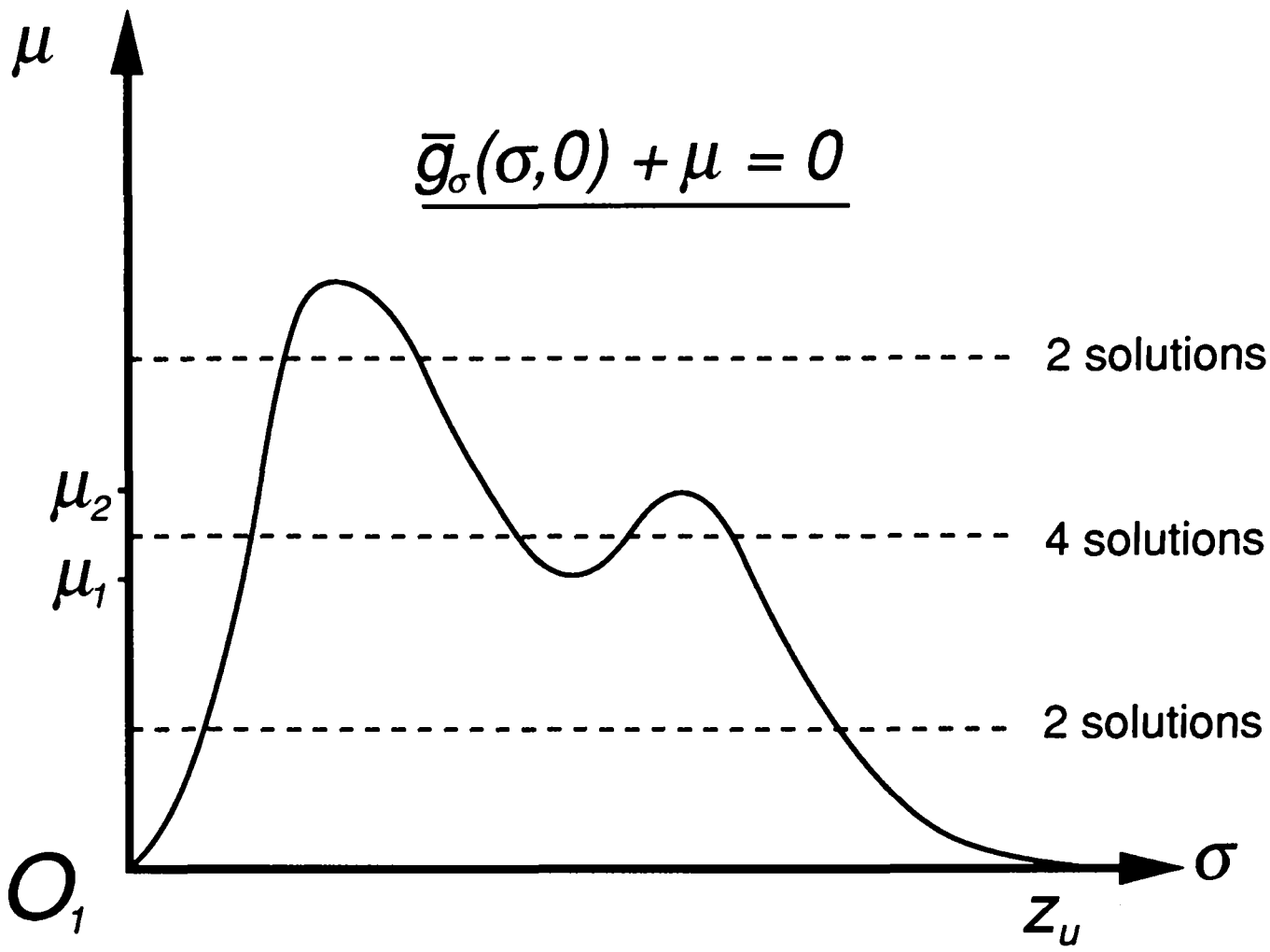

Figure 2.17: Bimodal $-\bar{g}_\sigma(\sigma, 0)$

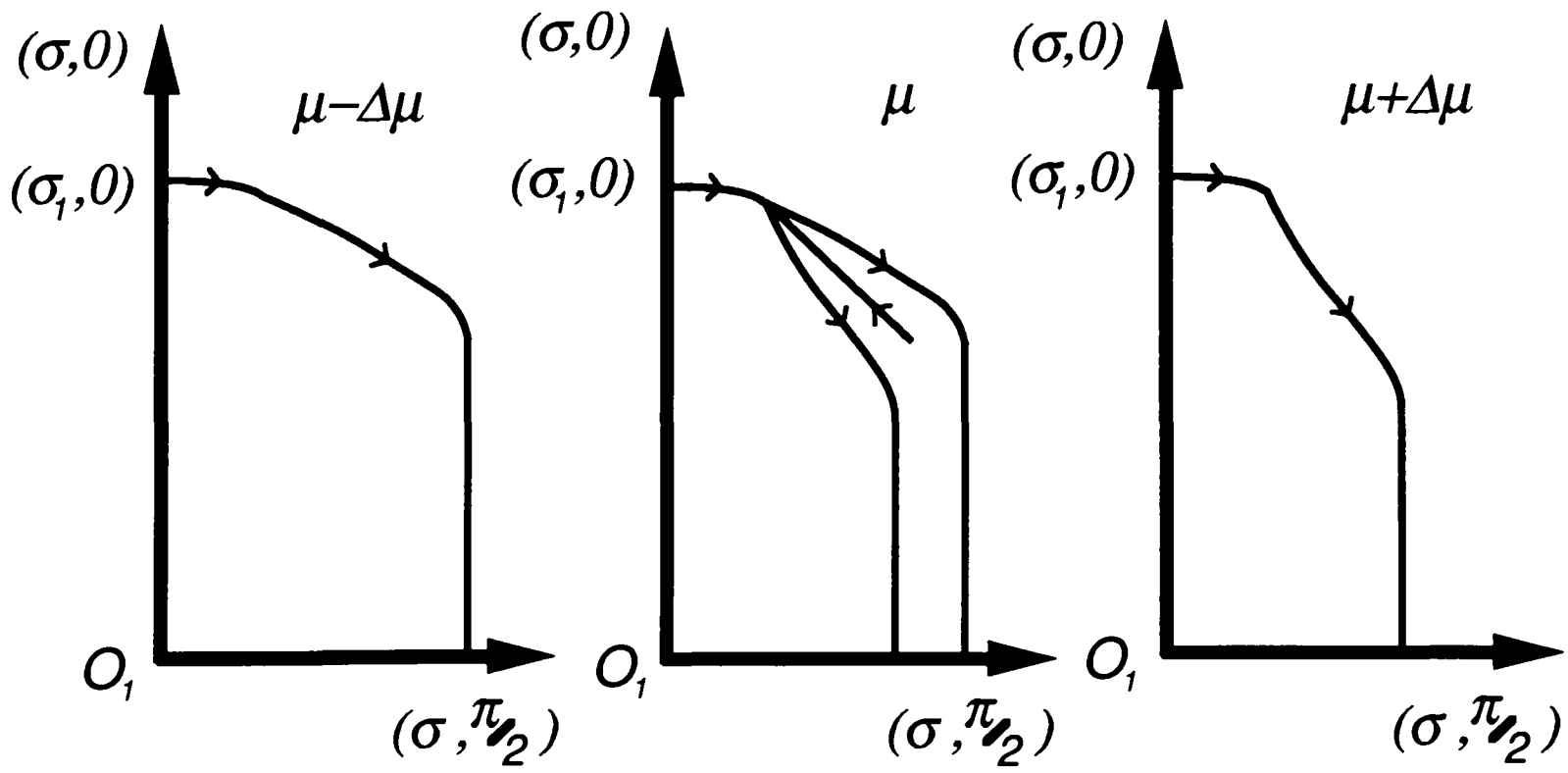

Figure 2.18: Structurally unstable phase phase plane; saddlenode bifurcation.

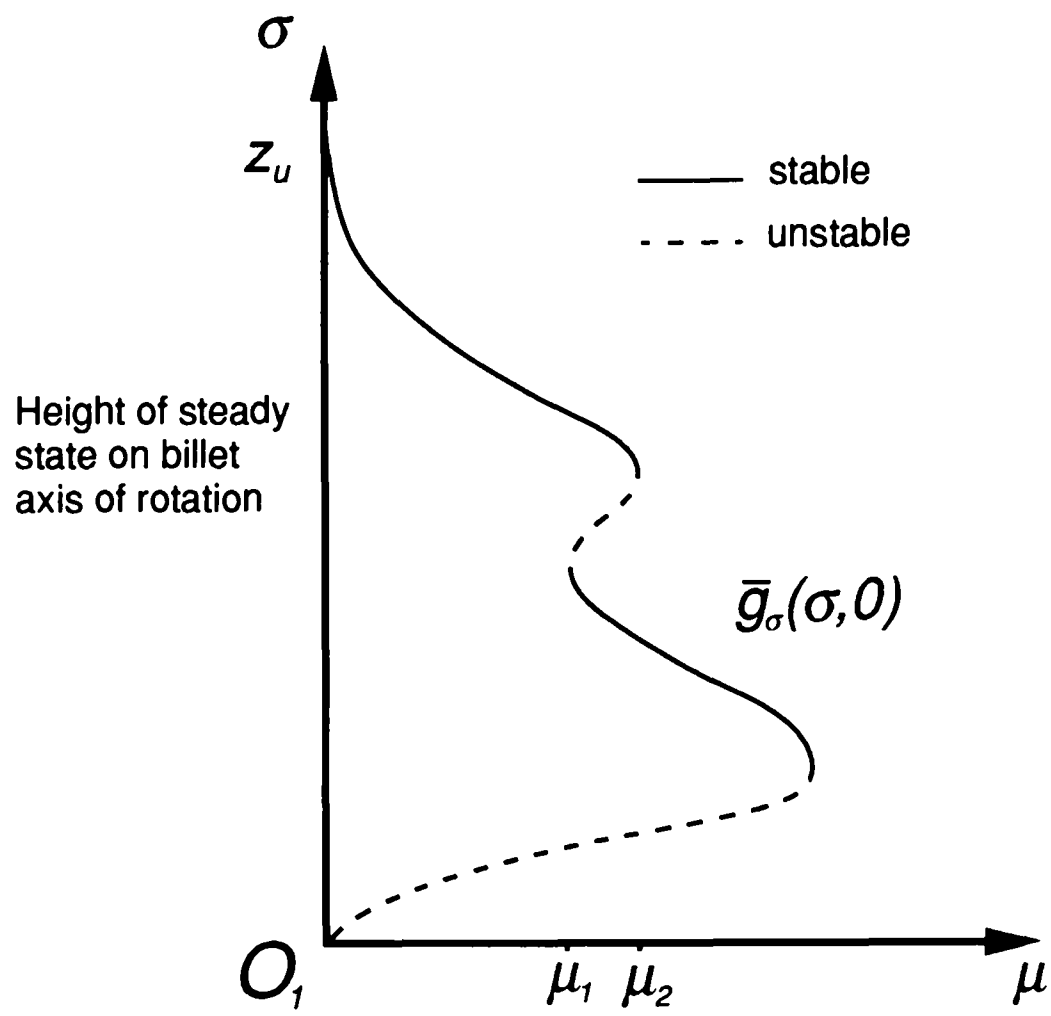

Figure 2.19: Possible hysteresis due to bimodal $-\bar{g}_\sigma(\sigma,0)$; bifurcation points μ_1 and μ_2.

unstable separatrix from $(\sigma_1,0)$ will be perturbed only slightly, but is felt beyond the first saddle point that this separatrix approaches. Although such instability would appear to be a theoretical possibility, it has not been observed computationally. In the absence of additional EP's for $\theta \in (0,a_1)$, the phase plane when only two solutions of (2.78) exist can be represented schematically by either Fig. 2.15a or Fig. 2.15b.

The second case, when four solutions of (2.78) exist, is more interesting still. Those EP's for which the gradient of $\bar{g}_\sigma(\sigma,0)$ is positive are saddle points that have unstable separatrices extending out into the phase plane. If the possibility of structurally unstable phase planes as described above is discounted, then each of these will potentially correspond to a steady state crown profile, with similar local stability properties as for the unimodal case. Each of the other two EP's on the σ-axis is either a node, or a saddle coupled with an unstable node/spiral in $\theta > 0$. In neither case will there be a steady state profile.

There is now also the possibility of a second type of structural instability in the phase plane. The two values μ_1 and μ_2 marked on Fig. 2.19 represent values at which there is a transition between there being one and two stable steady states. On increasing μ through the bifurcation value μ_1, a second stable steady state comes into existence. A transient profile that has been approaching the upper steady state will continue to do so only if sufficiently close, otherwise it will approach the new lower steady state. On increasing μ through the second bifurcation point, μ_2, the upper steady state ceases to exist. A transient solution of (2.71) that was close to the upper steady state must now "drop" towards the lower steady state. Hence, values of μ close to μ_1 and μ_2 represent unstable operating regimes. The transposed graph of $\bar{g}_\sigma(\sigma,0)$ represents a hysteresis curve for the bifurcations that occur, see Fig. 2.19. The existence of multiple steady states and the occurrence of this type of instability are investigated computationally in the following two chapters.

2.4 Summary

- A physically based mathematical model has been formulated, yielding non-dimensional equations, (2.42) and (2.43), which approximate the conservation of mass within the metal spray and at the billet surface.

- Equation (2.43) describes three dimensional growth of the billet surface, incorporates the nonlinear effects of shadowing, and allows directly for variations in

  1. the metal mass flow rate,
  2. the spray distribution within the spray cone,
  3. the rotation and scanner motions,
  4. the withdrawal rate, and
  5. the collector size and initial position.

  The various approximations made are discussed in the text.

- There is one important dimensionless group in the model equations;

$$\epsilon \equiv \frac{2\pi}{\hat{\omega}_0}\frac{\hat{U}_0}{R} \ll 1,$$

  which is the ratio of the rotation ($\approx$ scanner) and withdrawal timescales. Significant billet growth takes place over the timescale ϵ^{-1}, but variations in the spray mass flux occur on the rotation/scanner timescale. This makes numerical solution of (2.43) infeasible.

- For an identifiable subclass, $\mathcal{S}_1$, of billet crown profiles it is possible to define a "sticking efficiency", γ, which depends only on position within the crown frame of reference, (and hence remove the nonlinearity from (2.43)). For such billet crowns, under reasonable assumptions, one is able to apply an averaging method and derive an $o(\epsilon)$ asymptotic approximation, to the three dimensional billet growth, that is valid over the length of the production run. When the uniform boundedness of a certain integral, (defined by (2.64)), is assumed the approximation becomes $O(\epsilon)$.

- An averaged equation is derived, (2.71), describing the axisymmetric growth of billet surfaces in $\mathcal{S}_1$ on the slow timescale $\eta = \epsilon t$.

- Analysis of the averaged equations shows that for constant ratio, μ, of withdrawal rate and mass flow rate, if the averaged mass flux along the billet axis is unimodal, then the equation (2.71) has a unique steady state. If this steady state solution is in $\mathcal{S}_1$, then it corresponds to a steady state billet crown shape.

- These steady states are inherently stable, in a weak geometric sense. This is explained, and a theorem is proven giving sufficient conditions for a much stronger form of stability for the steady state solutions to (2.71), (see theorem 2.3.1). Both forms of stability are nonlinear, allowing finite perturbations from the steady state to decay, and thus indicate a very useful model/process property.

- When the averaged mass flux along the billet axis is not unimodal, it is most likely to be bimodal. In this case it is shown that it is possible for more than one stable steady state crown profile to coexist for a given ratio of withdrawal and mass flow rates. This situation also admits the possibility of hysteresis, (or a catastrophe), in the model process as the ratio of withdrawal and mass flow rates is varied. This and other structural instabilities are discussed.

Chapter 3

Steady State Billet Growth

The previous chapter established analytically the possibility of steady state billet crown shapes existing under the assumptions of the model. The existence of a steady state billet crown allows the growth of axisymmetric billets of constant radius, with control being exerted primarily through regulation of the ratio, μ, of withdrawal rate to mass flow rate. Since heat flow into the billet occurs only through spray deposition on the billet crown surface, the geometry of the billet crown will have a large influence on solidification, and on the subsequent quality of deposited material. It is therefore necessary to gain an understanding of how the steady state crown geometry is affected by variations in μ and by variations in the atomiser scanning pattern.

This understanding is developed in this chapter. Section one outlines the numerical methods used. In section two, generic features of steady state growth dynamics are described, using as a simple example a fixed angle spray. Section three explores variations in these features, with spray cone radius and with fixed spraying angle. A sinusoidal atomiser scanning pattern is introduced in section four, and a range of scanning angles is considered. In section five this is repeated for a more realistic scanning pattern. Section six combines knowledge gained from the earlier sections, and from the analysis in chapter two, into loosely defined constraints on the axis mass flux distribution, $-\bar{g}_\sigma(\sigma,0)$. An inverse problem is considered; that of finding a scanner pattern for which the constraints on $-\bar{g}_\sigma(\sigma,0)$ are satisfied. An optimisation method is proposed for the solution of this problem and example results, that indicate the feasibility of such a method, are presented. The chapter concludes with a summary.

3.1 Computational details

To compute slow-time axisymmetric billet growth it is first neccesary to evaluate the averaged mass flux distribution vectorfield, $\bar{\boldsymbol{g}}$ of equation (2.69). This requires that both $g(r')$ and γ be specified.

A truncated normal distribution is assumed for the spray distribution function, (following [87]); $g(r')$ is defined by

$$g(r') = \begin{cases} K_1(\exp^{-K_2 r'^2} - \exp^{-K_2 r_s^2}), & 0 \leq r' \leq r_s, \\ 0, & r_s < r' < \infty. \end{cases} \tag{3.1}$$

For fixed spray cone radius, r_s, the constant K_2 is chosen so that

$$\int_0^{r_s} \exp^{-K_2 r'^2} r' \mathrm{d}r' = .95 \int_0^{\infty} \exp^{-K_2 r'^2} r' \mathrm{d}r', \tag{3.2}$$

with K_1 chosen to conserve the mass flow between the atomiser and spray cone, according to equation (2.37).

In assigning a functional form for the shadowing coefficient, γ, one wishes to be able to compute as wide a range of billet surface geometries as is possible. Equation (2.56), which is valid for surfaces in $\mathcal{S}_1$, assumes that all spray above the lower spray boundary is deposited on the billet, whilst spray from the "overlapping" mass flux vectorfield, $\bar{\boldsymbol{g}}_2$, can only be deposited above the lower spray boundary. This is rather restrictive, especially when dealing with billet surfaces such as in Fig. 2.9a, or with the start of production runs where the collector is positioned low on the axis of rotation. The following procedure correctly computes $\bar{\boldsymbol{g}}$ for surfaces in $\mathcal{S}_1$, but is also able to handle these other cases.

1. Setting $\gamma \equiv 1$ in (2.69), and integrating firstly over $\tau_1 \in [0,1]$, and then over $\tau_2 \in [0,1/2]$ and $\tau_2 \in [1/2,1]$ separately, defines two vectorfields $\bar{\boldsymbol{g}}_1$ and $\bar{\boldsymbol{g}}_2$ respectively, see Fig. 3.1.

   A cylindrical polar coordinate system, (r_1, z_1), is defined within the crown frame of reference. Integration of (2.69) to give a value for $\bar{\boldsymbol{g}}_1$ and $\bar{\boldsymbol{g}}_2$ at (r_1, z_1) is performed using the midpoint rule, giving second order accuracy. An integration step $\Delta\tau_1 \approx .01$ is used to integrate over the scanner period. The integration step, $\Delta\tau_2$, used to integrate over the rotation, is chosen according to the time interval over which there is a non-zero mass flux through (r_1, z_1); typically $\Delta\tau_2 \sim 10^{-2}$ also. Values of these vectorfields are computed and stored at points on a regular mesh.[1] In later evaluation of the vectorfields, linear interpolation from the stored values is used.

2. For any axisymmetric billet crown surface, (i.e. steady or transient), assume a representation in terms of a sequence of surface points, (σ_i, θ_i), (or (r_1^i, z_1^i) in the cylindrical crown coordinate system). Computation of $\bar{\boldsymbol{g}}$ from $\bar{\boldsymbol{g}}_1$ and $\bar{\boldsymbol{g}}_2$ proceeds as follows.

   (a) Start where the surface meets the billet axis of rotation; assume that

   $$\bar{\boldsymbol{g}} = \bar{\boldsymbol{g}}_1 + \bar{\boldsymbol{g}}_2,$$

   i.e. all spray is deposited.

   (b) Move through the sequence of surface points, moving away from the billet axis of rotation along the surface. At each point, (σ_i, θ_i), compute the surface normal vector, $\boldsymbol{n}$, using the linear surface segment between (σ_i, θ_i) and the previous surface point considered.

   (c) Compute $\bar{\boldsymbol{g}}_1.\boldsymbol{n}$ and $\bar{\boldsymbol{g}}_2.\boldsymbol{n}$ at (σ_i, θ_i). Define

   $$\gamma_{1,i} = \begin{cases} 1, & \bar{\boldsymbol{g}}_1.\boldsymbol{n} < 0, \\ 0, & \bar{\boldsymbol{g}}_1.\boldsymbol{n} \geq 0, \end{cases} \tag{3.3}$$

   $$\gamma_{2,i}^{*} = \begin{cases} 1, & \bar{\boldsymbol{g}}_2.\boldsymbol{n} < 0, \\ 0, & \bar{\boldsymbol{g}}_2.\boldsymbol{n} \geq 0, \end{cases} \tag{3.4}$$

[1] For results in this thesis a mesh spacing $\Delta r_1 = \Delta z_1 = 0.02$ in radial and vertical directions, r_1 and z_1 respectively, has been used throughout.

and

$$\gamma_{2,i} = \gamma^*_{2,i} \prod_{j \in J_i} \gamma_{2,j}, \tag{3.5}$$

where J_i is the set of surface points that have been considered before (σ_i, θ_i); $\gamma_{2,i} = 1$ initially, on the billet axis of rotation.

(d) Set

$$\bar{\boldsymbol{g}} = \gamma_{i,1}\bar{\boldsymbol{g}}_1 + \gamma_{i,2}\bar{\boldsymbol{g}}_2. \tag{3.6}$$

For a large proportion of billet surfaces, $\bar{\boldsymbol{g}}_1.\boldsymbol{n} \leq 0$ for $\theta \in [0, \pi/2]$ and $\bar{\boldsymbol{g}}_2.\boldsymbol{n}$ increases through zero only once for $\theta \in [0, \pi/2]$. For such surfaces, (including those in S_1), the above approach allows the accurate computation of $\bar{\boldsymbol{g}}$ and is quick to implement.

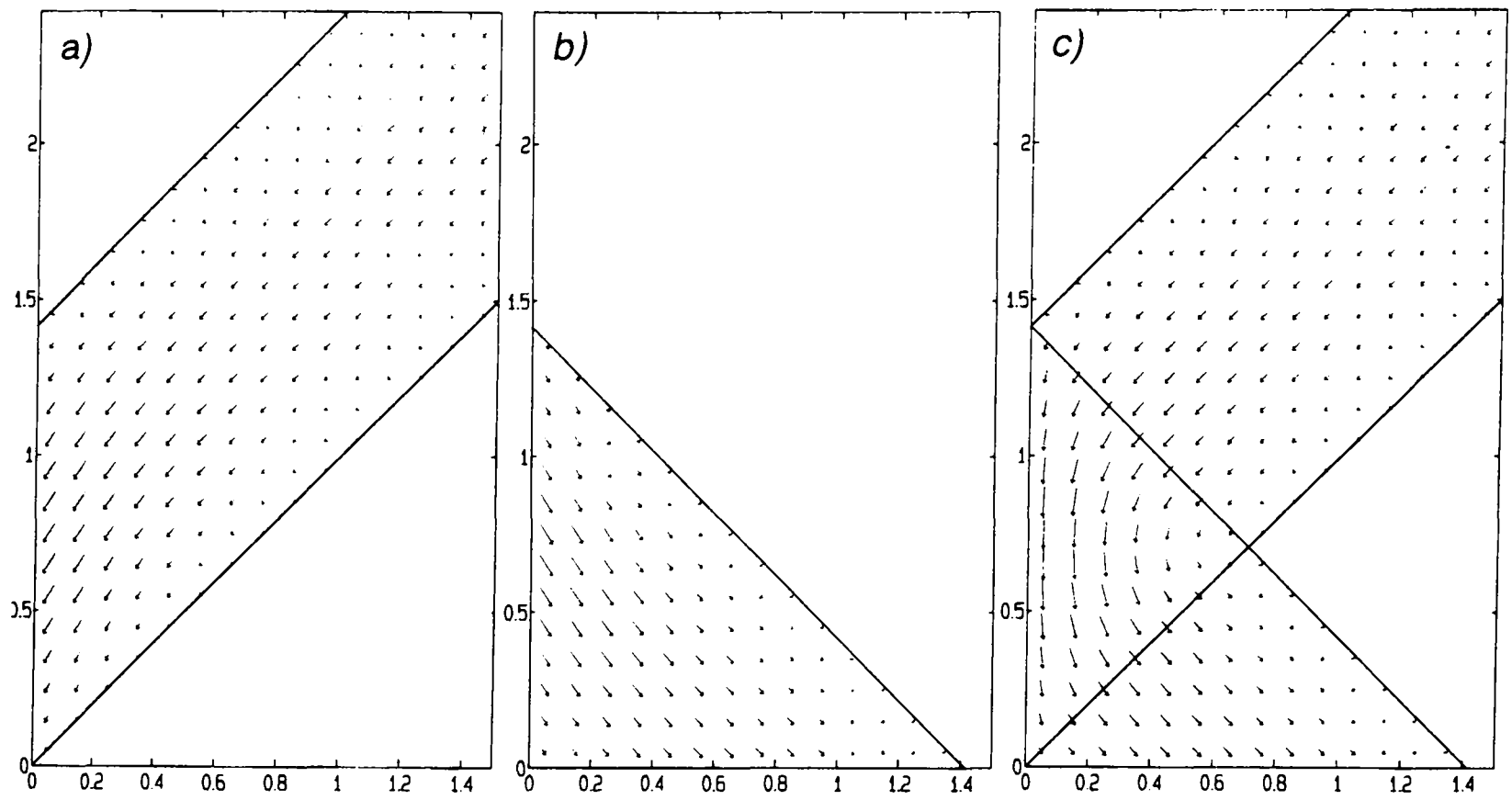

Figure 3.1: Computed mass flux distribution vectorfields on a regular grid, $r_s = 1/2$, $a(t) = 45°$; a) $\bar{\boldsymbol{g}}_1$, b) $\bar{\boldsymbol{g}}_2$, c) $\bar{\boldsymbol{g}}_1 + \bar{\boldsymbol{g}}_2$.

To compute a steady state crown shape the solutions of

$$\bar{g}_\sigma(\sigma, 0) + \mu = 0, \tag{3.7}$$

are found by computing the turning points of $\bar{g}_\sigma(\sigma, 0)$ and using the bisection method on each interval containing a solution. For each solution, $\sigma = f_0$, of (3.7) for which

$$\frac{\partial \bar{g}_\sigma}{\partial \sigma}(f_0, 0) > 0,$$

a steady state, $\sigma - f(\theta) = 0$, to equation (2.71) is found by integrating equation (2.72) forward in θ from the initial condition

$$f(0) = f_0. \tag{3.8}$$

The numerical integration is caried out using a second order Runge–Kutta method, (modified Euler), with fixed step $\Delta\theta = \frac{\pi}{800}$. Exploiting equation (2.82), the initial condition (3.8) is replaced by

$$f(\Delta\theta) = f_0, \tag{3.9}$$

as an initial condition for the numerical solution; $f(\theta)$ being integrated forward over $\theta \in [\Delta\theta, \pi/2]$. This avoids the problems of computing $\mathcal{H}$ on the billet axis, (where it takes values $-\infty$, 0 and $+\infty$), and introduces a local error of $O(\Delta\theta^2)$ only.

3.2 Fixed angle sprays: generic features

For a fixed angle spray, $a(t)$ = constant, computation of the mass flux distribution fields is very quick, involving only integration over the rotational movement. The billet axis flux distribution function, $-\bar{g}_\sigma(\sigma, 0)$, is given simply by

$$-\bar{g}_\sigma(\sigma, 0) = g(r'[\sigma, 0]) \cos a, \tag{3.10}$$

see Fig. 3.2. Thus (3.7) is easily solved.

In Fig. 3.3 are plotted computed steady state billet crown profiles in the (r_1, z_1)-plane for $a = 45°$, $r_s = 1/2$. Values of μ of

$$\mu = .5 + k\Delta\mu: \quad \Delta\mu = .5, \ k = 0, ..., 17$$

have been taken. From Fig. 3.2 it is seen that $-\bar{g}_\sigma(\sigma, 0) \approx 10$ at its maximum value. Hence, this choice of μ adequately covers the range of solutions to (3.7).

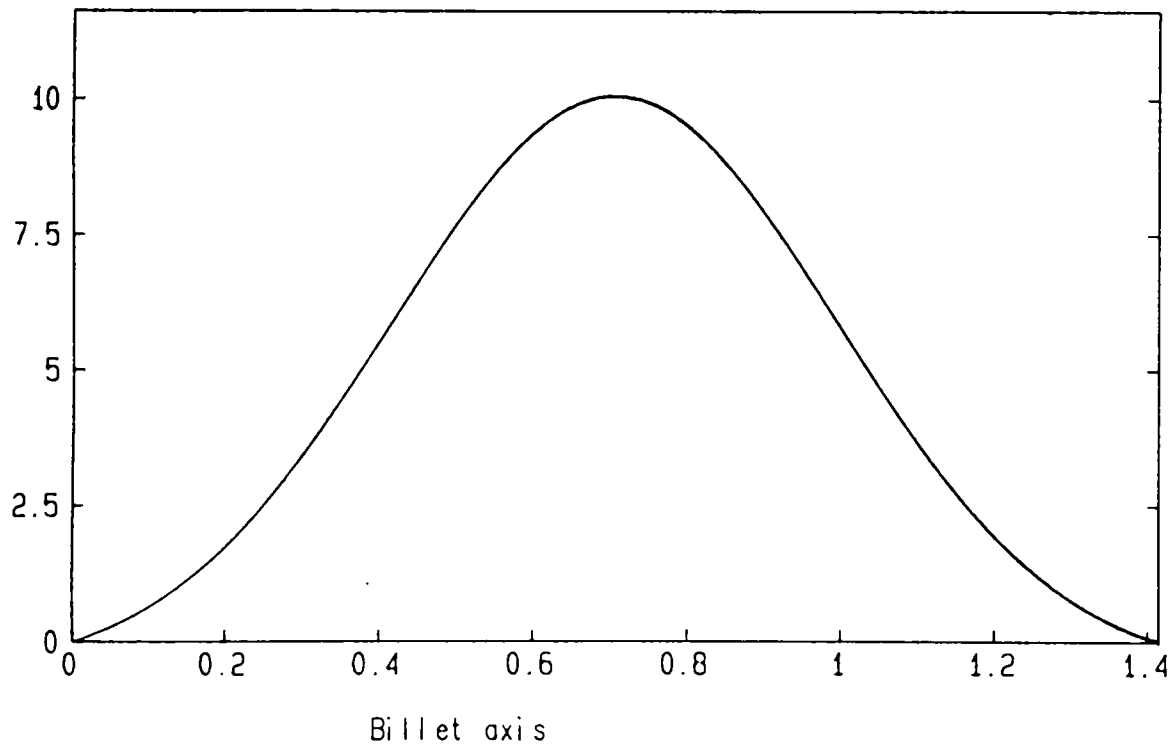

Figure 3.2: Axis flux distribution, $-\bar{g}_\sigma(\sigma, 0)$, for a fixed angle spray; $r_s = 1/2$, $a = 45°$.

With increasing ratio, μ, of withdrawal rate to mass flow rate, the steady state crown profiles form a series of nested curves. The outermost steady states, (small μ), are concave and lie in $\mathcal{S}_1$. As μ increases the steady state profiles become markedly more dome shaped and the height at which they intercept the billet axis of rotation decreases. Eventually, ($\mu \approx 3.6$), the steady states lie completely below the overlapping spray boundary, so that some of the averaged spray will pass over the top of the billet and will not be deposited. For these steady states $\bar{\boldsymbol{g}}_2 . \boldsymbol{n} \to 0$, and the averaging approximation might not be uniformly valid

over the whole billet surface, or on the timescale ϵ^{-1}, (see the discussion in chapter two, section 2.2.2, and Fig. 2.10b).

When μ is small, and the billet crown collects all of the spray, the steady state billet radius, r_b, should be given by

$$\mu = \frac{1}{r_b^2}. \tag{3.11}$$

For steady state crown shapes corresponding to

$$\mu = .5 + k\Delta\mu: \quad \Delta\mu = .25, \ k = 0, ..., 34,$$

(i.e. including those in Fig. 3.3), values of r_b and $\mu^{-1/2}$ were compared to produce Fig. 3.4. Fig. 3.4 illustrates the validity of the mass balance, (3.11), for small μ, (i.e. $\mu \leq 3.6$). In this range, equation (3.11) is satisfied with an error of order 10^{-3}, which gives a measure of the accuracy of the computation of both the mass flux distribution and the steady state profiles.

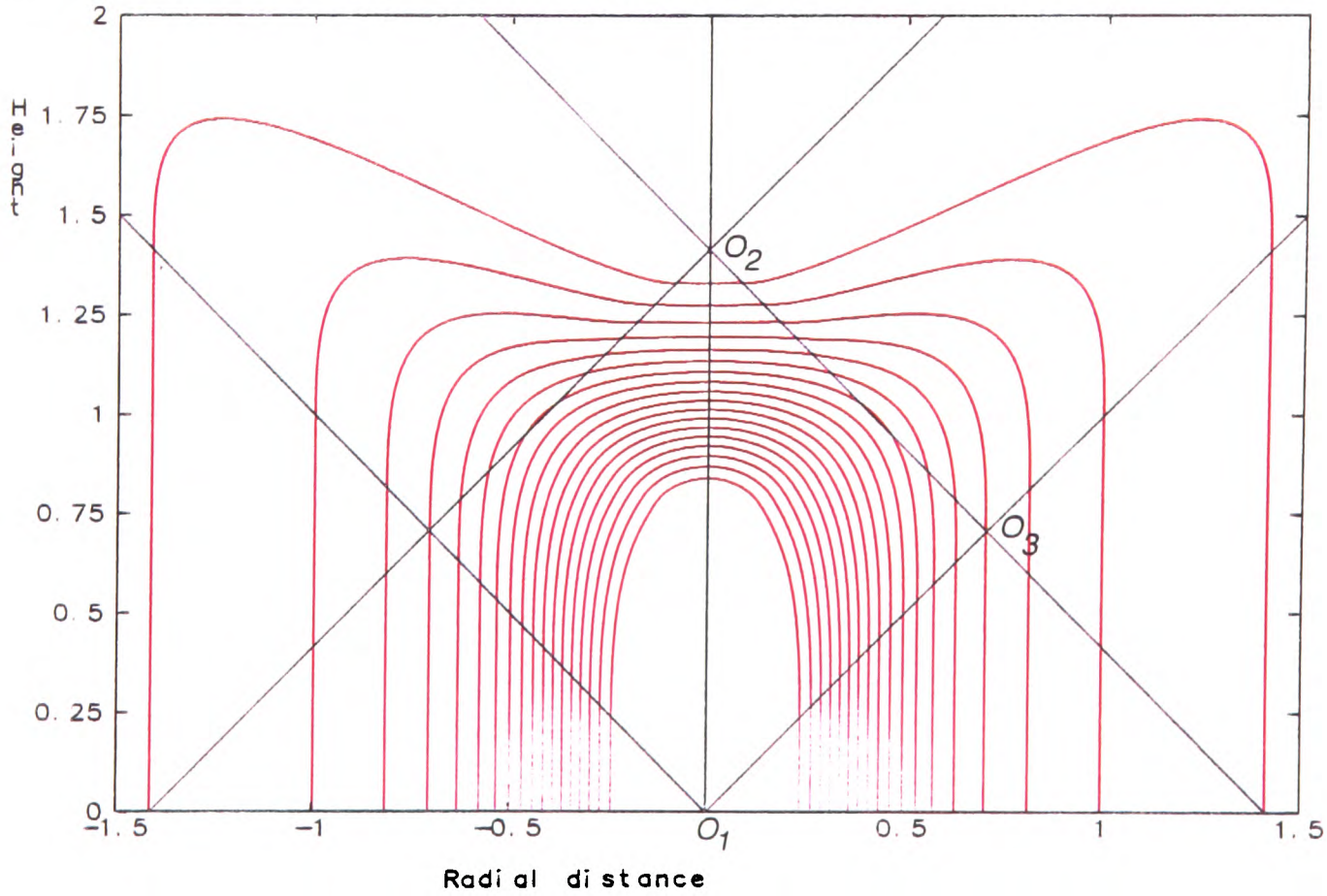

Figure 3.3: Family of nested steady state crown profiles; $r_s = 1/2$, $a = 45°$, $\mu = .5 + k\Delta\mu: \quad \Delta\mu = .5, \ k = 0, ..., 17$.

Concave steady states present a number of physical problems for production. Firstly, the concavity will be difficult to detect visually, since from a side view the billet crown will appear to be flat-topped. This has obvious repercussions for any control system based on height measurement, (see [99]), should such a steady state profile be approached. Secondly, the flight distance of different points on the billet crown from the atomiser has its greatest variation with concave profiles. This is due to both their larger size and to their particular shape. Hence, the thermal condition of the spray on deposition will have its greatest variation for billet surfaces that approach these steady states, and this may be reflected in the microstructure of the finished billet. Lastly, concave surfaces are probably more concave in reality than are predicted by the model. More spray is likely to stick at the outer radius of the billet, where the spray will be wetter and the impact angle of droplets impinging on the surface will be less oblique, than close to the billet axis. Thus,

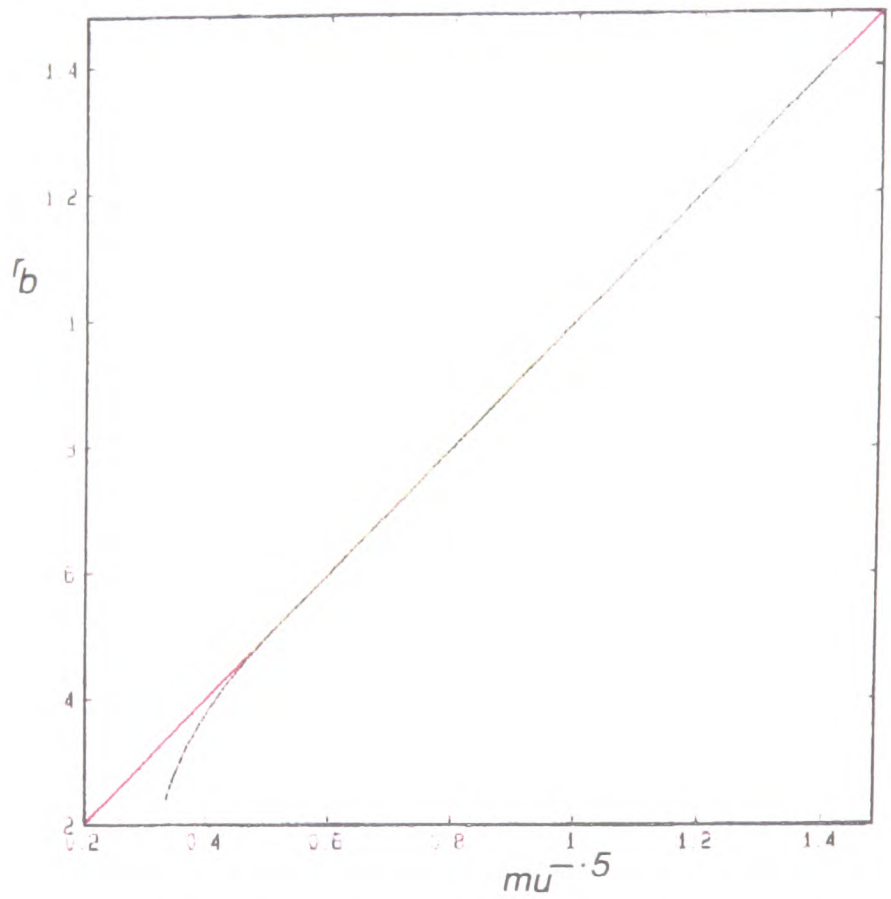

Figure 3.4: Validity of the mass balance

the assumption of there being only small local variations from the mean sticking efficiency, will be less valid for this geometry.

Of clear interest is the stability of steady states such as those illustrated in Fig. 3.3. In Fig. 3.5 the stability of the steady states corresponding to $\mu = .5,\ 1,\ 4$ and 9 has been analysed according to theorem 2.3.1. This theorem provides sufficient conditions for a finite perturbation, $\tilde{f}(\theta, \eta)$, to a steady state solution of equation (2.71), $\sigma = f(\theta)$, to be decreasing in absolute value on an interval $\theta \in [0, b] \subseteq [0, a_1]$. The areas shaded in Fig. 3.5 are those areas where, for each value of μ and for the vectorfield $\bar{\boldsymbol{g}} = \bar{\boldsymbol{g}}_1 + \bar{\boldsymbol{g}}_2$, the conditions of theorem 2.3.1 are not met.

It is seen from Fig. 3.5 that for each steady state considered it is possible to define an interval of stability, $[0, b] \subset [0, \pi/4]$, but that the conditions of theorem 2.3.1 may not be satisfied on the whole interval $[0, \pi/4]$. This suggests that parts of the steady states considered are not stable, in the "strong" sense implied by theorem 2.3.1. In fact, one can see from the proof of theorem 2.3.1 that, when only condition a) of the theorem holds, along an interval of the steady state, then the perturbation will grow in size. Condition a) of theorem 2.3.1 holds in those parts of the (σ, θ)-phase plane where θ is increasing along all phase paths.

In order to interpret Fig. 3.5 more clearly the vector field $-\mu \boldsymbol{k}_1 - \bar{\boldsymbol{g}}_1 - \bar{\boldsymbol{g}}_2$ is computed. This vectorfield gives the relative velocity of all possible points on the billet surface, within the crown frame of reference, assuming that all spray is deposited. In Figs. 3.6 and 3.7 the spray boundaries and the steady state profiles for $\mu = .5,\ 1,\ 4$ and 9 have been superimposed onto the respective vectorfields. This gives the (r_1, z_1) "phase plane" for each fixed value of μ, illustrating possible transient growth of the billet crown profile towards the steady state. Away from $\sigma = 0$ there is a $1-1$ mapping between this phase plane and the (σ, θ) phase plane discussed in chapter two, with the main features of the phase plane being preserved. Whilst the (σ, θ) phase plane was convenient for the previous analysis the (r_1, z_1) phase plane is physically more intuitive here.

Evident in both Figs. 3.6 and 3.7 is a saddle point where the steady state profile intercepts the billet axis

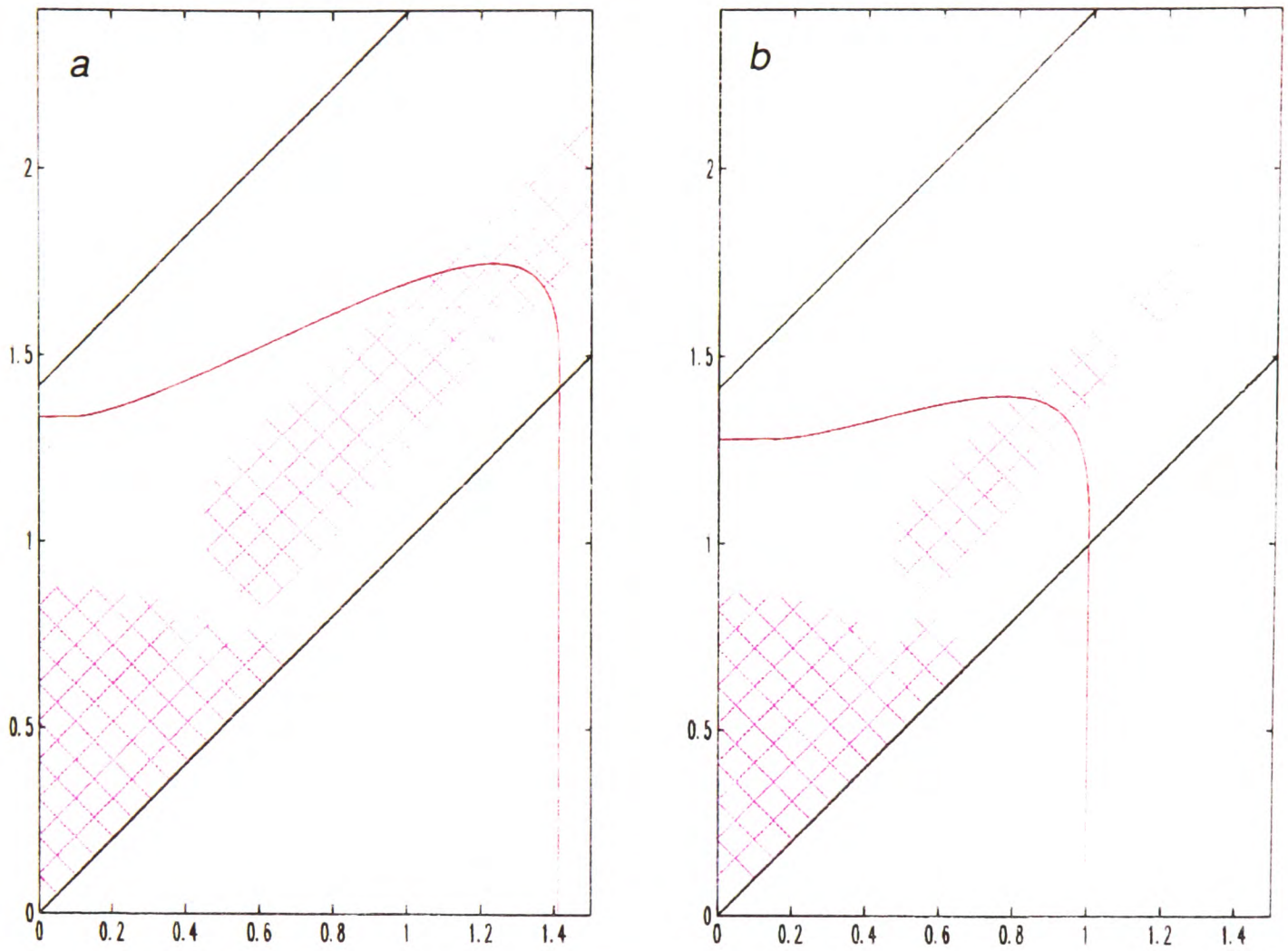

Figure 3.5: Stability of steady state crown profiles, $r_s = 1/2$, $\alpha = 45°$; a) $\mu = .5$, b) $\mu = 1$, c) $\mu = 4$, d) $\mu = 9$. Conditions of theorem 2.3.1 fail in shaded areas.

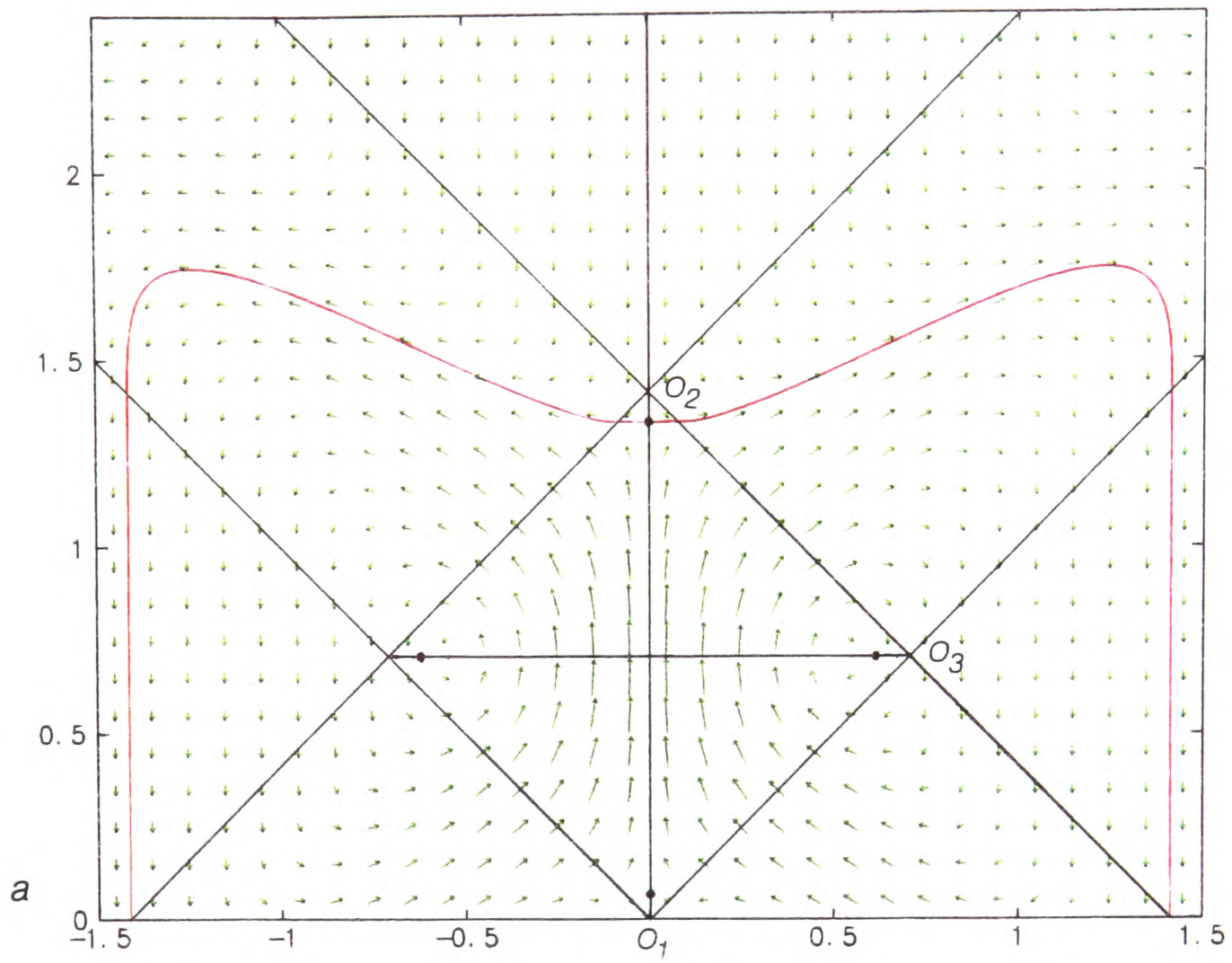

Figure 3.6: (r_1, z_1)-phase plane, $r_s = 1/2$, $a = 45°$; a) $\mu = .5$, equilibrium points and the line $\mathcal{L}(\lambda)$ are marked, b) $\mu = 1$. Surface velocity vectors - green, steady states - red, spray boundaries - black.

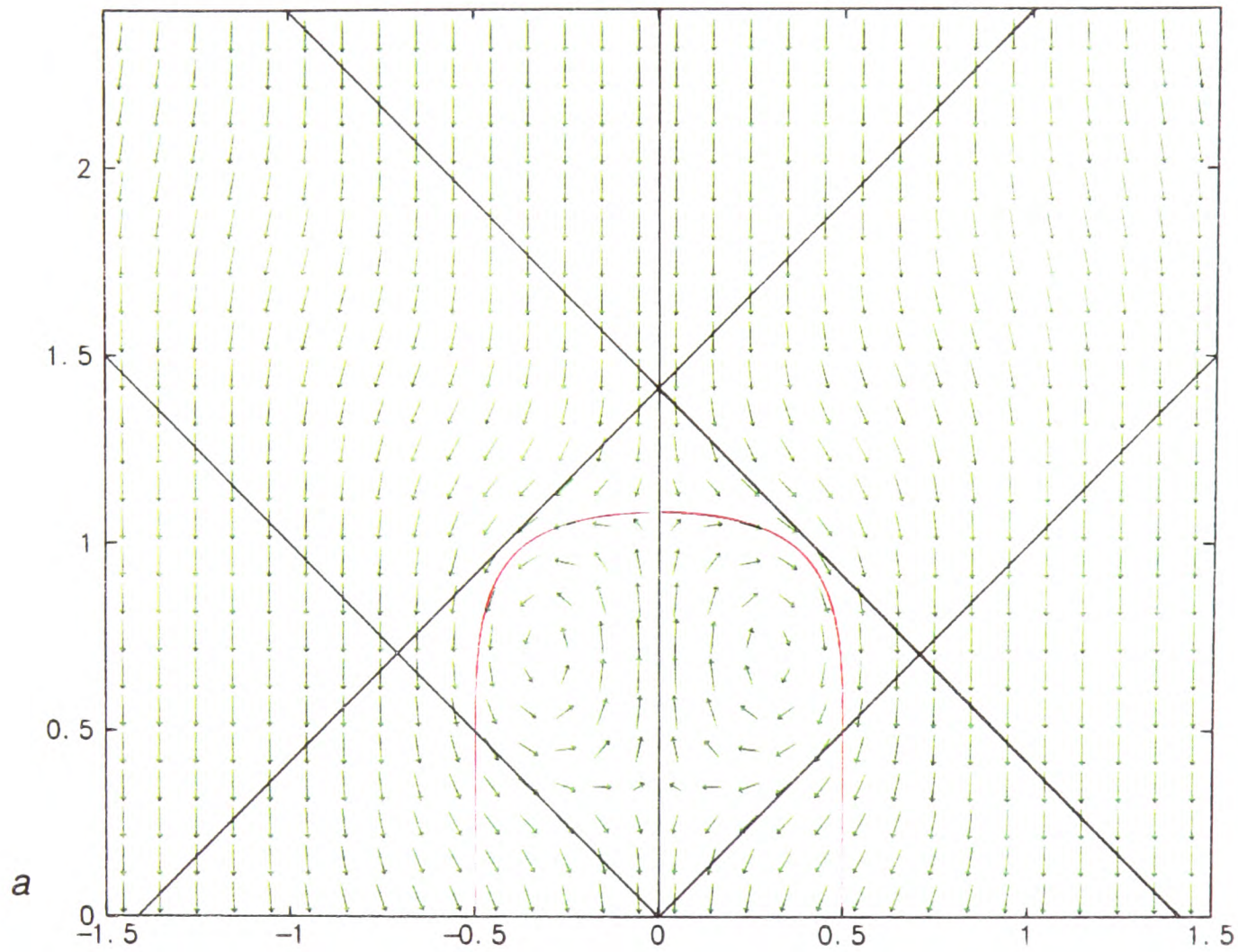

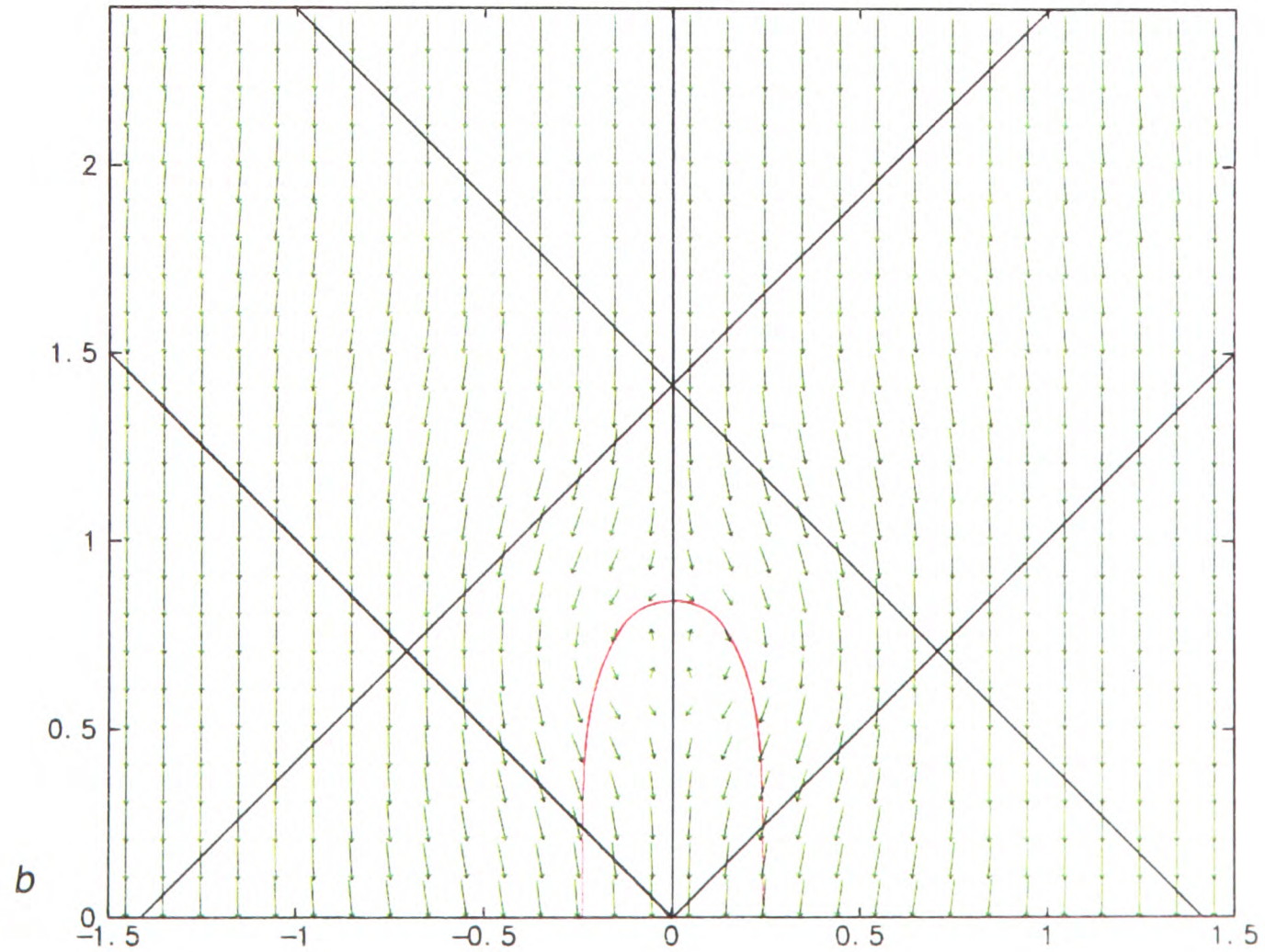

Figure 3.7: (r_1, z_1)-phase plane, $r_s = 1/2$, $a = 45°$; a) $\mu = 4$, b) $\mu = 9$. Surface velocity vectors - green, steady states - red, spray boundaries - black.

of rotation, and it is clear that the steady state profile does represent the unstable separatrix of the saddle. Further down on the billet axis of rotation, can be seen a second saddle point, corresponding to the second, (unstable), solution of (3.7). The line $\mathcal{L}(\lambda)$, (discussed in chapter two, section 2.3.3), where the mass flux component perpendicular to the billet axis of rotation is zero, is a straight line in the case of a fixed angle spray. It runs perpendicular to the billet axis of rotation and extends out to O_3. Along this line are further equilibrium points, which in this case are unstable spirals. The distance of these equilibrium points from the billet axis of rotation decreases as μ increases. These features are marked out in Fig. 3.6a, for clarity.

Remarks

1. It is emphasised that these phase portraits correspond to the situation for which all spray is deposited on a given surface, (i.e. $\overline{\boldsymbol{g}} = \overline{\boldsymbol{g}}_1 + \overline{\boldsymbol{g}}_2$). For billet surfaces where this is not the case the radial component of the mass flux arriving at points on $\mathcal{L}(\lambda)$ might not cancel out, and for such surfaces the unstable spirals will not exist.

2. Here and later on in the thesis, arrows used to graphically represent vectorfields at points on a regular grid have a shaft length drawn which is proportional to the square root of the magnitude of the vectorfield at that point, rather than directly proportional. The reason for this is that $\|\overline{\boldsymbol{g}}\|$ decreases approximately proportionate to r_1^2, so that choice of a linear shaft scaling produces phase portraits for which the features are difficult to see at a distance from the billet axis.

There are two distinct shaded regions in the (r_1, z_1)-planes shown in Fig. 3.5.

- The first region occurs closer to the origin and appears to be associated with the phase plane dynamics of the unstable spiral and lower saddle point. One can see from Figs. 3.6 and 3.7 that in some parts of the shaded region, (e.g. close to the billet axis of rotation and above the lower saddle), a transient surface profile will still grow towards the steady state. In those parts of the region both conditions of theorem 2.3.1 have failed, (see the remarks following the proof of theorem 2.3.1). In other parts of this region only one of the conditions has failed. For billet radii, $r_b \approx 1$, that are growing close to the steady state, this region is of little practical interest.

- The second shaded region in Fig. 3.5 runs close and roughly parallel to the lower spray boundary, up towards the atomiser. This region appears to only occur for smaller μ, and appears to be connected with the steady state profile turning round sharply before exiting the lower spray boundary. Since in Fig. 3.6, θ is observed to increase along the phase paths in this region, it is clear that only condition b) of theorem 2.3.1 has failed here. Hence, perturbations from the steady state will grow in this region. The instability here seems to arise because phase paths lying close to the steady state diverge from it as they turn around and follow it from the spray region. This is seen more clearly in Fig. 3.8, which has "zoomed-in" on this part of Fig. 3.6b, for $\mu = 1$. This feature seems to be particularly evident when the steady state is concave, since in this case the surface profile must turn sharply before crossing the lower spray boundary.

The second unstable region disappears as μ is increased from 1.6 to 1.75, as the steady state profiles contract and become convex, see Fig. 3.9. For larger μ the steady state profiles contract still further and parts of the surface can become influenced by the unstable spiral, (e.g. Figs. 3.5c and 3.5d).

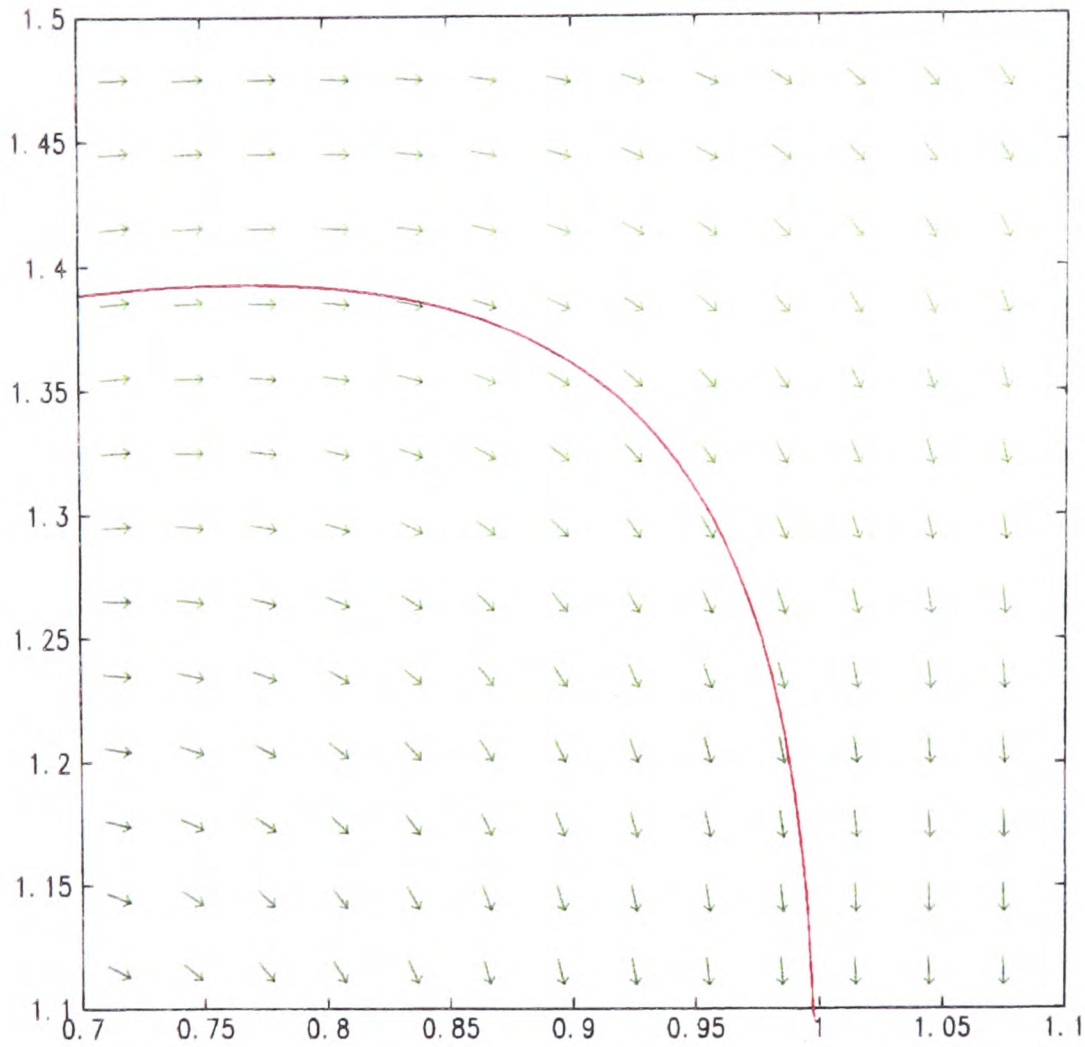

Figure 3.8: Divergence of phase paths from the steady state; $r_s = 1/2$, $a = 45°$, $\mu = 1$.

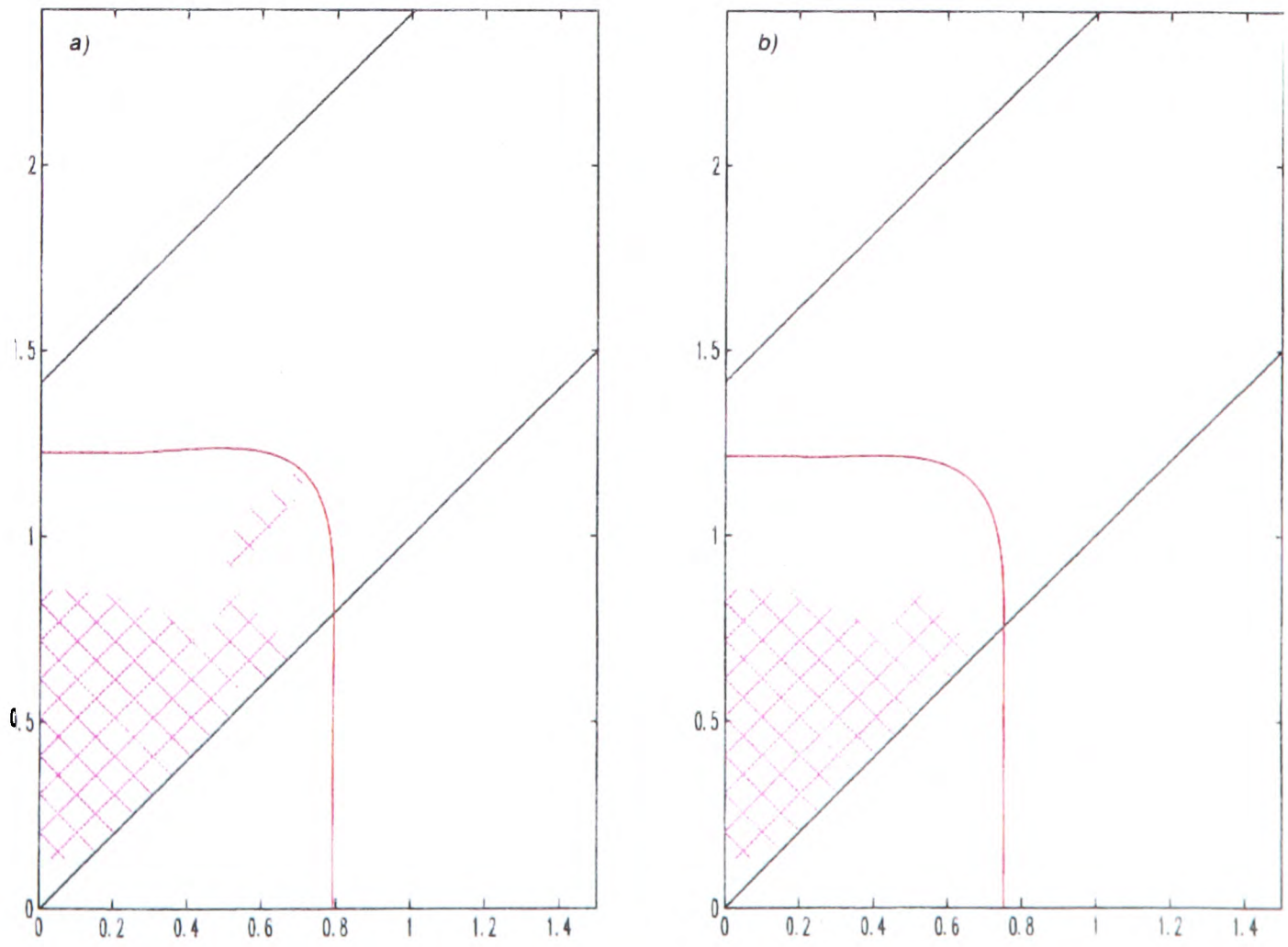

Figure 3.9: Completely stable steady state; $r_s = 1/2$, $a = 45°$, a) $\mu = 1.6$, b) $\mu = 1.75$.

3.3 Fixed angle sprays: variations with a and r_s

Families of steady state profiles for $r_s = 1/2$ and fixed spraying angles, $a = 35°$ and $a = 55°$, are plotted in Fig. 3.10. These may be compared with Fig. 3.3 to illustrate process variation with fixed spraying angle, a. There are two main features of this variation.

Firstly, as the spraying angle decreases, steady state profiles become increasingly concave. Larger steady states have their radius fixed by μ through (3.11). This in turn fixes the point at which the profile crosses the lower spray boundary. For small spraying angle, a, these crossing points are higher relative to O_2 than for large a, and hence the tendency toward concavity.

Secondly, and not obvious from Fig. 3.10, is that the distance of the steady state profiles from the atomiser nozzle increases significantly with decreasing spraying angle, a. The vertical height above O_1 of the steady state initial condition is given by the solution of (3.7). For moderate spraying angles, changing the angle of a fixed angle spray has little effect on either the size of the axis mass flux distribution function, $-\bar{g}_\sigma(\sigma, 0)$, or on the distance, z_u, between O_1 and O_2 on the axis of rotation, (which defines the range of values of σ for which $-\bar{g}_\sigma(\sigma, 0) > 0$). This is shown by there only being a gradual shift in displacement below O_2, of steady states the axis of rotation, between Figs. 3.10a, 3.3 and 3.10b. However, there will clearly be a shift in the point of interception of the upper spray boundary with the axis of rotation, (i.e. O_2), when the spraying angle, a, is changed. The vertical displacement of O_2 below the vertical position of the atomiser is given by $z_n + z_c - z_u$. For an atomiser positioned a radial distance, $r_n = 2$, from the billet axis, different values of spraying angle, a, produce the changes in $z_n + z_c - z_u$ shown in Table 3.1.

Spraying angle a	$z_n + z_c - z_u$
35°	1.985
45°	1.293
55°	0.790

Table 3.1: Vertical displacement of O_2 below the atomiser nozzle height; $r_n = 2$, $r_s = 1/2$.

For larger radius billets the variation in flight distance, D_F, with spraying angle is somewhat offset, due to the variation in concavity. These billet profiles are in any case undesirable, for the reasons mentioned in the previous section. Variation in D_F across the billet surface occurs in a more consistent manner for the smaller radius, convex, steady states. Thus, for convex billet profiles, variation of a represents one route for changing D_F in a more or less uniform way across the billet surface.

Variations with spraying angle, a, are further illustrated in Fig. 3.14, where (r_1, z_1)-phase planes have been plotted for $\mu = 1$ and for the two new values of a. The change in concavity is especially clear. The dynamics of the phase plane are qualitatively similar to those of Figs. 3.6 and 3.7. Regions of the phase plane within which sufficient conditions for stability are not met, have been shaded in Figs. 3.15a and 3.15b. The same steady state profiles for $\mu = 1$ as in Fig. 3.11, are examined. Both profiles have stable intervals that start at the billet axis and finish as the billet surface turns to leave the lower spray boundary.

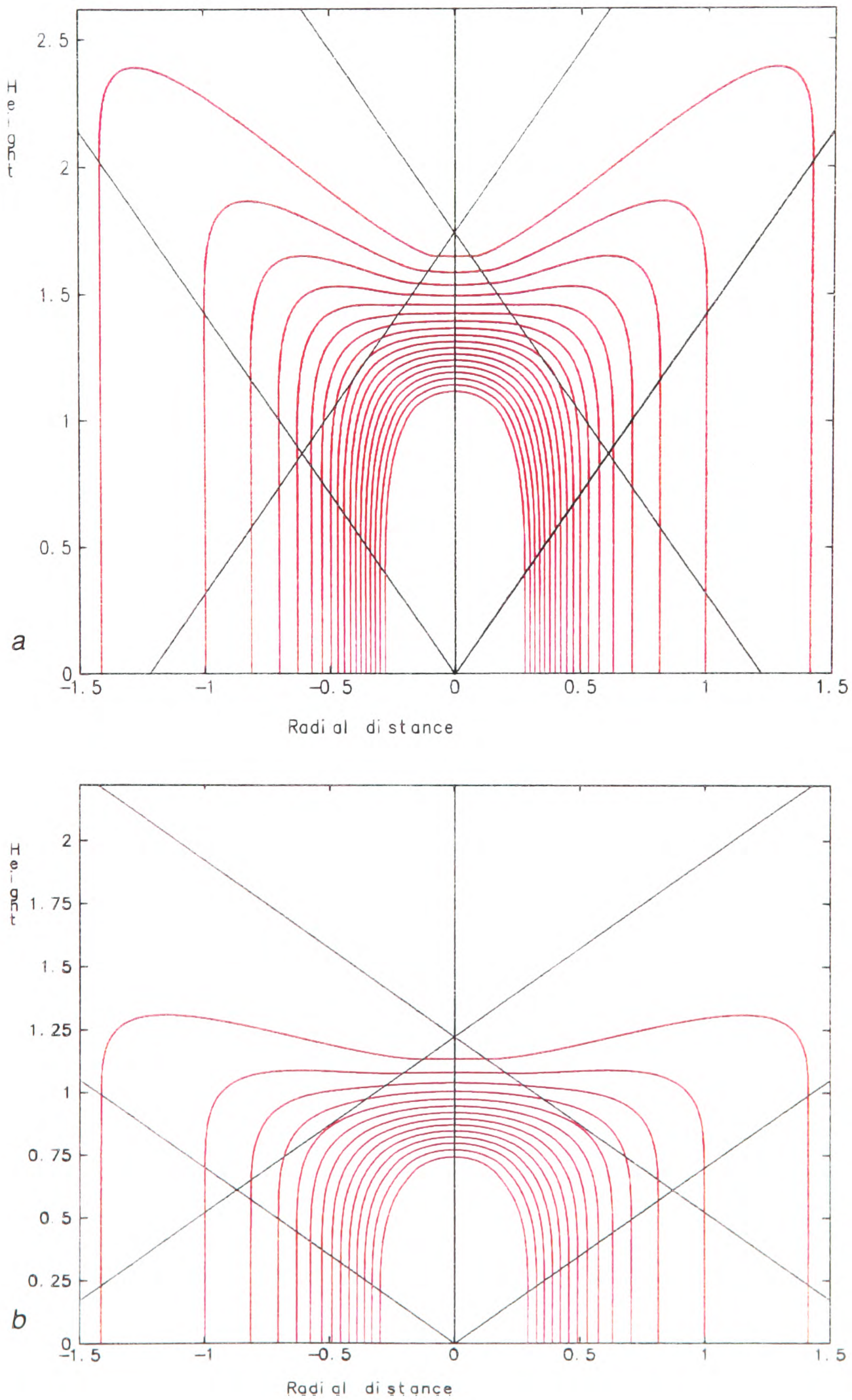

Figure 3.10: Families of steady state billet crowns, $r_s = 1/2$; a) $a = 35°$, $\mu = .5 + k\Delta\mu$: $\Delta\mu = .5$, $k = 0, ..., 17$, b) $a = 55°$, $\mu = .5 + k\Delta\mu$: $\Delta\mu = .5$, $k = 0, ..., 13$.

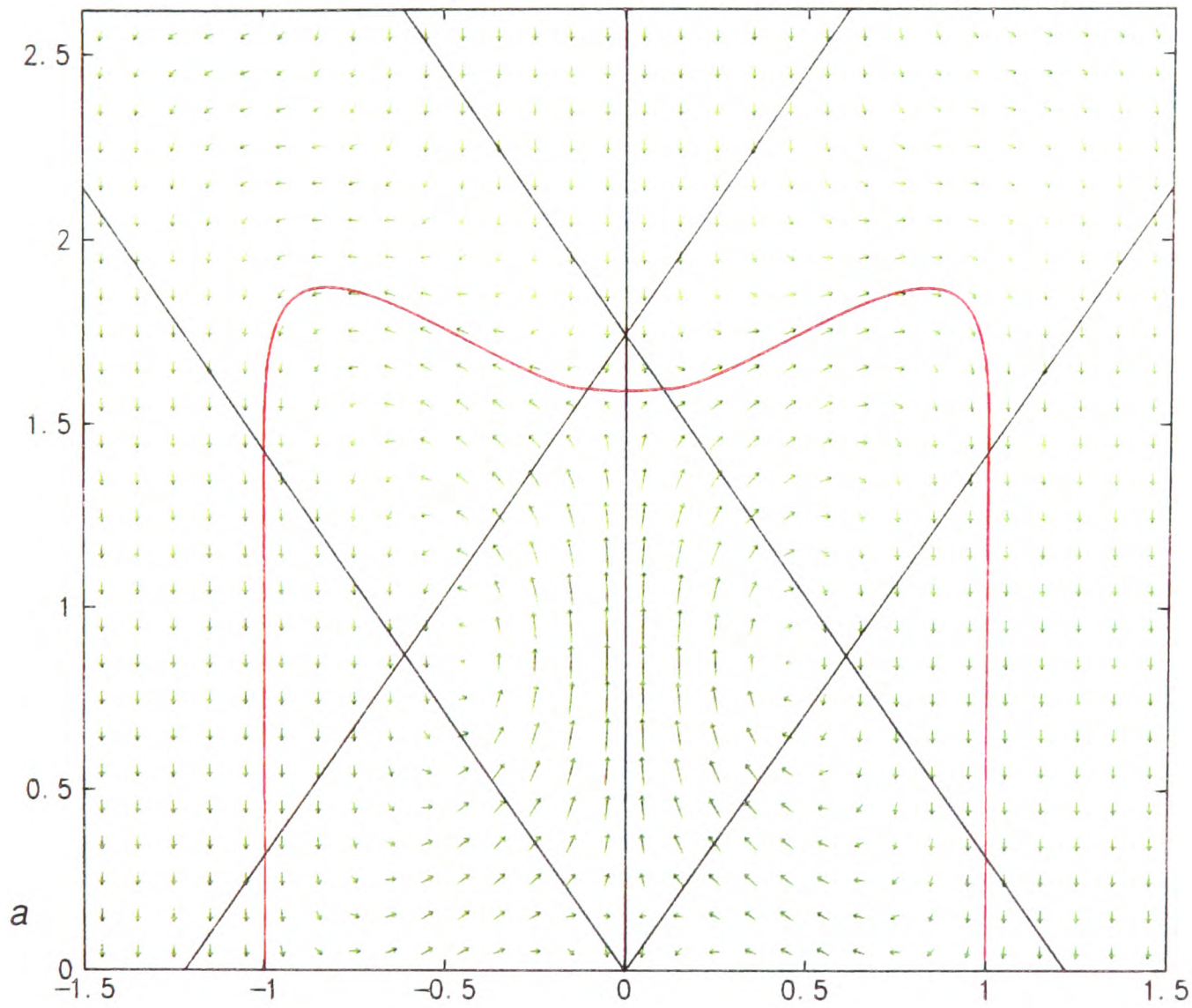

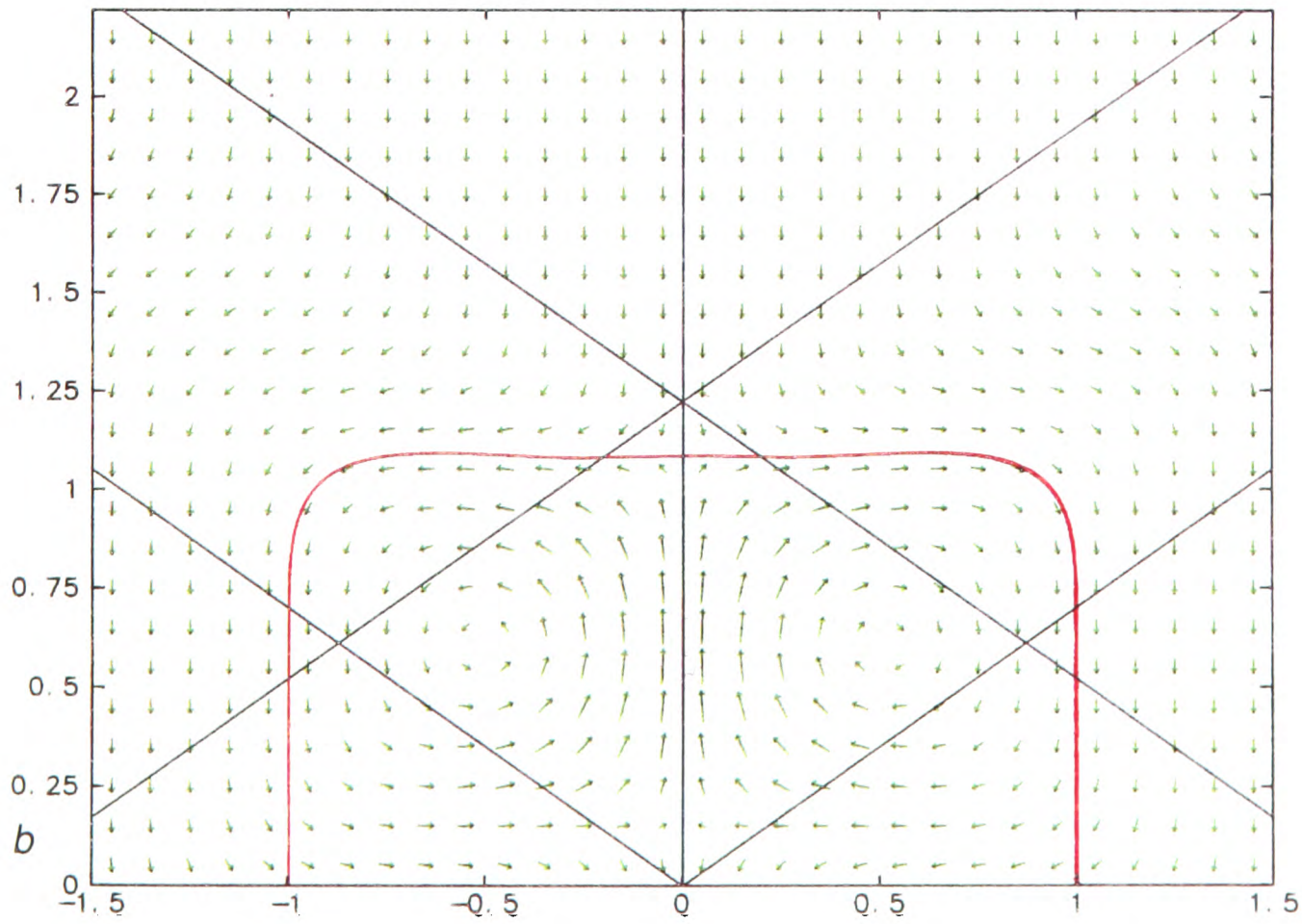

Figure 3.11: (r_1, z_1)-phase plane, $r_s = 1/2$, $\mu = 1$; a) $a = 35°$, b) $a = 55°$. Surface velocity vectors - green, steady states - red, spray boundaries - black.

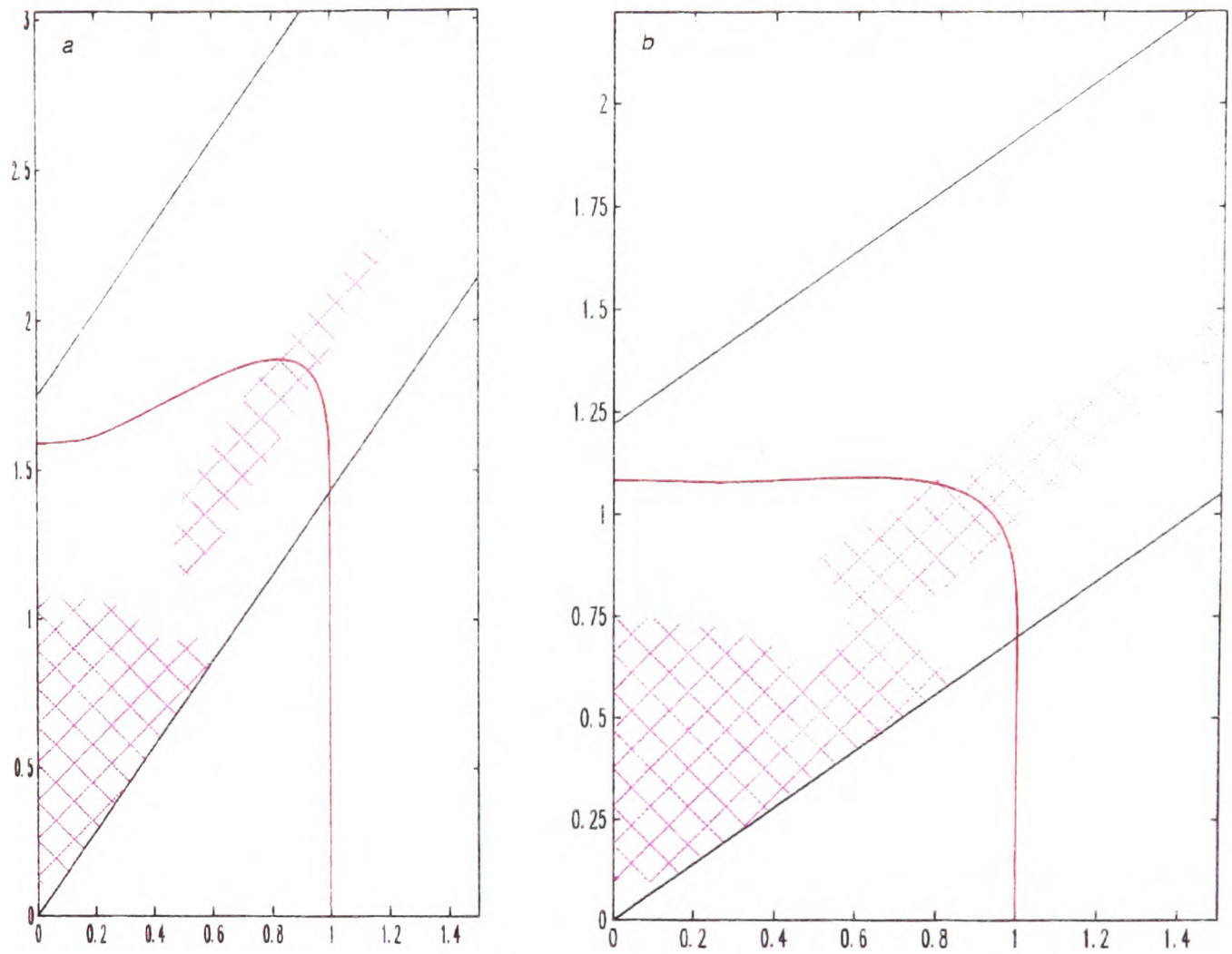

Figure 3.12: Stability of steady states, $r_s = 1/2$, $\mu = 1$; a) $a = 35°$, b) $a = 55°$.

Varying the spray cone radius, r_s

The second way in which some control might be exerted over steady state growth, is by variation of the spray cone radius, r_s. This could be achieved

1. by increasing the radial distance of the atomiser nozzle from the axis of rotation, r_n, (i.e. increasing the flight distance, D_F, and exploiting the natural divergence of the spray cone),
2. through atomiser redesign, or
3. through variation of the metal and gas flow rates through the atomiser. [2]

Each of these possibilities is likely also to have an effect on the thermal condition of the metal spray, and for this reason it is worth examining geometrically, the effect of this action. Families of steady state crown profiles are plotted in Fig. 3.13 for $a = 45°$ and for spray cone radii $r_s = 1/3$ and $r_s = 2/3$. These may be compared with Fig. 3.3 to show variation over a range of spray cone radii. Two main effects are observed.

Firstly, steady states appear to become increasingly concave when decreasing r_s. Within the global frame of reference, the "diamonds" formed by the intersecting spray boundaries in Figs. 3.13a, 3.3 and 3.13b will all lie nested inside one another with decreasing r_s. Thus, at the same fixed radius, a steady state profile must climb higher, (to cross the lower spray boundary), and descend lower, (to its point of interception with the billet axis), for small r_s than it would have to for large r_s.

Secondly, there is a significant difference in the vertical displacement of steady state profiles below O_2 on the axis of rotation. For $r_s = 1/3$ the steady states in Fig. 3.13a are much less spaced out than those in Fig.

[2] Both metal and gas flow rate variations will occur during a production run and must be controlled, see [55].

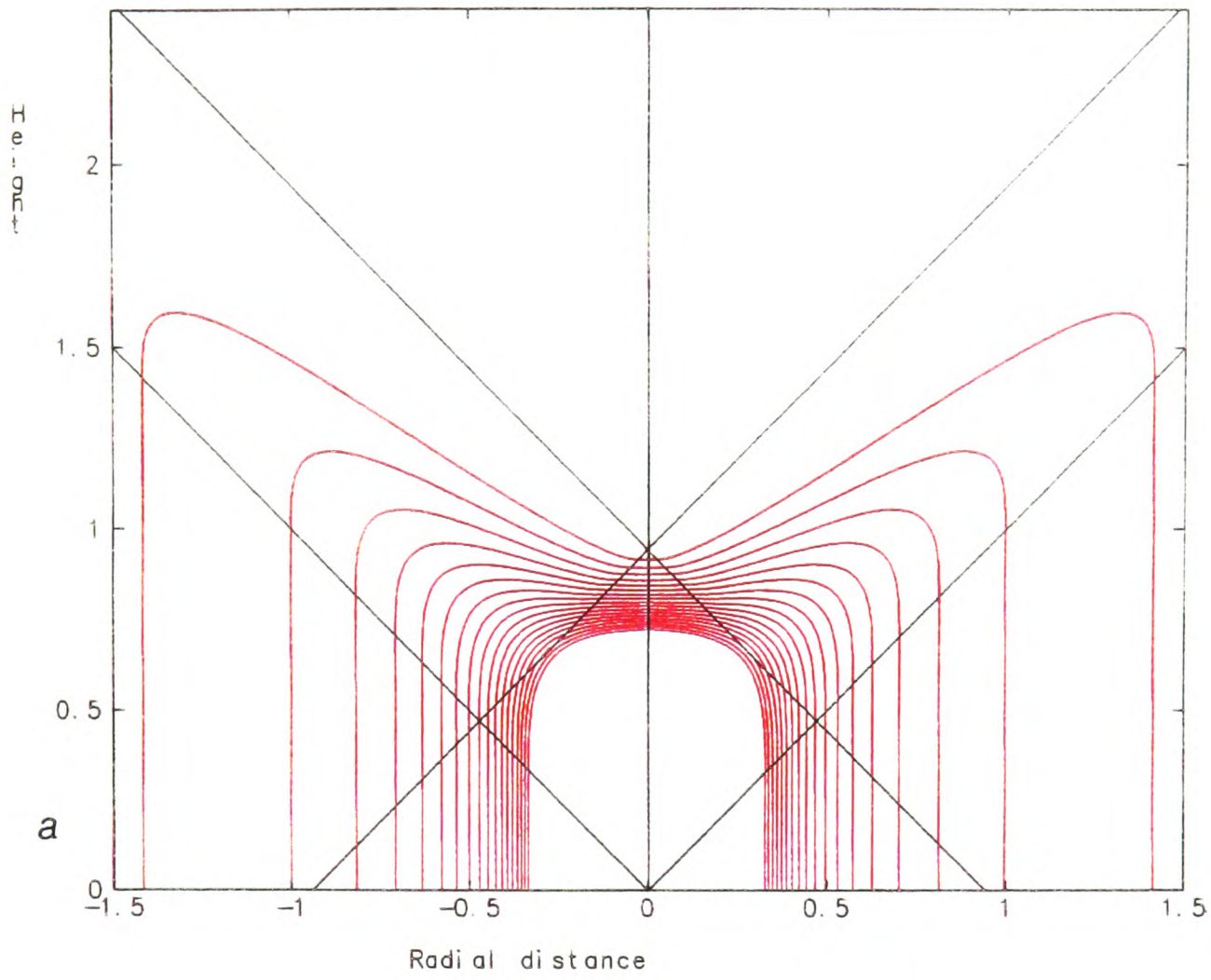

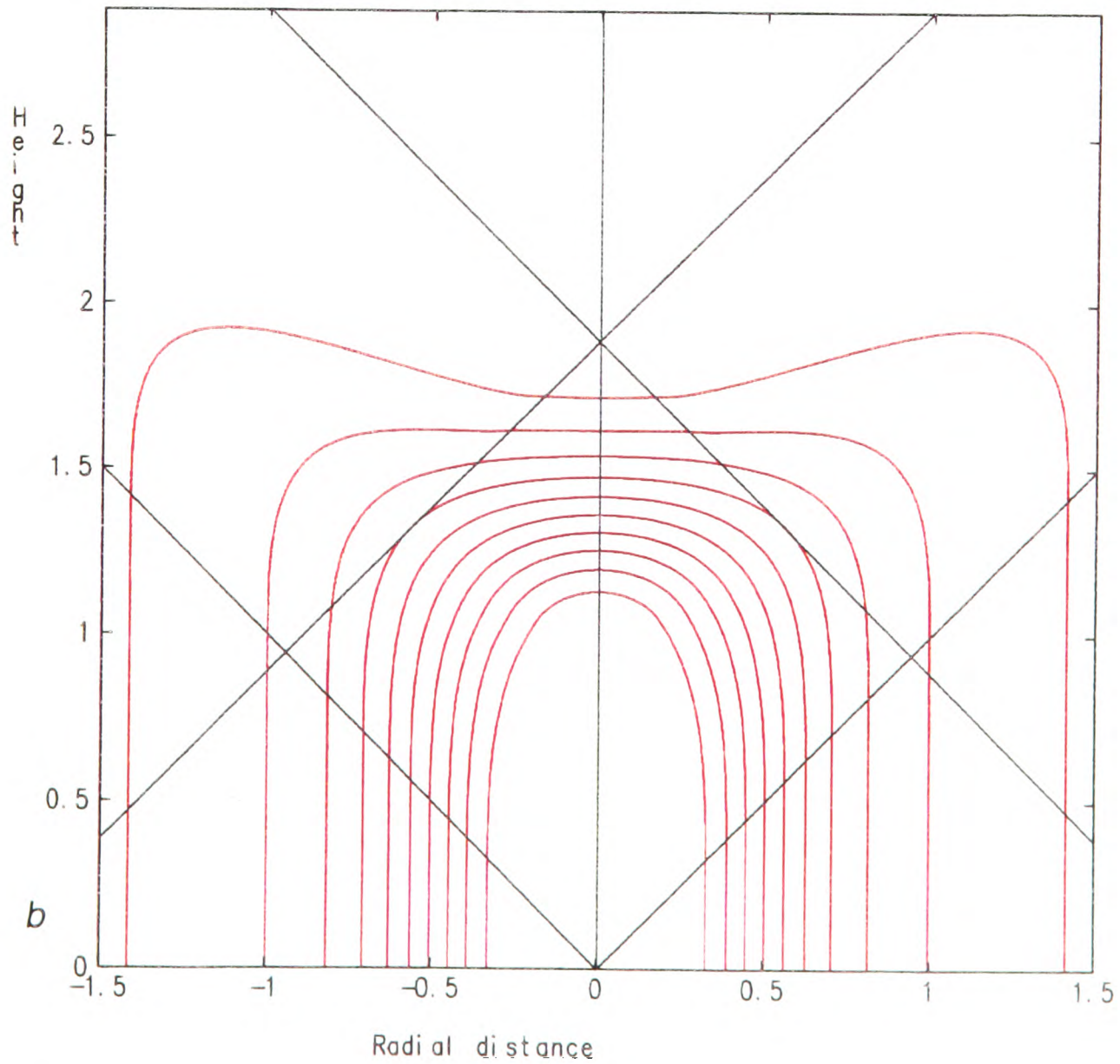

Figure 3.13: Families of steady state billet crowns, $a = 45°$; a) $r_s = 1/3$, $\mu = .5 + k\Delta\mu$: $\Delta\mu = .5$, $k = 0, ..., 17$, b) $r_s = 2/3$, $\mu = .5 + k\Delta\mu$: $\Delta\mu = .5$, $k = 0, ..., 9$.

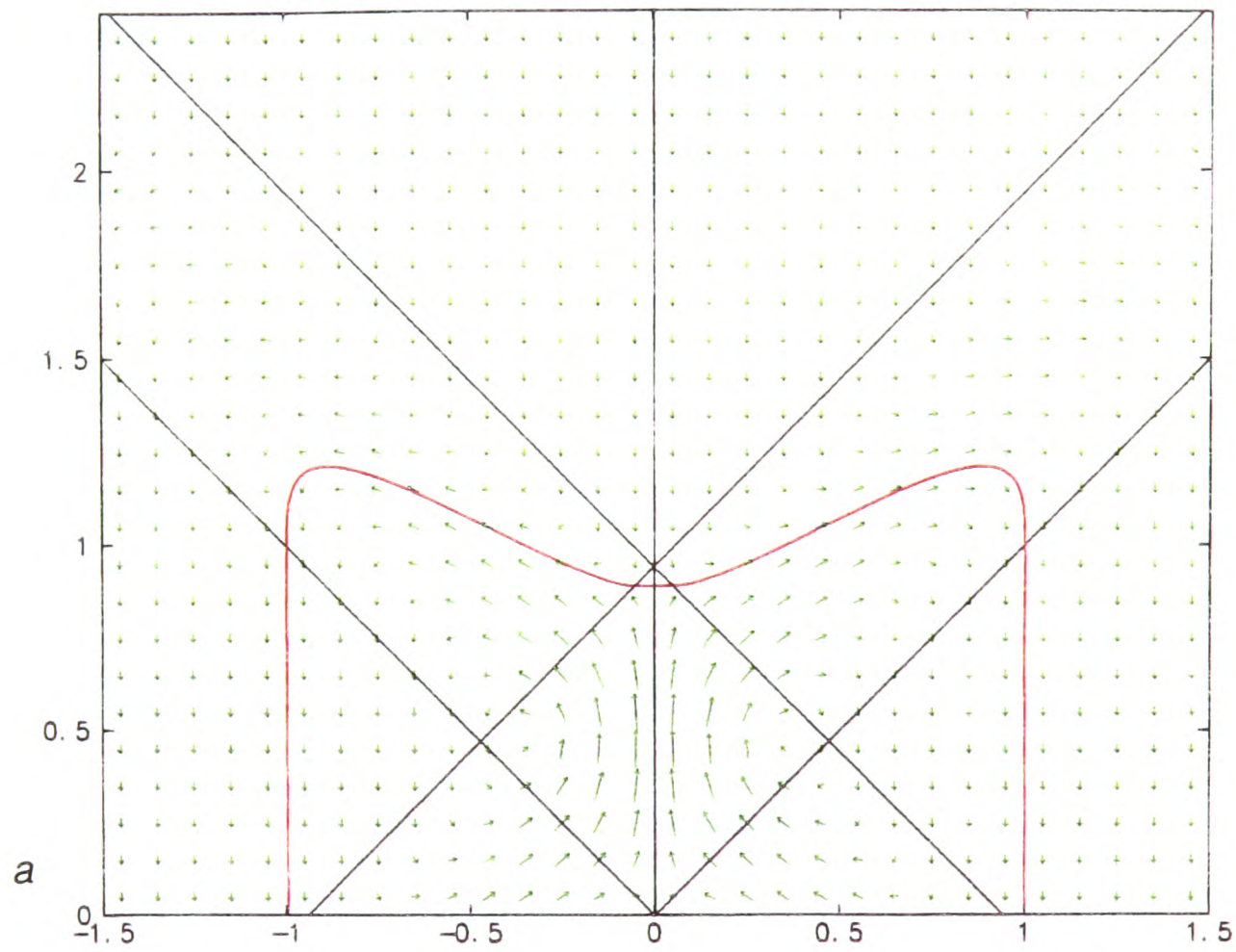

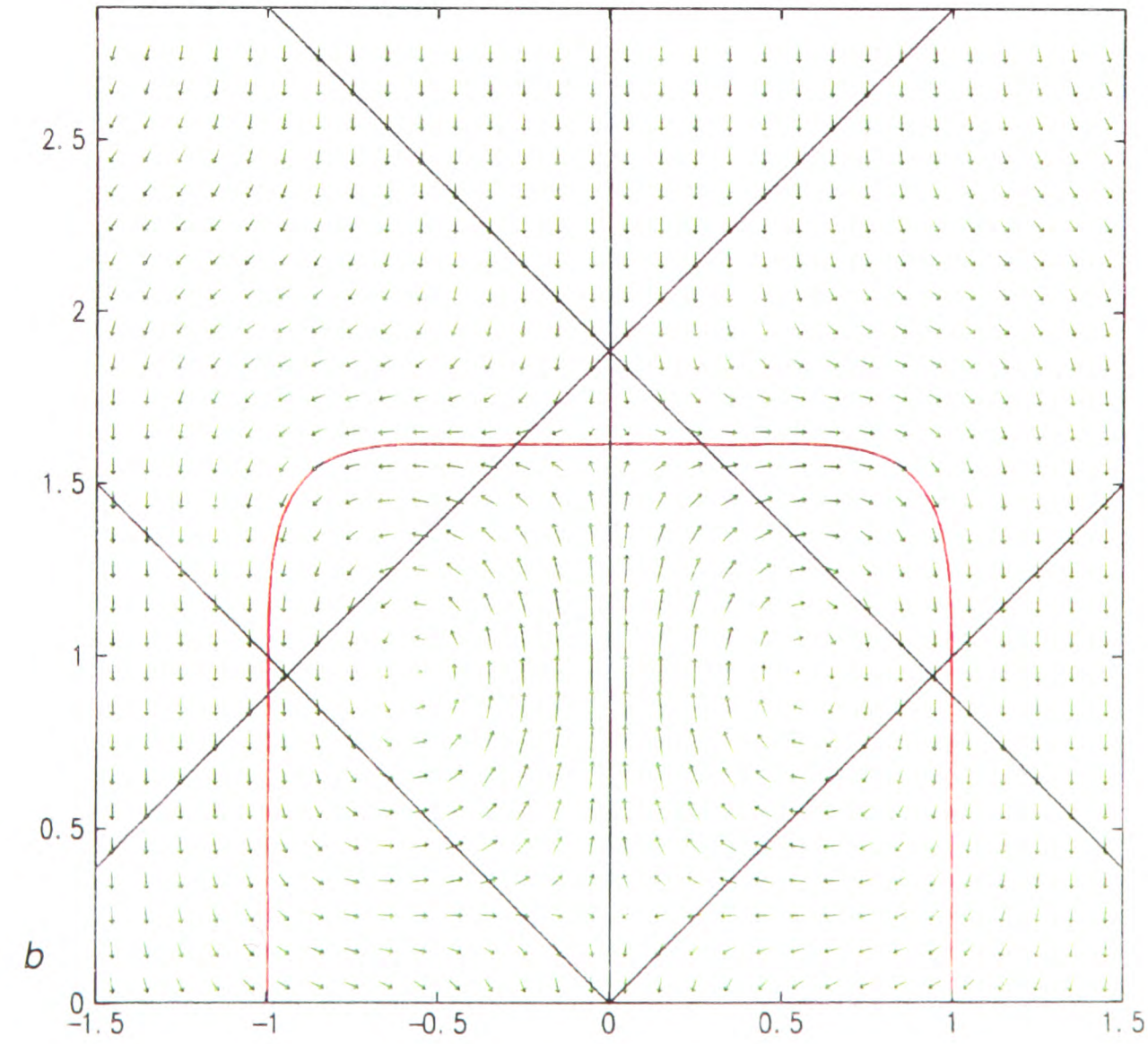

Figure 3.14: (r_1, z_1)-phase plane, $a = 45°$, $\mu = 1$; a) $r_s = 1/3$, b) $r_s = 2/3$. Surface velocity vectors - green, steady states - red, spray boundaries - black.

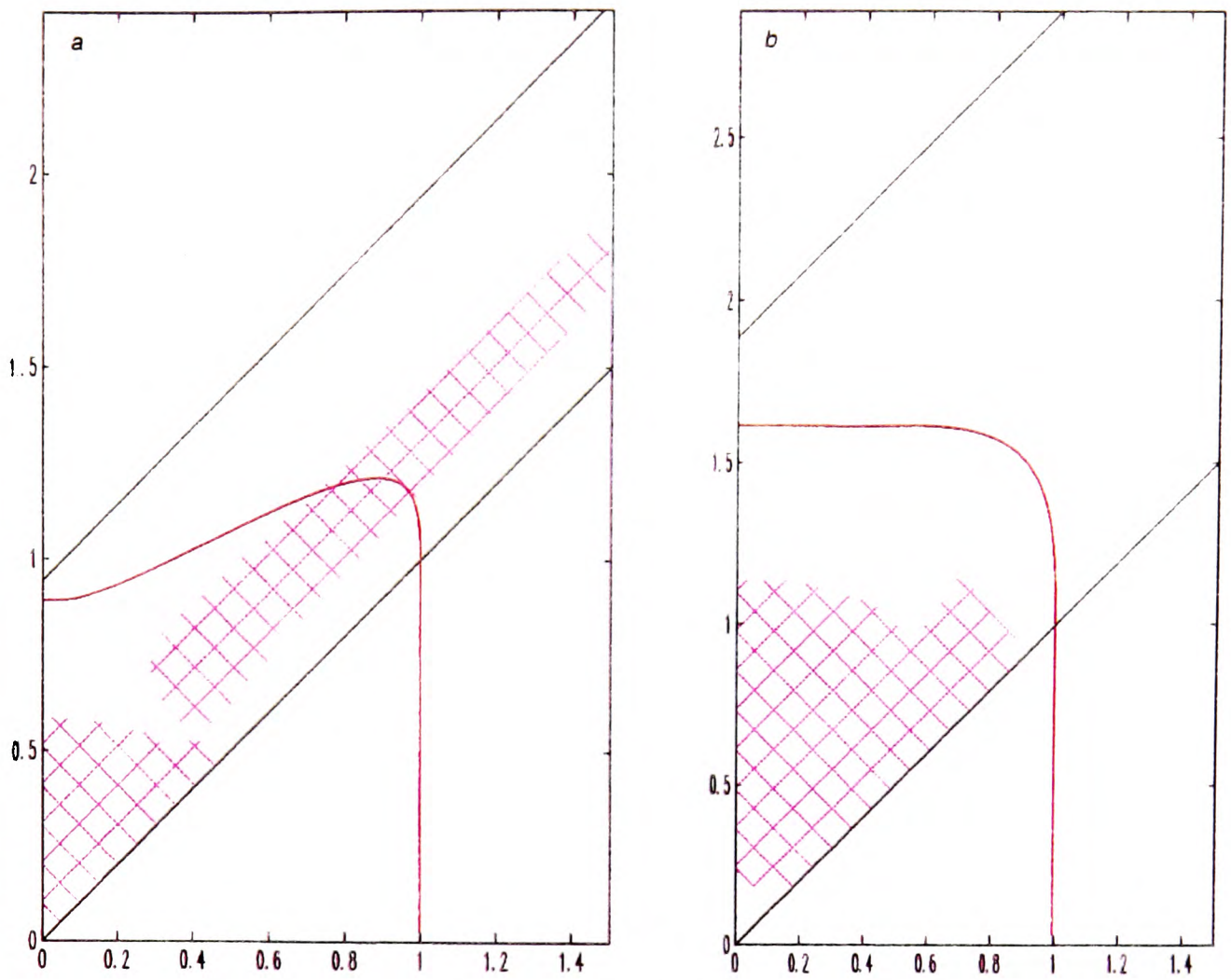

Figure 3.15: Stability of steady states, $a = 45°$, $\mu = 1$; a) $r_s = 1/3$, b) $r_s = 2/3$.

3.13b, where $r_s = 2/3$. This results from the decrease in $g(r')$, and hence $-\bar{g}_\sigma(\sigma, 0)$, caused by increasing r_s. For larger r_s, surface height movement will be more easily measured and more responsive to changes in μ.

A third effect that is observed when the spray cone radius is changed is an increase in flight distance, D_F, with decreasing r_s. This effect is however much less pronounced than for the variations in spraying angle, a, discussed above. This is because variations in the vertical displacement, $z_n + z_c - z_u$, of O_2 below the atomiser, are not as great as when changing the spraying angle, a, see Table 3.2.

Spray cone radius, r_s	$z_n + z_c - z_u$
1/3	1.528
1/2	1.293
2/3	1.057

Table 3.2: Vertical displacement of O_2 below the atomiser nozzle height; $r_n = 2$, $a = 45°$.

Geometric differences are further emphasised by looking at the (r_1, z_1)-phase planes corresponding to $\mu = 1$, for both $r_s = 1/3$ and $r_s = 2/3$, see Fig. 3.14. The underlying phase plane dynamics are similar to those described previously. However, the steady state for $r_s = 2/3$ is now completely stable, (according to theorem 2.3.1), see Fig. 3.15.

3.4 Sinusoidal atomiser scanner patterns

The previous sections have shown that considerable variation in steady state crown profile may be achieved through regulation of μ and by setting an appropriate scanner angle and spray cone radius. In reality, the dimensional spray cone radius, $\hat{r}_s$, is fixed approximately by the atomiser design and consequent restrictions on the ranges of melt and gas flow rates that produce stable atomisation. Also, because the thermal condition of the spray varies with flight distance, arbitrary selection of a fixed scanner angle, a, is not feasible. Thus, the problem is typically one of having to grow a billet of approximate radius R under the above physical constraints, where for commercial reasons, one usually wants R to be as large as possible.

From the numerical results in sections 3.2 and 3.3, it is evident that in trying to do this with a fixed angle spray the problems associated with concavity of the billet crown will occur, i.e. measurement, instability. These problems appear to be alleviated by using a larger radius spray cone, which results in the steady state profiles becoming increasingly convex and stable, (e.g. Fig. 3.15), whilst maintaining approximately the same fight distance, D_F, from the atomiser nozzle. However, since in practice one is not able to change r_s arbitrarily, the same effect is sought after by scanning the narrow spray cone through an angle $a(t)$. Writing

$$a(t) = \alpha_1 + \alpha_2 \alpha(t), \tag{3.12}$$

for $\alpha(t) \in [-1, 1]$, provides a convenient characterisation of the scanning angle $a(t)$. The angle α_1 is referred to as the **fixed scanner angle** and the angle α_2 is referred to as the **scanning range**. The atomiser scans through $\alpha_1 \pm \alpha_2$ degrees, according to the chosen **scanner function**, $\alpha(t)$. Fixed parameters,

$$\begin{aligned} r_n &= 2.27, \\ r_s &= 1/3, \\ \alpha_1 &= 35^\circ, \\ \alpha(t) &= \sin \frac{2\pi t}{t_s}, \end{aligned}$$

are used for the computations in this section. The effect of increasing α_2 from zero is studied.

Fig. 3.16 shows the flux distribution function, $-\bar{g}_\sigma(\sigma, 0)$, that results from taking $\alpha_2 = 0^\circ$, 3°, 6° and 9°. As α_2 increases from zero the function $-\bar{g}_\sigma(\sigma, 0)$ changes from being unimodal to bimodal. At the same time, since the interval $(0, z_u)$, (i.e. the range over which $\bar{g}_\sigma(\sigma, 0) \neq 0$), increases and the function $g(r')$ is spread over an increasingly large range of the axis of rotation, the magnitude of $\bar{g}_\sigma(\sigma, 0)$ decreases. The scanning range, α_2, at which $-\bar{g}_\sigma(\sigma, 0)$ first becomes bimodal will clearly depend upon r_s and the exact scanning pattern $\alpha(t)$ employed.

At a scanning range of $\pm 3^\circ$ the function $-\bar{g}_\sigma(\sigma, 0)$ is still unimodal, and is only slightly skewed towards the upper spray boundary, O_2, at $(z_u, 0)$, see Fig. 3.16b. The family of possible steady states is qualitatively very similar to that for a fixed angle spray. These are shown in Fig. 3.17. For $\mu = 1$ the steady state profile is distinctly concave and becomes unstable as it turns to cross the lower spray boundary, see Fig. 3.18. Such a scanning range is likely to be useful only for spraying smaller radius billets.

For a scanning range of $\pm 6^\circ$ the function $-\bar{g}_\sigma(\sigma, 0)$ is bimodal, with the larger mode nearest to $(z_u, 0)$. For $\mu \approx 6.8$ and higher there are now two steady state solutions to (2.71), for each value of μ that allows 4

solutions of (3.7). The two families of steady states are plotted in Fig. 3.19a. The second family of steady states lies nested within the first; 19 profiles are plotted in Fig. 3.19a, 16 profiles are plotted from the outer family and 3 from the inner family.

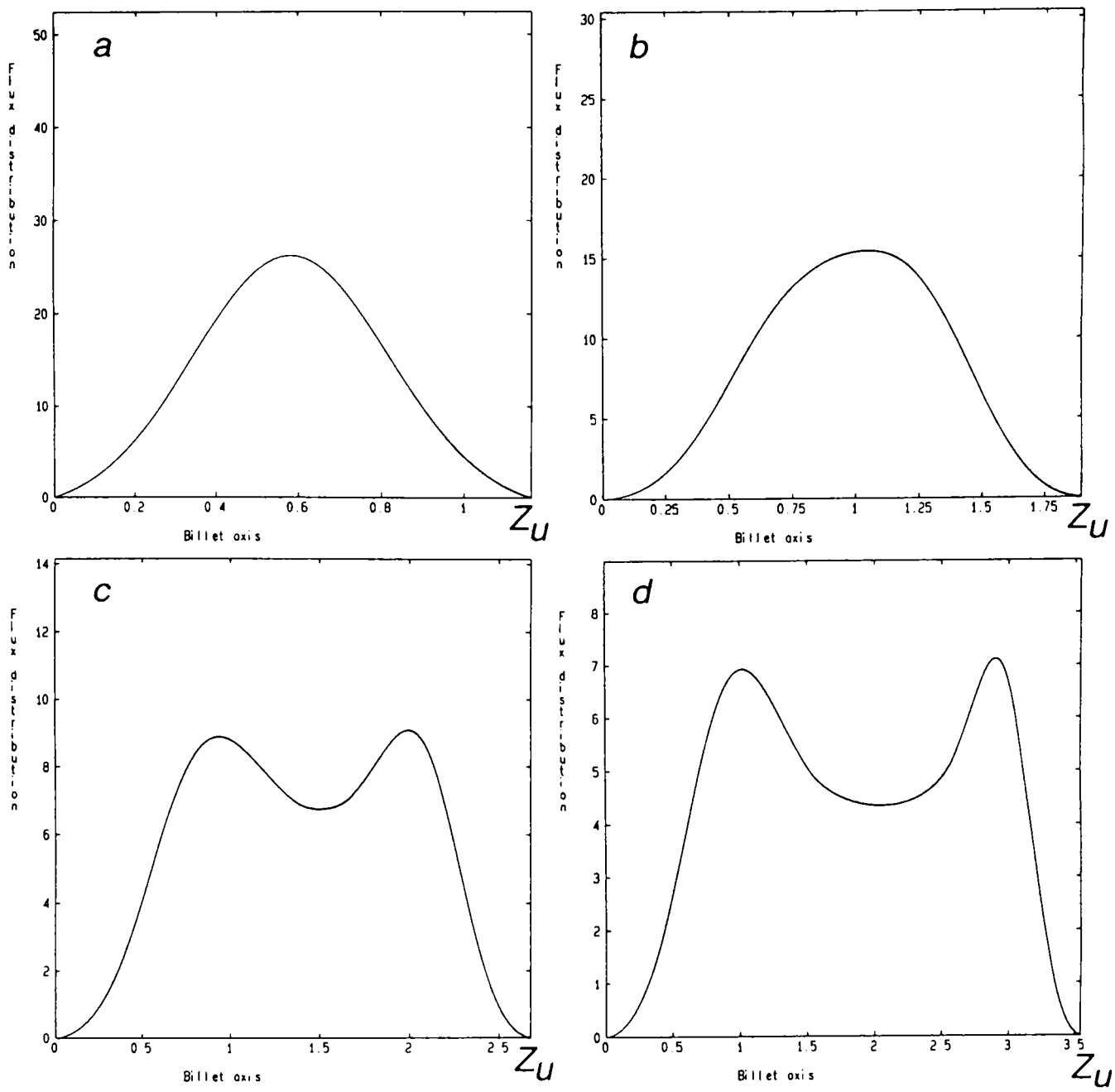

Figure 3.16: Axis flux distribution, $-\bar{g}_\sigma(\sigma, 0)$. Parameters, $r_s = 1/3$, $r_n = 2.27$, $a(t) = \alpha_1 + \alpha_2 \sin \frac{2\pi t}{t_s}$: $\alpha_1 = 35°$; a) $\alpha_2 = 0°$, b) $\alpha_2 = 3°$, c) $\alpha_2 = 6°$, d) $\alpha_2 = 9°$.

Interestingly, the two families of steady states give rise to a continuous range of steady state billet radii that may be achieved, (i.e. as is also true for a unimodal function, $-\bar{g}_\sigma(\sigma, 0)$), but there is a jump in the range of heights at which steady states intercept the axis of rotation. The bimodality of $-\bar{g}_\sigma(\sigma, 0)$ is reflected in the slightly more angular shape of the steady state profiles in Fig. 3.19a, than those seen earlier. In Fig. 3.19b are plotted two steady states which coexist for $\mu = 7$.

Further changes resulting from increasing the scanning range can be seen in the (r_1, z_1)-phase plane. For $\mu = 1$, the steady state at a scanning range $\alpha_2 = 6°$ is now only slightly concave, see Fig. 3.19c. In Fig. 3.19c, as well as the steady state, the spray boundaries and the surface velocity vectorfield, the r_1 and z_1-nullclines have also been plotted. The two nullclines are both plotted in blue. They may be easily distinguished since, the vectorfield is vertical at all points that lie only on a r_1-nullcline, and is horizontal at all points that lie only on a z_1-nullcline, (i.e. the line $\mathcal{L}(\lambda)$ discussed previously is a r_1-nullcline). The nullclines intersect at equilibrium points in the phase plane and are a useful conceptual tool, since they divide the phase plane into regions, in each which the surface velocity vectorfield is in one of four main directions.

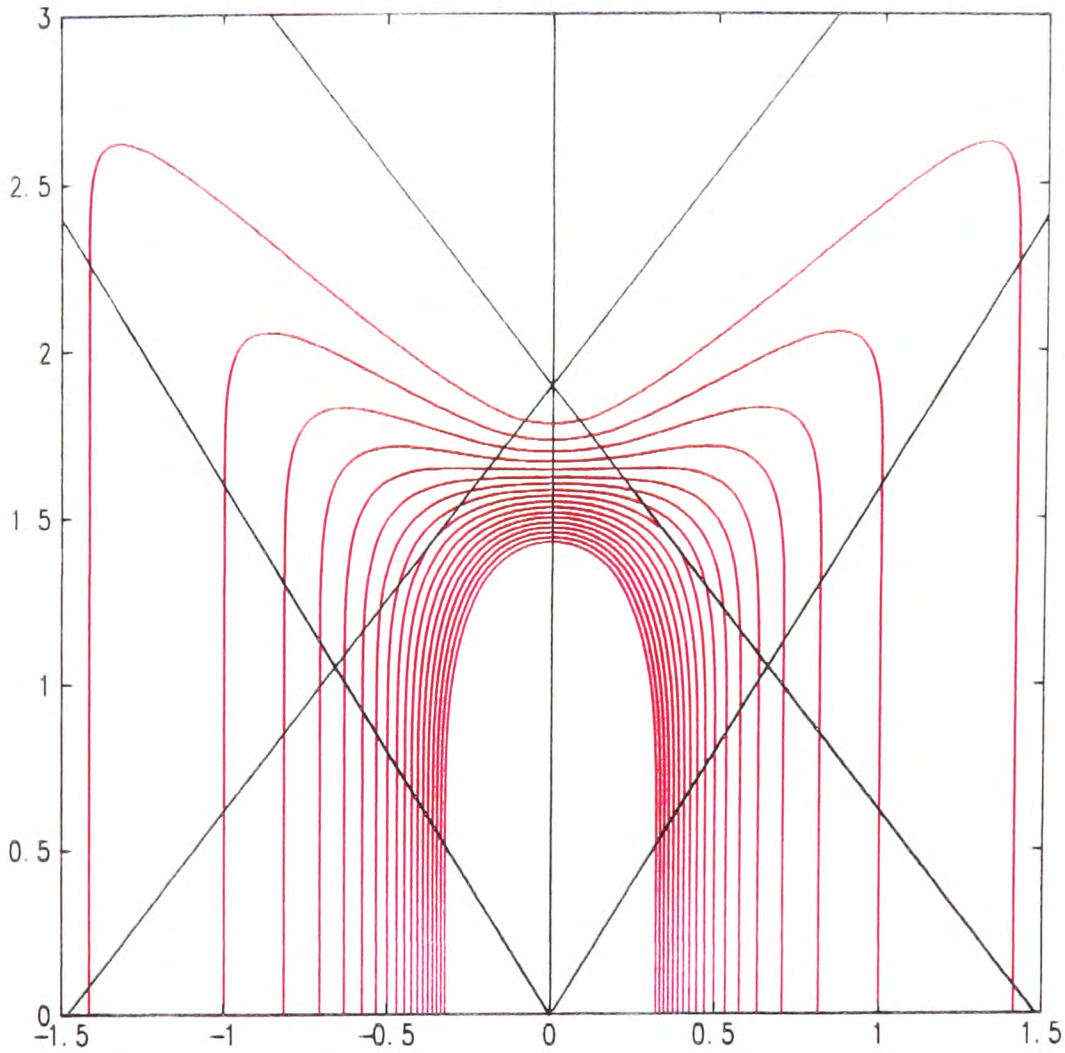

Figure 3.17: Steady state family for $\mu = .5 + k\Delta\mu$: $\Delta\mu = .5$, $k = 0, ..., 17$. Parameters, $r_s = 1/3$, $r_n = 2.27$, $a(t) = \alpha_1 + \alpha_2 \sin \frac{2\pi t}{t_s}$: $\alpha_1 = 35°$, $\alpha_2 = 3°$.

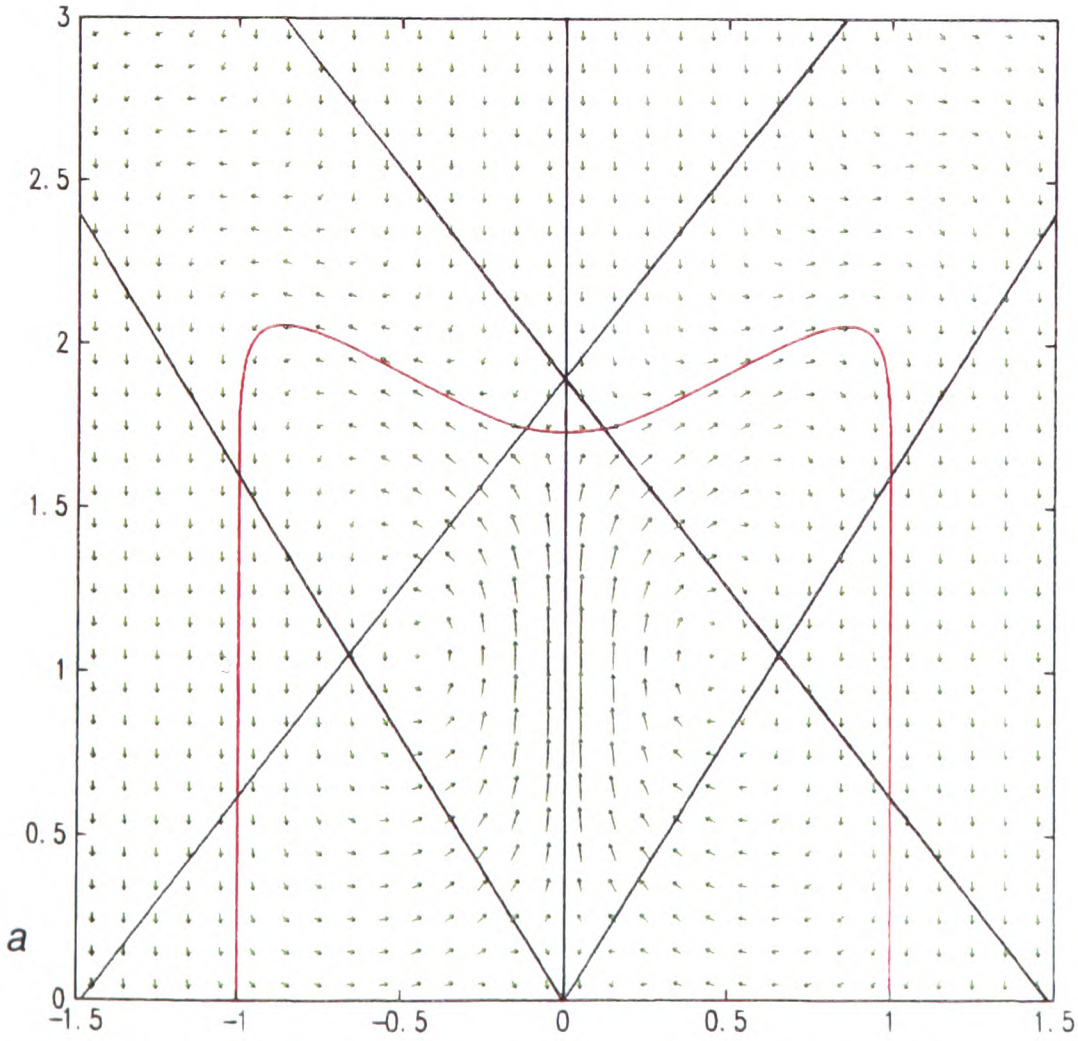

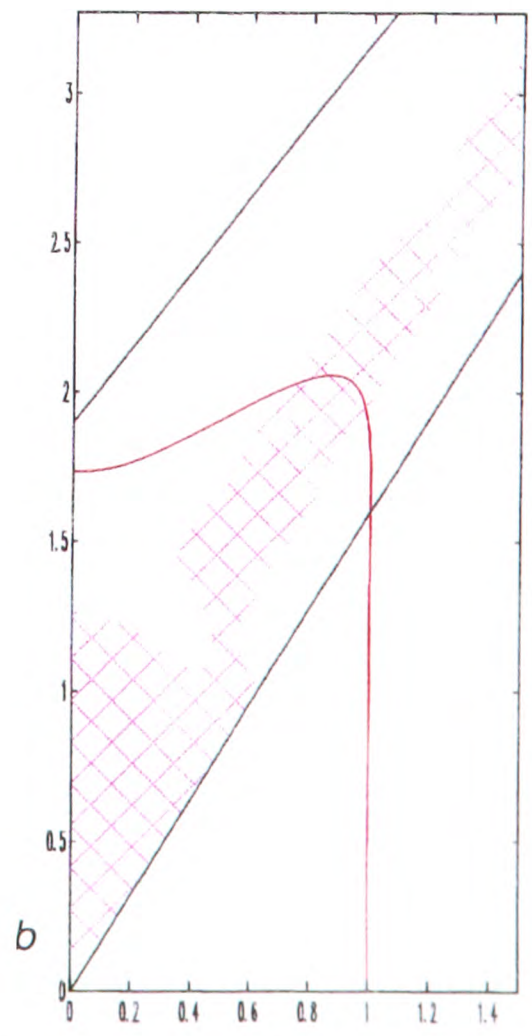

Figure 3.18: Parameters, $\mu = 1$, $r_s = 1/3$, $r_n = 2.27$, $a(t) = \alpha_1 + \alpha_2 \sin \frac{2\pi t}{t_s}$: $\alpha_1 = 35°$, $\alpha_2 = 3°$; a) (r_1, z_1)-phase plane: surface velocity vectors - green, steady states - red, spray boundaries - black, b) steady state stability: shaded areas are where the conditions of theorem 2.3.1 do not hold.

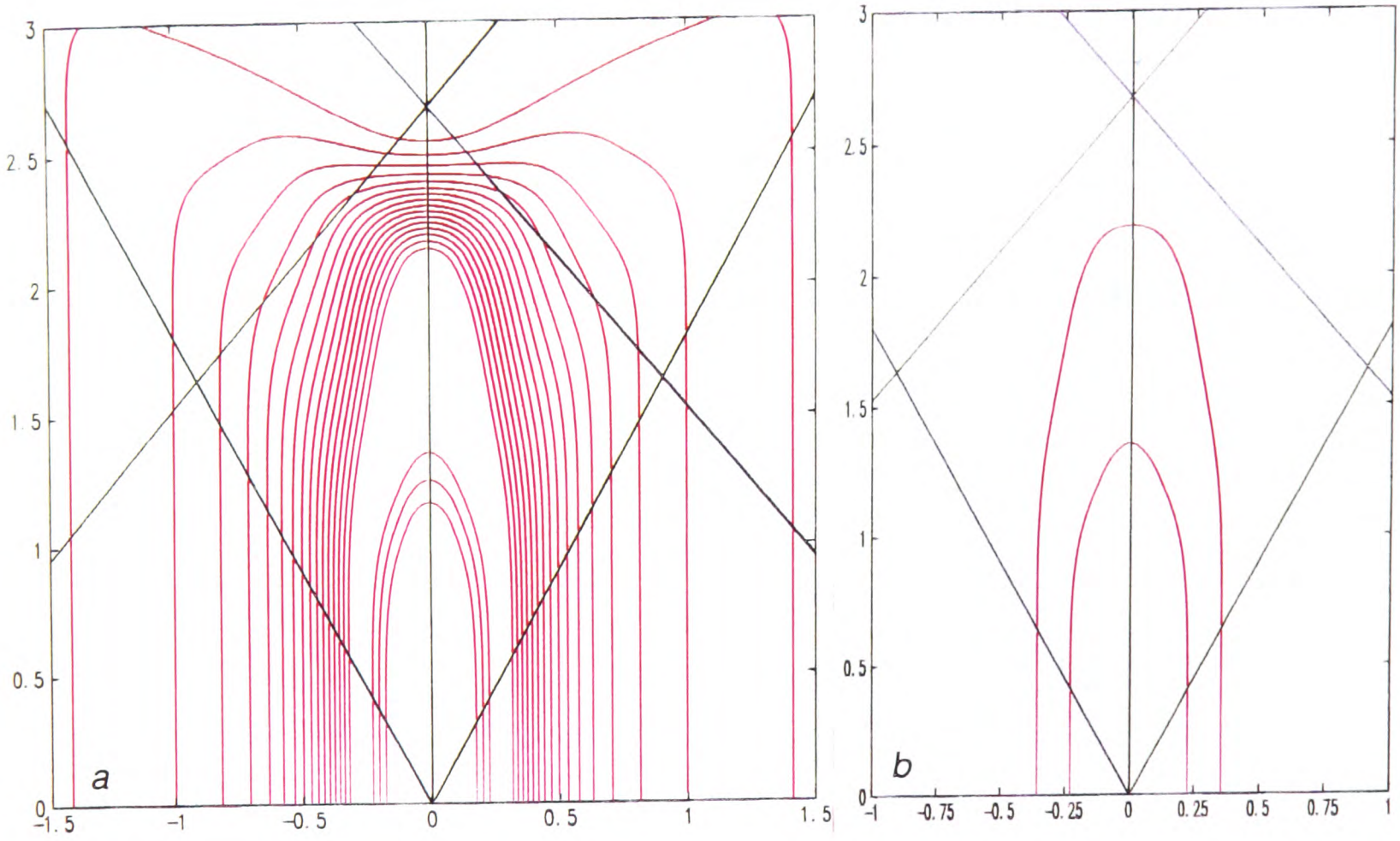

Figure 3.19: Parameters, $r_s = 1/3$, $r_n = 2.27$, $a(t) = \alpha_1 + \alpha_2 \sin \frac{2\pi t}{t_s}$: $\alpha_1 = 35°$, $\alpha_2 = 6°$; a) Steady state families for $\mu = .5 + k\Delta\mu$: $\Delta\mu = .5$, $k = 0, ..., 15$, b) Coexisting steady states at $\mu = 7$, c) (r_1, z_1)-phase plane at $\mu = 1$: surface velocity vectors - green, steady states - red, spray boundaries - black, nullclines - blue, d) Steady state stability for $\mu = 1$: shaded areas are where the conditions of theorem 2.3.1 fail.

The r_1-nullclines in Fig. 3.19c run outwards from the billet axis towards the interception of the lower and overlapping spray boundaries, O_3, and in the smaller of the two blue loops. The billet axis of rotation is also a r_1-nullcline. In the case of a unimodal $g_\sigma(\sigma, 0)$, the second, small looped, r_1-nullcline would not exist. The z_1-nullcline seen in Fig. 3.19c is the larger of the two blue loops. The two nullclines intersect at the unstable spirals which can be seen in Fig. 3.19c.

In Fig. 3.19d it is seen that the angular nature of the steady state for $\mu = 1$ results in two unstable intervals along its profile, where the conditions of theorem 2.3.1 are not met. In each shaded region the phase paths diverge from the steady state as they follow it around each angular section.

As μ is increased the r_1 nullclines remain unchanged and the looped z_1-nullcline contracts within itself towards the region where the mass flux is more concentrated. Due to the shape of the uppermost r_1-nullcline, as the z_1 nullcline contracts and the steady states become nested within one another the unstable spirals will get progressively closer to the steady state. This may have consequences for the interval of stability of steady states at higher values of μ. Further down the billet axis of rotation the contracting z_1-nullcline may intersect the looped r_1-nullcline, giving rise to new equilibrium points. Eventually, as μ is increased sufficiently for there to be two steady state profiles there will also be two looped z_1-nullclines, (see Fig. 3.20a & b).

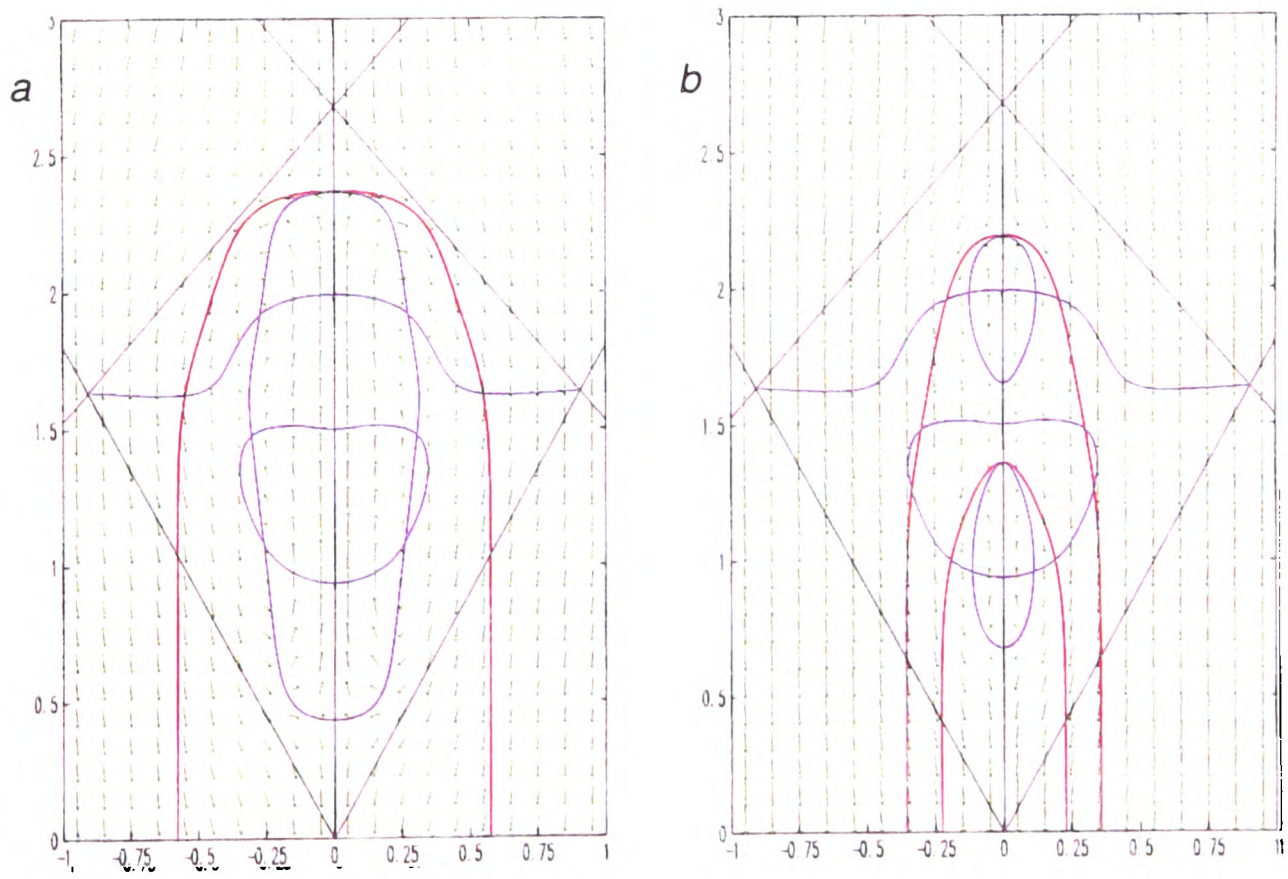

Figure 3.20: Parameters, $r_s = 1/3$, $r_n = 2.27$, $a(t) = \alpha_1 + \alpha_2 \sin \frac{2\pi t}{t_s}$: $\alpha_1 = 35°$, $\alpha_2 = 6°$; a) New equilibrium points in the (r_1, z_1)-phase plane at $\mu = 3$, b) Two looped z_1-nullclines and two coexisting steady states in the (r_1, z_1)-phase plane at $\mu = 7$.

For a scanning range of $\pm 9°$ the family of steady states are more convex, but also more angular, (see Fig. 3.21a, where only the outermost family of steady states has been plotted). Dual steady states and multiple equilibrium points, away from the axis of rotation, both occur at lower values of μ than with smaller scanning ranges, see Fig. 3.21b. Again there is evidence of steady state instability, due to angular shape and due to the shape of the uppermost r_1-nullcline, see Fig. 3.21c.

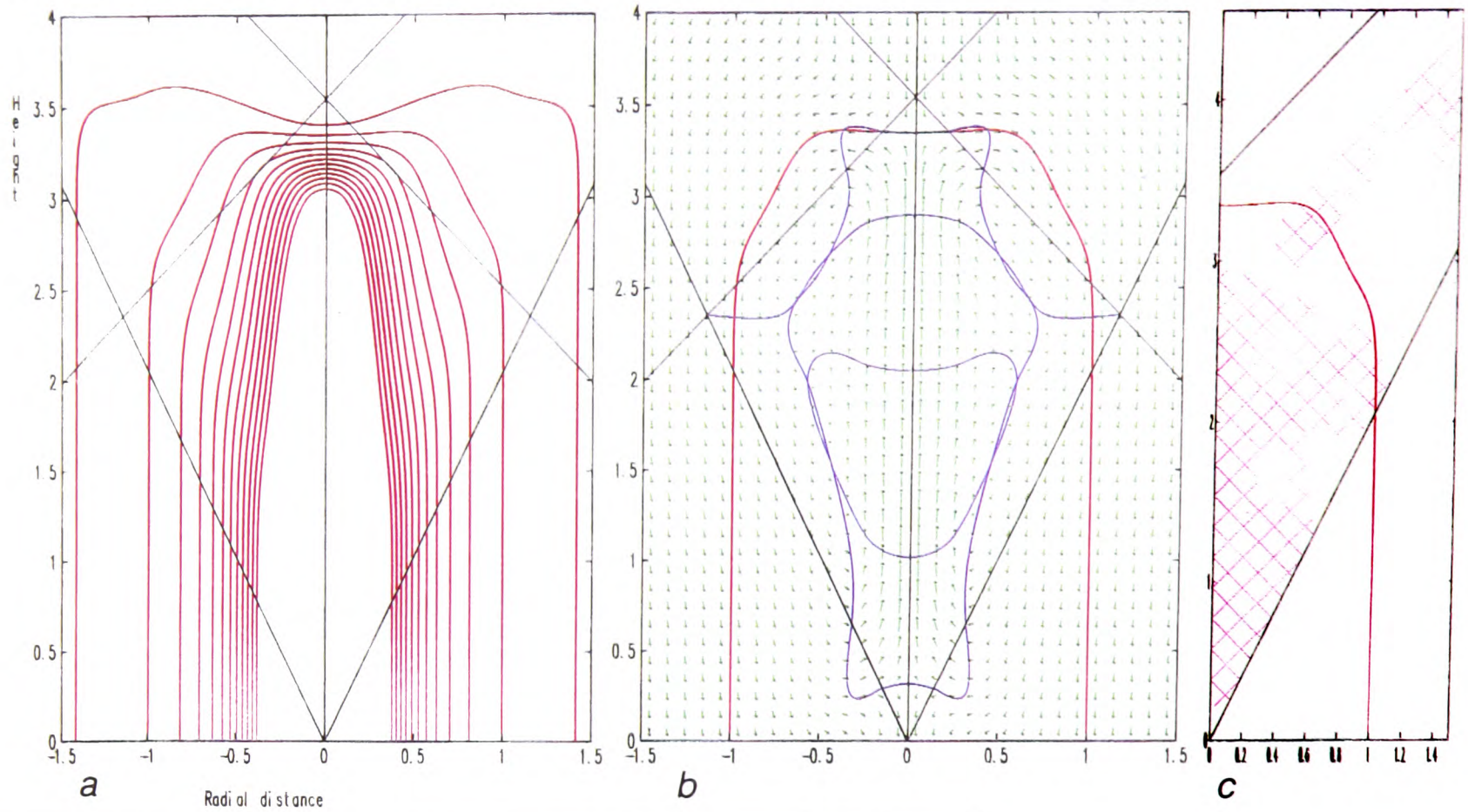

Figure 3.21: Parameters, $r_s = 1/3$, $r_n = 2.27$, $a(t) = \alpha_1 + \alpha_2 \sin \frac{2\pi t}{t_s}$: $\alpha_1 = 35°$, $\alpha_2 = 9°$; a) Outer family of steady states for $\mu = .5 + k\Delta\mu$: $\Delta\mu = .5$, $k = 0, ..., 11$, b) (r_1, z_1)-phase plane at $\mu = 1$, c) Steady state stability, $\mu = 1$.

Fig. 3.22 magnifies those regions of Fig. 3.21b within which extra equilibrium points lie. In the uppermost region, (Fig. 3.22a), the two nullclines intersect and then nearly touch again. Here there is a single unstable spiral, but for slightly larger μ there will be two unstable spirals separated by a saddle point. In the lower region, (Fig. 3.22b), there is a saddle and an unstable spiral.

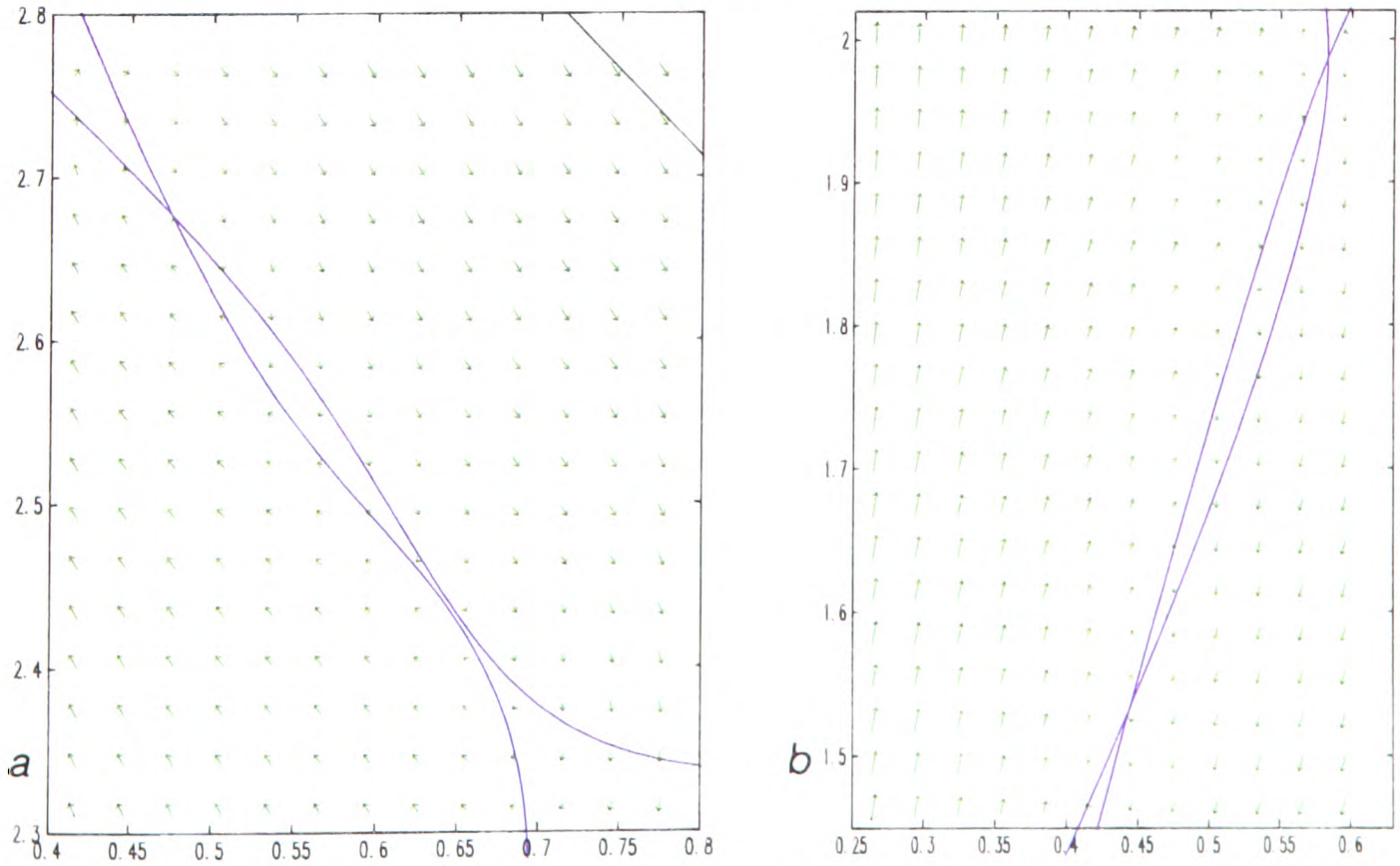

Figure 3.22: Parameters, $r_s = 1/3$, $r_n = 2.27$, $a(t) = \alpha_1 + \alpha_2 \sin \frac{2\pi t}{t_s}$: $\alpha_1 = 35°$, $\alpha_2 = 9°$; Additional equilibrium points in the (r_1, z_1)-phase plane at $\mu = 1$. Surface velocity vectors - green, nullclines - blue.

3.5 More realistic scanning patterns

The results of the previous section indicate that by employing a sinusoidal atomiser scanner motion with a large enough scanning angle it is possible to produce a convex steady state crown shape of a desired radius. However, there are two worrying features that appear to be associated with the use of a sinusoidal scanning function, $\alpha(t)$, for large scanning ranges, α_2.

1. The steady states produced when $-\bar{g}_\sigma(\sigma, 0)$ is bimodal are quite angular.
   (a) Sharp angular changes in steady state shape appear to lead to unstable intervals of the steady state profile.
   (b) Sharp angular changes in steady state shape imply sharp changes in both the heat and mass flux normal to the billet surface.
2. The shape of the uppermost of the two r_1-nullclines that extend away from the axis of rotation is undesirable. The unstable spirals that lie at the intersections of this nullcline with the z_1-nullcline, are quite close to the steady state crown surface, (e.g. Figs. 3.19c and 3.21b), and will get closer with increasing μ. This may then effect the stability of segments of the steady state profiles.

The points of intersection of the r_1-nullclines with the billet axis are the turning points of $-\bar{g}_\sigma(\sigma, 0)$. For bimodal $-\bar{g}_\sigma(\sigma, 0)$ there are three turning points. It is conjectured that the r_1-nullcline which starts from the maximum value of $-\bar{g}_\sigma(\sigma, 0)$ will run out to the point of intersection of the lower and overlapping spray boundaries, O_3, whilst the two r_1-nullclines that start from the other two turning points of $-\bar{g}_\sigma(\sigma, 0)$ will join in a loop.

This conjecture is supported by the results of the previous section and, if true, will be responsible for point 2, listed above. The r_1-nullclines represent those lines along which the mass flux component perpendicular to the billet axis is zero. The shape of $-\bar{g}_\sigma(\sigma, 0)$ in Figs. 3.16c and 3.16d suggests that a sinusoidal scanning angle results in a larger distribution of mass flux towards the upper spray boundary. It is this distribution that results in both the proximity of the uppermost r_1-nullcline to the steady state surfaces, and in the extent to which this nullcline penetrates the (r_1, z_1) plane from the billet axis. In order to lessen both effects it is necessary to employ a scanning angle which distributes the mass flux more towards the lower spray boundary.

Fig. 3.23 shows a typical production scanner function, $\alpha(t)$. The periodic function $\alpha(t)$, in Fig. 3.23, is negative for a larger proportion of the time than it is positive. Thus, the objective outlined in the above paragraph should be achieved by this function.

The more intuitive motivation for using a scanning motion which spends a greater proportion of the time directing spray close to the lower spray boundary is that the spray here will be deposited on the outside of the billet and there is more surface area here. It is this reasoning that has traditionally driven the design of scanner angle functions, $\alpha(t)$, that are used in production.[3]

[3]The reasoning is not entirely correct since, the results of this chapter show that billet radius can be fixed, and the billet crown allowed to grow to the shape that is necessary to capture the right amount of mass for that radius.

In this section the effect of using the scanner function of Fig. 3.23 with a variety of scanning ranges, α_2, is examined. Other parameters are fixed, (as before), to allow comparison with the results of the previous section.

$$\begin{aligned} r_n &= 2.27, \\ r_s &= 1/3, \\ \alpha_1 &= 35°. \end{aligned}$$

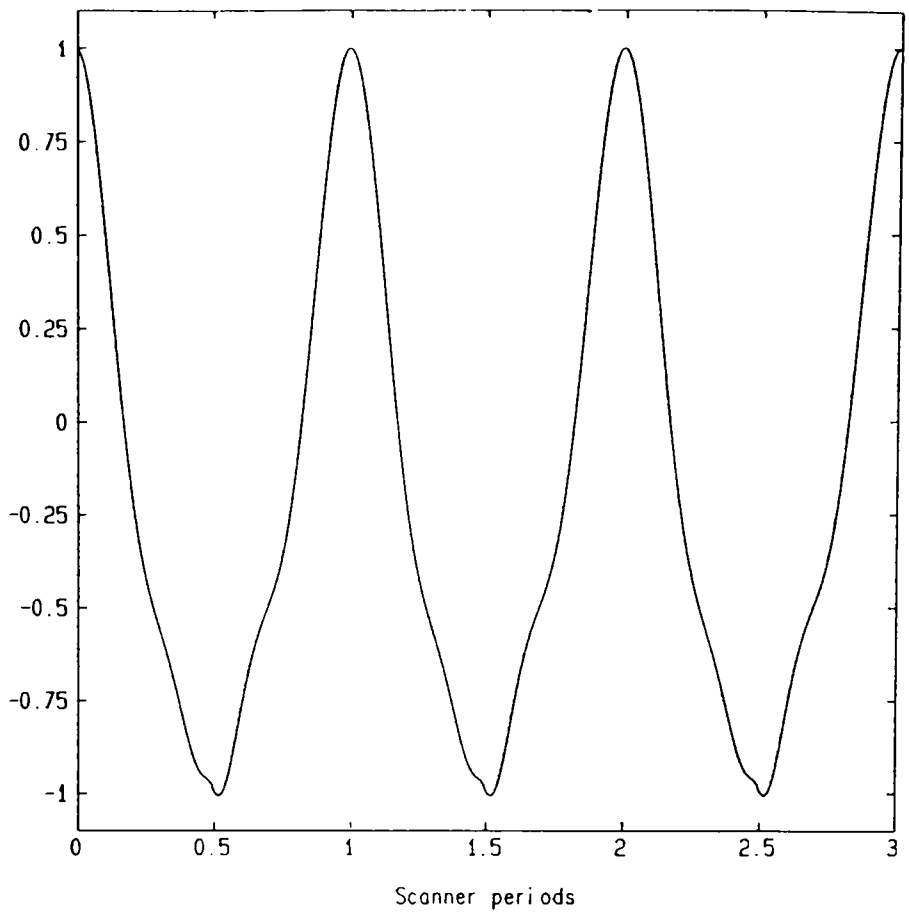

Figure 3.23: Typical production scanner function, $\alpha(t)$.

Fig. 3.24 shows the effect on $-\bar{g}_\sigma(\sigma, 0)$ of increasing α_2, using the scanner function of Fig. 3.23. For $\alpha_2 = 3°$ the function $-\bar{g}_\sigma(\sigma, 0)$ is still unimodal. Comparison of Fig. 3.24b with Fig. 3.16b shows that the distribution is now skewed slightly towards O_1, rather than towards O_2. As α_2 is increased further, bimodality of $-\bar{g}_\sigma(\sigma, 0)$ again results. However, a larger value of α_2 is needed before the distribution becomes bimodal. The maximum value of $-\bar{g}_\sigma(\sigma, 0)$ is now attained at the lower of the two modes.

For $\alpha_2 = 6°$ and $\alpha_2 = 9°$ the families of steady states are plotted in Fig. 3.25. In each case there are two families of nested steady states, separated on the billet axis of rotation. The steady states appear to be more convex than those produced with a sinusoidal scan, but are still quite angular. The continuous range of possible billet radii is well illustrated. The implication of this is that, although there is a large drop in height of the steady states on the axis of rotation, the amount of spray that is collected by the billet crown varies continuously.

The phase plane for $\mu = 1$, with scanning range $\alpha_2 = 6°$, reveals most clearly the effect of changing the scanner angle function. The smaller upper mode of $-\bar{g}_\sigma(\sigma, 0)$ now gives rise to a very small, looped r_1-nullcline. As conjectured, the second, lower r_1-nullcline runs from O_3 to the axial position of the second, larger, mode of $-\bar{g}_\sigma(\sigma, 0)$, see Fig. 3.26. Thus now, when μ is increased, the unstable spirals in the phase plane move downwards, in the same direction as the contracting nested steady state family.

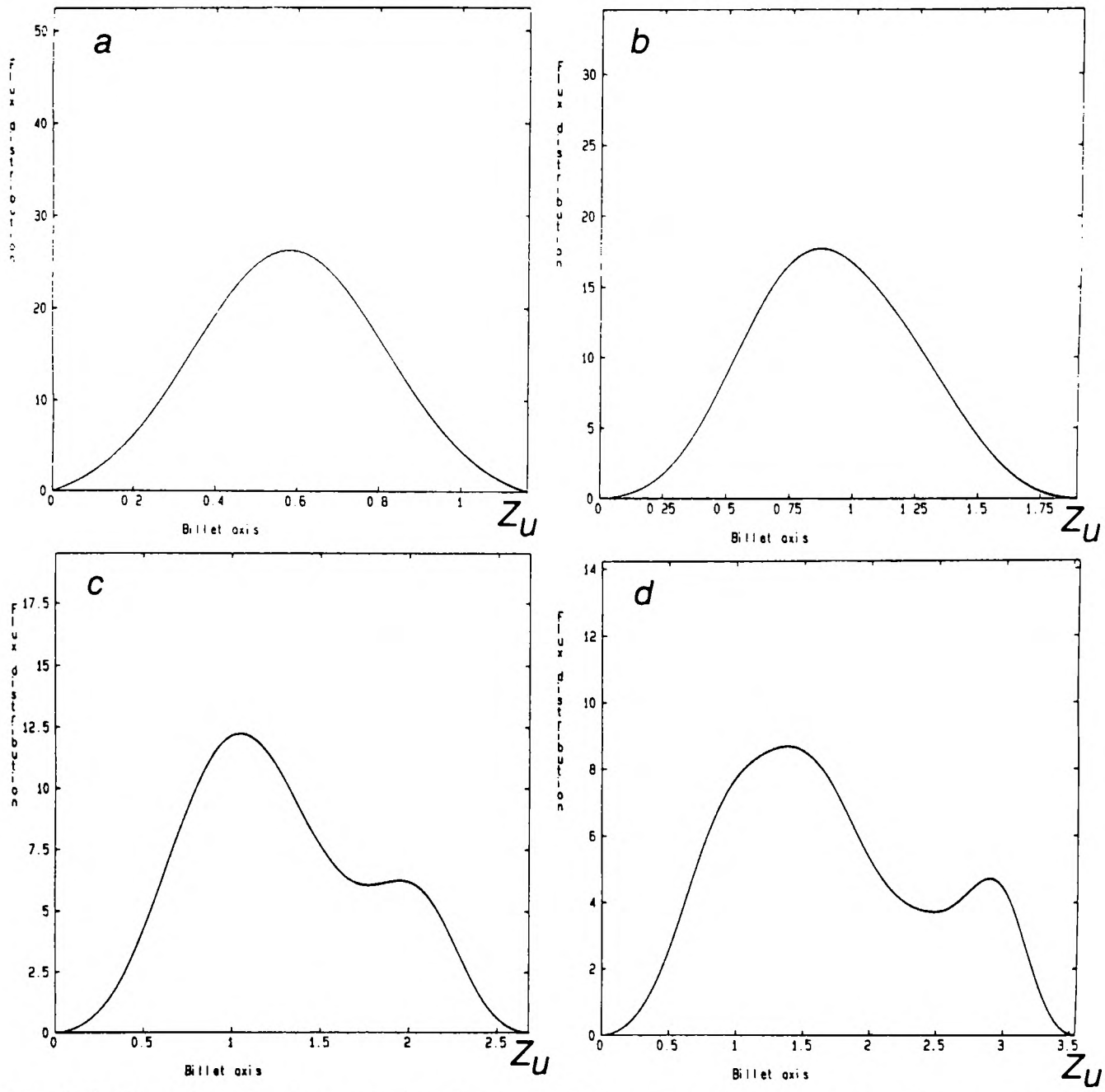

Figure 3.24: Axis flux distribution, $-\bar{g}_\sigma(\sigma, 0)$, $r_s = 1/3$, $r_n = 2.27$, $\alpha_1 = 35°$; a) $\alpha_2 = 0°$, b) $\alpha_2 = 3°$, c) $\alpha_2 = 6°$, d) $\alpha_2 = 9°$.

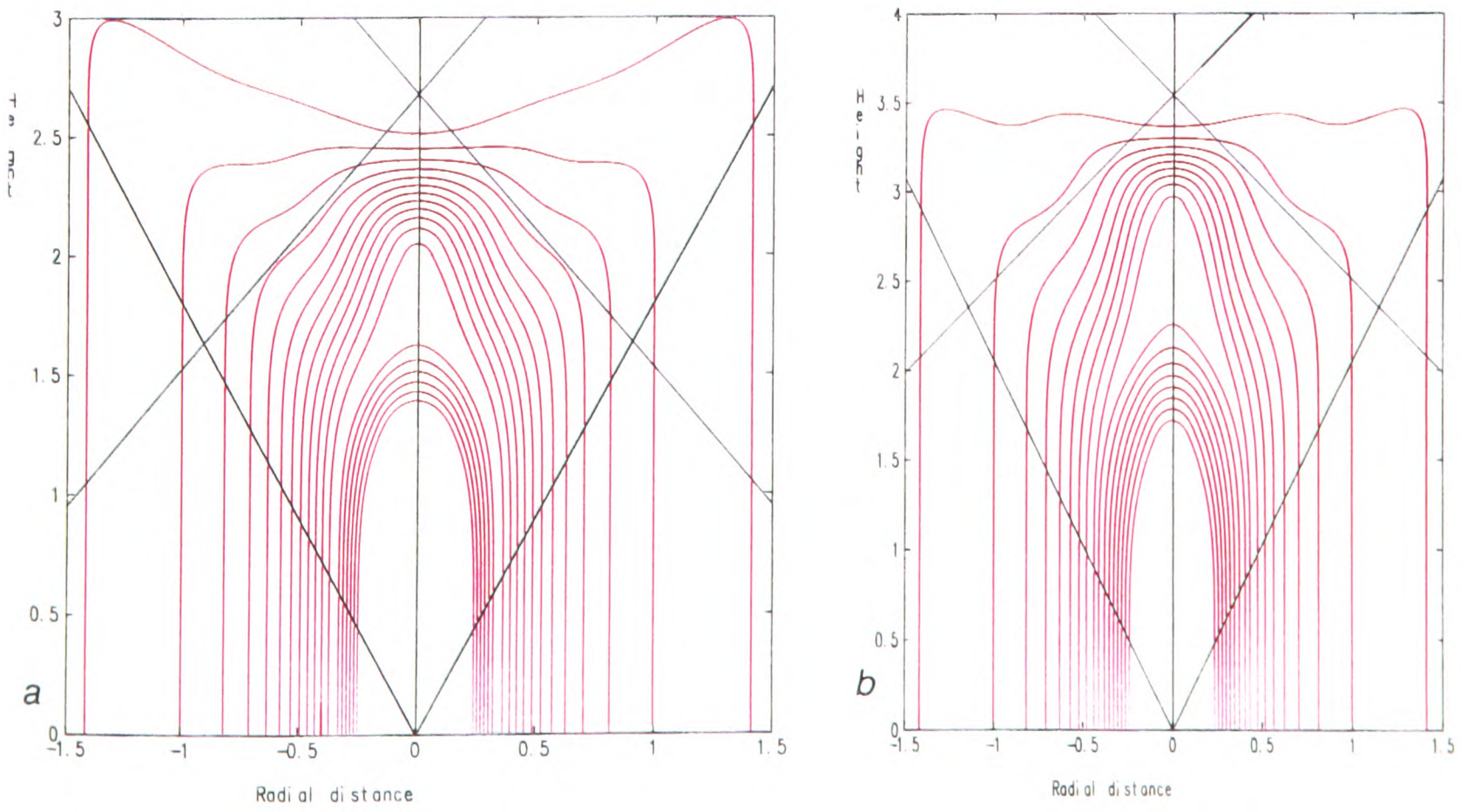

Figure 3.25: Steady state families, $r_s = 1/3$, $r_n = 2.27$, $\alpha_1 = 35°$; a) $\alpha_2 = 6°$, b) $\alpha_2 = 9°$.

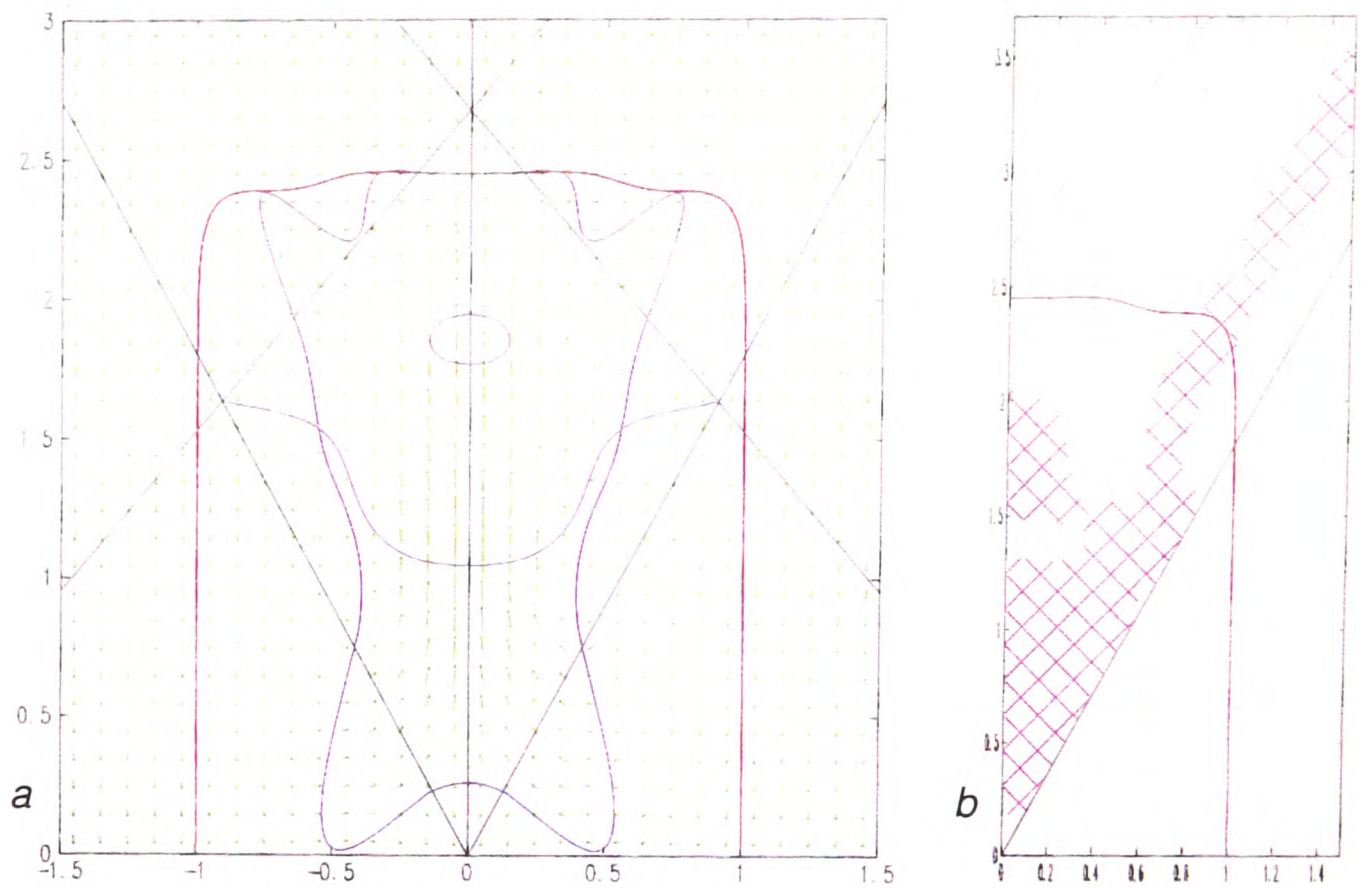

Figure 3.26: (r_1, z_1)-phase plane and steady state stability, $\mu = 1$; $r_s = 1/3$, $r_n = 2.27$, $\alpha_1 = 35°$, $\alpha_2 = 6°$.

Again there are instability problems where the steady state is angular. Fig. 3.26b also shows a shaded area on the billet axis, which covers the uppermost looped r_1-nullcline, as not satisfying the conditions of theorem 2.3.1. However, it is clear from the phase plane in Fig. 3.26a that a transient surface will grow towards the steady state in this region also. Similar comments apply to the case $\alpha_2 = 9°$, see Fig. 3.27.

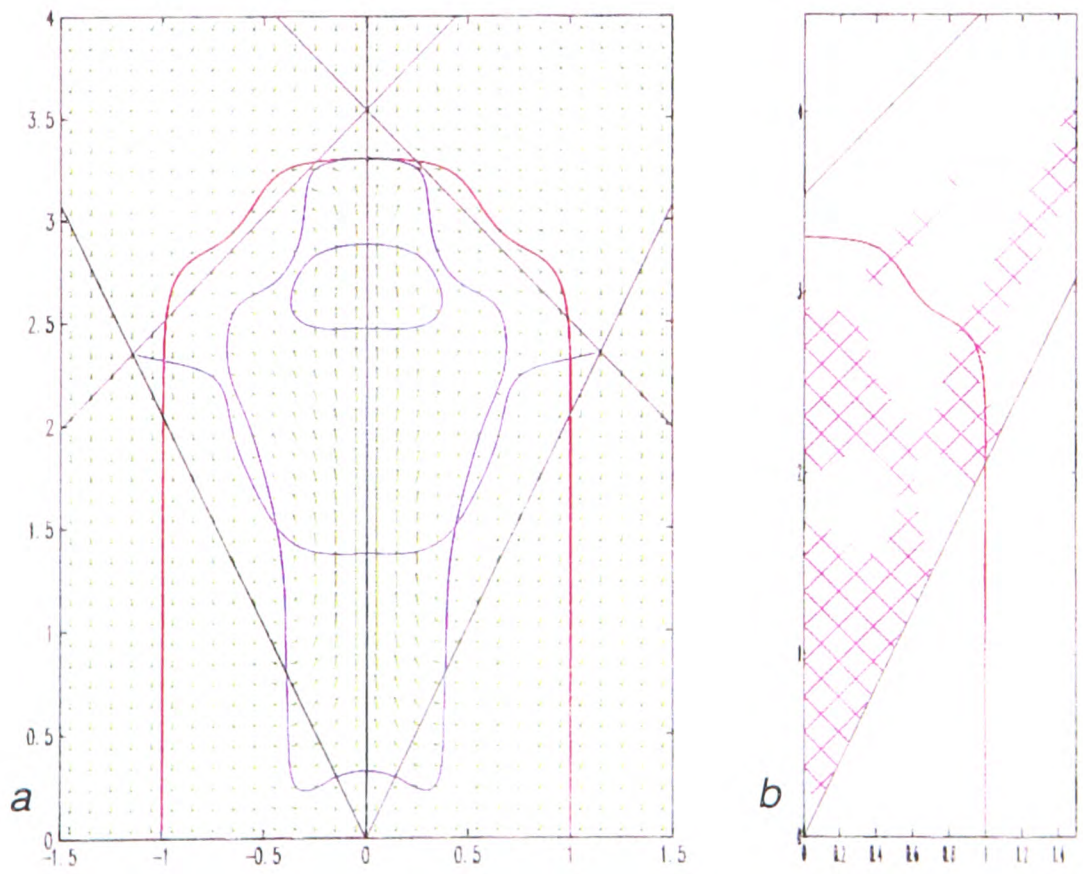

Figure 3.27: (r_1, z_1)-phase plane and steady state stability, $\mu = 1$; $r_s = 1/3$, $r_n = 2.27$, $\alpha_1 = 35°$, $\alpha_2 = 9°$.

3.6 Scanner angle design

From a purely dynamical point of view, to produce a billet of radius $r_b \approx 1$ by control of the ratio μ, of withdrawal rate to mass flow rate, it would be desirable to have a wide range of μ which produce as stable as possible steady states over an interval of radii containing r_b. The past sections of this chapter have shown that considerable variation in the shape of a steady state billet crown of radius r_b can be achieved through use of different scanner patterns, $a(t)$. The main features of billet shape and of the axis flux distribution, $-\bar{g}_\sigma(\sigma, 0)$, that are considered desirable may be summarised as follows.

1. The range of steady states should be convex. The phase plane plots show that radial motion of billet surfaces at small displacements from steady state radii, r_b, is much less than the corresponding vertical motion closer to the billet axis. Hence, billet height will generally be more responsive than billet radius to changes in μ, and it will be important to achieve accurate height measurement, see [99].

2. The distribution $-\bar{g}_\sigma(\sigma, 0)$ should be unimodal. In this way there will be at most one steady state for any value of μ. There will also be only a single r_1-nullcline, $\mathcal{L}(\lambda)$, that extends out from the axis of rotation.

3. The distribution $-\bar{g}_\sigma(\sigma, 0)$ should be skewed towards O_1, rather than O_2. This has the effect of positioning the line $\mathcal{L}(\lambda)$, and consequently any additional equilibrium points, further away from the steady state profiles, (to see the effect of skewing the distribution, $-\bar{g}_\sigma(\sigma, 0)$, this way for a bimodal $-\bar{g}_\sigma(\sigma, 0)$, compare Figs. 3.19c and 3.26a).

In practice, for a given desired dimensional radius, R, the angle, α_1, and the spray cone radius, r_s, are fixed approximately by the desired spray flight distance and the design features of the atomiser respectively. Given these, the scanning range, α_2, is also approximately fixed by the requirement that the steady states be convex, (e.g. in the above sections a scanning range $\alpha_2 \approx 6°$, or larger, was needed before steady states of radius $r_b \approx 1$ became convex). In order to incorporate these features into the process it becomes useful to devise some way of including the above loose constraints on $-\bar{g}_\sigma(\sigma, 0)$ in selection of an appropriate scanner pattern, $a(t)$. The problem may be addressed as follows.

- Given r_n, r_s, α_1, α_2 select a "target" axis flux distribution, $-\bar{g}^T_\sigma(\sigma, 0)$, which satisfies the above constraints.

- Define an objective function $\Delta\bar{g}_\sigma$ by

$$\Delta\bar{g}_\sigma = \left\| \bar{g}^T_\sigma - \bar{g}_\sigma \right\|, \tag{3.13}$$

  where $\|\cdot\|$ is a norm to be chosen later. Minimisation of $\Delta\bar{g}_\sigma$ over a range of possible $\alpha(t)$, results in an "optimal" scanner pattern, $a(t)$. It is hoped that the optimal $a(t)$ will produce an averaged mass flux distribution vectorfield, $\bar{g}$, that allows a single family of nested steady states, convex over a range of radii, including r_b, and suitably stable.

Setting $t = \tau_1 t_s$ the function $\alpha(t)$ can be written as $\alpha(\tau_1)$, for $\tau_1 \in [0, 1]$. Periodicity of the scanner is satisfied by requiring $\alpha(0) = \alpha(1)$, and $\alpha(\tau_1)$ must range between values of ± 1. Mechanical constraints on $\alpha(\tau_1)$ are

in the form of bounds on $|\alpha''(\tau_1)|$ at its turning points.[4] For a given $\alpha(\tau_1)$ these convert into bounds on the maximum scanner frequency that may be used. To reduce any such constraints $\alpha(\tau_1)$ is required to be symmetric about $\tau_1 = 1/2$, and to be monotone on $[0, 1/2]$.

As an example of how this optimisation technique might be used, two cubic splines are chosen as basis functions to represent $\alpha(\tau_1)$ on $[0, 1/2]$. Differentiability of $\alpha(\tau_1)$ requires that

$$\begin{aligned} \alpha(0) &= 1, \\ \alpha'(0) &= 0, \\ \alpha(1/2) &= -1, \\ \alpha'(1/2) &= 0, \end{aligned}$$

so that $\alpha(\tau_1)$ is completely specified by the spline knot, $\tau_1^* \in (0, 1/2)$, by $\alpha(\tau_1^*) \in (-1, 1)$ and by $\alpha'(\tau_1^*) < 0$. This choice of basis functions for finding optimal $\alpha(\tau_1)$ thus implies

$$\Delta\bar{g}_\sigma = \Delta\bar{g}_\sigma(\tau_1^*, \alpha(\tau_1^*), \alpha'(\tau_1^*)).$$

For comparison with the previous results of this chapter, model parameters are set at $r_n = 2.27$, $r_s = 1/3$, $\alpha_1 = 35°$, $\alpha_2 = 6°$. Preselection of r_n, r_s, α_1 and α_2, fixes z_u, the vertical distance between O_1 and O_2. At both O_1 and O_2, $\bar{g}_\sigma(\sigma, 0)$ and $\bar{g}_\sigma^T(\sigma, 0)$ are zero. The target distribution function chosen is shown in Fig. 3.28. It clearly satisfies all the above, loose, constraints on the axis flux distribution.

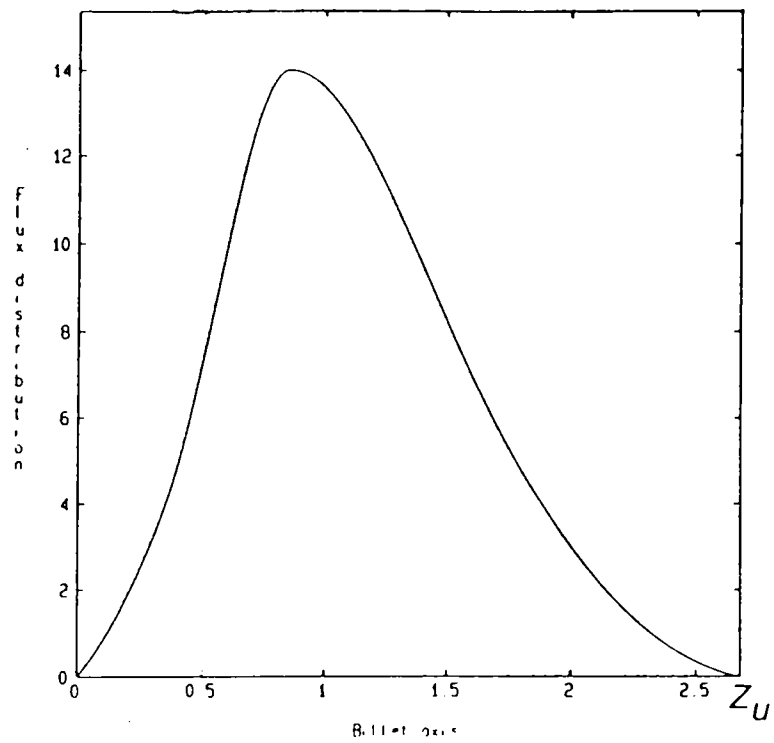

Figure 3.28: Target axis mass flux distribution $\bar{g}_\sigma^T(\sigma, 0)$; $r_s = 1/3$, $r_n = 2.27$, $\alpha_1 = 35°$, $\alpha_2 = 6°$.

Dividing the interval $\sigma \in (0, z_u)$ into N equal subintervals, separated by points $\{\sigma_k\}_{k=0}^N$, the norm in (3.13) is chosen, (for this example), to be given by

$$\begin{aligned} \Delta\bar{g}_\sigma(\tau_1^*, \alpha(\tau_1^*), \alpha'(\tau_1^*)) &= \frac{1}{N-1} \sum_{k=1}^{N-1} |\bar{g}_\sigma(\sigma_k, 0) - \bar{g}_\sigma^T(\sigma_k, 0)| + \\ &\quad [\bar{g}_\sigma(\sigma_{k+1}, 0) - g_\sigma(\sigma_{k-1}, 0) - \bar{g}_\sigma^T(\sigma_{k+1}, 0) + g_\sigma^T(\sigma_{k-1}, 0)]^2. \end{aligned} \tag{3.14}$$

[4] Here, $'$ denotes differentiation with respect to τ_1.

The minimisation problem can then be solved using NAG routine E02JAF, which employs a quasi-Newton algorithm, incorporating the bounds on τ_1^*, $\alpha(\tau_1^*)$ and $\alpha'(\tau_1^*)$, and using function values $\Delta\bar{g}_\sigma(\tau_1^*, \alpha(\tau_1^*), \alpha'(\tau_1^*))$ only. Graphical results from the minimisation, in the form of the axis flux distribution, $-\bar{g}_\sigma(\sigma, 0)$, and optimal scanner function, $\alpha(\tau_1)$, are shown in Fig. 3.29.

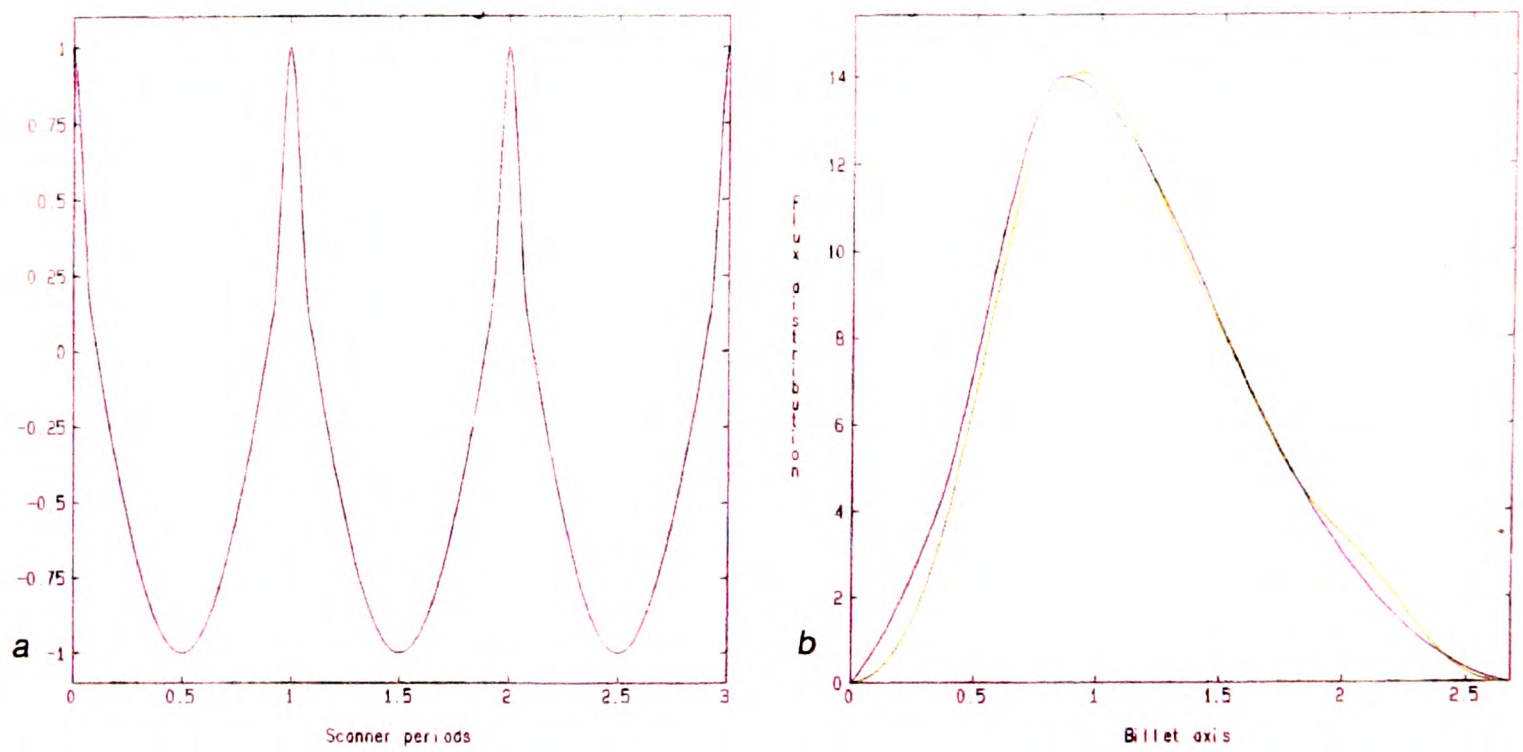

Figure 3.29: Minimisation results, $r_s = 1/3$, $r_n = 2.27$, $\alpha_1 = 35°$, $\alpha_2 = 6°$; a) Solution scanner angle function $\alpha(t)$, b) Target axis mass flux distribution, $\bar{g}_\sigma^T(\sigma, 0)$, (black) and solution axial mass flux distribution, $\bar{g}_\sigma(\sigma, 0)$, (green).

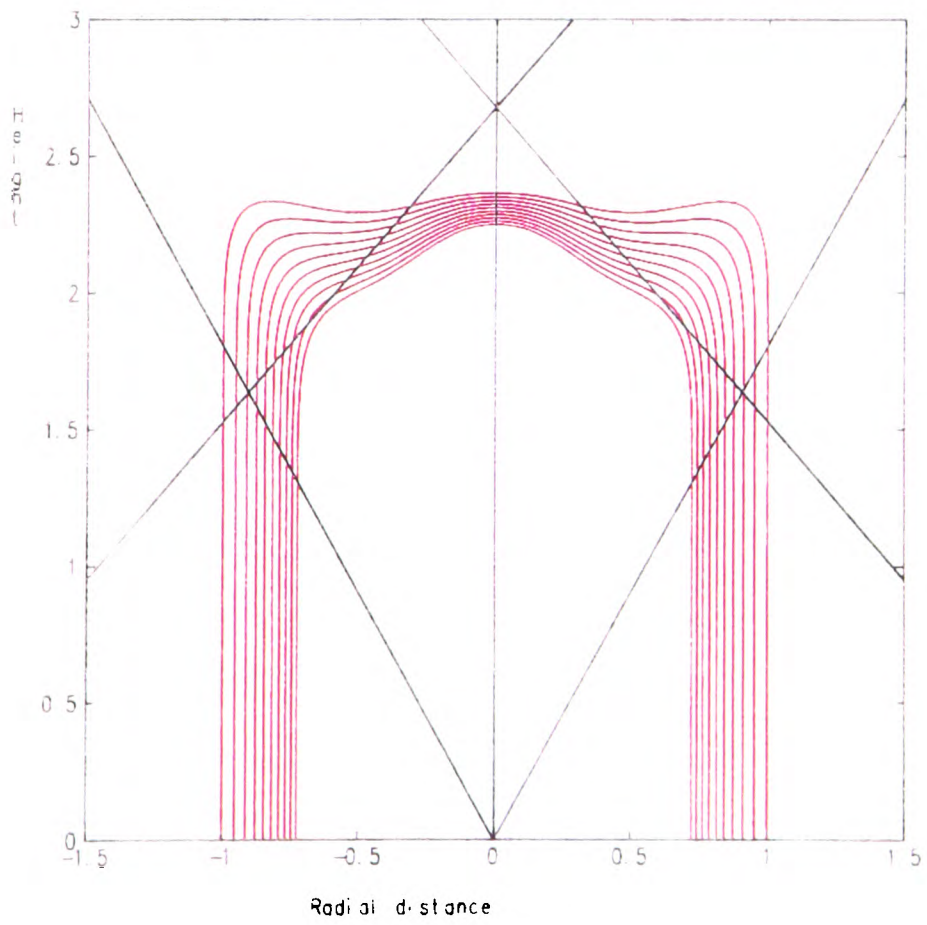

Figure 3.30: Minimisation results: steady state family $\mu = 1. + k\Delta\mu$: $\Delta\mu = .1$, $k = 0, ...9$, $r_s = 1/3$, $r_n = 2.27$, $\alpha_1 = 35°$, $\alpha_2 = 6°$.

For this scanner angle function there is a unique family of steady state crown profiles which become convex at $\mu \approx 1.1$, see Fig. 3.30. With increasing μ the unstable spirals in the phase plane move towards the billet axis, along $\mathcal{L}(\lambda)$, and away from the steady states, see Fig. 3.31.

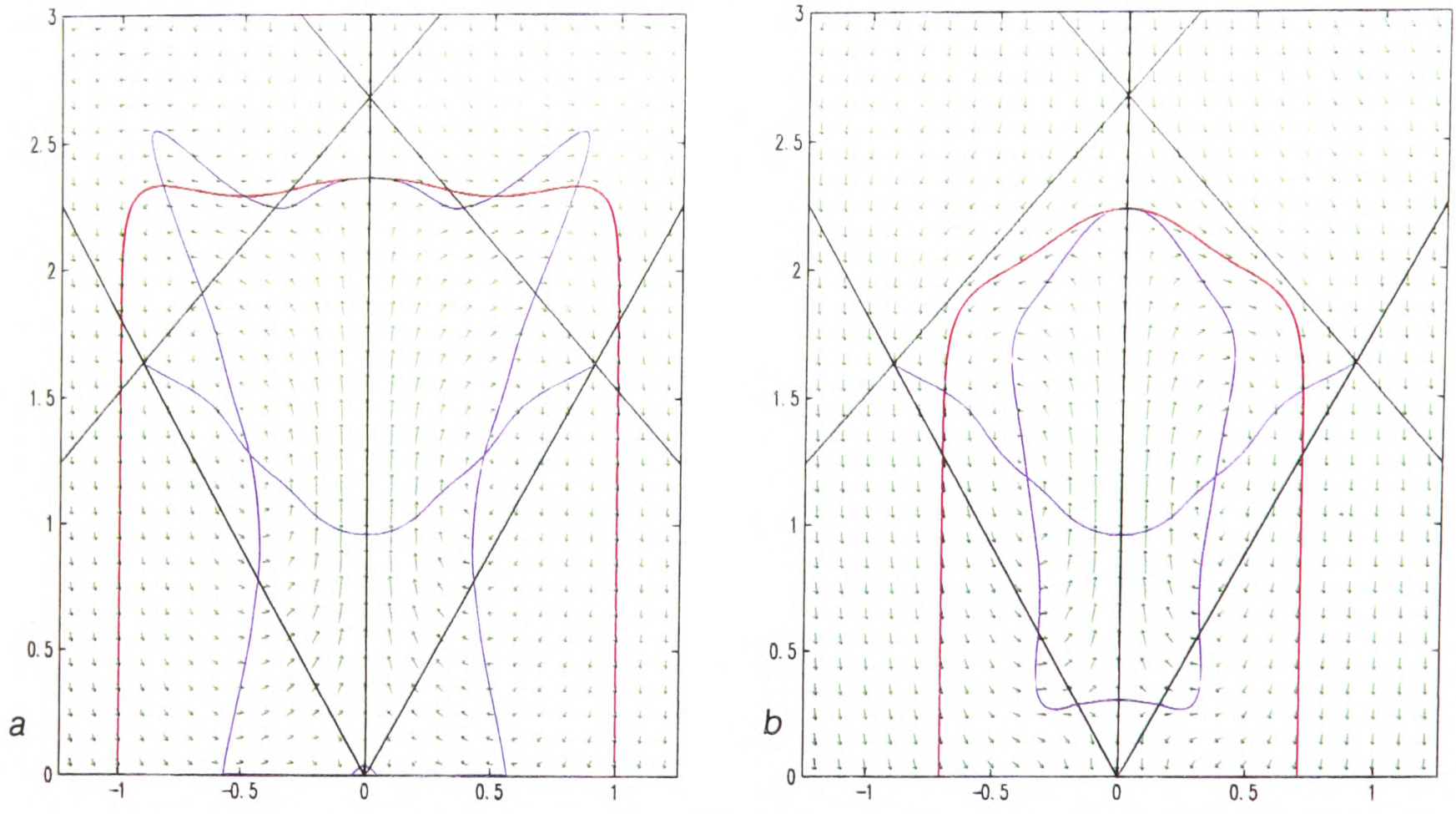

Figure 3.31: Minimisation results: (r_1, z_1)-phase planes, $r_s = 1/3$, $r_n = 2.27$, $\alpha_1 = 35°$, $\alpha_2 = 6°$; a) $\mu = 1$, b) $\mu = 2$.

3.7 Summary

- Computation of steady state billet crown surfaces using the methods outlined in section 3.1 shows that for unimodal axis mass flux distribution $-\bar{g}_\sigma(\sigma, 0)$ the steady state surfaces form a single family of nested curves with increasing ratio, μ, of withdrawal rate to mass flow rate.
- Steady states are increasingly convex with increasing μ.
- Numerical computations of billet radius, r_b, are in very good agreement with analytic predictions, (3.11). Even for larger μ, when some mass misses the billet, the mass balance (3.11) still provides a reasonable guide to steady state billet radius.
- For fixed angle sprays decreasing the spraying angle produces steady states that are increasingly concave and which are situated at a greater distance from the atomiser. Increasing the spray cone radius produces more convex steady states whilst maintaining approximately the same flight distance.
- Computed steady states are all stable to finite perturbations along some interval of their length. The interval of stability extends from the billet axis some way out towards the lower spray boundary.
- Commonly, the interval of stability is terminated where the steady state profile turns to cross the lower spray boundary. Here the phase paths diverge from the steady state.

- The size of the interval of stability and the size of finite perturbations from the steady state which will decay can both be influenced by other features in the phase plane, such as the proximity of unstable spirals to the steady state.

- The vertical component of a displaced billet crown surface velocity towards a steady state, across most of the top of the billet, is greater than the radial velocity component towards the steady state, along the sides of the billet. Hence, any control algorithm employed should exploit this greater sensitivity.

- Because the interval of stability frequently does not extend to the lower spray boundary, greater "weighting" should be given to the significance of variations in surface height measurements that are taken from closer to the billet axis.

- Concave steady state crown shapes do not allow simple visual measurement of surface height, due to obscuration. Concave steady states also imply a greater variation in the thermal condition of deposited spray, across the billet surface, than for convex surfaces. Thus, concave steady states should be avoided.

- Use of a scanning atomiser distributes the mass flux more widely, generally producing more convex steady states with increasing scanning angle.

- For large enough scanning range, the axis mass flux distribution function, $-\bar{g}_\sigma(\sigma, 0)$, becomes bimodal and there exist two nested families of steady state crown profiles. In this case there will be a range of μ over which two stable steady states will coexist for each value of μ.

- Bimodal $-\bar{g}_\sigma(\sigma, 0)$ is often reflected in angular steady state crown shapes.

- A sinusoidal scanner angle function produces bimodal $-\bar{g}_\sigma(\sigma, 0)$ with maximum mode closest to the upper spray boundary. This results in the tendency for additional equilibrium points in the phase plane to be closer to the steady state surfaces than with corresponding fixed angle sprays and unimodal $-\bar{g}_\sigma(\sigma, 0)$. More realistic scanner angle functions, such as those used in production, distribute the mass more towards the lower spray boundary.

- By suitably defining a target axis flux distribution, $-\bar{g}^T_\sigma(\sigma, 0)$, and solving a minimisation problem a scanner function can be derived, for which $-\bar{g}_\sigma(\sigma, 0)$ remains unimodal for a wider range of scanning angles than with current production scanner functions. This eliminates the possibility of catastrophic transient motions between coexisting steady states, whilst also moving any possible additional equilibrium points in the phase plane away from the steady state profiles. This might be exploited either in the more reliable production of standard sized billets or in attempting to produce larger diameter convex billets.

- Definition of the target axis flux distribution is only loosely constrained by the requirements that $-\bar{g}^T_\sigma(\sigma, 0)$ be unimodal and skewed toward O_1. It is not sensible to impose further constraints, since any such constraints should properly come from consideration of the heat flow characteristics of the steady state rather than be motivated by growth dynamics.

Chapter 4

Transient Billet Growth

This chapter focuses on solution of the averaged equation for transient slow-time axisymmetric billet growth, i.e.

$$\frac{\partial F_0}{\partial \eta}(\boldsymbol{x}_1, \eta) = [u(\eta)\boldsymbol{k}_1 + \dot{m}(\eta)\overline{\boldsymbol{g}}(F_0, \boldsymbol{x}_1)].\boldsymbol{\nabla} F_0(\boldsymbol{x}_1, \eta). \tag{4.1}$$

Here, $\boldsymbol{x}_1$ and η are respectively, the position vector within the crown frame of reference and the slow-time variable, (i.e. $\eta = \epsilon t$). Cylindrical coordinates, $\boldsymbol{x}_1 = (r_1, z_1)$, are used within the crown frame of reference; $\boldsymbol{k}_1$ denotes the unit vector in the direction of the billet axis of rotation. The functions $u(\eta)$ and $\dot{m}(\eta)$ are respectively the withdrawal rate and the mass flow rate through the atomiser. The billet surface is defined by

$$F_0(\boldsymbol{x}_1, \eta) = 0, \tag{4.2}$$

with suitable initial conditions at $\eta = 0$. The function $\overline{\boldsymbol{g}}(F_0, \boldsymbol{x}_1)$ is the axisymmetric averaged mass flux distribution vectorfield. This is computed for any surface by the methods outlined in chapter three, (section 3.1). This computation relies on F_0, although for those surfaces for which the averaging approximation, F_0, is properly valid one is able to express $\overline{\boldsymbol{g}}$ as a function of $\boldsymbol{x}_1$ only.

Computational details of the numerical method employed in solution of (4.1) are presented in section one. A numerical investigation of different strategies which might be adopted for controlling the intial stages of a production run is carried out in section two. The ability of the model to simulate well real billet growth that has occurred on a production run is demonstrated in section three. Section four examines the generic transient motion that occurs between steady state billet crowns following a small step change in the ratio, μ, of withdrawal rate to mass flow rate. A model simulation of the "catastrophic" transient growth that can occur between two coexisting steady states is presented in section five. The chapter concludes with a brief summary.

4.1 Computational details

Within a cylindrical crown coordinate system, movement of a point (r_1, z_1) on the billet surface is governed by the equations

$$\frac{\mathrm{d}r_1}{\mathrm{d}\eta} = -\dot{m}(\eta)\overline{g}_{r_1}(F_0, r_1, z_1), \tag{4.3}$$

$$\frac{\mathrm{d}z_1}{\mathrm{d}\eta} = -\dot{m}(\eta)\bar{g}_{z_1}(F_0, r_1, z_1) - u(\eta), \tag{4.4}$$

where $\bar{g}_{r_1}(F_0, r_1, z_1)$ and $\bar{g}_{z_1}(F_0, r_1, z_1)$ are respectively the r_1 and z_1 components of the averaged mass flux distributon vector field, $\bar{\boldsymbol{g}}(F_0, r_1, z_1)$. Initial conditions for the axisymmetric surface $F_0(r_1, z_1, \eta) = 0$ are given by

$$F_0(r_1, z_1, 0) = \begin{cases} z_1 - z_c, & 0 \le r_1 \le r_c, \\ r_1 - r_c, & 0 \le z_1 \le z_c. \end{cases} \tag{4.5}$$

In the numerical scheme, k_{tot} points $\{(r_1^k, z_1^k)\}_{k=1}^{k_{tot}}$ are selected on the initial surface, $F_0(r_1, z_1, 0) = 0$. The points are initially spaced a maximium distance $\mathrm{d}s_{max}$ apart. The point (r_1^{ktot}, z_1^{ktot}) always lies on the billet axis of rotation, and the initial spacing of points is also chosen so that a surface point lies at the sharp corner of the collector.[1] The separation of points according to the **mesh spacing**, $\mathrm{d}s_{max}$, continues along the top of the collector and down the sides of the collector until $k = k_{spbd}$, which is defined as the last point along the surface for which $\|\bar{\boldsymbol{g}}(F_0, r_1^k, z_1^k)\| > 0$, i.e.

$$k < k_{spbd} \Longrightarrow \|\bar{\boldsymbol{g}}(F_0, r_1^k, z_1^k)\| = 0.$$

For $k < k_{spbd}$, no billet growth occurs and a coarse spacing of surface points is selected, sufficient to represent the collector geometry, see Fig. 4.1.

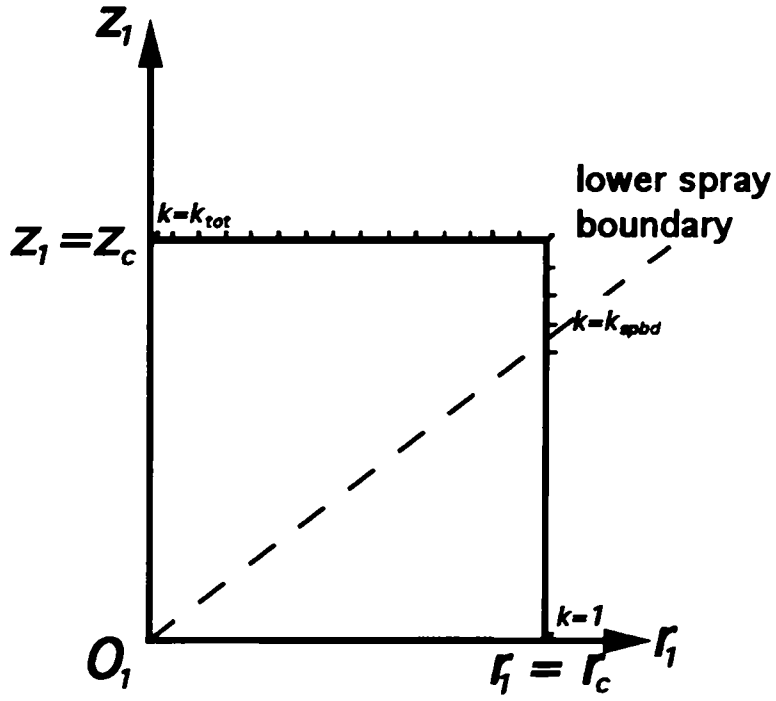

Figure 4.1: Choice of initial surface points for integration

Advance of the surface approximation over one time step proceeds as follows.

1. At time η a timestep $\mathrm{d}\eta$ is selected for the next integration step by

$$\mathrm{d}\eta = -\frac{\mathrm{d}s_{max}}{\max[\dot{m}(\eta)\bar{\boldsymbol{g}}(F_0, 0, z_1^{k_{tot}}), u(\eta)]}. \tag{4.6}$$

[1]The solutions to hyperbolic problems such as (4.1) are not generally smoother than their data. Although not particularly important for consideration of billet growth, it is important for the billet solidification algorithm, (which is developed in chapter seven), that the initial sharp geometry of the collector is preserved. It is this that has motivated the numerical method used here. Integration of (4.3) and (4.4) along the characteristic projections of (4.1) is preferred to an adaptation of either the box or Lax-Wendroff schemes, (which would both seem sensible for an equation such as (4.1)), since these methods tend to smooth out discontinuities that are propogated naturally along the characteristics.

(This selection ensures that growth is of order $\mathrm{d}s_{max}$ on each iteration.)

2. For $k = k_{tot}, k_{tot} - 1, ..., k_{spbd}$, compute $\overline{g}(F_0, r_1^k, z_1^k)$ using the methods in chapter three, section 3.1.

3. For $k = k_{tot}, k_{tot} - 1, ..., , 2, 1$, integrate forward (4.3) and (4.4) to give $(r_1^k(\eta + \mathrm{d}\eta), z_1^k(\eta + \mathrm{d}\eta))$ from $(r_1^k(\eta), z_1^k(\eta))$, using a second order Runge-Kutta scheme, (Improved Euler).

4. For $k = 1, 2, 3, ..., k_{tot} - 1, k_{tot}$; if

$$\left\|(r_1^k, z_1^k) - (r_1^{k-1}, z_1^{k-1})\right\| > \mathrm{d}s_{max}$$

then add an extra surface point at the midpoint of (r_1^k, z_1^k) and (r_1^{k-1}, z_1^{k-1}).

5. Renumber surface points including any new surface points and update the total number, k_{tot}.

6. Update k_{spbd} using new values of $(r_1^k(\eta + \mathrm{d}\eta), z_1^k(\eta + \mathrm{d}\eta))$.

Addition of new surface points is necessary to preserve an accurate surface representation, since it can be seen from the phase plane plots of the chapter three that points on adjacent characteristic curves will diverge from each other. Because $\mathrm{d}\eta \sim \mathrm{d}s_{max}$ and $\eta = O(1)$ the scheme maintains $O([\mathrm{d}s_{max}]^2)$ accuracy in computing points on the characteristic curves throughout the integration. Linear interpolation between adjacent surface points then preserves this accuracy at new surface points.

For a higher order scheme it is necessary not only to increase the order of the integration scheme used for (4.3) and (4.4), but also to use a more accurate method for approximating the surface profile between computed surface points. The computations carried out in the following sections all take $\mathrm{d}s_{max} = .01$.

4.2 Choice of initial conditions

For scanner functions, $\alpha(t)$, that produce either unimodal or bimodal axis flux distributions, $\overline{g}_\sigma(\sigma, 0)$, the desired operating point for steady state billet growth will be the uppermost steady state crown profile. The lower steady state, (if and when it exists), will be of smaller radius and will have a reduced material yield.

Collectors of different radii may be used, but their geometry is otherwise fixed. Collector radius is chosen to correspond to the desired billet radius, i.e. $r_c \approx 1$. The initial vertical displacement of the collector top below the atomiser nozzle, z_n, and both the withdrawal velocity, $u(\eta)$, and mass flow rate, $\dot{m}(\eta)$, for the initial part of the run, must then be selected in order to eliminate unwanted features of the transient growth towards steady state. In this section certain generic **start-up strategies** for the initial part of a production run, (i.e. in terms of z_n, $u(\eta)$ and $\dot{m}(\eta)$), are examined. Fixed model parameters are

$$\begin{aligned} r_n &= 2.27, \\ r_s &= 1/2, \\ r_c &= 1, \\ \alpha_1 &= 35^\circ, \\ \alpha_2 &= 6\tfrac{1}{2}^\circ, \end{aligned}$$

and the scanner function shown in Fig. 3.23 is used.

4.2.1 Delayed billet withdrawal

Delayed billet withdrawal is a strategy that is typically adopted during manual control of the billet growth. The operator is able to watch a side profile of the billet crown growth on a video monitor. Withdrawal is delayed until the operator is able to see the crown shape form, and is instigated by the billet radius exceeding its desired value or by suspected billet crown concavity formation.

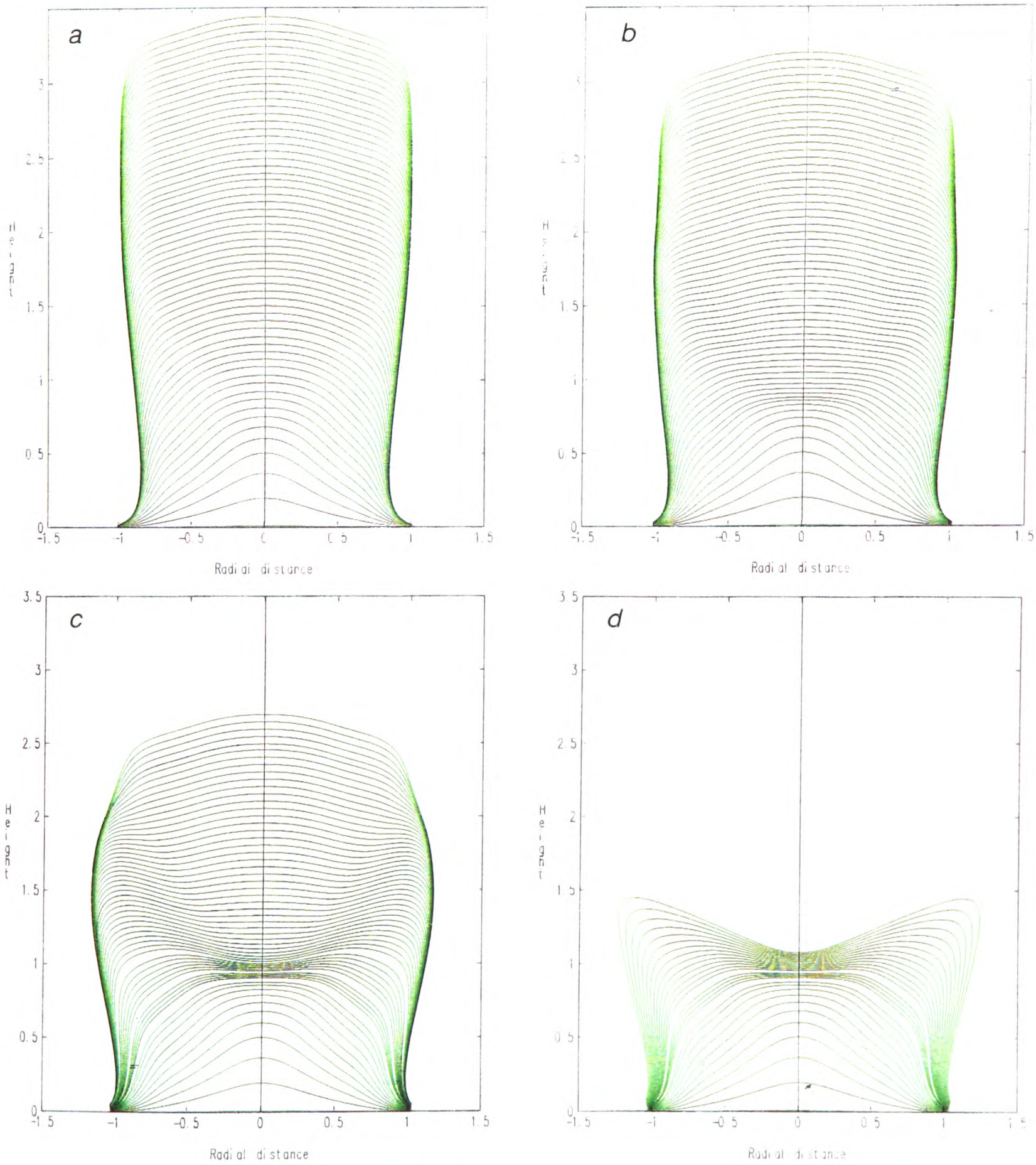

Figure 4.2: Delayed billet withdrawal, varying the delay; a) $\eta_s = 1/4$, b) $\eta_s = 1/2$, c) $\eta_s = 1$, d) $\eta_s = 2$.

Fig. 4.2 shows billet surface profiles for times $\eta \in [0, 3]$, plotted at intervals $d\eta \approx .05$, (dependent on the integration timestep). The collector is initially displaced a vertical distance $z_n = 3$ below the atomiser nozzle. A constant mass flow rate of $\dot{m}(\eta) = 1$ is adopted throughout, with a stepped withdrawal rate given

by

$$u(\eta) = \begin{cases} 0, & 0 \leq \eta \leq \eta_s, \\ 1, & \eta_s < \eta \leq 3. \end{cases} \tag{4.7}$$

Figs. 4.2a, 4.2b and 4.2c show the effect of using delays $\eta_s = 1/4,\ 1/2$ and 1 respectively. Initially the billet is seen to develop into a conical "hat" shape, which becomes progressively square as the delay is extended. When the withdrawal rate is increased at $\eta = \eta_s$ the billet crown grows towards the steady state crown shape for $\mu = 1$.

The shorter delays in Figs. 4.2a & 4.2b result in "necking" of the formed billet close to the collector. This can result in a reduction in the length of billet that it is later possible to machine down to a desired radius. The same problem does not arise with the longer delay of Fig. 4.2c. Here, the longer delay instead results in a bulging out of the billet radius and in a slight concavity developing before the withdrawal rate is increased. This bulge will also contribute to machining wastage.

Perhaps a more serious worry than these machining related issues is the nonuniformity of deposit layering during this initial period of growth. Initial cooling of the billet will be dominated by heat losses through the collector and top surface, with the sides becoming more important as the billet grows taller. The uneven layering is thus likely to result in wider variation in solidification behaviour at different parts of the billet than would be caused by a more even layering. This may have serious consequences for the quality of material formed at the base of the billet. In Fig. 4.2c, just before the withdrawal rate is stepped up, the variation between thicker layers and the very thin layers found both near the billet axis of rotation and on the billet sides is particularly large.

Fig. 4.2d shows the effect of having $u(\eta) = 0$, $\dot{m}(\eta) = 1$ for $\eta \in [0, 2]$. The layers in each of Figs. 4.2a, 4.2b & 4.2c before the withdrawal rate is incresed correspond to layers in Fig. 4.2d. The thin/thick layering pattern emerges as the growth on the billet axis approaches the upper spray boundary and that on the sides grows out to the lower spray boundary, whilst the surface in between these two regions grows up towards the atomiser. This uneven layering pattern would appear to be an unavoidable consequence of withdrawal being delayed for too long.

4.2.2 Immediate billet withdrawal

Delayed withdrawal seems to have the inherent problem of judging the length of delay to be long enough to avoid possible necking of the billet base but short enough to avoid very uneven layering. An alternative strategy for the initial period of growth is to have no withdrawal delay and to experiment only with varying the vertical displacement of the collector top surface below the atomiser nozzle, z_n.

Fig. 4.3 shows billet surface profiles for times $\eta \in [0, 3]$, again plotted at intervals $\mathrm{d}\eta \approx .05$, (dependent on the integration timestep). Constant mass flow rate, $\dot{m}(\eta) = 1$, and constant withdrawal rate, $u(\eta) = 1$, are adopted throughout. Figs. 4.3a, 4.3b, 4.3c & 4.3d correspond to initial vertical displacements of the collector top below the atomiser nozzle of $z_n = 3,\ 2\frac{2}{3},\ 2\frac{1}{3}$ & 2 respectively.

Fig. 4.3a may be compared with the delayed withdrawal computations of the previous section; the necking problem is particularly severe. Gradual raising of the collector initial position results in a lessening of the necking effect, until it is eliminated at $z_n \approx 2\frac{1}{3}$, see Fig. 4.3c. A second consequence of raising the

collector plate is that the layering becomes increasingly uniform across the billet top. In Fig. 4.3d, where the high positioning of the collector results in a bulge, which must be machined, the layering within the billet is still fairly uniform, (in contrast to Fig. 4.2c).

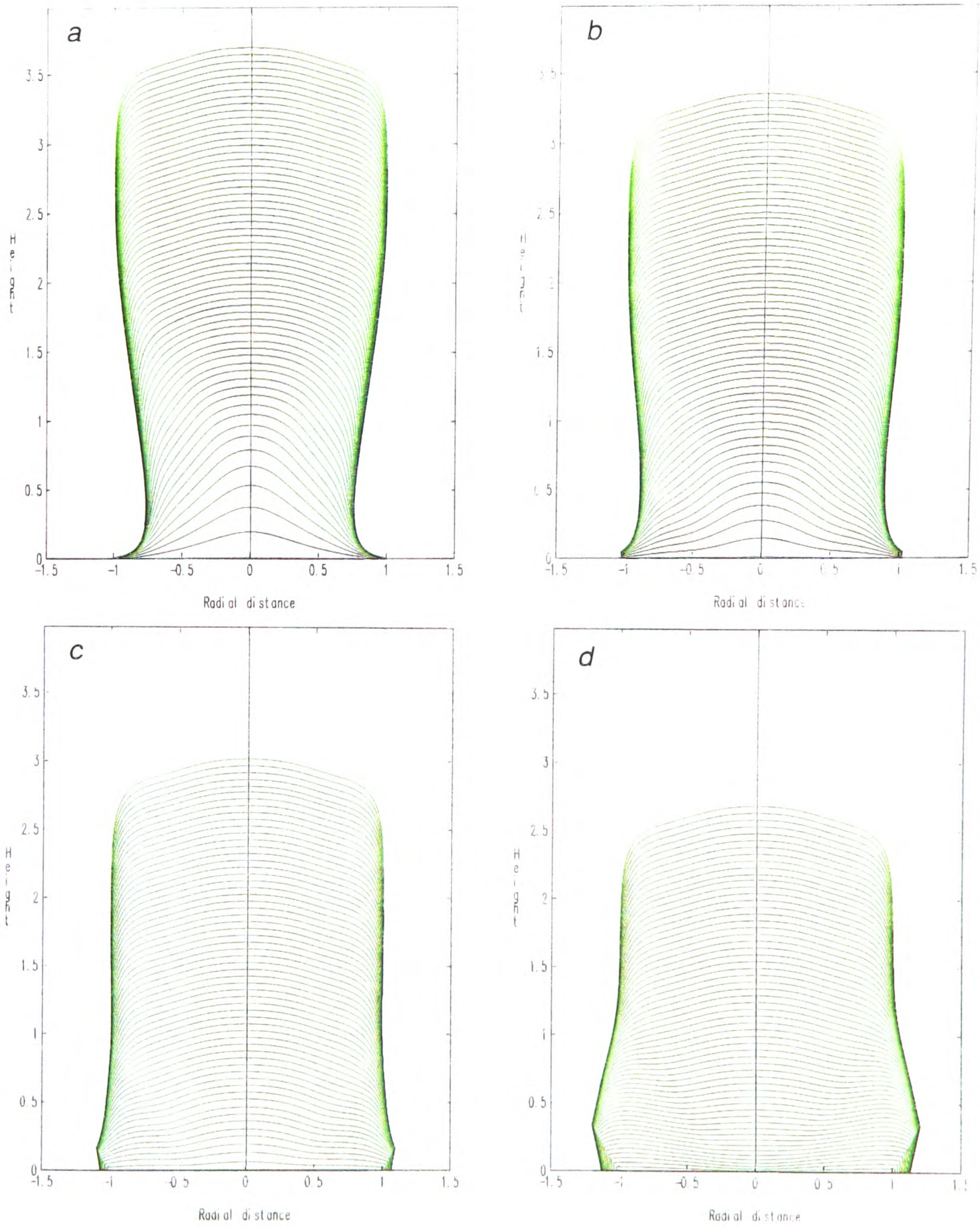

Figure 4.3: Varying the collector height; a) $z_n = 3$, b) $z_n = 2\frac{2}{3}$, c) $z_n = 2\frac{1}{3}$, d) $z_n = 2$.

4.2.3 Comments and recommendations

The "hat" shaped billet crowns are commonly observed during the initial stages of manually controlled production runs. It is thus gratifying to see that, for parameters that approximate those in the real plant, a similar effect is seen in the model. The "hat" shapes arise not only because of the delayed withdrawal but also because of the low initial position of the collector plate; as is illustrated by the initial crown shapes of Fig. 4.3a, where there has been no delay.

The effect of raising the collector initial position is best understood with reference to the phase plane for $\mu = 1$, see Fig. 4.4. For the chosen model parameters the origin of the crown coordinate system, O_1, is displaced a vertical distance $z_n + z_c = 5.223$ below the atomiser nozzle. Hence the start positions of Fig. 4.3 correspond to initial collector top surface heights above O_1 of $z_c = 2.223,\ 2.556,\ 2.89$ and 3.223. These start positions have been marked in thick black in Fig. 4.4. Initial growth of the "hat" shaped crowns in Figs. 4.3a & 4.3b can then be inferred from the observed horizontal variation in the surface velocity vector field in Fig. 4.4 at the heights $z_1 = 2.223$ and $z_1 = 2.556$. Choice of $z_c \approx 2.89$ places the collector almost directly at the position of the steady state profile. Larger choices of z_c place the collector above the steady state in Fig. 4.4. Here horizontal variations in the surface velocity field are less pronounced. Hence, the more uniform transition towards steady state that is observed.

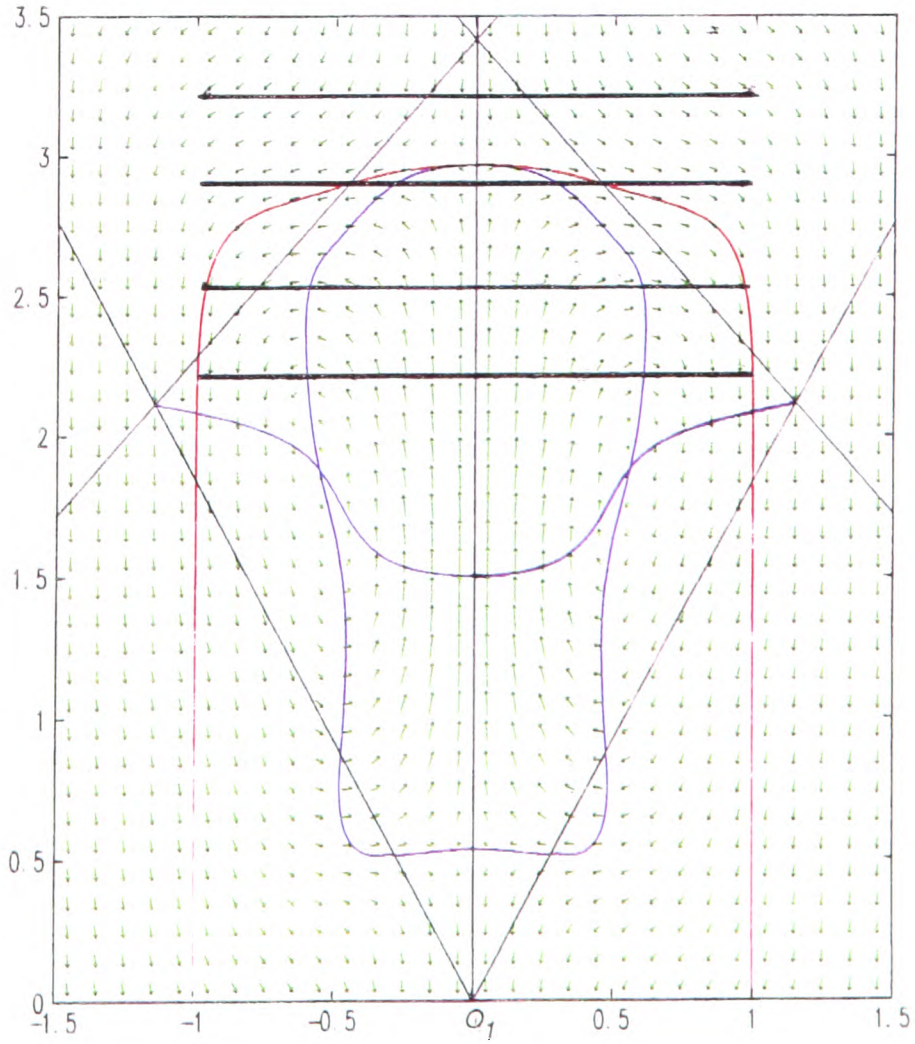

Figure 4.4: (r_1, z_1)-phase plane, $\mu = 1$. Surface velocity vectors - green, steady state - red, spray boundaries - thin black, nullcines - blue, collector start positions - thick black.

Recommended strategy

A strategy that is recommended, on the basis of the numerical results in this section, is to position the collector plate high and withdraw it immediately the deposition starts. Initial positioning of the collector too high may result in a slight initial concavity but this soon disappears. Adoption of this strategy is likely to lead to more even layering in the initial part of the billet. One problem with practical implementation of such a strategy is that the initial mass flow rate and yield must be known so that the correct initial withdrawal rate may also be chosen.

Discussion of other problems peculiar to control of the start-up phase of production runs may be found in [99]. Metal mass flow rate control for a spray-forming production plant has been considered recently in [55]. Initial run strategies in which the collector position has been raised and the withdrawal delay reduced, (i.e. from those practices previously adopted), are now commonly used for production runs.

4.3 Production run simulation

During production, height measurements of the billet surface in the crown frame of reference are made, at six radial distances, equally spaced from the billet axis of rotation. Measurements of billet radius are then made at two different fixed distances below the lowest of the six height measurements. These eight surface points are used with the withdrawal rate to provide an estimate of the deposition rate on the billet crown surface. This estimate is used in an algorithm for the on-line control of billet radius, [99]. Measurement of metal mass flow rate through the atomiser is also made throughout a production run, see [55].

Surface height and radius measurements taken during a production run may be compared directly with model output that is produced using mass flow rates and withdrawal rates that approximate those measured. Fig. 4.5 shows as an example, the results of doing this for Alcan/Cospray production run reference number D26NG706. Aluminium alloy 2618 is sprayed. Fig. 4.5a shows the measured billet profiles, mass flow rate and withdrawal rate.[2] The first measured billet profiles are not shown, due to the difficulties of obtaining accurate visual measurement during the early stages of the run, see [99]. Fig. 4.5b shows the mass flow rate and withdrawal rate approximated by piecewise linear functions and the billet profiles predicted by the model using these process functions. Linear interpolation is used between both measured and modelled surface points, the surfaces being plotted at time intervals of 19.8 seconds, (in the case of the model results this interval is only accurate to the nearest timestep). Model parameters used are $\hat{r}_n = .34\text{m}$, $\hat{r}_s = .075\text{m}$, $\hat{r}_c = .15\text{m}$, $\alpha_1 = 35°$ and $\alpha_2 = 6\frac{1}{2}°$. The scanner angle function shown in Fig. 3.23 has been used.

The model simulation captures well the qualitative features of the measured data. Both modelled and measured billets are slightly necked near their bases, then bulge out slightly before becoming approximately straight sided. The slightly hat shaped initial surface profiles that become more domed as the withdrawal rate is stepped up are also predicted; as is the overall thickness of layering, the billet height and radius. However, the model crown profiles are generally less rounded than the measured profiles, and the necking effect is less pronounced in the model.

[2]Data supplied by J. Heath and J. Myerscough. Measurements made via methods described in [55, 99].

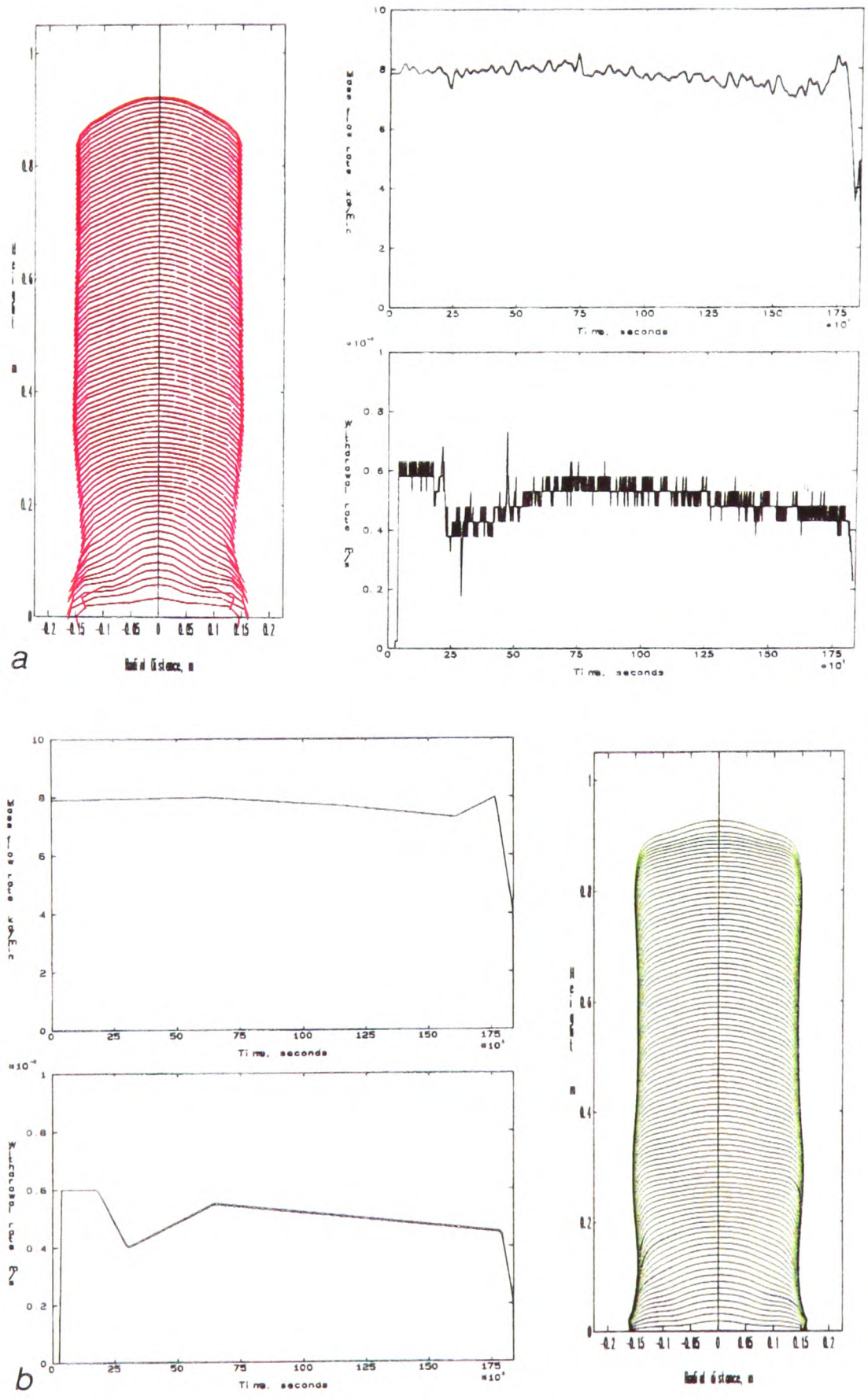

Figure 4.5: Results of simulating run reference number D26NG706; a) Measured, b) Modelled.

The difference in crown shape may be attributable to a number of factors. Firstly, the spray cone radius may vary with atomising conditions and is difficult to measure during production. A value $\hat{r}_s \in [.05, .075]$m is realistic. There will be some variation in the crown shape produced by a simulation over this range of values. Secondly, the model assumption of a spray sticking efficiency that is uniform over the whole of the billet crown may be inaccurate. Lastly, the spray distribution within the spray cone, (which has been assumed to be a truncated normal distribution), may vary. Given these possible variations, (resulting from the model formulation), Fig. 4.5 provides encouraging evidence for the model's validity.

4.4 Generic transient motion

Model control of the slow-time transient motion of the billet surface, to grow a billet of uniform radius, is achieved through control of the ratio, μ, of withdrawal rate to mass flow rate. In this section are examined the generic transient motions of the billet surface between steady states, that result from small increases and decreases in μ. Fixed model parameters are $r_n = 2.27$, $r_s = 1/2$, $r_c = 1$, $z_n = 2\frac{1}{3}$ $\alpha_1 = 35°$ and $\alpha_2 = 6\frac{1}{2}°$, and the scanner angle function shown in Fig. 3.23 is used. The model is integrated for $\eta \in [0, 6]$.

The first computation assumes a consant mass flow rate, $\dot{m}(\eta) = 1$, with a stepped withdrawal rate

$$u(\eta) = \begin{cases} 1, & 0 \leq \eta < 3, \\ 1.235, & 3 \leq \eta \leq 6. \end{cases} \tag{4.8}$$

This step change in $u(\eta)$ is chosen to result in a change in the steady state growth from a steady state billet crown of radius 1 to a steady state billet crown of radius 0.9.

Fig. 4.6 shows the process functions $\dot{m}(\eta)$ and $u(\eta)$, together with the predicted billet growth. Transition to the smaller radius steady state in response to the step change in $u(\eta)$ is smooth. The layer thickness increases due to the constant mass flow rate and reduced radius. To maintain layer thickness through such a transition requires that the same step increase in μ be implemented by lowering $\dot{m}(\eta)$ and keeping $u(\eta)$ constant.

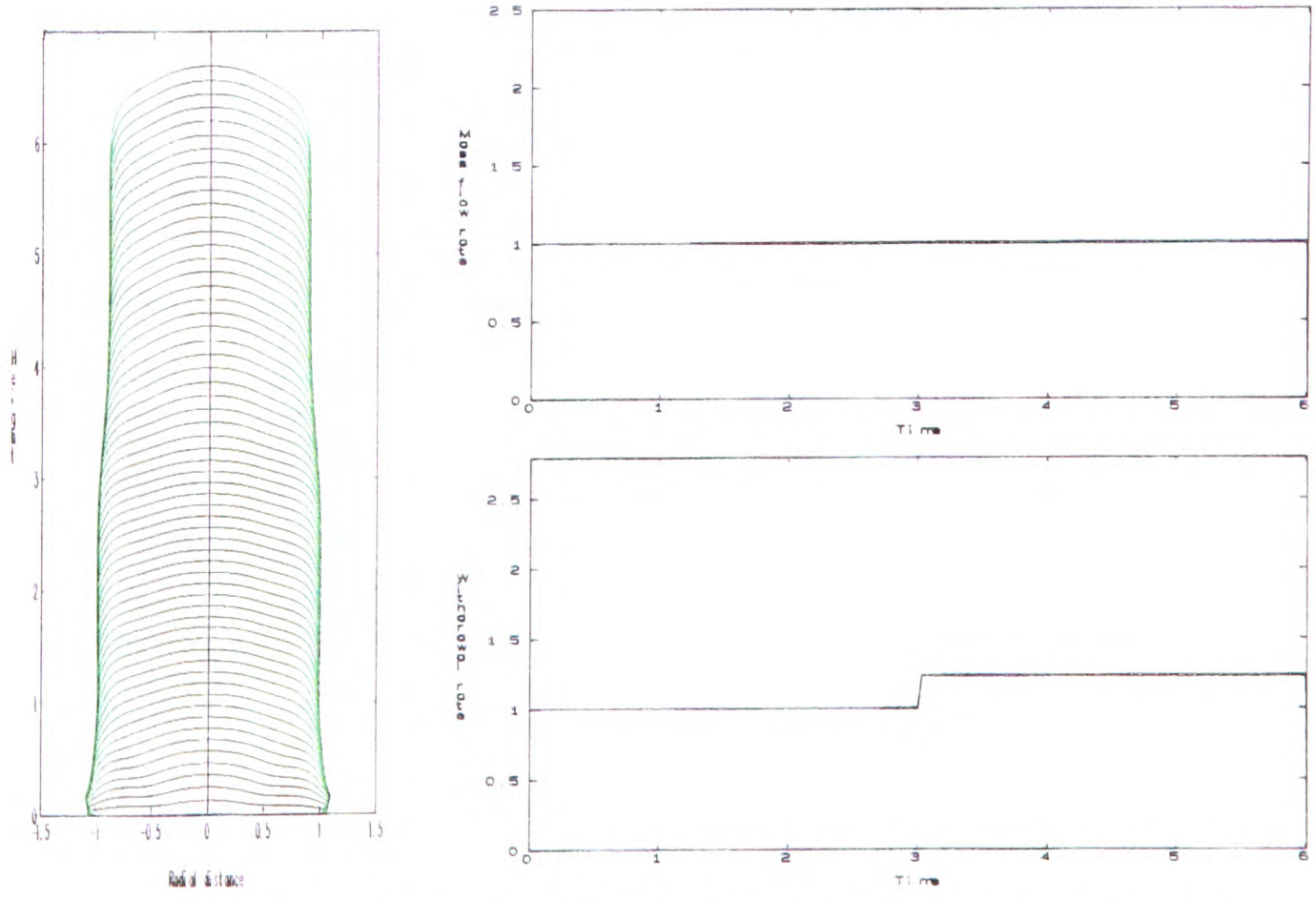

Figure 4.6: Step increase in $u(\eta)$; transition to a small diameter steady state.

In Fig. 4.7 are shown a series of surface profiles in the crown frame of reference. These profiles are the same as those shown in the full billet view of Fig. 4.6, but effectively correspond to the "operator's eye" view of the transition. Each picture corresponds to an interval $\Delta\eta = 1$ of the billet growth and plots crown profiles separated by intervals $\delta\eta \approx 0.1$, (accurate to the nearest integration timestep).

Running through Figs. 4.7a, 4.7b, 4.7c, 4.7d, 4.7e & 4.7f, the following features can be seen. Firstly,

transition from the angular collector into the steady state of radius 1. The steady state is approached fastest on the billet axis of rotation, and then spreads outwards. Transition times are $O(0.1)$ close to the billet axis of rotation and $O(1)$ further out. The steady state shape is reached at all points by $\eta \approx 2$, see Fig. 4.7c. At $\eta = 3$ the step increase in withdrawal results in the crown profile dropping towards the new steady state, Fig 4.7d. Again fastest transition is close to the billet axis of rotation, with the shoulder and sides of the billet crown converging last, Fig. 4.7e. Eventually the new steady state is reached.

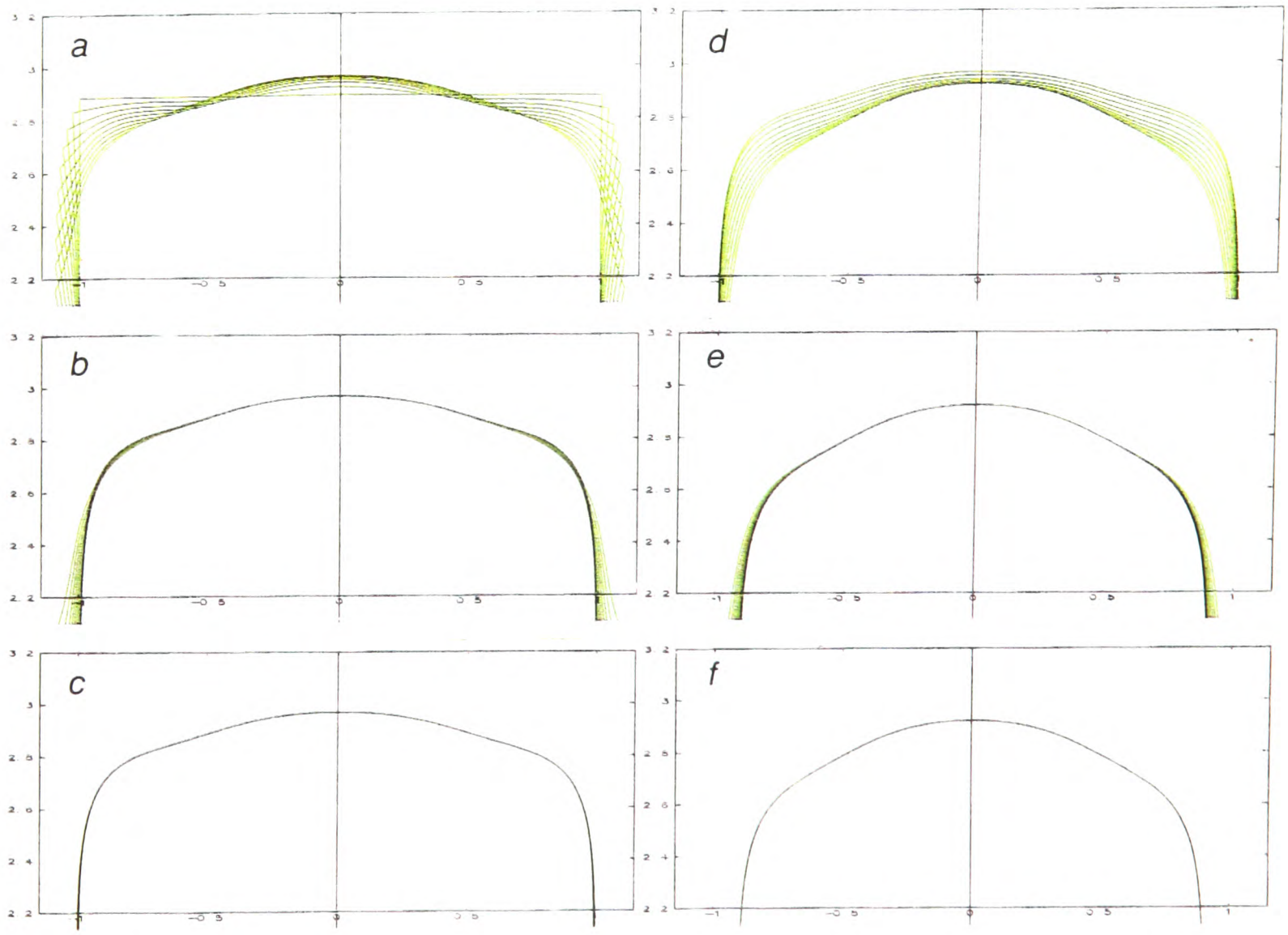

Figure 4.7: Step increase in $u(\eta)$; transient crown profiles, a) $\eta \in [0,1]$, b) $\eta \in [1,2]$, c) $\eta \in [2,3]$, d) $\eta \in [3,4]$, e) $\eta \in [4,5]$, f) $\eta \in [5,6]$.

The second computation studies the reverse transition from a smaller radius steady state to a larger radius steady state. A constant mass flow rate, $\dot{m}(\eta) = 1$, is assumed, with a stepped withdrawal rate

$$u(\eta) = \begin{cases} 1.235, & 0 \leq \eta < 3, \\ 1, & 3 \leq \eta \leq 6. \end{cases} \tag{4.9}$$

Fig. 4.8 shows the process functions $\dot{m}(\eta)$ and $u(\eta)$, together with the predicted billet growth. Fig. 4.9 shows the transitory motions in the crown frame of reference; again over time intervals $\Delta\eta = 1$ with surface plots separated by intervals $\delta\eta \approx 0.1$, (accurate to the nearest integration timestep). The pattern is broadly similar to that for the first computation. Steady state transition times vary between $O(0.1)$ and $O(1)$ dependant on surface position. The faster transition times occur at points closer to the billet axis, so that the spreading motion, that is evident close to the steady state in the phase plane plots of chapter three, is observed in the computed transient motion.

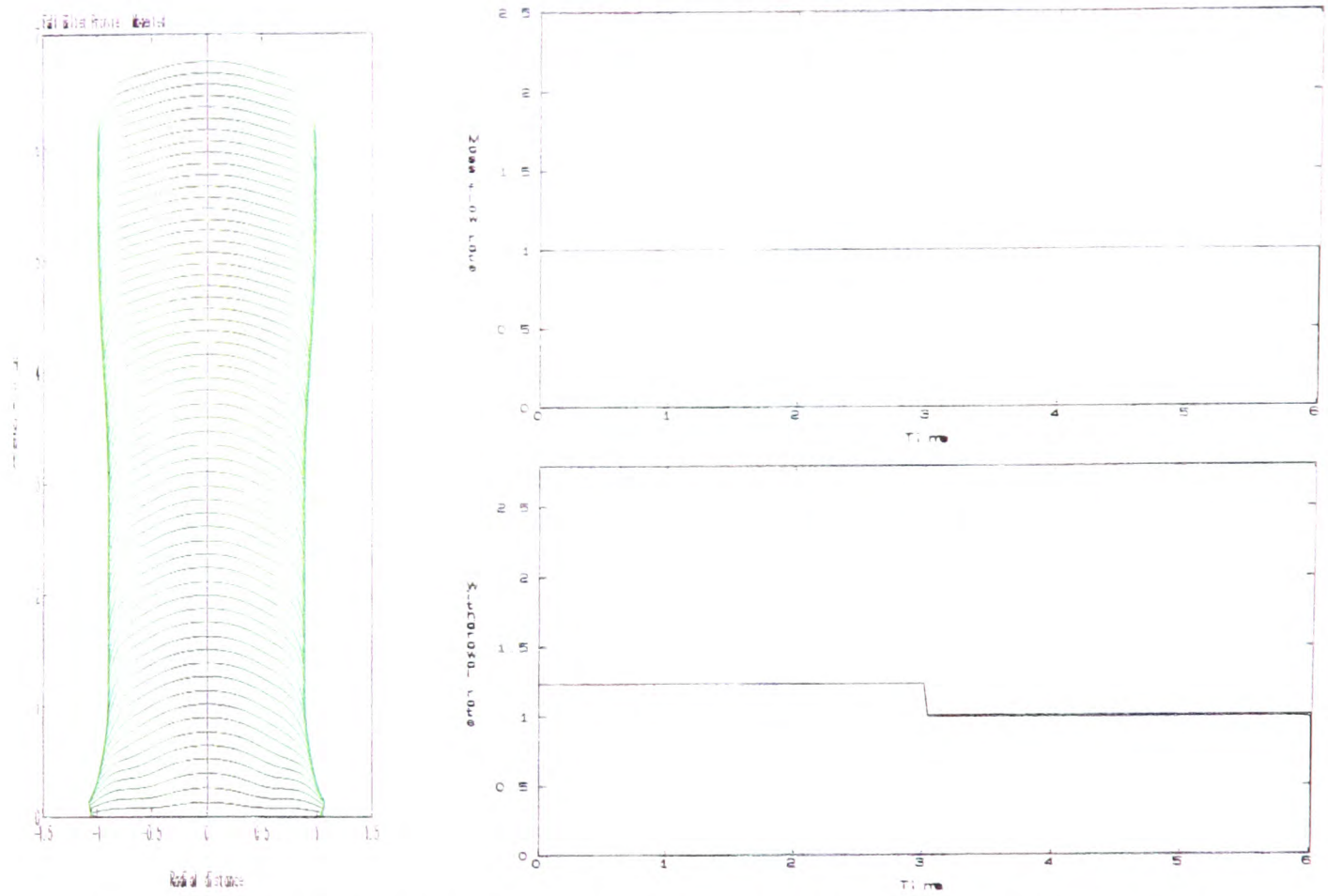

Figure 4.8: Step decrease in $u(\eta)$; transition to a larger diameter steady state.

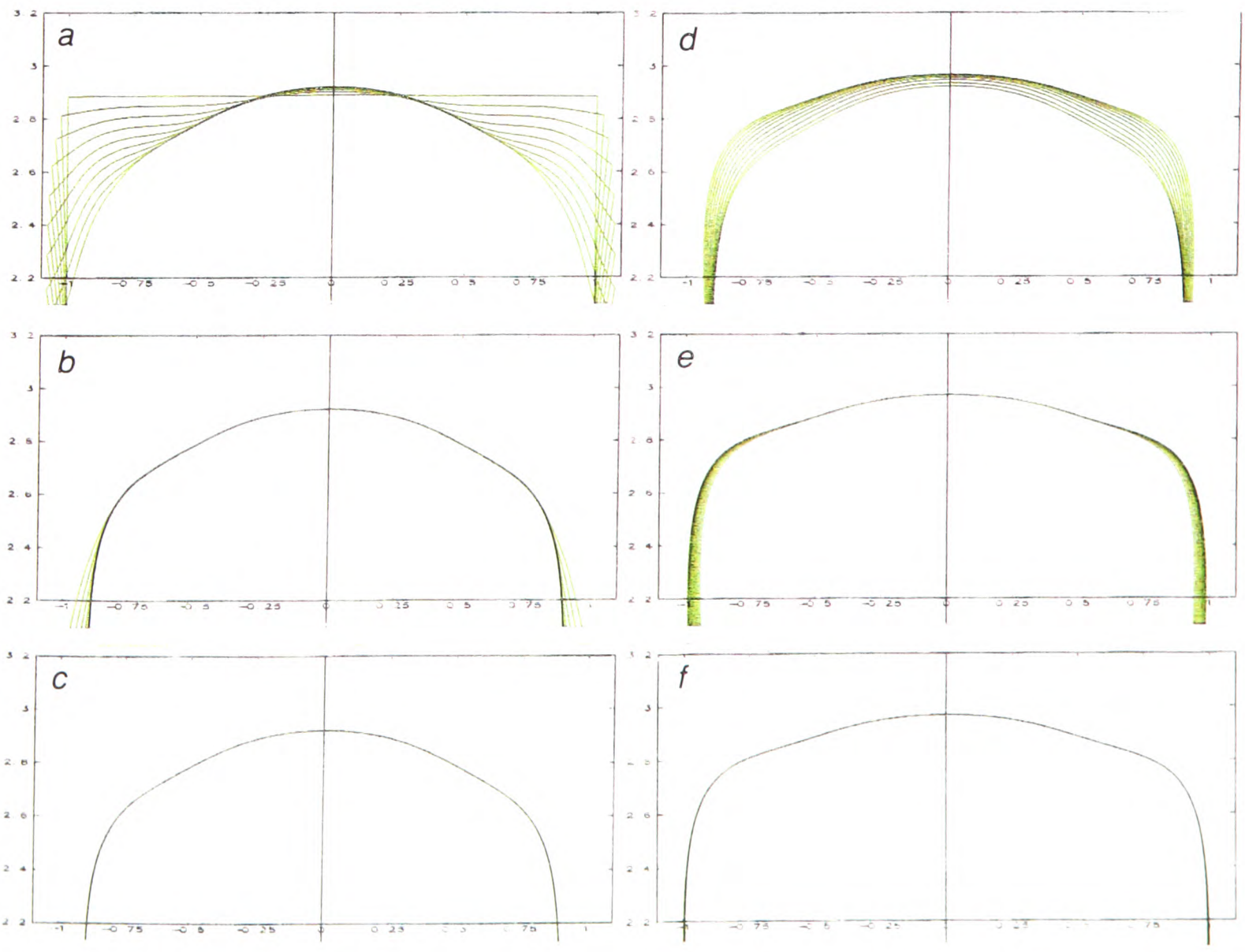

Figure 4.9: Step decrease in $u(\eta)$; transient crown profiles, a) $\eta \in [0,1]$, b) $\eta \in [1,2]$, c) $\eta \in [2,3]$, d) $\eta \in [3,4]$, e) $\eta \in [4,5]$, f) $\eta \in [5,6]$.

4.5 Hysteresis

In chapter two it was commented that for bimodal distributions of mass flux along the billet axis of rotation a small fluctuation in μ could result in a transition between two coexisting steady states. Such transitions represent a problem for control, due to their unpredictability.

Those bimodal axis flux distributions, $-\bar{g}_\sigma(\sigma,0)$, that have been encountered until now have had modes at values $-\bar{g}_\sigma(\sigma,0) \approx 5$, or larger, (see for example Fig. 3.24). Since, for a properly scaled problem one expects $\mu \approx 1$, hysteresis is unlikely to occur during normal production. However, a variety of factors may combine to increase this likelihood. Perturbations in the scanner function, $\alpha(t)$, may occur due to machine wear, and in the spray cone radius, r_s, due to poor control of atomisation.

As an example, averaging of the scanner function, $\alpha(t)$ of Fig. 4.10a, with $\alpha_1 = 35°$, $\alpha_2 = 7°$ and $r_s = .4$ produces the axis flux distribution shown in Fig. 4.10b. Bifurcation from one to two steady states now takes place at $\mu \approx 2.8$, see Fig. 4.11. Using this scanner pattern, and the corresponding averaged mass flux field, it is possible to simulate billet growth through hysteresis.

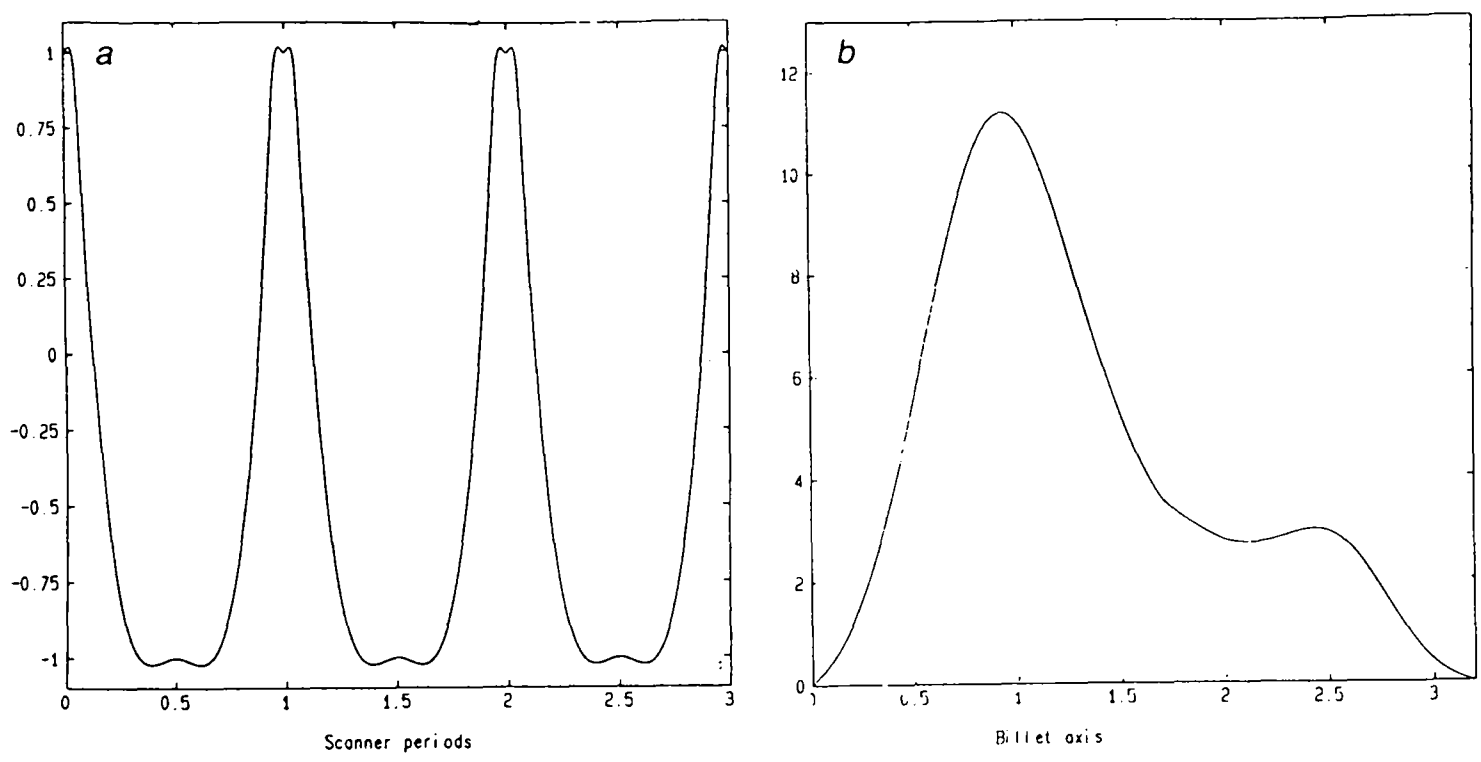

Figure 4.10: a) Perturbed scanner angle function. b) Resulting bimodal axis flux distribution, $-\bar{g}_\sigma(\sigma,0)$.

Fig. 4.12 shows a chosen mass flow rate and withdrawal rate. The withdrawal rate is kept constant and the mass flow rate drops suddenly at $\eta \approx 1$, then recovers to its previous level. This scenario might represent that of a sudden partial metal flow nozzle blockage in the atomiser, which eventually clears itself. Also shown in Fig. 4.12 is the full grown billet, with layers plotted at intervals $\delta\eta \approx .05$.

The billet initially grows towards a rather pointed steady state, belonging to the outer family of steady states in Fig. 4.11. This is followed by a series of very thin layers as the mass flow rate drops. During this time the value of μ is such that no steady state exists in the outer family. Consequently, the billet crown drops. When the metal mass flow rate recovers, there again exist two steady states. By this time the billet crown has dropped so far that it continues to move towards the steady state from the inner family of steady states in Fig. 4.11.

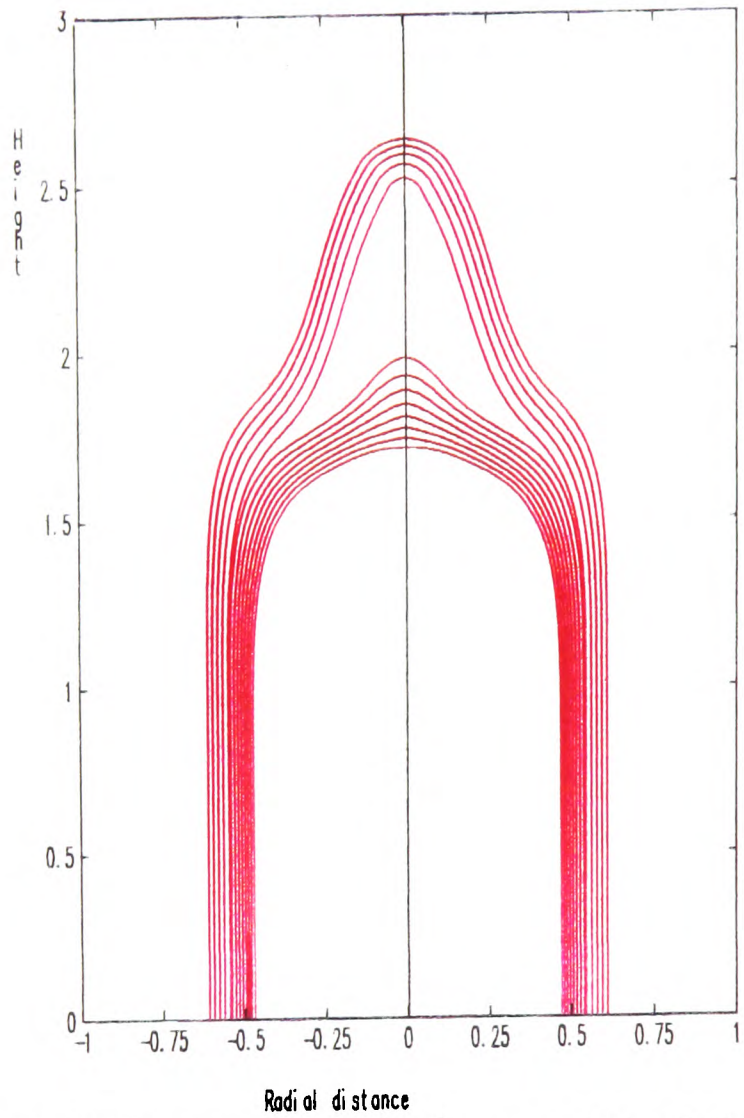

Figure 4.11: Families of steady states; outer family - $\mu = 2.5 + 0.1k$: $k = 0, 1, 2, 3$. inner family - $\mu = 2.8 + 0.1k$: $k = 0, 1, 2, 3, 4, 5, 6, 7$.

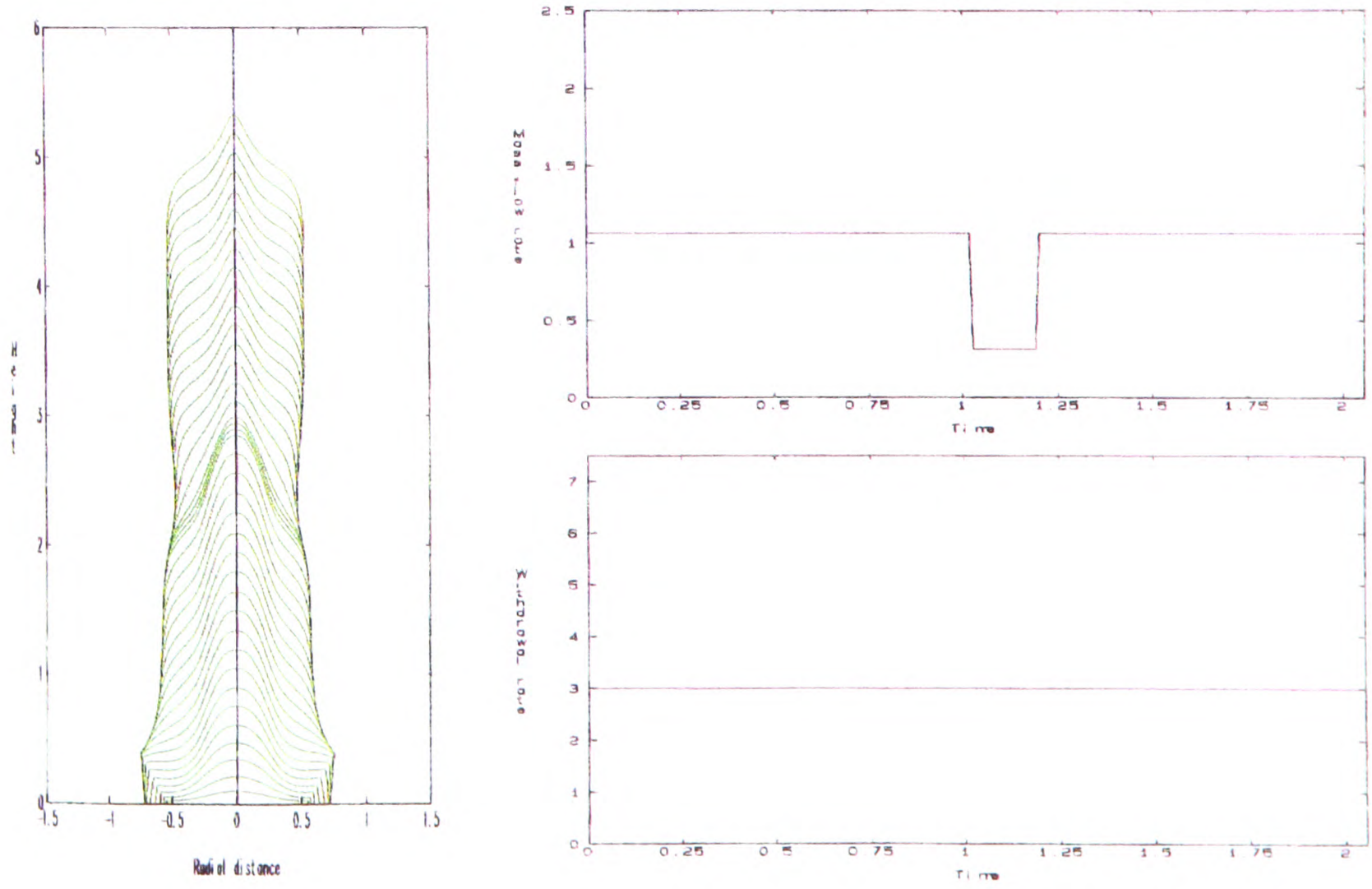

Figure 4.12: Simulated hysteresis due to sudden drop in mass flow rate.

In Fig. 4.13 are shown the same surface profiles in the crown frame of reference, with approximately ten surface profiles separated by time intervals $\delta\eta \approx .05$ per picture. Figs. 4.13a & 4.13b show the initial transient from the collector shape converging to a pointed steady state, for $\eta < 1$. Figs. 4.13c & 4.13d show the rapid drop of the billet crown as the mass flow rate drops off, followed by the growth out into the lower steady state.

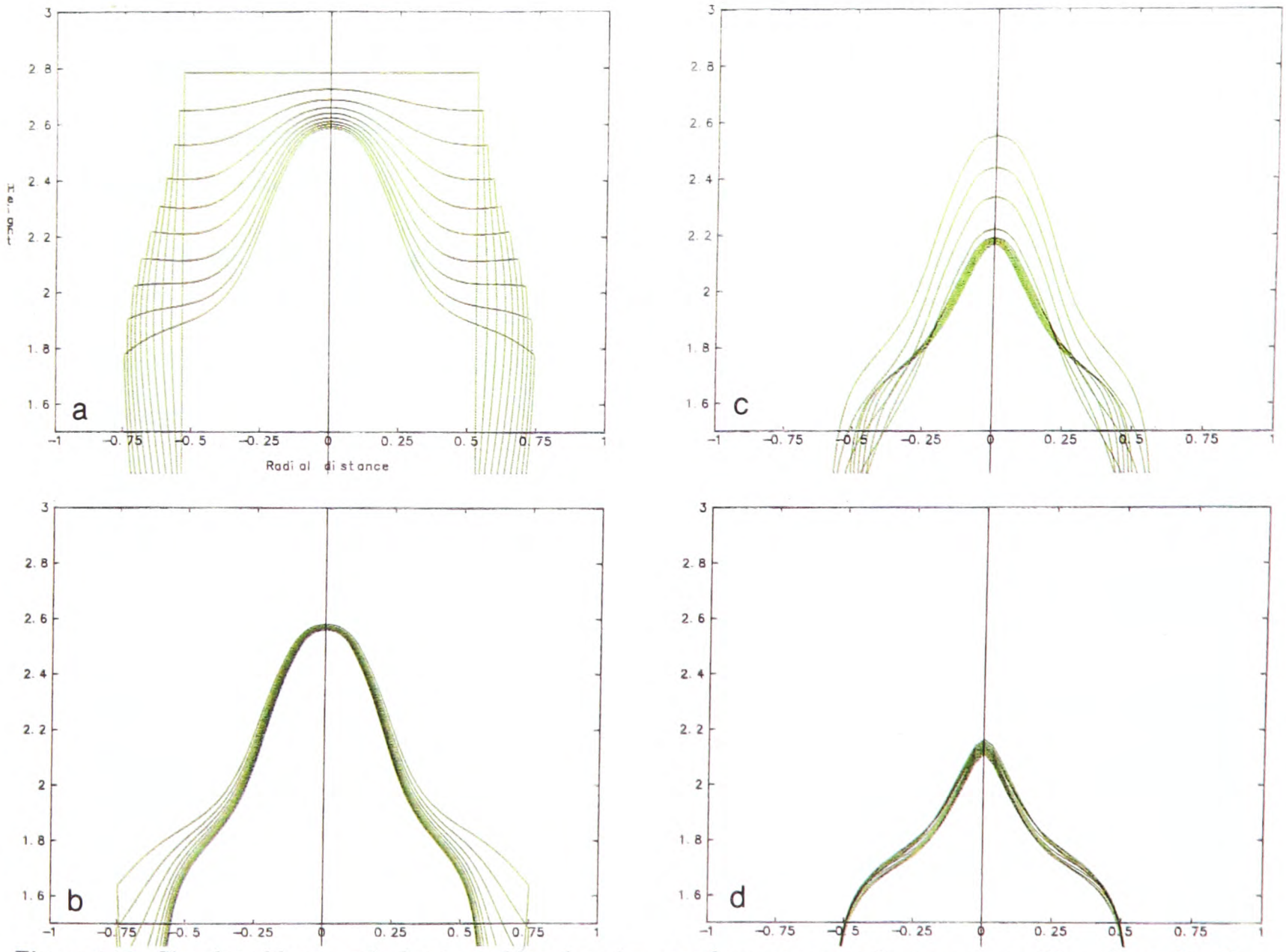

Figure 4.13: Simulated hysteresis due to sudden drop in mass flow rate; transient crown profiles, a) $\eta \in [0, .5]$, b) $\eta \in [.5, 1]$, c) $\eta \in [1, 1.5]$, d) $\eta \in [1.5, 2]$.

4.6 Summary

- Computation of transient billet motion, by a method based on integration along the characteristics of (4.1), produces a numerical approximation to the solution of (4.1) that is second order accurate in the mesh spacing ds_{max}.
- This integration method succeeds in preserving the initial sharp, corner geometry of the collector throughout the integration.
- Numerical experiments show that initial positioning of the collector too far below the atomiser nozzle can result in severe "necking" of the finished billet close to the collector plate.
- The "necking" effect may be alleviated by introduction of a delay before the billet is withdrawn. However, delayed withdrawal may result in uneven layering and convexity of the billet crown.
- Raising of the initial collector position also reduces the amount of "necking", and appears to preserve even layering.
- Initial "hat" shaped billet crowns are predicted by the model, in accordance with initial billet crown geometries commonly observed during production.
- Further validity for the model is provided by its ability to simulate real measured billet growth reasonably well, capturing most essential features.
- During transitions between neighbouring steady states the parts of the billet crown closest to the billet axis approach the new steady state fastest. Complete transition occurs on an $O(1)$ timescale, with convergence close to the billet axis taking place on an $O(0.1)$ timescale.
- The model is able to simulate hysteresis between coexisting steady state crown shapes.

Chapter 5

Heat Flow within the Billet

This short chapter deals with the derivation, and some analysis, of the field equations and boundary conditions for the heat flow that occurs within the billet during solidification. Section one derives and discusses the basic non-dimensional field equations and boundary conditions. The limitations of these equations lead to the derivation, in sections two and three, of different approximations to the heat flow that occurs in different parts of the billet. In section two a boundary layer approximation is derived, governing rapid heat flow close to the billet surface, where thin layers of metal spray are deposited intermittently. In section three a "slow-time" approximation is derived, governing heat flow within the bulk of the billet. These two approximations are considered further in chapters six and seven respectively.

5.1 Field equations

Unlike a pure metal, typical spray-formed aluminium alloys release their latent heat of freezing over a range of temperatures, ($\approx 80°C$). The fact that the metal spray is only partially liquid upon impact and is deposited intermittently in thin layers, combined with the evidence of fine scale, low segregation, relatively homogeneous end-product microstructure, suggests that liquid phase convection is not usually an important heat transfer mechanism in spray-forming solidification. Thus, in agreement with other spray-forming solidification studies, [6, 7, 43, 49, 50, 87, 89, 90], solidification is assumed to be conduction controlled.

Neglecting fluid flow and species conservation effects, consideration of the heat content within an arbitrary volume, V, of the billet bounded by a surface, S, produces the energy balance

$$\frac{\partial}{\partial \hat{t}} \int_V \hat{H} \, \mathrm{d}V = \oint_S \hat{K}^* \frac{\partial \hat{T}}{\partial n} \mathrm{d}S, \tag{5.1}$$

where $\hat{H}$ and $\hat{K}^*$ are respectively the heat content per unit volume, or enthalpy, and the thermal conductivity. The temperature of the billet is denoted $\hat{T}$. As previously stated, the operator $\frac{\partial}{\partial n}$ denotes the partial derivative in the direction of the outward normal (to S) and $\hat{\bullet}$ denotes a dimensional quantity.

Assuming a uniform alloy composition over the freezing range, the fraction of liquid present in the alloy at temperature $\hat{T}$ is denoted by $f_l(\hat{T})$. The function $f_l(\hat{T})$ has been determined empirically for the alloys considered in this thesis, [44]. For these alloys $f_l(\hat{T})$ increases monotonically with $\hat{T}$ over the freezing range.

The enthalpy of the metal is related to the temperature by

$$\hat{H}(\hat{T}) = \int_0^{\hat{T}} \rho c d\hat{T} + f_l(\hat{T})\rho L. \tag{5.2}$$

The constant L in (5.2) is the latent heat. The functions ρ and c are the material density and specific heat capacity of the metal. These functions and the thermal conductivity, $\hat{K}^*$, all vary with temperature. However, the variation in ρ and c over the freezing range is typically quite small; ρ and c are thus assumed constant. In contrast, thermal conductivities of the solid and liquid phases differ by a factor of about two. A "mixture based" thermal conductivity, $\hat{K}^*$, is defined by

$$\hat{K}^*(\hat{T}) = (1 - f_l(\hat{T}))K_s(\hat{T}) + f_l(\hat{T})K_l(\hat{T}), \tag{5.3}$$

where K_s and K_l denote the (constant) thermal conductivities of the solid and liquid phases of the alloy respectively, ($K_l \approx \frac{1}{2}K_s$).

For suitable liquid fraction functions, (continuous and increasing is sufficient), $\hat{H}(\hat{T})$ will be strictly monotone. This guarantees that $\hat{H}$ may be used as the independent variable in (5.1) instead of $\hat{T}$. With further assumptions on the smoothness of $\hat{H}$ spatially within the billet, application of the divergence theorem to (5.1) and reliance on the arbitrary choice of V yields

$$\frac{\partial \hat{H}}{\partial \hat{t}}(\hat{\mathbf{x}}_0, \hat{t}) = \hat{\boldsymbol{\nabla}}.[\hat{K}^*(\hat{T})\hat{\boldsymbol{\nabla}}\hat{T}(\hat{\mathbf{x}}_0, \hat{t})], \qquad \hat{\mathbf{x}}_0 \in \Omega(\hat{t}), \tag{5.4}$$

which is the dimensional field equation for the heat flow. Recall from chapter two that $\Omega(\hat{t})$ denotes the volume, within the billet frame of reference, that is occupied by the billet at time $\hat{t}$. The function, $\hat{K}(\hat{H})$, is defined by

$$\hat{K}(\hat{H}) = \hat{K}^*(\hat{T})\frac{\mathrm{d}\hat{T}}{\mathrm{d}\hat{H}}. \tag{5.5}$$

The monoticity of $\hat{T}(\hat{H})$ guarantees that $\hat{K}(\hat{H})$ is positive, and it can easily be shown that both $\hat{K}(\hat{H})$ and $\frac{\mathrm{d}\hat{K}}{\mathrm{d}\hat{H}}$ are bounded. The field equation (5.4) becomes

$$\frac{\partial \hat{H}}{\partial \hat{t}}(\hat{\mathbf{x}}_0, \hat{t}) = \hat{\boldsymbol{\nabla}}.[\hat{K}(\hat{H})\hat{\boldsymbol{\nabla}}\hat{H}(\hat{\mathbf{x}}_0, \hat{t})], \qquad \hat{\mathbf{x}}_0 \in \Omega(\hat{t}). \tag{5.6}$$

Solution of (5.6) requires the prescription of boundary and of initial conditions.

5.1.1 Boundary Conditions

The position of the billet surface, $\partial\Omega(\hat{t})$, is given (see chapter two for details) at time $\hat{t}$ by

$$\partial\Omega(\hat{t}) = \{\hat{\mathbf{x}}_0 \in \mathcal{R}^3 : \hat{F}(\hat{\mathbf{x}}_0, \hat{t}) = 0\}, \tag{5.7}$$

where evolution of $\hat{F}$ is governed by

$$\rho\frac{\partial \hat{F}}{\partial \hat{t}} = \hat{\Gamma}\hat{\boldsymbol{G}}_0.\hat{\nabla}\hat{F}. \tag{5.8}$$

In (5.8) $\hat{\Gamma}$ is the sticking efficiency and $\hat{\boldsymbol{G}}_0$ is the spray mass flux vector field.

The simplifying assumption is made that the molten spray droplets impinge and coalesce instantaneously[1]

[1]Deposition and spreading times for individual droplets are in the range $10^{-6} - 10^{-5}$ seconds. Thermal equillibriation between droplet and billet proceeds on a timescale of order $\sim 10^{-4}$ seconds. See the discussion in chapter one, section 1.2.3. Both of these are much shorter than other process timescales.

onto an infinitessimally thin surface layer with position given by (5.8). A point $P \in \partial\Omega(\hat{t})$ moves instantaneously in the direction of the outward normal to $\hat{F}(\hat{\mathbf{x}}_0, \hat{t}) = 0$ at P with a speed $\hat{v}_P$

$$\hat{v}_P = -\frac{\partial \hat{F}}{\partial \hat{t}} |\hat{\nabla} \hat{F}|^{-1},$$

that is determined by the deposition at P, through (5.8). This deposition results in a net flux of heat across $\partial\Omega(\hat{t})$ at P equal to

$$\hat{v}_P(\hat{H}_{spray} - \hat{H}), \tag{5.9}$$

where $\hat{H}_{spray}$ is the mass averaged enthalpy of the spray.

As well as the heat influx due to deposition there is a cooling effect due to heat conduction from the billet into a thin layer of gas that passes rapidly over the surface. There may also be some radiation into the surrounding gas, but this effect is much smaller.[2] A linear heat transfer law is assumed to account for the forced convective cooling and additional radiative cooling. The net flux of heat across $\partial\Omega(\hat{t})$ due to combined cooling effects is given by

$$h_{gas}(\hat{T} - \hat{T}_{gas}), \tag{5.10}$$

where h_{gas} is a heat transfer coefficient and $\hat{T}_{gas}$ is the gas temperature. Combining (5.9) and (5.10) produces the boundary condition

$$-\hat{K}(\hat{H})\frac{\partial \hat{H}}{\partial n} = h_{gas}(\hat{T} - \hat{T}_{gas}) + \hat{v}_P(\hat{H}_{spray} - \hat{H}), \qquad \hat{\boldsymbol{x}}_0 \in \partial\Omega(\hat{t}) : \hat{z}_0 > \hat{z}_c, \tag{5.11}$$

see Fig. 5.1.

Remark The boundary condition (5.11), (usually with a separate radiative term), has been used in previous models of spray-forming deposit solidification, e.g. [6, 7, 49, 50, 87, 89, 90]. However, its validity is not proven. In using (5.11) the assumption is made implicitly that the mass and heat flux in the spray may be averaged both spatially and temporally prior to impact, and that this average heat flux may then be applied to the surface. The reality is much more complicated, with each surface point experiencing irregularly interspersed time intervals during which droplet deposition and forced convective cooling are taking place. Thus, there is a challenging homogenisation problem which needs to be explored.

The billet is bounded by the line $z_0 = z_c$ in the billet frame of reference; this represents the boundary between billet and collector. The collector is not initially heated. Solidification of the initial layers of deposited billet is thus very rapid, with imperfect contact resulting due to shrinkage. A linear heat transfer law is assumed to model the heat flow between the two imperfectly contacting media, i.e.

$$\hat{K}(\hat{H})\frac{\partial \hat{H}}{\partial z_0} = h_{collector}(\hat{T} - \hat{T}_{collector}), \qquad \hat{\boldsymbol{x}}_0 \in \partial\Omega(\hat{t}) : \hat{z}_0 = \hat{z}_c. \tag{5.12}$$

In (5.11) h_{gas}, $\hat{T}_{gas}$ and $\hat{H}_{spray}$ may all vary with position and time, as may $h_{collector}$ and $\hat{T}_{collector}$ in (5.12). Each of h_{gas}, $\hat{T}_{gas}$, $\hat{H}_{spray}$, $h_{collector}$ and $\hat{T}_{collector}$ needs to be supplied, either empirically or otherwise, as process parameters. The surface position and normal velocity may be calculated approximately by the methods of chapter four.

[2] Assuming surface and gas temperatures of approximately 850K and 450K, and surface emissivity in the range $0.1 - 0.4$, black body radiation accounts for between 2700 and 11000 W/m^2 of the surface heat flux. Surface heat transfer coefficients are estimated to be approximately 1000W/m^2/°C (billet crown) and 300W/m^2/°C (billet sides). Thus, radiation probably accounts for much less than 10% of the total heat flux.

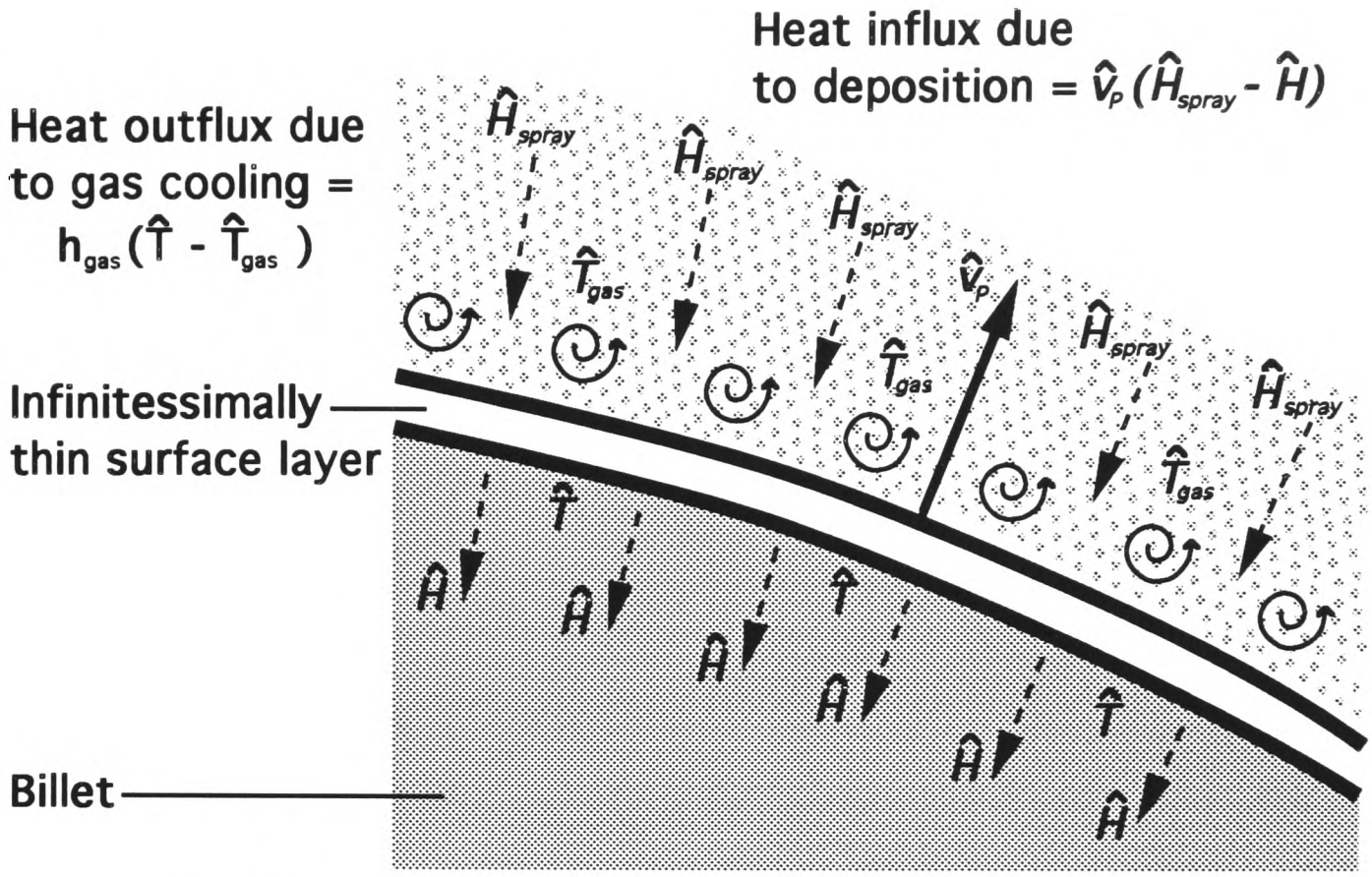

Figure 5.1: Schematic of the deposition boundary condition derivation.

5.1.2 Non-dimensionalisation

For the purpose of future simplification, independent and dependent variables in (5.6), (5.11) and (5.12) are scaled with typical values to yield dimensionless variables, i.e.

$$\begin{aligned} x &= \frac{\hat{x}}{R}, & t &= \frac{\hat{\omega}_0 \hat{t}}{2\pi}, \\ T &= \frac{\hat{T} - \hat{T}_s}{\Delta \hat{T}}, & H &= \frac{\hat{H} - \hat{H}_s}{\rho c \Delta \hat{T}}, \\ K &= \frac{\rho c \hat{K}}{K_s}, & v_P &= \frac{2\pi \hat{v}_P}{\hat{\omega}_0 R}. \end{aligned} \tag{5.13}$$

The length-scale R and timescale $\frac{2\pi}{\hat{\omega}_0}$ are as in chapter two, section 2.1.3. Temperatures have been scaled with the freezing range

$$\Delta \hat{T} \equiv \hat{T}_l - \hat{T}_s; \tag{5.14}$$

$\hat{T}_l$ and $\hat{T}_s$ being respectively the liquidus and solidus temperatures of the alloy. Hence non-dimensionally, the alloy is fully solid for $T \leq 0$ and fully liquid for $T \geq 1$. The enthalpy has been scaled with $\rho c \Delta \hat{T}$; $\hat{H}_s$ denotes the enthalpy at the solidus temperature, $\hat{T}_s$. From (5.2) it can be seen that the alloy is fully solid for $H \leq 0$ and fully liquid for $H \geq 1 + \frac{L}{c\Delta \hat{T}}$. The non-dimensional quantity $\frac{L}{c\Delta \hat{T}}$, (similar to the inverse of a Stefan number), represents the ratio of the latent heat to the specific heat that is released during freezing; typically

$$\frac{L}{c\Delta \hat{T}} \approx 4$$

for the aluminium alloys considered in this thesis.

Equations (5.6), (5.11) and (5.12) become

$$\frac{\partial H}{\partial t} = \frac{\epsilon}{Pe} \nabla . [K(H) \nabla H], \qquad x_0 \in \Omega(t), \tag{5.15}$$

$$-K(H)\frac{\partial H}{\partial n} = B_{gas}(T(H) - T_{gas}) + \frac{Pe}{\epsilon}v_P(H - H_{spray}), \qquad \boldsymbol{x}_0 \in \partial\Omega(t) : z_0 > z_c, \tag{5.16}$$

$$K(H)\frac{\partial H}{\partial z_0} = B_{collector}(T(H) - T_{collector}), \qquad \boldsymbol{x}_0 \in \partial\Omega(t) : z_0 = z_c. \tag{5.17}$$

These equations describe the heat flow occurring within the billet on the rotation timescale.

It is assumed that billet growth is governed by the approximate form of equation (5.8) that is given by the non-dimensional model equation (2.43), in chapter two. The surface normal velocity, v_P, is given by

$$v_P = -\frac{\partial F}{\partial t}|\nabla F|^{-1},$$

and in the billet frame of reference, (2.43), becomes

$$\frac{1}{\epsilon}\frac{\partial F}{\partial t}(\boldsymbol{x}_0, t) = \gamma(\dot{m}g\boldsymbol{k}', F)\dot{m}(t)g(r'[\boldsymbol{x}_0, t])\boldsymbol{k}'(t).\nabla F(\boldsymbol{x}_0, t), \qquad \boldsymbol{x}_0 \in \partial\Omega(t). \tag{5.18}$$

In (5.18) γ is a simplified sticking efficiency, $\dot{m}(t)$ is the mass flow rate through the atomiser, $g(r')$ is the mass flux distribution function within the spray cone, $r' \leq r_s$, and $\boldsymbol{k}'$ is the unit vector in the direction of the spray cone axis at time t. All functions are non-dimensional.

The Peclet number

The dimensionless groups that appear above in (5.15) are

$$\epsilon \equiv \frac{2\pi\hat{U}_0}{\hat{\omega}_0 R} \ll 1, \tag{5.19}$$

which is the ratio of the rotation and withdrawal timescales, (introduced in chapter two), and

$$Pe \equiv \frac{\rho c\hat{U}_0 R}{K_s}, \tag{5.20}$$

which is a **Peclet** number. The Peclet number compares the relative importance of conduction and convection in heat transfer. Large Peclet numbers indicate the dominance of the "convective diffusivity", $\hat{U}_0 R$, over the thermal diffusivity. Convective effects in this problem are due to billet growth, which occurs at a rate $\approx \hat{U}_0$. The convective element of heat transfer in this problem is made clear by shifting to the crown coordinate system, when (5.15) becomes

$$\frac{\partial H}{\partial t} = \epsilon u(t)\frac{\partial H}{\partial z_1} + \frac{\epsilon}{Pe}\nabla.[K(H)\nabla H].$$

Rewriting the Peclet number as

$$Pe = (\frac{R}{\hat{U}_0})^{-1}(\frac{\rho cR^2}{K_s}), \tag{5.21}$$

and rescaling time with ϵ on the left hand side of (5.15), it can be seen that an alternative interpretation of the Peclet number, (on the slow billet growth timescale, $\eta = \epsilon t$), is as the ratio of the timescales for conduction/solidification and for billet growth. Large Peclet number would imply that the solidification timescale is longer than the growth timescale resulting in a billet with a high liquid fraction, since the heat from the spray would not be dissipated rapidly enough. Conversely, a small Peclet number would imply that

heat flowing in through the billet crown is rapidly dissipated in the bulk of the billet. The billet may in this case be very dry, and this also implies the potential for faster production through increased mass flow rate and withdrawal rate.

Not surprisingly, typical production parameters give

$$Pe = O_S(1). \tag{5.22}$$

Fig. 5.2 plots $\frac{R}{\hat{U}_0}$ against $\frac{\rho c R^2}{K_s}$ for a number of successful production runs of aluminium alloy 2618. The production rig produces several different alloys, and these are produced in batches to reduce the risk of cross-contamination of alloying elements. Batches of the same alloy may be separated by a period of months, during which time modifications in the process and/or in operating procedures may conceivably occur. This is illustrated well in Fig. 5.2 where the operational Peclet number shifts from about 1.8 to about 1.4, between earlier and later batches.

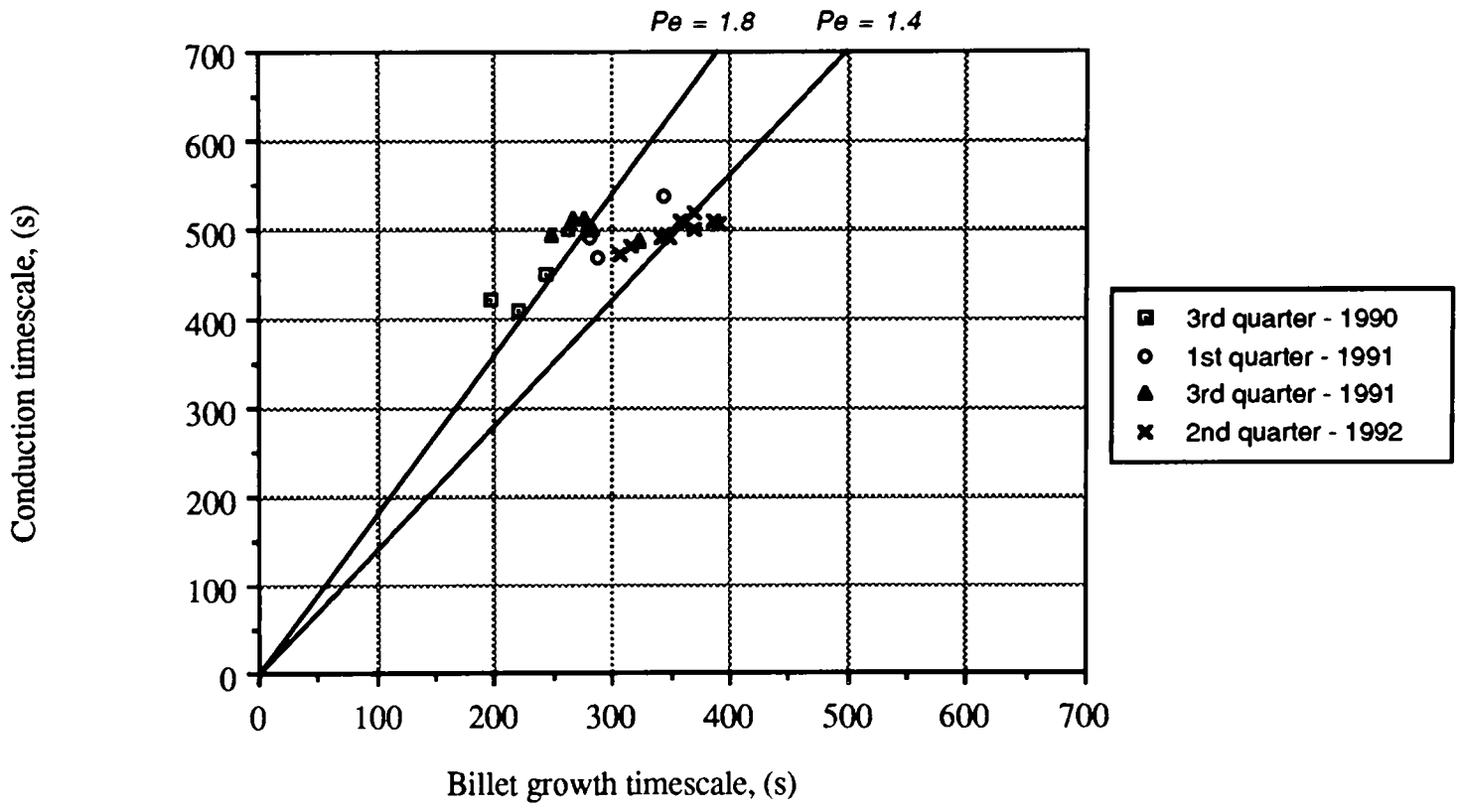

Figure 5.2: Plot of $\frac{R}{\hat{U}_0}$ against $\frac{\rho c R^2}{K_s}$ for successful production runs of aluminium alloy 2618.

Changes in Peclet number will represent changes in the solidification characteristics of the bulk of the billet.[3] The situation is clearly more complicated, since changes in Peclet number may also coincide with changes in boundary heat fluxes. However, an operational Peclet number can easily be computed from the average process parameters, (measured on any production run), and can be monitored over a large number of production runs. This makes it ideally suited to the application of a diagnostic control technique such as Statistical Process (or Quality) Control.

Maintenance of near constant Peclet number between production runs makes physically intuitive sense when Pe is interpreted as the ratio of solidification and billet growth timescales. Constant Pe implies

[3]This part of the billet spray-forming process is analagous to a continuous casting process, once the collector is sufficiently distant from the billet top surface. It is well known that the "casting speed" in continuous casting is of prime importance in determining the solidification front, see e.g. [123].

constant $\hat{U}_0 R$. Thus, ignoring for the moment changes in boundary effects, an increase in billet target radius R should be accompanied by a decrease in withdrawal rate $\hat{U}_0$ to maintain Pe constant. The mass balance for a billet of constant radius, R,

$$\hat{\dot{M}}_0 \overline{Y} = \rho \pi R^2 \hat{U}_0,$$

then implies that the quantity

$$\frac{\hat{\dot{M}}_0 \overline{Y}}{R}$$

also be maintained constant. This gives a simple indication of how to vary mass flow rates and withdrawal rates with production of different sized billets.

Boundary conditions

In the boundary condition equations (5.16) and (5.17), B_{gas} and $B_{collector}$ are **Biot** numbers, defined by

$$B_{gas} = \frac{h_{gas} R}{K_s}, \tag{5.23}$$

$$B_{collector} = \frac{h_{collector} R}{K_s}. \tag{5.24}$$

The gas Biot number will be largest on the top of the billet, where the atomising gas jets impinge, and will be smaller on the billet sides, where the flow becomes more laminar. Estimates derived from the production rig, [2], indicate that h_{gas} decreases from about $1000\text{W/m}^2/^\circ\text{C}$ on the billet crown to about $300\text{W/m}^2/^\circ\text{C}$ on the billet sides, whilst the collector heat transfer coefficient, $h_{collector}$, is approximately $2000\text{W/m}^2/^\circ\text{C}$. Thus, for a typical aluminium alloy and production billet radius,

$$.15 < B_{gas} < .5, \text{ and } B_{collector} \approx 1. \tag{5.25}$$

5.1.3 Temperature and thermal conductivity functions

With the above scaling and previous assumptions the material functions, $T(H)$ and $K(H)$, that appear in (5.15), (5.16) and (5.17) are given by

$$T(H) = H - \frac{L}{c\Delta\hat{T}} f_l(H), \tag{5.26}$$

$$K(H) = [1 - (1 - \frac{K_l}{K_s}) f_l(H)] \frac{\mathrm{d}T}{\mathrm{d}H}(H). \tag{5.27}$$

For simplicity, $K(H)$ is referred to as the thermal conductivity. For the later numerical solution of the heat flow equations, the functions $T(H)$ and $K(H)$ must be readily computable from a "lookup table". This minimises computational time and allows the incorporation of temperature dependent densities and specific heats as simple model modifications, (i.e. the field equations and boundary conditions remain unchanged in form).

Experimental data is supplied, [44], for all the material constants above and for the temperatures, T_k, at which $5k$ % of the alloy will be liquid, $k = 0, 1, ..., 20$. Outside the freeezing range the functions $T(H)$ and $K(H)$ are easily calculable. Within the freeezing range 21 values H_k of the enthalpy H are calculated at the temperatures T_k using

$$T_k = H_k - .05k \frac{L}{c\Delta\hat{T}}, \qquad k = 0, 1, ..., 20. \tag{5.28}$$

Using these values for $T(H_k) = T_k$, and additional points just outside the freeezing range, estimates of the gradient $\frac{dT}{dH}(H_k)$ are made at each point, H_k. A formula described in [36] is used,[4] which is especially suited to locally monotone data. The data points $T(H_k)$ and estimates of the derivatives are then used to construct a monoticity preserving piecewise cubic Hermite interpolant, approximating $T(H)$.

For future computational speed in evaluating $T(H)$, the freezing range, $H \in [0, 1 + L/c\Delta\hat{T}]$, is divided into 100 equal intervals, separated by 101 mesh points and at each mesh point the cubic interpolant is used to give an approximate value for $T(H)$. For later computations a linear interpolant is evaluated using these stored values.

At the 21 enthalpy values, H_k, estimates of $K(H_k)$ are made using

$$K(H_k) = (1 - .05k[1 - \frac{K_l}{K_s}])\frac{dT}{dH}(H_k), \qquad k = 0, 1, ..., 20, \tag{5.29}$$

where the values $\frac{dT}{dH}(H_k)$ are estimated using the above cubic interpolant for $T(H)$. From these values for $K(H_k)$ and others chosen just outside the melting range the method of [36] is again used to estimate the derivatives $\frac{dK}{dH}(H_k)$. The estimates of $K(H_k)$ and $\frac{dK}{dH}(H_k)$ are used to construct a piecewise cubic Hermite interpolant approximating $K(H)$, and from this a linear approximant is constructed for fast evaluation of $K(H)$, just as described for $T(H)$.

Examples of the two functions $T(H)$ and $K(H)$, computed by this method, are shown in Fig. 5.3 for the aluminium alloy 2618. The spray deposited on the billet crown will typically be less than 80 % liquid. This provides an upper bound to the billet liquid fraction. It can be seen from Fig. 5.3 that for typical billet temperatures, the approximations of $T(H)$ and $K(H)$ from the experimental data will be quite smooth; $T(H)$ typically increases and $K(H)$ typically decreases, with H.

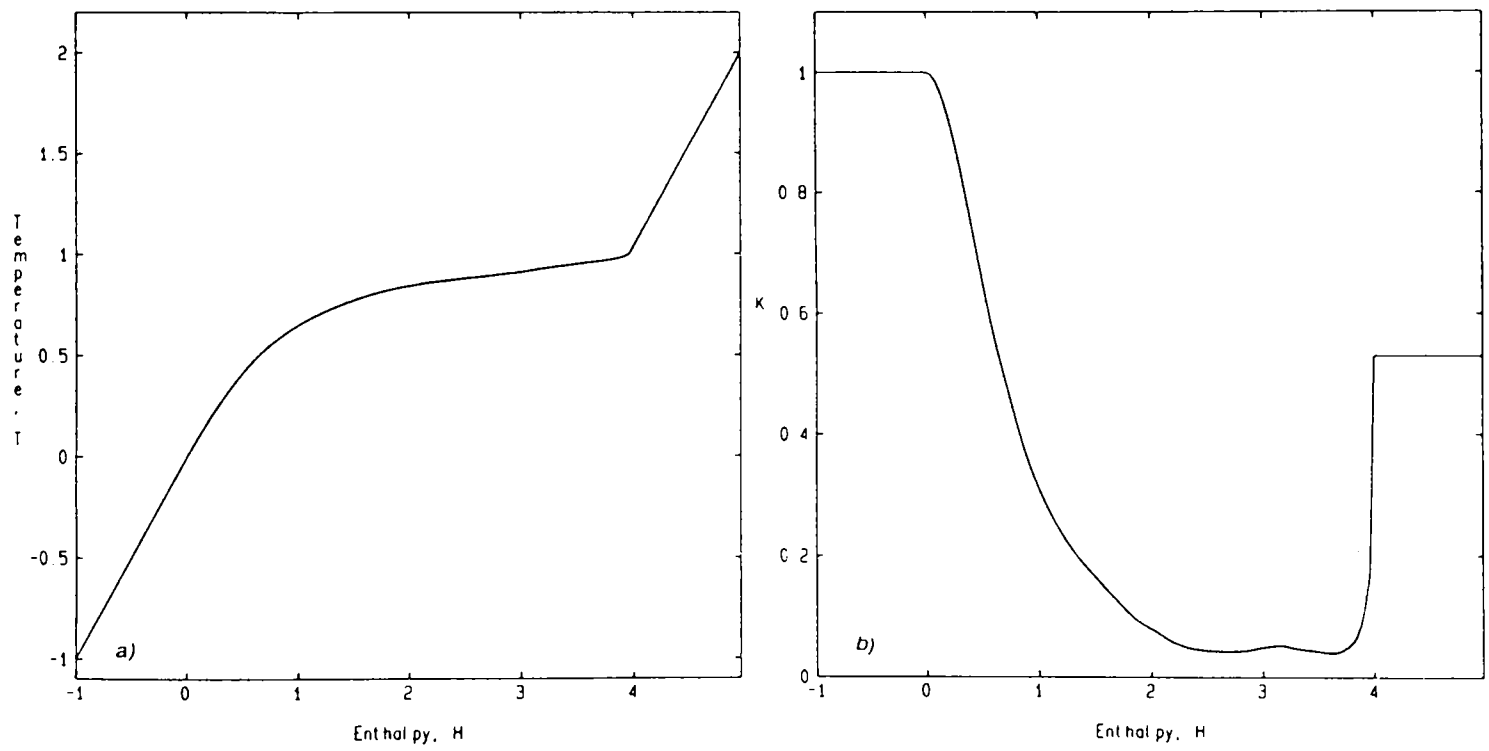

Figure 5.3: The functions $T(H)$ and $K(H)$ for aluminium alloy 2618.

[4]This formula is utilised by NAG routine E01BEF, an adapted version of which is used here.

5.1.4 Model limitations and requirements

There are severe limitations in the usefulness of equation (5.15), (and its boundary conditions), as a model. Analytic solution is not possible, and numerical solution is hampered by problems that are similar to, (but much worse than), those of the billet growth model equation (2.43), of chapters two, three and four. The production run timescale is $O(\epsilon^{-1})$, but the rapid changes occurring in the boundary condition (5.16) mean that a small timestep must be used in any numerical algorithm. The three dimensional heat flow problem within the billet is horrendous, not least because of the mesh size that would be required to capture the small surface movements. Any direct solution method would be likely to require an adaptive mesh near the billet surface, and this adds further complexity.

The model provided by equations (5.15), (5.16) and (5.17) also fails to emphasize those parts of the solidification process that are likely to be most relevant to the different mechanisms of microstructure formation. Equation (5.15) suggests that, on the billet length-scale and rotation timescale, enthalpy changes are negligible. However, close to the billet surface (5.16) suggests that larger fluctuations in the enthalpy may occur, due to the intermittent deposition of spray, coupled with strong convective cooling from the gas. Rescaling time with ϵ in (5.15) shows that $O(1)$ changes in enthalpy on the billet length-scale occur on the slow timescale, $\eta = \epsilon t$.

- Close to the billet surface, where deposition is taking place, solidification must be very rapid. The rapid rotational motion of the billet means that the billet cannot contain a large mushy region that has a high fraction liquid.[5] Thus, most of the latent heat deposited with each layer of spray must be rapidly dissipated, either into the billet bulk by conduction or into the atomising gas by forced convection and radiation. The cooling rates close to the billet surface will control microsegregation, and will also largely determine the grain size. The mechanisms of porosity formation that were outlined in chapter one, section 1.2.3, are also heavily influenced by the fraction liquid in this region alone.

- In the bulk of the billet, fluctuations in enthalpy will be much slower than those that are "forced" at the billet surface, due to the diffusive nature of heat flow. The solidus isotherm marks the boundary of the mushy region within the billet. In this region there is the possibility of both macrosegregation and grain coarsening occurring. These large scale features are also likely to be affected most by changes in billet shape.

Sensible model requirements include the following.

1. To be able to investigate heat flow both close to the surface and within the bulk of the billet.

2. To be able to investigate the major effects of variations in process parameters on the heat flow in each of these regions, either analytically or numerically.

[5] Semi-solid alloys can be thought of as either "mushes" or "slurries", [33]. The former is conceptualised as a porous solid, with pores filled with liquid phase. The latter is conceptualised as largely liquid, with small solid particles suspended in the liquid phase. A reasonably solid mush might withstand the strong centrifugal forces exerted on the billet, by rotation; a slurry is likely to end up on the walls of the spray chamber. It is not clear at what fraction liquid the transition from mush to slurry takes place.

3. If numerical analysis is required then the model equations should permit an efficient enough solution to allow parametric studies to be feasible.

Satisfying these model requirements should enable one to gain both qualitative and quantitative understanding of the relevance of the different mechanisms of microstructure formation in spray-forming, and also to understand how the individual mechanisms may be influenced by changes in the process parameters. To satisfy the above requirements it is necessary to develop approximations to (5.15), (5.16) and (5.17). These approximations are developed in the following two sections.

5.2 Boundary layer approximation

For axisymmetric averaged billet growth, as in chapters two, three and four, both radial and longitudinal variations in solidification behaviour are of interest. In order to determine the cooling rates most likely to control local variations in grain size and microsegregation, as well as to understand the likelihood of different mechanisms of porosity formation occurring, it is necessary to consider transient heat flow close to the billet surface. In this region, during deposition, rapid enthalpy variation is likely to occur on the rotation timescale. Derivation of approximate model equations, describing transient heat flow within a small neighbourhood of a surface point, P, over a short time interval, is as follows.

The position of P in a cartesian billet frame of reference is denoted

$$\boldsymbol{x}_{P,0}(t) \equiv (x_{P,0}(t), y_{P,0}(t), z_{P,0}(t)), \tag{5.30}$$

and motion of P is given by

$$\frac{\mathrm{d}\boldsymbol{x}_{P,0}}{\mathrm{d}t}(t) = v_P(t)\boldsymbol{n}_P(t), \tag{5.31}$$

where $\boldsymbol{n}_P(t)$ is the unit outward normal vector to the billet surface at P. Transient heat flow is considered only within a neighbourhood

$$\|\boldsymbol{x}_0 - \boldsymbol{x}_{P,0}\| = O((\frac{\epsilon}{Pe})^{1/2}) \tag{5.32}$$

of the surface point, P.

The billet surface position is assumed to have an axisymmetric $O(\epsilon)$ asymptotic approximation, uniformly valid on the timescale ϵ^{-1}, that is given by the averaged billet growth equations of chapter two, i.e.

$$F(\boldsymbol{x}_0, t) \sim F_0(\boldsymbol{x}_0, \eta) + O(\epsilon). \tag{5.33}$$

At P, orthogonal unit vectors $\tilde{\boldsymbol{i}}(t)$, $\tilde{\boldsymbol{j}}(t)$ and $\tilde{\boldsymbol{k}}(t)$ are chosen so that

$$\tilde{\boldsymbol{k}}(t) \equiv -\frac{\boldsymbol{\nabla} F_0}{|\boldsymbol{\nabla} F_0|} = -\boldsymbol{n}_P(t) + O(\epsilon), \tag{5.34}$$

with $\tilde{\boldsymbol{i}}(t)$ and $\tilde{\boldsymbol{j}}(t)$ then fixed arbitrarily to form a right handed system, e.g. see Fig. 5.4. Position, $\tilde{\boldsymbol{x}}$, in this new surface coordinate system and position, $\boldsymbol{x}_0$, in the billet coordinate system are related by

$$\tilde{\boldsymbol{x}} = (\tilde{\boldsymbol{i}}.[\boldsymbol{x}_0 - \boldsymbol{x}_{P,0}], \tilde{\boldsymbol{j}}.[\boldsymbol{x}_0 - \boldsymbol{x}_{P,0}], \tilde{\boldsymbol{k}}.[\boldsymbol{x}_0 - \boldsymbol{x}_{P,0}]). \tag{5.35}$$

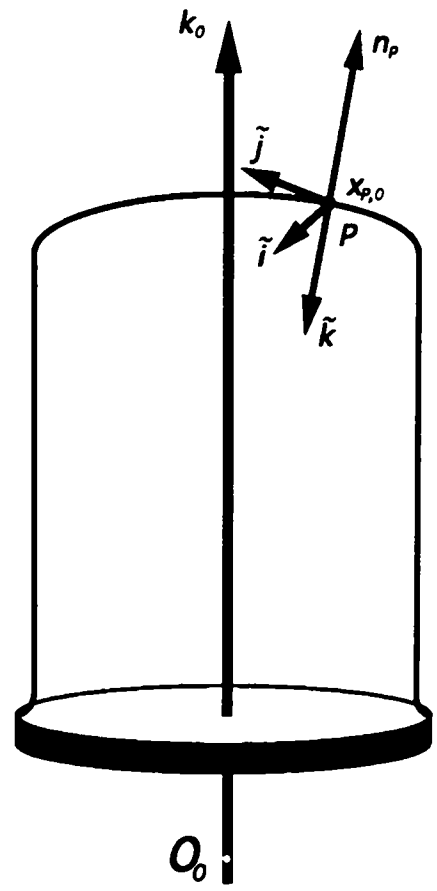

Figure 5.4: Surface fixed boundary layer coordinate system.

On the rotation timescale it is assumed that tangential thermal gradients are $O(1)$ and that thermal gradients normal to the surface vary on the diffusive length-scale, $(\frac{\epsilon}{Pe})^{1/2}$. The distance, $\tilde{z}$, in the direction of $\tilde{\boldsymbol{k}}$ is rescaled with this length-scale, thus introducing a boundary layer coordinate, ζ, defined by

$$\tilde{z} = \zeta(\frac{\epsilon}{Pe})^{1/2}. \tag{5.36}$$

The left hand side of (5.15), in the new coordinate system, becomes

$$\begin{aligned} \frac{\partial H}{\partial t} \quad &+ \quad (\frac{\partial \tilde{\boldsymbol{i}}}{\partial t}.[\boldsymbol{x}_0 - \boldsymbol{x}_{P,0}], \frac{\partial \tilde{\boldsymbol{j}}}{\partial t}.[\boldsymbol{x}_0 - \boldsymbol{x}_{P,0}], \frac{\partial \tilde{\boldsymbol{k}}}{\partial t}.[\boldsymbol{x}_0 - \boldsymbol{x}_{P,0}]).(\frac{\partial}{\partial \tilde{x}}, \frac{\partial}{\partial \tilde{y}}, (\frac{Pe}{\epsilon})^{1/2}\frac{\partial}{\partial \zeta})H. \\ &- \quad v_P(\tilde{\boldsymbol{i}}.\boldsymbol{n}_P, \tilde{\boldsymbol{j}}.\boldsymbol{n}_P, \tilde{\boldsymbol{k}}.\boldsymbol{n}_P).(\frac{\partial}{\partial \tilde{x}}, \frac{\partial}{\partial \tilde{y}}, (\frac{Pe}{\epsilon})^{1/2}\frac{\partial}{\partial \zeta})H. \end{aligned} \tag{5.37}$$

With the above assumptions, changes in $\tilde{\boldsymbol{i}}$, $\tilde{\boldsymbol{j}}$ and $\tilde{\boldsymbol{k}}$ on the rotation timescale are $O(\epsilon)$. From (5.32), it then follows that the first vector product in (5.37) contains only terms of $O(\epsilon)$. From (5.34), it follows that the first two terms in the second vector product in (5.37) are also $O(\epsilon)$. Thus, the above expression, (5.37), for the left hand side of (5.15) becomes

$$\frac{\partial H}{\partial t} = \frac{\partial H}{\partial t} + (\frac{Pe}{\epsilon})^{1/2} v_P \frac{\partial H}{\partial \zeta} + O(\epsilon). \tag{5.38}$$

Transformation of the right hand side of (5.15) produces

$$\frac{\epsilon}{Pe}\nabla.[K(H)\nabla H] = \frac{\partial}{\partial \zeta}[K(H)\frac{\partial H}{\partial \zeta}] + O(\epsilon). \tag{5.39}$$

Combining (5.38) and (5.39), retaining only terms of $O(\epsilon^{1/2})$ and larger, gives

$$\frac{\partial H}{\partial t} + (\frac{Pe}{\epsilon})^{1/2} v_P \frac{\partial H}{\partial \zeta} = \frac{\partial}{\partial \zeta}[K(H)\frac{\partial H}{\partial \zeta}], \tag{5.40}$$

which, for $\zeta > 0$, provides an $O(\epsilon^{1/2})$ asymptotic approximation to the transient enthalpy variations normal to the billet surface at P. The boundary condition (5.16) becomes

$$K(H)\frac{\partial H}{\partial \zeta} = (\frac{\epsilon}{Pe})^{1/2} B_{gas}(T(H) - T_{gas}) + (\frac{Pe}{\epsilon})^{1/2} v_P(H - H_{spray}), \qquad \zeta = 0. \tag{5.41}$$

An $O(\epsilon)$ approximation to the surface velocity is gained from substituting $F_0(\boldsymbol{x}_0, \eta)$ in the right hand side of (5.18), i.e.

$$\frac{1}{\epsilon}\frac{\partial F}{\partial t}(\boldsymbol{x}_0, t) \sim \gamma(\dot{m}g\boldsymbol{k}', F_0)\dot{m}(\eta)g(r'[\boldsymbol{x}_0, t])\boldsymbol{k}'(t).\boldsymbol{\nabla}F_0(\boldsymbol{x}_0, \eta) + O(\epsilon). \tag{5.42}$$

This may be used in (5.40) and (5.41) to give v_P explicitly. Defining $v(t)$ and β by

$$v(t) = -\frac{(\epsilon Pe)^{1/2}\gamma(\dot{m}g\boldsymbol{k}', F_0)\dot{m}(\eta)g(r')\boldsymbol{k}'(t).\boldsymbol{\nabla}F_0}{|\boldsymbol{\nabla}F_0|}, \tag{5.43}$$

$$\beta = (\frac{\epsilon}{Pe})^{1/2}B_{gas}, \tag{5.44}$$

(all functions evaluated at P), it is easily shown that

$$(\frac{\epsilon}{Pe})^{1/2}v(t) = v_P + O(\epsilon).$$

For $\zeta \sim (\frac{Pe}{\epsilon})^{1/2}$, (i.e. at distances much greater than the diffusive length-scale, $(\frac{\epsilon}{Pe})^{1/2}$, from the billet surface),

$$\frac{\partial H}{\partial \tilde{z}} = O(1), \tag{5.45}$$

since terms in (5.16) are $O(1)$. Thus, again retaining only terms of $O(\epsilon^{1/2})$,

$$\frac{\partial H}{\partial \zeta} \to 0, \qquad \zeta \to \infty. \tag{5.46}$$

Boundary layer equations

The boundary layer approximation is given by

$$\frac{\partial H}{\partial t} = -v(t)\frac{\partial H}{\partial \zeta} + \frac{\partial}{\partial \zeta}[K(H)\frac{\partial H}{\partial \zeta}], \qquad \zeta > 0, \tag{5.47}$$

$$K(H)\frac{\partial H}{\partial \zeta} = \beta(T(H) - T_{gas}) + v(t)(H - H_{spray}), \qquad \zeta = 0, \tag{5.48}$$

$$\frac{\partial H}{\partial \zeta} \to 0, \qquad \zeta \to \infty. \tag{5.49}$$

Terms in equation (5.47) are all $O(1)$, except possibly the convective term, $v(t)\frac{\partial H}{\partial \zeta}$. The function $v(t)$ has the form of an intermittent pulse as the scanning and rotation movements interact in depositing metal spray at irregular intervals at point P. From (5.43) it is seen that when P is not under the spray cone then

$$v(t) = 0,$$

and when P is under the spray cone then

$$v(t) \sim (\epsilon Pe)^{1/2}\dot{m}(\eta)g(r').$$

Typically, $\dot{m}(\eta) \approx 1$ and $g(r') \approx r_s^{-2}$; where the spray cone radius, r_s, has a value in the range $[1/3, 1/2]$ for usual process production parameters. Thus, although $\epsilon \ll 1$, values of $v(t)$ that can occur during deposition are not $\ll 1$.

Through equation (5.48) it can be seen that $O(1)$ variations in $v(t)$ result in $O(1)$ transient enthalpy gradients at the boundary layer surface, $\zeta = 0$. On a slower timescale the averaging methods of chapter two indicate that time averaged values of $v(t)$ are $O((\epsilon Pe)^{1/2})$, which then balance with the convective cooling

term in (5.48). The $O((\epsilon Pe)^{1/2})$ parameter, β, appearing in (5.48) may also vary with time as local gas velocities and pressures change. These changes are however, unlikely to be as sudden as those in $v(t)$ and are very hard to quantify. Thus, the boundary layer Biot number, β, will be assumed to vary only with choice of surface point, P.

5.2.1 Validity and limitations

The boundary layer approximation takes a point, P, initially at a fixed radial distance from the billet axis of rotation and looks at the heat flow in the direction normal to the surface at that point. The approximation is expected to be valid for

$$\zeta \ll (\frac{Pe}{\epsilon})^{1/2}, \tag{5.50}$$

and to give a good physical representation of the transient heat flow in this region.

Clearly the boundary layer approximation will not be immediately valid during the initial stages of billet growth, when the collector represents an effective heat sink and when the billet and boundary layer thickness are comparable.

The ζ-axis is fixed to P, and will change its orientation as the surface changes shape. Thus, fixed points along the ζ-axis will not continue to represent fixed points in the billet very well over large integration periods. Similarly, the radial distance of P from the billet axis of rotation will change as P moves in the direction of the surface normal vector. Time averaged values of $v(t)$ are $O((\epsilon Pe)^{1/2})$. Thus, billet shape changes that are significant in the boundary layer will occur on a timescale $(\epsilon Pe)^{-1/2}$, and to retain a physical representation of fixed points along the ζ-axis it is required that the time period, Dt, throughout which the boundary layer equations are integrated satisfies

$$\mathrm{D}t \ll \frac{1}{(\epsilon Pe)^{1/2}}. \tag{5.51}$$

The restrictions, (5.50) and (5.51), on ζ and Dt respectively, are not too severe and will allow the parametric investigation of the effects on boundary layer solidification behaviour of changes in billet shape, mass flow rate, spray enthalpy, gas temperature, rotation rate and scanner pattern.

5.2.2 Far-field behaviour

The far-field boundary condition, (5.49), implies that a constant value for H is approached as $\zeta \to \infty$, say $H \to H_\infty$. Suppose now that $H \to H_\infty$ sufficiently fast for the improper integral

$$\boldsymbol{H}(t) \equiv \int_0^\infty [H(\zeta, t) - H_\infty] \mathrm{d}\zeta \tag{5.52}$$

to be differentiable. The derivative of $\boldsymbol{H}(t)$ is obtained after a little algebra,

$$\frac{\mathrm{d}\boldsymbol{H}}{\mathrm{d}t}(t) = -\beta(T(H(0,t)) - T_{gas}) - v(t)(H_\infty - H_{spray}). \tag{5.53}$$

The functional $\boldsymbol{H}$ is representative of the total heat in the boundary layer. From (5.53) changes in $\boldsymbol{H}(t)$ are seen to result from heat losses to the surrounding gas, (first term), and from convection of heat right through the boundary layer at speed $v(t)$, (second term). The boundary layer represents a region of the billet within

which transient heat transfer mechanisms are in operation during deposition and should not "on average" gain or lose heat. To do so would imply a heat source or sink in the boundary layer, which is unrealistic since there are none in the billet as a whole and since the boundary layer heat flow is one dimensional. Hence, the right hand side of (5.53) averaged over time should equal zero. The function $v(t)$ is almost periodic, (see chapter two), and assuming that the surface enthalpy is also almost periodic, the time average of the right hand side of (5.53) will exist.

Consider now the time averaged boundary layer equations

$$\frac{\partial H}{\partial t} = -\overline{v}\frac{\partial H}{\partial \zeta} + \frac{\partial}{\partial \zeta}[K(H)\frac{\partial H}{\partial \zeta}], \qquad \zeta > 0, \tag{5.54}$$

$$K(H)\frac{\partial H}{\partial \zeta} = \beta(T(H) - T_{gas}) + \overline{v}(H - H_{spray}), \qquad \zeta = 0, \tag{5.55}$$

$$\frac{\partial H}{\partial \zeta} \rightarrow 0, \qquad \zeta \rightarrow \infty, \tag{5.56}$$

overbars denoting time averaged values. These equations have the constant steady state solution

$$H(\zeta, t) = \overline{H},$$

to which solutions from arbitrary initial conditions converge to as $t \rightarrow \infty$, in the "energy norm"

$$\boldsymbol{E}(t) \equiv \int_0^\infty [H(\zeta, t) - \overline{H}]^2 \mathrm{d}\zeta. \tag{5.57}$$

The constant $\overline{H}$ is the (unique) solution of

$$\beta(T(\overline{H}) - T_{gas}) + \overline{v}(\overline{H} - H_{spray}) = 0. \tag{5.58}$$

The time averaged right hand side of (5.53) set equal to zero is

$$\beta(\overline{T(H(0,t))} - T_{gas}) + \overline{v}(H_\infty - H_{spray}) = 0. \tag{5.59}$$

By comparison with (5.58) it is seen that

$$\overline{T(H(0,t))} > T(\overline{H}) \quad \Rightarrow \quad H_\infty < \overline{H}$$

and

$$\overline{T(H(0,t))} < T(\overline{H}) \quad \Rightarrow \quad H_\infty > \overline{H}.$$

The above two possibilities imply a net flow of heat through the boundary layer, respectively into and out of the billet, contradicting the far field boundary condition (5.49). Hence, it follows that

$$\overline{H} = H_\infty, \tag{5.60}$$

i.e. that the far field boundary layer enthalpy is determined by averaging the boundary condition at $\zeta = 0$.

5.2.3 Boundedness of the boundary layer transient

In order to examine the departure of the transient boundary layer solution from the steady solution, $\overline{H}$, to the averaged problem, the norm (5.57) is differentiated. After some algebra this produces

$$\begin{aligned}\frac{\mathrm{d}\boldsymbol{E}}{\mathrm{d}t}(t) = & -2\int_0^\infty K(H)[\frac{\partial H}{\partial \zeta}]^2 \mathrm{d}\zeta - [v(t) + 2\beta\frac{\mathrm{d}T}{\mathrm{d}H}(H^*)][H(0,t) - \overline{H}]^2 \\ & + 2[H_{spray} - \overline{H}][v(t) - \overline{v}][H(0,t) - \overline{H}].\end{aligned} \tag{5.61}$$

The first two terms in (5.61) are negative always. The third term will be predominantly positive, since periods of time when $v(t) > \overline{v}$ are likely to result in $H(0,t) > \overline{H}$ and $v(t) < \overline{v}$ is likely to result in $H(0,t) < \overline{H}$. Thus, fluctuations from $\overline{H}$ may occur. However, since the second term in (5.61) is quadratic in $[H(0,t) - \overline{H}]$ it is seen that fluctuations from $\overline{H}$ will be bounded with respect to the norm $\boldsymbol{E}(t)$.

5.3 Slow-time Heat Flow

The boundary layer approximation will give an approximation to the heat flow occurring close to those parts of the billet surface that receive deposition from the spray. At places on the billet surface which receive no deposition, (i.e. the sides and base), large scale fluctuations in the boundary conditions imposed do not occur on the rotation timescale. For Peclet numbers of $O_S(1)$ conduction here occurs on the slower billet growth timescale.

Section 5.2 shows that the boundary layer has the effect of averaging the rapid transient surface heat fluxes as $\zeta \to \infty$. Within the bulk of the billet it is these averaged heat fluxes that are important. This prompts the study of the "slow-time" heat flow model

$$\frac{\partial H}{\partial \eta} = \frac{1}{Pe}\nabla.[K(H)\nabla H], \qquad \boldsymbol{x}_0 \in \Omega(t), \tag{5.62}$$

$$-K(H)\frac{\partial H}{\partial n} = B_{gas}(T(H) - T_{gas}) + Pe\overline{v}(H - H_{spray}), \qquad \boldsymbol{x}_0 \in \partial\Omega(t) : z_0 > z_c, \tag{5.63}$$

$$K(H)\frac{\partial H}{\partial z_0} = B_{collector}(T(H) - T_{collector}), \qquad \boldsymbol{x}_0 \in \partial\Omega(t) : z_0 = z_c, \tag{5.64}$$

which is obtained by rescaling t with ϵ to give the slow-time variable η, and by averaging the surface normal velocity v_P to give $\overline{v}$. The billet is assumed to be axisymmetric. The averaged billet growth model of chapter two is used to give $\overline{v}$ as

$$\overline{v} \equiv -\frac{\partial F_0}{\partial \eta}|\nabla F_0|^{-1}, \tag{5.65}$$

where, in the billet frame of reference, evolution of $F_0(\boldsymbol{x}_0, \eta)$ is governed by

$$\frac{\partial F_0}{\partial \eta}(\boldsymbol{x}_0, \eta) = \dot{m}(\eta)\overline{\boldsymbol{g}}(F_0, \boldsymbol{x}_1[\boldsymbol{x}_0, \eta]).\nabla F_0(\boldsymbol{x}_0, \eta), \qquad \boldsymbol{x}_0 \in \partial\Omega(t). \tag{5.66}$$

In (5.66), $\dot{m}(\eta)$ is the mass flow rate, (assumed to vary on the slow timescale), and $\overline{\boldsymbol{g}}$ is the axisymmetric averaged mass flux distribution vectorfield. See chapter two for further details.

Validity

The above derivation has been intuitive, rather than deductive, and no rigorous attempt will be made to justify its validity. An outline of a method that might be used to demonstrate the validity of this approximation is as follows.

1. Define smooth mappings from the three dimensional moving billet boundaries in both the transient problem, (5.15), (5.16) & (5.17), and the slow-time problem, (5.62), (5.63) & (5.64), onto a fixed three dimensional volume.

2. The mapping of the moving boundary onto a fixed domain should preserve the parabolicity of (5.15) and (5.62), but the equations now have coefficients which are dependant on time and position within the fixed volume. Assuming that the two initial billet domains are $O(\epsilon)$ approximations of each other, uniformly on the timescale ϵ^{-1}, it should be possible to choose the mappings so that the transformed equations have coefficients and boundary conditions which are $O(\epsilon)$ approximations of each other, also uniformly on the timescale ϵ^{-1}.

3. Subtracting the two equations should, to leading order, give a nonlinear parabolic operator to which a maximum principle can be applied, (e.g. theorem 12, page 187, in [110]).

Usefulness of the slow-time equations

The slow-time heat flow equations should provide an approximation to the heat flow occurring in the bulk of the billet. The billet surface position and normal velocity are given by the approximations of chapter two. Thus, the billet growth is assumed to be axisymmetric. For axisymmetric initial and boundary conditions the heat flow may then also be assumed to be axisymmetric about the billet axis of rotation. Analytic solution of (5.62), (5.63) and (5.64) will not be possible, due to the irregular geometry and the nonlinearity. Instead a numerical method must be used, and for this the reduced dimensionality of the problem produced by the symmetry assumption results in a considerable computational saving.

Matching with the boundary layer approximation

The slow-time heat flow equations and the boundary layer approximation may be viewed as different components of the same asymptotic expansion of the enthalpy within the growing billet. The boundary layer approximation is the first term in an *inner* expansion of the enthalpy close to the deposition surface. The slow-time heat flow is the first term in an *outer* expansion of the enthalpy within the bulk of the billet.

As $\zeta \to (\frac{Pe}{\epsilon})^{1/2}$ the boundary layer approximation becomes invalid as the heat flow becomes multi-dimensional, whilst the slow-time approximation becomes invalid as the deposition surface is approached from within the billet and more rapid transients exist. For a uniformly valid approximation the two expansions must be matched in some intermediate region. This matching is not attempted, since the main focus of the analysis has been to provide approximations to the heat flow in different regions of the billet which are more manageable than the full equations. The slow-time equations in particular, although simplified, still represent a challenging numerical problem on their own, without having to think about matching with the boundary layer.

It should be noted that the far-field enthalpy, $\overline{H}$, of the boundary layer approximation, as $\zeta \to \infty$, is different to the enthalpy that will be computed at the billet surface using the slow-time approximation. The former is governed by equation (5.58), whilst the latter is governed by equation (5.63). Although both enthalpies rely on the time-averaged boundary heat fluxes, the slow-time approximation also allows conduction into the billet. On the slow timescale, multi-dimesional heat flow occurs over the billet length-scale. Thus, for example, cooling effects through the billet sides and base can be felt at the deposition surface in the slow-time approximation, but not in the boundary layer approximation. This difference may result in significant heat fluxes within the matching layer.

5.4 Summary

- A simplified, conduction controlled model of alloy solidification is adopted, that neglects species conservation, shrinkage and fluid flow effects. This is justified by the low liquid fractions present in the deposited spray and by the relative homogeneity of the finished material.

- The latent heat of solidification is released over a range of temperatures. The main change in the physical properties of a typical sprayed alloy over the freezing range is that the thermal conductivity of the fully liquid alloy is approximately half that of the fully solid alloy. Changes in material density and specific heat capacity with temperature are slight and are ignored in the model formulation.

- Non-dimensionalisation of the equations and boundary conditions shows that enthalpy changes on the rapid rotation timescale are $O(\epsilon)$ within the bulk of the billet, with $O(1)$ changes occurring only close to the deposition surface. The non-dimensional parameter ϵ is the ratio of the timescales for rotation and billet growth.

- On the slower billet growth timescale solidification is parameterised by the Peclet number,

$$Pe = \frac{\rho c \hat{U}_0 R}{K_s},$$

representing the ratio of the conduction/solidification timescale and the billet growth timescale. Typical production parameters have $Pe = O_S(1)$, as is illustrated in Fig. 5.2. The application of diagnostic control technique such as Statistical Process (Quality) Control is recommended. A simplified analysis is presented, indicating how to vary mass flow rates and withdrawal rates when growing different radii billets, retaining the same Peclet number.

- A boundary layer approximation is derived, governing the rapid variations in enthalpy occurring close to the surface, and in a direction normal to the billet surface. The approximation is expected to be valid for $\zeta \ll (Pe/\epsilon)^{1/2}$, (where ζ is the boundary layer coordinate), and for integration time periods $\mathrm{D}t \ll (Pe\epsilon)^{-1/2}$.

- A "slow-time" approximation is derived, driven by the time-averaged deposition and cooling effects at the boundary. This gives the enthalpy variations in the bulk of the billet as it grows.

Chapter 6

Billet Boundary Layer Heat Flow

This chapter deals with the solution of the boundary layer equations, derived in chapter five, section 5.2. These equations approximate the rapid heat flow occurring close to the deposition surface of the billet; they are given by

$$\frac{\partial H}{\partial t} = -v(t)\frac{\partial H}{\partial \zeta} + \frac{\partial}{\partial \zeta}[K(H)\frac{\partial H}{\partial \zeta}], \qquad \zeta > 0, \tag{6.1}$$

$$K(H)\frac{\partial H}{\partial \zeta} = \beta(T(H) - T_{gas}) + v(t)(H - H_{spray}), \qquad \zeta = 0, \tag{6.2}$$

$$\frac{\partial H}{\partial \zeta} \rightarrow 0, \qquad \zeta \rightarrow \infty. \tag{6.3}$$

The computational details are covered in section one. Section two presents results showing the variation in boundary layer heat flow with radial distance from the billet axis of rotation, for typical process parameters. Section three examines the effects of varying the billet crown shape, and section four examines the effects of changing the rotation and scanner frequencies. There is a brief discussion in section five, and the chapter ends with a summary.

6.1 Computational Details

Equation (6.1) is a nonlinear advection–diffusion equation. The nonlinearity of the conductivity, $K(H)$, and the irregularity of the surface normal velocity, $v(t)$, make analytic solution impossible. The constants β, T_{gas} and H_{spray} are fixed, either by experimentation or by the construction of more complex submodels. Numerical solution requires that $v(t)$ be specified. The surface normal velocity, $v(t)$, is given by

$$v(t) = -\frac{(\epsilon Pe)^{1/2}\gamma(\dot{m}g\boldsymbol{k}', F_0)\dot{m}(\eta)g(r')\boldsymbol{k}'(t).\nabla F_0}{|\nabla F_0|}, \tag{6.4}$$

where $F_0 = 0$ gives the time averaged position of the billet surface; γ, $\dot{m}(\eta)$, $g(r')$ and $\boldsymbol{k}'(t)$ are respectively the sticking efficiency, the metal mass flow rate, the spray cone mass flux distribution function and the unit vector in the direction of the spray cone axis. The non-dimensional groups ϵ and Pe have been discussed in chapters two and five respectively.

To calculate the boundary layer heat flow at a fixed surface point over a short interval of time, first note the following.

- Boundary layer heat flow is driven by the slow-time billet growth, since in (6.4), the function F_0 must be computed. Thus, either the methods of chapter three or chapter four must be used, depending on whether the underlying slow-time growth is steady state or transient respectively.

- Although *a priori* computation of the slow-time billet growth is a complication, it should be noted that

  1. The computationally expensive multi-dimensional slow-time heat flow computations are not required, and

  2. Computation of the slow-time billet growth needs only to be done once, and the data stored, when computing the boundary layer heat flow below any number of surface points.

- The computed slow-time billet growth in chapters three and four has been axisymmetric about the billet axis of rotation. Thus, this growth may be represented by coordinates r_1 and z_1 in a cylindrical billet crown coordinate system, (r_1, ϕ_1, z_1), where ϕ_1 measures azimuthal axis about the billet axis of rotation.

  Fig. 6.1 shows the locus of the point of interception of the spray cone axis with a unit disc fixed horizontally within the crown coordinate system. The disc height is determined by solving equation (2.78), and thus represents approximately the top surface of a steady state billet crown produced with ratio, $\mu = 1$, of withdrawal rate to mass flow rate. The scanner pattern illustrated in Fig. 3.23 has been used and the locus has been followed over approximately three rotations of the billet. Figs. 6.1a and 6.1b show the locus for two different scanner periods.

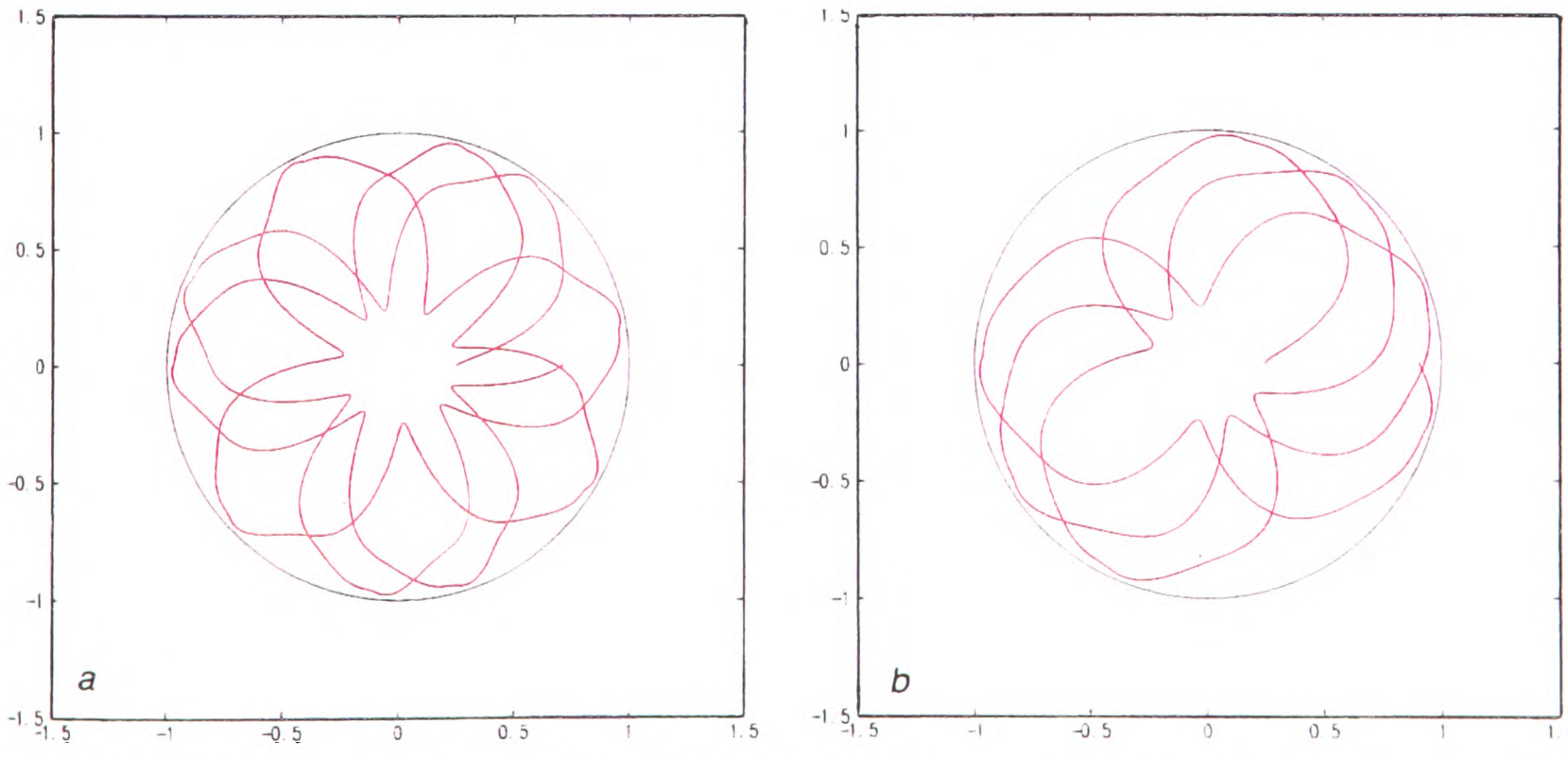

Figure 6.1: Loci of the point of interception of the spray cone axis with a fixed horizontal unit disc, $\alpha_1 = 35°$, $\alpha_2 = 6°$, $t \in [0, 3]$; a) $t_s = 5/17$, b) $t_s = 5/11$.

The function $g(r')$, in (6.4), is evaluated at the billet surface. The perpendicular distance from the spray cone axis, r', of a point with cylindrical polar billet crown coordinates (r_1, ϕ_1, z_1) is given by

$$r' = [x'^2 + y'^2]^{1/2}, \tag{6.5}$$

$$x' = (r_n - r_1 \cos[\phi_1 + \phi_n(t)]) \cos a(t) + (z_1 - z_n - z_c) \sin a(t), \tag{6.6}$$

$$y' = r_1 \sin[\phi_1 + \phi_n(t)]. \tag{6.7}$$

The functions $\phi_n(t)$ and $a(t)$ are respectively the azimuthal angle, (about the z_1 axis), of the atomiser nozzle and the angle that the spray cone axis makes with the vertical. The constants r_n, z_n and z_c are introduced in chapter two, section 2.1, (see also Figs. 2.1 and 2.2).

The amount of deposition taking place at a given point depends on the proximity of that point to the spray cone axis at any time. Thus, it can be seen, both from Fig. 6.1 and from equations (6.6) and (6.7), that the pattern of deposition experienced over a short time interval can vary with both distance, r_1, from the billet axis of rotation and with azimuthal angle, ϕ_1, as well as with variations in scanner and rotation periods.

Since the observed billet growth is axisymmetric about the billet axis of rotation, one wants to choose ϕ_1 so that the time-average of the surface normal velocity, $v(t)$, at (r_1, ϕ_1, z_1), taken over the interval of integration of the boundary layer equations, Dt, is equal to the (axisymmetric) slow-time surface normal velocity.

- An initial condition must be specified for the boundary layer equations.

6.1.1 Presolution algorithm

The preceding points indicate that a number of computational tasks must be performed before numerical solution of (6.1), (6.2) and (6.3) can be carried out. The following algorithm is used.

1. Specify β, T_{gas} and H_{spray} using submodels or experimental estimates, (see section 6.1.3).

2. Select those radial distances from the billet axis of rotation at which an investigation of boundary layer heat flow is desired.

3. Select process parameters for averaged billet growth. Set initial conditions for averaged billet growth. Compute averaged billet growth. For each preselected radial distance from the billet axis store

   (a) billet surface height,

   (b) surface normal velocity, and

   (c) surface normal vector cosines,

   all at each timestep during the integration.

4. Select one of the preselected radial distances from the billet axis of rotation.

   (a) Select start and finish times, t_1 and t_2, for boundary layer computation. Check that the integration time interval, D$t = t_2 - t_1$, satisfies the constraint (5.51).

   (b) Use the stored data to provide approximate values of r_1, z_1, at the surface point, and of the surface normal vector, $\nabla F_0 |\nabla F_0|^{-1}$.

(c) Use the above values in integrating $v(t) = v(\phi_1, t)$ over the interval $[t_1 - 1, t_2]$, and find ϕ_1 such that $v(\phi_1, t)$ integrates to the averaged value previously stored. Fix ϕ_1 at this value to define $v(t)$ through (6.4).

(d) Set initial conditions for equation (6.1).

(e) Solve the boundary layer equations (6.1), (6.2) and (6.3) numerically for this surface point over the selected time interval, (see section 6.1.2).

5. Reselect a different surface point and/or time interval:- go to 4, above.

6.1.2 Numerical solution algorithm

Complications arising in a straightforward numerical solution of (6.1), (6.2) and (6.3) come from the nonlinearity of $K(H)$ and $T(H)$, from the convective term and from the semi-infinite spatial solution domain. Nonlinearity in (6.1) and (6.2) will carry over to either finite difference or finite element discretisations, requiring special treatment and possibly affecting the stability of the numerical method. Similarly, convective terms can cause numerical instability if improperly treated.

Replacement of the semi-infinite domain

For numerical solution using a finite difference method the semi-infinite spatial domain, $\zeta \in [0, \infty)$, must be replaced by a finite interval, with (6.3) satisfied at a finite limit. For a variety of one dimensional linear heat equations on semi-infinite domains, the solution is damped like $\exp^{\zeta^2/4Kt}$ as $\zeta \to \infty$, see e.g. [21]. Thus, when the far-field temperature remains constant, (and when Kt is finite), replacement of the semi-infinite domain with a finite domain has little effect on the behaviour of the underlying mathematical equation, (which one approximates numerically). Inclusion of a convective term in the linear equations does not affect this underlying far-field behaviour of the analytic solutions, e.g. [12]. Although (6.1) is nonlinear, the thermal conductivity, $K(H)$, is positive and bounded above by 1. Hence physically, a similar diffusive/damping effect is expected as $\zeta \to \infty$ as with the linear problems.

Instead of (6.1), (6.2) and (6.3), numerical solution is sought for the equations

$$\frac{\partial H}{\partial t} = -v(t)\frac{\partial H}{\partial \zeta} + \frac{\partial}{\partial \zeta}[K(H)\frac{\partial H}{\partial \zeta}], \qquad \zeta \in (0, Z), \tag{6.8}$$

$$K(H)\frac{\partial H}{\partial \zeta} = \beta(T(H) - T_{gas}) + v(t)(H - H_{spray}), \qquad \zeta = 0, \tag{6.9}$$

$$\frac{\partial H}{\partial \zeta} = 0, \qquad \zeta = Z. \tag{6.10}$$

Initial conditions

In step 4c of the presolution algorithm above, the azimuthal angle ϕ_1 has been set by averaging $v(t)$ over the interval $[t_0, t_2]$, where

$$t_0 = t_1 - 1,$$

rather than the chosen interval of interest, $[t_1, t_2]$. Constant initial conditions are set at $t = t_0$, and the equations are integrated for one rotation period. This allows the enthalpy transients to develop before the

interval of interest, $[t_1, t_2]$, is reached. Initial condition, $\overline{H}$, are set by solving

$$0 = \beta(T(\overline{H}) - T_{gas}) + \overline{v}(\overline{H} - H_{spray}), \tag{6.11}$$

using a bisection method. Recall that $\overline{H}$ is the far field enthalpy of the boundary layer approximation, discussed in chapter five, section 5.2.

Algorithm statement

The interval $\zeta \in [0, Z]$ is covered by a regular mesh with spacing $\Delta\zeta$. Meshpoints ζ_j are defined by

$$\zeta_j = (j - 1/2) \times \Delta\zeta, \qquad \Delta\zeta = \frac{Z}{J}. \tag{6.12}$$

At time $t = t^n$ the enthalpy, H, is approximated by the mesh function H_j^n, such that

$$H_j^n \approx H(\zeta_j, t^n): \qquad j = 0, .., J. \tag{6.13}$$

Initial conditions at $t = t^0 \equiv t_0$ are

$$H_j^0 = \overline{H}, \qquad j = 0, .., J. \tag{6.14}$$

To advance the approximation from timestep n to timestep $n+1$ the following two stage scheme is used.

- **Stage 1:** (Predictor)

$$\frac{2(H_j^{n+1/2} - H_j^n)}{\Delta t_n} = \frac{K(H_{j-1/2}^n)(H_{j-1}^{n+1/2} - H_j^{n+1/2}) + K(H_{j+1/2}^n)(H_{j+1}^{n+1/2} - H_j^{n+1/2})}{\Delta\zeta^2} + \frac{v(t^{n+1/2})}{2\Delta\zeta}(H_{j-1}^n - H_{j+1}^n), \qquad j = 1, .., J-1, \tag{6.15}$$

$$K(H_{1/2}^{n+1/2})\frac{H_1^{n+1/2} - H_0^{n+1/2}}{\Delta\zeta} = \beta[T(H_{1/2}^{n+1/2}) - T_{gas}] + v(t^{n+1/2})[H_{1/2}^{n+1/2} - H_{spray}], \tag{6.16}$$

$$H_J^{n+1/2} = H_{J-1}^{n+1/2}, \tag{6.17}$$

- **Stage 2:** (Corrector)

$$\frac{H_j^{n+1} - H_j^n}{\Delta t_n} = \frac{K(H_{j-1/2}^{n+1/2})(H_{j-1}^{n+1} - H_j^{n+1}) + K(H_{j+1/2}^{n+1/2})(H_{j+1}^{n+1} - H_j^{n+1})}{2\Delta\zeta^2} + \frac{K(H_{j-1/2}^{n+1/2})(H_{j-1}^n - H_j^n) + K(H_{j+1/2}^{n+1/2})(H_{j+1}^n - H_j^n)}{2\Delta\zeta^2} + \frac{v(t^{n+1/2})}{2\Delta\zeta}(H_{j-1}^{n+1/2} - H_{j+1}^{n+1/2}), \qquad j = 1, .., J-1, \tag{6.18}$$

$$K(H_{1/2}^{n+1})\frac{H_1^{n+1} - H_0^{n+1}}{\Delta\zeta} = \beta[T(H_{1/2}^{n+1}) - T_{gas}] + v(t^{n+1})[H_{1/2}^{n+1} - H_{spray}], \tag{6.19}$$

$$H_J^{n+1} = H_{J-1}^{n+1}. \tag{6.20}$$

In the above, t_n is the timestep between times t^n and t^{n+1}, $H_j^{n+1/2}$ is a mesh function approximating H at time $t = t^n + \frac{1}{2}\Delta t_n$. Other fractional subscripts and superscripts are defined by

$$H_{j\pm1/2}^n = \frac{1}{2}(H_j^n + H_{j\pm1}^n),$$

$$t^{n+1/2} = t^n + \frac{1}{2}\Delta t_n.$$

Comments on the algorithm

The two-stage, two-level finite difference scheme, described above, is a simple adaptation of two different "predictor-corrector" schemes described in [92].[1] The scheme is consistent, and for a timestep Δt_n, has a local truncation error $O(\Delta t_n^2)+O(\Delta\zeta^2)$. Convergence of the scheme is not proven here, but the methods used in [92] should (straightforwardly) demonstrate that convergence in the time direction is at least $O(\Delta t_n^{3/2})$, and is $O(\Delta\zeta^2)$ spatially. Analagously to predictor corrector schemes used for ordinary differential equations, the predictor step, (stage 1), has local truncation error

$$O(\Delta t_n) + O(\Delta\zeta^2),$$

wheras the corrector step, (stage 2), has local truncation error

$$O(\Delta t_n^2) + O(\Delta\zeta^2).$$

It is the use of the two stages in conjunction that produces the

$$O(\Delta t_n^2) + O(\Delta\zeta^2)$$

local truncation error for the scheme as a whole. The use of two stages also dispenses with the need for costly iteration in solving large systems of nonlinear difference equations. A further advantage of this scheme, over alternative predictor-corrector methods, is that there is no need to evaluate derivatives of $K(H)$ and $T(H)$. This is particularly important when these functions have been approximated from experimental data.

The scheme retains its second order accuray through the use of central differences at both internal and boundary meshpoints. In both first and second stages the boundary conditions (6.9) and (6.10) have been approximated centrally, at $\zeta = 0$ and $\zeta = Z$ respectively, through the use of the "fictitious" meshpoints ζ_0 and ζ_J which lie outside the interval $[0, Z]$.

The boundary conditions (6.16) and (6.19) are the only nonlinear difference equations to be solved in the scheme. The remaining equations are linear and each stage of the scheme may be written in matrix form as a tridiagonal matrix equation, i.e. (6.15) and (6.18) may be written as

$$-a_j u_{j-1}^n + b_j u_j^n - c_j u_{j+1}^n = d_j, \qquad j = 1, .., J-1. \tag{6.21}$$

For stage 1 or for stage 2 the coefficients a_j, b_j, c_j and d_j may be easily found from (6.15) or (6.18) respectively.

The chosen differencing approximation of the convective term in (6.15) and (6.18) ensures that the matrices are diagonally dominant. Solution for $\{H_j^{n+1/2}\}_{j=0}^J$ and $\{H_j^{n+1}\}_{j=0}^J$ is then accomplished by the Thomas algorithm. This algorithm first sets

$$e_J = 1, \qquad f_J = 0, \tag{6.22}$$

and computes

$$e_j = \frac{a_j}{b_j - c_j e_{j+1}}, \qquad j = J-1, .., 1 \tag{6.23}$$

$$f_j = \frac{d_j + c_j f_{j+1}}{b_j - c_j e_{j+1}}, \qquad j = J-1, .., 1. \tag{6.24}$$

[1] The two schemes adapted are the CPC and MPC schemes in [92].

This is followed by solution of the relevant nonlinear boundary difference equation. For stage 1 (6.16) is solved by substituting for

$$H_1^{n+1/2} = e_1 H_0^{n+1/2} + f_1,$$

and solving the resulting nonlinear equation for $H_0^{n+1/2}$, using a bisection method. For stage 2 (6.19) is solved by substituting for

$$H_1^{n+1} = e_1 H_0^{n+1} + f_1,$$

and solving the resulting nonlinear equation for H_0^{n+1}, again using a bisection method.

Having found either $H_0^{n+1/2}$ or H_0^{n+1} values of $H_j^{n+1/2}$ or H_j^{n+1} respectively are found from the relevant forward recurrence

$$H_j^{n+1/2} = e_j H_{j-1}^{n+1/2} + f_j, \qquad j = 1, .., J, \tag{6.25}$$

(stage 1), or

$$H_j^{n+1} = e_j H_{j-1}^{n+1} + f_j, \qquad j = 1, .., J, \tag{6.26}$$

(stage 2).

Timestep restrictions

Build up of error in computing e_j is avoided, since it is easily shown that $|e_j| \leq 1 \ \forall j$. Build up of error in computing f_j is avoided if

$$1 > \frac{\Delta t_n}{2\Delta\zeta^2} \max_{j=1,..,J-1} \{|K(H_{j+1/2}^n) - K(H_{j-1/2}^n)|, |K(H_{j+1/2}^{n+1/2}) - K(H_{j-1/2}^{n+1/2})|\}. \tag{6.27}$$

Since

$$K(H_{j+1/2}^n) - K(H_{j-1/2}^n) \approx \Delta\zeta \frac{\mathrm{d}K}{\mathrm{d}H}(H_j^n),$$

equation (6.27) represents an $O(\Delta\zeta)$ restriction on the timestep, Δt_n, used.

A further restriction is placed on Δt_n by the surface velocity $v(t)$. Since $v(t)$ takes the form of an intermittent pulse and heat inflow to the boundary layer only takes place when $v(t) > 0$ there is a real need not to "miss" the pulse. When $v(t) > 0$ the pulse duration, $\mathrm{D}t_{pulse}$, is computed. Defining

$$L_1 \equiv \frac{\Delta t_n}{2\Delta\zeta^2} \max_{j=1,..,J-1} \{|K(H_{j+1/2}^n) - K(H_{j-1/2}^n)|, |K(H_{j+1/2}^{n+1/2}) - K(H_{j-1/2}^{n+1/2})|\}, \tag{6.28}$$

$$\Delta t_{pulse} \equiv \frac{\mathrm{D}t_{pulse}}{10}, \tag{6.29}$$

selection of Δt_{n+1} is determined by

$$L_2 = \max\{\frac{10}{9} L_1, \Delta t_n\}, \tag{6.30}$$

$$\Delta t_{n+1} = \min\{\Delta\zeta, \Delta t_{pulse}, \frac{\Delta t_n}{L_2}\}. \tag{6.31}$$

This selection satisfies the restriction (6.27) on Δt_n for the new timestep Δt_{n+1}, whilst adequately representing even very brief pulsed surface velocities $v(t)$.

6.1.3 Model parameters used

Computational results that are presented in the remainder of this chapter are all computed using the material properties of aluminium alloy 2618. The functions $K(H)$ and $T(H)$ for this alloy have been shown in Fig. 5.3.

Derivation of submodels describing h_{gas}, $\hat{T}_{gas}$ and $\hat{H}_{spray}$ is beyond the scope of this thesis. Variation in boundary layer heat flow with these parameters is not explored, and for the remainder of this chapter these parameters are fixed.

$$h_{gas} = 1000 \text{ W/m}^2/^\circ\text{C}, \tag{6.32}$$

$$\hat{T}_{gas} = 200 \ ^\circ\text{C}. \tag{6.33}$$

These values are consistent with estimates derived from the production plant, [2]. The spray enthalpy is set at a value corresponding to 50% liquid fraction, by mass, in the arriving spray, (see e.g. [43]). This is computed using the function in Fig. 6.2, showing the enthalpy as a function of the fraction liquid for alloy 2618. All computations in this chapter assume a Peclet number

$$Pe = 1.887.$$

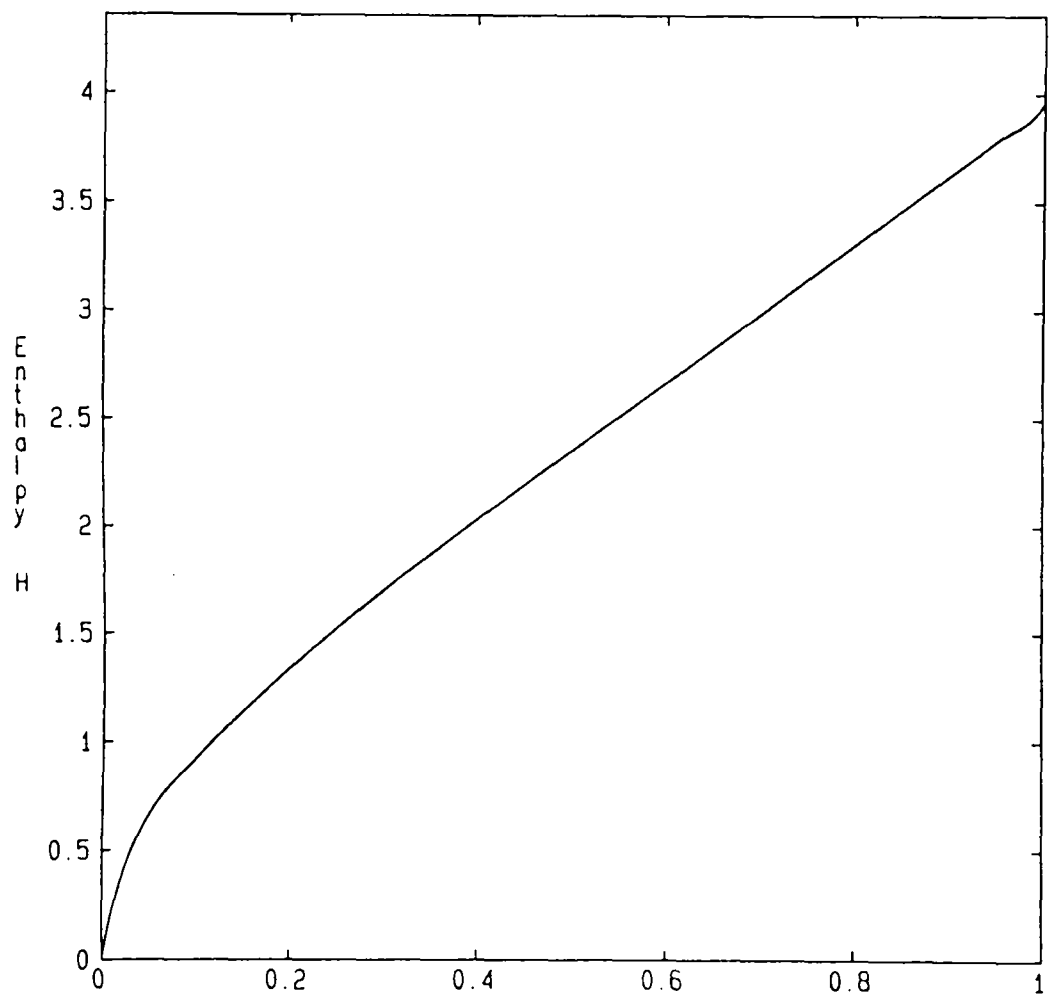

Figure 6.2: Aluminium alloy 2618; non-dimensional enthalpy vs. fraction liquid.

For all computations presented in this chapter a mesh spacing $\Delta\zeta = .02$ was used and $Z = 3$. Further mesh refinement produces little effect, and for typical boundary conditions imposed there is negligible departure of H_j^n from $\overline{\overline{H}}$ with this value of Z.

The presolution algorithm selects an azimuthal angle ϕ_1 at which $v(t)$ averages over $[t_0, t_2]$ to the axisymmetric averaged surface normal velocity, $\bar{v}$. Efficiency of this part of the algorithm may be monitored;

$$|[\mathrm{D}t + 1] \times \bar{v} - \int_{t_0}^{t_2} v(t)\mathrm{d}t| = O(10^{-6}) \tag{6.34}$$

being a typical accuracy for the results of this chapter, (recall $\overline{v} \sim (\epsilon Pe)^{1/2}$, and $\epsilon Pe = O(10^{-3})$).

6.2 Typical radial heat flow variations

Radial variations in boundary layer heat flow occur because of variation in β, T_{gas}, H_{spray} and the surface normal velocity, $v(t)$, between different points. Whilst the first three of these parameters are held constant in this chapter, $v(t)$ will vary with surface position, due to both the underlying geometry of the surface and to the differing interaction between scanner and rotation motions at each point. In this section some of the generic physical differences that affect the boundary layer heat flow are examined.

For the underlying billet growth, constant mass flow rates and withdrawal rates, $\dot{m}(\eta) = 1$ and $u(\eta) = 1$, are assumed. The billet is allowed to grow towards the steady state corresponding to $\mu = 1$ for the chosen scanner angle function. The boundary layer heat flow is then computed at points along the steady state surface, upon which the scanner and rotation motions of the spray cone are superimposed to deliver $v(t)$. For this section an averaged mass flux distribution is assumed that corresponds to scanner angles $\alpha_1 \doteq 35°$, $\alpha_2 = 6°$, and to spray cone radius $r_s = 1/3$. The assumed scanner function, and steady state crown shape that corresponds to $\mu = 1$ are both shown in Fig. 6.3. The top of the steady state crown surface is mainly horizontal, with a slight "kink" at $r_1 \approx 1/2$. The scanner angle is the same as in Fig. 3.23. The ratio, ϵ, of rotation timescale to withdrawal timescale, is $\epsilon = 9.6 \times 10^{-4}$. These parameters are representative of those that are used on a production rig.

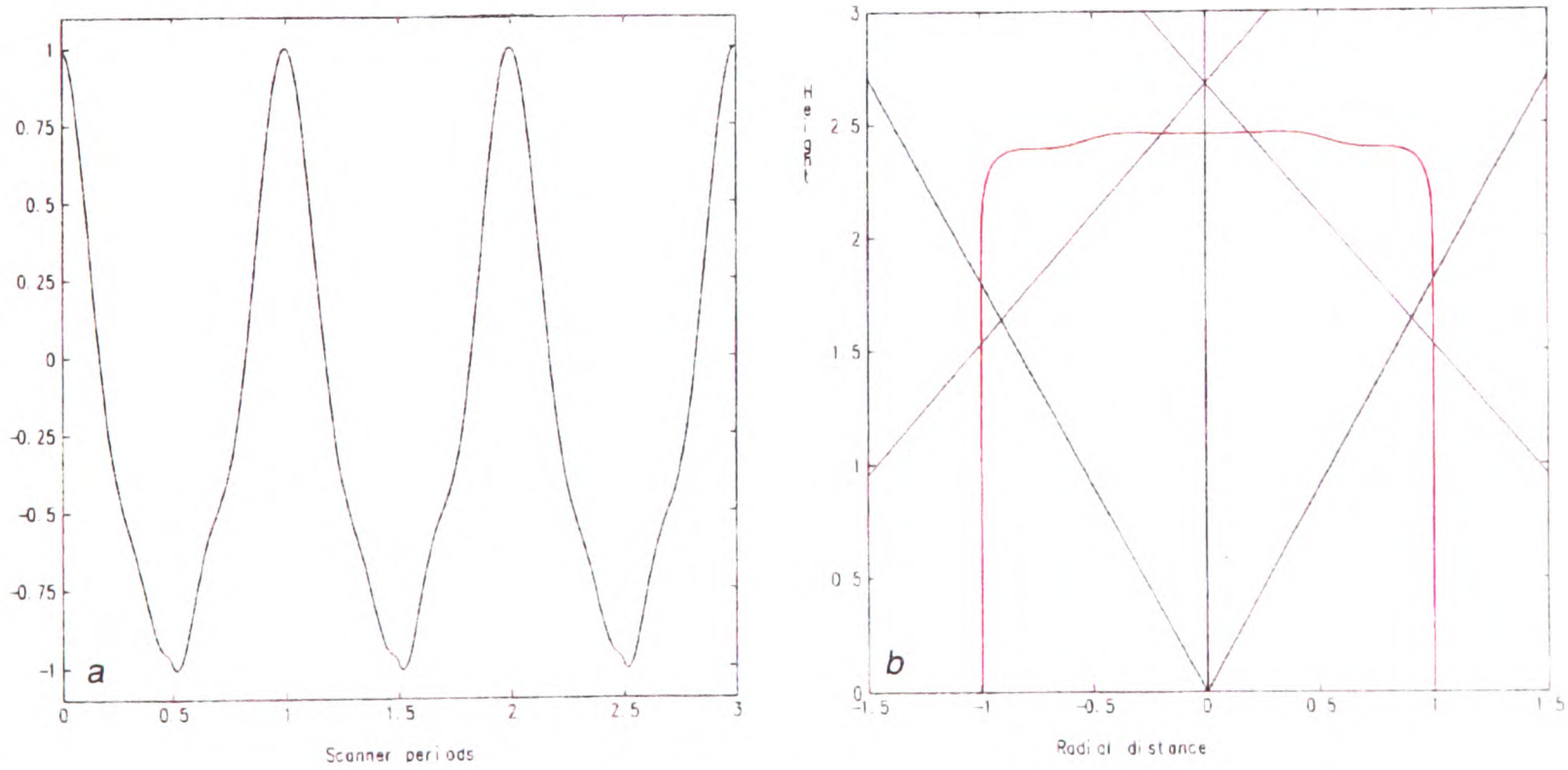

Figure 6.3: a) Scanner angle function, $\alpha(t)$. b) Spray boundaries and steady state produced at $\mu = 1$ with spray cone radius, $r_s = 1/3$, fixed scanning angle, $\alpha_1 = 35°$, and scanning range, $\alpha_2 = 6°$.

Results have been computed for a scanner period $t_s = 5/17$ over a time interval $Dt = 3$, following convergence of the slow-time billet growth to the steady state. Boundary layer heat flow results are shown for radial distances $r_1 = 0$, $1/4$, $1/2$ and $3/4$ from the billet axis of rotation.

In Fig. 6.4 are shown plots of the surface normal velocity $v(t)$, (Figs. 6.4a, b, e & f), and also a comparison of the averaged and instantaneous billet growth in the normal direction, (Figs. 6.4c, d, g & h),

for the four radial distances selected. At all four radial distances the instantaneous velocity pulse is $O_S(1)$, and the averaged normal velocity is

$$\overline{v} \approx .045 = O((\epsilon Pe)^{1/2}).$$

The averaged normal growth for $r_1 = 0$, $1/4$ and $3/4$, (Figs. 6.4c, d & h), is slightly larger than that at $r_1 = 1/2$, (Fig. 6.4g). This is attributable to the slightly sloped surface at $r_1 = 1/2$. In a steady state, all points on the billet crown have vertical velocity $u(\eta)$, but only for those points at which the surface is horizontal does this coincide with the surface normal velocity.

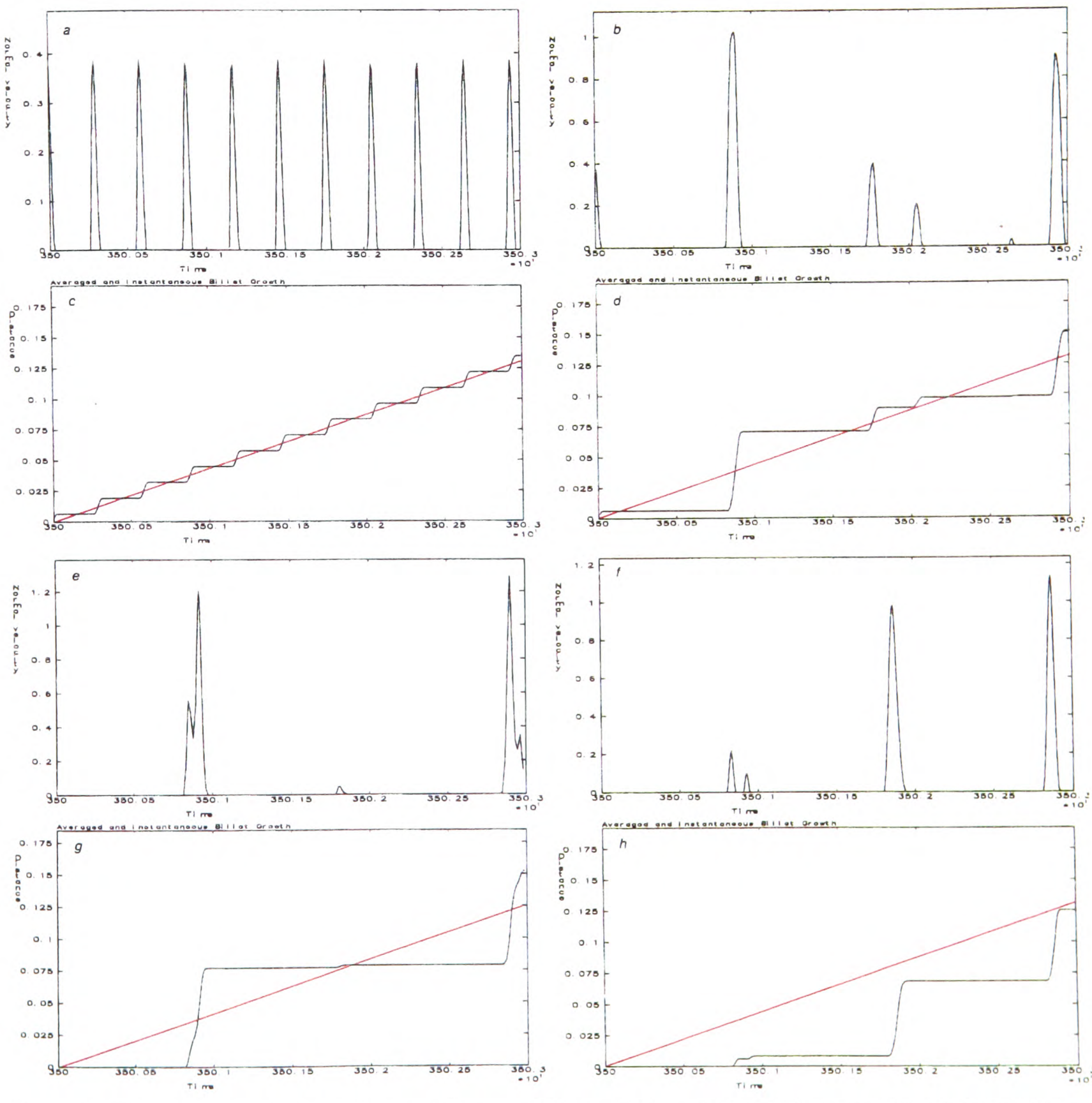

Figure 6.4: Model parameters: $\mu = 1$, $r_s = 1/3$, $\alpha_1 = 35°$, $\alpha_2 = 6°$, $\epsilon = 9.6 \times 10^{-4}$, $t \in [t_1, t_2] = [3500, 3503]$. Surface normal velocity pulse: a) $r_1 = 0$, b) $r_1 = 1/4$, e) $r_1 = 1/2$, f) $r_1 = 3/4$. Comparison of instantaneous, (black), and averaged, (red), normal growth: c) $r_1 = 0$, d) $r_1 = 1/4$, g) $r_1 = 1/2$, h) $r_1 = 3/4$.

Fig. 6.4a shows a series of regular pulses at $r_1 = 0$, smaller and sharper, but less intense, than those

at the larger radial distances. Fig. 6.1a, showing the approximate locus of the spray cone axis, indicates that the spray cone axis never crosses the billet axis. Thus, the smaller velocity pulses result from regular intermittent deposition from the spray cone edge, where the mass flux density is less. The scanner period $t_s = 5/17$ is evident in there being approximately three pulses per time unit.

Fig. 6.4b shows at $r_1 = 1/4$ a pulse pattern of interspersed larger, (≈ 1), and smaller pulses. Interpretation of Fig. 6.4b with Fig. 6.1a indicates the likelihood that at this radial distance the smaller double set of velocity pulses correspond to an azimuthal position on the disc of Fig. 6.1a in the centre of one of the "petal" shapes at $r_1 = 1/4$. Such a position will receive deposition from the outside of the spray cone twice in quick succession. Following the locus in Fig. 6.1a both backwards and forwards, each over one billet rotation, it can be seen that the larger pulses in Fig. 6.4b correspond to deposition at earlier and later times as the centre of the spray cone passes close by. Similar interpretation may be made of the pulse patterns in Figs. 6.4e & f. These positions, further from the billet axis, do not neccessarily receive deposition on every rotation of the billet.

Fig. 6.5 shows the variation in surface temperature, $T(H^n_{1/2})$, for $t \in [t_1, t_2]$ at each of the above radial positions, (Figs. 6.5a, b, e & f), and translates this into the surface fraction liquid, (Figs. 6.5c, d, g & h). Also shown for comparison with the surface temperature is the far field temperature, $T(\overline{H})$, (in red in Figs. 6.5a, b, e & f). Most noticeable in comparing Figs. 6.4 and 6.5 is that the surface temperature transient mimics the surface normal velocity pulse, as is to be expected. However, fluctuations in surface temperature are characterised by sharp rises, due to rapid heating by the metal pulse, followed by slower decays caused by domination of the gas cooling effect as the pulse dies away.

That there is no overall rise in surface temperature with time, but rather an oscillation about the far field temperature, confirms numerically the analysis of chapter five, leading to the definition of $\overline{H}$. The oscillation about $T(\overline{H})$ is characterised by large, sharp increases above the far field temperature occurring on short time intervals interspersed with smaller decreases below the far field temperature, occurring on longer time intervals.

The smaller and more frequent deposition pulses at $r_1 = 0$ result in fluctuations in surface temperature and fraction liquid at the billet centre, that are much less pronounced than the fluctuations occurring at larger radial distances. For example, the peak surface fraction liquid at $r_1 = 0$ is $< 3\%$, (Fig. 6.5c), compared with $> 6\%$ for $r_1 = 1/4$, $1/2$ or $3/4$. As discussed in chapter one, maintenance of a high surface liquid fraction at any point for a significant time period might result in poor material quality, due to fluid instability on the billet surface, (i.e. waves and/or bubbles caused by the atomising gas jets). This radial variation in solidification characteristics might then translate into a noticeable radial porosity variation in the finished billet.

The lower time-averaged growth-rate that was evident at $r_1 = 1/2$ in Fig. 6.4 is reflected by the lower far field temperature in Fig. 6.5e than in Figs. 6.5a, b & f. aluminium alloy 2618 has solidus temperature and freezing range,

$$\hat{T}_s = 541°\mathrm{C}, \tag{6.35}$$

$$\Delta\hat{T} \approx 90°\mathrm{C}. \tag{6.36}$$

Hence, the difference in far field temperature translates dimensionally into a $4 - 5°C$ temperature difference.

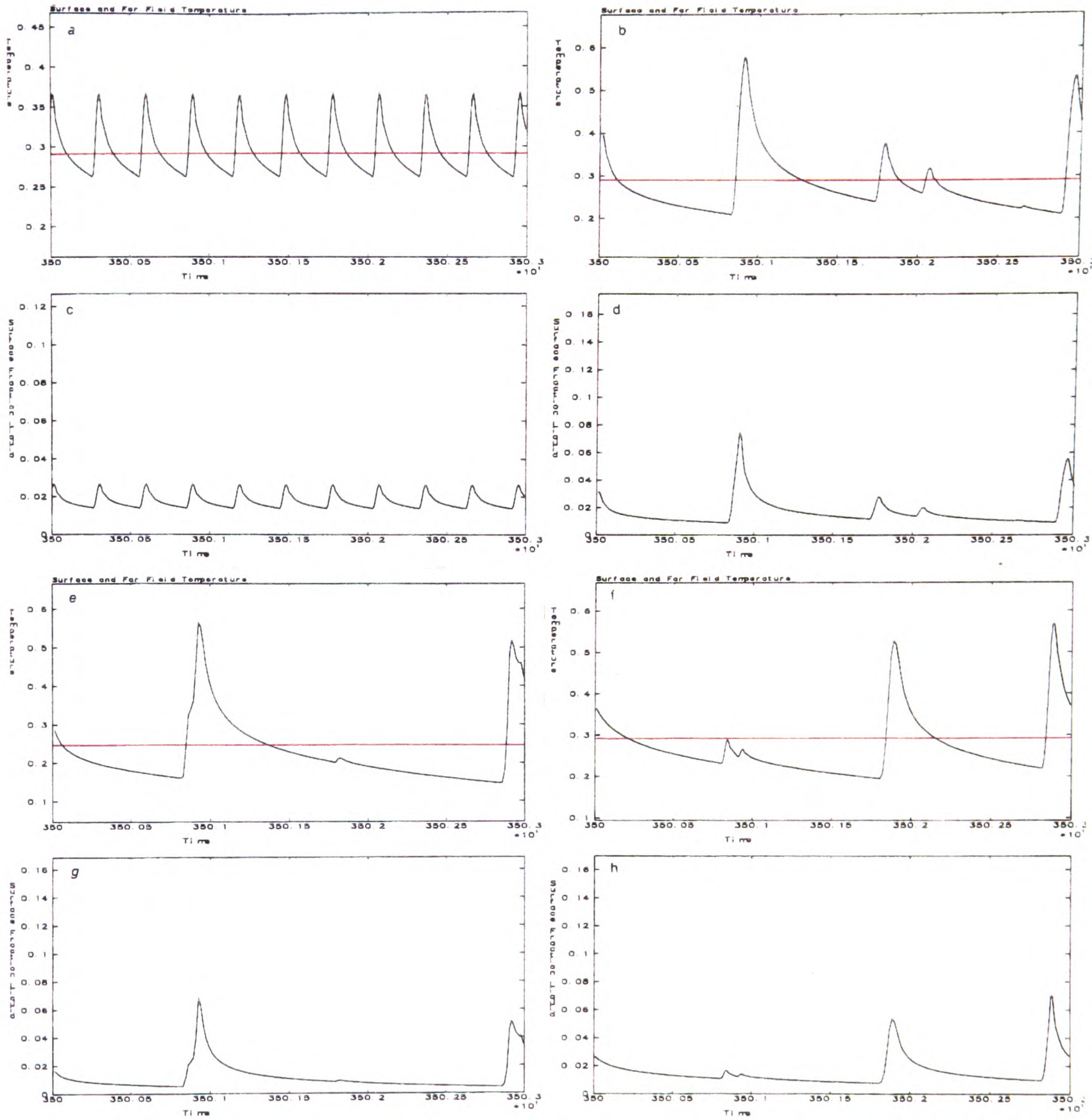

Figure 6.5: Model parameters: $\mu = 1$, $r_s = 1/3$, $\alpha_1 = 35°$, $\alpha_2 = 6°$, $\epsilon = 9.6 \times 10^{-4}$, $t \in [t_1, t_2] = [3500, 3503]$. Comparison of surface, (black), and far field, (red), temperatures: a) $r_1 = 0$, b) $r_1 = 1/4$, e) $r_1 = 1/2$, f) $r_1 = 3/4$. Surface fraction liquid: c) $r_1 = 0$, d) $r_1 = 1/4$, g) $r_1 = 1/2$, h) $r_1 = 3/4$.

Fig. 6.6 plots the under surface isotherms at each of the selected surface points over the time interval $[t_1, t_2]$. The vertical axes in Figs. 6.6a, b, c & d correspond to distance in the direction of the outward surface normal, measured in units of the boundary layer length scale. At $t = t_1$ the positive ζ-axis correponds to the negative coordinate on the vertical axes in Figs. 6.6a, b, c & d. As deposition occurs the boundary layer axis remains fixed to the billet surface in Figs. 6.6a, b, c & d, and the growth is illustrated. The vertical graph axes in Figs. 6.6a, b, c & d, thus represent fixed material positions in the billet, measured in a direction normal to the growing billet surface.

In Figs. 6.6a, b, c & d the isotherms are drawn using only the values of H_j^n for which $\zeta_j \in [0, 2]$, although the computation uses values $\zeta_j \in [0, 3]$. For $\zeta \in [2, 3]$ there is very little of interest happening. The billet

surface is represented in Figs. 6.6a, b, c & d by a shaded block of width $\frac{1}{2}\Delta\zeta$ at $\zeta = 0$, between times t^n and t^{n+1}. This then obscures any isotherms extended into the region $\zeta \in [-\frac{1}{2}\Delta\zeta, 0]$, (where the value of H_0^n has been used in the contouring subroutine), and also shows the variation in timestep used during the computation, when $v(t) > 0$.

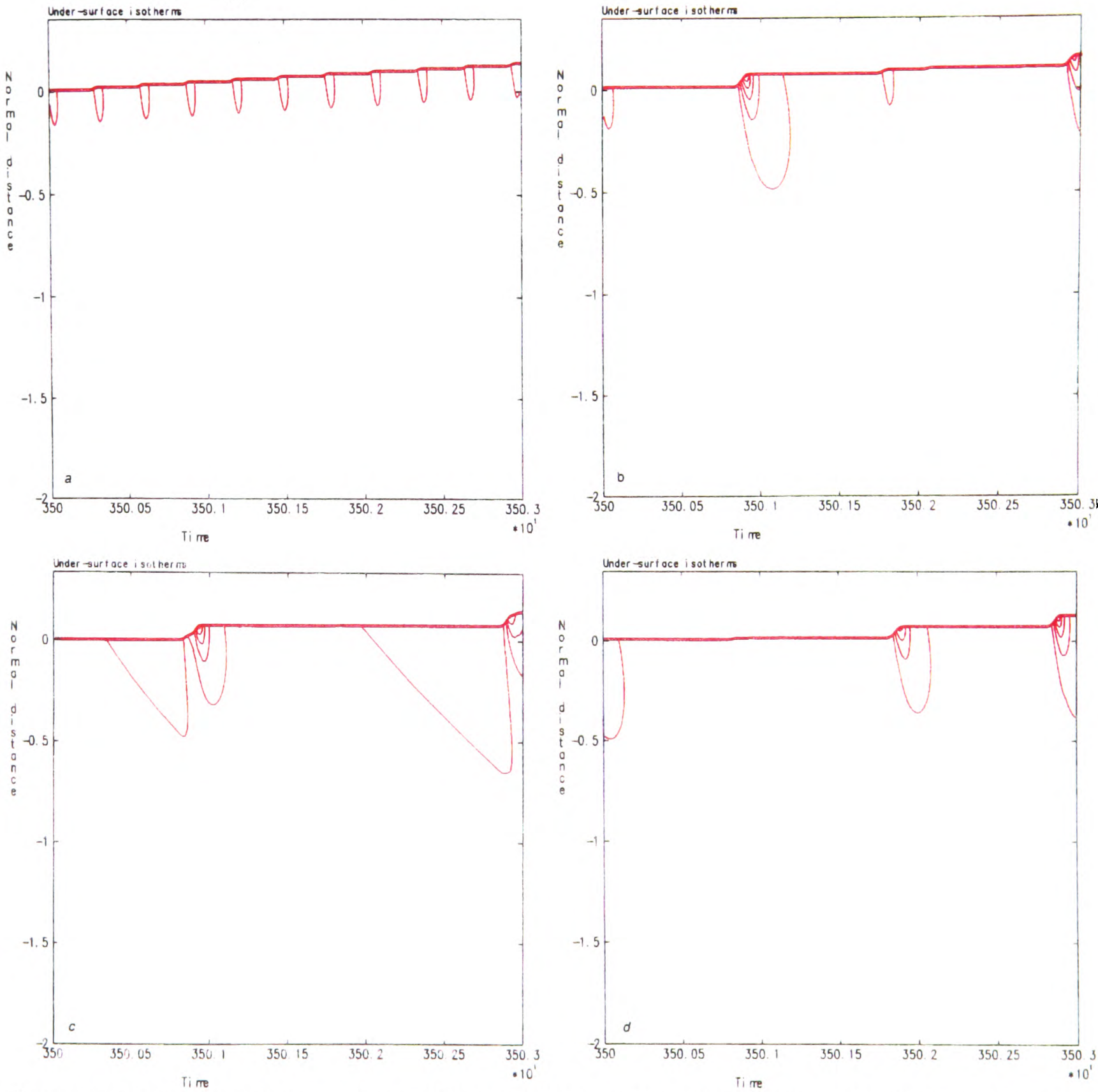

Figure 6.6: Model parameters: $\mu = 1$, $r_s = 1/3$, $\alpha_1 = 35°$, $\alpha_2 = 6°$, $\epsilon = 9.6 \times 10^{-4}$, $t \in [t_1, t_2] = [3500, 3503]$. Under surface isotherms: a) $r_1 = 0$, b) $r_1 = 1/4$, c) $r_1 = 1/2$, d) $r_1 = 3/4$. Colour code: red $\Rightarrow$ 1% fraction liquid intervals, green $\Rightarrow$ solidus line, blue $\Rightarrow$ intervals of 5% of temperature freezing range below solidus temperature.

Isotherms in Figs. 6.6a, b, c & d, (and in similar figures to follow subsequently), are coloured red, blue or green. The red isotherms represent successive increments of 1% liquid fraction, the green isotherm is the solidus isotherm and blue isotherms represent successive negative temperature increments of 5% of the freezing range, below the solidus temperature. Used in conjunction with the surface liquid fraction plots of

Fig. 6.5, the isotherms are easily identified.

At the billet centre, Fig. 6.6a, the small rapid deposition pulses result in small regular penetration of the 1% isotherm into the billet. At greater radial distances, Figs. 6.6b, c & d, show that the larger surface temperature variations seen in Fig. 6.5 also result in deeper pulse penetration; compare a maximum 1% liquid fraction isotherm penetration of $\zeta \approx .15$ at the billet centre with $\zeta \approx .5$ at the other surface points.

6.3 Changes in crown shape

To examine in more detail the sorts of changes in heat flow that may result from underlying changes in billet crown shape, similar computations to the above have been carried out using the same scanner angle function $\alpha(t)$ as in Fig. 6.3a and with the same scanner fixed angle, $\alpha_1 = 35°$, but with scanner angle ranges, $\alpha_2 = 3°$ & $9°$. Spray cone radius is kept at $r_s = 1/3$. Constant mass flow rates and withdrawal rates, $\dot{m}(\eta) = 1$ and $u(\eta) = 1$, are again assumed and the billet is allowed to grow towards the steady state corresponding to $\mu = 1$ for each scanner angle function. In both cases the rotation rate and scanner period are kept at the same values as in the previous section, i.e. $\epsilon = 9.6 \times 10^{-4}$, $t_s = 5/17$.

Fig. 6.7 shows the steady state crown shapes for $\mu = 1$ corresponding to the two different values of α_2. The steady state corresponding to $\alpha_2 = 3°$ is concave, that corresponding to $\alpha_2 = 9°$ is convex. Both steady states exhibit large variations in surface gradient with radial distance from the billet axis of rotation.

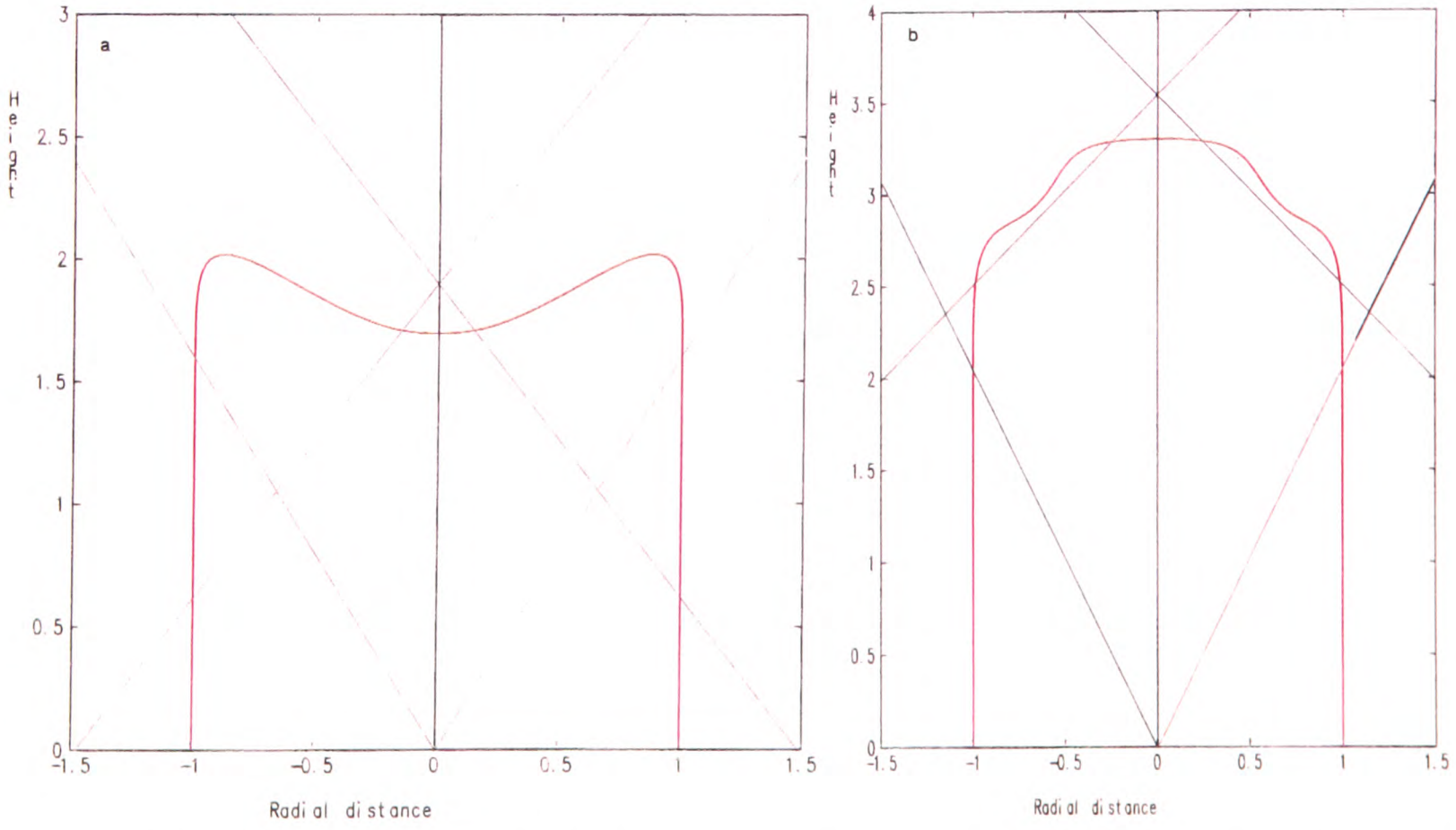

Figure 6.7: Model parameters: $\mu = 1$, $r_s = 1/3$, $\alpha_1 = 35°$. Spray boundaries and steady state shapes; a) $\alpha_2 = 3°$, b) $\alpha_2 = 9°$.

The boundary layer heat flow is computed at points along the steady state surfaces over same time interval as in the previous section, of length $Dt = 3$, and at radial distances $r_1 = 0$, $1/4$, $1/2$ and $3/4$.

Fig. 6.8 shows the variation in far field temperature, surface temperature and surface fraction liquid, for

$t \in [t_1, t_2]$ at each radial positions with $\alpha_2 = 3°$.

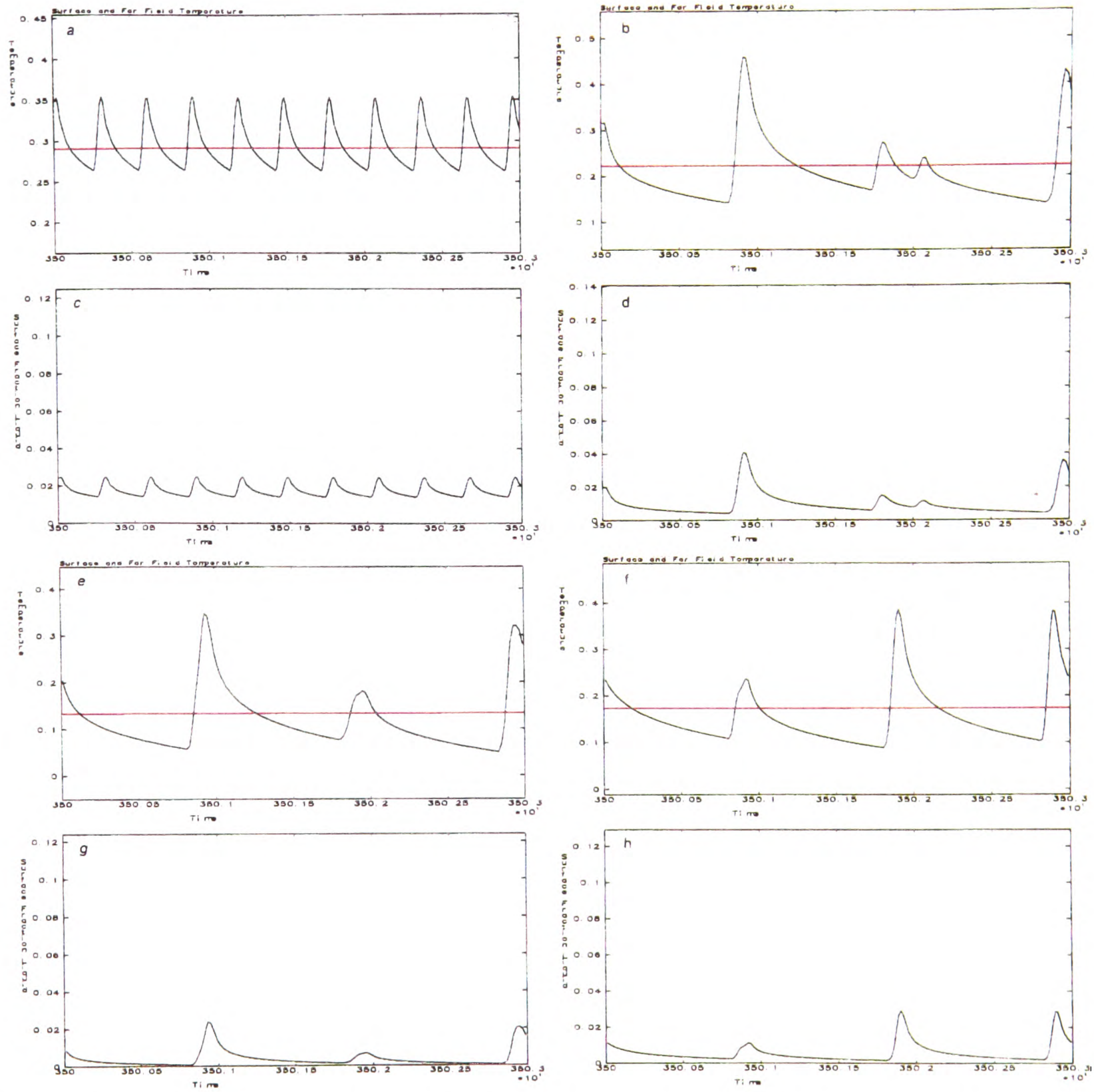

Figure 6.8: Model parameters: $\mu = 1$, $r_s = 1/3$, $\alpha_1 = 35°$, $\alpha_2 = 3°$, $\epsilon = 9.6 \times 10^{-4}$, $t \in [t_1, t_2] = [3500, 3503]$. Comparison of surface, (black), and far field, (red), temperatures: a) $r_1 = 0$, b) $r_1 = 1/4$, e) $r_1 = 1/2$, f) $r_1 = 3/4$. Surface fraction liquid: c) $r_1 = 0$, d) $r_1 = 1/4$, g) $r_1 = 1/2$, h) $r_1 = 3/4$.

The billet centre position, $r_1 = 0$, (Figs. 6.8a & c), exhibits a very similar heat flow to that for the 6° scan considered in the previous section. Frequency, amplitude and shape of the surface temperature and fraction liquid fluctuations are similar, as is the far field temperature. Identical far field temperature is to be expected because of the identical surface gradient and averaged growth rate.

Further from the billet axis of rotation the small, regular, frequent pulses at $r_1 = 0$ are replaced by larger and more irregular fluctuations in surface temperature, (Figs. 6.8b, e & f), and surface fraction liquid, (Figs. 6.8d, g & h). Most noticeable in Figs. 6.8b, e & f however, is the radial variation in far field temperature about which the surface temperature fluctuations occur. The lowest far field temperature, in Fig. 6.8e at

$r_1 = 1/2$, corresponds to the smallest averaged surface normal velocity, indicated by the steepest surface gradient there, (see Fig. 6.7a).

In comparison with Fig. 6.5, (resulting from a nearly horizontal steady billet crown), away from the billet axis of rotation the smaller averaged surface normal velocities implied by the steeper gradients of the concave steady state result in lower far field temperatures. This effect is also felt on the instantaneous surface normal velocity, as is evidenced by the smaller fluctuations in surface temperature about the far field temperatures in Figs. 6.8b, e & f, compared with Figs. 6.5b, e & f.

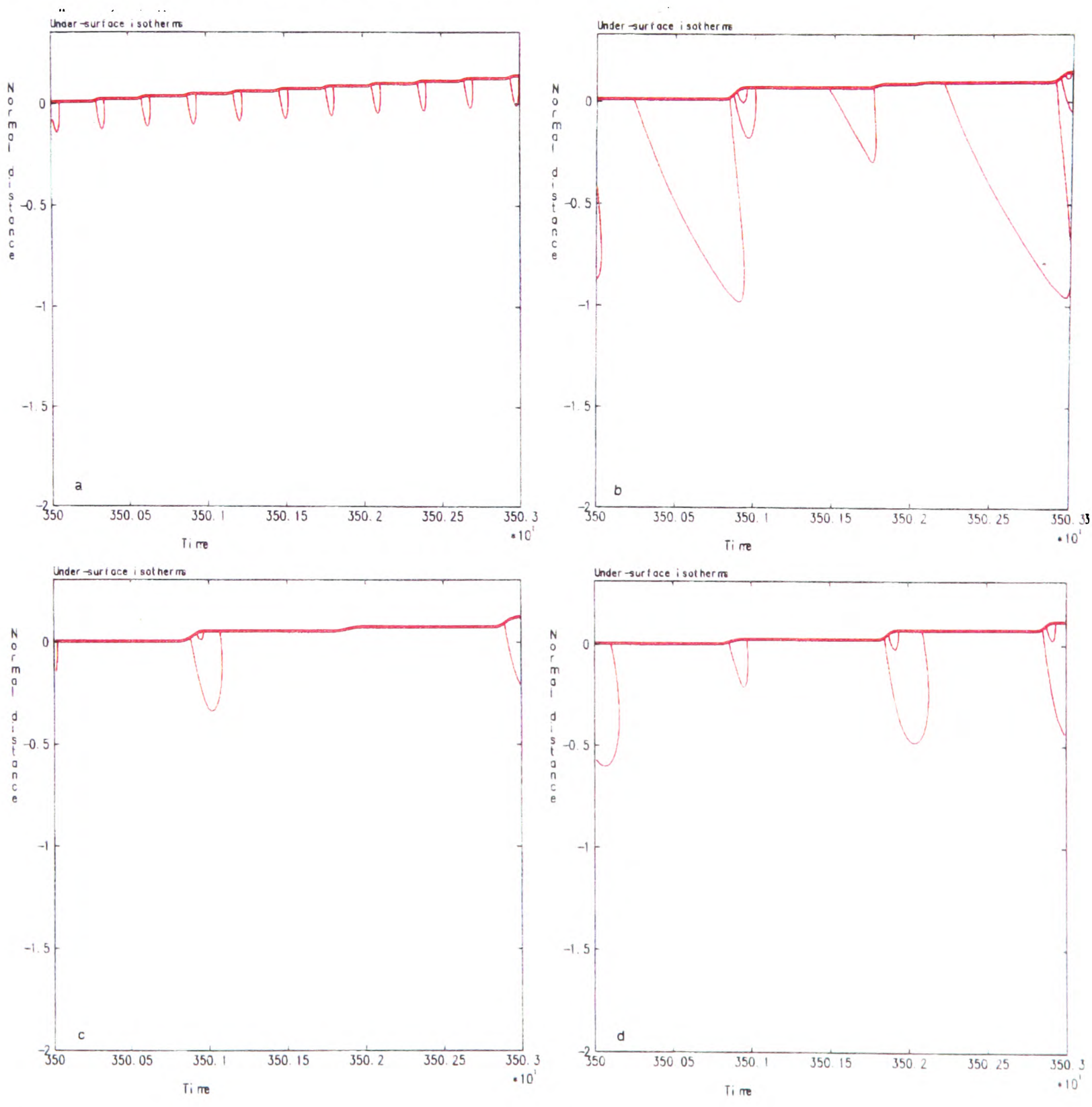

Figure 6.9: Model parameters: $\mu = 1$, $r_s = 1/3$, $\alpha_1 = 35°$, $\alpha_2 = 3°$, $\epsilon = 9.6 \times 10^{-4}$, $t \in [t_1, t_2] = [3500, 3503]$. Under surface isotherms: a) $r_1 = 0$, b) $r_1 = 1/4$, c) $r_1 = 1/2$, d) $r_1 = 3/4$. Colour code: red $\Rightarrow$ 1% fraction liquid intervals, green $\Rightarrow$ solidus line, blue $\Rightarrow$ intervals of 5% of temperature freezing range below solidus temperature.

Under surface isotherms corresponding to the 3° scanning range have been plotted in Fig. 6.9 for each

of the radial distances. The billet centre has very similar solidification behaviour to that plotted for the 6° scanning range in Fig. 6.6a. At other surface points the penetration distance of the coldest isotherms under the surface is similar to the 6° scanning range, but the fluctuations occurring nearer the surface are of smaller amplitude.

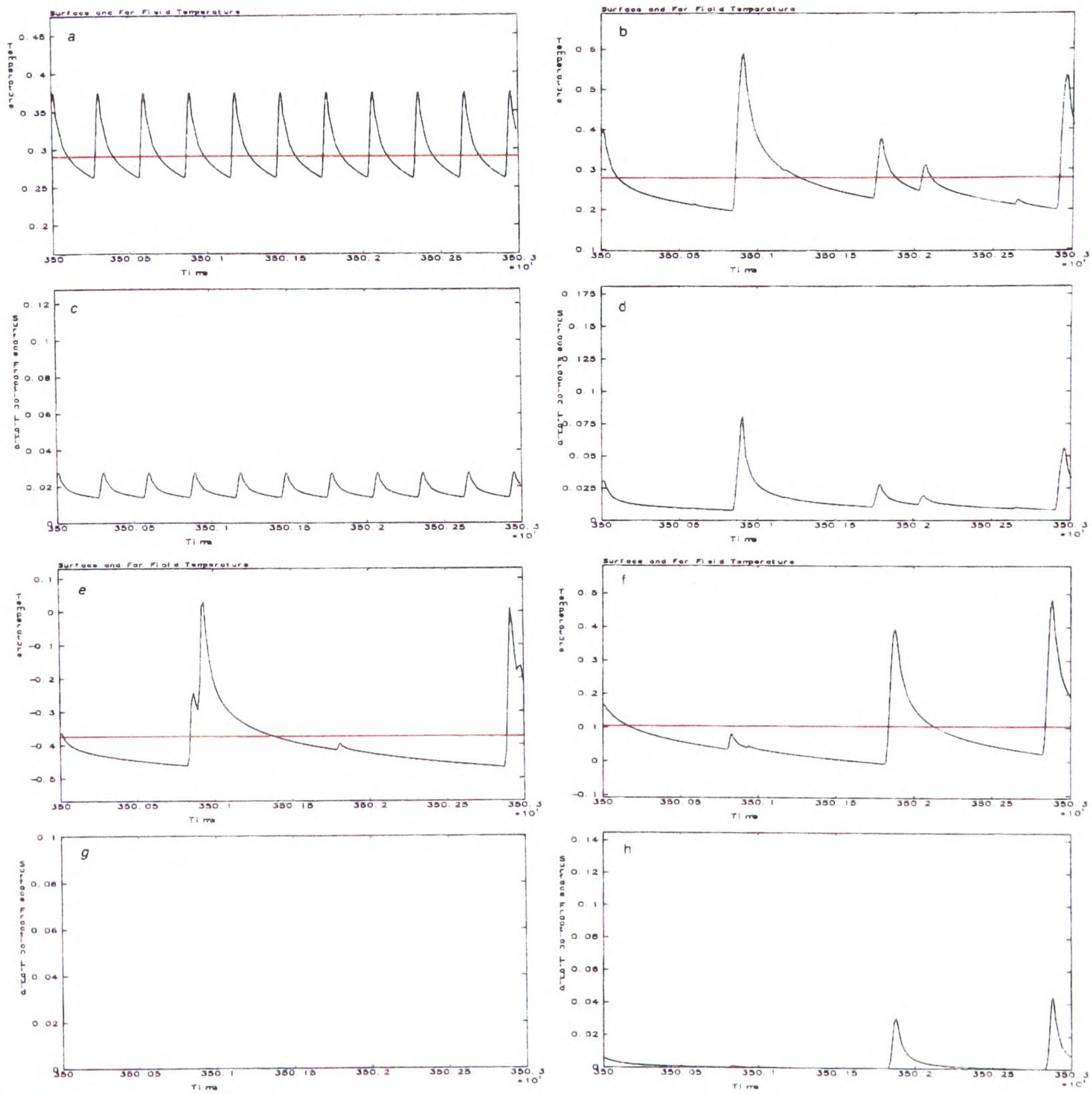

Figure 6.10: Model parameters: $\mu = 1$, $r_s = 1/3$, $\alpha_1 = 35°$, $\alpha_2 = 9°$, $\epsilon = 9.6 \times 10^{-4}$, $t \in [t_1, t_2] = [3500, 3503]$. Comparison of surface, (black), and far field, (red), temperatures: a) $r_1 = 0$, b) $r_1 = 1/4$, e) $r_1 = 1/2$, f) $r_1 = 3/4$. Surface fraction liquid: c) $r_1 = 0$, d) $r_1 = 1/4$, g) $r_1 = 1/2$, h) $r_1 = 3/4$.

For the 9° scanning range, surface temperature and fraction liquid variations, together with far field temperatures, are plotted in Fig. 6.10. At $r_1 = 0$ and $r_1 = 1/4$ the steady state in Fig. 6.7b is nearly horizontal. Comparison of Figs. 6.10a, b, c & d with Figs. 6.5a, b, c & d shows little difference. In contrast, at $r_1 = 1/2$ and $r_1 = 3/4$ the gradient of the steady state in Fig. 6.7b is very steep. Although the transient surface temperature pulse shapes in Figs. 6.10e & f are similar to those in Figs. 6.5e & f, (indicating similar

surface normal velocity pulse patterns), the far field temperatures are much lower.

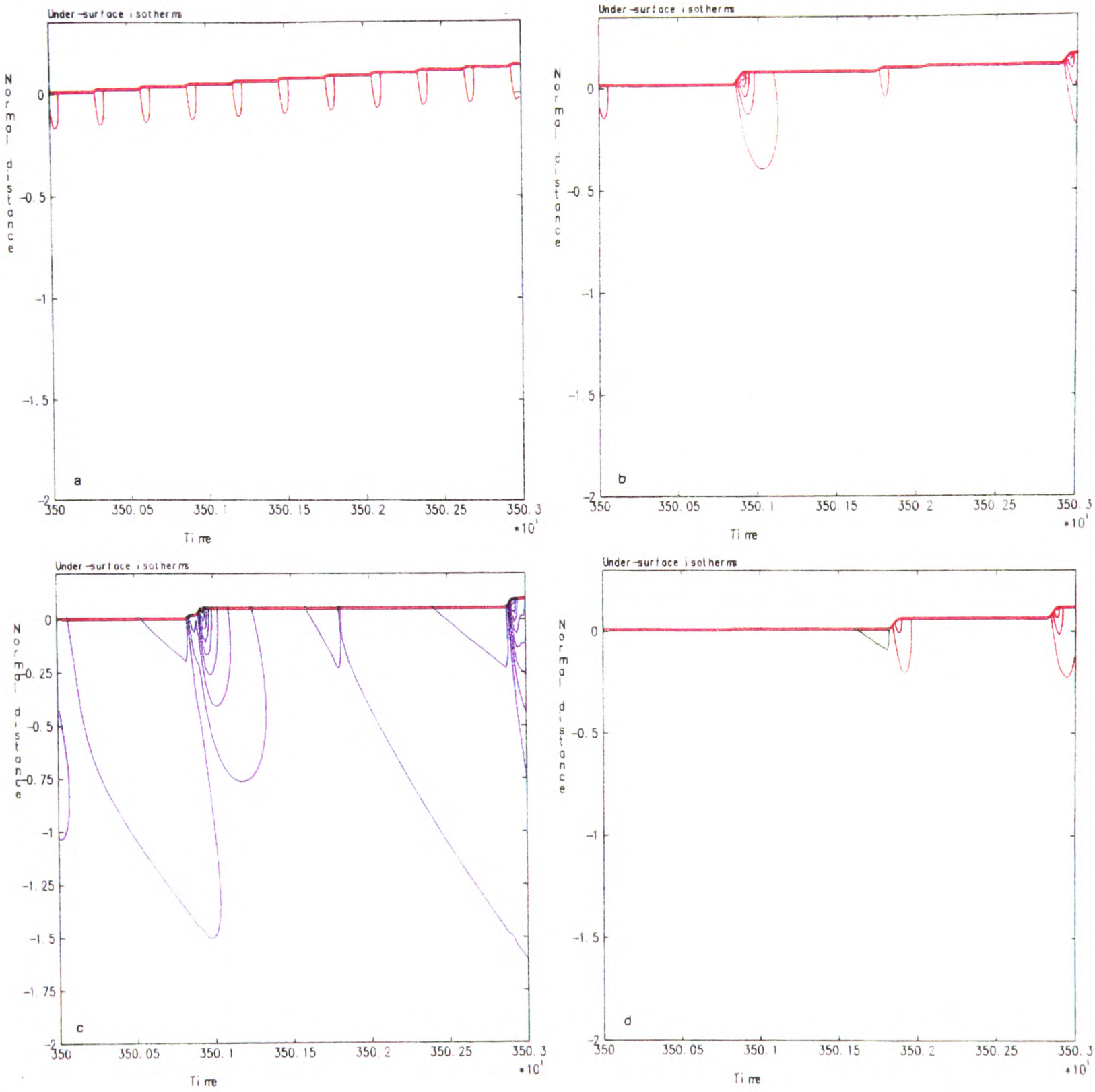

Figure 6.11: Model parameters: $\mu = 1, r_s = 1/3, \alpha_1 = 35°, \alpha_2 = 9°, \epsilon = 9.6 \times 10^{-4}, t \in [t_1, t_2] = [3500, 3503]$. Under surface isotherms: a) $r_1 = 0$, b) $r_1 = 1/4$, c) $r_1 = 1/2$, d) $r_1 = 3/4$. Colour code: red $\Rightarrow$ 1% fraction liquid intervals, green $\Rightarrow$ solidus line, blue $\Rightarrow$ intervals of 5% of temperature freezing range below solidus temperature.

This difference is further exemplified by study of the under surface isotherms, see Fig. 6.11. Figs. 6.11a & b are very similar to Figs. 6.6a & b. The greatest contrast is between Figs. 6.11c and 6.6c. In the former case the boundary layer is completely solid. Temperature fluctuations occur between the solidus temperature and approximately $.4 \times \Delta\hat{T}$ below the solidus temperature. This is compared with fluctuations corresponding to $\approx 7\%$ of liquid fraction in Fig. 6.6c. This change, due to surface shape change, seems very drastic when measured in terms of the temperature drop. However, since the ratio of latent of solidification

to specific heat is

$$\frac{L}{c_p \Delta \hat{T}} \approx 4,$$

it can be seen that similar levels of energy fluctuation are taking place in the two cases. Penetration of the isotherms in Fig. 6.11c is particularly deep. This might be attributable to the higher thermal conductivity of the solid phase.

In order to explain the similarity in the results closer to the billet axis of rotation, the loci of the point of interception of the spray cone axis with a horizontal fixed unit disc, ($\approx$ steady state crown), are shown in Fig. 6.12 for each of the two scanning ranges in this section. The disc height is fixed by the height of each of the steady state crown shapes in Fig. 6.7. Close to the billet axis, where the steady states are nearly horizontal, this gives a good representation of the loci of the point of interception of the spray cone axis with the billet surface. It can be seen that at $r_1 = 0$ and $r_1 = 1/4$ the loci will be quite similar.

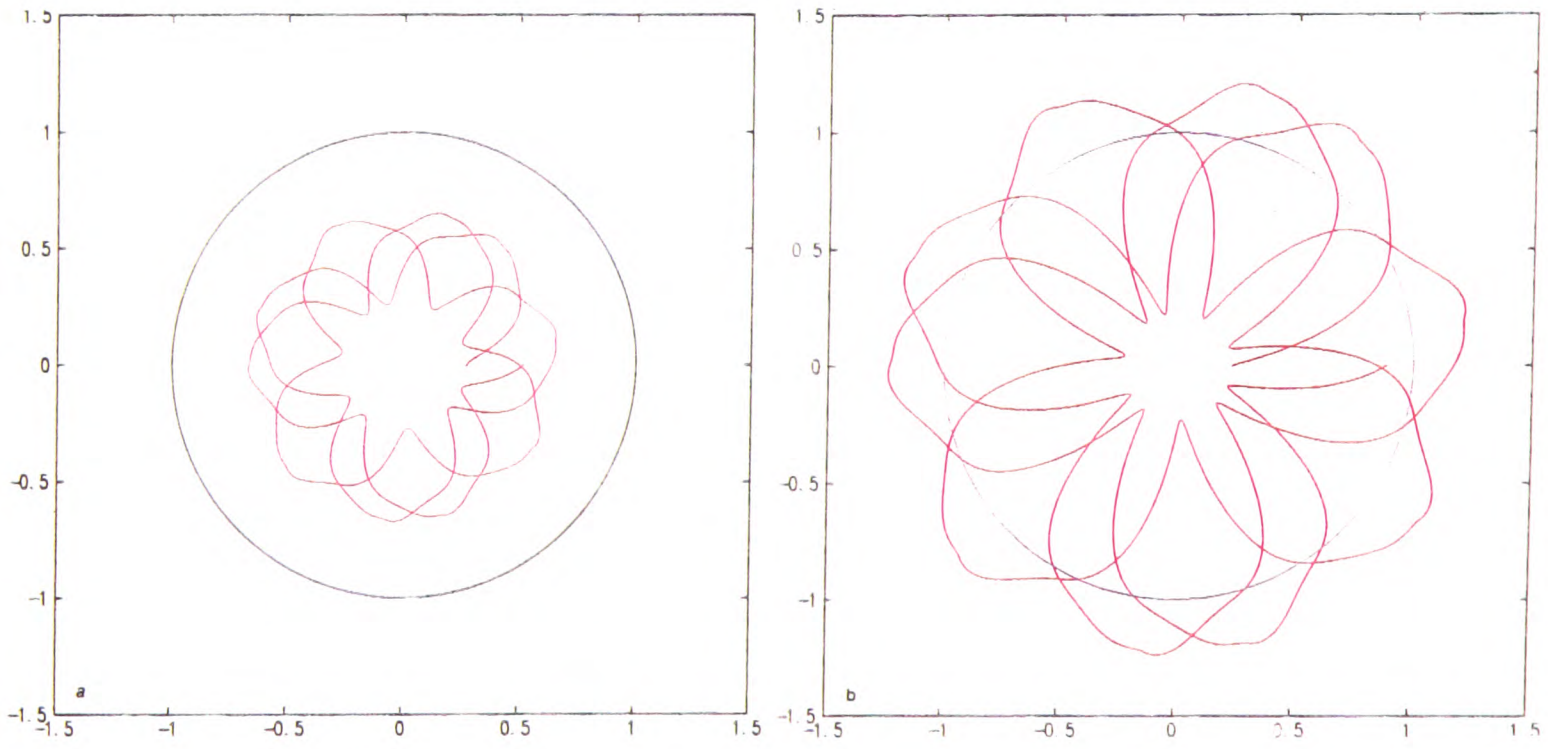

Figure 6.12: Loci of the point of interception of the spray cone axis with a fixed horizontal unit disc, $\alpha_1 = 35°$, $t \in [0, 3]$, $t_s = 5/17$; a) $\alpha_2 = 3°$, b) $\alpha_2 = 9°$.

6.4 Changing rotation and scanner frequencies

Effects of varying rotation and scanner frequencies on model behaviour have not yet been explored. Clearly any variation in either scanner or rotation frequency alone will change the velocity pulse pattern experienced at any particular surface point. The range of possible different velocity pulse patterns will be inexhaustable, and exploration of this variation is unlikely to be productive.

Changing the rotation and scanner frequencies has the effect of either shortening or lengthening both the typical velocity pulse duration and the typical interval between pulses. In order to explore this effect in isolation, (i.e. without also changing the way the scanner and rotation motions interact), both scanner and rotation frequencies are changed together. In the model, this has the effect of varying the ratio, ϵ, of rotation timescale to withdrawal timescale, whilst leaving all other parameters unchanged. In this section, unchanged model parameters are $r_s = 1/3$, $\alpha_1 = 35°$, $\alpha_2 = 6°$, $u(\eta) = 1$, $\dot{m}(\eta) = 1$, $t_s = 5/17$.

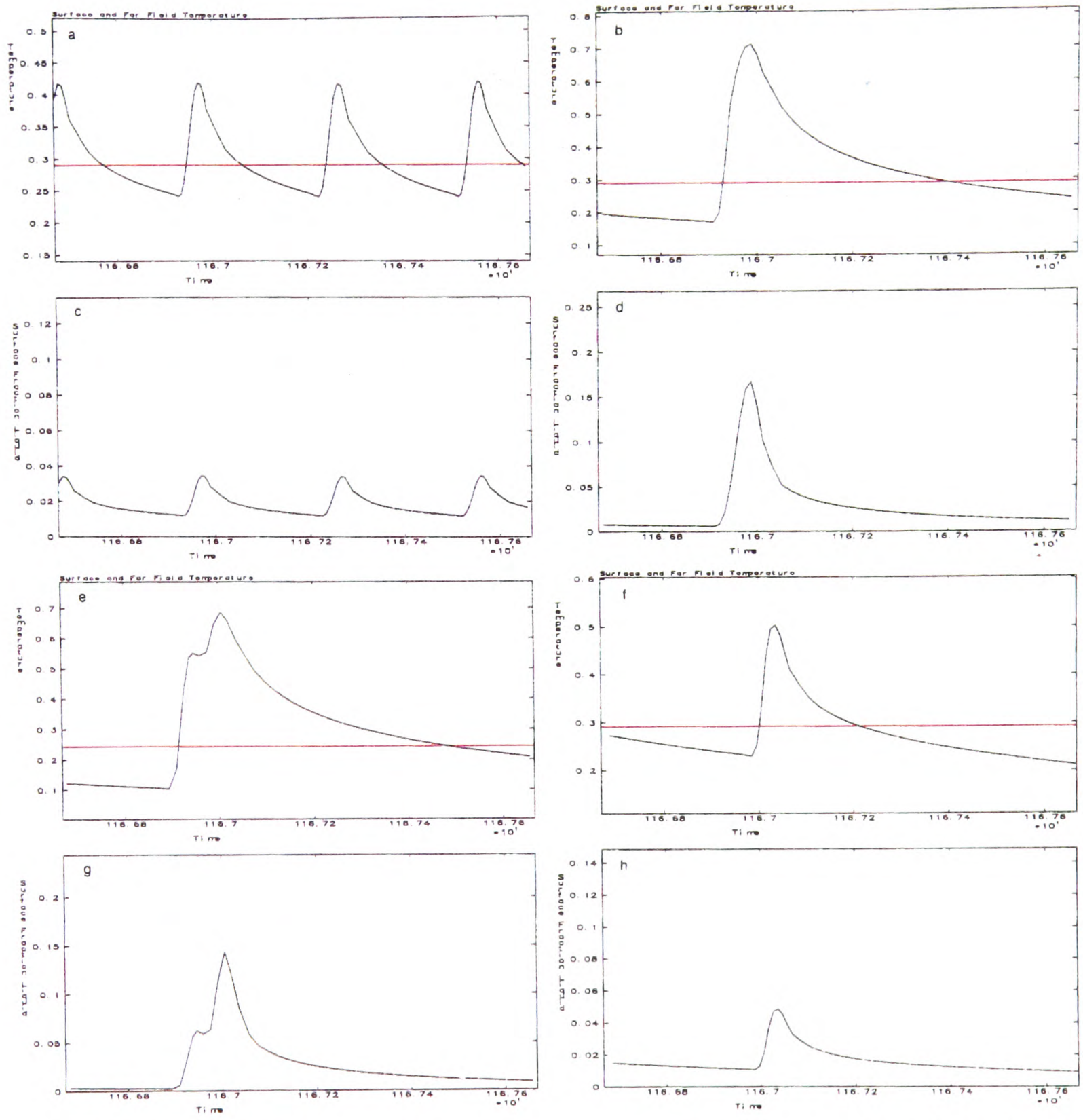

Figure 6.13: Model parameters: $\mu = 1$, $r_s = 1/3$, $\alpha_1 = 35°$, $\alpha_2 = 6°$, $\epsilon = 2.88 \times 10^{-3}$, $t \in [t_1, t_2] = [1166.67, 1167.67]$. Comparison of surface, (black), and far field, (red), temperatures: a) $r_1 = 0$, b) $r_1 = 1/4$, e) $r_1 = 1/2$, f) $r_1 = 3/4$. Surface fraction liquid: c) $r_1 = 0$, d) $r_1 = 1/4$, g) $r_1 = 1/2$, h) $r_1 = 3/4$.

The scanner angle function, $\alpha(t)$, in Fig. 6.3a is used and the billet is again allowed to grow towards the steady state of Fig. 6.3b before the boundary layer equations are integrated. The results in section 6.2 were for $\epsilon = 9.6 \times 10^{-4}$; two further values of ϵ are examined in this section;

$$\epsilon = 2.88 \times 10^{-3},$$

$$\epsilon = 3.2 \times 10^{-4}.$$

The larger value of ϵ is three times larger than the value of ϵ used in sections 6.2 and 6.3, whilst the smaller value of ϵ is three times smaller than the value in sections 6.2 and 6.3. Variation of ϵ has two effects on the physical interpretation of results from the boundary layer approximation. Firstly, the physical timescale is proportional to ϵ. Secondly, the physical length-scale is proportional to $\epsilon^{1/2}$.

In the following computations the same physical time interval is retained for both values of ϵ. Whilst the time interval in sections 6.2 and 6.3 corresponded to three billet rotation periods, the same time interval will correspond to one and nine rotation periods for $\epsilon = 2.88 \times 10^{-3}$ and $\epsilon = 3.2 \times 10^{-4}$ respectively. For plots of the under-surface isotherms, the physical length-scale corresponding to $\epsilon = 2.88 \times 10^{-3}$ will be three times that corresponding to $\epsilon = 3.2 \times 10^{-4}$.

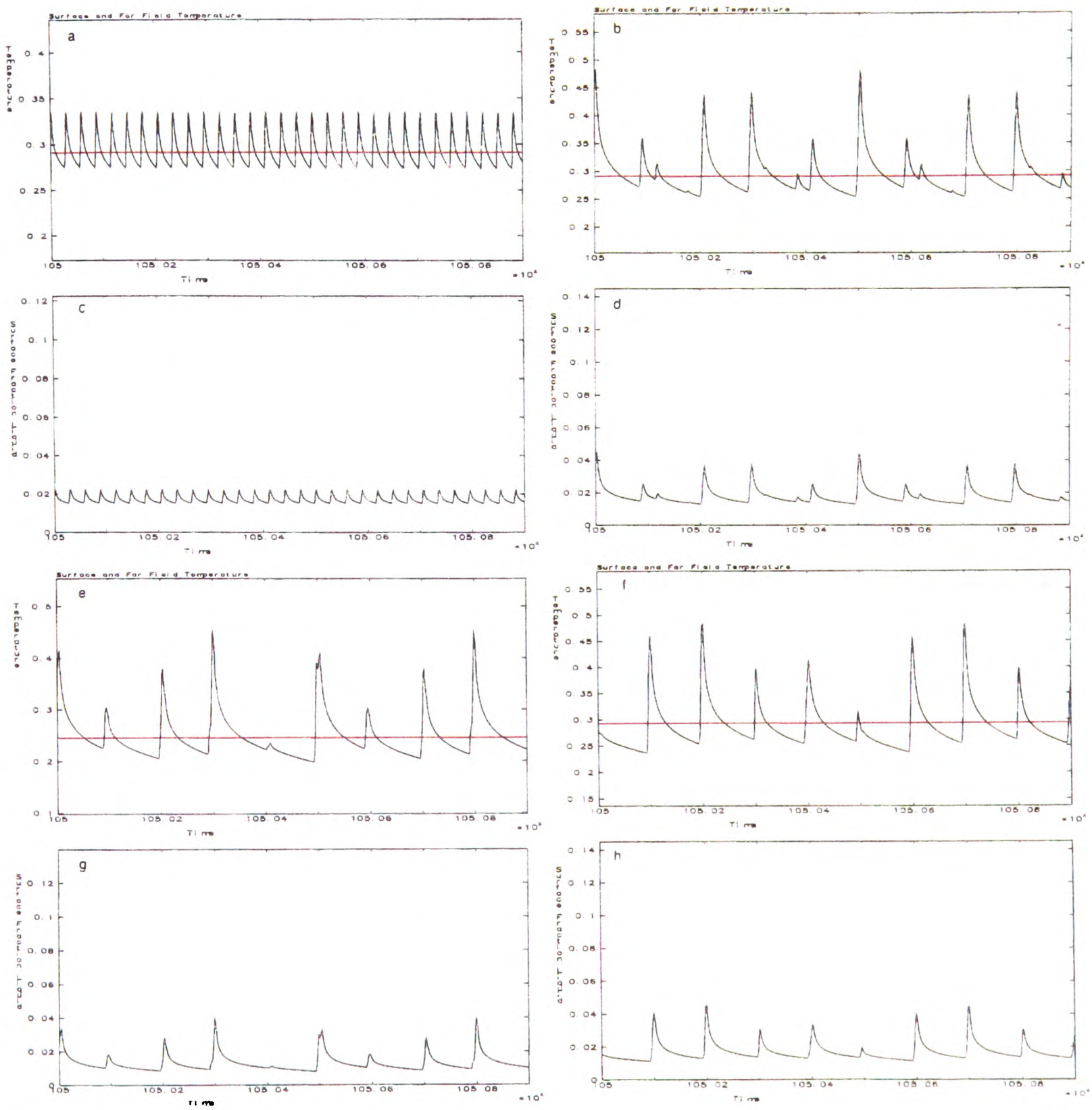

Figure 6.14: Model parameters: $\mu = 1$, $r_s = 1/3$, $\alpha_1 = 35°$, $\alpha_2 = 6°$, $\epsilon = 3.2 \times 10^{-4}$, $t \in [t_1, t_2] = [10500, 10509]$. Comparison of surface, (black), and far field, (red), temperatures: a) $r_1 = 0$, b) $r_1 = 1/4$, e) $r_1 = 1/2$, f) $r_1 = 3/4$. Surface fraction liquid: c) $r_1 = 0$, d) $r_1 = 1/4$, g) $r_1 = 1/2$, h) $r_1 = 3/4$.

Fig. 6.13 shows the variation in far field temperature, surface temperature and surface fraction liquid at radial positions $r_1 = 0$, $1/4$, $1/2$ and $3/4$ for $\epsilon = 2.88 \times 10^{-3}$. Fig. 6.14 shows the variation in far field temperature, surface temperature and surface fraction liquid at radial positions $r_1 = 0$, $1/4$, $1/2$ and $3/4$ for $\epsilon = 3.2 \times 10^{-4}$. Figs. 6.13 & 6.14 can be compared with Fig. 6.5, ($\epsilon = 9.6 \times 10^{-4}$). The far field

temperatures are the same for the three different values of ϵ, at each radial position. Far field temperatures are determined by the solution of (6.11) and this does not change with ϵ.

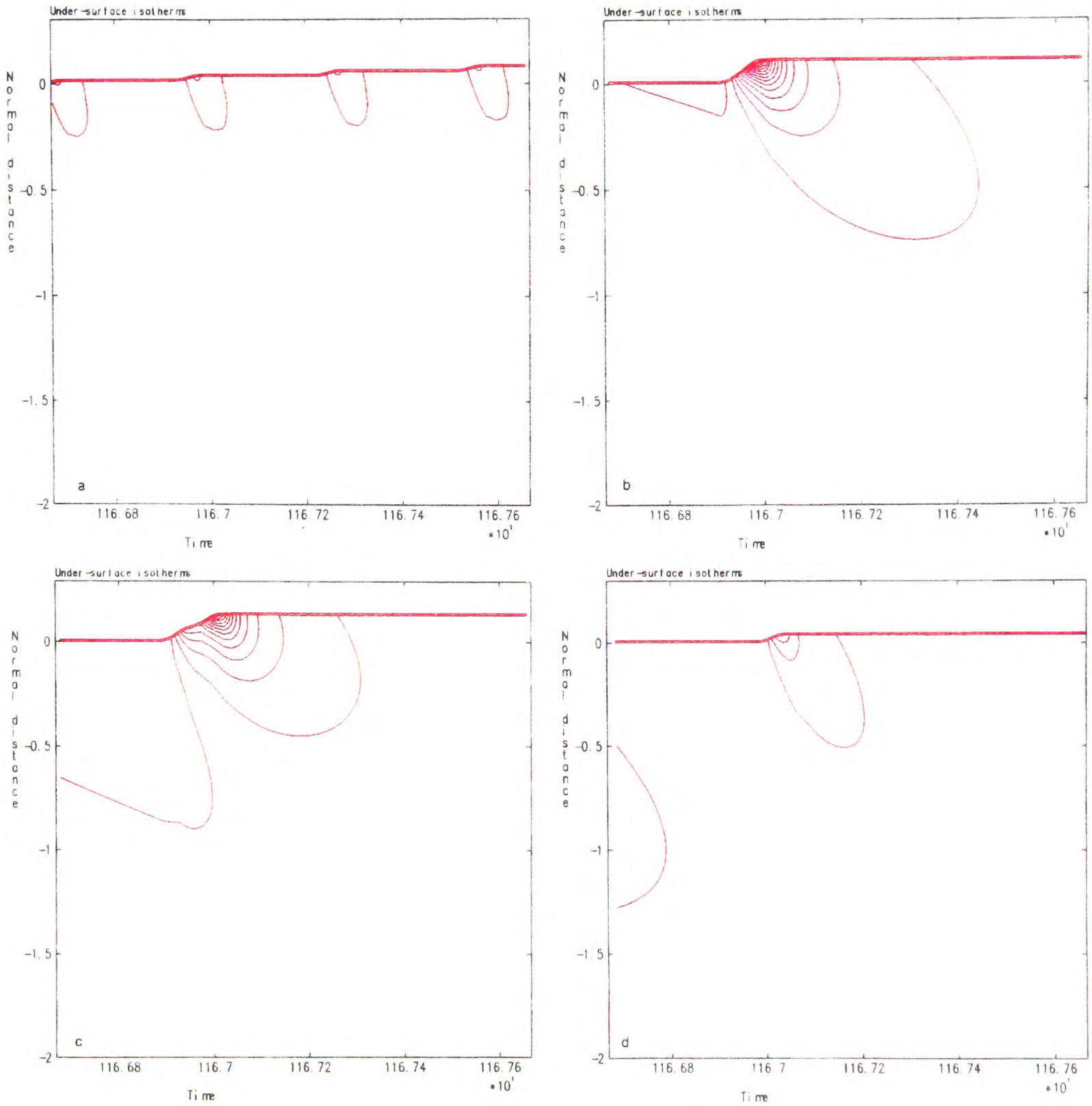

Figure 6.15: Model parameters: $\mu = 1$, $r_s = 1/3$, $\alpha_1 = 35°$, $\alpha_2 = 6°$, $\epsilon = 2.88 \times 10^{-3}$, $t \in [t_1, t_2] = [1166.67, 1167.67]$. Under surface isotherms: a) $r_1 = 0$, b) $r_1 = 1/4$, c) $r_1 = 1/2$, d) $r_1 = 3/4$. Colour code: red $\Rightarrow$ 1% fraction liquid intervals, green $\Rightarrow$ solidus line, blue $\Rightarrow$ intervals of 5% of temperature freezing range below solidus temperature.

The different rotation and scanner rates of Figs. 6.13 and 6.14 have most effect on the fluctuating surface temperature and fraction liquid transients. In Fig. 6.13, at each radial position, the pulses are less frequent and of a larger amplitude than the corresponding pulses in Fig. 6.14. The drop in peak surface fraction liquid with ϵ is very noticeable. The lower rotation and scanner frequencies also allow higher fractions of liquid to persist on the billet surface for significantly longer periods of time; hence increasing the likelihood of fluid instabilities occurring.

Figs. 6.15 and 6.16 show the under surface isotherms at the four radial distances for the two values of ϵ. Comparison of the two figures reveals that the effect of changing rotation and scanner rates is not confined to the billet surface. Since the physical length-scale in Fig. 6.15 is three times that of Fig. 6.16, the results show that the penetration depth increases significantly with ϵ.

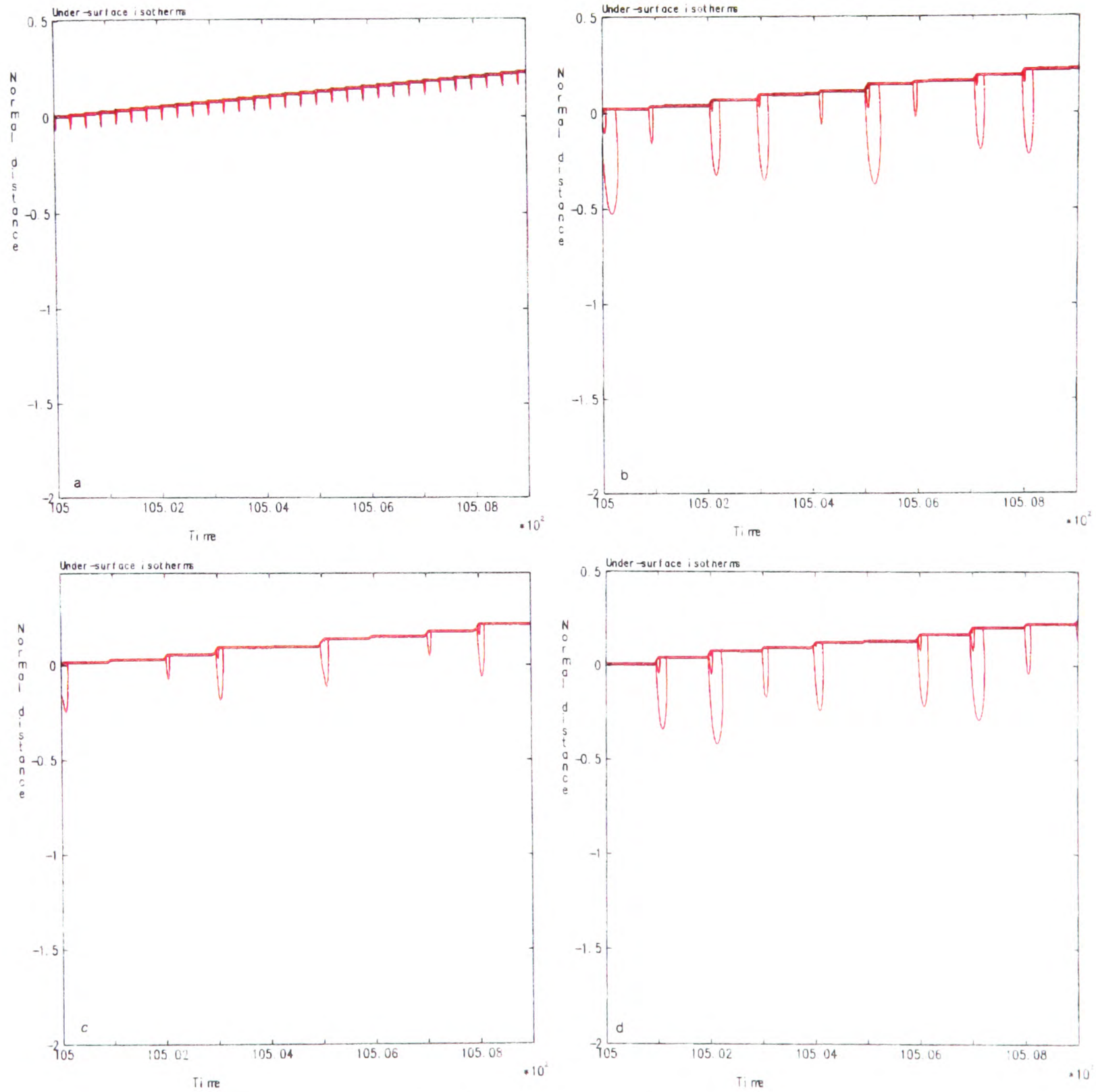

Figure 6.16: Model parameters: $\mu = 1$, $r_s = 1/3$, $\alpha_1 = 35°$, $\alpha_2 = 6°$, $\epsilon = 3.2 \times 10^{-4}$, $t \in [t_1, t_2] = [10500, 10509]$. Under surface isotherms: a) $r_1 = 0$, b) $r_1 = 1/4$, c) $r_1 = 1/2$, d) $r_1 = 3/4$. Colour code: red $\Rightarrow$ 1% fraction liquid intervals, green $\Rightarrow$ solidus line, blue $\Rightarrow$ intervals of 5% of temperature freezing range below solidus temperature.

6.5 Discussion

Mechanisms of porosity formation have been discussed in chapter one, section 1.2.3. Most of the published literature, (from which this understanding has developed), relates to one dimensional geometries, where one is able to talk of a uniform "layer thickness", at all points on the deposit. In billet spray-forming, as the results of this chapter have shown, interaction of the scanner and rotation motions result in considerably more complexity. Porosity levels within spray-formed billets exhibit complex local variations which are hard to characterise, [96]. Such variations can be economically investigated using the boundary layer model.

The four deposition/microstructre regimes that were outlined in section 1.2.3 cannot be easily distinguished when deposition is intermittent. For example, a very thick layer deposited on a relatively cold billet surface may experience a number of different regimes during its deposition; first the metal layer is chilled by the billet into a splat-like structure, then as it grows thicker, it heats through the incremental solidification regime, finally becoming very liquid. Alexander, [1], has suggested six different qualitative limits, relating to layer thickness, that may be relevant to this type of deposition.

The results of section 6.3 are supported by recent microstructural analysis by Mingard, [94]. Radial variations in porosity have been found at radial distances at which there are correspondingly sharp changes in surface gradient.

The results of section 6.4 are in agreement with recent experimental results, [95]. Variation of rotation rate, (through a similar range to that in section 6.4), was found to produce high levels of porosity in the deposited material for both very high and very low rotation rates. The porosity found at the very high rotation rates seemed to result from a very "dry" microstructure, with little bonding between layers. At very low rotation rates there was evidence of the porosity being caused by fluid instability on the billet surface, with gas pores found in the sprayed deposit on analysis.

Dimensionally, the boundary layer length-scale is typically of the order of millimetres. Splat thicknesses are thought to lie in the range

$$5 - 10\ \mu\text{m},$$

(see the discussion in chapter one, section 1.2.3). Thus, the sort of isotherm penetration distances that have been shown in this chapter suggest that remelting and refreezing processes occur across

$$\sim 10^2$$

flattened layers of deposited droplets. This not only lends some validity to the use of a continuum approximation, over the short boundary layer length-scale, but also shows that the boundary layer length-scale is appropriate for the investigation of observed microstructural variations.

For typical process parameters, as in section 6.2, the dimensional cooling rates of the surface following deposition are $\sim 10^3$C/s. This is important, since the implication here is that cooling rates of a similar order to those that are found in other rapid solidification processes may also be found in the boundary layer. Previous continuum modelling work has not exposed this feature, since it has generally considered cases of continuous deposition.

The results presented in this chapter have given only a brief demonstration of the usefulness of the

boundary layer approximation. Development of submodels relating the predicted boundary layer heat flow fluctuations to microstructural characteristics, (e.g. grain size, porosity levels), would be a sensible extension.

Variations in h_{gas}, $\hat{T}_{gas}$ and $\hat{H}_{spray}$ have not been explored in this chapter. Local variations in the heat transfer coefficient, h_{gas}, are likely to occur, due to variation in the turbulent gas velocity across the surface. Directing additional gas cooling jets onto the billet surface would also influence h_{gas}. Gas temperature and spray enthalpy will vary with the ratio of metal and gas mass flow rates through the atomiser, with the temperature of the molten metal, and with the atomised droplet size distribution, (this influences the efficiency of heat transfer between the metal spray and atomising gas). For larger radius billets there may also be a significant variation in flight distance from the atomiser at points across the billet surface, and this will translate into a variation in H_{spray}. Thus, the sensitivity of the model to each of these parameters needs to be systematically explored in order to give some guidance in assessing the potential risk of process change.

6.6 Summary

- Computation of the boundary layer heat flow first requires that the slow time billet growth equations be solved to give an approximation to the surface position and unit normal vector.

- Instantaneous surface normal velocity at a fixed radial distance, r_1, from the billet axis of rotation varies with the azimuthal angle, ϕ_1, about the billet axis of rotation. For computation of the boundary layer heat flow over a given time interval it is necessary to first find ϕ_1, such that the instantaneous surface normal velocity averaged over the time interval is equal to the axisymmetric averaged surface normal velocity on that interval.

- Numerical solution of the boundary layer equations is accomplished using a two level, two stage finite difference scheme. A regular spatial mesh spacing, $\Delta\zeta$, is used and a variable timestep

$$\Delta t_n = O(\Delta\zeta)$$

  is chosen to preserve the stability of the scheme, and to ensure adequate representation of pulsed surface normal velocities.

- The numerical scheme has local truncation error

$$O(\Delta\zeta^2) + O(\Delta t_n^2).$$

  Convergence is believed to be $O(\Delta\zeta^2)$ spatially and at least $O(\Delta t_n^{3/2})$ in the tiime direction.

- The irregular and intermittent pulsed deposition on the billet surface produces corresponding irregular and intermittent fluctuations in the surface temperature and surface fraction liquid.

- Surface cooling rates in the boundary layer model are $\sim 10^3$C/s, following deposition, for typical process parameters.

- Underneath the billet deposition surface the pulsed heat flow can result in remelting and refreezing processes extending to a depth representing $\sim 10^2$ layer thicknesses of flattened, deposited droplets.

- Surface enthalpy/temperature fluctuates about a far field value which is determined by setting the time averaged boundary heat flux equal to zero.

- On the billet axis of rotation the deposition pulses are typically regular, more frequent and smaller than at other radial distances from the billet axis of rotation. Accordingly, the amplitude of surface enthalpy fluctuations about the far field enthalpy is generally less at the billet axis of rotation than elsewhere.

- Convexity and concavity of the billet surface do not directly effect the boundary layer heat flow, (since this is a more local process), although associated variations in surface gradient can.

- Far field enthalpies underneath points at which there is a steep surface gradient are significantly lower than far field enthalpies underneath points where the surface is nearly horizontal. This is due to the reduced averaged surface normal velocity at these points.

- Variation in rotation and scanner frequency does not effect the computed far field enthalpy/temperature in the boundary layer approximation.

- Reduction of the rotation and scanner frequencies results in surface deposition pulse patterns in which the pulses are larger, last for longer, and are more intermittent. This results in larger and more persistent fluctuations in the surface temperature about the far field value. The temperature/enthalpy transients also penetrate to a deeper distance below the billet surface.

Chapter 7

Slow-time Billet Heat Flow

This chapter considers the heat flow that occurs on the billet length-scale and on a much slower timescale than does the boundary layer heat flow of the previous chapter. Slow-time heat flow in the billet frame of reference is governed by

$$\frac{\partial H}{\partial \eta} = \frac{1}{Pe}\nabla.[K(H)\nabla H], \qquad \boldsymbol{x}_0 \in \Omega(\eta), \tag{7.1}$$

$$-K(H)\frac{\partial H}{\partial n} = B_{gas}[T(H) - T_{gas}] + Pe\bar{v}[H - H_{spray}], \qquad \boldsymbol{x}_0 \in \partial\Omega(\eta) : z_0 > z_c, \tag{7.2}$$

$$K(H)\frac{\partial H}{\partial z_0} = B_{collector}[T(H) - T_{collector}], \qquad \boldsymbol{x}_0 \in \partial\Omega(\eta) : z_0 = z_c. \tag{7.3}$$

At slow-time, $\eta = \epsilon t$, the billet occupies the region $\Omega(\eta)$ in the billet frame of reference and has boundary denoted $\partial\Omega(\eta)$. Equation (7.1) is parameterised by the Peclet number, Pe, which has been discussed in chapter five. In equation (7.2), the partial derivative in the direction of the outward surface normal vector is denoted by $\frac{\partial}{\partial n}$; B_{gas}, T_{gas} and H_{spray} are respectively the gas Biot number, the gas temperature and the mass averaged enthalpy of the spray. In equation (7.3), $B_{collector}$ and $T_{collector}$ are respectively, the Biot number governing the heat transfer between the base of the billet and the collector, and the collector temperature.

The time averaged surface normal velocity, $\bar{v}$ in equation (7.2), is given by

$$\bar{v} \equiv -\frac{\partial F_0}{\partial \eta}|\nabla F_0|^{-1}, \tag{7.4}$$

where

$$\partial\Omega(\eta) \equiv \{\boldsymbol{x}_0 \in \mathcal{R}^3 : \; F_0(\boldsymbol{x}_1[\boldsymbol{x}_0, \eta], \eta) = 0\}. \tag{7.5}$$

Evolution of $F_0(\boldsymbol{x}_1[\boldsymbol{x}_0, \eta], \eta)$ is governed by

$$\frac{\partial F_0}{\partial \eta}(\boldsymbol{x}_1[\boldsymbol{x}_0, \eta], \eta) = \dot{m}(\eta)\bar{\boldsymbol{g}}(F_0, \boldsymbol{x}_1[\boldsymbol{x}_0, \eta]).\nabla F_0(\boldsymbol{x}_1[\boldsymbol{x}_0, \eta], \eta), \qquad \boldsymbol{x}_0 \in \partial\Omega(\eta), \tag{7.6}$$

where $\dot{m}(\eta)$ is the metal mass flow rate and $\bar{\boldsymbol{g}}$ is the axisymmetric averaged mass flux distribution vector field. See chapters two, three and four for further details.

With the assumption of symmetry about the billet axis of rotation, the equations (7.1), (7.2), (7.3) and (7.6) represent a nonlinear, two dimensional, parabolic free boundary problem in which the position of both

the billet surface and the isotherms within the billet must be found. With the further assumptions that have been made in chapter two, the problem of determining the billet surface position uncouples from the heat flow problem. This leaves a two dimensional, nonlinear, parabolic initial and boundary value problem to be solved in an irregular expanding domain.

For clarity in describing the numerical algorithm used, the subscripts on r_0 and z_0, (respectively denoting radial distance from the billet axis of rotation and vertical distance above O_0, as measured in the billet frame of reference), will be dropped for the remainder of this section. Thus, assuming symmetry about the billet axis of rotation, position within a cylindrical billet coordinate system is denoted by (r, z). Equations (7.1), (7.2), (7.3), and the symmetry condition at the billet axis of rotation become

$$\frac{\partial H}{\partial \eta} = \frac{1}{Pe}\{\frac{1}{r}\frac{\partial}{\partial r}[rK(H)\frac{\partial H}{\partial r}] + \frac{\partial}{\partial z}[K(H)\frac{\partial H}{\partial z}]\}, \quad (r,z) \in \Omega(\eta), \tag{7.7}$$

$$-K(H)\frac{\partial H}{\partial n} = B_{gas}[T(H) - T_{gas}] + Pe\bar{v}[H - H_{spray}], \quad (r,z) \in \partial\Omega(\eta) : r > 0,\ z > z_c, \tag{7.8}$$

$$K(H)\frac{\partial H}{\partial z} = B_{collector}[T(H) - T_{collector}], \quad (r,z) \in \partial\Omega(\eta) : r > 0,\ z = z_c, \tag{7.9}$$

$$\frac{\partial H}{\partial r} = 0, \quad r = 0,\ z > z_c. \tag{7.10}$$

It is these equations that are solved in this chapter.

The computational method used to solve (7.7), (7.8), (7.9) and (7.10) is presented in considerable detail in section one. The algorithm is quite complex, and is summarised in section 7.1.10 for convenience. Various features of the method are discussed in section two. Section three presents results demonstrating the flexibility of the algorithm employed. Section four looks at heat flow during the initial phases of billet growth. Section five briefly examines numerically the question of existence of thermal steady states, and also tests, numerically for one case, the simplistic predictions of chapter five concerning how to spray different radii billets to give similar temperature variations. The chapter concludes with a summary.

7.1 Computational method; description

Let R and Z denote the radial and vertical limits of the billet growth, measured in the cylindrical billet coordinate system. Defining mesh spacings Δr and Δz in r and z directions respectively, the region $(r, z) \in [-\frac{1}{2}\Delta r, R] \times [z_c - \frac{1}{2}\Delta z, Z]$ is covered by a regular mesh. Meshpoints (r_i, z_j) are defined by

$$r_i = (i - 1/2) \times \Delta r, \quad i = 0, 1, ..., I, \tag{7.11}$$

$$z_j = z_c + (j - 1/2) \times \Delta z, \quad j = 0, 1, ..., J, \tag{7.12}$$

see Fig. 7.1. For computations carried out in this chapter equal mesh spacings in the r and z-directions were used, i.e.

$$\Delta r = \Delta z. \tag{7.13}$$

Thus, only Δz is used in the following description.

For $n \geq 1$, timestep n is defined by $\eta \equiv \eta_n$. The position of the billet surface is computed from its position at timestep $n-1$ using the method outlined in chapter four. The computed billet surface contour, and its reflection in the billet axis of rotation, form a curve in the (r, z)-plane which divides the total set of meshpoints, defined above by (7.11) and (7.12), into two distinct subsets. The subset of meshpoints, at timestep n, comprising those meshpoints lying within the billet boundary, together with those meshpoints (r_0, z_j) for which (r_1, z_j) lies within the billet boundary, and those meshpoints (r_i, z_0) for which (r_i, z_1) lies within the billet boundary, is denoted Ω^n. See Fig. 7.2a for clarity.

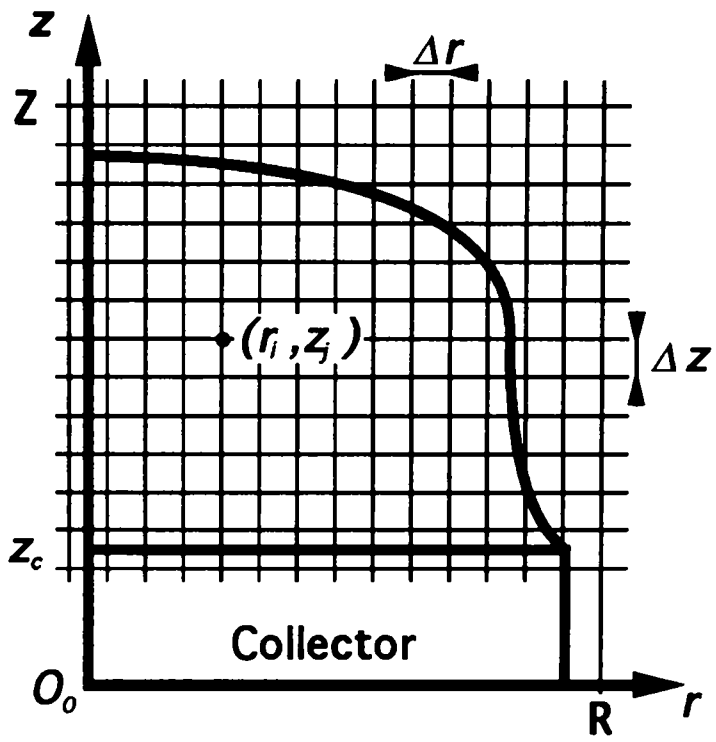

Figure 7.1: Definition of meshpoints, (r_i, z_j).

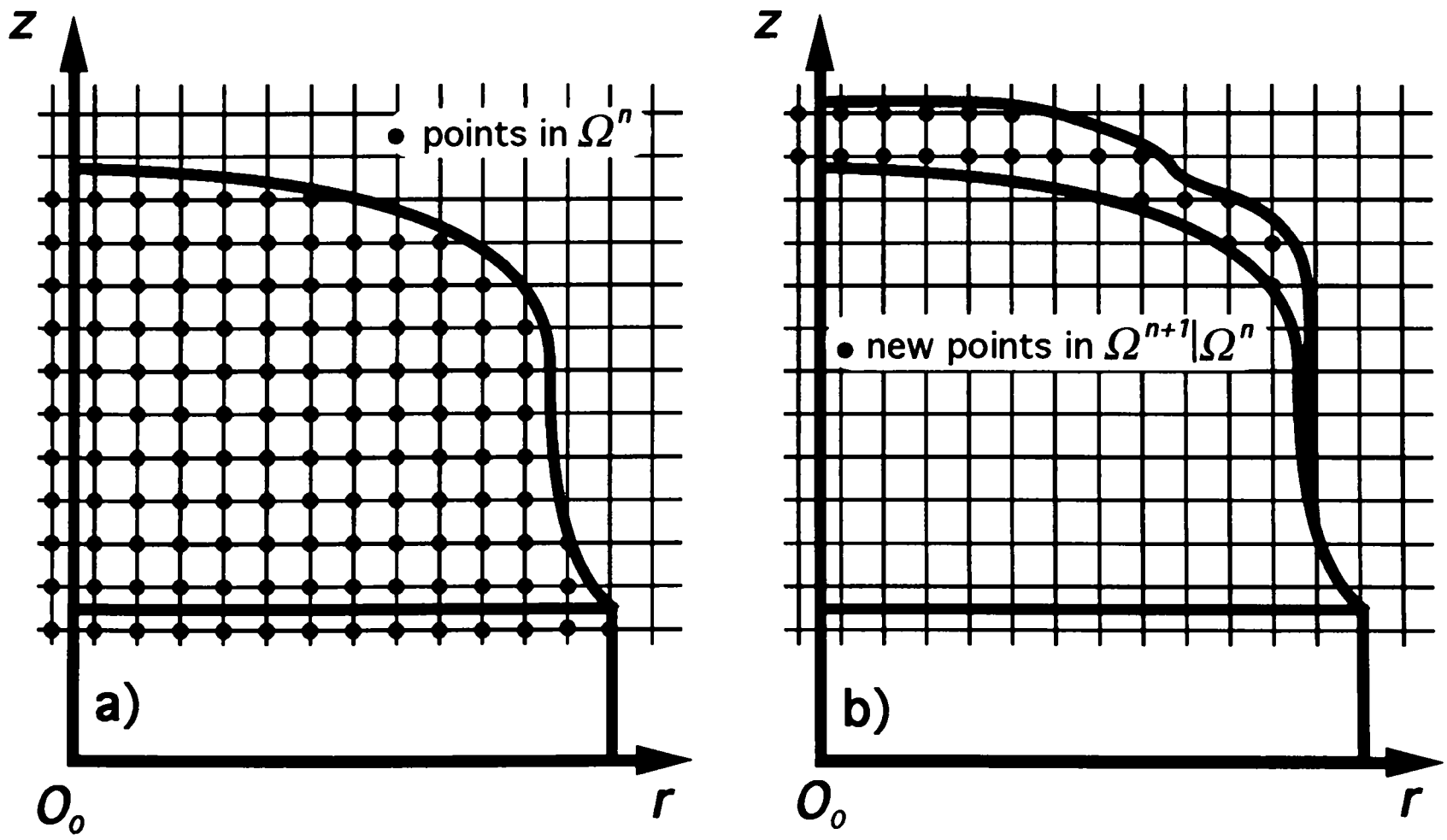

Figure 7.2: a) Definition of Ω^n, b) Old and new meshpoints on timestep n.

The enthalpy, $H(r, z, \eta)$, in equations (7.7), (7.8), (7.9) and (7.10) is approximated by the mesh function $H^n_{i,j}$ at all $(r_i, z_j) \in \Omega^n$, i.e.

$$H^n_{i,j} \approx H(r_i, z_j, \eta_n). \tag{7.14}$$

Given the mesh function $H^n_{i,j}$, defined at all $(r_i, z_j) \in \Omega^n$, new values $H^{n+1}_{i,j}$ are computed at all $(r_i, z_j) \in \Omega^{n+1}$, using finite difference approximations to (7.7), (7.8), (7.9) and (7.10). The set $\Omega^{n+1}|\Omega^n$ comprises the set of **new meshpoints** entering the billet on timestep n. For each $(r_i, z_j) \in \Omega^{n+1}|\Omega^n$, a value must be assigned to $H^{n+1}_{i,j}$ on the nth timestep, without there being a previous value, $H^n_{i,j}$, to utilise, see Fig. 7.2b.

The set Ω^n may be partitioned into either vertical or horizontal "chains" of meshpoints. Vertical chains of meshpoints may be identified by the index i of their radial distance from the billet axis of rotation, r_i. Due to the irregularly shaped billet boundary, at any particular radial distance, r_i, there may be more than one vertical chain of meshpoints lying within Ω^n.

Let $k^{v,n}_i$ denote the number of vertical chains of meshpoints at $r = r_i$, lying within Ω^n. Denote by $C^{v,n}_{i,k}$ the kth vertical chain lying within Ω^n at radial position $r = r_i$, for $k = 1, .., k^{v,n}_i$. Similarly, let $k^{h,n}_j$ denote the number of horizontal chains of meshpoints lying within Ω^n at height $z = z_j$, and denote by $C^{h,n}_{j,k} : k = 1, .., k^{h,n}_j$ the kth horizontal chain lying within Ω^n at height $z = z_j$. These definitions are illustrated in Fig. 7.3.

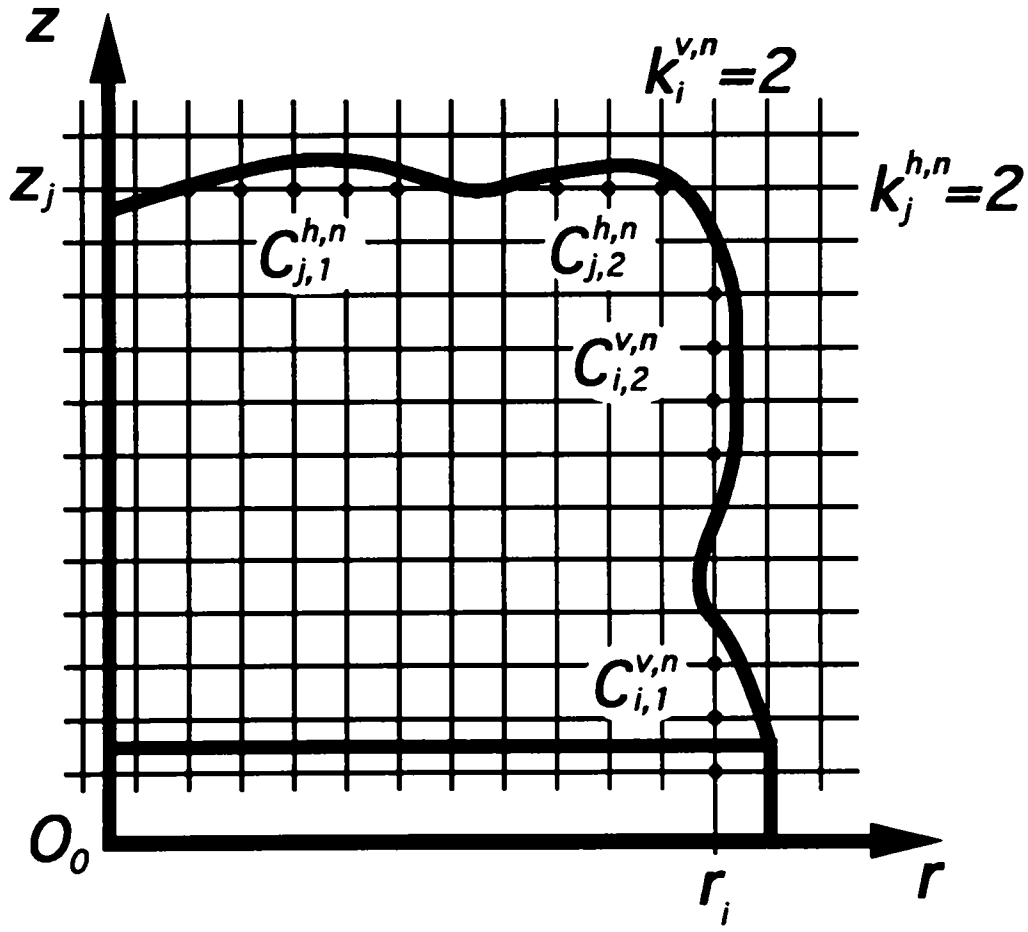

Figure 7.3: Notation describing horizontal and vertical chains on timestep n.

Meshpoints at the "start" and "finish" of $C^{v,n}_{i,k}$ are denoted $(r_i, z_{j^n_{st,i,k}})$ and $(r_i, z_{j^n_{fin,i,k}})$ respectively. Meshpoints at the "start" and "finish" of $C^{h,n}_{j,k}$ are denoted $(r_{i^n_{st,j,k}}, z_j)$ and $(r_{i^n_{fin,j,k}}, z_j)$ respectively. The "start" and "finish" endpoints of a particular horizontal or vertical chain are distinguished by adopting the convention that

$$j^n_{st,i,k} \leq j^n_{fin,i,k}, \tag{7.15}$$

$$i^n_{st,j,k} \leq i^n_{fin,j,k}. \tag{7.16}$$

7.1.1 Computing $H_{i,j}^{n+1}$ $\forall(r_i, z_j) \in \Omega^n$

To advance the approximation from timestep n to timestep $n+1$ at all points $(r_i, z_j) \in \Omega^n$ the following four stage scheme is used.

- **Stage 1:** (Vertical chain solver, I)

  For $i = 1, ..., I,\ k = 1, ..., k_i^{v,n}$, at meshpoints $(r_i, z_j) \in C_{i,k}^{v,n}$ solve for $H_{i,j}^{n+*}$, which satisfies

$$H_{i,j}^{n+*} - H_{i,j}^{n} = \nu^n\{K(H_{i,j+1/2}^{n})(H_{i,j+1}^{n+*} - H_{i,j}^{n+*}) + K(H_{i,j-1/2}^{n})(H_{i,j-1}^{n+*} - H_{i,j}^{n+*})\}, \quad (7.17)$$

  for $j = j_{st,i,k}^n + 1, ..., j_{fin,i,k}^n - 1$, together with conditions at $j = j_{st,i,k}^n$ and $j = j_{fin,i,k}^n$, which will be discussed in the following sections. Having solved (7.17) for $i = 1, ..., I,\ k = 1, ..., k_i^{v,n}$, stage 1 is completed by setting

$$H_{0,j}^{n+*} = H_{1,j}^{n+*}; \qquad j = j_{st,0,k}^n, ..., j_{fin,0,k}^n,\ k = 1, ..., k_0^{v,n}, \quad (7.18)$$

  which represents the symmetry condition, (7.10).

- **Stage 2:** (Vertical chain solver, II)

  For $i = 1, ..., I,\ k = 1, ..., k_i^{v,n}$, at meshpoints $(r_i, z_j) \in C_{i,k}^{v,n}$ solve for $H_{i,j}^{n+1*}$, which satisfies

$$H_{i,j}^{n+1*} - H_{i,j}^{n} = \nu^n\{K(H_{i,j+1/2}^{n+*})(H_{i,j+1}^{n+1*} - H_{i,j}^{n+1*}) + K(H_{i,j-1/2}^{n+*})(H_{i,j-1}^{n+1*} - H_{i,j}^{n+1*})\}, \quad (7.19)$$

  for $j = j_{st,i,k}^n + 1, ..., j_{fin,i,k}^n - 1$, together with conditions at $j = j_{st,i,k}^n$ and $j = j_{fin,i,k}^n$, which will be discussed in the following sections. Having solved (7.19) for $i = 1, ..., I,\ k = 1, ..., k_i^{v,n}$, stage 2 is completed by setting

$$H_{0,j}^{n+1*} = H_{1,j}^{n+1*}; \qquad j = j_{st,0,k}^n, ..., j_{fin,0,k}^n,\ k = 1, ..., k_0^{v,n}. \quad (7.20)$$

- **Stage 3:** (Horizontal chain solver)

  For $j = 1, ..., J,\ k = 1, ..., k_j^{h,n}$, at meshpoints $(r_i, z_j) \in C_{j,k}^{h,n}$ solve for $H_{i,j}^{n+1**}$, which satisfies

$$\begin{aligned} H_{i,j}^{n+1**} - H_{i,j}^{n+1*} = \nu^n\{&\frac{i}{i-1/2}K(H_{i+1/2,j}^{n+1*})(H_{i+1,j}^{n+1**} - H_{i,j}^{n+1**}) \\ &+\frac{i-1}{i-1/2}K(H_{i-1/2,j}^{n+1*})(H_{i-1,j}^{n+1**} - H_{i,j}^{n+1**})\}, \end{aligned} \quad (7.21)$$

  for $i = i_{st,j,k}^n + 1, ..., i_{fin,j,k}^n - 1$, together with conditions at $i = i_{st,j,k}^n$ and $i = i_{fin,j,k}^n$, which will be discussed in the following sections. Having solved (7.21) for $j = 1, ..., J,\ k = 1, ..., k_j^{h,n}$, stage 3 is completed by solving

$$K(H_{i,1/2}^{n+1**})\frac{H_{i,1}^{n+1**} - H_{i,0}^{n+1**}}{\Delta z} = B_{collector}[T(H_{i,1/2}^{n+1**}) - T_{collector}], \quad (7.22)$$

  for $H_{i,0}^{n+1**}$ at $i = i_{st,0,k}^n, ..., i_{fin,0,k}^n,\ k = 1, ..., k_0^{h,n}$. Equation (7.22) is a nonlinear equation for $H_{i,0}^{n+1**}$ and is solved using Newtons method, with $H_{i,0}^{n+1*}$ taken as an initial guess for $H_{i,0}^{n+1**}$.

- **Stage 4:** (Consistency step)

An interior set of meshpoints, $\tilde{\Omega}^n \subset \Omega^n$, is defined by

$$(r_i, z_j) \in \tilde{\Omega}^n \Longleftrightarrow \{(r_i, z_j), (r_i, z_{j+1}), (r_i, z_{j-1}), (r_{i+1}, z_j), (r_{i-1}, z_j)\} \in \Omega^n, \tag{7.23}$$

see Fig. 7.4. For meshpoints $(r_i, z_j) \in \tilde{\Omega}^n$ solve for $H_{i,j}^{n+1}$, which satisfies

$$\begin{aligned} H_{i,j}^{n+1} - H_{i,j}^{n} &= \nu^n \{K(H_{i,j+1/2}^{n+1**})(H_{i,j+1}^{n+1**} - H_{i,j}^{n+1}) + K(H_{i,j-1/2}^{n+1**})(H_{i,j-1}^{n+1**} - H_{i,j}^{n+1}) \\ &\quad + \frac{i}{i-1/2} K(H_{i+1/2,j}^{n+1**})(H_{i+1,j}^{n+1**} - H_{i,j}^{n+1}) + \\ &\quad \frac{i-1}{i-1/2} K(H_{i-1/2,j}^{n+1**})(H_{i-1,j}^{n+1**} - H_{i,j}^{n+1})\}. \end{aligned} \tag{7.24}$$

Having solved for $H_{i,j}^{n+1}$ at meshpoints $(r_i, z_j) \in \tilde{\Omega}^n$, stage 4 is completed by computing $H_{i,j}^{n+1}$ at meshpoints $(r_i, z_j) \in \Omega^n | \tilde{\Omega}^n$. The procedure for doing so is described in the following sections.

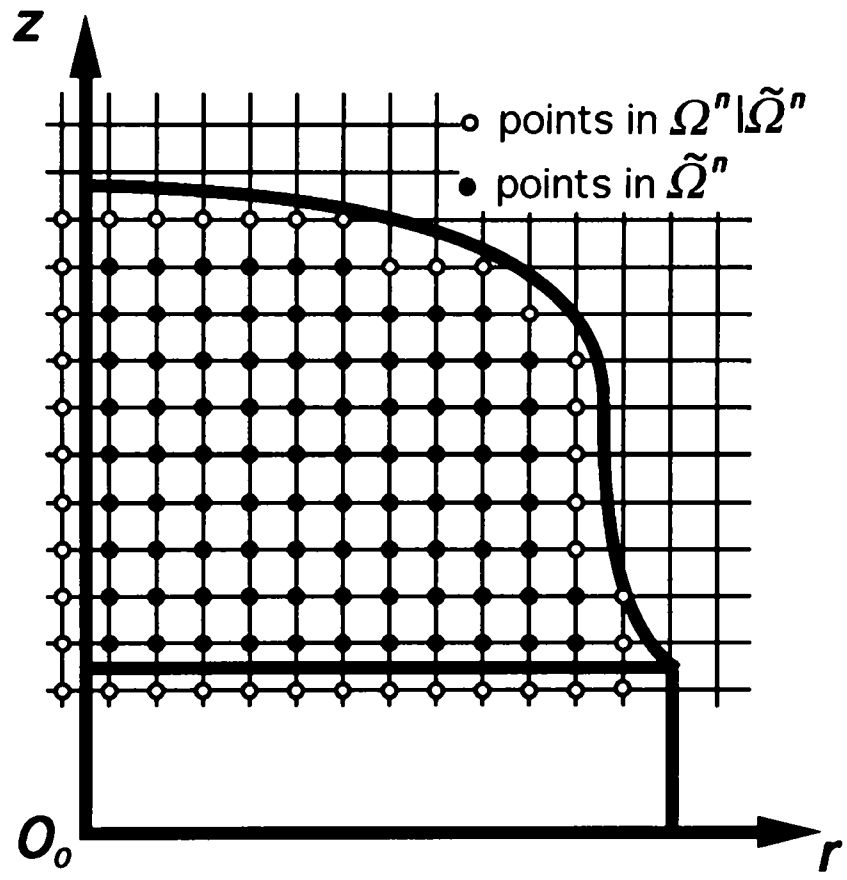

Figure 7.4: Definition of $\tilde{\Omega}^n$.

Stage 4 is repeated iteratively by replacing $H_{i,j}^{n+1**}$ with the computed values of $H_{i,j}^{n+1}$ and recomputing new values of $H_{i,j}^{n+1}$ with (7.24). During iterations of stage 4

$$\max_{(r_i, z_j) \in \Omega^n} |H_{i,j}^{n+1} - H_{i,j}^{n+1**}|$$

is monitored. Convergence is assumed to be satisfactory when

$$\max_{(r_i, z_j) \in \Omega^n} |H_{i,j}^{n+1} - H_{i,j}^{n+1**}| < .003. \tag{7.25}$$

This is typically found to take 2-3 iterations, and an upper limit of 10 iterations is allowed for in the algorithm.

In equations (7.17), (7.19), (7.21) and (7.24)

$$\nu^n \equiv \frac{\Delta \eta_n}{Pe \Delta z^2}, \tag{7.26}$$

and fractional subscripts that appear are defined by, e.g.

$$H^n_{i,j+1/2} \equiv \frac{1}{2}[H^n_{i,j} + H^n_{i,j+1}]. \tag{7.27}$$

7.1.2 Boundary conditions at the billet surface

In order to compute $H^{n+1}_{i,j}$ $\forall(r_i, z_j) \in \Omega^n$, using stages 1 to 4 above, it is necessary to provide values for $H^{n+*}_{i,j}$, $H^{n+1*}_{i,j}$, $H^{n+1**}_{i,j}$ and $H^{n+1}_{i,j}$ at the end meshpoints of each vertical and horizontal chain in Ω^n. Note that meshpoints $(r_i, z_j) \in \Omega^n | \tilde{\Omega}^n$ must lie at the endpoints of vertical and/or horizontal chains, (e.g. see Fig. 7.4).

Where vertical or horizontal chains in Ω^n start at the collector plate or at the billet axis of rotation respectively, the boundary conditions (7.9) and (7.10) may be utilised. Otherwise, the billet surface cuts gridlines

$$r = r_i,$$

and

$$z = z_j,$$

at points which are not necessarily meshpoints. At each of these points the boundary condition (7.8) must be satisfied approximately, and this information can be used to provide the end conditions at the start and finish meshpoints of chains in Ω^n.

Given the position of the billet surface at time η_n, and computed values of $H^n_{i,j}$, $\forall(r_i, z_j) \in \Omega^n$, the new position of the billet surface is computed at time η_{n+1}. A piecewise cubic Hermite interpolant is used to give a continuously differentiable representation of the billet surface between computed surface points. This allows a normal velocity vector to be computed which is continuous along the billet surface. At each point of intersection of the new billet surface at time η_{n+1} with a gridline, the (r, z) position, the surface normal vector cosines, and values for B_{gas}, T_{gas}, $\bar{v}$ and H_{spray} are stored.

- **Stage 1:** when a vertical chain starts or finishes at a point of intersection of the billet surface with a gridline the following procedure is adopted.

  1. The inward surface normal is followed into the billet until a gridline is crossed.
  2. On each gridline that is crossed by the inward normal a check is performed to ascertain whether or not there are sufficient adjacent collinear meshpoints, lying on that gridline and within Ω^n, to give an $O(\Delta z^3)$ approximation to $H(r, z, \eta_n)$ at the point of intersection, (i.e. three adjacent collinear meshpoints are required).
  3. The procedure is repeated until two suitable points of intersection of the inward normal with internal gridlines have been located. Denote these points by B and C, and suppose that B and C lie at distances $s_B\Delta z$ and $s_C\Delta z$ from the billet surface. Let $s_B < s_C$; see Fig. 7.5.
  4. Denote by H^n_B and H^n_C the $O(\Delta z^3)$ approximations to $H(r, z, \eta_n)$ at the points B and C, and denote the point on the billet surface by A, with enthalpy H^n_A. An $O(\Delta z^2)$ approximation to the normal derivative of the enthalpy at A is provided by

$$\frac{\partial H}{\partial n} \approx \frac{s_B^2 H^n_C - s_C^2 H^n_B + (s_C^2 - s_B^2) H^n_A}{s_B s_C (s_C - s_B)\Delta z} \tag{7.28}$$

5. A value for H_A^n is computed by using a bisection method to solve

$$K(H_A^n)\frac{s_B^2 H_C^n - s_C^2 H_B^n + (s_C^2 - s_B^2)H_A^n}{s_B s_C(s_B - s_C)\Delta z} = B_{gas}(T(H_A^n) - T_{gas}) + Pe\bar{v}(H_A^n - H_{spray}). \quad (7.29)$$

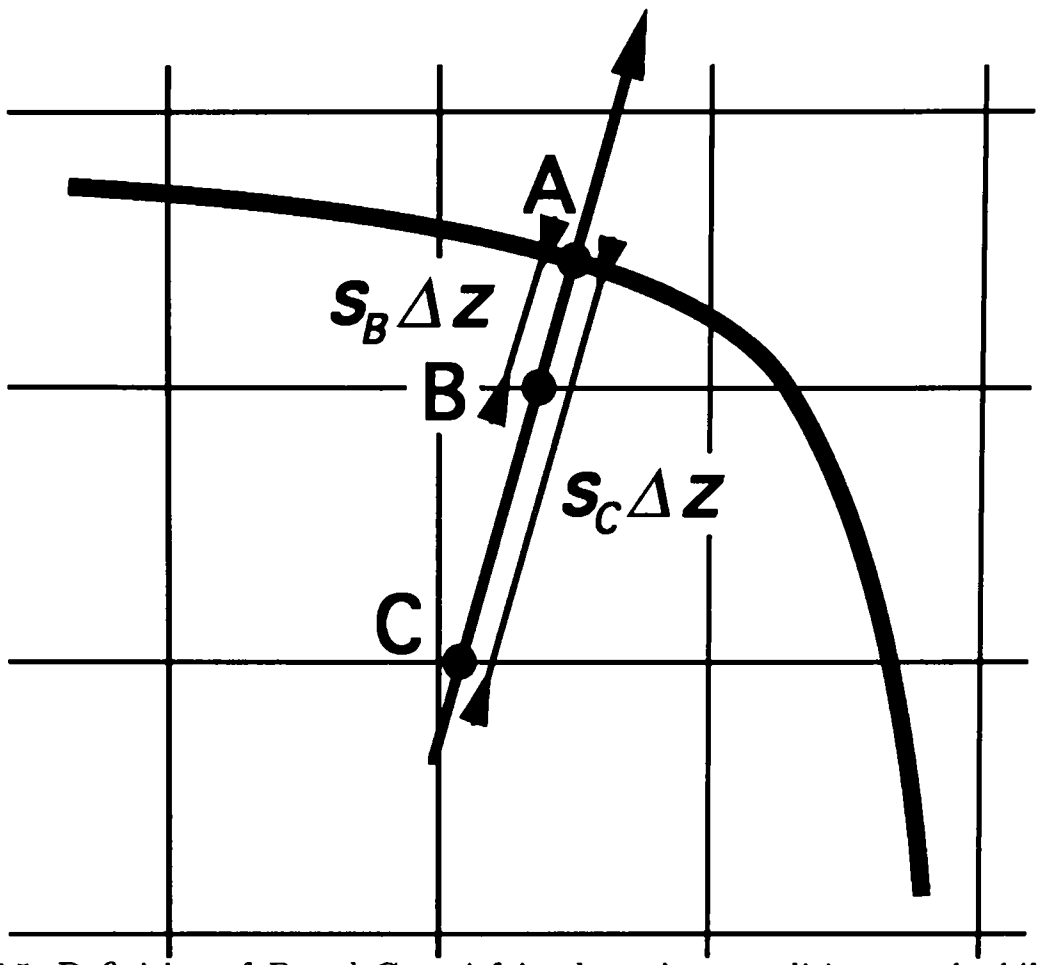

Figure 7.5: Definition of B and C; satisfying boundary conditions at the billet surface.

- **Stage 2:** when a vertical chain starts or finishes at a point of intersection of the billet surface with a gridline the following procedure is adopted.

  1. The inward surface normal is followed into the billet until a gridline is crossed.
  2. On each gridline that is crossed by the inward normal a check is performed to ascertain whether or not there are sufficient adjacent collinear meshpoints, lying on that gridline and within Ω^n, to give an $O(\Delta z^3)$ approximation to H^{n+*} at the point of intersection from the values of $H_{i,j}^{n+*}$, which have been computed above in stage 1.
  3. The procedure is repeated until two suitable points of intersection of the inward normal with internal gridlines have been located. Denote these points by B and C, and suppose that B and C lie at distances $s_B\Delta z$ and $s_C\Delta z$ from the billet surface. Let $s_B < s_C$.
  4. Denote by H_B^{n+*} and H_C^{n+*} the $O(\Delta z^3)$ approximations to H^{n+*} at the points B and C, and denote the point on the billet surface by A, with $H^{n+*} \equiv H_A^{n+*}$ at A. A value for H_A^{n+*} is computed by using a bisection method to solve

$$K(H_A^{n+*})\frac{s_B^2 H_C^{n+*} - s_C^2 H_B^{n+*} + (s_C^2 - s_B^2)H_A^{n+*}}{s_B s_C(s_B - s_C)\Delta z} = B_{gas}(T(H_A^{n+*}) - T_{gas}) + Pe\bar{v}(H_A^{n+*} - H_{spray}). \quad (7.30)$$

- **Stage 3:** when a horizontal chain starts or finishes at a point of intersection of the billet surface with a gridline the following procedure is adopted.

1. The inward surface normal is followed into the billet until a gridline is crossed.
2. On each gridline that is crossed by the inward normal a check is performed to ascertain whether or not there are sufficient adjacent collinear meshpoints, lying on that gridline and within Ω^n, to give an $O(\Delta z^3)$ approximation to H^{n+1*} at the point of intersection from the values of $H_{i,j}^{n+1*}$, which have been computed in stage 2.
3. The procedure is repeated until two suitable points of intersection of the inward normal with internal gridlines have been located. Denote these points by B and C, and suppose that B and C lie at distances $s_B\Delta z$ and $s_C\Delta z$ from the billet surface. Let $s_B < s_C$.
4. Denote by H_B^{n+1*} and H_C^{n+1*} the $O(\Delta z^3)$ approximations to H^{n+1*} at the points B and C, and denote the point on the billet surface by A, with $H^{n+1*} \equiv H_A^{n+1*}$ at A. A value for H_A^{n+1*} is computed by using a bisection method to solve

$$K(H_A^{n+1*})\frac{s_B^2 H_C^{n+1*} - s_C^2 H_B^{n+1*} + (s_C^2 - s_B^2)H_A^{n+1*}}{s_B s_C(s_B - s_C)\Delta z} = B_{gas}(T(H_A^{n+1*}) - T_{gas}) + Pe\bar{v}(H_A^{n+1*} - H_{spray}). \quad (7.31)$$

- **Stage 4:** when a horizontal chain starts or finishes at a point of intersection of the billet surface with a gridline the following procedure is adopted.

1. The inward surface normal is followed into the billet until a gridline is crossed.
2. On each gridline that is crossed by the inward normal a check is performed to ascertain whether or not there are sufficient adjacent collinear meshpoints, lying on that gridline and within Ω^n, to give an $O(\Delta z^3)$ approximation to H^{n+1} at the point of intersection from the values of $H_{i,j}^{n+1}$, which have been computed in an iteration stage 4.
3. The procedure is repeated until two suitable points of intersection of the inward normal with internal gridlines have been located. Denote these points by B and C, and suppose that B and C lie at distances $s_B\Delta z$ and $s_C\Delta z$ from the billet surface. Let $s_B < s_C$.
4. Denote by H_B^{n+1} and H_C^{n+1} the $O(\Delta z^3)$ approximations to H^{n+1} at the points B and C, and denote the point on the billet surface by A, with $H^{n+1} \equiv H_A^{n+1}$ at A. A value for H_A^{n+1} is computed by using a bisection method to solve

$$K(H_A^{n+1})\frac{s_B^2 H_C^{n+1} - s_C^2 H_B^{n+1} + (s_C^2 - s_B^2)H_A^{n+1}}{s_B s_C(s_B - s_C)\Delta z} = B_{gas}(T(H_A^{n+1}) - T_{gas}) + Pe\bar{v}(H_A^{n+1} - H_{spray}). \quad (7.32)$$

7.1.3 Chain end conditions; completing stages 1, 2, 3 & 4

Following the above procedure in stages 1, 2 and 3 gives approximate values for H^n, H^{n+*}, H^{n+1**} and H^{n+1} actually on the billet surface, close to a chain endpoint. The procedures described in this section are then used to solve for $H_{i,j}^{n+*}$, $H_{i,j}^{n+1*}$ and $H_{i,j}^{n+1**}$ in stages 1, 2 and 3 respectively, whenever there are at least three meshpoints in a chain, i.e.

$$j_{st,i,k}^n + 1 < j_{fin,i,k}^n : \text{ stages 1 \& 2,}$$
$$i_{st,j,k}^n + 1 < i_{fin,j,k}^n : \text{ stage 3.}$$

The special treatment necessary for shorter chains in stages 1, 2 and 3 is covered in the next section. Also described in this section is the procedure used in stage 4 for assigning values to $H_{i,j}^{n+1}$ when $(r_i, z_j) \in \Omega^n | \tilde{\Omega}^n$.

- **Stage 1:**

1. Use $H^n_{i,j^n_{fin,i,k}-1}$ and $H^n_{i,j^n_{fin,i,k}-2}$, together with the computed chain end boundary value for H^n, to give an $O(\Delta z^3)$ approximation to $H^n_{i,j^n_{fin,i,k}}$. This provides an $O(\Delta z^3)+O(\Delta\eta_n)$ approximation to $H^{n+*}_{i,j^n_{fin,i,k}}$.
2. Write equation (7.17) in the form of a tri-diagonal system of simultaneous equations, i.e.

$$- a_{i,j}^{n+*} H_{i,j-1}^{n+*} + b_{i,j}^{n+*} H_{i,j}^{n+*} - c_{i,j}^{n+*} H_{i,j+1}^{n+*} = d_{i,j}^{n+*}, \tag{7.33}$$

   where $a_{i,j}^{n+*}$, $b_{i,j}^{n+*}$, $c_{i,j}^{n+*}$ and $d_{i,j}^{n+*}$ are defined by reference to equation (7.17).
3. Set

$$e^{n+*}_{i,j^n_{fin,i,k}} = 0, \tag{7.34}$$

$$f^{n+*}_{i,j^n_{fin,i,k}} = H^{n+*}_{i,j^n_{fin,i,k}}, \tag{7.35}$$

   and for $j = j^n_{fin,i,k} - 1, ..., j^n_{st,i,k} + 1$, define iteratively

$$e_{i,j}^{n+*} = \frac{a_{i,j}^{n+*}}{b_{i,j}^{n+*} - c_{i,j}^{n+*} e_{i,j+1}^{n+*}}, \tag{7.36}$$

$$f_{i,j}^{n+*} = \frac{d_{i,j}^{n+*} + c_{i,j}^{n+*} f_{i,j+1}^{n+*}}{b_{i,j}^{n+*} - c_{i,j}^{n+*} e_{i,j+1}^{n+*}}, \tag{7.37}$$

4. If the vertical chain does not start at the collector, derive an $O(\Delta z^3) + O(\Delta\eta_n)$ approximation to $H^{n+*}_{i,j^n_{st,i,k}}$ by interpolating from $H^n_{i,j^n_{st,i,k}+1}$, $H^n_{i,j^n_{st,i,k}+2}$ and the boundary value computed for H^n at the chain start.
5. If the vertical chain does start at the collector, define $H^{n+*}_{i,j^n_{st,i,k}}$ by solving the system

$$K(H_{i,1/2}^{n+*}) \frac{H_{i,1}^{n+*} - H_{i,0}^{n+*}}{\Delta z} = B_{collector}[T(H_{i,1/2}^{n+*}) - T_{collector}], \tag{7.38}$$

$$H_{i,1}^{n+*} = e_{i,1}^{n+*} H_{i,0}^{n+*} + f_{i,1}^{n+*}. \tag{7.39}$$

6. For $j = j^n_{st,i,k} + 1, ..., j^n_{fin,i,k}$, compute values for $H_{i,j}^{n+*}$ from

$$H_{i,j}^{n+*} = e_{i,j}^{n+*} H_{i,j-1}^{n+*} + f_{i,j}^{n+*}. \tag{7.40}$$

- **Stage 2:**

1. Use $H^{n+*}_{i,j^n_{fin,i,k}-1}$ and $H^{n+*}_{i,j^n_{fin,i,k}-2}$, together with the computed chain end boundary value for H^{n+*}, to give an $O(\Delta z^3)$ approximation to $H^{n+*}_{i,j^n_{fin,i,k}}$. This provides an $O(\Delta z^3)+O(\Delta\eta_n)$ approximation to $H^{n+1*}_{i,j^n_{fin,i,k}}$.
2. Write equation (7.19) in the form of a tri-diagonal system of simultaneous equations, i.e.

$$- a_{i,j}^{n+1*} H_{i,j-1}^{n+1*} + b_{i,j}^{n+1*} H_{i,j}^{n+1*} - c_{i,j}^{n+1*} H_{i,j+1}^{n+1*} = d_{i,j}^{n+1*}, \tag{7.41}$$

   where $a_{i,j}^{n+1*}$, $b_{i,j}^{n+1*}$, $c_{i,j}^{n+1*}$ and $d_{i,j}^{n+1*}$ are defined by reference to equation (7.19).

3. Set

$$e^{n+1*}_{i,j^n_{fin,i,k}} = 0, \tag{7.42}$$

$$f^{n+1*}_{i,j^n_{fin,i,k}} = H^{n+1*}_{i,j^n_{fin,i,k}}, \tag{7.43}$$

and for $j = j^n_{fin,i,k} - 1, ..., j^n_{st,i,k} + 1$, define iteratively

$$e^{n+1*}_{i,j} = \frac{a^{n+1*}_{i,j}}{b^{n+1*}_{i,j} - c^{n+1*}_{i,j} e^{n+1*}_{i,j+1}}, \tag{7.44}$$

$$f^{n+1*}_{i,j} = \frac{d^{n+1*}_{i,j} + c^{n+1*}_{i,j} f^{n+1*}_{i,j+1}}{b^{n+1*}_{i,j} - c^{n+1*}_{i,j} e^{n+1*}_{i,j+1}}. \tag{7.45}$$

4. If the vertical chain does not start at the collector, derive an $O(\Delta z^3) + O(\Delta \eta_n)$ approximation to $H^{n+1*}_{i,j^n_{st,i,k}}$ by interpolating from $H^{n+*}_{i,j^n_{st,i,k}+1}$, $H^{n+*}_{i,j^n_{st,i,k}+2}$ and the boundary value computed for H^{n+*} at the chain start.

5. If the vertical chain does start at the collector, define $H^{n+1*}_{i,j^n_{st,i,k}}$ by solving the system

$$K(H^{n+1*}_{i,1/2}) \frac{H^{n+1*}_{i,1} - H^{n+1*}_{i,0}}{\Delta z} = B_{collector}[T(H^{n+1*}_{i,1/2}) - T_{collector}], \tag{7.46}$$

$$H^{n+1*}_{i,1} = e^{n+1*}_{i,1} H^{n+1*}_{i,0} + f^{n+1*}_{i,1}. \tag{7.47}$$

6. For $j = j^n_{st,i,k} + 1, ..., j^n_{fin,i,k}$, compute values for $H^{n+1*}_{i,j}$ from

$$H^{n+1*}_{i,j} = e^{n+1*}_{i,j} H^{n+1*}_{i,j-1} + f^{n+1*}_{i,j}. \tag{7.48}$$

- **Stage 3:**

1. Write equation (7.21) in the form of a tri-diagonal system of simultaneous equations, i.e.

$$-a^{n+1**}_{i,j} H^{n+1**}_{i-1,j} + b^{n+1**}_{i,j} H^{n+1**}_{i,j} - c^{n+1**}_{i,j} H^{n+1**}_{i+1,j} = d^{n+1**}_{i,j}, \tag{7.49}$$

where $a^{n+1**}_{i,j}$, $b^{n+1**}_{i,j}$, $c^{n+1**}_{i,j}$ and $d^{n+1**}_{i,j}$ are defined by reference to equation (7.21).

2. If the horizontal chain does not start at the billet axis of rotation then use $H^{n+1*}_{i^n_{st,i,k}+1,j}$ and $H^{n+1*}_{i^n_{st,i,k}+2,j}$, together with the computed chain start boundary value for H^{n+1*}, to give an $O(\Delta z^3)$ approximation to $H^{n+1*}_{i^n_{st,i,k},j}$. This provides an approximation to $H^{n+1**}_{i^n_{st,i,k},j}$ which is $O(\Delta z^3)+O(\Delta \eta_n)$. Then set

$$e^{n+1**}_{i^n_{st,i,k},j} = 0, \tag{7.50}$$

$$f^{n+1**}_{i^n_{st,i,k},j} = H^{n+1**}_{i^n_{st,i,k},j}. \tag{7.51}$$

3. Otherwise, if the horizontal chain does start at the billet axis of rotation set

$$e^{n+1**}_{i^n_{st,i,k},j} = 1, \tag{7.52}$$

$$f^{n+1**}_{i^n_{st,i,k},j} = 0. \tag{7.53}$$

4. For $i = i^n_{st,i,k} + 1, ..., i^n_{fin,i,k} - 1$, define iteratively

$$e^{n+1**}_{i,j} = \frac{c^{n+1**}_{i,j}}{b^{n+1**}_{i,j} - a^{n+1**}_{i,j} e^{n+1**}_{i-1,j}}, \tag{7.54}$$

$$f^{n+1**}_{i,j} = \frac{d^{n+1**}_{i,j} + a^{n+1**}_{i,j} f^{n+1**}_{i-1,j}}{b^{n+1**}_{i,j} - a^{n+1**}_{i,j} e^{n+1**}_{i-1,j}}. \tag{7.55}$$

5. By interpolating from $H^{n+1*}_{i^n_{fin,i,k}-1,j}$, $H^{n+1*}_{i^n_{fin,i,k}-2,j}$ and the computed boundary value for H^{n+1*}, derive an $O(\Delta z^3) + O(\Delta \eta_n)$ approximation to $H^{n+1**}_{i^n_{fin,i,k},j}$.

6. For $i = i^n_{fin,i,k} - 1, ..., i^n_{st,i,k}$, compute values for $H^{n+1**}_{i,j}$ from

$$H^{n+1**}_{i,j} = e^{n+1**}_{i,j} H^{n+1**}_{i+1,j} + f^{n+1**}_{i,j}. \tag{7.56}$$

- **Stage 4:**

1. At the finish of each vertical chain of length greater than two meshpoints use $H^{n+1}_{i,j^n_{fin,i,k}-1}$ and $H^{n+1}_{i,j^n_{fin,i,k}-2}$, together with the computed chain end boundary value for H^{n+1}, to give an $O(\Delta z^3)$ approximation to $H^{n+1}_{i,j^n_{fin,i,k}}$.

2. At the start of each vertical chain of length greater than two meshpoints which does not start at the collector, interpolate from $H^{n+1}_{i,j^n_{st,i,k}+1}$, $H^{n+1}_{i,j^n_{st,i,k}+2}$ and the boundary value computed for H^{n+1} at the chain start to give an $O(\Delta z^3)$ approximation to $H^{n+1}_{i,j^n_{st,i,k}}$.

3. If a vertical chain starts at the collector solve for $H^{n+1}_{i,0}$ in

$$K(H^{n+1}_{i,1/2}) \frac{H^{n+1}_{i,1} - H^{n+1}_{i,0}}{\Delta z} = B_{collector}[T(H^{n+1}_{i,1/2}) - T_{collector}]. \tag{7.57}$$

4. For each horizontal chain of length greater than two meshpoints where the finish meshpoint does not also lie at the end of a vertical chain considered above, use $H^{n+1}_{i^n_{fin,i,k}-1,j}$, $H^{n+1}_{i^n_{fin,i,k}-2,j}$ and the computed boundary value for H^{n+1} to give an $O(\Delta z^3)$ approximation to $H^{n+1}_{i^n_{fin,i,k},j}$.

5. For each horizontal chain of length greater than two meshpoints where the start meshpoint is neither on the billet axis of rotation, nor lies at the end of a vertical chain considered above, use $H^{n+1}_{i^n_{st,i,k}+1,j}$, $H^{n+1}_{i^n_{st,i,k}+2,j}$ and the computed boundary value for H^{n+1} to give an $O(\Delta z^3)$ approximation to $H^{n+1}_{i^n_{st,i,k},j}$.

6. If a horizontal chain starts at the billet axis of rotation set

$$H^{n+1}_{i^n_{st,i,k},j} = H^{n+1}_{i^n_{st,i,k}+1,j}. \tag{7.58}$$

7. At any meshpoints in $\Omega^n | \tilde{\Omega}^n$ not considered above set $H^{n+1}_{i,j} = H^{n+1**}_{i,j}$.

7.1.4 Short chains; solving stages 1, 2 & 3

- **Stage 1:**

1. Let $(r_i, z_j) \in \Omega^n$ be a meshpoint in a short vertical chain, (i.e. a chain which contains ≤ 2 meshpoints). Let the billet surface intercept the gridline $r = r_i$ at distances $s_{st}\Delta z$ below and $s_{fin}\Delta z$ above (r_i, z_j) respectively, see Fig. 7.6.

2. Compute boundary values of H^n, say H^n_{st} and H^n_{fin}, at the chain ends, (where the billet surface intercepts the mesh), as previously described.

3. Define approximations to H^n at the points lying half way between (r_i, z_j) and the start and finish points of the chain by

$$H^n_{st+1/2} \equiv \frac{1}{2}(H^n_{st} + H^n_{i,j}), \tag{7.59}$$

$$H^n_{fin-1/2} \equiv \frac{1}{2}(H^n_{fin} + H^n_{i,j}). \tag{7.60}$$

4. Compute $H^{n+*}_{i,j}$ from

$$H^{n+*}_{i,j} - H^n_{i,j} = \nu^n \frac{2}{s_{st} + s_{fin}} \{K(H^n_{fin-1/2}) \frac{(H^n_{fin} - H^{n+*}_{i,j})}{s_{fin}} + K(H^n_{st+1/2}) \frac{(H^n_{st} - H^{n+*}_{i,j})}{s_{st}}\}. \tag{7.61}$$

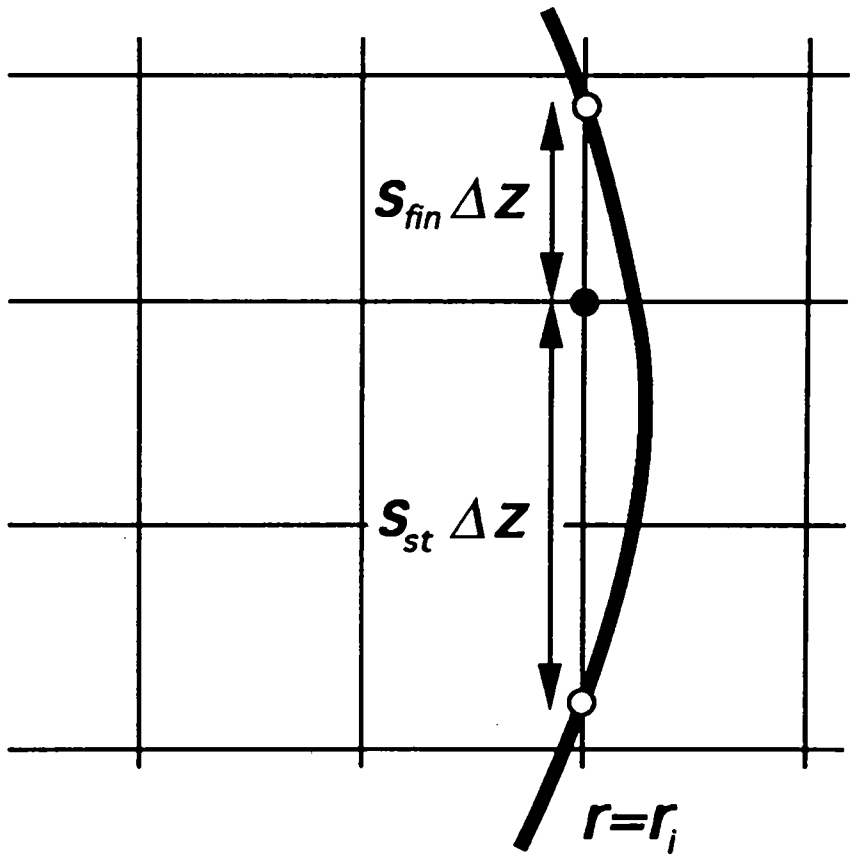

Figure 7.6: Start and finish points of short chains.

- **Stage 2:**

1. Let $(r_i, z_j) \in \Omega^n$ be a meshpoint in a short vertical chain. Let the billet surface intercept the gridline $r = r_i$ at distances $s_{st}\Delta z$ below and $s_{fin}\Delta z$ above (r_i, z_j) respectively.

2. Compute boundary values of H^{n+*}, say H^{n+*}_{st} and H^{n+*}_{fin}, at the chain ends, (where the billet surface intercepts the mesh), as previously described.

3. Define approximations to H^{n+*} at the points lying half way between (r_i, z_j) and the start and finish points of the chain by

$$H^{n+*}_{st+1/2} \equiv \frac{1}{2}(H^{n+*}_{st} + H^{n+*}_{i,j}), \tag{7.62}$$

$$H^{n+*}_{fin-1/2} \equiv \frac{1}{2}(H^{n+*}_{fin} + H^{n+*}_{i,j}). \tag{7.63}$$

4. Compute $H_{i,j}^{n+1*}$ from

$$H_{i,j}^{n+1*} - H_{i,j}^{n} = \nu^n \frac{2}{s_{st}+s_{fin}}\{K(H_{fin-1/2}^{n+*})\frac{(H_{fin}^{n+*} - H_{i,j}^{n+1*})}{s_{fin}} + K(H_{st+1/2}^{n+*})\frac{(H_{st}^{n+*} - H_{i,j}^{n+1*})}{s_{st}}\}. \quad (7.64)$$

- **Stage 3:**

1. Let $(r_i, z_j) \in \Omega^n$ be a meshpoint in a short horizontal chain. Let the billet surface intercept the gridline $z = z_j$ at distances $s_{st}\Delta z$ to the left of and $s_{fin}\Delta z$ to the right of (r_i, z_j) respectively.

2. Compute boundary values of H^{n+1*}, say H_{st}^{n+1*} and H_{fin}^{n+1*}, at the chain ends, (where the billet surface intercepts the mesh), as previously described.

3. Define approximations to H^{n+1*} at the points lying half way between (r_i, z_j) and the start and finish points of the chain by

$$H_{st+1/2}^{n+1*} \equiv \frac{1}{2}(H_{st}^{n+1*} + H_{i,j}^{n+1*}), \quad (7.65)$$

$$H_{fin-1/2}^{n+1*} \equiv \frac{1}{2}(H_{fin}^{n+1*} + H_{i,j}^{n+1*}). \quad (7.66)$$

4. Compute $H_{i,j}^{n+1**}$ from

$$H_{i,j}^{n+1**} - H_{i,j}^{n} = \frac{2\nu^n}{s_{st}+s_{fin}}\{(1+\frac{1/2}{i-1/2}s_{fin})K(H_{fin-1/2}^{n+1*})\frac{(H_{fin}^{n+1*} - H_{i,j}^{n+1**})}{s_{fin}} + (1-\frac{1/2}{i-1/2}s_{st})K(H_{st+1/2}^{n+1*})\frac{(H_{st}^{n+1*} - H_{i,j}^{n+1**})}{s_{st}}\}. \quad (7.67)$$

7.1.5 Computing $H_{i,j}^{n+1}$; $\forall (r_i, z_j) \in \Omega^{n+1}|\Omega^n$

The previous sections describe how $H_{i,j}^{n+1}$ is computed at all $(r_i, z_j) \in \Omega^n$. New meshpoints, $(r_i, z_j) \in \Omega^{n+1}|\Omega^n$, are also added to the growing billet on each timestep, (see Fig. 7.2b). The following procedure is used to assign values to $H_{i,j}^{n+1}$ at these meshpoints.

1. The stored boundary data for the billet surface at time η_{n+1} is used with the newly computed values of $H_{i,j}^{n+1}$ in Ω^n to give values of H^{n+1} at all points of interception of the billet surface with vertical and horizontal gridlines. The method used is analagous to that described above in section 7.1.2.

2. New meshpoints $(r_i, z_j) \in \Omega^{n+1}|\Omega^n$ that lie on the extension of an existing vertical chain within Ω^n, and within a distance $2\Delta z$ of the start or finish meshpoint of the existing vertical chain, are assigned values. Values are determined by interpolating between the boundary value that has been assigned to H^{n+1} at the end of the existing vertical chain, and the values of $H_{i,j}^{n+1}$ at the two closest meshpoints in the existing vertical chain. If the chain contains only one meshpoint then a lower order approximation is achieved by the interpolation.

3. New meshpoints $(r_i, z_j) \in \Omega^{n+1}|\Omega^n$ that lie on the extension of an existing horizontal chain within Ω^n, within a distance Δz of the start or finish meshpoint of the existing horizontal chain, and which have not previously been assigned a value, are assigned values. Values are determined by interpolating

between the boundary value that has been assigned to H^{n+1} at the end of the existing horizontal chain, and the values of $H_{i,j}^{n+1}$ at the two closest meshpoints in the existing horizontal chain. If the chain contains only one meshpoint then a lower order approximation is achieved by the interpolation.

7.1.6 Timestep selection

A number of constraints are imposed on the timestep, $\Delta\eta_n$, that is selected. Firstly, use of the Thomas algorithm, as described in section 7.1.3, to solve the tri-diagonal matrix systems of equations which arise from stages 1, 2 and 3 imposes a timestep constraint. It is easily shown that

$$|e_{i,j}^{n+*}| \leq 1, \qquad \forall i,j, \tag{7.68}$$

$$|e_{i,j}^{n+1*}| \leq 1, \qquad \forall i,j, \tag{7.69}$$

$$|e_{i,j}^{n+1**}| \leq 1, \qquad \forall i,j. \tag{7.70}$$

Thus, the stability of the algorithm is assured. Rounding errors may however build up in computing $f_{i,j}^{n+*}$, $f_{i,j}^{n+1*}$ and $f_{i,j}^{n+1**}$. This is avoided if

$$c_{i,j}^{n+*} - a_{i,j}^{n+*} < 1, \qquad \forall i,j, \tag{7.71}$$

$$c_{i,j}^{n+1*} - a_{i,j}^{n+1*} < 1, \qquad \forall i,j, \tag{7.72}$$

$$a_{i,j}^{n+1**} - c_{i,j}^{n+1**} < 1, \qquad \forall i,j. \tag{7.73}$$

Defining L_1^n as the maximum of the left-hand sides of (7.71), (7.72) and (7.73), choice of $\Delta\eta_{n+1}$ is made to satisfy

$$\frac{\Delta\eta_{n+1}}{\Delta\eta_n} L_1^n \leq 0.8. \tag{7.74}$$

Contstraints (7.71) and (7.72) are very similar, and are of form

$$\begin{aligned} 1 > c_{i,j}^{n+*} - a_{i,j}^{n+*} &\approx c_{i,j}^{n+1*} - a_{i,j}^{n+1*}, \\ &\approx \frac{\Delta\eta_n}{Pe\Delta z} \frac{\mathrm{d}}{\mathrm{d}z} K(H_{i,j}^{n+1}). \end{aligned} \tag{7.75}$$

Hence, this represents a constraint of form

$$\Delta\eta_n \sim \Delta z.$$

However, typically H will increase with z, since spray is deposited near the top of the billet, and $K(H)$ will decrease with H over the range of fraction liquids typically encountered, (see e.g. Fig. 5.3). Thus, constraints (7.71) and (7.72) are usually satisfied trivially. It should be noted that this is a consequence of the "correct" choice of direction in which to solve the tri-diagonal systems in stages 1 and 2.

Contstraint (7.73) can be written as

$$1 > a_{i,j}^{n+1**} - c_{i,j}^{n+1**} \approx \frac{\Delta\eta_n}{Pe\Delta z} \{ \frac{\mathrm{d}}{\mathrm{d}r} K(H_{i,j}^{n+1}) - \frac{K(H_{i,j}^{n+1})}{r_i} \}. \tag{7.76}$$

This again represents a constraint of form

$$\Delta\eta_n \sim \Delta z.$$

The second term on the right hand side of (7.76) is always negative and is usually larger in magnitude than the first term. Thus, the "correct" choice of direction in which to solve the tri-diagonal systems in stage 3 has again resulted in a constraint that will typically be satisfied trivially.

A second form of timestep restriction results from the moving boundary. Although in itself the moving boundary has little effect on the heat flow computation, since this is carried out on Ω^n, the speed of the moving boundary does effect the number of new meshpoints that are added to the billet on each timestep. Since the local truncation error at newly added meshpoints will be of lower order than elsewhere, it is desirable to control the rate at which new meshpoints are added to the billet

The following two growth related restrictions are imposed.

1. L_2^n is defined as the maximum surface normal velocity that is stored at time η_{n+1} at the points of interception of the billet surface with the gridlines. Choice of $\Delta\eta_{n+1}$ satisfies

$$\Delta\eta_{n+1} \leq \frac{\Delta z}{2L_2^n}. \tag{7.77}$$

2. Let $\Delta\eta_{n+1*}$ be the maximum timestep which satisfies both constraints, (7.74) and (7.77), and let L_3^n be defined as the maximum increase in the length of a vertical chain in Ω^n between times η_n and η_{n+1}. If $L_3^n > \Delta z/2$ then

$$\Delta\eta_{n+1} = [\frac{\Delta z}{2L_3^n}]^3 \Delta\eta_{n+1*}. \tag{7.78}$$

If $L_3^n \leq \Delta z/2$, but $L_3^{n-k} > \Delta z/2$ for some $k \leq 10$ then

$$\Delta\eta_{n+1} = L_4^{n,k} \Delta\eta_{n+1*}, \tag{7.79}$$

where

$$L_4^{n,k} \equiv [\frac{\Delta z}{2L_3^{n-k}}]^3 + \frac{k}{10}\{1 - [\frac{\Delta z}{2L_3^{n-k}}]^3\}. \tag{7.80}$$

Otherwise,

$$\Delta\eta_{n+1} = \Delta\eta_{n+1*}. \tag{7.81}$$

The first growth related constraint is straightforward and ensures explicitly for the next timestep that new meshpoints in $\Omega^{n+2}|\Omega^{n+1}$ lie within $\Delta z/2$ of meshpoints in Ω^{n+1}. The second constraint severely restricts the timestep during periods when there is significant growth in the radial direction, (e.g. when there is significant transient growth towards a steady state), but has little effect when the billet growth is predominantly vertical.

7.1.7 Initial conditions

Initial conditions for the numerical solution are set by assuming an initially uniform deposit of thickness $2\Delta z$ on top of the collector plate. The collector plate initial vertical displacement below the atomiser is increased by a distance $2\Delta z$, so as to leave the initial conditions for the billet growth computation unchanged. Thus, for $0 < r_i < r_c$, $k_i^{v,0} = 1$,

$$j_{st,i,1}^0 = 0, \tag{7.82}$$

$$j_{fin,i,1}^0 = 2, \tag{7.83}$$

and for $0 < z_j < 2\Delta z$, $k_j^{h,0} = 1$,

$$i_{st,j,1} = 0, \tag{7.84}$$

$$i_{fin,j,1} = \text{int}[\frac{r_c}{\Delta z} + \frac{1}{2}], \tag{7.85}$$

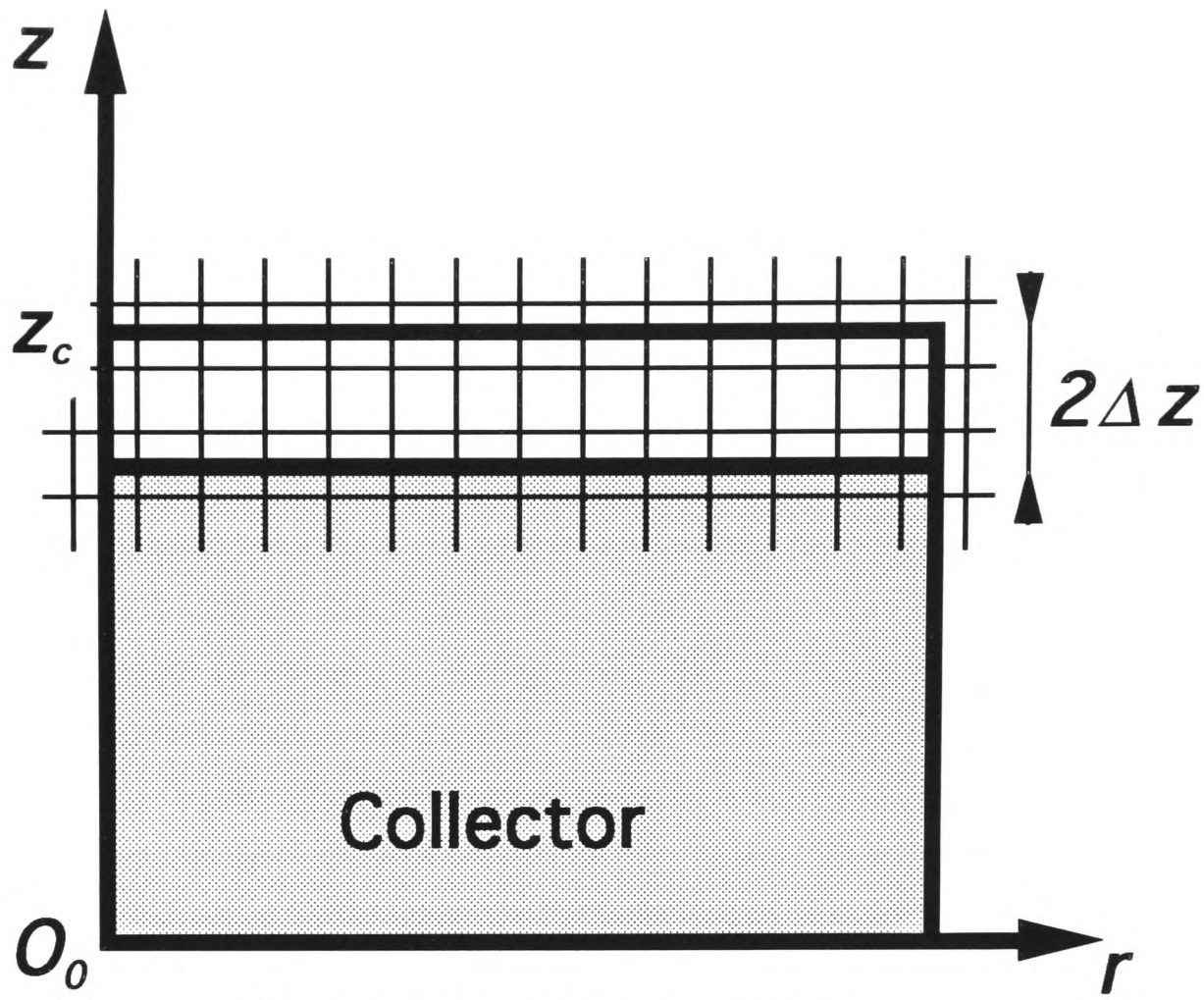

Figure 7.7: Assumed initial conditions

see Fig. 7.7.

Initial values for H are chosen by assuming a constant vertical enthalpy gradient through the thin initial deposit at each radial distance, r_i. This gradient is chosen so as to satisfy a finite difference analogue of the boundary condition (7.8) at the billet top surface. Linear interpolation using $H^0_{i,1}$ and $H^0_{i,2}$ gives

$$\begin{aligned} H(r_i, z_{2\frac{1}{2}}, \eta_0) &\approx 2H^0_{i,2} - H^0_{i,1}, \\ \frac{\partial H}{\partial z}(r_i, z_{2\frac{1}{2}}, \eta_0) &\approx H^0_{i,2} - H^0_{i,1}. \end{aligned}$$

Using the above approximations $H^0_{i,1}$ and $H^0_{i,2}$ are made satisfy

$$K(H^0_{i,2\frac{1}{2}})\frac{H^0_{i,2} - H^0_{i,1}}{\Delta z} = B_{gas}[T(H^0_{i,2\frac{1}{2}}) - T_{gas}] + Pe\overline{v}[H^0_{i,2\frac{1}{2}} - H_{spray}]. \tag{7.86}$$

Another condition is required to determine both $H^0_{i,1}$ and $H^0_{i,2}$. This second condition is given by assuming that the heat content of the initial thin layer of deposit is governed by the boundary heat fluxes. At each $r_i < r_c$ the solution, $\overline{H}_i$, of

$$0 = B_{collector}[T(\overline{H}_i) - T_{collector}] + B_{gas}[T(\overline{H}_i) - T_{gas}] + Pe\overline{v}[\overline{H}_i - H_{spray}], \tag{7.87}$$

is computed using a bisection method. A second condition for $H^0_{i,1}$ and $H^0_{i,2}$ is then given by

$$H^0_{i,1} + H^0_{i,2} = 2\overline{H}_i. \tag{7.88}$$

Finally, linear interpolation is used to give $H^n_{i,0}$ from the values of $H^0_{i,1}$ and $H^0_{i,2}$, preserving the constant vertical enthalpy gradient through the deposit.

7.1.8 Treatment of the collector

The collector is treated as a cylindrical slab of material, with constant density, specific heat capacity and thermal conductivity denoted $\rho_{collector}$, $c_{collector}$ and $K_{collector}$ respectively. The collector thickness is denoted $\hat{Z}_{collector}$. A uniform collector initial temperature, $\hat{T}^0_{collector}$, is assigned and an axisymmetric temperature profile is assumed to exist within the collector at later times.

Heat flows into the collector through the base of the billet. The sides and bottom of the collector are assumed insulated throughout the process. Thus, the collector acts as an initial heat sink for the spray that is first deposited, and then diminishes in importance as it itself heats up and as the billet grows larger.

Temperature profiles within the collector are computed explicitly on timestep n. Values of $H^n_{i,1/2}$ at the billet base are used as boundary conditions throughout the timestep, to integrate the collector temperature forward to time η_{n+1}. This collector temperature is then used in the implicit scheme described above for computing the billet enthalpy on timestep n. A completely standard 5-point explicit, centrally differenced finite difference scheme is used, with a much coarser spatial mesh than that used for the billet heat flow computation. If necessary, the time is advanced from η_n to η_{n+1} over a number of smaller substeps when computing the collector temperature, in order to preserve the stability of the explicit scheme.

For computations carried out in this chapter the following parameters are assumed.

$$\begin{aligned}
\rho_{collector} &= 2560\ kg/m^3, \\
c_{collector} &= 1300\ J/kg/C, \\
K_{collector} &= 180\ W/m/C, \\
\hat{T}^0_{collector} &= 25\ C, \\
h_{collector} &= 2000\ W/m^2/C, \\
\hat{Z}_{collector} &= .03\ m.
\end{aligned}$$

7.1.9 B_{gas}, T_{gas}, and H_{spray}

Derivation of accurate submodels to describe B_{gas}, T_{gas}, and H_{spray} is beyond the scope of this thesis. However, the assumptions of constant B_{gas}, T_{gas}, and H_{spray} across the billet surface, which were made in chapter six so that the effects of changes in billet shape, scanner and rotation rates could be studied in isolation, are here invalid. This is because on the slow timescale, variations in B_{gas}, T_{gas}, and H_{spray} along the billet surface can have a significant effect on the heat flow in other parts of the billet.

The heat transfer coefficient, h_{gas}, is thought to decrease smoothly from a value of approximately 1000 $W/m^2/C$ on the billet crown to a value of approximately 300 $W/m^2/C$ along the billet sides, [2]. The transition from billet crown to billet sides typically occurs within a distance $\approx \hat{r}_s$ above the lower spray boundary, as the mass flux tends to zero at the spray edge. A simple model which captures this feature is given by

$$B_{gas}(r_1, z_1) = \begin{cases} B_{gas,1}, & z_{1,*} \leq z_1, \\ B_{gas,2} + (B_{gas,1} - B_{gas,2}) \dfrac{\|\bar{\boldsymbol{g}}(r_1, z_1)\|}{\|\bar{\boldsymbol{g}}(r_1, z_{1,*})\|}, & r_1 \cot a_1 < z_1 < z_{1,*}, \\ B_{gas,2}, & z_1 \leq r_1 \cot a_1, \end{cases} \tag{7.89}$$

where,

$$z_{1,*} \equiv \frac{r_1 \cos a_1 + r_s}{\sin a_1},$$

and for the purposes of the results presented in this chapter,

$$B_{gas,1} = \frac{1000R}{K_s}, \tag{7.90}$$

$$B_{gas,2} = \frac{300R}{K_s}. \tag{7.91}$$

Recall, r_1 and z_1 measure the radial and vertical distances from O_1 respectively, within the crown frame of reference. The angle a_1 is the minimum angle that the spray cone axis makes with the vertical; R and K_s are respectively, the chosen process length-scale and the thermal conductivity of the solid phase of the alloy.

For given atomising gas pressures and metal mass flow rates the spray fraction liquid, $f_{l,spray}$, is known to decrease with distance from the atomiser; (for measurements and computations see e.g. [6, 7, 13, 38, 43, 45, 46, 50, 74, 87, 89]). The exact spray fraction liquid at a given distance from the atomiser nozzle will also depend on the local droplet size distribution and gas velocity, as well as other factors such as the melt superheat. See the discussion in chapter one, section 1.2.2.

A very simplified model, which roughly approximates the spray fraction liquid variations at typical flight distances that have been computed for representative process parameters in [43], is given by

$$f_{l,spray}(\hat{z}_d) = 1 - \hat{z}_d, \tag{7.92}$$

where $\hat{z}_d$ is the dimensional distance from the atomiser nozzle. This model is used to compute H_{spray} at the billet surface for all results presented in this chapter.

In the absence of further data a constant gas temperature,

$$\hat{T}_{gas} = 200\ C, \tag{7.93}$$

is assumed for the results presented in this chapter.

7.1.10 Summary of algorithm

The following summarises the main steps in the algorithm for computing the numerical solution to (7.7), (7.8), (7.9) and (7.10).

1. Set initial conditions for billet growth.
2. Set initial conditions for billet heat flow.
3. To advance the solution from time η_n to time η_{n+1} do the following:
   (a) Select timestep.
   (b) Compute new billet boundary.
   (c) Store boundary data.
   (d) Compute $H_{i,j}^{n+*} : \forall (r_i, z_j) \in \Omega^n$ by solving the tri-diagonal systems in stage 1 on all vertical chains in Ω^n.

(e) Compute $H_{i,j}^{n+1*}$: $\forall(r_i, z_j) \in \Omega^n$ by solving the tri-diagonal systems in stage 2 on all vertical chains in Ω^n.

(f) Compute $H_{i,j}^{n+1**}$: $\forall(r_i, z_j) \in \Omega^n$ by solving the tri-diagonal systems in stage 3 on all horizontal chains in Ω^n.

(g) Compute $H_{i,j}^{n+1}$: $\forall(r_i, z_j) \in \Omega^n$ by solving stage 4; iterate stage 4 if necessary.

(h) Compute $H_{i,j}^{n+1}$: $\forall(r_i, z_j) \in \Omega^{n+1}|\Omega^n$ by interpolating from boundary values of H^{n+1} and computed values of $H_{i,j}^{n+1}$ in Ω^n.

7.2 Computational method; discussion

The criteria that one hopes to satisfy with an algorithm for the numerical solution of equations (7.7), (7.8), (7.9) and (7.10) are rather less stringent than those one might hope to satisfy when solving a simpler boundary value problem.

Firstly, a high order scheme is not required. Heat flow is a diffusive phenomena, with internal variations bounded by those at the boundary. The boundary layer model of chapter six provides high resolution information about the rapid heat flow that occurs close to the billet surface. The slow-time model is intended to provide insight into processes occurring on a much larger length-scale, that are infiuenced by more global and longer term variations in boundary conditions. Thus, fine resolution is unlikely to be needed to expose such features.

Secondly, although for a simpler boundary value problem one might hope to demonstrate the consistency, stability and convergence of the algorithm, here this is unlikely to be achieved without great effort. Instead, apart from consistency, the main objectives to be aimed for in devising a numerical method for (7.7), (7.8), (7.9) and (7.10) are that the method be both quick and robust. Additionally, one might attempt to devise a method which retains as much conceptual simplicity as is possible. By being "robust", one implies not only that the method be numerically stable, but also that the algorithm is able to reliably cope with a wide range of process parameters and billet geometries.

Complications in computing the solution to equations (7.7), (7.8), (7.9) and (7.10) arise from the problem being two dimensional, nonlinear, and from the irregular expanding domain. Ways to cope with the expanding domain can be divided into either "front-fixing" methods or "front-tracking" methods. Much published work that deals with deposit heat flow in spray forming processes employs front-fixing methods, [6, 7, 87, 88, 89]. In contrast, this thesis uses a front-tracking method to deal with the moving billet surface.

7.2.1 Front-tracking and front-fixing methods

The contrast between these two overall solution strategies is best illustrated through consideration of the one dimensional analogue of equations (7.7), (7.8), (7.9) and (7.6), i.e.

$$\frac{\partial H}{\partial \eta} = \frac{1}{Pe}\frac{\partial}{\partial z}.[K(H)\frac{\partial H}{\partial z}], \qquad z \in [0, Z(\eta)], \tag{7.94}$$

$$-K(H)\frac{\partial H}{\partial z} = B_{gas}[T(H) - T_{gas}] + Pe\bar{v}[H - H_{spray}], \qquad z = Z(\eta), \tag{7.95}$$

$$K(H)\frac{\partial H}{\partial z} = B_{collector}[T(H) - T_{collector}], \qquad z = 0, \tag{7.96}$$

$$Z(\eta) = \int_0^\eta \overline{v}(\tau)\mathrm{d}\tau. \tag{7.97}$$

Here the heat flow is one dimensional and the growing billet has been replaced by the expanding interval $z \in [0, Z(\eta)]$, with $\overline{v}(\eta)$ specified.

In a **front-tracking** method the above equations are discretised in a standard way, using a mesh fixed in the spatial domain, and the numerical approximation is advanced from timestep n to timestep $n+1$ using the resulting difference equations. The progress of the moving boundary, $z = Z(\eta)$, is tracked as it crosses successive meshpoints. Problems that arise in this sort of method include

- how to specify H on timestep $n+1$ at meshpoints that were not in the solution domain at timestep n,
- the need to either select the timestep so that the boundary condition (7.95) may be satisfied at a meshpoint on each timestep, or to devise a special treatment for satisfying (7.95) between meshpoints on each timestep without an unacceptable loss of accuracy,
- the time required to advance the numerical solution from time step n to timestep $n+1$ increases with n, due to the addition of extra meshpoints as the solution domain expands.

In a **front-fixing** method the coordinates of the expanding solution domain are mapped into a geometrically simpler domain. In the one dimensional example the mapping

$$\xi = \frac{z}{Z(\eta)}, \tag{7.98}$$

maps the solution domain into the unit interval, $\xi \in [0, 1]$, and transforms equations (7.94), (7.95) and (7.96) into

$$\frac{\partial H}{\partial \eta} = \frac{\xi\overline{v}}{Z(\eta)}\frac{\partial H}{\partial \xi} + \frac{1}{PeZ(\eta)^2}\frac{\partial}{\partial \xi}.[K(H)\frac{\partial H}{\partial \xi}], \qquad \xi \in [0, 1], \tag{7.99}$$

$$-\frac{K(H)}{Z(\eta)}\frac{\partial H}{\partial \xi} = B_{gas}[T(H) - T_{gas}] + Pe\overline{v}[H - H_{spray}], \qquad \xi = 1, \tag{7.100}$$

$$\frac{K(H)}{Z(\eta)}\frac{\partial H}{\partial \xi} = B_{collector}[T(H) - T_{collector}], \qquad \xi = 0. \tag{7.101}$$

Whilst the problems associated with the front-tracking method are avoided by this transformation, problems that arise are

- additional complexity in the field equations and boundary conditions to be solved,
- additional computation in mapping between domains,
- loss of resolution in the physical solution domain as $Z(\eta)$ becomes large,
- initial timestep restrictions when $Z(\eta)$ is small if an explicit method is used.

For a properly one dimensional problem, (e.g. uniform sprayed metal strip), the additional complexity in the field equations and boundary conditions is not very severe. Published work here has generally used an explicit finite difference method to solve equations such as (7.99), (7.100) and (7.101), e.g. [6, 7, 87, 88]. It is

noticable however, that the published work considers only sprayed metal strip and thin discs of up to a few centimetres in thickness. Clearly, in computing physically larger domains the assumption that the heat flow will be one dimensional becomes questionable. However, this is only part of the problem. Other problems are firstly, that using an explicit method to integrate over the longer time period that will be required for large $Z(\eta)$ is very expensive computationally, and secondly, that either the accuracy will decrease with $Z(\eta)$ or it will be neccessary to refine the grid in the ξ domain. The latter choice not only negates one of the advantages of this type of method over a front-tracking method, but also further restricts the size of timestep used.

Where the problem is two dimensional, the situation becomes much more complicated. Billet geometries can be complex, and the first problem to be overcome is to choose a suitable two dimensional analogue of (7.98). Wavy sided billets and billets with irregular crown shapes can cause transformations such as

$$\xi = \frac{z}{Z(\eta, r)}, \tag{7.102}$$

$$\varrho = \frac{r}{R(\eta, z)}, \tag{7.103}$$

(where $z = Z(\eta, r)$ and $r = R(\eta, z)$ define the billet surface), to become double valued, e.g. see Fig. 7.8. If the billet geometry is more regular, the use of transformations such as (7.102) and (7.103) will still result in extremely complex field equations. For example,

$$\begin{aligned} \frac{\partial}{\partial z} &= \frac{\partial \xi}{\partial z}\frac{\partial}{\partial \xi} + \frac{\partial \varrho}{\partial z}\frac{\partial}{\partial \varrho}, \\ &= \frac{1}{Z}\frac{\partial}{\partial \xi} - \frac{\varrho}{R}\frac{\partial R}{\partial z}\frac{\partial}{\partial \varrho}. \end{aligned}$$

Thus, it can be seen that transformation of (7.7) will contain mixed derivatives of up to second order in ξ and ϱ, as well as derivatives of $Z(\eta, r)$ and $R(\eta, z)$ with respect to r and z respectively, of up to second order. Hence, it is not enough to estimate the billet surface position through a billet growth model, but estimates of surface gradient and curvature must also be made.

Additional complexity also results in transfoming the boundary condition (7.8) to the normalised coordinates. Here, the normal derivative will result in boundary conditions of type

$$A(\varrho, \xi, \eta, H)\frac{\partial H}{\partial \varrho} + B(\varrho, \xi, \eta, H)\frac{\partial H}{\partial \xi} = C(\varrho, \xi, \eta, H, B_{gas}, T_{gas}, H_{spray})$$

to be satisfied on the billet boundary. Proper numerical treatment of such boundary conditions, in order to preserve accuracy would require much care.

Mathur *et al.* claim the use of a two dimensional front-fixing method in the only published two dimensional results, [89]. In [89] the growth of, and heat flow within small well shaped billets is presented. However, a statement of the equations actually solved and a description of the numerical algorithm used is omitted. This work has been discussed further in chapter one, section 1.2.5.

In summary, use of a front-fixing method to solve equations (7.7), (7.8), (7.9) and (7.10) has been rejected for the following reasons.

- The transformed field equations are extremely complex in two dimensions, and require computation of the surface position, velocity, gradient and curvature for their solution.

- The transformed boundary conditions contain tangential derivative as well as normal derivative terms.
- Loss of accuracy in computing heat flow within large production scale billets, or excessive timestep restrictions due to the use of a very fine mesh.
- Additional mapping problems may arise with complex geometries.

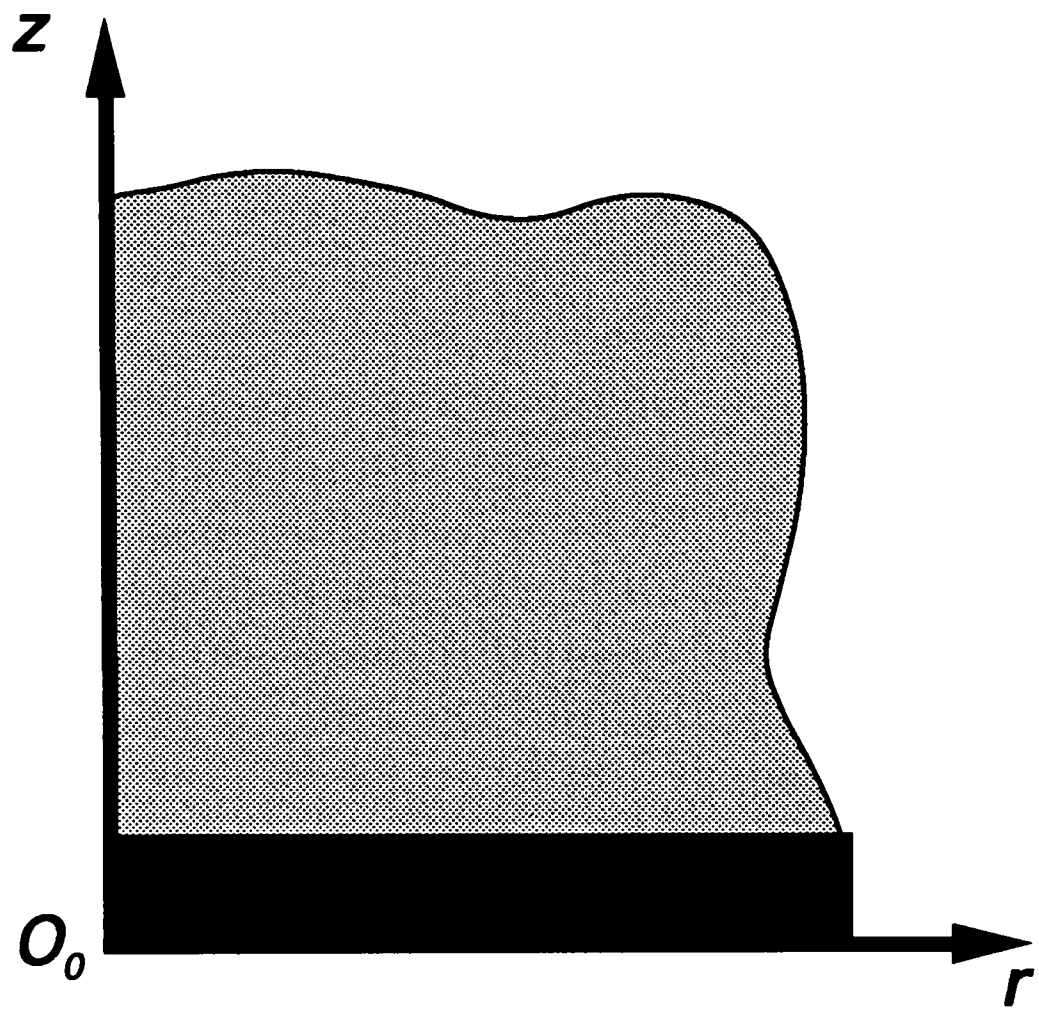

Figure 7.8: Problems with simple transformations

7.2.2 ADI and LOD methods

In one dimension, two step finite difference methods for parabolic problems may be broadly classified as either explicit or implicit. Explicit methods enjoy the advantage of being extremely easy to implement, and in general involve fewer floating point multiplications per timestep. However, they are also hampered by severe restrictions on the size of timestep which may be used while still preserving numerical stability. Implicit methods enjoy the advantage of being numerically more stable, (unconditionally sometimes), and those methods which may be written in the form of tri-diagonal matrix equations can also be solved efficiently by use of the Thomas algorithm. Although more floating point multiplications per timestep are generally required when solving an implicit difference scheme, the possible use of larger timesteps often makes the implicit method more economical. Even when the equations are nonlinear, use of a predictor-corrector method such as in chapter six, can retain the economy of the implicit method.

When solving a two dimensional parabolic problem, the timestep restrictions on an explicit method are even more severe. However, now the straightforward use of an implicit method entails the inversion of a large matrix, which is no longer tri-diagonal. Thus, the economical Thomas algorithm can no longer be used to perform the inversion, and the choice between straightforward explicit and implicit methods is not as simple as in the one dimensional case.

In an effort to retain the economy and stability of the implicit methods used for one dimensional problems, alternating direction implicit, (ADI), methods were first proposed in the 1950's, [29, 105]. These methods essentially split the two dimensional implicit difference scheme into two stages, each of which involves the solution of a tri-diagonal matrix equation. Each tri-diagonal matrix equation results from the use of an implicit discretisation in the direction of one coordinate axis, and only an explicit discretisation in the direction of the other axis. The direction of the implicit discretisation alternates over the two stages, (see e.g. [40, 147] for a discussion). Such methods are frequently used for multi-dimensional unsteady heat flow computations in the metals processing industry, e.g. [67, 137].

Also developed in parallel to the ADI schemes, were certain methods which approximate the two dimensional problem, again with two stages involving the solution of tri-diagonal systems, but with the discretisation at each stage approximating the heat flow only in one direction, [146]. These locally one dimensional, (LOD), schemes have some advantages over ADI methods in terms of computational speed, but have been criticised since although the two stages combine to provide a consistent approximation to the underlying differential equation neither stage alone is consistent.

The lack of consistency of the two stages of an LOD method with the differential equation can cause problems in how to interpret the mesh function that is solved for in the first stage. This interpretation is important, since boundary conditions must be assigned in order to compute the intermediate mesh function. Thus, in general, an ADI method is to be preferred. For an ADI method the interpretation of the intermediate mesh function computed by the first stage is often more straightforward.

Gourlay and Mitchell, [41], have investigated the relationship between the different approximations produced by ADI and LOD schemes with varying degrees of implicitness. In particular they show the equivalence of the two methods for the fully implicit method, so that the fully implicit LOD method may be regarded as both an LOD and an ADI method. It is this LOD method that is most commonly used.

Although in [146] Yanenko originally proposed the LOD method for numerical solution of the Dirichlet problem for the linear heat equation on a rectangular region, the method has since been generalised to arbitrary regions, to mixed boundary conditions and to some nonlinear parabolic equations, [121]. Various convergence results are given in [57, 58, 121]; convergence rates being at least first order in both temporal and spatial directions. The better convergence rates result from rectangular regions, linear problems and Dirichlet boundary conditions.

7.2.3 Generalisation to the slow-time heat flow problem

The numerical algorithm described in section 7.1 of this chapter is based on a fully implicit discretisation of equation (7.7), adjusted to cope with the nonlinearity and the moving boundary. After iteration of stage 4 of the algorithm, the equations

$$\begin{aligned} H_{i,j}^{n+1} - H_{i,j}^{n} \;=\; & \nu^n \{ K(H_{i,j+1/2}^{n+1})(H_{i,j+1}^{n+1} - H_{i,j}^{n+1}) + K(H_{i,j-1/2}^{n+1})(H_{i,j-1}^{n+1} - H_{i,j}^{n+1}) \\ & + \frac{i}{i-1/2} K(H_{i+1/2,j}^{n+1})(H_{i+1,j}^{n+1} - H_{i,j}^{n+1}) + \frac{i-1}{i-1/2} K(H_{i-1/2,j}^{n+1})(H_{i-1,j}^{n+1} - H_{i,j}^{n+1}) \}, \end{aligned} \tag{7.104}$$

are satisfied at all meshpoints $(r_i, z_j) \in \tilde{\Omega}^n$. Convergence of this method for a nonlinear parabolic equation such as (7.7), on an arbitrary smooth region, and with mixed boundary conditions, is discussed by Samarskii,

[120]. A generalisation to the case of an expanding domain has not been found in the literature.

Stages 1, 2 and 3, used alone, provide a one dimensionally derived estimate to the implicit nonlinear difference equations, (7.104). Stages 1 and 2 correspond to the first stage of the fully implicit LOD scheme that would at internal meshpoints be given by

$$H_{i,j}^{n+1*} - H_{i,j}^{n} = \nu^n\{K(H_{i,j+1/2}^{n+1*})(H_{i,j+1}^{n+1*} - H_{i,j}^{n+1*}) + K(H_{i,j-1/2}^{n+1*})(H_{i,j-1}^{n+1*} - H_{i,j}^{n+1*})\}, \tag{7.105}$$

$$H_{i,j}^{n+1} - H_{i,j}^{n+1*} = \nu^n\{\frac{i}{i-1/2}K(H_{i+1/2,j}^{n+1*})(H_{i+1,j}^{n+1} - H_{i,j}^{n+1}) + \frac{i-1}{i-1/2}K(H_{i-1/2,j}^{n+1*})(H_{i-1,j}^{n+1} - H_{i,j}^{n+1})\}. \tag{7.106}$$

Equation (7.105) is nonlinear and would require some form of iterative process to be satisfied exactly. The two stages above, (7.105) and (7.106), combine to give a consistent approximation to (7.7). From (7.106) it can be seen that $H_{i,j}^{n+1*}$ is an $O(\Delta\eta)$ approximation to $H_{i,j}^{n+1}$.

Stages 1 and 2 of the numerical method described, approximate (7.105) by a predictor corrector method, with stage 2 being effectively the first iteration towards an exact solution of (7.105). Additionally, whilst stage 1 has used the new boundary position and function values, together with a normal derivative estimated from $H_{i,j}^{n}$, to satisfy (7.8), stage 2 of the algorithm estimates the normal derivative in (7.8) from values of $H_{i,j}^{n+*}$ that have been computed in stage 1. Thus, the two stages used to approximate (7.105) involve an iteration of the boundary values of H^{n+1*} as well as the internal values, $H_{i,j}^{n+1*}$. This iterative application of the normal derivative boundary condition is suggested in [147].

Stage 3 of the algorithm then corresponds directly to (7.106) above. The boundary condition (7.8) is satisfied using a normal derivative estimated from values of $H_{i,j}^{n+1*}$. Thus, at both internal and boundary meshpoints the values of $H_{i,j}^{n+1**}$ are estimates of the values $H_{i,j}^{n+1}$, given by (7.104), and have been derived only from approximations of the nonlinear diffusive operator at time η_{n+1}. The values of $H_{i,j}^{n+1**}$ computed in stage 3 of the algorithm therefore give a good first approximation to the iterated final values, $H_{i,j}^{n+1}$, computed in stage 4, not only at internal meshpoints, but also close to the boundary.

Instead of stage 4 in the algorithm the LOD method could be used alone, with iteration used to solve (7.105) exactly and (7.106) replaced by

$$H_{i,j}^{n+1} - H_{i,j}^{n+1*} = \nu^n\{\frac{i}{i-1/2}K(H_{i+1/2,j}^{n+1})(H_{i+1,j}^{n+1} - H_{i,j}^{n+1}) + \frac{i-1}{i-1/2}K(H_{i-1/2,j}^{n+1})(H_{i-1,j}^{n+1} - H_{i,j}^{n+1})\}, \tag{7.107}$$

which could again be solved via iteration. Initial attempts to use this methodology were unsuccessful. In iterating to an exact solution of (7.105) and (7.107) the problem of inconsistency of either stage with (7.7) emerges. The computation of the billet surface is carried out at points separated by a distance $\sim \mathrm{d}s_{max}$, where $\mathrm{d}s_{max}$ is chosen to satisfy

$$\mathrm{d}s_{max} \approx \Delta z.$$

Thus, any oscillations in boundary errors that are attributable to using a numerical procedure to solve for the billet surface position will occur on approximately the same spatial frequency as the mesh spacing. Such errors will typically be very small, but may grow larger in periods of more rapid transient growth when additional surface points are being added to the computation. Although small, these errors are

propagated, (diffused), horizontally into the billet by the horizontal second stage of the LOD method. This is demonstrated in Fig. 7.9, where an artificial $O(\Delta z)$ boundary error has been introduced. Use of an iterative technique, to satisfy (7.107), exactly exagerates the effect since it allows spurious boundary corrections to be diffused even deeper into the billet. On a fixed domain, with smooth boundary conditions, this effect is unlikely to be so severe. The moving boundary causes additional changes in the values assigned to meshpoints at the end of chains within the billet and allows for additional rounding errors.

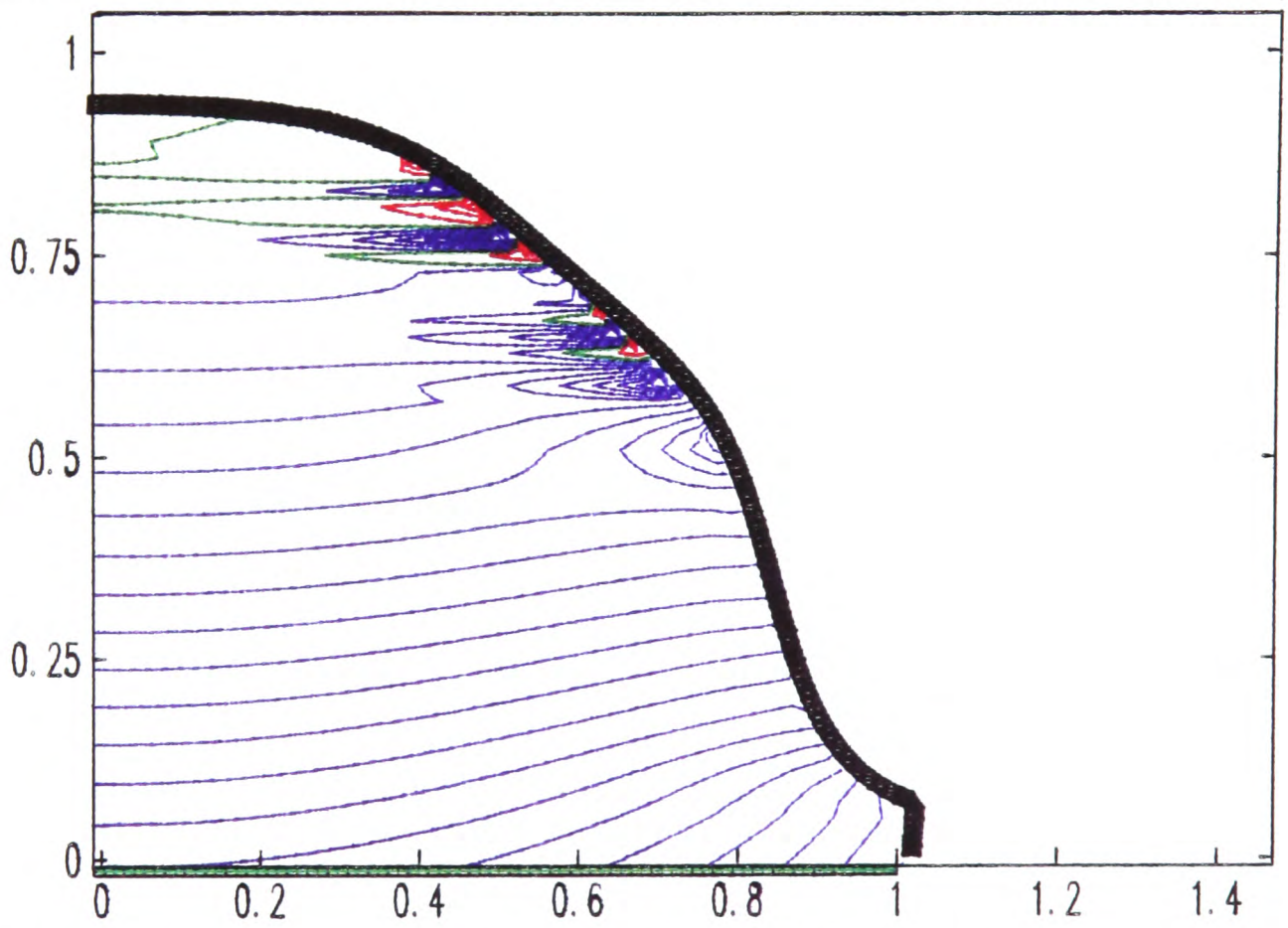

Figure 7.9: An example of boundary error propogation in the LOD method; red blue and green curves show computed isotherms within a billet cross-section, (black).

The above example explains the reason for stage 4 of the numerical scheme. Stage 4 provides a consistent approximation to (7.7) that is normally missing from the LOD method. The consistent approximation provided by stage 4 dissipates boundary errors two dimensionally that could otherwise be propagated horizontally into the billet. In effect the LOD method is used in stages 1, 2 and 3 to provide predicted values, $H_{i,j}^{n+1**}$, which are then corrected at internal meshpoints by stage 4. Thus, the scheme as a whole may be viewed as a predictor-corrector method.

The scheme benefits from the reduced computation time of the LOD method over a comparable ADI method in providing predicted values for stage 4. One might question whether, by using an ADI method, stage 4 could be dispensed with. This is possible, but should not lead to any time saving. Iteration of stage 4 helps to smooth the computed temperature fields. The largest updates in the iteration of stage 4 are usually found near the billet surface, and are caused by the lower order of approximation of the boundary condition (7.8) there, and by associated rounding errors. These features would not be diminished by using an ADI method. Additionally, use of an ADI method would discard another advantage of the LOD method for this particular application; that of its conceptual simplicity. In applying the LOD method, at each timestep it is only necessary to store the end positions of each vertical and horizontal chain. Then in advancing the approximation over one timestep boundary conditions need only be applied at the ends of these chains,

(i.e. since the heat flow is one dimensional). However, the ADI method may also require the evaluation of boundary conditions at intermediate points in chains close to the boundary, see Fig. 7.10. This not only leads to more computation, but also requires the derivation of a more complex method for storing and coding boundary data.

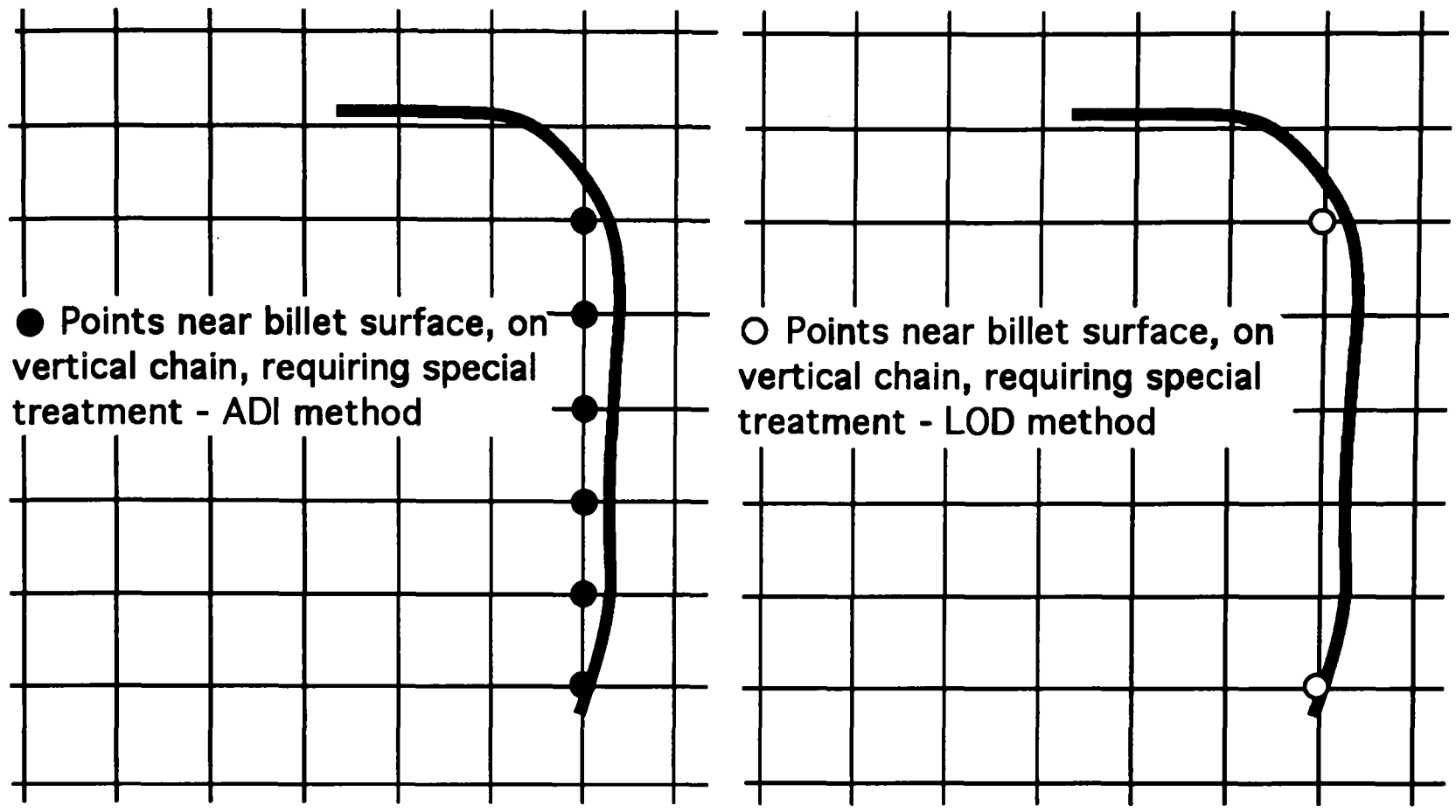

Figure 7.10: Increased boundary condition computation requirements of an ADI method in comparison to an LOD method.

7.2.4 Accuracy and stability

The consistency of the algorithm at internal meshpoints is self evident, and will give a local truncation error of order

$$O(\Delta z^2) + O(\Delta \eta_n),$$

at these meshpoints. On short horizontal or vertical chains the local truncation error increases to

$$O(\Delta z) + O(\Delta \eta_n).$$

The interpolation of the chain end meshpoints using the closest boundary values and two meshpoints within the chain gives an error of size

$$O(\Delta z^3)$$

in approximating the endpoint value. This value is then used in the difference schemes in stages 1, 2, 3 and 4; thus giving rise to a local truncation error of order

$$O(\Delta z) + O(\Delta \eta_n),$$

at these meshpoints. At newly added meshpoints a value is assigned. The approximation is again

$$O(\Delta z^3),$$

giving rise to a local truncation error of order

$$O(\Delta z) + O(\Delta \eta_{n+1}),$$

on the following timestep. With $ds_{max} = \Delta z$ the surface position is computed to order

$$O(\Delta z^2),$$

and a similar order error is involved in approximating the normal derivative in boundary condition (7.8). Other boundary conditions are approximated by central differences using the fictitious meshpoints at $z = z_c - 1/2\Delta z$ and $r = -1/2\Delta z$; both having error

$$O(\Delta z^2).$$

Thus, the algorithm is believed to provide a consistent approximation to (7.7) at all meshpoints.

Under the timestep restrictions discussed in section 7.1.6 the algorithm is numerically stable. It has been pointed out that these restrictions are not severe, and may be lessened by solution of the tri-diagonal matrix systems in an appropriate direction. At most they imply

$$\Delta \eta_n \sim \Delta z.$$

Compared with an explicit method, where the timestep restriction would be

$$\Delta \eta_n \sim \Delta z^2,$$

the implicit algorithm outlined requires approximately $2+k$ times as many floating point multiplications per meshpoint on each timestep, where k is the number of iterations of stage 4. Thus, for $\Delta z < \frac{1}{2+k}$ the implicit algorithm will be more efficient. Use of the LOD method in stages 1, 2 and 3 to provide the initial guess for stage 4 means that only two to three iterations of stage 4 are usually required. Thus, for example with the results computed in the remainder of this chapter, where $\Delta z = .02$, the method represents approximately a ten-fold saving in CPU!

No attempt will be made to demonstrate convergence of the numerical method. Typically, convergence proofs for nonlinear parabolic equations make use of some *a priori* estimates of the analytic solution. Here no proof has been attempted of the existence and uniqueness of the analytic solution, so none will be made for the numerical method. An educated guess would be that, if the method converges, its rate of convergence will be $O(\Delta z) + O(\Delta \eta_n)$.

Without making the numerical method a good deal more complicated it is doubtful whether the spatial accuracy of the method can be improved. Higher order interpolations at the billet surface could be used to improve the spatial accuracy there, but this accuracy will remain diminished on the shorter chains. To improve the temporal accuracy, one could use an intermediate timestep. Disadvantages with doing so might include the need to compute the billet surface position at the intermediate timestep and the greater storage requirements.

7.3 Algorithm capabilities

Using the algorithm described in section 7.1 the transient slow-time heat flow was computed within the billet illustrated in Fig. 7.11a. This figure has been produced using the transient growth model of chapter four, and has resulted from the model metal mass flow rates and withdrawal rates that are illustrated in Fig. 7.11b. The surface profiles are plotted at intervals $\Delta\eta \approx .1$, and show a wide variation in layering both across the billet surface and over the duration of the modelled run. To compute the heat flow within this billet the algorithm must contend with the following

- Wide variations in surface velocity, ($\Rightarrow$ heat influx).
- Sharp changes in the mass flow rate.
- Variation in all the other boundary heat flux parameters, both across the surface and during the run.
- Periods of billet growth at a wide range of different angles to the gridlines.
- A geometry that would defeat many front fixing methods.

A billet such as that in Fig. 7.11a would require much wasteful machining to achieve a satisfactory cylindrical shape for extrusion, and would almost certainly be rejected by a production quality control following microstructural analysis. A model with the capability of computing the isotherms within such billets, during formation, is thus of great value in providing insight into real causes of production failure.

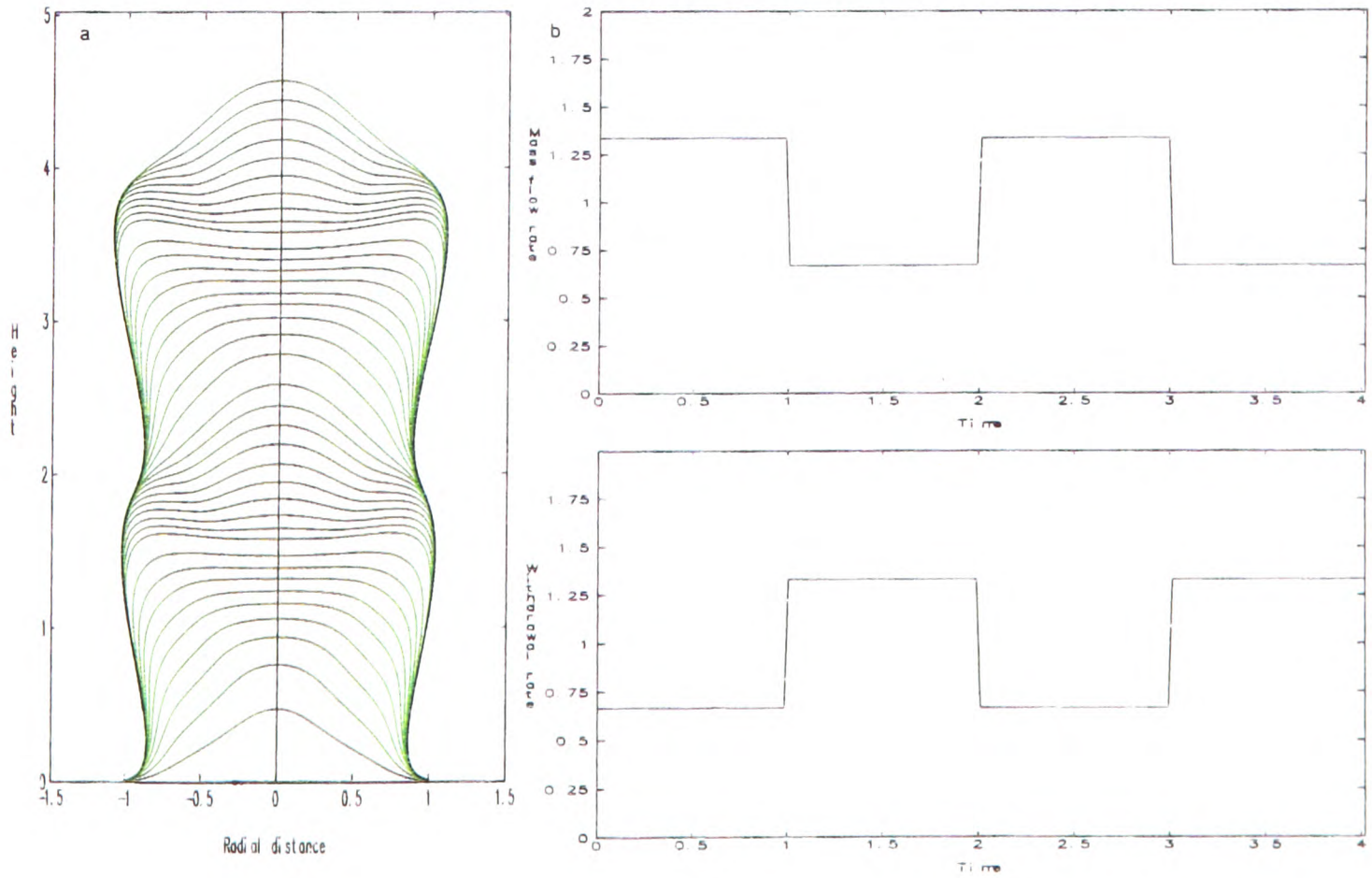

Figure 7.11: a) Billet surface contours plotted at intervals $\Delta\eta \approx 0.1$, b) Mass flow rate and withdrawal rate used in a). Model parameters: start position $z_n = 3$.

In computing the heat flow within this billet, the Peclet number has been fixed at

$$Pe = 1.887,$$

and mesh spacings

$$\Delta z = \mathrm{d}s_{max} = .02$$

are used for the heat flow and surface growth algorithms, see Fig. 7.12. The model alloy chosen is 2618. Other model parameters are $a_1 = 35°$, $a_1 = 6.5°$, $r_n = 2.27$, $r_s = 1/2$, $r_c = 1$; the scanner angle function shown in Fig. 3.23 is assumed. Unless otherwise stated, these parameters remain fixed for the remainder of the results computed and presented in this chapter.

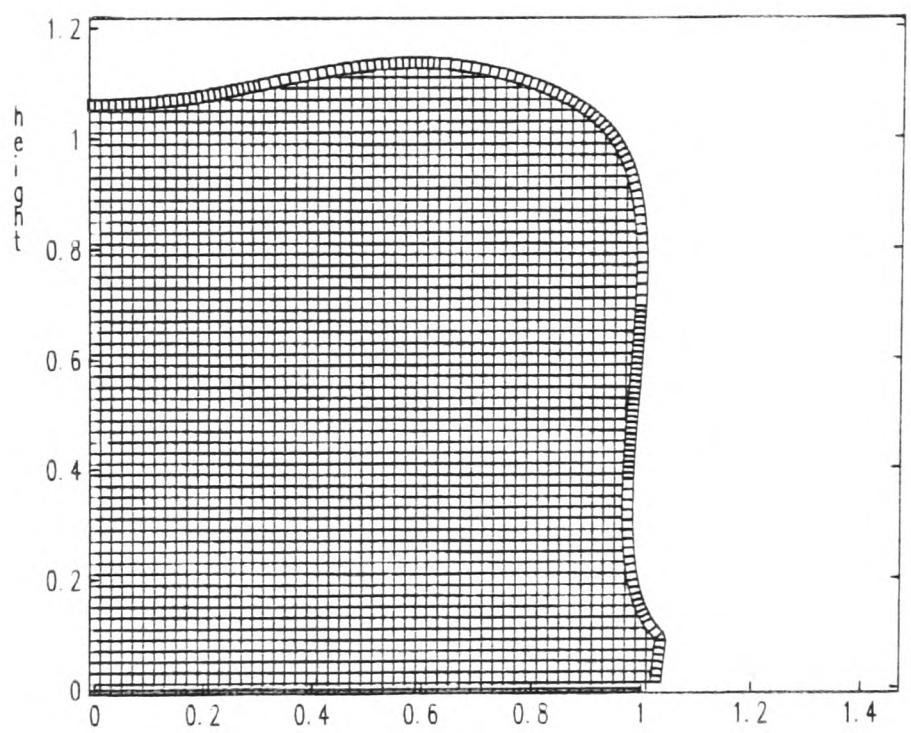

Figure 7.12: Example of mesh used for heat flow computations in this chapter.

Fig. 7.13 shows the isotherms that have been computed within a cross-section of the axisymmetric billet, at intervals $\Delta\eta = .5$, throughout the modelled run. In these figures the green isotherm plotted represents the solidus isotherm. Red curves represent successive temperature increments, each equivalent to 1% fraction liquid, above the solidus temperature. Blue curves represent increments of 10% of the freezing range of the alloy, below the solidus temperature.

Significant temperature transients can be observed in Fig. 7.13, with the billet changing from being nearly fully solid, (Figs 7.13c, f & g), to having quite significant liquid fractions, (Figs 7.13a, b, d, e & h). Corresponding variations in both vertical and radial temperature gradients throughout the billet and throughout the length of the run are also observed.

The isotherms in Fig. 7.13 are smooth throughout the run, even close to the billet surface, thus demonstrating the capabilities of the algorithm in using a fixed, square mesh to cope with a boundary that is both curved and moving. The equations are fully nonlinear in regions where the isotherms are red, (see in particular Figs 7.13a & e), and linear elsewhere. It is clear that the nonlinearity causes no difficulties for the algorithm. It is also clear from Fig. 7.13 that the algorithm is able to cope well with geometries involving multiple chains of vertical and/or horizontal meshpoints, (e.g. 7.13g), such as could cause difficulties for a front-fixing method.

This computation took approximately 15 minutes of CPU on the Oxford University VAX 6000/620, a dual processor machine giving 35 MIPS of processing power on each processor. The model parameters chosen

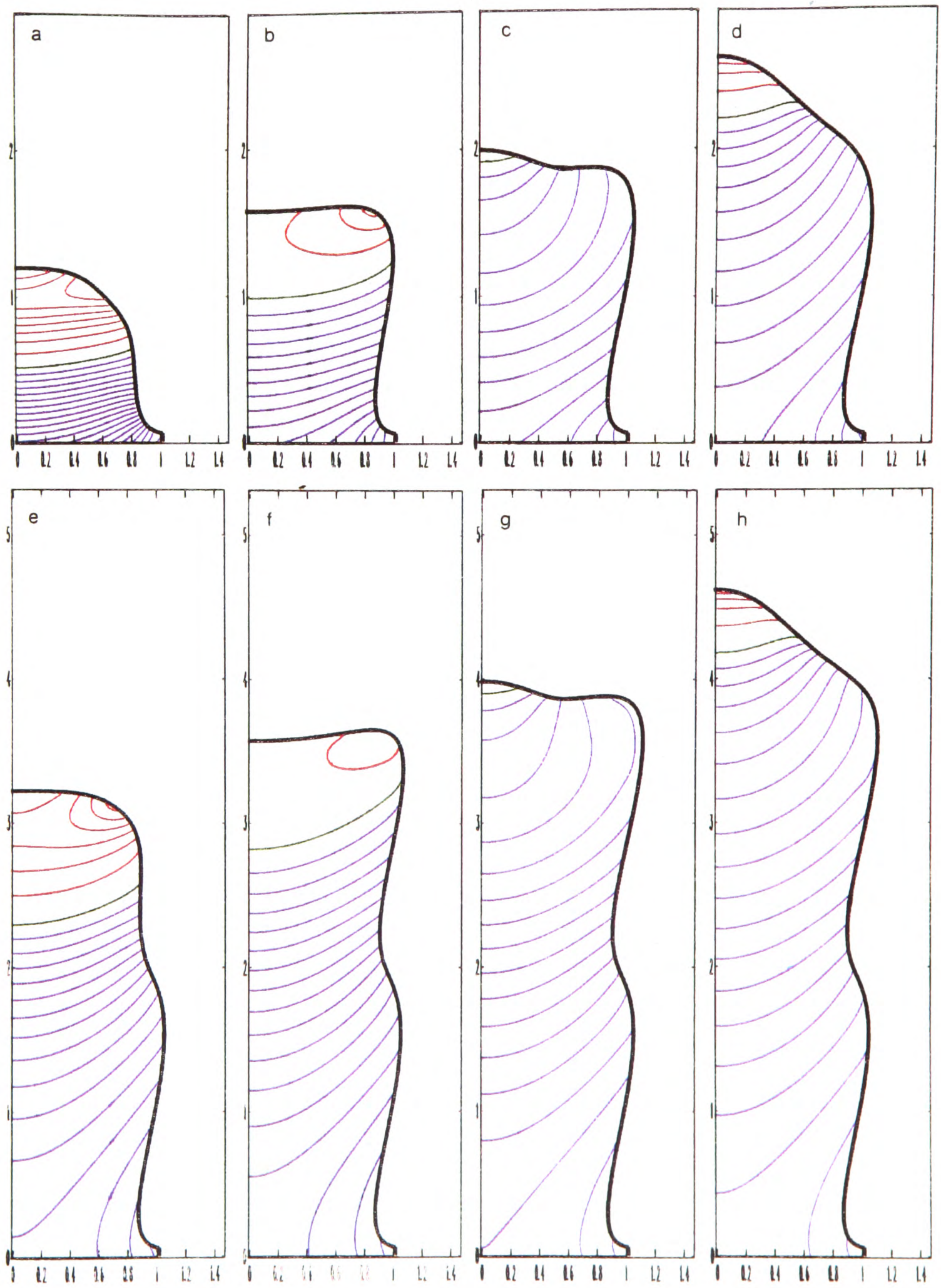

Figure 7.13: Billet cross-sectional isotherms; a) $\eta = .5$, b) $\eta = 1$, c) $\eta = 1.5$, d) $\eta = 2$, e) $\eta = 2.5$, f) $\eta = 3$, g) $\eta = 3.5$, h) $\eta = 4$. Black - billet surface, red - isotherms for increments of 1% fraction liquid above solidus, green - solidus isotherm, blue - isotherms for increments, $\Delta H = 0.1$, below solidus.

are in the range of real process parameters. Faster computation would result during a modelled run in which there were fewer transients and/or from using a larger mesh size. With the increasing availability of desktop workstations, within this processing power range, the possibilities of real-time heat flow simulation and of designing solidification control algorithms, based on this model, become realities.

The fine mesh size used throughout the chapter is chosen for consistency with the next section, where the initial stages of a modelled run are investigated, and it is desirable to minimise errors due to approximation of the initial conditions. Over a longer period of time the initial errors become less significant, and use of a coarser mesh would be quite acceptable. For a moving boundary problem with

$$\Delta\eta_n \sim \frac{1}{2}\Delta z,$$

(as is suggested by the timestep restrictions that have been imposed), there are K_n meshpoints inside the billet at time η_n, where

$$K_n \sim \frac{\eta_n}{\Delta z^2} \approx \frac{n}{2\Delta z}.$$

Thus, supposing the model is integrated over the interval $\eta \in [0, \eta_{fin}]$, there will be approximately N timesteps, where

$$N \sim \frac{2\eta_{fin}}{\Delta z}.$$

If the average CPU time per meshpoint, per timestep is denoted k_{CPU} the total CPU cost is then given approximately by

$$\text{CPU} \approx k_{CPU} \sum_{n=1}^{N} K_n \sim \frac{k_{CPU}\eta_{fin}^2}{\Delta z^3}. \tag{7.108}$$

Equation (7.108) demonstrates that significant computational savings will be made when a reduction in accuracy is accepted. For the explicit method applied to this problem the cost, (preserving stability), would be

$$\text{CPU} \sim \frac{2k_{CPU}\eta_{fin}^2}{\Delta z^4}.$$

7.4 Start up strategies

In chapter four, section 4.2, a number of generic strategies for controlling the initial phase of billet growth were examined. These strategies were described in terms of the initial vertical displacement of the collector below the atomiser nozzle, z_n, and the process withdrawal and mass flow rates, $u(\eta)$ and $\dot{m}(\eta)$. Considerable variation in the initial pattern of layering of the deposited spray was found to result from firstly, delaying withdrawal of the billet for a short period, and secondly from varying z_n. This section presents results of computations of slow-time heat flow, in the initial stages of billet growth, for three of the eight cases that were considered in section 4.2.

Results for the case $z_n = 3$, $\dot{m}(\eta) = 1$ and

$$u(\eta) = \begin{cases} 0, & 0 \le \eta \le 1, \\ 1, & 1 \le \eta \le 3, \end{cases}$$

are shown in Figs 7.14 and 7.15. The layering that occurs during the initial stages of billet growth has been shown in Fig. 4.2c. Fig. 7.14 shows isotherms in the billet cross-section at times $\eta \approx 0,\ 0.2,\ 0.4,\ 0.6,\ 0.8.$

During this time the billet initially grows up rapidly in the centre towards the upper spray boundary. On approaching the upper spray boundary, growth in the centre of the billet slows and is overtaken by growth outwards and up into the spray region. Fig. 7.15 shows isotherms in the billet cross-section at times $\eta \approx 1,\ 2,\ 3$, during which time the billet grows both upwards and outwards.

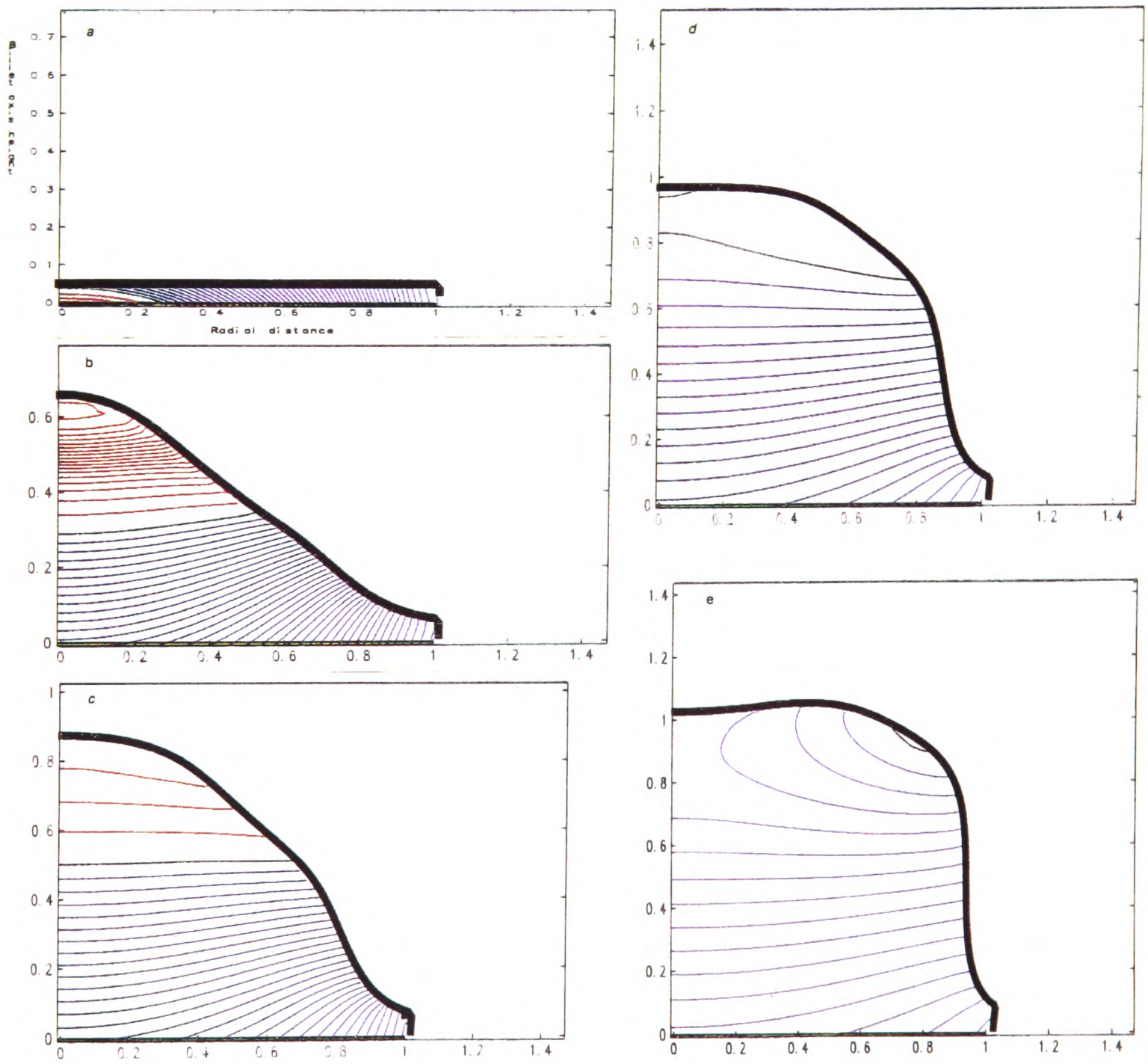

Figure 7.14: Billet cross-sectional isotherms; low start and delayed withdrawal, $z_n = 3$: a) $\eta = 0$, b) $\eta = .2$, c) $\eta = .4$, d) $\eta = .6$, e) $\eta = .8$.

Fig. 7.14a shows the initial conditions imposed along an assumed uniform initial deposit of thickness $2\Delta z$, see section 7.1.7. Fig. 7.14b shows the effect of the initial rapid central growth. Fraction liquids in excess of 18% are found near the top of the billet. The growth during this phase is too fast to allow conduction into the collector and into the rest of the billet to have any great effect. The looped 18% fraction liquid isotherm in Fig. 7.14b indicates that the billet growth on the axis of rotation is already just beginning to decelerate. The presence of such high fraction liquids close to the billet surface in the slow-time heat flow computations suggests that even higher surface fraction liquids will be present locally on a more rapid timescale. In such cases there will be the possibility of pore formation in the mushy surface layer, due to disturbance by the atomising gas.

The continued deceleration of the central portion of the billet surface can be seen in Figs 7.14c and 7.14d. The looped isotherm in Fig. 7.14b and the two solidus isotherms in Fig. 7.14d indicate regions of the billet within which solidification is no longer unidirectional. This suggests the possibility of solute being trapped under the billet surface. The shift of the solidus isotherm location between Figs 7.14d and 7.14e reflects the shift in billet growth direction. In Fig. 7.15 it can be seen that the temperature transients persist as the billet is withdrawn and changes shape further.

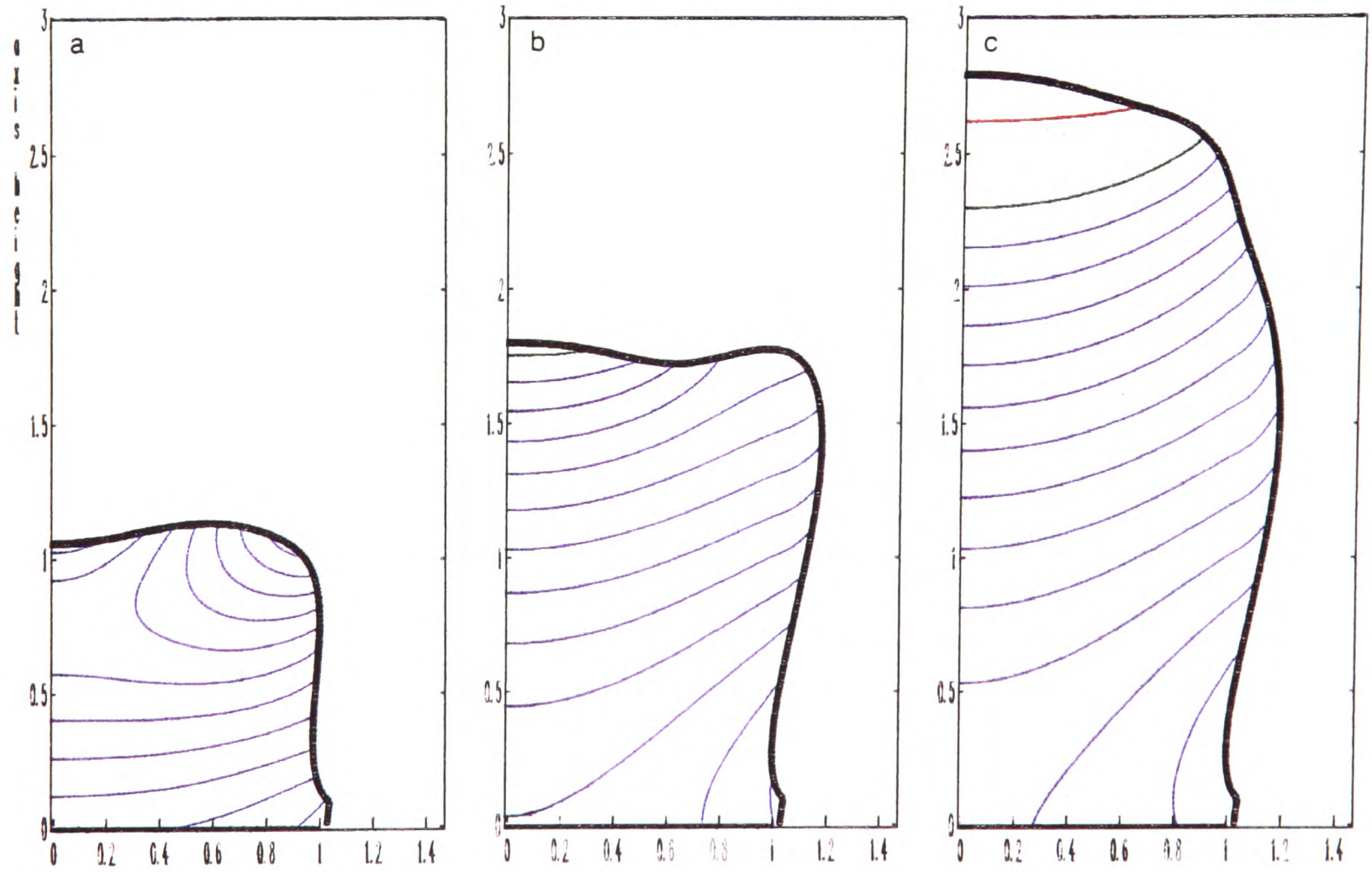

Figure 7.15: Billet cross-sectional isotherms; low start and delayed withdrawal, $z_n = 3$: a) $\eta = 1$, b) $\eta = 2$, c) $\eta = 3$.

In Figs 7.16 and 7.17 are shown results for the case $z_n = 3$, $\dot{m}(\eta) = 1$, $u(\eta) = 1$. In this case the immediate withdrawal of the collector from a relatively low initial position results in sustained rapid growth of the centre of the billet upwards, and an eventual "necking" of the billet close to the collector. Surface contours at intervals $\Delta\eta \approx 0.1$ are plotted in Fig. 4.3a. Fig. 7.16 shows isotherms in the billet cross-section at times $\eta \approx 0.2,\ 0.4,\ 0.6,\ 0.8$. The initial condition at $\eta = 0$ is the same as in Fig. 7.14a. Fig. 7.17 shows isotherms in the billet cross-section at times $\eta \approx 1,\ 2,\ 3$, during which time the billet grows both upwards and outwards.

Fig. 7.16a shows the effect of the initial rapid central growth. Fraction liquids in excess of 23% are found near the top of the billet. The growth during this phase is too fast to allow conduction into the collector and into the rest of the billet to have any great effect. The immediate withdrawal of the collector has the effect of preventing the billet growth from reaching the upper spray boundary, and keeps the billet top surface in a part of the averaged spray where there is still significant mass flux. The sides of the billet are withdrawn out of the spray more rapidly than in the delayed withdrawal case, and so receive little deposition. This results in the billet necking in, thus reducing the total heat flux down through the billet. These factors combine to

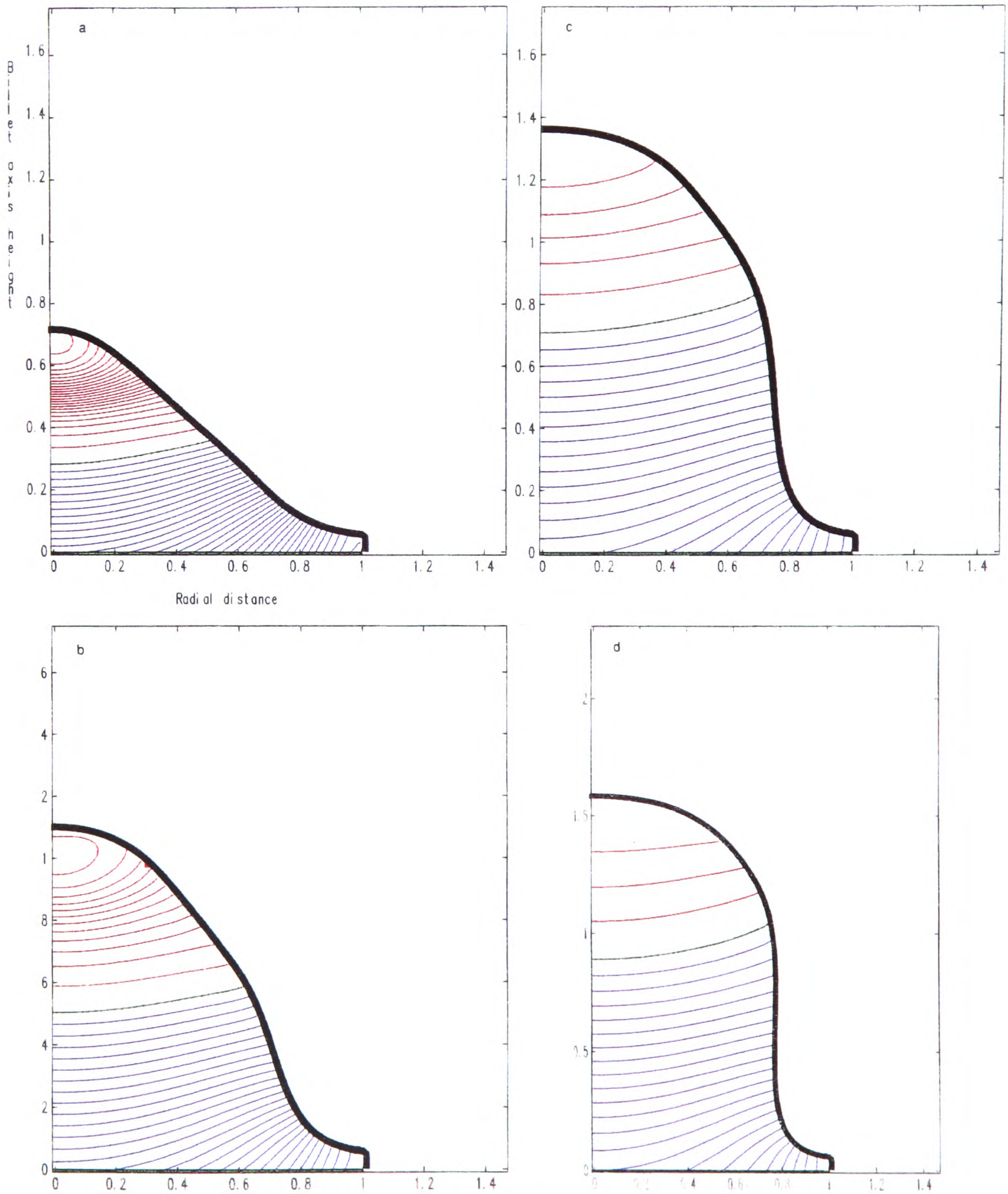

Figure 7.16: Billet cross-sectional isotherms; low start and immediate withdrawal, $z_n = 3$: a) $\eta = .2$, b) $\eta = .4$, c) $\eta = .6$, d) $\eta = .8$.

sustain the high liquid fraction near the billet top surface for a longer period than in the delayed withdrawal case.

By looking at successive billet growth increments along the billet axis of rotation in Fig. 7.16, it is clear that on the billet axis of rotation the billet surface has reached its steady state position soon after $\eta = .4$. The looped 23% fraction liquid isotherm in Fig. 7.16a and the looped 12% fraction liquid isotherm in Fig. 7.16b indicate the deceleration of the billet growth as the steady state growth rate is approached on the billet axis of rotation.

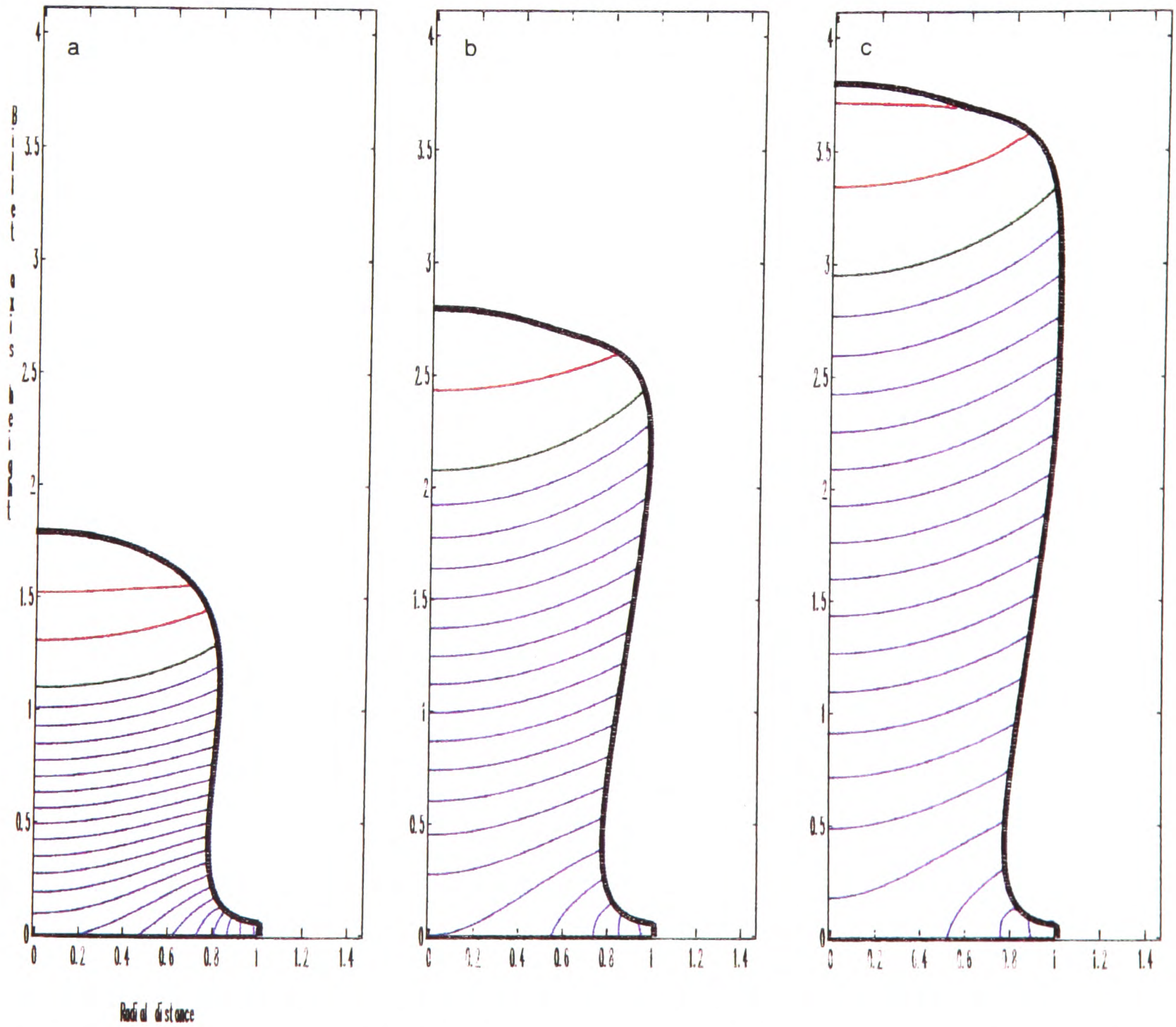

Figure 7.17: Billet cross-sectional isotherms; low start and immediate withdrawal, $z_n = 3$: a) $\eta = 1$, b) $\eta = 2$, c) $\eta = 3$.

As the billet sides continue to grow outwards and the billet becomes larger, the importance of heat conduction down through the billet diminishes. The billet continues to cool, (Figs 7.17a, b), and the significance of the necking diminishes. At $\eta = 3$, comparison of Figs 7.15c and 7.17c shows that the top surface temperatures, and the radial and longitudinal thermal gradients are very similar in the two cases.

In Figs 7.18 and 7.19 are shown results for the case $z_n = 2\frac{1}{3}$, $\dot{m}(\eta) = 1$, $u(\eta) = 1$. In this case the immediate withdrawal of the collector from an optimally chosen initial position results in fairly uniform

growth of the billet surface towards its dynamic steady state. Necking is avoided and machining wastage is minimal. Surface contours at intervals $\Delta\eta \approx 0.1$ are plotted in Fig. 4.3c, and show very even layering of deposited spray. Fig. 7.18 shows isotherms in the billet cross-section at times $\eta \approx 0,\ 0.2,\ 0.4,\ 0.6,\ 0.8$. Fig. 7.19 shows isotherms in the billet cross-section at times $\eta \approx 1,\ 2,\ 3$.

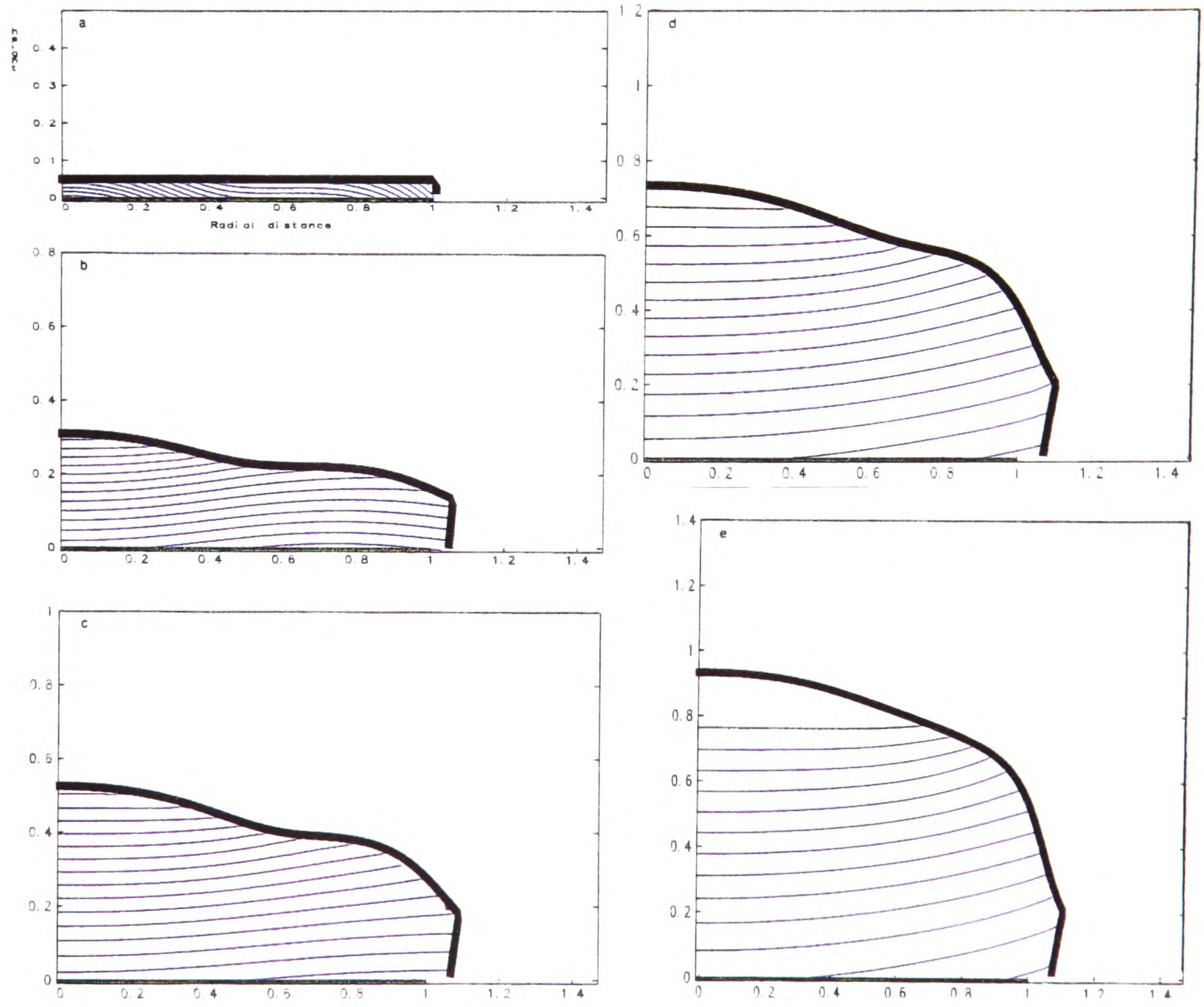

Figure 7.18: Billet cross-sectional isotherms; optimal start and immediate withdrawal, $z_n = 2\frac{1}{3}$: a) $\eta = 0$, b) $\eta = .2$, c) $\eta = .4$, d) $\eta = .6$, e) $\eta = .8$.

Fig. 7.18a shows the assumed initial conditions for the heat flow computations. These initial conditions are different to the two cases featured above. Firstly, the spray fraction liquid is greater for the higher start position, since the collector is closer to the atomiser nozzle in this case. Secondly, the surface normal velocities at the closer position are reduced, and vary less across the radius of the collector. These two counterbalancing effects combine to produce an initial temperature distribution in Fig 7.18a in which initial thermal gradients and overall temperature variations are much reduced.

Rapid convergence of the billet surface to its dynamic steady state is evident from Figs 7.18 and 7.19. The main noticeable change during the initial period of growth in Fig. 7.18 is a gradual reduction in longitudinal thermal gradients as the billet grows taller. The radial thermal gradients appear to remain unchanged, and the solidification appears to be unidirectional everywhere at all times. A second feature, (more noticeable

with Fig. 7.19), is that the top surface becomes slightly hotter as it grows away from the influence of the collector.

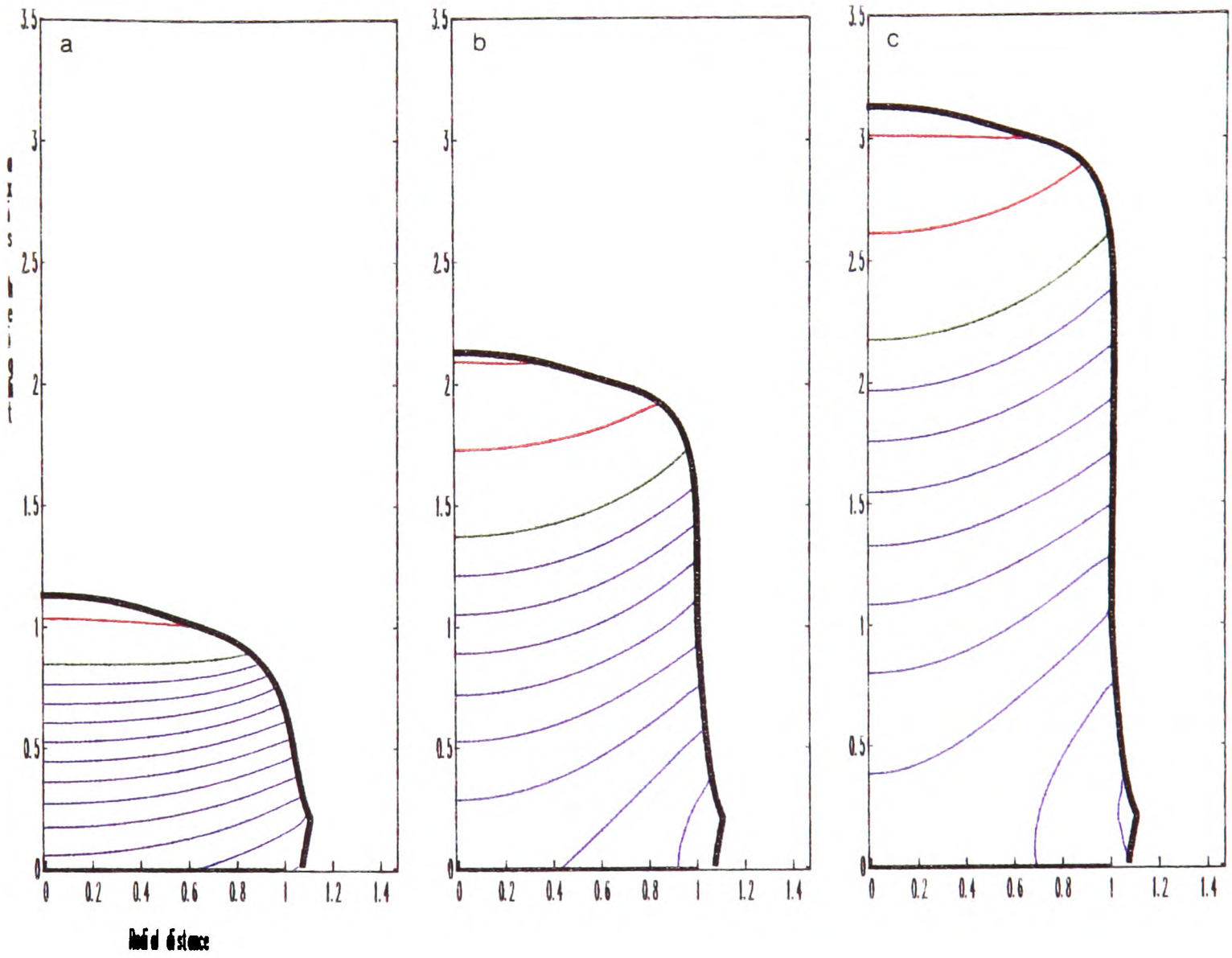

Figure 7.19: Billet cross-sectional isotherms; optimal start and immediate withdrawal, $z_n = 2\frac{1}{3}$: a) $\eta = 1$, b) $\eta = 2$, c) $\eta = 3$.

Figs 7.14, 7.15, 7.16, 7.17, 7.18 and 7.19 have demonstrated that there are considerable differences in the initial thermal behaviour of the billet, depending on the initial strategy adopted. These differences manifest in differing solidification rates at different heights and radial distance from the billet axis of rotation in each case. This is further illustrated in Figs 7.20 and 7.21, where temporal variations in heat flow along vertical sections, at the billet axis of rotation and at a half radius, (i.e. $r = 1/2$), respectively, are plotted for each of the above strategies. In these figures the black line represents the billet top surface height above the collector and the red, green and blue curves are isotherms, as described before.

The main variation is found at $r = 0$, where much higher cooling rates and vertical thermal gradients are experienced initially for the lower collector start position. Also clear in Figs 7.20a and 7.20b is that for the lower collector start position, solidification is not unidirectional initially. The difference between Figs 7.20a and 7.21a, and between Figs 7.20b and 7.21b shows that significant radial thermal gradients persist for some time in these two cases.

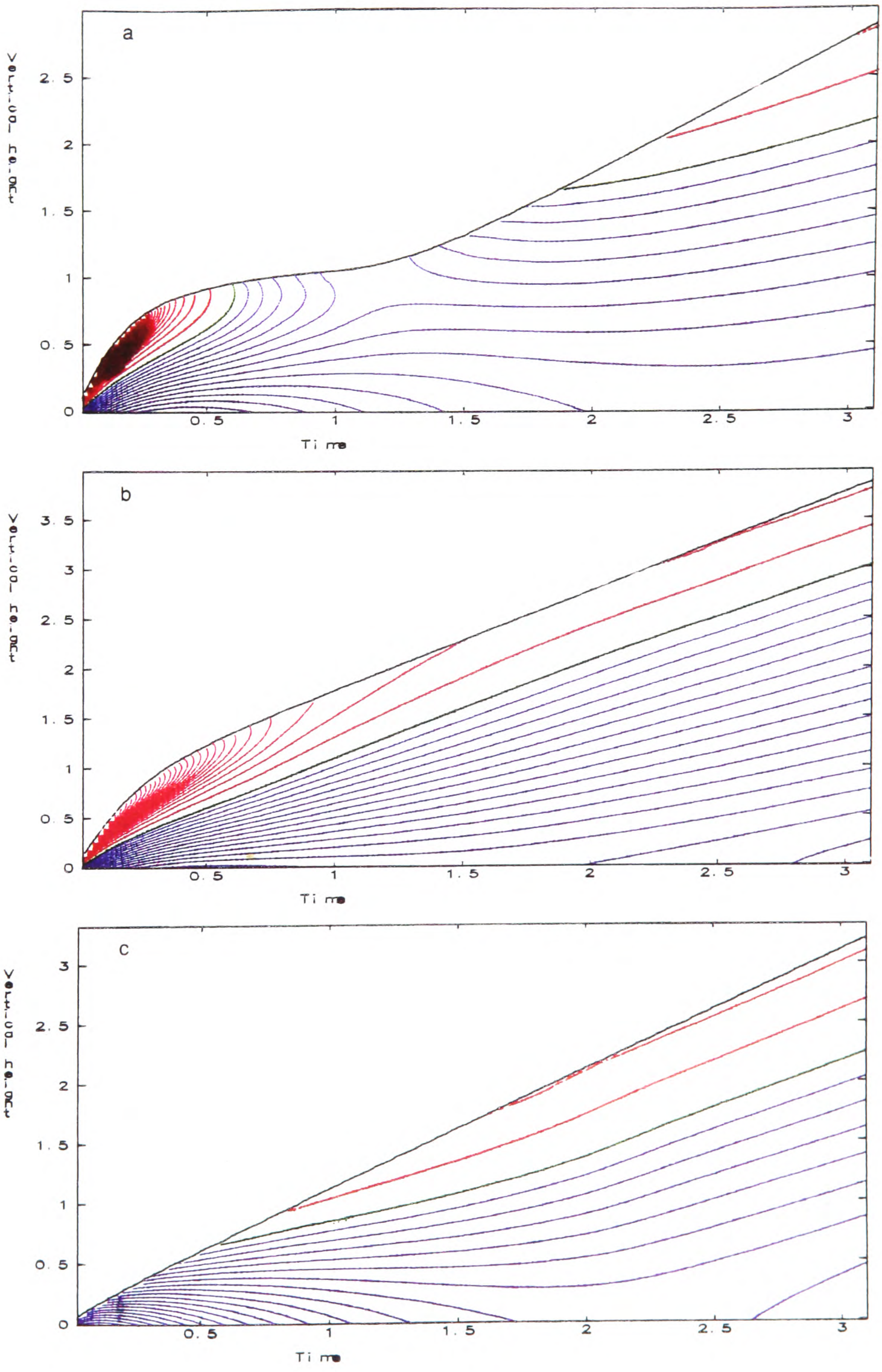

Figure 7.20: Temporal heat flux variations along vertical sections at $r = 0$; a) low start and delayed withdrawal, b) low start and immediate withdrawal, c) optimal start and immediate withdrawal.

Figure 7.21: Temporal heat flux variations along vertical sections at $r = 1/2$; a) low start and delayed withdrawal, b) low start and immediate withdrawal, c) optimal start and immediate withdrawal.

7.5 Slow-time steady state heat flow

In Figs 7.20 and 7.21 convergence of the billet crown shape to its steady state is marked by the linear increase in height of the top surface with time. For each of the above three example start up strategies, the shape of the top part of the billet crown is similar at time $\eta = 3$, (see Figs 4.2 and 4.3). Since maintaining a steady billet crown shape implies that the same deposition and cooling effects will also be maintained on the billet crown, it becomes pertinent to question whether or not there will exist a steady state temperature distribution in the billet crown, following convergence of the billet growth to a steady state crown shape.

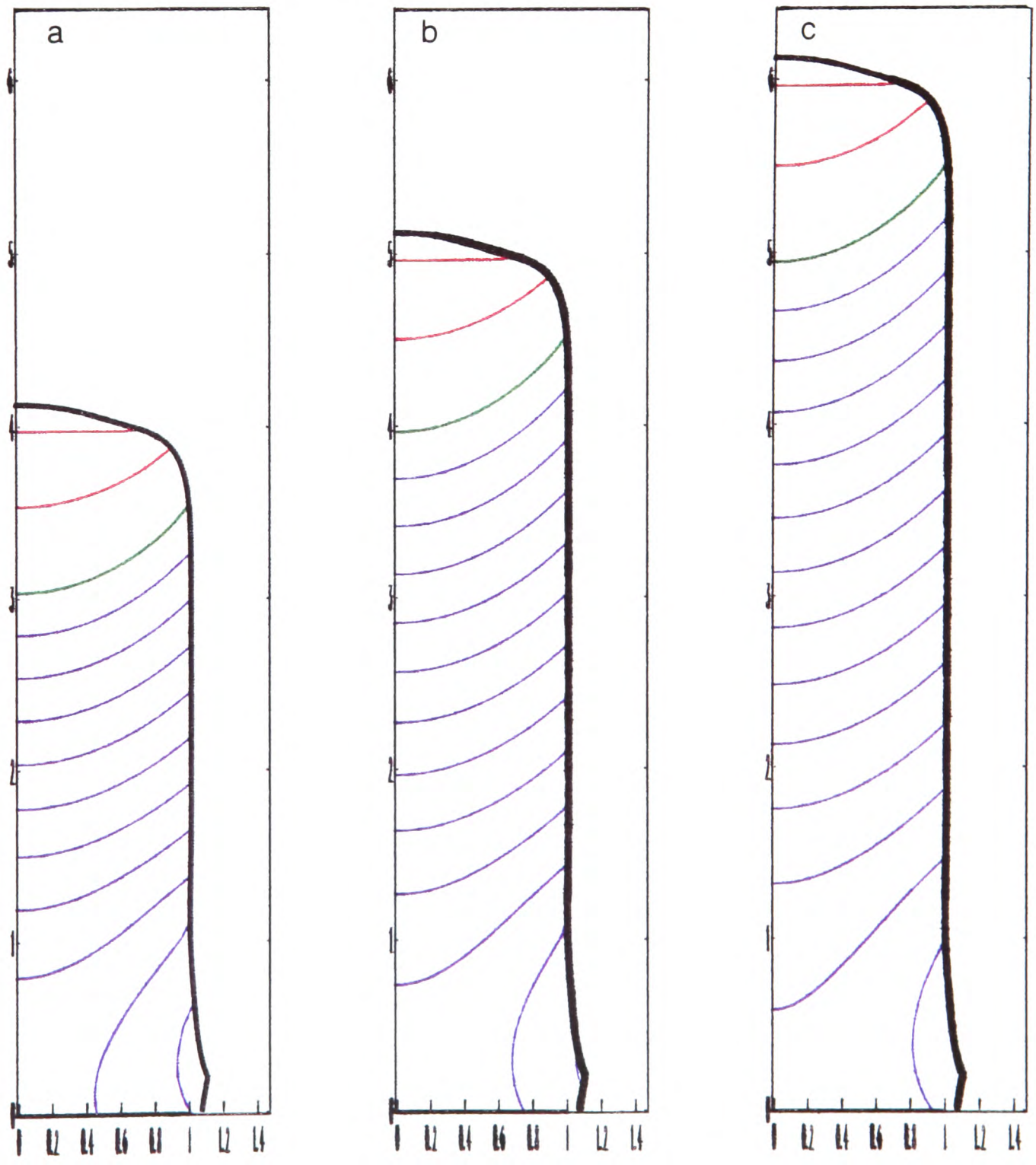

Figure 7.22: Billet cross-sectional isotherms, optimal start and immediate withdrawal; a) $\eta = 4$, b) $\eta = 5$, c) $\eta = 6$.

Figs 7.20 and 7.21 indicate that the answer to this question is probably yes. The isotherms closest to the billet top surface in Figs 7.20b, 7.20c, 7.21b and 7.21c run progressively more parallel to the billet top surface, suggesting the evolution of constant thermal gradients, measured in the crown frame of reference. Extending the computation for the optimal start position case up until time, $\eta = 6$, produces the results in

Fig. 7.22, which show isotherms and billet growth at times, $\eta = 4,\ 5,\ 6$. Comparing Fig. 7.22 with Fig. 7.19 one can see that the pattern of isotherms that has been computed near the top of the billet does indeed become steady, as the billet grows taller, and as the effect of the collector diminishes.

Thermal time histories of the billet at fixed heights above the collector, $z - z_c = 2,\ 3,\ 4,\ 5$, are shown in Fig. 7.23. Not only do these figures show more clearly the convergence to the thermal steady state, but they also illustrate well the implication that, if a steady state crown temperature distribution can be achieved, the solidification of different points along the length of the billet will be identical. It can also be seen from Fig. 7.23 that although there is a radial temperature gradient, solidification histories computed at different radial positions are very similar. Thus, attaining a steady state crown heat flux should help considerably in producing a billet of fairly uniform microstructure, and presumably material/mechanical properties.

A second example of a steady state billet crown heat flux is given in Fig. 7.24. For these computations, the billet length-scale, R, has been reduced to 3/4 of its previous value, and constant dimensional mass flow rate and withdrawal rate have been chosen so that $\hat{\dot{M}}_0 R^{-1}$ and $\hat{U}_0 R$ are kept constant. As suggested in chapter five, this retains the same Peclet number, (and hopefully similar solidification characteristics), whilst a different radius billet is grown. The similarity is not complete however, since the non-dimensional groups in the boundary conditions (7.8) and (7.9) are also changed.

The scanner angle function of Fig. 3.23 has again been used, with $a_1 = 35°$ and $a_2 = 6°$. Other parameters are as before. The steady state crown shape in Fig. 7.24 is slightly different to that produced in Fig. 7.22. A steady state billet crown heat flux is again clearly attained, (soon after the steady crown shape is reached). The billet as a whole is a little hotter than the larger radius billet, but with similar, (non-dimensional), thermal gradients throughout. The increased temperature is probably due to the decreased gas and collector Biot numbers, that result from reducing R.

Comments

Whilst following the suggestions of chapter five for changing billet radius appears in this case to give a billet of approximately the same temperature, the evidence is not conclusive. It should also be said that it is not clear that maintaining similar temperatures in billets of different radiius is an appropriate goal to aim for, (i.e. because dimensional thermal gradients and solidification rates will change also and may be more relevant).

The existence of steady state billet crown heat flows is clearly of some importance, and requires far more attention than has been been possible here. Direct computation of steady states should be possible, without the time consuming unsteady heat flow computations of this chapter. This then opens up the possibility of a systematic study of how to achieve similar solidification histories within different radii billets. Other interesting research possibilities that could then be considered are the inclusion of a temperature, (and geometry), dependant sticking efficiency in the model and finally, solution of the inverse heat conduction problem, i.e. "Given a desired material solidification history, what are the billet geometry and boundary conditions required to achieve it?".

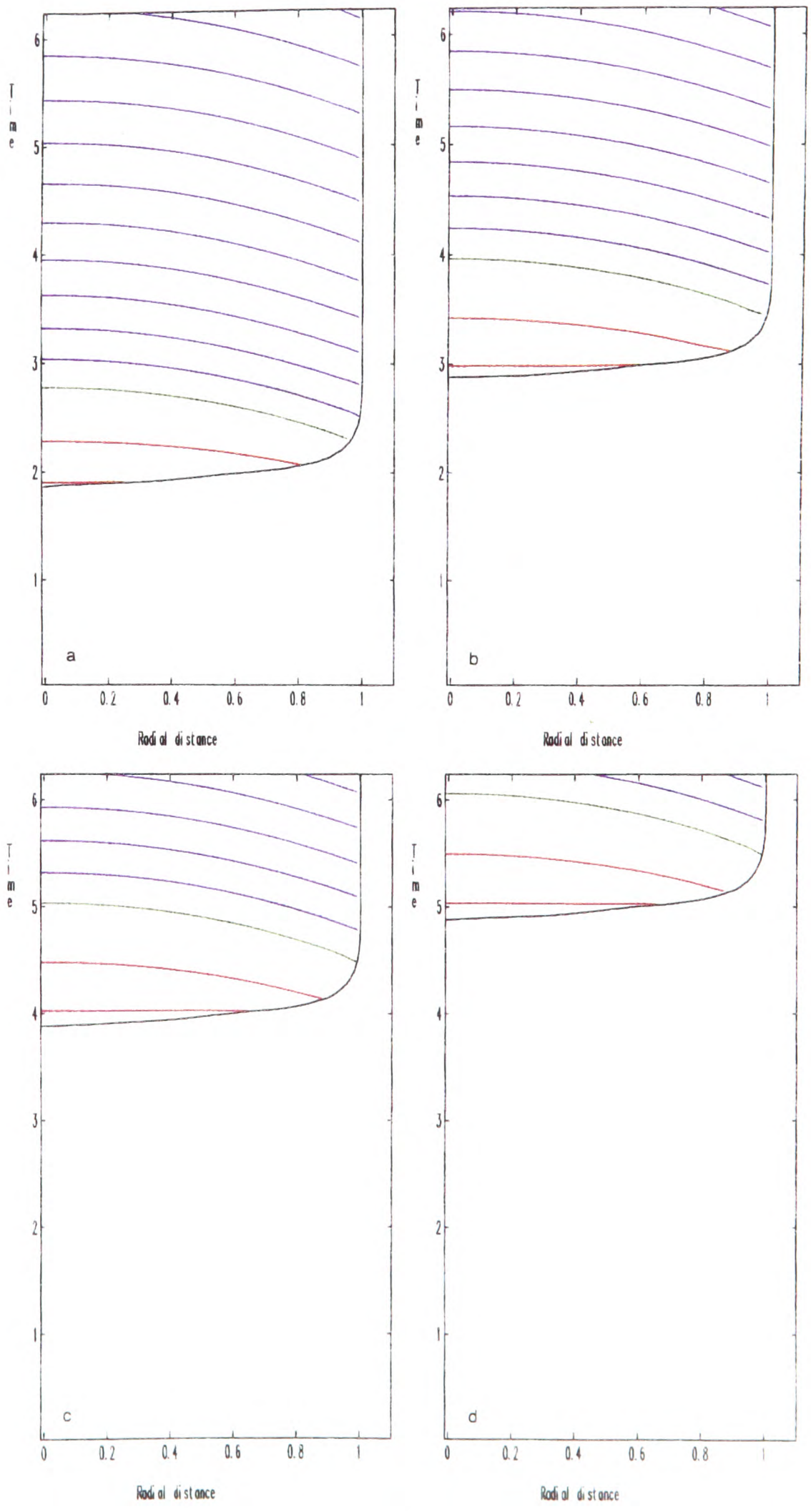

Figure 7.23: Temporal heat flux variations along radial sections; a) $z = z_c + 2$, b) $z = z_c + 3$, c) $z = z_c + 4$, d) $z = z_c + 5$.

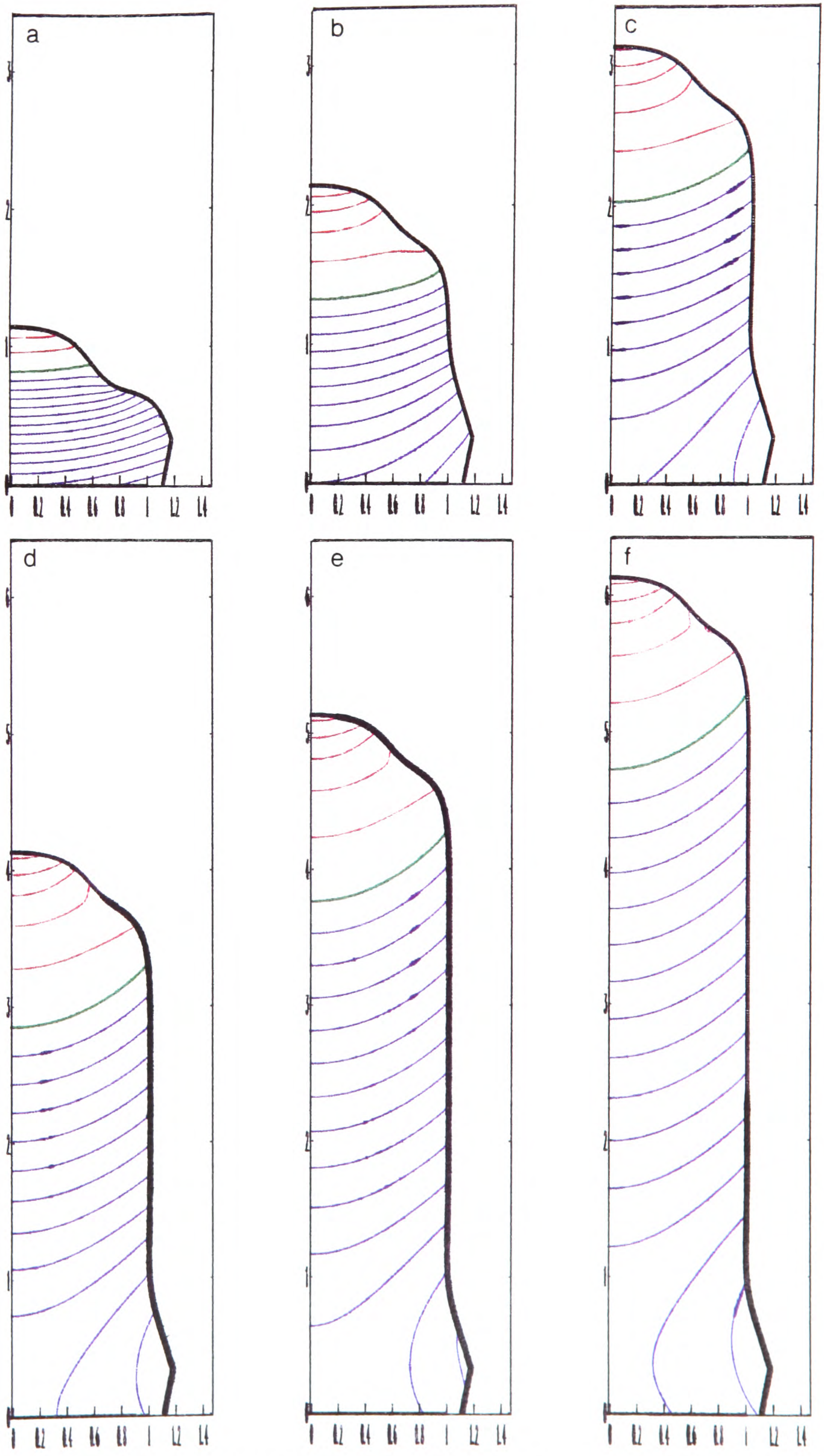

Figure 7.24: Billet cross-sectional isotherms; a) $\eta = 1$, b) $\eta = 2$, c) $\eta = 3$, d) $\eta = 4$, e) $\eta = 5$, f) $\eta = 6$.

7.6 Summary

- An implicit, two step, finite difference algorithm is devised, which approximates the slow-time heat flow equations, (7.7), (7.8), (7.9) and (7.10), consistently. The local truncation error is

$$O(\Delta z^2) + O(\Delta \eta_n)$$

at internal meshpoints and

$$O(\Delta z) + O(\Delta \eta_n)$$

close to the billet surface, where Δz and $\Delta \eta_n$ are spatial and temporal mesh spacings respectively.

- A front-tracking method is used, rather than a front-fixing method, to cope with the moving boundary.

- The algorithm is stable under a timestep restriction of form

$$\Delta \eta_n = O(\Delta z).$$

This timestep restriction represents a considerable CPU saving over a simpler algorithm based on a two step explicit method.

- The algorithm is fully able to cope with a wide range of billet geometries and process conditions.

- The algorithm uses an implicit LOD method to predict the enthalpy on each new timestep, and then corrects the prediction iteratively so that a set of fully implicit, nonlinear, 6-point difference equations are satisfied everywhere within the billet.

- The algorithm is fast enough to run in real time on currently availabe workstations. This opens up the possibility of real time simulation, and developing solidification control algorithms.

- Total CPU usage is approximately proportional to $\eta_{fin}^2 \Delta z^{-3}$, where η_{fin} is the end time of the run.

- Computation of the heat flow in the initial stages of a modelled production run suggests that the collector plate should initially be positioned high and be withdrawn immediately at an appropriate rate. This has the effect of allowing more rapid and uniform growth towards a steady state. The computed heat flow, associated with this strategy, shows moderate radial and longitudinal thermal gradients and relatively uniform cooling rates throughout the billet.

- Delayed billet withdrawal and/or a low collector start position are found to result in rapid heating of the billet centre, large thermal gradients and large variation in cooling rates throughout the billet. Associated with these phenomena are the possibilities of solute trapping, (when the solidification is not unidirectional), and porosity formation due, (to disturbance of the mushy billet surface by the atomising gases).

- Steady state billet crown heat flows are believed to exist, driven by steady state crown geometries. These allow extremely similar thermal histories to be experienced by all points within the billet.

Chapter 8

Conclusions

This thesis has developed mathematical models describing the growth and solidification of cylindrical spray-formed, aluminium alloy billets. This chapter summarises the main results of the thesis, in section one. Section two discusses further research on spray-forming.

8.1 Main results

The mathematical models that have been fomulated in this thesis describe three dimensional billet growth and billet solidification. Under the physical model assumptions, the equations that are formulated, conserve both mass and heat at the billet surface. The physical assumptions/simplifications that underly these model equations are similar to those that have been made previously in the literature for one dimensional spray-forming geometries.

8.1.1 Billet growth

The main billet growth model equations are derived in chapter two, section 2.1, and are presented in non-dimensional form in section 2.1.4, (equations (2.42) and (2.43)). Equations (2.42) and (2.43) describe conservation of mass in the spray and at the billet surface, respectively. Equation (2.43) is a first order quasi-linear partial differential equation. The nonlinearity arises from the possibility of one part of the surface "shadowing" another part of the surface from the spray.

The three process motions, withdrawal, rotation and atomiser scan, are represented directly in (2.43). Equation (2.43) is parameterised by a single dimensionless parameter, ϵ, representing the ratio of the rotation and withdrawal timescales; typically $\epsilon \ll 1$.

The size of ϵ prompts the use of an averaging method. The averaged equations that are derived describe changes in billet surface profile with respect to the "slow" time variable, $\eta = \epsilon t$. For a suitably defined class of billet surfaces, $\mathcal{S}_1$, (see section 2.2.2), one can effectively linearise equation (2.43). The averaging method then produces an $o(\epsilon)$ asymptotic approximation to the three dimensional surface movement, valid on the timescale ϵ^{-1}. The order of approximation may reasonably be assumed to be $O(\epsilon)$.

Provided that synchronisation of the scanner and rotation movements does not occur, the averaged equa-

tions are axisymmetric about the billet axis of rotation. If the surface remains within $\mathcal{S}_1$, the approximation remains valid throughout the length of the modelled process run. This application of the averaging method is interesting because one is able to make a direct physical interpretation of those situations in which the method fails, (see the discussion at the end of section 2.2.2).

The averaged equation for axisymmetric billet growth, (2.71), offers considerable advantages over (2.43), both in terms of computational efficiency of its solution and in the potential for analytic results. Analysis of (2.71) shows the following, (see section 2.3 and chapters three and four).

- For a given atomiser scanner motion, equation (2.71) is parameterised solely by the non-dimensional ratio, μ, of withdrawal rate to mass flow rate.
- For a constant ratio, μ, if the averaged mass flux along the billet axis is unimodal, then equation (2.71) has a unique steady state. If this steady state solution is in $\mathcal{S}_1$, then it corresponds to a steady state billet crown shape.
- Numerical results show that, for a unimodal axis mass flux, the steady state solutions of (2.71) form a series of nested surfaces. The radius of the steady state billets can be determined simply, via a mass balance, for a wide range of μ.
- Steady states are shown to be stable in a weak geometric sense, (via a phase plane analysis). A theorem giving sufficient conditions for a much stronger form of stability is also proven. Numerical results show that these sufficient conditions are met for most steady states, along an interval of the steady state profile that starts at the billet axis. Along this interval, finite perturbations from the steady state will decay.
- Numerical results, demonstrating variation in steady state shape and stability with different scanning motions have been presented in chapter three, and are summarised in section 3.7.
- A bimodal averaged mass flux along the billet axis admits the possibility of there existing two steady states at the same value of μ. The resulting possible growth dynamics are discussed, and co-existence of steady states is demonstrated numerically. Co-existing steady states allow hysteresis, as is demonstrated numerically in chapter four, section 4.5. A simple optimisation technique is devised which enables scanner motions to be designed that do not allow multiple steady states to co-exist, under the model assumptions, (section 3.6).
- Direct numerical solution of (2.71) allows the investigation of transient billet growth, in chapter four. This is used to investigate suitable control strategies to be adopted, during the initial part of a production run, in order to minimise machining wastage. Results that show the successful use of the model to simulate a real production run have been presented, (section 4.3 and Fig. 4.5). Generic transient motions between steady states are also studied.

8.1.2 Billet solidification

The main billet heat flow model equations are derived in chapter five, section 5.1, and are presented in non-dimensional form in section 2.1.2, (equations (5.15), (5.16) and (5.17)). Equations (5.15), (5.16) and

(5.17) describe conservation of heat within the billet and at the billet surface. Equation (5.15) is a second order quasi-linear parabolic partial differential equation. The nonlinearity arises from the release of latent heat during solidification, and from the different physical properties of the solid and liquid phases of the alloys that are typically sprayed.

Heat flow within the billet is reliant on the billet surface being specified through the billet growth model. The equations (5.15), (5.16) and (5.17) contain a number of non-dimensional groups. On the rotation/scanner timescale, changes in enthalpy are $O(\epsilon)$ in the bulk of the billet, and larger near the billet surface where deposition is taking place. On the slow timescale of the averaged growth, (described above), the field equation (5.15) is parameterised by a Peclet number, Pe, which represents the ratio of the conduction and billet growth timescales. Typically, $Pe = O_S(1)$, which indicates that both convective and conductive mechanisms are responsible for heat flow within the billet.

Boundary heat fluxes are described by (5.16) and (5.17). These equations are parameterised by the gas and collector Biot numbers, by the gas and collector temperatures, by the enthalpy of the spray and by the surface normal velocity, (as well as by ϵ and Pe).

A boundary layer approximation is derived, (see section 5.3), governing heat flow close to the billet surface, where deposition is taking place. The boundary layer equations are one dimensional; a boundary layer coordinate is fixed to the billet surface, with length measured in the direction of the inward surface normal vector. These equations are solved numerically in chapter six, using a predictor-corrector, finite difference method.

- The irregular and intermittent pulsed deposition on the billet surface, (due to the interaction of the scanner and rotational motions), produces correspondingly irregular fluctuations in billet surface temperature.
- Surface cooling rates following pulsed deposition are $\sim 10^3$C/s, with remelting and refreezing processes occurring across $\sim 10^2$ layers of flattened deposited droplets. Typically, the boundary layer length-scale is $\sim 3 - 4$mm.
- The enthalpy in the boundary layer fluctuates about a far field value, which may be determined directly by the solution of a single nonlinear equation, (see section 5.2.2).
- Radial variations in boundary layer heat flow are observed. These variations, and other observed variations with surface gradient, rotation and scanner frequencies are summarised in section 6.6.

A "slow-time" heat flow model is also derived, (see section 5.3), governing the heat flow in the bulk of the billet. This varies with the slow-time variable, η, and is driven by the averaged billet growth equation for axisymmetric growth, (2.71). Numerical solution of the equations for slow-time heat flow, (7.7), (7.8), (7.9) and (7.10), is technically complicated, due to the following.

1. The field equation, (7.7), is nonlinear.
2. The billet surface is moving and the billet geometry is irregular.

3. The boundary condition, (7.8), is nonlinear, of the third kind, and must be satisfied on the moving surface.

This is accomplished in chapter seven.

- An implicit, two step, finite difference algorithm is devised, which consistently approximates the slow-time heat flow equations, (7.7), (7.8), (7.9) and (7.10). The local truncation error is $O(\Delta z^2)+O(\Delta\eta_n)$ at internal meshpoints and $O(\Delta z)+O(\Delta\eta_n)$ closer to the billet surface, where Δz and $\Delta\eta_n$ are spatial and temporal mesh spacings respectively.

- The algorithm is stable under a timestep restriction of form $\Delta\eta_n = O(\Delta z)$. Total CPU usage is approximately proportional to $\eta_{fin}^2\Delta z^{-3}$, where η_{fin} is the end (slow) time of the run. This represents a considerable CPU saving over a simpler algorithm, based on a two step explicit method. The algorithm is fast enough to run in real time on currently availabe workstations.

- The algorithm is fully able to cope with a wide range of billet geometries and process conditions.

- Computation of the heat flow in the initial stages of a modelled production run suggests that the collector plate should initially be positioned high and be withdrawn immediately at an appropriate rate. This has the effect of allowing more rapid and uniform growth towards a steady state. The computed heat flow, associated with this strategy, shows moderate radial and longitudinal thermal gradients and relatively uniform cooling rates throughout the billet.

- Delayed billet withdrawal and/or a low collector start position are found to result in rapid heating of the billet centre, large thermal gradients and large variation in cooling rates throughout the billet.

- Thermal steady states are believed to exist, driven by steady state crown geometries. These allow extremely similar thermal histories to be experienced by all points within the billet.

8.1.3 Validation

The models derived in the thesis all rely on a number of approximations. These approximations may be arranged heirarchically.

1. Real world observations of the spray-forming process are given a physical interpretation.

2. This physical understanding is translated into mathematical equations.

3. The mathematical equations are approximated asymptotically, either to make analysis possible, or to make numerical solution feasible.

4. The asymptotically derived equations are solved numerically.

For complex physical processes there is therefore a great deal of scope for the errors in each stage of the model's development to increase. Validation of the model comes from its ability to make predictions which correspond quantitatively and/or qualitatively with observation.

Billet growth

In chapter two various arguments were forwarded for the validity of the various physical assumptions made in deriving the model equations. Relaxation of some of these assumptions is discussed in the next section, on further research. A large part of chapter two was devoted towards the validity of the averaging method in providing an asymptotic approximation to the full model equations. The numerical methods used in chapters three and four, to integrate the steady state and transient growth equations, are well established.

Stable steady state dynamics, such as those described in chapters two and three, are believed to underly real billet growth.

- Billets of near constant radius that are produced often have a crown shape that is observed to remain fairly stationary in the crown frame of reference.
- The existence of a nested series of steady states, that become increasingly convex and small, with increasing μ, is also confirmed by experience from the production rig. This trend has also been observed, (but not explained), in early technical advice, [103].
- Billet crown shapes, for billets of near constant radius, are slightly convex and do correspond approximately to those steady state crown shapes predicted by the model using the production scanning angle function of Fig. 3.23, with appropriate fixed scanning angle and scanning range.
- Extremely effective methods for on-line control of billet shape have been developed and implemented, [99]. The methods developed in [99] rely solely on controlling the withdrawal rate, (thus changing μ), in response to changes in billet shape. The importance of height measurements over radial measurements, (confirmed by the phase plane plots), is also fundamental to the method in [99].

The ability of the model to simulate transient billet growth in a real production run, (section 4.3 and Fig. 4.5), supports its validity. Many of the other effects modelled in chapter four are also observed on real production billets.

- Necking of the billet near its base when the collector is positioned too low and when it is withdrawn too quickly at the start of a run.
- Bulging out of the billet near its base when withdrawal is delayed for too long.
- Initial rapid growth of the billet centre upwards, to form a "hat" shape.

Hysteresis can also occur in production, (see [99]), the effects being qualitatively similar to those shown in section 4.5.

Billet solidification

Two billet heat flow models have been developed. In chapter six, section 6.5, computed results from the boundary layer model have been discussed in the context of recent experimental results by Mingard, [94, 95]. There appears to be quite good qualitative agreement between observed microstructural variations, (due to changes in the process parameters), and corresponding variations in the boundary layer heat flow, (combined

with an understanding of how this affects microstructure). Validity of the boundary layer approximation necessarily relies upon restriction to a thin layer close to the billet surface, and to a short enough integration time interval, (see chapter five, section 5.2.1).

Validity of the slow-time heat flow equations, as an approximation to the full three dimensional problem, has not been proven but is discussed in chapter five, section 5.3. The numerical solution method in chapter seven is consistent and stable.

In the initial stages of production runs, when there is rapid vertical growth of the centre of the billet into a hat shape, the billet is observed to glow hotly. Large thermal gradients predicted by the model in the lower part of the billet during the low and delayed start conditions, (section 7.4), can be reflected in the finished product by the following.

- Shrinkage porosity very close to the collector, (reminiscent of splat cooling).
- "Hot tears" running either vertically or radially, [103], thought to result from contraction stresses in the hotter central areas of the billet base.
- Gas porosity, blown into the more liquid central part of the billet base.

The suggestions of a thermal steady state existing, (section 7.5), are supported by pyrometer measurements of the billet top surface temperature, which attain a (noisy) steady value, following convergence of the billet growth. Lastly, the vertical temperature gradients predicted by the model along the side of the billet, (Fig. 7.22), are similar to those measured along the sides of production billets, on entering the spray chamber some few minutes after the end of a production run, (after degasing), [2].

8.2 Further research

Given the process complexity, there is wide scope for further research in this area. As in chapter one, upstream parts of the process are also considered.

8.2.1 Upstream in the process

There is enormous potential for quantitative research into the atomisation stage of the process. However, it is likely that such research will be largely empirical in nature and that its direct applicability will be confined to the particular atomiser geometry.

A more mathematical treatment of spray transport and solidification should be possible with the focus on establishing qualitative, (as well as quantitative), understanding of the sensitivity of critical downstream process parameters, (such as the spray enthalpy), on other upstream process parameters.

Spray impact and consolidation is an area where there is a growing body of knowledge, from other fields, which has yet to be applied to spray-forming. Consideration of the homogenisation problems at the billet surface, (i.e. validating the continuum approximations), would be very challenging, particularly as individual droplet behaviour will depend on droplet size as well as other local physical conditions.

8.2.2 Billet growth

Chapters three and four have not exhausted the possibilities of parametric study with the current model. Examples include the following.

- With increased fixed scanning angle, (e.g. $80-90°$), and by raising the collector considerably, the same model can be used for spraying tubes, (i.e. on the sides of the collector), without further modification. There are no shadowing effects in tube spraying; thus, the dynamics of steady state tube geometries should be a simple extension.[1]
- Effects of collector size and radial distance from the atomiser have not been investigated. Different collector shapes could also be incorporated.
- The results presented in section 3.6, on scanner angle design, demonstrate the feasibility of this method. There is much room for further experimentation.

Further research on billet growth can be separated into consideration of what happens either when some of the model assumptions are relaxed, or when the model is extended to some new situation.

Relaxing model assumptions

The three biggest assumptions that have been made in the billet growth model formulation have been

1. Consideration only of type A shadowing.
2. Specification of the mass flux vectorfield as being confined within a cylinder and having a distribution function, $g(r')$, which does not change with any other process parameters.

[1] This is very similar to the icing of an overhead cable, described in [134].

3. Specification of a constant sticking efficiency, influenced only by shadowing.

Allowing type B shadowing would not be particularly mathematically difficult to incorporate in the model. It would however, make the averaging method very difficult to apply, and result in considerable computational expense.

Allowing a mass flux characterisation in which the spray cone is not cylindrical and in which the spray distribution depends in a simple parametric way on the mass flow rate, (as well as perhaps on atomising gas flow rates?), would be mathematically interesting. If the spray distribution remains unimodal within a spray cone that is diverging slightly, steady states should exist, as before. However, steady states will now be parameterised by both the mass flow rate and the withdrawal rate, rather than just by their ratio, μ. This introduces the possibility of non-uniqueness of steady states at any value of μ, even when the axis mass flux distribution remains unimodal.

The specification of a constant sticking efficiency has allowed the uncoupling of growth and heat flow models. Inclusion of a thermal component of the sticking efficiency, (dependant on the spray and surface liquid fractions), causes greater computation since both problems must be computed together. However, in the case of a thermal steady state existing in the billet crown, it may be possible to compute the thermal steady state directly. This then allows a sensible investigation of the coupling of billet growth and solidification models. This could again prove interesting mathematically since it again allows the possibility of non-uniqueness.

Model extensions

In attempting to grow progressively larger billets, one eventually comes up against a limiting mass flow rate at which the atomiser is capable of producing "stable" atomisation, (i.e. predictable). At this point, to grow larger radius billets, (e.g. to fit larger extrusion presses or to machine larger products from), one has to consider the feasibility of additional atomisers within the spray chamber. Extensions of the present model could easily be made to incorporate this feature.

8.2.3 Billet solidification

Points of common interest for the further development of the heat flow models include the following.

- Consideration of the question of well posedness for each model.
- Consideration of matching the slow-time and the boundary layer approximations.

Clearly, any of the modifications and extensions of the billet growth analysis, suggested in the above sections, will also have effects on billet solidification.[2]

Upstream

Both heat flow models rely on the specification of various non-dimensional parameters, determining their boundary conditions, e.g. Biot numbers, atomising gas temperature, spray enthalpy, collector temperature.

[2] Whilst the growth model could be adapted to tube spraying without modification, the heat flow models require some further work.

Each of these parameters is determined upstream in the process, and has been rather loosely approximated. Further work might focus on attempting to model these parameters and their local variations.

Downstream

A final objective of modelling billet solidification, in both heat flow models, has been to gain insight into microstructure formation. An obvious extension of the models is to include simple "downstream" predictive models for various microstructural features, (e.g. boundary layer model - grain sizes, gas porosity, microsegregation; slow-time model - macrosegregation, grain coarsening).

Boundary layer model

Variations in boundary layer heat flow with boundary layer Biot number, with gas temperature and with spray enthalpy have not been considered. In parallel with developing (upstream) models for approximating these parameters better, model sensitivity should be explored. Additionally, one could consider the following.

- Proving convergence of the numerical algorithm.
- Numerical investigation of variation in boundary layer heat flow at surface points close to each other. The boundary layer approximation has assumed tangential thermal gradients to be $O(1)$, in it derivation. The validity of this assumption could be tested.
- Azimuthal variations in boundary layer heat flow over short time intervals.
- Consideration of the effects of varying the surface velocity pulse "shape", (i.e. through $g(r')$).

Slow-time heat flow

- Consideration of the validity of the slow-time equations as an approximation to the heat flow within the bulk of the billet.
- Convergence of the numerical algorithm used. Possible improvements in accuracy.
- Parametric investigation of the effects of varying Peclet and Biot numbers, spray enthalpy and gas temperature.
- Improved modelling of the collector and investigation of effects such as; using collectors made of different materials, allowing heat loss from the collector.
- Direct formulation and economical solution of equations for thermal steady state billet crowns.
- Consideration of an inverse heat conduction problem. Given a solidus isotherm, positioned within the billet crown, determine a (steady state) billet crown geometry and surface temperature distribution to achieve it.

8.3 Concluding remarks

Mathematical modelling of spray-forming is a difficult problem. The different sub-processes involved are interrelated in an ill-defined and nonlinear fashion. Much of the physics of the various problems is not completely understood. This work serves as an example of the usefulness of combining physical, mathematical, asymptotic and numerical approximations to generate fundamental quantitaive and qualitative understanding of a complex industrial process.

Appendix A

A.1 Coordinate Transformations

A.1.1 Cartesian Global ↔ Cartesian Spray

$$\begin{aligned} \hat{\boldsymbol{x}} &= \hat{\boldsymbol{x}}' \boldsymbol{B}'(\hat{t})^T, \\ \hat{\boldsymbol{x}}' &= \hat{\boldsymbol{x}} \boldsymbol{B}'(\hat{t}), \end{aligned}$$

with

$$\boldsymbol{B}'(\hat{t}) = \begin{pmatrix} -\cos a(\hat{t}) & , & 0 & , & -\sin a(\hat{t}) \\ 0 & , & 1 & , & 0 \\ \sin a(\hat{t}) & , & 0 & , & -\cos a(\hat{t}) \end{pmatrix} \tag{A.1}$$

A.1.2 Cartesian Global ↔ Cartesian Crown

$$\begin{aligned} \hat{\boldsymbol{x}} &= (\hat{\boldsymbol{x}}_1 - \hat{\boldsymbol{x}}_{n,1}) \boldsymbol{B}_1(\hat{t})^T, \\ \hat{\boldsymbol{x}}_1 &= \hat{\boldsymbol{x}}_{n,1} + \hat{\boldsymbol{x}} \boldsymbol{B}_1(\hat{t}), \end{aligned}$$

with

$$\boldsymbol{B}_1(\hat{t}) = \begin{pmatrix} \cos \phi_n(\hat{t}) & , & -\sin \phi_n(\hat{t}) & , & 0 \\ \sin \phi_n(\hat{t}) & , & \cos \phi_n(\hat{t}) & , & 0 \\ 0 & , & 0 & , & 1 \end{pmatrix} \tag{A.2}$$

A.1.3 Cartesian Global ↔ Cartesian Billet

$$\begin{aligned} \hat{\boldsymbol{x}} &= (\hat{\boldsymbol{x}}_0 - \hat{\boldsymbol{x}}_{n,0}) \boldsymbol{B}_1(\hat{t})^T, \\ \hat{\boldsymbol{x}}_0 &= \hat{\boldsymbol{x}}_{n,0} + \hat{\boldsymbol{x}} \boldsymbol{B}_1(\hat{t}). \end{aligned}$$

A.1.4 Cartesian Spray ↔ Cartesian Crown

$$\begin{aligned} \hat{\boldsymbol{x}}' &= (\hat{\boldsymbol{x}}_1 - \hat{\boldsymbol{x}}_{n,1}) \boldsymbol{B}_0(\hat{t})^T, \\ \hat{\boldsymbol{x}}_1 &= \hat{\boldsymbol{x}}_{n,1} + \hat{\boldsymbol{x}}' \boldsymbol{B}_0(\hat{t}), \end{aligned}$$

with

$$\boldsymbol{B}_0(\hat{t}) = \boldsymbol{B}'(\hat{t})^T \boldsymbol{B}_1(\hat{t}) = \begin{pmatrix} -\cos\phi_n(\hat{t})\cos a(\hat{t}) & , & \sin\phi_n(\hat{t})\cos a(\hat{t}) & , & \sin a(\hat{t}) \\ \sin\phi_n(\hat{t}) & , & \cos\phi_n(\hat{t}) & , & 0 \\ -\cos\phi_n(\hat{t})\sin a(\hat{t}) & , & \sin\phi_n(\hat{t})\sin a(\hat{t}) & , & -\cos a(\hat{t}) \end{pmatrix} \tag{A.3}$$

A.1.5 Cartesian Spray ↔ Cartesian Billet

$$\begin{aligned} \hat{\boldsymbol{x}}' &= (\hat{\boldsymbol{x}}_0 - \hat{\boldsymbol{x}}_{n,0})\boldsymbol{B}_0(\hat{t})^T, \\ \hat{\boldsymbol{x}}_0 &= \hat{\boldsymbol{x}}_{n,0} + \hat{\boldsymbol{x}}'\boldsymbol{B}_0(\hat{t}). \end{aligned}$$

Bibliography

[1] P.W. Alexander. Modelling the Cospray deposition process; preliminary report. Cospray, internal report, February 1991.

[2] P.W. Alexander, I.A. Frigaard, J. Heath, and K.P. Mingard. Experimental studies carried out on the Cospray spray-forming production rig in 1991 and 1992 at Alcan International Laboratories, Banbury, U.K.

[3] P.W. Alexander and O.L.R. Jacobs. Geometric models of cylindrical ingots grown by spray deposition. Unpublished paper, August 1990.

[4] V. Anand, A.J. Kaufman, and N.J. Grant. Rapid solidification of a modified 7075 aluminium alloy by ultrasonic gas atomisation. In R. Mehrabian, B.H. Kear, and M. Cohen, editors, *Rapid solidification processing, principles and technologies, II*, pages 273–286. Baton Rouge, 1980.

[5] T. Ando, E.J. Lavernia, and N.J. Grant. A TEM study of the microstructures of a modified 7075 and X2020 aluminium alloys produced by Liquid Dynamic Compaction. *Materials Letters*, 5:17–28, 1986.

[6] S. Annavarapu. *Spray casting of steel strip: Modelling and experimental studies.* PhD thesis, Drexel University, 1989.

[7] S. Annavarapu, D. Apelian, and A. Lawley. Spray casting of steel strip: Process analysis. *Metallurgical Transactions A*, 21A:3237–3255, 1990.

[8] S. Annavarapu, R.D. Doherty, D. Apelian, A. Lawley, and P. Mathur. Fundamental aspects of consolidation and microstructure development during spray casting. In *Proceedings of the International Conference on Spray Forming, Swansea*, 1990.

[9] D. Apelian, G. Gillen, and A. Leatham. Near net shape manufacturing via the Osprey process. In *Processing of structural metals by rapid solidification*, pages 107–125. American society for the Metals Industries, 1987.

[10] P.C. Baker, G. Poots, and G.G. Rodgers. Ice accretion on cables of various cross-sections. *I.M.A. Journal of Applied Mathematics*, 36:11–28, 1986.

[11] G.K. Batchelor. *An introduction to fluid mechanics.* Cambridge University Press, 1967.

[12] A.E. Benfield. The temperature in an accumulating snoowfield. *Monthly Notices of the Royal Astronomical Society, Geophysical Supplement*, 6:139–147, 1951.

[13] B.P. Bewlay and B. Cantor. Modelling of spray deposition: measurements of particle size, gas velocity, particle velocity, and spray temperature in gas atomised sprays. *Metallurgical Transactions B*, 21B:899–912, 1990.

[14] D. Bradley. On the atomization of liquids by high velocity gases. *Journal of Physics D*, D6:1724–1736, 1973.

[15] J.B. Brennan. Formation of metal strip under controlled pressures. U.S. Patent number 2639490, May 1953.

[16] J.B. Brennan. Apparatus and method for producing metal strip. U.S. Patent number 2864137, December 1958.

[17] R.H. Bricknell. The structure and properties of a nickel-base superalloy produced by Osprey atomisation-deposition. *Metallurgical Transactions A*, 17A:583–591, 1986.

[18] R.G. Brooks. Method and apparatus for manufacturing precision articles from molten articles. U.S. Patent number 3826301, July 1974.

[19] R.G. Brooks. Method and apparatus for making shaped articles from sprayed molten metal or metal alloy. U.S. Patent number Re 31767, December 1984.

[20] S.R. Cant, H. Iacovides, B.E. Launder, M.A. Leschziner, and A.P. Watkins. Notes in support of the UMIST short course on turbulence modelling for CFD applications, 1992. Course held September, 1992.

[21] H.S. Carslaw and J.C. Jaeger. *Conduction of Heat in Solids.* Clarendon, 1959.

[22] R.A. Castleman. The mechanism of the atomization of liquids. *Bureau of Standards Journal of Research*, 6:369–376, 1931.

[23] S. Chandrasekhar. *Hydrodynamic and hydromagnetic stability*, chapter XII. Clarendon, London, 1961.

[24] A.U. Chatwani and F.V. Bracco. Computation of dense spray jets. In *International Conference on Liquid Atomisation and Spray Systems*, 1985.

[25] C.J. Clark and N. Dombrowski. Aerodynamic instability and disintegration of inviscid liquid sheets. *Proceedings of the Royal Society of London*, A.329:467–478, 1972.

[26] S.R. Coriell and R.F. Sekerka. Interface stability during rapid solidification. In R. Mehrabian, B.H. Kear, and M. Cohen, editors, *Rapid solidification processing, principles and technologies, II*, pages 35–49. Baton Rouge, 1980.

[27] A.D. Craik. Wind-generated waves iin thin liquid films. *Journal of Fluid Mechanics*, 26:369–392, 1966.

[28] N. Dombrowski and W.R. Jones. The aerodynamic instability and disintegration of viscous liquid sheets. *Chemical Engineering Science*, 18:203–214, 1963.

[29] J. Douglas. On the numerical integration of $u_{xx} + u_{yy} = u_t$ by implicit methods. *Journal of the Society for Industrial and Applied Mathematics*, 3:42–65, 1955.

[30] R.W. Evans, A.G. Leatham, and R.G. Brooks. The Osprey preform process. *Powder Metallurgy*, 28:13–20, 1985.

[31] H.C. Fielder, T.F. Sawyer, R.W. Kopp, and A.G. Leatham. The spray forming of superalloys. *Journal of Metals*, 39:28–33, 1987.

[32] A.M. Fink. *Almost periodic differential equations*, volume 377 of *Lecture notes in Applied Mathematics.* Springer-Verlag, 1974.

[33] M.C. Flemings. Behaviour of metal alloys in the semi-solid state. *Metallurgical Transactions*, 22B:269–293, 1991.

[34] Fluent. Flow Simulation Limited, Sheffield, S1 4ES, U.K.

[35] R.P. Fraser, P. Eisenklam, N. Dombrowski, and D. Hasson. Drop formation from rapidly moving liquid sheets. *A.I.Ch.E. Journal*, 88:672–680, 1962.

[36] F.N. Fritsch and J. Butland. A method for constructing local monotone piecewise cubic interpolants. *S.I.A.M. Journal of Scientific and Statistical Computation*, 5:300–304, 1984.

[37] E.N. Ganic and K. Mastanaiah. Investigation of droplet deposition from a turbulent gas stream. *International Journal of Multiphase Flow*, 7:401–422, 1981.

[38] G. Gillen, P. Mathur, D. Apelian, and A. Lawley. Spray deposition: the interaction of material and process parameters. *Progress in Powder Metallurgy*, 42:753–773, 1986.

[39] T. Gillespie and E. Rideal. On the adhesion of drops and particles on impact at solid surfaces. *Journal of Colloid Science*, 10:281–298, 1955.

[40] A.R. Gourlay. Splitting methods for time dependant partial differential equations. In D.A.H. Jacobs, editor, *The state of the art in numerical analysis.* Academic press, London, 1967.

[41] A.R. Gourlay and A.R. Mitchell. The equivalence of certain alternating direction and locally one-dimensional difference methods. *S.I.A.M. Journal of Numerical Analysis*, 6:37–46, 1969.

[42] N.J. Grant. A review of various atomisation processes. In R. Mehrabian, B.H. Kear, and M. Cohen, editors, *Rapid solidification processing, principles and technologies*, pages 230–245. Baton Rouge, 1977.

[43] P.S. Grant. *Spray forming of aluminium alloys.* PhD thesis, Oxford University, 1991.

[44] P.S. Grant and B. Cantor. Experimental work conducted under contract for Alcan International Ltd, Banbury, U.K; private communication of 29th May, 1990.

[45] P.S. Grant and B. Cantor. Modelling of spray forming. *Cast Metals*, 4:140–151, 1991.

[46] P.S. Grant, B. Cantor, S. Rogers, and L. Katgerman. A computer model for droplet and particle trajectories and thermal profiles in spray forming. *Cast Metals*, 3:227–232, 1991.

[47] P.S. Grant, W.T. Kim, and B. Cantor. Spray forming of aluminium-copper alloys. *Materials Science and Engineering*, A134:1111–1114, 1991.

[48] M. Gupta, F. Mohamed, and E.J. Lavernia. Spray atomisation and deposition of an Al-Cu-Li-Zr alloy. In *Aluminium–Lithium V*, 1992.

[49] E.M. Gutierrez, E.J. Lavernia, G.M. Trapaga, and J. Szekely. A mathematical model of the Liquid Dynamic Compaction process. part 2: Formation of the deposit. *International Journal of Rapid Solidification*, 4:125–150, 1988.

[50] E.M. Gutierrez, E.J. Lavernia, G.M. Trapaga, J. Szekely, and N.J. Grant. A mathematical model of the spray deposition process. *Metallurgical Transactions A*, 20A:71–85, 1989.

[51] A. Haenlein. Disintegration of a liquid jet. Technical report 659, National advisory committee for aeronautics, 1932.

[52] W.W. Hagerty and J.F. Shea. A study of the stability of plane fluid sheets. *Journal of Applied Mechanics*, 22:509–514, 1955.

[53] T.J. Hanratty. Interfacial instabilities caused by air flow over a thin liquid layer. In *Waves on fluid interfaces*, pages 221–259. Academic Press, 1983.

[54] P.N. Hansen, G. Hartmann, and L. Kallien. Numerical simulation of rapid solidification processes: powder and spray-forming technologies. In *Proceedings of the International Conference on Solidification Processing, Institute of Metals, Sheffield*, 1987.

[55] J. Heath. Metal flow rate control in an aluminium spray-forming process. Master's thesis, Oxford University, 1993. To be submitted.

[56] J.M. Hill. *One-dimensional Stefan problems; an introduction.* John Wiley and Sons, New York, 1987.

[57] B.E. Hubbard. Alternating direction schemes for the heat equation in a general domain. *S.I.A.M Journal of Numerical Analysis*, 2:448–463, 1965.

[58] B.E. Hubbard. Some locally one-dimensional difference schemes for parabolic equations in an arbitrary region. *Mathematics of Computation*, 20:53–59, 1966.

[59] H. Jones. Cooling rates in freezing slabs. *Materials Science and Engineering*, 5:297–299, 1969.

[60] H. Jones. Observations on a structural transition in aluminium alloys hardened by rapid solidification. *Materials Science and Engineering*, 5:1–18, 1969.

[61] D.W. Jordan and P. Smith. *Nonlinear Ordinary Differential Equations.* Oxford University Press, 1977.

[62] W. Kahl and J. Leupp. High performance Aluminium produced by spray deposition. In *Proceedings of the International Conference on Spray Forming, Swansea*, 1990.

[63] J.B. Keller and S. Kogelman. Asymptotic solutions of initial value problems for nonlinear partial differential equations. *S.I.A.M. Journal of Applied Mathematics*, 4:748–758, 1970.

[64] J. Kevorkian. Perturbation techniques for oscillatory systems with slowly varying coefficients. *S.I.A.M. Review*, 3:391–461, 1987.

[65] K.A. Kojima, R.E. Lewis, and M.J. Kaufman. Microstructural characterisation and mechanical properties of a spray-cast Al-Li-Cu-Mg-Zr alloy. In *Aluminium–Lithium V*, 1992.

[66] M.S. Krol. On a galerkin-averaging method for weakly non-linear wave equations. *Mathematical Methods in the Applied Sciences*, 11:649–664, 1989.

[67] B. Lally, L. Biegler, and H. Henhein. Finite difference heat transfer modelling for continuous casting. *Metallurgical Transactions B*, 21B:761–770, 1990.

[68] P.J. Larcombe, G. Poots, P.L. Skelton, and M. Shillor. Mathematical models for ice accretion on conductors using free streamline theory. part 1: single conductor. *I.M.A. Journal of Applied Mathematics*, 41:217–236, 1988.

[69] R.W. Lardner. Asymptotic solutions of nonlinear wave equations using the methods of averaging and two-timing. *Quarterly Journal of Applied Mathematics*, 35:225–238, 1977.

[70] E.J. Lavernia. The evolution of microstructure during spray atomisation and deposition. *International Journal of Rapid Solidification*, 5:47–85, 1989.

[71] E.J. Lavernia, E. Gomez, and N.J. Grant. The structure and properties of Mg-Al-Zr and Mg-Zn-Zr alloys produced by Liquid Dynamic Compaction. *Materials Science and Engineering*, 95:225–236, 1987.

[72] E.J. Lavernia and N.J. Grant. Structures and properties of a modified 7075 aluminium alloy produced by liquid dynamic compaction. *International Journal of Rapid Solidification*, 2:93–106, 1986.

[73] E.J. Lavernia and N.J. Grant. Spray Deposition of Metals: A Review. *Materials Science and Engineering*, 98:381–394, 1988.

[74] E.J. Lavernia, E.M. Gutierrez, J. Szekely, and N.J. Grant. A mathematical model of the Liquid Dynamic Compaction process. part 1: Heat flow in gas atomisation. *International Journal of Rapid Solidification*, 4:89–124, 1988.

[75] A. Lawley. Rapidly solidified powder processes - atomisation models and mechanisms. In *Processing of structural metals by rapid solidification*, pages 31–40. American society for the Metals Industries, 1987.

[76] A. Lawley. *Atomization - the production of metal powders*, chapter 6. Metal powder industries federation, 1992.

[77] A. Lawley, P. Mathur, D. Apelian, and A. Meystel. Spray forming: process fundamentals and control. *Powder Metallurgy*, 33:109–111, 1990.

[78] A. Leatham and A. Ogilvy. Making thixotropic metal by spray casting. U.K. Patent number 2172900A, October 1986.

[79] A. Leatham and A. Ogilvy. Method of manufacture of a thixotropic deposit. U.S. Patent number 4804034, February 1989.

[80] A.G. Leatham, R.G. Brooks, J.S. Coombs, and A.J.W. Ogilvy. The past, present and future developments of the Osprey preform process. In *Proceedings of the International Conference on Spray Forming, Swansea*, 1990.

[81] S. Lefschetz. *Differential equations: geometric theory.* Interscience, New York, 1963.

[82] C.G. Levi and R. Mehrabian. Heat flow during rapid solidification of undercooled metal droplets. *Metallurgical Transactions A*, 13A:221–234, 1982.

[83] H. Lubanska. Correlation of spray ring data for gas atomization of liquid metals. *Journal of Metals*, 22:45–49, 1970.

[84] J. Madejski. Solidification of droplets on a cold surface. *International Journal of Heat and Mass Transfer*, 19:1009–1013, 1976.

[85] T.J. Mahoney and A.M. Sterling. The breakup of laminar newtonian liquid jets in air. In *International Conference on Liquid Atomisation and Spray Systems*, 1978.

[86] H. Martin. Heat and mass transfer between impinging gas jets and solid surfaces. In J.P. Hartnett and T.F. Irvine, editors, *Advances in Heat and Mass Transfer*, volume 13. Academic Press, 1977.

[87] P. Mathur. *Analysis of the spray deposition process.* PhD thesis, Drexel University, 1988.

[88] P. Mathur, S. Annavarapu, D. Apelian, and A. Lawley. Process control, modelling and applications of spray casting. *Journal of Metals*, 41:23–28, 1989.

[89] P. Mathur, S. Annavarapu, D. Apelian, and A. Lawley. Spray casting: an integral model for process understanding and control. *Materials Science and Engineering*, A142:261–276, 1991.

[90] P. Mathur, D. Apelian, and A. Lawley. Analysis of the spray deposition process. *Acta Metallurgica*, 37:429–443, 1989.

[91] V.G. McDonell, E.J. Lavernia, and G.S. Samuelsen. Simultaneous measurement of metal atomizer particle size and velocity using phase Doppler interferometry. In E.J. Lavernia, H. Henein, and I. Anderson, editors, *Synthesis and analysis in materials processing: advances in characterisation and diagnostics of ceramics and metal particulate processing.* The minerals, metals and materials society, 1989.

[92] P.C. Meek and J. Norbury. Two-stage, two-level finite difference schemes for non-linear parabolic equations. *I.M.A. Journal of Numerical Analysis*, 2:335–356, 1982.

[93] P.J. Meschter, J.K. Gregory, R.J. Lederich, J.E. O'Neal, E.J. Lavernia, and N.J. Grant. Microstructures and properties of rapid solidification processed aluminium-high lithium alloys. *Journal de Physique*, 48:C3–317 – C3–325, 1987.

[94] K.P. Mingard. Private communication, July 1992.

[95] K.P. Mingard. Metallurgical quality control; progress report. Cospray/T.C.S. internal report, March 1991.

[96] K.P. Mingard. Summary of metallurgical studies. Cospray/T.C.S. internal report, December 1990.

[97] A.L. Moran and W.A. Palko. Evaluation of near net shape alloy 625 tubular preforms for seawater piping. *Progress in Powder Metallurgy*, 43:711–721, 1987.

[98] A.L. Moran and D.R. White. Developing intelligent control for spray forming processes. *Journal of Metals*, 42:21–24, 1990.

[99] J. Myerscough. *On-line geometric control of a spray deposition process.* PhD thesis, Oxford University, 1993.

[100] K. Ogata, E. Lavernia, G. Rai, and N.J. Grant. Structure and properties of a rapidly solidified superalloy produced by Liquid Dynamic Compaction. *International Journal of Rapid Solidification*, 2:21–35, 1986.

[101] H.N. Oguz and A. Prosperetti. Surface tension effects in the contact of liquid surfaces. *Journal of Fluid Mechanics*, 203:149–171, 1989.

[102] P.J. O'Rourke and F.V. Bracco. Modelling of drop interactions in thick sprays and comparison with experiments. *Journal of the Institute of Mechanical Engineers*, pages 101–116, 1980.

[103] Osprey. Technical note, undated.

[104] I. Parker. Droplets of destiny. *Aerospace Composites and Materials*, 4:7–9, 1992.

[105] D.W. Peaceman and H.H. Rachford. The numerical solution of parabolic and elliptic differential equations. *Journal of the Society for Industrial and Apllied Mathematics*, 3:28–41, 1955.

[106] Phoenics. Cham Limited, London, SW19 5AU, U.K.

[107] M. Pilch and C.A. Erdman. Use of breakup time data and velocity history data to predict the maximum size of stable fragments for acceleration-induced breakup of a liquid drop. *International Journal of Multiphase Flow*, 13:741–757, 1987.

[108] G. Poots and G.G. Rodgers. The icing of a cable. *Journal of the Institute of Mathematics and its Applications*, 18:203–217, 1976.

[109] P Predecki, A.W. Mullendore, and N.J. Grant. A study of the splat cooling technique. *Transactions of the Metallurgical Society of AIME*, 233:1581–1586, 1965.

[110] M.H. Protter and H.F. Weinberger. *Maximum principles in differential equations.* Prentice-Hall, New Jersey, 1967.

[111] B.H. Rabin, G.R. Smolik, and G.E. Korth. Characterisation of entrapped gases in rapidly solidified powders. *Materials Science and Engineering*, A124:1–7, 1990.

[112] G. Rai, E. Lavernia, and N.J. Grant. Powder size and distribution in ultrasonic gas atomization. *Journal of Metals*, 37:22–26, 1985.

[113] W.T. Reid. *Ordinary differential equations.* John Wiley & Sons, New York, 1971.

[114] R.D. Reitz. Modelling atomization processes in high-pressure vaporizing sprays. *Atomization and Spray Technology*, 3:309–337, 1987.

[115] R.D. Reitz and F.V. Bracco. *Mechanisms of breakup of round liquid jets*, volume 3, chapter 10, pages 233–249. Gulf Publications, New Jersey, 1986.

[116] R.D. Reitz and R. Diwakar. Effect of drop breakup on fuel sprays. Technical Report 860469, S.A.E. Technical paper series, February 1986.

[117] N.K. Rizk, A.A. Mostafa, and H.C. Moniga. Modelling of gas turbine fuel nozzles. *Atomization and Spray Technology*, 3:241–260, 1987.

[118] S. Rogers and L. Katgerman. Heat transfer and solidification of a stream of molten metal during atomisation by an impinging gas jet. In *Proceedings of the 5th International conference on numerical methods in thermal problems, Montreal*, pages 1806–1817, 1987.

[119] R.C. Ruhl. Cooling rates in splat cooling. *Materials Science and Engineering*, 1:313–320, 1967.

[120] A.A. Samarskii. On the convergence and accuracy of homogeneous difference schemes for one-dimensional and multidimensional parabolic equations. *U.S.S.R. Journal of Computational Mathematics and Mathematical Physics*, 2(4):654–696, 1962.

[121] A.A. Samarskii. On an economical difference method for the solution of a multidimensional parabolic equation in an arbitrary region. *U.S.S.R. Journal of Computational Mathematics and Mathematical Physics*, 2(5):894–926, 1963.

[122] J.A. Sanders and F. Verhulst. *Averaging methods in nonlinear dynamical systems*, volume 59 of *Applied Mathematical Science.* Springer-Verlag, 1985.

[123] R. Siegel. Analysis of solidification interface shape during continuous casting of a slab. *International Journal of Heat and Mass Transfer*, 21:1421–1430, 1978.

[124] A.R.E. Singer. Note on the Spray Strip and Spray Tube process. Confidential, Department of Materials, University of Wales, University College Swansea, August 1968.

[125] A.R.E. Singer. The principles of spray rolling of metals. *Metals and Materials*, 4:246–257, 1970.

[126] A.R.E. Singer. Aluminium and aluminium alloy strip produced by spray deposition and rolling. In *Proceedings of the International Conference on the effective and economic use of the special characteristics of Aluminium and its alloys, Zurich*, September 1972.

[127] A.R.E. Singer. Improvements relating to the fabrication of articles. U.K. Patent number 1262471, February 1972.

[128] A.R.E. Singer. Method of forming composite metal strip. U.S. Patent number 3775156, November 1973.

[129] A.R.E. Singer. Spraying atomised particles. U.K. Patent number 1455862, November 1976.

[130] A.R.E. Singer. A future for spray forming. In *Proceedings of the International Conference on Spray Forming, Swansea*, 1990.

[131] A.R.E. Singer. Metal matrix composites made by spray forming. *Materials Science and Engineering*, A135:13–17, 1991.

[132] A.R.E. Singer and R.W. Evans. Incremental solidification and forming. *Metals Technology*, 10:61–68, 1983.

[133] A.R.E. Singer and S. Ozbek. Metal matrix composites produced by spray codeposition. *Powder Metallurgy*, 28:72–78, 1985.

[134] P.L. Skelton and G. Poots. Approximate predictions of ice accretion on an overhead transmission line which rotates with constant angular velocity. *I.M.A. Journal of Applied Mathematics*, 40:23–35, 1988.

[135] H.B. Squire. Investigation of the instability of a moving liquid film. *British Journal of Applied Physics*, 4:167–169, 1953.

[136] J. Sun and M.M. Chen. A theoretical analysis of heat transfer due to particle impact. Technical Report 86-WA/HT-89, The American Society of Mechanical Engineers, 1986.

[137] B.G Thomas, I.V. Samarasekera, and J.K. Brimacombe. Comparison of numerical modelling techniques for complex two-dimensional, transient heat-conduction problems. *Metallurgical Transactions B*, 15B:307–318, 1984.

[138] G. Trapaga and J. Szekely. Mathematical modeling of the isothermal impingement of liquid droplets in spraying processes. *Metallurgical Transactions B*, 22B:901–914, 1991.

[139] A. Unal. Effect of processing variables on particle size in gas atomization of rapidly solidified aluminium powders. *Materials Science and Technology*, 3:1029–1039, 1987.

[140] A. Unal, M.J. Naylor, and H.B. McShane. Modelling of metal powder production using a wax atomiser. *Powder Metallurgy*, 33:260–268, 1990.

[141] D.P. Wang. Finite amplitude effect on the stability of a jet of circular cross-section. *Journal of Fluid Mechanics*, 34:299–313, 1968.

[142] G.X. Wang and E.F. Matthys. Modelling of heat transfer and solidification during splat cooling: effect of splat thickness and splat/substrate thermal contact. *International Journal of Rapid Solidification*, 6:141–174, 1991.

[143] W.G. Watson. Thermal and microstructural characterization of spray cast copper alloy strip. In *Proceedings of the International Conference on Spray Forming, Swansea*, 1990.

[144] C. Weber. The disintegration of a liquid jet. *Ztschr. Angew. Math and Mech.*, 11:136–154, 1931. English translation.

[145] T.C. Willis. Spray deposition process for metal matrix composites manufacture. *Powder Metallurgy*, 31:485–488, 1988.

[146] N.N. Yanenko. On a difference method for calculation of the multidimensional equation of heat flow. *Dokl. Akad. Nauk SSSR*, 125:1207–1210, 1959.

[147] N.N. Yanenko. *The method of fractional steps.* Springer-Verlag, 1971.

[148] M.C. Yuen. Nonlinear capilliary instability of a liquid jet. *Journal of Fluid Mechanics*, 313:151–163, 1986.

[149] A.J. Yule. Notes in support of the 5th UMIST short course on atomiser and spray technology, 1989. Course held January, 1991.